NAPIER UNIVERSITY

DEPARTMENT OF CIVIL AND TRANSPORTATION ENGINEERING

"AN EXPERIMENTAL INVESTIGATION ON THE FLOW CHARACTERISTICS OF OPEN-CHANNEL SLOT FLOW"

A THESIS SUBMITTED IN FULFILMENT OF
THE REQUIREMENTS FOR THE DEGREE OF
DOCTOR OF PHILOSOPHY
IN CIVIL ENGINEERING

BY

DARREN PAUL KEOGH BEng MPhil

FEBRUARY 2000

ACKNOWLEDGEMENTS

I would like to thank my supervisor Dr Paul S. Addison for his patience, guidance and understanding throughout this project, to whom I am greatly indebted.

The additional support provided from the Department of Civil and Transportation Engineering is also appreciated. In particular, I would especially like to thank Mr John Callaghan for his excellent workmanship in constructing the experimental equipment vital to this project.

Thanks is also given to Dr Gareth Pender of the Department of Civil Engineering, University of Glasgow, for his input and collaborative work on this project.

Finally, I must thank my parents and Miss Shirley Douglas for their patience and support during the period of this research.

SUMMARY

This thesis is the culmination of an experimental study on the flow characteristics which develop in open-channel slot flow. Although the current literature provides much information on the flow downstream of a backward facing step (BFS), there is little information on the effect of a forward facing step (FFS) located beyond this, a condition known as slot flow and experienced in many engineering flow problems.

The aim of this research was to investigate the influence of a FFS at varying distances downstream of a BFS. This was achieved through the accurate measurement of slot flow fields using laser-Doppler velocimetry.

In order to conduct this LDV investigation, various pieces of laboratory equipment had to be designed and constructed. This primarily involved the construction of a purpose built laboratory flume capable of supporting LDV measurements and a range of channel geometries and flow conditions.

The thesis contributes much information on the flow which is generated beyond a BFS, and the effects of a FFS at various locations beyond this. The relationships between both the upstream flow depth and Reynolds number on the reattachment length are presented in greater detail than that currently provided in the literature. The results indicate that a FFS located within a distance of 15-20 step heights from a BFS will influence the resulting flow characteristics. When the FFS is located beyond this, both the BFS and FFS may be treated independently.

The mean flow characteristics are examined in detail, illustrating the mean velocity distribution before flow separation, immediately after separation, and beyond flow reattachment. The velocity distribution downstream of a BFS was confirmed to have a Gaussian form. An expression for this is presented which describes this more accurately than that given currently in the literature. The location of flow reattachment, R_L, was found to occur in the region of 5-9 step heights downstream of the BFS, however, the FFS influenced this value when located within 2-3 step heights of reattachment. The flow effects created by the BFS were observed to exist at a distance of approximately 40 step heights downstream of the step. Although the relaxation of the mean velocity distribution to the thin shear layer state occured after a distance of approximately 27 step heights, the relaxation of the turbulence intensities occured at the greater distance of 40 step heights. The turbulence intensities which develop throughout the entire flow field have the property that $u'>w'>v'$. It was also observed that the levels of turbulence generated in the slot shear layer were less than those which developed in the FFS shear layer.

AN EXPERIMENTAL INVESTIGATION OF OPEN-CHANNEL SLOT FLOW

CONTENTS PAGE No.

CHAPTER 3: EXPERIMENTAL APPARATUS

LIST OF FIGURES

CHAPTER 4

LIST OF TABLES

LIST OF PLATES

CHAPTER 3

NOTATION

A_s - slot aspect ratio (slot length/slot height)
B - channel width
C - Chezy's constant
F - Froude number
g - gravity
h - flow depth
H - flume design height
H_S - slot height
k - turbulent kinetic energy (TKE) per unit volume
k_{max} - maximum TKE in slot
k_{up} - maximum TKE upstream of slot (main channel)
l - characteristic (unit) length
L - flume design length
m - hydraulic mean depth
N - refractive index (also used for number of samples from point measurement)
n - Manning's friction factor
Q - flowrate (m^3s^{-1})
Q_O - upstream flowrate
Re - Reynolds number
Re_{crit} - critical Reynolds number above which flow becomes turbulent
R_{Lmax} - maximum reattachment length
R - hydraulic radius
R_L - reattachment length
$R_{L(s)}$ - reattachment length obtained in main investigation
S - slope of the channel = $\partial h/L \equiv \sin\theta$
S_e - the slope of the energy grade line
T - duration of sample record (seconds)
U - longitudinal component of velocity ($=u + u'$)
u - mean longitudinal velocity (also used to represent $\bar{u}$) (ms^{-1})
u_{max} - maximum streamwise velocity in the upstream channel
u_{Rmax} - maximum (negative) velocity in the recirculation zone
U_s - free stream velocity
u_o - mean upstream longitudinal velocity
u' - fluctuating velocity (also used to represent u'_{RMS})
$u*$ - friction velocity
U^+ - $u/u*$
V - vertical component of velocity ($=v + v'$)
V – orthogonal velocity component
W - lateral component of velocity ($=w + w'$)
x - longitudinal distance
y - vertical distance
y_o - upstream flow depth
Y^+ - $yu*/\nu$
y_S - slot flow depth
z - lateral distance
δ - boundary layer thickness
ρ - mass density of fluid medium
μ - coefficient of dynamic viscosity
ν - coefficient of kinematic viscosity
τ - shear stress

G - rate of turbulent energy generation

ε - rate of turbulent dissipation (also used for eddy viscosity)

$\xi \equiv y/h$.

θ_i - angle of incidence

θ_r - angle of refraction

CHAPTER 1

INTRODUCTION

CHAPTER 1

INTRODUCTION

1.1 INTRODUCTION

Science and engineering have benefited enormously over the last 30 years with the advent of computers and the associated improvement in technology. With the cost of this new technology decreasing and its use becoming more widespread, the scientific community has taken advantage of these and become reliant and adept at using them to its potential.

The application of theoretical fluid mechanic equations, such as the Navier-Stokes equations for turbulent flow, to even the most basic of flow types, requires the solution to a vast number of calculations, only achievable using computers.

Prior to this application of computer technology, complex fluid mechanic problems were solved through experimental investigations. This generated a whole new science of empirical and semi-empirical solutions. Indeed, much of the progress in fluid mechanics in the 20th Century focused on obtaining accurate empirical models and solutions. The development of the hot-film anemometer (HFA) and the laser-Doppler anemometer (LDA) within the last 30 years, has greatly increased the scope of experimental fluid mechanics, allowing the turbulent fluctuations of flow to be measured with reasonable accuracy.

Experimental fluid mechanics is still used today to solve real fluid engineering problems and is not just limited to bridging the gap to fluid theory. Experiments range from scale models of river courses to simplified hydraulic situations, such as the flow round bends and overbank flow. The cost and time factors associated with experimental investigations are shifting preference towards numerical solutions. Computational fluid dynamics (CFD) is now recognised as a powerful tool for solving hydraulic engineering problems at a fraction of the expense and time taken for an experimental approach. However, despite the advances in technology, the numerical equations used in CFD have proved difficult to solve. One of the main problems associated with this is the difficulty in modelling turbulence. The scientific community often utilises semi-empirical equations to achieve a short-term solution to flow problems. The empirical coefficients applied to these solutions however, are often not universal, and therefore require further investigation (Alfrink and van Rijn, 1983).

The integrity of computer models must therefore be validated by accurate experimental data. This normally takes the form of a simplistic flow condition which can be investigated both

experimentally and numerically. The phenomena of flow separation is well known, occurring in nearly all fluid flows when there is a rapid change in the boundary geometry, or the flow is subject to the presence of adverse pressure gradients. As the oncoming boundary layer separates, a recirculating region develops immediately downstream. A separated turbulent shear layer rapidly grows and reattaches to the surface at some point further downstream. The behaviour of this separated shear layer, its growth, its turbulent properties and the length of reattachment have been the focus of research within many engineering disciplines. Attempts have been made to develop advanced experimental and theoretical techniques in order to study this type of flow, however, it is only recently that these techniques have reached the required state of development to be of use in fluid mechanic problems. In the past, this type of investigation relied on flow visualisation or intrusive measurement techniques, which limited the investigation to mean velocity measurements.

One of the simplest flow conditions used to induce flow separation is the use of a two-dimensional backward facing step (BFS), see figure 1.1(a). The separated flow behind a backward, or rearward, facing step, has frequently been used as a condition for validating both numerical codes and experimental measurement techniques (Amano and Goel, 1985; Sohn, 1988; Grant et al, 1992; Barton, 1995; Allerborn et al, 1997). The attraction of this configuration for base line testing is due to its simplicity of geometry, the stability of the separated reversed flow region, and the wide range of mean flow and turbulence levels encountered (Grant et al, 1992). In order to analyse this flow, detailed information on the turbulent structure and the coherent vortices are required to evaluate the velocity distribution, bed shear stress and turbulence.

1.2 APPLICATION OF BFS FLOWS

A BFS geometry is directly applicable to a range of engineering fluid problems. The separation and recirculation processes are fundamental to the understanding of turbo-machinery passages, the stalling flow over an airfoil and the stabilisation of the flame in a gas turbine combustor. The aerodynamic efficiency of an airfoil or vehicle is reduced if there is a loss in lift and an increase in drag, the effects created by extensive separation and its associated lack of pressure recovery. There are many examples of BFS induced separation in open-channel flows. River channels undergoing a natural sudden expansion, both vertically or laterally, will demonstrate this process of flow separation. Many man-made alterations to river channels can also induce flow separation, such as the addition of bridge piers, sheet piles, submerged weirs and turbulence diffusers. Man-made hydraulic structures and

channels such as slipways, dams and canals can also experience a sudden expansion of geometry which will exhibit flow separation.

The use of a BFS to investigate flow separation is not only applicable to fixed bed problems. Flow over a mobile granular bed is a complex process because of the inter-relationship between the fluid and the bed material. The reverse flows and stagnant regions found in a recirculating zone affect the sediment transport which subsequently alters the geometry and location of the bed form. Backward-facing steps have been adopted as a base line study owing to the similarity in such investigations (Engel, 1981; Mendoza and Shen, 1990; Nezu and Nakagawa, 1993; Lee and Hwang, 1994; Nelson et al, 1995). These mostly concern open-channel flow, however, the closed-duct flow condition has also been investigated, applicable to the study of shallow ice-covered rivers (e.g. Smith and Ettema, 1997).

1.3 APPLICATION OF SLOT FLOWS

Variations of a sudden change in channel geometry have been developed to provide wider applications to engineering problems. One such example is the forward facing step (FFS), which produces a sudden decrease in a channel depth, see figure 1.1(b). Another variation is the existence of both a BFS and FFS close together, where the flow conditions created by one affects the other. This type of obstacle can take two forms: (1) a FFS followed by a BFS becomes a surface mounted obstacle (figure 1.2); and, (2) a BFS followed by a FFS becomes a trench or slot in the channel (figure 1.3). For a surface mounted obstacle, the FFS does little to affect the surrounding flow and therefore the affected flow field becomes primarily that for a BFS. A FFS located downstream of a BFS can produce two distinct slot flow types, these being differentiated in terms of the development of slot bed reattachment of the flow. When the FFS is close to the BFS, no reattachment occurs and a single recirculating cell dominates the slot. This case is shown in figure 1.3(a). When the FFS moves further downstream, slot bed reattachment occurs, and the flow in the slot is characterised by a recirculation zone upstream of reattachment, and a recovery period of the flow between reattachment and the FFS, figure 1.3(b). This type of flow is generally referred in the literature as 'trench' or 'slot' flow (Alfrink and van Rijn, 1983; and Fujita and Komura, 1992). When the downstream distance of the FFS is increased further still, the FFS no longer influences the flow immediately downstream of the BFS, and both the BFS and FFS may be treated independently.

Civil engineering projects such as submerged tunnels, pipelines, harbours, and storm surge barriers often require a trench or channel to be excavated in the channel bed. Knowledge of

the flow and turbulence field may be required to estimate the siltation rate of a dredged channel or the fluid forces acting on a submerged structure. Trenches dug along the approach to a harbour will have a continually evolving depth and profile under the combined action of backfilling and channel migration, created by deposition at the upstream side and erosion at the downstream side. Determining the optimum location of these trenches and the frequency of redredging, are therefore matters determined by the rates of bed-load and suspended sediment transport, which are subsequently controlled by the mean flow and turbulence structure (Basara and Younis, 1995).

The interaction of a floodplain with the underlying river has been widely investigated. The complex flow structures which develop at this boundary are responsible for erosion of the river banks and subsequent sedimentation downstream. As the flood subsides, the exposed river form can be significantly altered from its previous condition. Although these effects occur at different scales, from small streams to major rivers, its effects can have direct consequences for mankind. The Brahmaputra in Bangladesh and the Mississippi in the US being well known rivers where flooding has created large scale damage to property, disruption to civilised life, and has even resulted in the death of wildlife, livestock and humans.

The analysis of floodplain flow (also known as overbank, compound channel and two-stage channel flows) has been widely investigated, Toebes and Sooky (1967), Yen and Overton (1973), Rajaratnam and Ahmadi (1981), Krishnappan and Lau (1986), Keller and Rodi (1988), Sellin et al (1990), Ackers (1992), Pender (1992), Ervine et al (1993), Fares and Herbertson (1993), Greenhill and Sellin (1993), Sellin et al (1993), Willetts and Hardwick (1993), Ervine and Jasem (1995), Ervine and MacLeod (1999). Due to the complexity and individual nature of every river, this research focuses on simplified conditions. This normally takes the form of a sinuous meandering river, or a straight river channel skewed with the main floodplain flow, see figure 1.4. In some cases, the river channel can be skewed to the extent that the river will lie perpendicular to the direction of the floodplain. When this occurs, the cross-section through the floodplain longitudinally has the same geometry as a slot. This was investigated by Jasem (1990) in conjunction with skewed channels to the floodplain.

Another engineering problem which can be modelled using BFS and slot flow information is the pollution concentration of the air quality in an urban canyon (DePaul and Sheih, 1986; Hoydysh and Dabberdt, 1988; Nakamura and Oke, 1988; Hunter et al, 1990; Ca et al, 1995; Herbert et al, 1997; Addison et al 1999a and 1999b). An urban canyon comprises a road with its flanking buildings. This forms a basic geometric unit which can be used by planners to

model the flow of air within. The airflow and thermal characteristics are of importance to the safety and comfort of pedestrians because of potential problems arising from wind buffeting, wind chill, heat stress, driving rain, blowing snow and sand, and high concentrations of pollutants. Further, the influence of canyon geometry on building heat losses, or the demand for cooling, is of direct relevance to energy conservation. Hence, knowledge of canyon climate in relation to canyon geometry and external meteorological forcing forms an essential input to urban street design (Nakamura and Oke, 1988). When the above-roof wind direction is perpendicular to the canyon, the air flow within the canyon can exhibit characteristics similar to slot flow.

Many of the engineering problems associated with flow separation at a channel expansion can be understood with reference to the mean flow characteristics. However, another property of this flow type is the development of vortices at the point of flow separation. These vortices expand as they propagate downstream producing large oscillations of the flow. This hydrodynamic instability of the shear layer may lead to an effective variation in the hydrodynamic load and produce structural vibrations (Ethembabaoglu, 1978). An application of this type of hydrodynamic loading is in the structural design of tall buildings.

1.4 SCOPE OF THIS INVESTIGATION

Although many of the flow characteristics which occur downstream of a BFS are well documented, there are some aspects of this type of flow which are less well known. As the point of flow separation is fixed, much of what happens downstream of this is described by the reattachment of the shear layer. In open-channel flow, the Reynolds number and boundary layer thickness of the oncoming flow are found to influence the shear layer development and subsequently the reattachment length. Most of the examples documented in the literature to date are confined to a limited set of flow conditions, and therefore, a wider range of these influencing parameters need to be investigated in order to provide a more comprehensive account of this type of flow.

Investigations on open-channel flow (including BFS flows) include 3-dimensional studies which generally focus on the extent of sidewall contamination. When the channel has a large width to depth aspect ratio, a central 2-dimensional region exists which is representative of a channel of infinite width, with 3-dimensional flow limited to the near wall region. Although the mean flow properties are generally described using only a 2-dimensional analysis using U and V, the turbulent property of the lateral component, w', has generally been overlooked.

However, it is known that this component contributes more to the turbulent energy than the vertical component, and therefore this component should not be overlooked so readily.

The previous section highlighted the direct application of slot flow configurations to a variety of engineering problems. Although examples of slot flows are found in the literature, BFS flows have received more attention. There are, however, specific characteristics pertinent to slot flows which are not fully understood, this being primarily the influence of the FFS on the reattachment length of the shear layer.

The aim of the investigation detailed in this thesis was to **determine experimentally the flow characteristics which develop in open-channel slot flow, focusing on the influence of a FFS located within the vicinity of flow reattachment downstream of a BFS.**

This aim was achieved through the following objectives:

(1) **To undertake a preliminary study using the LDV system in a laboratory teaching flume**.

This teaching flume restricted the measurement of the lateral velocity component, *W*. Despite this, a 2-component investigation was undertaken to achieve the following:

- To provide the author with a detailed insight into LDV data acquisition, such as the accurate movement and position of the laser probe, and good working experience of the controlling software, FlowLite.

- To gain an insight into the mean and turbulent flow characteristics of open-channel slot flow using a limited set of physical and hydraulic conditions. This would include a BFS case and several slot flows of varying slot aspect ratio.

- To gain an understanding of the physical and hydraulic parameters required for the main investigation, and hence assist in the design specifications for the construction of the main flume.

(2) **To construct a purpose built experimental flume**.

This was necessary since a flume was required both to provide the correct physical and hydraulic conditions, and to facilitate 3-component LDV measurements.

On construction of this flume, several confirmatory investigations would be necessary prior to 3-component LDV measurements. This will include:

- A detailed survey of the main flume to confirm its suitability for such measurements. This would focus on the degree of workmanship of the flume and its ability to support the required experimental conditions.

- A method of obtaining statistically reliable results from LDV measurements.

(3) To undertake a comprehensive study of open-channel slot flow using the purpose built flume.

This consisted of the following areas of investigation:

- Measurements of rectangular open-channel flow were required to confirm the following:

  (i) The application of the law of the wall.
  (ii) The validity of the universal turbulence intensity functions for all 3-components.
  (iii) The symmetry of flow around the channel centreline.
  (iv) The extent of sidewall contamination and central zones of 2-dimensional flow.

- A detailed investigation of the reattachment length downstream of a BFS was required to establish the following relationships:

  (i) The effect of a change in oncoming flow depth, y_o.
  (ii) The effect of a change in upstream flow velocity, u_o.
  (iii) The influence of a FFS at varying distances from the BFS.
  (iv) The spanwise distribution of reattachment length.

An outline of the physical and hydraulic conditions for the main investigation would be based on the preceding information. Using various slot aspect ratios, the flow field upstream, within, and downstream of the slot would then be measured to determine the following key characteristics:

- The mean velocity distribution, primarily within the slot region.
- The development of the shear layer with respect to its inner and outer boundaries.
- Using the three-components of fluctuating velocity, their contribution within the shear layer and their subsequent dissipation.
- In the BFS case, the relaxation of the perturbed flow back to normal open-channel flow.

The remainder of this thesis documents the work undertaken in achieving these objectives, with the conclusions drawn from this work clearly indicating that the aim of the project was successfully achieved. A timetable of the key events which were undertaken during this project can be seen in table 1.1.

Table 1.1 – Timetable of Events

Event / Time	Year 1				Year 2				Year 3			
Literature Review	■■■	■■■	■■■	■■■								
Initial Investigation		■■■	■■■									
Main Flume Design		■■■										
Main Flume Construction			■■■	■■■	■■■	■■■						
Main Flume Calibration							■■					
Open-Channel Investigation								■■				
Reattachment Length Investigation								■■				
Slot Flow Data Acquisition									■■■	■■■	■■■	
Analysis										■■■	■■■	■■
Thesis Write-Up				■	■	■	■	■	■	■	■■■	■■■

A brief summary of the contents of each chapter in this thesis now follows.

Chapter 2 contains a detailed literature review. This introduces the fundamental flow equations used in open-channel flow, and also the flow conditions experienced before, during and after a BFS and FFS. The mean and fluctuating velocity characteristics of rectangular open-channel flow are explained with reference to the law of the wall and turbulence intensity models respectively. As the flow experiences the change in geometry, the flow characteristics are described by the development of a recirculation system and a free-shear layer boasting high turbulent activity. The recovery of the flow back to the 2-dimensional thin shear layer state is also discussed.

Chapter 3 details the experimental equipment used in this study. An overview of the LDV system is presented, followed by the design specifications for an accurate method of moving and supporting the laser probe. Two flumes were used in this study. An initial investigation was conducted using an existing teaching flume, whilst the main study was conducted in a purpose built flume. The main advantages of this new flume were its ability to support 3-component data acquisition using a 1-component LDV system, to provide fully developed 2-dimensional turbulent flow, and to facilitate various slot geometries. Details of the construction of this flume are given in this chapter.

Chapter 4 documents the initial flow investigation using slots of varying length. This concentrates on the mean velocity distribution and the turbulent kinetic energy generated both in the slot and at the FFS. The suitability of the main flume is assessed through a combination of flume channel properties and a rectangular open-channel flow investigation. The latter confirms the law of the wall, turbulence intensity distribution and flow 2-dimensionality. The integrity of the data measurements is also assessed in this chapter.

Chapter 5 details the main study. The first section presents a relationship of the reattachment length with respect to flow depth, Reynolds number and slot length. From this investigation, twelve different flow conditions were selected for detailed measurement. The mean velocity data provided information on the velocity profiles in the recirculation cell, the shear layer boundaries, the mass flow streamlines and the relaxation of the flow back to the thin shear layer state. The 3-component fluctuating velocities clearly illustrate the intensity and distribution of turbulence generation in the primary shear layer and at the FFS. The dissipation of this turbulent energy is also used to assess the relaxation of the flow back to the thin shear layer state.

Chapter 6 provides a summary of the aims and objectives of this study. These are addressed individually with general conclusions drawn from the investigation. The chapter concludes with a section on recommendations for future research.

Figure 1.1 - Recirculation Regions in Sudden Expansion and Contraction of Channel Geometry

(a) Backward Facing Step **(b) Forward Facing Step**

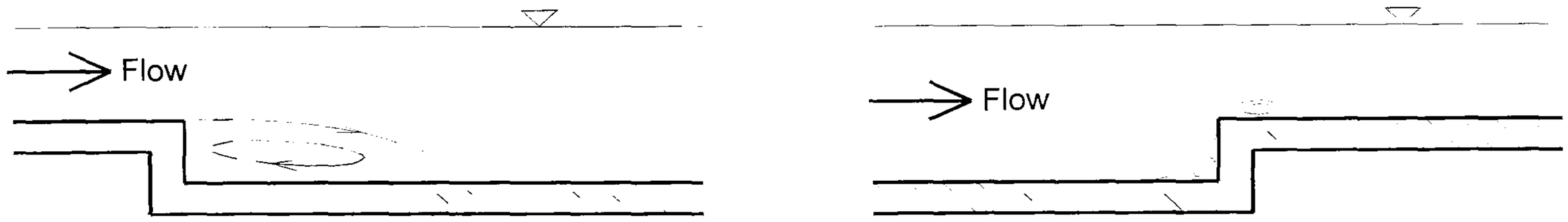

Figure 1.2 - Block Obstacle Produced from a FFS Followed by a BFS

(a) Small Distance Between Steps **(b) Large Distance Between Steps**

Figure 1.3 - Slot Configuration Produced from a BFS Followed by a FFS

(a) Small Distance Between Steps **(b) Large Distance Between Steps**

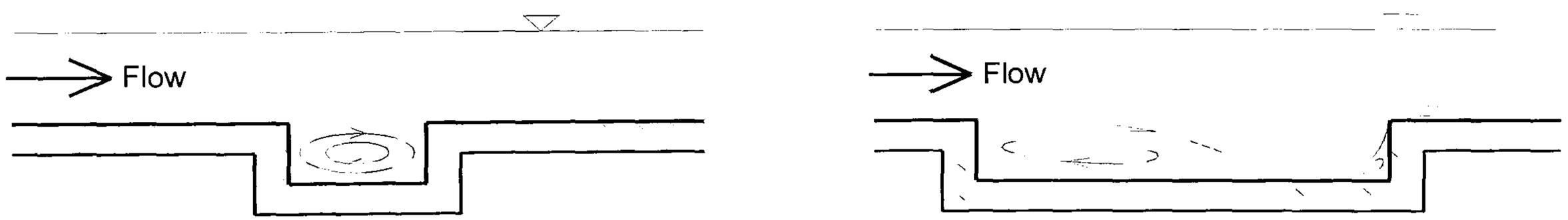

Figure 1.4 - Some Examples of Floodplain Flows

(a) Meandering River Channel

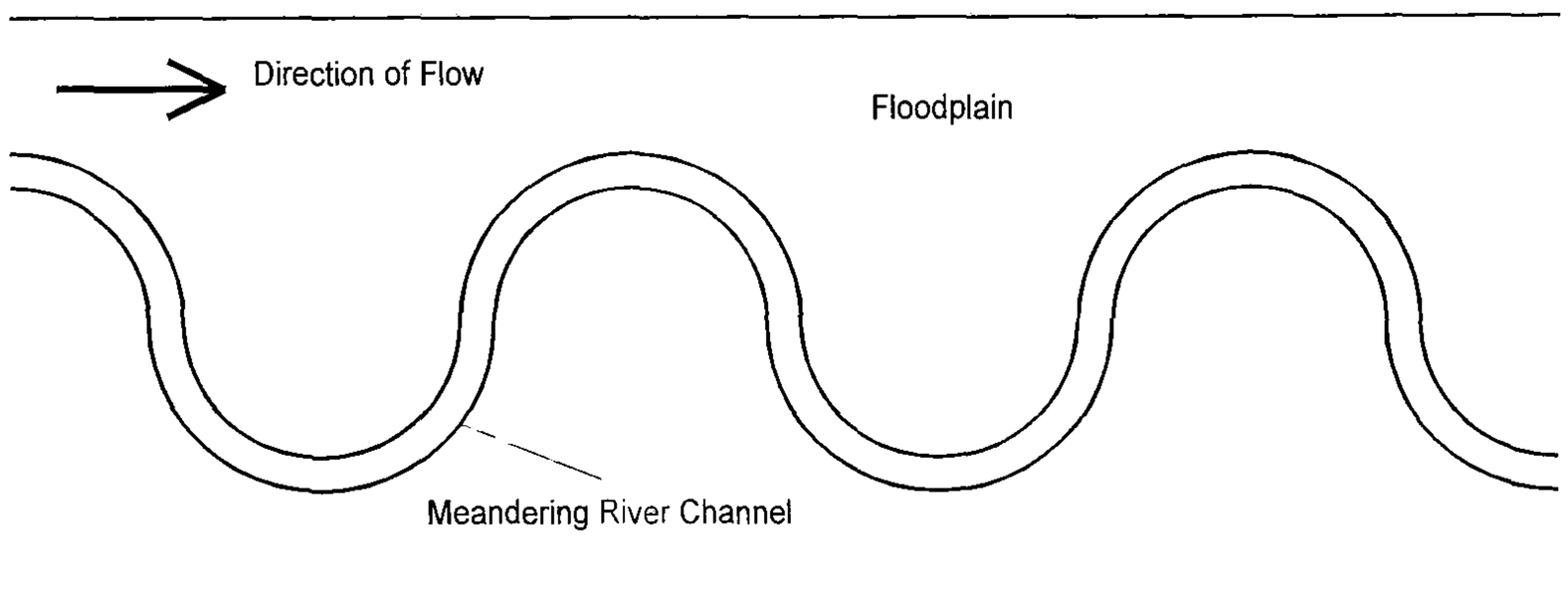

(b) Skewed River Channel (Various Angles)

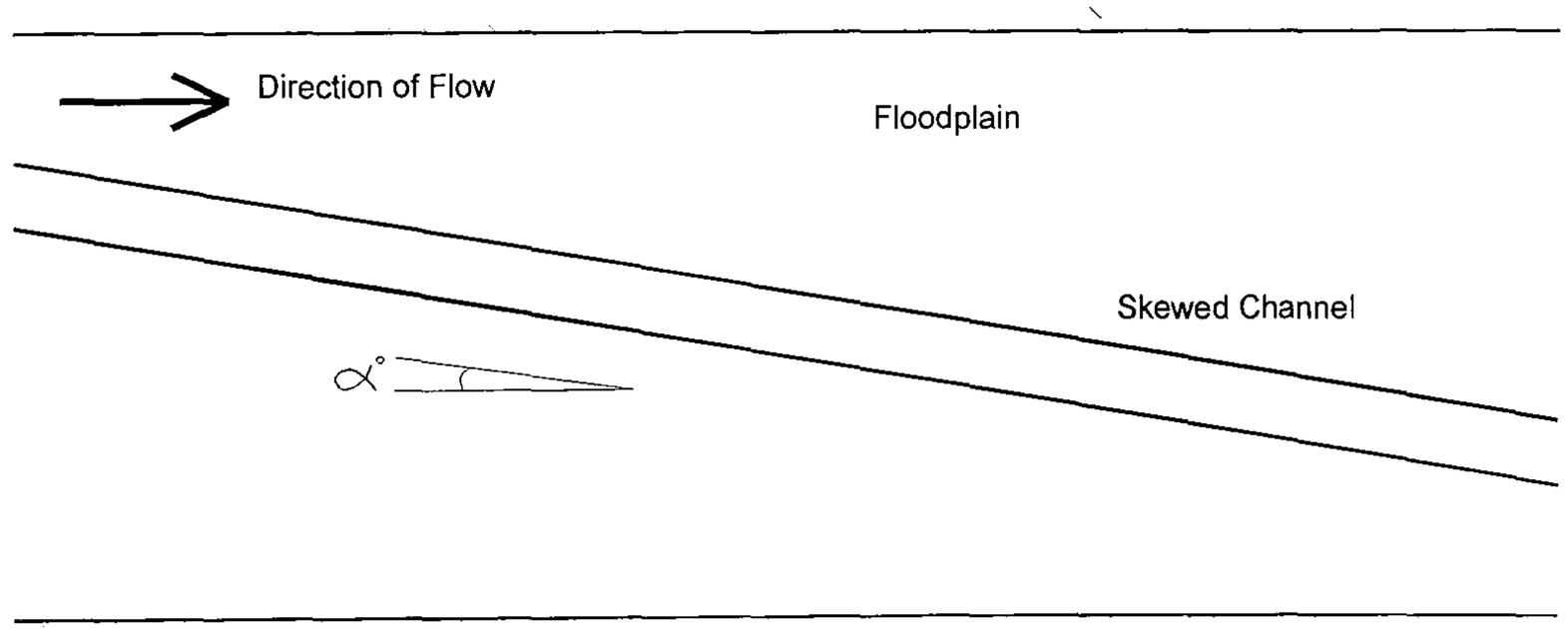

CHAPTER 2

LITERATURE REVIEW

2.1 INTRODUCTION

2.2 INTRODUCTION TO OPEN CHANNEL FLOW

2.2.1 Turbulence Phenomena

2.2.2 Boundary Layer Theory

2.2.3 Vertical Velocity Distribution Relationship

2.2.4 Friction Velocity

2.3 OPEN-CHANNEL FLOW DEVELOPMENT

2.3.1 Sub-Division of the Open-Channel Flow Field

2.3.2 The Velocity Defect Law and Cole's Wake Function

2.3.3 Free-Surface Effects

2.3.4 General Developments

2.4 UNIVERSAL FUNCTIONS FOR TURBULENCE INTENSITIES

2.4.1 Damping Function Extension for Turbulence Intensity

2.5 FLOW SEPARATION AND REATTACHMENT

2.5.1 Introduction to Backward Facing Step Flow

2.5.2 Defining Reattachment Length

2.5.3 Streamlines

2.5.4 Shear Layer Development

2.5.5 Plane Jet Considerations

2.5.6 The Coanda Effect

2.5.7 Shear Layer Thickness in BFS Flow

2.5.8 Inlet Conditions

2.5.9 Open-Channel BFS Flow

2.5.10 Two-Dimensional Flow and Side-wall Contamination

2.5.11 Lateral Expansion Studies

2.5.12 Forward Facing Step Flow

2.6 OPEN-CHANNEL SLOT FLOW

2.7 SUMMARY

2.7.1 Open-Channel Flow

2.7.2 Backward Facing Steps and Slot Flow

CHAPTER 2

LITERATURE REVIEW

2.1 INTRODUCTION

A basic understanding of fluid flow has existed for many centuries, with many engineering examples of water supply and flood control systems originating back to the Roman age. Significant developments in fluid flow were introduced by Bernoulli (both Johann and his son Daniel) and Euler in the 17th and 18th centuries, however, these findings applied to the concept of ideal fluid flow. The discovery of the distinction between laminar and turbulent flows by Reynolds (1883), and the presentation of the boundary-layer theory by Prandtl (1904) closed the gap between ideal and real fluid flow. Since then, our understanding of the mean velocity distribution and turbulence characteristics of fluid flow in both closed and open-channel flow have greatly improved. This increased awareness stems from a combination of theoretical and experimental research, which has subsequently led to the development of useful semi-empirical relationships. Although the use of computers, particularly in the last 30 years, has greatly increased the development towards a numerical solution for fluid flow, there still exists the need to produce highly accurate flow measurements. The ability to acquire such measurements has greatly improved in recent years with the advent of non-intrusive measurement techniques.

In this chapter, the fundamental properties of fluid flow are discussed which are pertinent to the flow conditions required in this study. This concentrates on the semi-empirical relationships derived for rectangular open-channel flow, and the characteristics of backward-facing step and slot flow in open-channels.

2.2 INTRODUCTION TO OPEN-CHANNEL FLOW

It was during the latter period of the 18th century that formulae which could represent the flow of water in a river channel began to be developed. The first attempt to express this problem by means of an algebraic formula, albeit purely empirical, was by the French engineer Chezy. This formula represents the cross-sectional average velocity and is expressed as follows:

$$u = CRS^{1/2} \qquad \textbf{Equation 2.1}$$

Where, u - mean velocity

R - hydraulic radius,

S - channel longitudinal slope,

C - Chezy's constant, $\sqrt{(2g/c_f)}$, where c_f is a friction factor (shear stress).

It was understood at this time that the flow is affected by the retarding force of friction created by the river bed, or more specifically that created around the wetted perimeter. Chezy's formula was the basis for much research in the 19th century, where extensions of the same algebraic form were introduced to create a more exact formula. The formula which became accepted at the time was that proposed by Manning (1890) which took the form:

$$u = \frac{1}{n} R^{2/3} S^{1/2}$$

Equation 2.2

Where n, is the Manning's friction factor which is related to Chezy's C as:

$$C = \frac{1}{n} R^{1/6}$$

Equation 2.3

Values for Manning's friction factor, n, are given for various materials in Chow (1959). Typical values of n range from 0.010 for smooth surfaces, such as glass and metal, to 0.100 for river beds with dense weeds.

The concept of ideal fluid flow ignored frictional forces. This simplified flow models, where the velocity profile was described by a uniform velocity profile throughout the section, see figure 2.1. Actual flow measurements in pipes and open channels reveal a profile affected by the influence of friction with the bed and side-walls, and therefore introduced the concept of real fluid flow, see figure 2.2.

One of the first detailed investigations into the effects of friction on the cross-sectional average velocity was by the Frenchman, Bazin (1865). In a purpose built channel 450m long with a width of 2m, he conducted a vast range of tests on rectangular channels with different types of channel surface. Using a pitot-static tube developed by Darcy, detailed velocity traverses were made throughout the test section. Bazin himself did not conclude a definitive formula for the cross-sectional average velocity of fluid flow, but was regarded more for the precision in his

results which were used by many scientists in later research. Indeed, these results were used by Kuelegan (1938) to verify the use of a valid relationship for the velocity profile in open-channel flow, see section 2.2.3.

2.2.1 Turbulence Phenomena

The understanding and definition of turbulence and the pioneering research in pipe flow have both contributed significantly to the development of the current knowledge of open channel flow. Although pipe flow and open-channel flow can be considered as two distinct subjects in their own right, the development of open-channel flow is described historically with contributions from turbulence and pipe flow.

A turbulent flow is characterised by a mean velocity, u, and fluctuating velocity component, u', in the streamwise direction, x. In general, the flow velocity, U, at an instant in time may be described by:

$$U = u + u' \qquad \textbf{Equation 2.4}$$

The same can be said for the vertical and lateral directions, y and z, whereby each has a velocity, V and W respectively, composed of a mean and fluctuating component:

$$V = v + v' \qquad \textbf{Equation 2.5}$$

$$W = w + w' \qquad \textbf{Equation 2.6}$$

A schematic diagram of the way in which the velocity, U, at a fixed position fluctuates in time is shown in figure 2.3. An example time series taken during this investigation is presented in Appendix C.

Due to the nature of turbulent fluid flow, it is impossible to trace and characterise mathematically the motion of individual particles. However, mathematical relationships may be obtained by considering the average motion of aggregates of fluid particles, or by statistical methods. One such method is to plot the probability distribution of the fluctuating velocity component, where it has been shown that the turbulent velocity probability distributions approach that of a Gaussian

distribution (Xinyu *et al*, 1995), as seen in figure 2.4. Appendix C includes an example distribution.

Turbulence is generated by friction effects at solid boundaries or by the interaction of fluid streams moving past each other with different velocities. In turbulent flow, the fluid particles are observed to travel in randomly moving fluid masses of varying sizes called *eddies*. These eddies cause a rapid and irregular pulsation of velocity about a well-defined mean value.

The first detailed study into the turbulence of fluid flow was conducted by Reynolds (1883), where he identified three distinct types of flow, namely laminar, transitional and turbulent, depending on the magnitude of the ratio of the inertial forces to the viscous forces. In order to classify these flow types, Reynolds introduced the non-dimensionalised parameter known as the Reynolds number:

$$R_e = \frac{\rho.u.l}{\mu} = \frac{u.l}{\nu} \qquad \textbf{Equation 2.7}$$

where, u - the average velocity of flow,

ρ - mass density of fluid medium,

μ - coefficient of dynamic viscosity,

l - characteristic length, and

ν - coefficient of kinematic viscosity.

Laminar flow occurs when the viscous force is greater than the inertial force, and thus the viscous force dominates the flow. In laminar flow the fluid particles move smoothly in a coherent fashion. Turbulent flow occurs when the viscous forces are small relative to the inertial forces, and hence the latter dominate the flow. In this case the particles move in an apparent random fashion. Transitional flow is one which cannot be described by either of these flow types. Reynolds showed that there was a critical value of the Reynolds number, Re_{crit}, above which the flow became turbulent. From his experiments he found this to be of the order of 2000 for pipe flow, however, a definite value for this critical value is somewhat ambiguous. For open-channel flow, the transitional phase can be in the region from 500 to 12,500. When a laminar flow reaches this critical value, the flow tends to become unstable and breaks down into a turbulent state, whereby the flow field becomes full of irregular eddying motions (Prandtl, 1952).

In general, the intensity of turbulence increases with Re and the scale of turbulence increases with boundary dimensions. The largest eddy size expected is of the order of a characteristic length of the flow, e.g. pipe radius, channel width or depth etc..

2.2.2 Boundary Layer Theory

Whether a solid body is pulled through a mass of water, or a flow exists over a stationery surface, the effect of drag between the solid object and the flow is the same. The total drag on a solid body is made up of two components, namely the form, or pressure drag and the skin friction drag. The form drag is dependent on the pressure forces acting on the body, and the skin friction drag is dependent on the shearing forces acting between the body and the fluid.

The skin friction drag over a flat plate is similar in principle to the flow over a channel bed. Indeed, in order to analyse the effects of the fluid viscosity on the velocity gradient near a solid boundary, the concept of the flat plate with infinite width has traditionally been used. A velocity gradient exists perpendicular to the surface of the plate. This is because the particles of the fluid adjacent to the surface are stationary whilst those at an arbitrarily small distance above the surface move with some velocity. This condition of zero fluid velocity at the surface is known as the *no slip* boundary condition, and the layer of fluid between the surface and the free stream fluid is termed the boundary layer. Outside this boundary layer the fluid behaves as if it had no viscosity, and since the boundary layer is thin compared to the typical longitudinal length scale, the pressure difference across the layer is negligible.

Figure 2.5 illustrates the stages of boundary layer development in an open-channel. Consider a flat surface with a flow applied with a velocity, u, which exists outside the boundary layer. The boundary layer thickness, δ, has been shown both theoretically and experimentally to depend on the flow velocity, density, viscosity and a length scale. The boundary layer does not merge into the main flow with a definite boundary, and therefore the thickness of the layer is generally taken as the distance from the surface where the velocity, u, is 99% of the free-stream velocity, U_S. As the laminar boundary layer thickens with distance from the leading edge, the boundary layer becomes unstable and transforms into a turbulent boundary layer. The random particle motion characterising turbulent flow results in a far more rapid growth of the boundary layer in the turbulent region.

Blasius (1908) developed a solution for the flow in a laminar boundary layer on a flat plate with zero pressure. A series of dimensionless profiles, dependent on the ratio of u/U_S, were used to describe the boundary layer at different locations along the flat plate. For the condition where u/U_S=0.99, the following solution describes the boundary layer thickness:

$$\delta = \frac{5.x}{\sqrt{R_x}}$$

Equation 2.8

where, x - distance from the leading edge, and

$$R_x = \frac{\rho.u.x}{\mu}$$

Equation 2.9

where, R_X - a Reynolds number based on longitudinal distance.

For turbulent flows, there are no exact solutions for obtaining the boundary layer thickness. One of the simplest expressions for the velocity distribution in a turbulent boundary layer was proposed by Prandtl (1932):

$$\frac{u}{U_s} = \left(\frac{y}{\delta}\right)^{\frac{1}{7}}$$

Equation 2.10

This empirically derived expression is known as the seventh-power law. Based on this assumption, the boundary layer thickness is given by:

$$\delta = \frac{0.37x}{R_x^{0.2}}$$

Equation 2.11

Even in a turbulent boundary layer, a very thin layer close to the boundary remains laminar, and is known as the laminar sub-layer.

2.2.3 Vertical Velocity Distribution Relationship

The Navier-Stokes equations for laminar flow can be extended to describe turbulent flow by the addition of terms involving the time averaged velocity fluctuations. The terms added are commonly referred to as Reynolds stresses. The resulting equation proved to contain too many unknowns, making a direct solution difficult. To overcome this problem, attempts were made to simplify the equations by developing empirical relationships between the Reynolds stresses and the mean values of the velocity components. Using this approach, Boussinesq (1897) suggested that the shear stress in turbulent flow could be represented as the sum of a stress due to purely molecular viscosity and a stress due to the turbulent transfer of momentum.

Viscosity produces stresses within the fluid due to the shearing of faster moving fluid layers over slower ones. The stress between two such layers is related to the rate of shearing of the two layers over each other. In the case of water, the viscous stress, τ, is linearly related to the rate of fluid shear through the viscosity (Rouse and Ince, 1957).

The viscous shear stress is given by:

$$\tau = \tau_{lam} + \tau_{turb} \qquad \textbf{Equation 2.12}$$

where,

$$\tau_{lam} = \mu.\frac{du}{dy} \qquad \textbf{Equation 2.13(a)}$$

$$\tau_{turb} = \varepsilon.\frac{du}{dy} \qquad \textbf{Equation 2.13(b)}$$

Where, ε - eddy viscosity

Taking the fluctuating velocities of fluid particles as u' and v' for the streamwise and vertical direction respectively, Reynolds confirmed that these turbulent velocities caused an effective shearing stress in turbulent flow, where:

$$\tau_{turb} = -\rho\overline{u'v'} \qquad \textbf{Equation 2.14}$$

in which $\overline{u'v'}$ is the mean value of the product $u'v'$. Terms of the form $-\rho.\overline{u'v'}$ are called Reynolds Stresses.

Prandtl (1952) proposed that small aggregations of fluid particles are transported by turbulence over a mean distance, l, from regions of one velocity to regions of another. In doing so they suffer changes in their general velocities of motion, the distance, l, being termed the *mixing length*. According to Batchelor (1950), the mixing length expression represents the equilibrium between the production and dissipation of the turbulent kinetic energy.

Consider the two-dimensional velocity profile in figure 2.6. A turbulent fluctuation v' at position 1 causes a discrete pulse of fluid to move from layer 1 to layer 2 a small distance, l (the mixing length). It may be seen that the turbulent fluctuation in the direction of flow, u', at position 2, is thus:

$$u' = -l.du/dy \qquad \textbf{Equation 2.15}$$

where u' is proportional to v', thus we can combine this expression with that of the Reynolds Stress, to get:

$$\tau_{turb} = -\rho\overline{u'v'} = \rho.l^2.\left(\frac{du}{dy}\right)^2 \qquad \textbf{Equation 2.16}$$

where the constant of proportionality between u' and v' is incorporated within l. Equation 2.16 is a (suggested) valid equation for shearing stress in turbulent flow. This leads to:

$$\varepsilon = \rho.l^2.\left(\frac{du}{dy}\right) \qquad \textbf{Equation 2.17}$$

since, $\tau_{turb} = \varepsilon.\dfrac{du}{dy}$

For flow near a boundary (wall), u and v must be zero. Close to the surface, Prandtl assumed that l became dependent on the distance from the surface, or:

$$l = \kappa.y \qquad \textbf{Equation 2.18}$$

where κ is called the *von Karman* constant. This value has been found experimentally to be about 0.4.

Hence:

$$\tau = \rho.\kappa^2.y^2.\left(\frac{du}{dy}\right)^2 \qquad \textbf{Equation 2.19}$$

Drawing from this analysis, the total shear stress can be written as:

$$\tau = \left(\mu.\frac{du}{dy} - \rho.\overline{u'v'}\right) \qquad \textbf{Equation 2.20}$$

where $\mu.dv/dy$ is the viscous stress and $-\rho.\overline{u'v'}$ is the turbulent (Reynolds) stress. Prandtl's mixing length theory is used here to derive the velocity distribution and other quantities because the results obtained are close to experimental data.

Prandtl further assumed the mixing length to be directly proportional to the distance from the boundary and that the shear stress was constant and hence equal to the boundary shear stress, τ_O, hence:

$$\tau_o = \rho(\kappa y)^2\left(\frac{du}{dy}\right)^2 \qquad \textbf{Equation 2.21}$$

therefore:

$$\frac{du}{dy} = \frac{1}{\kappa}\sqrt{\frac{\tau_o}{\rho}}.\frac{1}{y} \qquad \textbf{Equation 2.22}$$

The term $\sqrt{\frac{\tau_o}{\rho}}$ has the dimension of velocity and is called the friction velocity. This is represented by the symbol $u*$ or $v*$ for x and y respectively. On integration of equation 2.22 we get:

$$\frac{u}{u_*} = \frac{1}{\kappa}\log_e\frac{y}{y_o} \qquad \textbf{Equation 2.23}$$

or, it can be expressed as:

$$\frac{u}{u_*} = \frac{1}{\kappa}.\log_e y + C \qquad \textbf{Equation 2.24}$$

where y_O is the *boundary condition*, i.e. the distance from the boundary at which the velocity becomes zero, see figure 2.7.

This smooth bed observation can also be applied to flows over beds affected by wall roughness. This is important since many turbulent flows in hydraulic engineering (such as rough pipes and fluvial open-channels) occur over rough beds and complicated bed configurations. Observations by Nikuradse of friction head loss and velocity distribution on smooth and artificially roughened pipes conveying water, revealed that the forms of velocity distribution in the smooth and rough turbulent zones were different. For the smooth turbulent zone he assumed y_O to be proportional to $\nu/u*$, therefore equation 2.24 becomes:

$$\frac{u}{u_*} = \frac{A}{\kappa}.\log\frac{u_* y}{\nu} + C \qquad \textbf{Equation 2.25(a)}$$

For the rough turbulent zones, Nikuradse used the equivalent sand roughness parameter, k_S. For a uniform rough surface, the sand grain diameter can be used for the value of k_S. However, for irregular surfaces, the equivalent value of k_S can be more difficult to determine. The effects of roughness elements are usually classified in three categories:

(a) Hydraulically smooth bed ($k_s^+ < 5$).
(b) Incompletely rough bed ($5 \le k_s^+ \le 70$).
(c) Completely rough bed ($k_s^+ > 70$).

Where, k_s^+, is equivalent to the ratio of the length scales $k_s/(\nu/u*)$.

For rough beds, equation 2.24 can be rearranged to become:

$$\frac{u}{u_*} = \frac{A}{\kappa}\log\left(\frac{y}{k_s}\right) + \frac{A}{\kappa}\log\left(k_s^+\right) + C \qquad \textbf{Equation 2.25(b)}$$

From experimental data for hydraulically smooth channels, Nikuradse plotted $\frac{u}{u_*}$ against $\log(\frac{u_* y}{\nu})$ to get a straight line fitting the equation:

$$\frac{u}{u_*} = 5.75\log(\frac{u_* y}{\nu}) + 5.5 \qquad \textbf{Equation 2.26(a)}$$

Therefore, we have, A=2.3 and C=5.5, where κ=0.4, which represents the expression known as the *log law*. For flow close to the boundary, the velocity distribution is described by the viscous sub-layer law (equation 2.26b). The use of both these equations is referred to as the *inner law* or *law of the wall*. The distance from the surface at which this *inner law* or *law of the wall* analysis breaks down depends upon the particular flow considered.

$$u/u_* = u_* y/\nu \qquad \textbf{Equation 2.26(b)}$$

This expression is also used in the form, $U^+ = Y^+$.

The theoretical investigation of Prandtl and von Karman on flow through pipes, and the experimental studies of Nikuradse have led to rational formulae for velocity distribution and hydraulic resistance for turbulent flows over flat plates and in circular pipes. These formulae have been extended to open-channel flow. Although some general similarities exist between the flow through pipes and the flow through open channels, certain factors such as the presence of a free-surface, three-dimensional nature of the flow due to non-circular cross-section of the channel, and non-uniform distribution of the shear along the wetted perimeter, distinguish the open-channel flow from pipe flow. However, in wide open-channels the nature of flow is 2-dimensional, and the shear stress is constant along the bed. Thus, the formulae for pipes can be applied to those channels by changing the constants suitably to include the free surface effects. The velocity distribution in the middle region of such a channel is not influenced by the presence of the side walls, and the flow in that region may be considered as 2-dimensional in nature.

Kuelegan (1938) suggested that equation 2.26 which is valid for smooth pipes could also be extended to smooth, wide open-channels. Two main assumptions were made in applying this equation. The first assumption is that Karmans universal law of velocity distribution near a solid boundary is of general applicability. The other assumption is that the effects of the free-surface and secondary currents over the cross section of a channel is, in general, a small quantity which

can be merged in the surface characteristics entering the flow formulae. Furthermore, it is found that when the hydraulic radius is adopted as the characteristic length of a channel cross section, the resulting formulae become almost independent of the shape of the channel. Thus the formulae for flow in open-channels are identical in form with those for flow in circular pipes, the difference being in the values of the surface characteristics. Using Bazin's (1865) data, Kueligan confirmed the application of these formulae.

2.2.4 Friction Velocity

In order to investigate open-channel flow, the friction velocity u_* needs to be evaluated. This parameter is the most fundamental velocity scale with which to normalise both mean velocity and turbulence. Several methods have been proposed for the determination of this parameter. These are given as follows:

(1) From the channel slope under the conditions of normal and uniform flow, i.e. $dh/dx = 0$.

$$u_* = \sqrt{gRS} \qquad \textbf{Equation 2.27}$$

where, S - slope of the channel = $dh/L \equiv \sin\theta$,

g - gravity,

R - hydraulic radius (if flow is 2-dimensional then use depth of flow, h)

Of all the methods described here, this is the simplest and most widely used in turbulence research, e.g. Raichlen (1967), McQuivey and Richardson (1969), and Blinco and Partheniades (1971).

(2) An evaluation from the mean velocity distribution using the log-law. This can be used for open-channel flow on the assumption than von Karman's constant κ=0.4 and the integral constant A=5.5.

(3) From the measured Reynolds stress distribution. If Reynolds stresses are measured, then this has been shown to be the most accurate method (Nezu and Nakagawa, 1993b).

(4) If the viscous sub-layer can be measured, then u_* can be determined from the velocity distribution measured there using $U^+=Y^+$. Due to the difficulty of obtaining measurements in this region, then this method is limited in application.

(5) From direct measurements of wall shear stress with a Preston tube, however, although suitable to examine friction laws, this method is not considered to have a great accuracy for use in turbulence research.

In a study using the method of HFA, Nezu (1977a) reported that methods 1, 2 and 3 gave values of u_* within 30% of each other, however, in a more recent study using LDA, Nezu and Rodi (1986) showed that using the same methods (1, 2 and 3) yielded values of u_* within 5% of each other.

2.3 OPEN-CHANNEL FLOW DEVELOPMENT

Over the past twenty years, extensive experimental research has been performed on the mean flow and turbulence structure of open-channel flow with the aid of hot-film anemometry (HFA), laser-Doppler anemometry (LDA) and various visualisation methods. It was thereby established that, as with boundary layers and closed duct flows, open channel flows also consist of two regions: a near wall region (inner region) and an outer region near the free surface. The near wall region is controlled by the inner variables, namely the kinematic viscosity, ν, and the friction velocity, u_*, and its features are virtually the same as those observed in boundary layers and closed channel flow. On the other hand, the outer region is controlled by the flow depth, h, and the maximum velocity, u_{max}. The free surface exercises an influence only on this outer region. One noticeable influence is the damping of the vertical fluctuations by the surface. Associated with this is a reduction in eddy viscosity near the surface as compared with the central region of closed channel flow.

2.3.1 Sub-Division of the Open-Channel Flow Field

It is accepted that the open channel flow field has three distinct sub-regions resulting from the adverse effects created by the bed and the free-surface, each of which have their own sets of equations describing the flow in that region, see figure 2.8.

(1) *Inner* or *Wall Region* ($0 < y/h < 0.2$): This region compares to the inner layer described in boundary layer theory. The length scale of the turbulent structure in this region is controlled by the inner variables with respect to the law of the wall, $\nu/u*$, and the velocity scale is dependent on the friction velocity, u_*. Also, the rate of turbulent energy generation, G, exceeds the dissipation rate, ε, as bursting phenomena occurs most violently near a wall, i.e. $y^+<50$ (where $y^+ = yu*/\nu$).

Xinyu et al (1995) divided this region into a further 3 sub-divisions:

(a) Viscous sub-layer ($0 < y^+< 8$). This is a very thin layer where the viscous influence is dominant.

(b) Buffer Layer ($8 < y+ < 30$). They concluded that this region boasts the most production and dissipation of turbulent energy.

(c) Log-Law Layer ($30 < y+ < 0.2$ R*). Using a linear regression technique to analyse the velocity distribution, it was found that von Karman's constant, κ, was indeed constant at 0.4. In addition, the constant, A, from the log-law equation was found to vary depending on distance from the side-wall, but in the centreline A=0.6. The turbulence intensity u'/u_* occurring in the log-law layer was found to be constant, suggesting that a constant shear layer may exist in open channel flow like that in boundary layers. A similar phenomena was found in turbulent pipe flows (Perry and Abell, 1975).

(2) *Intermediate, or wake region* ($0.2 < y/h < 0.6$). This region is not strongly influenced by either the wall properties or the free-surface. The length scale in this region is the depth, y, and the velocity scale is governed by equation 2.21. The turbulent energy budget in this region maintains near equilibrium, $G \approx \varepsilon$. In this region U^+ deviates gradually from the log-law profile.

(3) *Free-surface region* ($0.6 < y/h < 1.0$). The turbulent structure in this region is governed by the outer variable, with the length scale being the flow depth, h, and the velocity scale being the maximum mainstream velocity u_{max}. Owing to the damping of turbulence by the free-surface, the dissipation rate exceeds the generation rate. Therefore, turbulent energy must be supplied from the wall region to the free-surface by turbulent diffusion.

Both the intermediate and free-surface region are collectively known as the outer-region.

2.3.2 The Velocity Defect Law and Cole's Wake Function

The log-law proposed by Kuelegan (1938) was initially used to describe the velocity distribution throughout the depth of open-channel flows. It has since been shown that the log-law is only valid in the wall region. The deviation of the flow from the log-law could be accounted for by introducing a wake function, as was introduced by Coles (1956) for boundary layers, and not by altering the values of von Karmans constant, κ, and the constant, A, in equation 2.26.

From experiments, Coleman (1981) extended equation 2.26 to suit the profile in the outer region of the flow, whereby the deviation in the outer region is best described by a wake function $w(\xi)$:

$$\frac{u}{u_*} = 5.75\log(\frac{u_* y}{\nu}) + 5.5 + w(\xi) \qquad \textbf{Equation 2.28}$$

where:

$$w(\xi) = \frac{2\Pi}{\kappa}.\sin^2(\frac{\pi}{2}.\xi) \qquad \textbf{Equation 2.29}$$

This function being the same as that introduced by Coles (1956) for boundary layers. In equation 2.29, Π is the Coles parameter expressing the strength of the wake function. From their experimental data, Nezu and Rodi (1986) found this parameter to have a value of 0.2 in open-channel flow. Xinyu *et al* (1995) concluded from their results that the value of the Coles parameter, Π, was closer to 0.3.

Although several empirical formulae have been proposed for the outer region (e.g. Sarma et al, 1983, Coleman and Alonso, 1983), Cole's wake function has proven to be the most acceptable extension of the log-law. A formula for the velocity defect law is obtained from equations 2.28 and 2.29:

$$U^+_{\max} - U^+ = -\frac{1}{\kappa}\ln\left(\frac{y}{h}\right) + \frac{2\Pi}{\kappa}\cos^2\left(\frac{\pi y}{2h}\right) \qquad \textbf{Equation 2.30}$$

where, $U^+_{\max} = u_{\max} / u_*$.

If Π=0, then equation 2.28 reduces to the usual defect law, and therefore, Cole's parameter describes the deviation from the log-law in the outer-region.

2.3.3 Free-Surface Effects

In turbulent flow, the eddies which are generated impinge on the water surface, causing a slight upward deflection of the free-surface. This generates an excess hydrostatic pressure which pushes back the eddies, and hence the vertical turbulent motion is damped by the presence of the free-surface (Celik and Rodi, 1984). This phenomenon is similar to the effect when the eddies impinge on solid walls, however, the process in this situation is complicated by the presence of shear forces. It has been shown by Thomas and Hancock (1977) that when a solid boundary moves at the same velocity as the adjacent turbulent fluid, there is no velocity gradient or shear stresses generated, and the situation developed is similar to that of a free-surface.

2.3.4 General Developments

From extensive research in wide rectangular open-channels many general conclusions have been established. The flow is symmetrical about the vertical plane equi-distant from the two side-walls of the flume, with each half-section being divided into two regions, one in the central portion of the channel, and the other in the vicinity of the wall. This central region exists for channels of aspect ratio greater than approximately 5-10 (De Brederode and Bradshaw, 1972; Berbee and Ellzey, 1989), where the aspect ratio, A_r is defined as the ratio of the width, B, to the depth, h. The vertical velocity curve in the central region of the flow is logarithmic from the surface to a point very close to the floor, with each curve appearing to be identical over the width of the central region (Tracy and Lester, 1961).

Another feature which is widely documented is the phenomenon of *dip*, defined as the ratio of the depth below the free surface where maximum velocity occurs in the vertical section to the total depth of flow in the channel. This feature is normally associated with turbulent flow through a rectangular open-channel of small aspect ratio, where the maximum velocity does not occur at the free surface, however, it can also feature in profiles in the vicinity of side-walls for flow in wide open-channels (Tracy and Lester, 1961). Steffler *et al* (1985) also describe this feature near the side wall, where the velocity profiles were found to drop off from the log-law line, thereby exhibiting a significant dip in the velocity profile near the water surface, characteristics also described by Sarma *et al* (1983). Vanoni (1941) reported that in reference to two-dimensional channels, the logarithmic velocity distribution was justified by his data to be far below the free-surface. Similarly the maximum velocities occurred below the free-surface thereby exhibiting dip in the vertical profile.

A study into the velocity distribution for smooth rectangular channel flow with different aspect ratios was carried out by Steffler *et al* (1985). In this case, the measurements were recorded using LDA. It was found that the longitudinal velocity measurements in the viscous sub-layer were found to agree well with the linear form of the law of the wall. For values of the normalised distance, y^+, greater than about 30 in the central region of the channel, the mean velocity measurement agreed well with the logarithmic form of the law of the wall with the coefficient set of 5.75 and 5.5 for A/κ and C in equation 2.25a.

2.4 UNIVERSAL FUNCTIONS FOR TURBULENCE INTENSITIES

Two distinct methods have been utilised for investigating the turbulent nature of fluid flow. The first of these is the point or probe system, whereby a device is introduced into the flow to measure velocity fluctuations, allowing a picture of the flow to be gradually constructed from a series of point measurements. The more reliable of these measurement techniques being the hot-film anemometer (HFA) and laser-Doppler anemometry (LDA). The other method is particle image velocimetry (PIV), which uses image processing from still photographic recordings to obtain the (two-component, in-plane) instantaneous velocities of the flow. An important advantage of PIV is its ability to obtain spatial information about the properties of turbulence in time varying unsteady flows (Grant *et al*, 1992).

The first documented research into the measurement of all three components of turbulence intensity, u', v', and w', in open-channels was by Nakagawa *et al* (1975) using the method of HFA. Universal expressions for turbulence intensities, normalised with the friction velocity were later investigated for various values of Reynolds and Froude numbers in smooth open-channels. These findings were compared with results from pipe flows and closed-channel flows.

Nakagawa *et al* (1975) proposed a power-law distribution for u'/u_*, however, a more acceptable set of universal functions for u', v', and w' was proposed by Nezu (1977a). Based on the k-ε turbulence model, the following semi-theoretical relationships for turbulent energy and turbulence intensities were proposed (Nezu, 1977a):

$$\frac{k}{u_*^2} = D.\exp(-2C_k\xi)$$

Equation 2.31

$$\frac{u'}{u_*} = D_u.\exp(-C_k\xi)$$ **Equation 2.32**

$$\frac{v'}{u_*} = D_v.\exp(-C_k\xi)$$ **Equation 2.33**

$$\frac{w'}{u_*} = D_w.\exp(-C_k\xi)$$ **Equation 2.34**

where, k = turbulent kinetic energy $\equiv (u'^2 + v'^2 + w'^2) / 2$,

D, D_u, D_v, D_w and C_k = empirical constants,

$\xi \equiv y/h$.

These relationships were found to give a better fit in the intermediate region, $0.1 < y/h < 0.6$ than the power laws proposed by Nakagawa *et al* (1975). This region corresponds to the equilibrium region ($50 < y^+ < 0.6R*$) in which the turbulent energy production is approximately in balance with the viscous dissipation. The initial results taken by Nezu (1977) were obtained using hot-film anemometry and compared to pipe-flow data obtained by Laufer (1954) and Clark (1968). From these initial results, Nezu (1977) evaluated the following empirical constants for equations 2.31 - 2.34:

$C_k = 1.0$ $D = 4.78$ $D_u = 2.30$ $D_v = 1.27$ $D_w = 1.63$

These values proved to be independent of Reynolds and Froude numbers, and thus the following relationships were established:

$$\frac{k}{u_*^2} = 4.78\exp(-2y/h)$$ **Equation 2.35**

$$\frac{u'}{u_*} = 2.30\exp(-y/h)$$ **Equation 2.36**

$$\frac{v'}{u_*} = 1.27\exp(-y/h)$$ **Equation 2.37**

$$\frac{w'}{u_*} = 1.63 \exp(-y/h)$$

Equation 2.38

These results also confirmed the relation among wall turbulence intensities such that $u' > w' > v'$.

2.4.1 Damping Function Extension for Turbulence Intensity

The distributions of u', v' and w' in the near wall region ($y^+ < 50$) can in principle be obtained from a model that provides for bursting phenomena, but the resulting equations proved to be too complicated. It has been shown that the following expression can be applied to the viscous sub-layer:

$$\frac{u'}{u_*} = Cy^+$$

Equation 2.39

where, C = constant, found experimentally to be approximately equal to 0.3.

To obtain the distribution for u'/u_* in the near wall region ($y^+<50$), a semi-empirical formula using a damping function Γ was introduced (Nezu, 1977):

$$\frac{u'}{u_*} = D_u.\exp(-C_u.\xi)\Gamma + 0.3y^+(1-\Gamma)$$

Equation 2.40

where,

$$\Gamma = 1 - \exp(\frac{-y^+}{B})$$

Equation 2.41

In this expression, the damping coefficient B, has a value 10 (as opposed to $B = 26$ when used in van Driest's damping function for the u distribution in the near wall region) since the measurements taken by Nezu (1977) indicated that the u'-distribution has a maximum near $y^+ = 10$, implying that viscous effects on the u-fluctuations appear to be important only for $y^+ < 10$.

Nezu and Rodi (1986) measured in detail the distribution of turbulent intensity for the flow in a smooth bed flume with a two-dimensional LDA. Through the regression analysis of their experimental results and the data obtained by Clark (1968), Blinco and Partheniades (1971), Nezu (1977) and Steffler et al (1985), they obtained D_u=2.26 and C_u=0.88 which are similar to the values of D_u=2.30 and C_u=1.0 given earlier by Nezu (1977). Similarly, it was shown that D_v = 1.23 and C_v = 0.67.

2.5 FLOW SEPARATION AND REATTACHMENT

The boundary-layer concept, discussed in section 2.2.2, assumes a uniform pressure of the fluid outside the boundary-layer. There are, however, situations when the pressure varies in the direction of flow, which has subsequent effects on the fluid behaviour. The simplest model for describing this process was proposed by Prandtl, whereby the flow over a curved surface results in a change in the pressure gradient. Figure 2.9 illustrates this concept, where it is assumed that the radius of curvature is large compared with the boundary layer thickness, δ. The fluid accelerates as it deflects round the surface, until at point *B* the velocity just outside the boundary-layer is a maximum. The acceleration of the flow satisfies continuity, thereby the pressure at this point is at a minimum. The pressure gradient, *dp/dx*, from *A* to *B* is negative and the net pressure force on an element in the boundary layer is in the forward direction.

The acceleration of the flow reduces beyond *B*, therefore the pressure increases, and so the net pressure force on an element in the boundary layer opposes the forward flow. The fluid closest to the surface of the curve has less momentum than the fluid further away, and so this net pressure force affects the forward flow in this region the greatest. Eventually, the fluid close to the surface of the curve is brought to a standstill. The value of *du/dy* at the surface becomes zero, as illustrated at point *C*. Immediately downstream from this point, the fluid can no longer follow the contour of the surface, whereby it folds back on itself producing reversed flow, point *D*. This is caused by the reduction of velocity in the boundary layer combined with the positive (adverse) pressure gradient which opposes the forward direction of the flow. This phenomena is termed *separation*, and begins at the separation point, defined where $(du/dy)_{y=0}$ becomes zero. The line of zero velocity which divides the forward and reverse flow begins at the separation point, and is known as the separation streamline. The reverse flow produces large irregular eddies which dissipate energy as heat. This disturbed region can continue downstream for some distance.

Separation occurs with both laminar and turbulent boundary layers, however, laminar layers are more likely to separate than turbulent layers. This is because the increase in velocity with distance from the surface is less rapid in laminar layers, and therefore the adverse pressure gradient can more readily slow down the fluid close to the surface. Turbulent boundary layers can exist for longer with an adverse pressure gradient prior to separation, however, no matter what the flow type, the greater the adverse pressure gradient the sooner separation occurs. The boundary layer rapidly thickens, and the assumption that δ is small may no longer be valid (Munson *et al*, 1990).

This phenomena does not always readily apply to engineering problems in the form described above, however, separation can be induced both naturally and artificially as a result of abrupt or rapid changes in channel geometry.

2.5.1 Introduction to Backward Facing Step Flow

Investigations into the flow characteristics of separated flow has been extensive over the last two decades, primarily due to the increased computational power now available to researchers. This has provided the opportunity for direct comparison of both numerical and experimental data, and thus provided greater confidence in numerical models. One of the simplest methods adopted by researchers to initiate flow separation is the use of a backward-facing step (BFS), i.e. a sudden expansion in the channel geometry. This produces a flow downstream of the step characterised by viscous interaction between ordinary channel flow and a large recirculating region, bounded by the base of the channel, see figure 2.10. Due to the complexities involved in the numerical analysis of such flows, they were seldom investigated. The numerical modelling of the effects of free-surface flows has proved to be difficult in open-channel flow, and therefore most investigations on separated flow have been conducted in closed-channels, a process which has been replicated experimentally using both air and water as the fluid medium.

It has been widely documented that there are three main types of separated flows, namely laminar, transitional and turbulent (Chapman *et al*, 1957). Both the laminar and transitional cases are based upon the incoming flow prior to separation being laminar, however, in the laminar case, the flow remains laminar beyond reattachment, and in the transitional case, the flow becomes turbulent prior to reattachment. In the turbulent case, the boundary layer is turbulent prior to separation, and is by far the most common case encountered in engineering applications.

2.5.2 Defining Reattachment Length

One of the first detailed papers on this subject was published by Abbot and Kline (1962). In their investigation using a BFS, they identified flow separation at the BFS which reattached to the channel bed at some distance further downstream. This length is the time-averaged distance from the wall to where the flow adjacent to the wall is zero, whereby flow slightly upstream has a negative velocity, and flow immediately downstream has a positive velocity. Using different inlet conditions (i.e. the flow conditions immediately before the step), such as the turbulence intensity and boundary-layer thickness, the reattachment length, R_L, did not alter, and the subsequent turbulence measurements downstream of the step did not alter. They concluded that the turbulence generated in the free-shear layer is far greater than the turbulence levels located in the channel prior to separation, thus suggesting that the flow pattern is independent of the upstream effects.

The length of this reattachment point has received much attention, as it is one of the most important parameters characterising separated flow. It has been shown by Eaton and Johnston (1981) that the reattachment length is sensitive to Reynolds number, initial turbulence levels and streamwise pressure gradient. Near the reattachment, the local turbulence intensity and Reynolds stresses reach their peak values, which can be attributed to the impingement of the unsteady shear layer onto the step's floor.

From figure 2.10, it can be seen that the flow separates as it reaches the step, producing a separation streamline which reattaches at some point along the step floor. The normalised distance at which reattachment occurs is generally defined by x_S/H_S, where x_S is the distance along the step floor and H_S is the step height. For laminar flow, the value of x_S/H_S is found to increase directly with Reynolds number. In an experimental study undertaken in a closed-channel, Armaly *et al* (1983) found that the flow turned from laminar to transitional flow at Re>1250. At this stage, it was observed that the reattachment length suddenly decreased, and continued to decrease further with increasing Reynolds number. This continued until the turbulent state was achieved. A secondary recirculation zone was also found to develop on the upper wall for Re>500 (Armaly *et al*, 1983; Sohn, 1988). As indicated in figure 2.10, a second recirculation bubble along the step floor was also observed by Armaly *et al* (1983). This bubble had not been reported before in the literature, and no other evidence has been found to substantiate it. However, it appeared in the early transitional stage, where the reattachment length experiences a sudden drop in its magnitude and is believed to be caused by the development of vortex shedding at the edge of the step. An increase in Reynolds number, still

within the transitional range, leads to the disappearance of this separation bubble. Similarly, the secondary recirculation bubble at the upper surface was found to move upstream as the Reynolds number increases, before disappearing when the flow becomes turbulent. With increasing Reynolds number the flow becomes unstable and breaks down into a turbulent state. When this occurs, it has been found that the reattachment length stabilises at a length varying between 6-9 step heights.

The reattachment length can be defined as the point where the separated shear layer reattaches to the surface. Two methods have been used to measure the time mean reattachment points. The first is to obtain the point where the time-averaged velocity close to the wall is equal to zero. The second method is to establish the point along the base of the step floor where 50% of the surface flow moves upstream, i.e. positive velocity. These methods can be combined to achieve a mean reattachment point. This was the procedure adopted by Shih and Ho (1994), where it was found that the difference between the two established points was only 0.1 step heights. Ötügen (1991) adopted the same technique and observed that during long observations, both methods gave the same reattachment point.

2.5.3 Streamlines

A concept widely adopted for fluid motion analysis is the use of streamlines. In a steady flow, the particles passing through the same point will follow the same path, and its velocity vector is everywhere tangent to the path. The lines that are tangential to the velocity vectors throughout the flow field are called streamlines.

In a two-dimensional flow, the velocity and displacement vectors of a fluid at a point, together with their orthogonal components, produce a velocity triangle and displacement triangle, both of which are similar (see figure 2.11a). Therefore:

$$\frac{dx}{u} = \frac{dy}{v} = \frac{ds}{\mathbf{V}} \qquad \textbf{Equation 2.42}$$

where, dx, dy and ds are the longitudinal, vertical and orthogonal displacements respectively, and u, v and $\mathbf{V}$ are the longitudinal, vertical and orthogonal velocities respectively. This constitutes the equation of a streamline, and since the streamlines describe the pattern of the flow, they are labelled by a numerical system relating to the flow rate. Thus, let *aa* and *bb* be

two streamlines in a flow bounded by solid boundaries AA and BB (see figure 2.11b). If the streamline aa is denoted by ψ_a, which will be labelled by a numerical value representing the flow rate per unit depth between the boundary AA and the streamline aa, then,

$$\psi_a = Q_{Oc} \qquad \textbf{Equation 2.43(a)}$$

and, similarly,

$$\psi_b = Q_{Oe} \qquad \textbf{Equation 2.43(b)}$$

It follows that,

$$d\psi = \psi_b - \psi_a = Q_{ce} = udy - vdx \qquad \textbf{Equation 2.44}$$

and ψ, which is called the stream function, is given by,

$$\psi = \int udy - \int vdx \qquad \textbf{Equation 2.45}$$

Thus, the stream function which is constant along a streamline, depends upon position co-ordinates. Therefore, by using different values of ψ, various lines in the x-y plane can be plotted, each representing a streamline. Therefore,

$$\psi = f(x,y) \qquad \textbf{Equation 2.46}$$

and hence, the total derivative:

$$d\psi = \frac{\partial \psi}{\partial x} dx + \frac{\partial \psi}{\partial y} dy \qquad \textbf{Equation 2.47}$$

Comparing equations 2.44 and 2.47, the relationship between the stream function and the velocity components are obtained:

$$u = \partial \psi / \partial y \qquad \textbf{Equation 2.48(a)}$$

and,

$$v = -\partial \psi / \partial x \qquad \textbf{Equation 2.48(b)}$$

Since the value of a stream function represents the flowrate between a given streamline described by the stream function and a reference boundary, it follows that it must be constant for the given streamline in order to satisfy the continuity equation combined with the requirement of no flow across a streamline.

The use of streamlines for flow analysis in the expanded region of a BFS flow reveals the recirculating region, bounded by the upstream corner of the BFS and the separating streamline, ψ=0. This separating streamline can also be used to identify the reattachment length, i.e. where the streamline meets the channel bed. This method has been used in BFS flow investigations such as Etheridge and Kemp (1977), and Nakagawa and Nezu (1987), where the streamline ψ=0 impacted the channel bed at the same reattachment point as that defined by the longitudinal mean velocity method. In these studies, two-dimensional flow has been assumed, and the mean streamlines have been constructed from the profiles of the mean longitudinal velocity. Constant values of $\psi/(uH_s)$ are used to plot the normalised streamlines, where H_s is the step height (or any characteristic length) and ψ is the streamfunction:

$$\psi \equiv \int_0^y u dy \qquad \textbf{Equation 2.49}$$

2.5.4 Shear Layer Development

An important feature observed in the transitional and turbulent phase is the development of a turbulent free-shear layer. This occurs as the faster main channel flow shears across the top of the slower fluid contained within the primary recirculation area. It is characterised by high turbulent activity generated by shearing of the two flows along the separation streamline. This area of high turbulent activity convects downstream producing a turbulent plume which gradually dissipates as the flow recovers. It has been documented that the effects of this shear layer can still be measured at a distance of 50 step heights downstream of the reattachment point (Bradshaw and Wong, 1972).

The Reynolds stresses have been shown to reach a maximum within the shear layer, especially at points along the separation streamline. Etheridge and Kemp (1978) have shown that the Reynolds shear stress in the u-v plane increases rapidly with the distance from the step, x_S, up to a maximum value occurring near reattachment.

Due to the hydrodynamic instability of this free-shear layer, the flow develops finite amplitude oscillations. This produces vortices which are small at first and amplify as they convect downstream at rates appropriate to their wavelengths (e.g. see Betts, 1972; Ethembabaoglu, 1978), giving rise to fluctuations in the velocity at points within the shear layer. Perturbations over a wide range of frequencies develop as the flow separates. These take the form of wavy patterns which develop into vortices.

2.5.5 Plane Jet Considerations

Flow in a channel which suddenly experiences a vertical expansion behaves similarly to a jet of fluid entering a region of stagnant or slower moving flow. When the channel is wide and the flow is 2-dimensional, the type of jet which is generated in the expanded region is known as a plane jet. Assuming this jet has a large, or semi-infinite height, then the flow characteristics are as shown in figure 2.12.

The initial state of the fluid in the expanded region is treated as being stagnant and is the same type of fluid. The shearing action which develops at the interface of the velocity discontinuity between the oncoming flow and the stagnant region induces turbulence and accelerates the stagnant flow. This also results in a loss of momentum of the original jet. The expanding region of fluid affected by this exchange of momentum is known as the mixing layer, or free-shear layer. The thickness of this region increases with streamwise distance, x.

If b is the distance between u/u_O=1 and u=0.5u_O, then the curves for the velocity distribution of u/u_O vs Y/b are similar throughout the shear layer for any distance x (Rajaratnam, 1976). If Q_O is the initial flow rate before the expansion, and Q is the flow rate in the jet at any section along x, then the ratio Q/Q_O has been shown to be greater than unity, and increases with x. This occurs because the jet draws fluid into itself at its boundary with the stagnant fluid. This process is known as entrainment which has a velocity component, v_e. For plane turbulent shear layers, it has been shown that v_e=0.033u_O (Liepmann and Laufer, 1947).

The lines OA and OB which correspond to u/u_O=1 and u/u_O=0 respectively, can be defined as the edges of this mixing layer, and the line OC corresponds to u=0.5u_O. For a plane jet, where $\bar{b}$ is the thickness of the shear layer at any distance x, it has been shown that $\bar{b}$=0.263x. The distance,

b, which is measured from ϕ_1 is found to be equal to $0.115x$. These findings correspond to the angles α_1 and α_2 being equal to 4.8^{o} and 9.5^{o} respectively.

Also, if y_1 and y_2 are the normal distances of the inner and outer edges of the shear layer, it has been shown that:

$$\frac{y_1}{b_o} = 1 - \frac{\bar{x}}{b_o}\tan\alpha_1 \qquad \textbf{Equation 2.50}$$

$$\frac{y_2}{b_o} = 1 + \frac{\bar{x}}{b_o}\tan\alpha_2 \qquad \textbf{Equation 2.51}$$

2.5.6 The Coanda Effect

The above scenario for jet type flows can be related to the expansion region experienced in backward facing step (BFS) flows. In this case however, the presence of the channel bed has a significant influence on the developing jet. The process of entrainment has been discussed, however, as the jet migrates from the BFS, there comes a point as the inner edge of the shear layer approaches the channel bed. When the jet can no longer draw fluid into itself due to the presence of the wall, it is found that the jet draws downwards onto the surface as shown schematically in figure 2.13. This is known as the 'Coanda' effect, and the jet becomes a wall attaching jet.

The area of fluid trapped between the jet and the upstream corner of the BFS is recirculated by the shearing action of the initial jet and this slower moving fluid mass. The flow also reattaches onto the wall at a point where the flow streamline is equal to zero. This is known as the separation streamline, and the distance at which this reattachment occurs from the BFS is known as the reattachment length, R_L (see section 2.5.2).

Plane jet flow describes a jet entering a region of stagnant flow, however, in many cases the fluid in the expanded region will have an initial independent velocity, u_1, where $u_1 < u_O$. The shear layer which develops in this case is known as the plane compound shear layer. Once again, the velocity profiles at any distance x, have been shown to display similarity (Rajaratnam, 1976).

2.5.7 Shear Layer Thickness in BFS Flow

The plane jet mixing layer thickness has been described as the distance between u/u_O=1 and u/u_O=0 for any distance x downstream of the step. This same definition applies to BFS flow. Ötügen *et al* (1992) described the shear layer thickness in a BFS flow as:

$$\delta_w = u_o \; / \left|\frac{du}{dy}\right|_m$$

Equation 2.52

Where, δ_w - is the vorticity thickness,

u_O - is the mean upstream velocity, and

$\left|\frac{du}{dy}\right|_m$ - is the local maximum of mean velocity gradient.

This latter term relies on the assumption that the velocity gradient in the shear layer is nearly constant, and therefore a constant velocity gradient exists between u/u_O=1 and u/u_O=0. Ötügen *et al* (1992) found that the shear layer grows in a non-linear fashion and that this is due to the adverse pressure gradient and the streamline curvature. This investigation included the growth of the shear layer in the spanwise direction, where it was observed that the central channel section gave similar growth rates of the shear layer. However, closer to the sidewalls the shear layer was found to have an increased growth as a result of the secondary flow which develops between the flow and the sidewalls. In another investigation by Ötügen (1991), the shear layer thickness was examined with respect to different expansion ratios, defined as the step height to upstream channel height, H_s/h. It was observed that smaller expansion ratios have an initially larger relative shear layer thickness, however, as the shear layer develops the larger ratios displayed a more rapid growth.

2.5.8 Inlet Conditions

The flow conditions prior to the BFS have been investigated in many studies. The knowledge of these will serve as control conditions with which to compare the resulting mean velocities and turbulence intensities. Indeed, many researchers have found that the flow characteristics which develop behind a BFS are greatly influenced by the initial flow conditions. However, there are

many studies which contradict this, suggesting that the shear layer turbulence overrides the initial turbulence levels.

Abbot and Kline (1962) found that the initial turbulence levels in their closed channel was in the region of 1-2% of the mean stream velocity under normal conditions. By introducing turbulence inducers upstream of the step, turbulence intensities between 1-18% of the mean stream velocity were examined for their effects on the flow beyond the step. They concluded that there was no appreciable change in the length of reattachment under these varying inlet conditions.

Shih and Ho (1994) measured the spanwise distribution of the streamwise velocity components upstream of the step. It was observed that both the mean velocity and the turbulence intensity profiles demonstrated that the flow prior to separation was two-dimensional, except very close to the side-walls. The displacement thickness of the side-wall boundary layer was of the same order of magnitude as that of the boundary layer. This was found to be 3% of the channel width. In conclusion, the 3-dimensional distortion effect produced by the side-wall boundary layer was of no great significance.

2.5.9 Open-Channel BFS Flow

There is not much information in the literature regarding flow over a backward facing step for open-channels, one reason for this being the difficulty of modelling this type of flow numerically. Despite this, the flow characteristics are much the same as that which develop in closed-channel BFS flow, where the main flow feature is still the primary recirculation zone. Due to the free-surface, the secondary recirculation zone appearing in the closed-channel does not occur, and there is no evidence of the second recirculation zone which appeared along the bottom of the slot as documented by Armaly *et al* (1983).

2.5.10 Two-Dimensional Flow and Side-wall Contamination

The effect of the side-walls have been shown to influence the flow in rectangular open-channels. This also affects the flow over backward facing steps. De Brederode and Bradshaw (1972) showed that the flow is primarily two-dimensional away from the side-walls for an aspect ratio greater than 10. In a study by Berbee and Ellzey (1989) the effect of the spanwise width on the shear layer behind a BFS was investigated. Using aspect ratios of 4 and 10, defined as the

channel width/slot height, they concluded that both the mean velocity profiles and turbulence intensities were constant across the width, regardless of Reynolds number, suggesting that the flow is primarily two-dimensional.

A study by Ötügen and Muckenthaler (1992) focused on the influence of the expansion ratio on the separation shear layer structure and reattachment behind a BFS at the mid-plane. In a channel with a width/height aspect ratio of 10, and expansion ratio (defined as the ratio of the downstream flow depth to upstream flow depth) of 2, it was shown that the spanwise uniformity of mean flow is significantly distorted within a short streamwise distance of the step, and by reattachment the 2-dimensional characteristic of the mean flow is limited to a relatively small region at the channel mid-plane. It appeared that the steamwise vortex pattern growing along each side-wall causes this 3-dimensional flow behaviour. This originates at the junction of the side-wall and the corner of the step, growing along the streamwise direction inducing a secondary flow pattern. This causes a rapid growth of spanwise non-uniformity of the velocity with axial distance.

Ötügen (1991) investigated the behaviour of the turbulent separated shear layer and subsequent reattachment downstream of a BFS. By varying the step height-to-upstream channel height ratio whilst maintaining the inlet conditions, this study showed that when the expansion ratio increased, there was a corresponding increase in turbulence intensity, particularly at the initial stage of separation. The increase in turbulent diffusion leads to a faster increase in the shear layer growth. Due to this increased growth of the shear layer thickness, the shear layer impinges on the channel bed at a shorter distance from the step. It was observed that this shear layer impinged the channel bed at a distance equivalent to the reattachment length obtained from the mean velocities. Ötügen goes on to say that it is unlikely that the reattachment length is a direct influence on shear layer turbulence, but rather it is a consequence of this increased turbulence activity.

The spanwise reattachment lengths were also investigated. In the central region of the channel, the reattachment lengths were shown to be uniform. Close to the side-walls, the reattachment length decreased. This is attributed to the higher shear layer turbulence measured near the walls upstream of reattachment, where complex 3-dimensional effects are to be expected due to the interaction between corner flow and boundary layer effects.

Isomoto and Honami (1989) showed that an increase in turbulence intensity prior to separation led to reduced reattachment lengths. It would therefore appear that the initial turbulence

intensity and the high turbulence intensities developed in the shear layer amalgamate, producing an increased shear layer growth.

Ötügen *et al* (1992) observed that the shear layer grows in a non-linear fashion, with larger shear-layer growth rates at increasing distance from the channel mid-plane, and likewise the difference in the growth rate is stronger at larger streamwise distances. In general, both the mean velocities and turbulence intensities have a spanwise uniformity limited to a central region of the channel.

Bhattacharrjee *et al* (1986) investigated the coherent flow structures which develop in the shear layer. In a channel with an aspect ratio of 16.24, similar coherent structures were found to extend across the entire span of the channel.

Shih and Ho (1994) have shown that the flow in the immediate vicinity of the step is highly 3-dimensional. As a result, the reattachment length was less in the centreline and greater towards the side-walls. Reattachment lengths as low as 4.3 step heights were observed in the centreline, which were approximately 20% shorter than those at the side-walls. In this study however, the aspect ratio of the channel was 3, and therefore this observation may only apply to narrow channels. Another observation made in this study, was the development of two counter rotating vortices in the horizontal plane immediately downstream of the step. This is likely to be attributed to the 3-dimensional secondary flows from both side-walls converging together.

2.5.11 Lateral Expansion Studies

Similar investigations have also been undertaken for lateral expansions as opposed to vertical expansions. Such flows can be of interest in understanding the cross-shear flows which develop in harbours and behind islands. A study by Babarutsi *et al* (1989) investigated the effect of bed friction on the reattachment length in such a flow. Flows where the horizontal length scale of the flows are two orders of magnitude larger than their depths are called shallow recirculating flows. In general, this study showed that when the flow depth was high, and hence the bed-shear had little influence on the flow, the reattachment length was comparable to BFS flows. As the flow depth reduced, there was an increase in the influence of the bed shear, resulting in a reduction in reattachment length, this being comparable to the flows near side-walls in BFS flows.

2.5.12 Forward Facing Step (FFS) Flow

The study of flow over forward facing steps (FFS) has received less attention to that of the BFS. Bradshaw and Galea (1967) report that the flow approaching a FFS experiences separation, and that in their investigation, flow separation occurred 1.2 step heights upstream of the step. The increase in turbulence intensity up to separation was found to be very small, and was attributable to low-frequency unsteadiness of the separation point. The flow approaching a FFS was also investigated by Dimaczek *et al* (1989), where it was observed that the flow in the region up to 1.5 step heights upstream of the FFS was 3-dimensional, and concluded that these effects were not created by side-wall effects.

2.6 OPEN-CHANNEL SLOT FLOW

Backward facing step flow is well documented in the literature, and that for a forward facing step has also been covered, however, the condition does arise when the flow undergoes a rapid expansion in channel geometry, i.e. BFS, followed by a sudden contraction, i.e. FFS. If these sudden changes are relatively close, i.e. the flow effects of one interferes with the other, then the resulting flow condition is that of a *slot* (also called cavity and trench). Conversely, if the FFS precedes the BFS, then the condition is that of a surface mounted obstacle.

For slots, there are several flow phenomena that can be generated, depending upon the flow conditions and the size of the slot. Figure 2.14 illustrates the type of flow characteristics that can develop in slot flow.

When the aspect ratio, A_s (defined as the length of the slot, L_S, divided by the height of the slot, H_S), is small (i.e. less than 5), the type of flow experienced is that illustrated in figure 2.14 (a), whereby a recirculating eddy dominates the slot region which is driven by the main flow with no reattachment within the slot. When the aspect ratio is increased to values greater than about 10, then the type of flow generated is like that illustrated in figure 2.14 (b), which is not dissimilar to that experienced in BFS flow. In this case, the separation streamline reattaches somewhere along the base of the slot, producing a primary recirculation zone, again driven by the faster moving main channel flow. The flow beyond the reattachment point continues along the slot until it is rapidly accelerated over the forward facing step. When the flow encounters the top of the FFS, it separates, reattaching to the channel bed at a small distance downstream. This produces a

smaller recirculation zone than that observed in the slot, and will be referred to as the secondary recirculation zone.

The interaction of the main flow and the slower moving primary recirculating region generates a separated shear layer. Depending on the aspect ratio of the slot, the flow will begin to overcome the effects of the BFS and relax towards the thin-shear layer state (Bradshaw and Wong, 1972), whereupon the velocity distribution will attempt to settle to normal flow conditions and the high level of turbulence will dissipate. As the flow progresses downstream, whether it has recovered or not, it will eventually come under the influence of the FFS. High velocities and turbulence activity is generated as the flow separates at the top of the FFS, producing a secondary recirculating zone and a secondary shear layer.

The distance at which the primary separation streamline reattaches itself to the main flow has been found to occur in the slot at a length of approximately 7 slot heights, which is the same as that observed in the case of backward-facing steps. However, Manson (1994) suggests that in some cases, reattachment does not occur until 10 slot heights, due to interference by the FFS.

2.7 SUMMARY

The fundamental flow characteristics required for this investigation have been presented. It is clear that rectangular open-channel flow is the basic flow type for this research, as it can be used to describe the initial flow conditions prior to separation, and the development of the flow beyond reattachment.

Although there are similarities between closed-channel flow and open-channel flow, the latter has not been examined to the same degree as the former, primarily due to the difficulty in analysing open-channel flow numerically. However, it is clear from the literature that similarities do exist.

From the literature review, the following points are highlighted as they are pertinent to this study.

2.7.1 Open-Channel Flow

(1) Turbulent flow is characterised by a mean velocity, u, and fluctuating velocity component, u', in the streamwise direction, x.

$$U = u + u' \qquad \textbf{Equation 2.4}$$

and similarly for the vertical and lateral directions, y and z respectively:

$$V = v + v' \qquad \textbf{Equation 2.5}$$

$$W = w + w' \qquad \textbf{Equation 2.6}$$

The fluctuating component, u', is converted to a root mean square value, $\sqrt{\overline{u'^2}}$, to describe the magnitude of departure from the mean value u. The value, $\sqrt{\overline{u'^2}}$ / u, is the relative intensity of turbulence.

(2) An equation describing the vertical velocity distribution was proposed by Nikuradse for pipe flow. Using Bazin's (1865) data, Kuelegan (1938) verified that the pipe-flow equation could also be used to describe a large proportion of the vertical velocity distribution in open-channel flow. This is known as the log-law equation:

$$\frac{u}{u_*} = 5.75\log(\frac{u_* y}{\nu}) + 5.5 \qquad \textbf{Equation 2.26}$$

(3) Further investigations in open-channel flow revealed that the flow field could be sub-divided into three distinct regions, these being:

(1) *Inner* or *Wall Region* ($0 < y/h < 0.2$)

(2) *Intermediate, or wake region* ($0.2 < y/h < 0.6$).

(3) *Free-surface region* ($0.6 < y/h < 1.0$).

Both the intermediate and free-surface region are collectively known as the outer-region.

(4) In the outer region, U deviates gradually from the log-law profile. Using Coles wake function, Coleman (1981) extended the log-law equation to describe the flow in this outer region:

$$\frac{u}{u_*} = 5.75\log(\frac{u_* y}{\nu}) + 5.5 + w(\xi) \qquad \textbf{Equation 2.28}$$

where $w(\xi)$ is described by the function:

$$w(\xi) = \frac{2\Pi}{\kappa}.\sin^2(\frac{\pi}{2}.\xi) \qquad \textbf{Equation 2.29}$$

(5) The flow in a channel is found to be symmetrical about the centreline. For wide open-channels, there exists 2 different regions. The first is a central region characterised by 2-dimensional flow, and the other is the side-wall region which has 3-dimensional characteristics. Although many different investigations have resulted in different definitions of wide channels, it appears that a width/depth aspect ratio greater than 10 would ensure a central 2-dimensional region, however, many investigations have shown that a central 2-dimensional region exists in channels with an aspect ratio of 5.

(6) In the central 2-dimensional region, the velocity profile is described as being logarithmic from the surface to a point very close to the floor, with each curve being identical across this central region.

(7) The velocity profile in the side-wall region is characterised by a phenomena known as *dip*. This is defined as the ratio of the depth below the surface where maximum velocity occurs. This phenomena has also been observed in rectangular channels of low aspect ratio.

(8) A universal set of equations has been given which describes the vertical distribution of the turbulence intensities, u', v', and w', in open-channels (Nezu, 1977). These are:

$$\frac{u'}{u_*} = 2.30\exp(-y/h) \qquad \textbf{Equation 2.36}$$

$$\frac{v'}{u_*} = 1.27\exp(-y/h) \qquad \textbf{Equation 2.37}$$

$$\frac{w'}{u_*} = 1.63\exp(-y/h)$$

Equation 2.38

(9) For the streamwise turbulence intensity, u', the distribution for u'/u_* in the near wall region ($y^+<50$), is better described using a damping function Γ (Nezu, 1977):

$$\frac{u'}{u_*} = D_u.\exp(-C_u.\xi)\Gamma + 0.3y^+(1-\Gamma)$$

Equation 2.40

where,

$$\Gamma = 1-\exp(\frac{-y^+}{B})$$

Equation 2.41

In this expression, the damping coefficient B, has a value 10.

(10) There are several methods described in the literature for obtaining the value of the friction velocity, u_*. One of the simplest methods is the use of the channel slope under the conditions of normal and uniform flow, i.e. $dh/dx = 0$, whereby:

$$u_* = \sqrt{gRS}$$

Equation 2.27

Nezu (1977a) reported that comparing this method with the log-law equation and the Reynolds stresses produced values of u_* within 30% of each other. Using LDA measurements, Nezu and Rodi (1986) showed that these methods gave values of u_* within 5% of each other.

2.7.2 Backward Facing Steps and Slot Flow

The backward facing step has been widely used by researchers to induce flow separation. Much of the earlier research used closed-channels in the investigation of BFS flow, owing to the numerical analysis of such flows being easier than their open-channel counter-part, and that many testing rigs used air and not water as the flow medium. Despite this, the findings have proven to be a valuable source of reference and information for the condition of open-channel BFS flow.

The following general points about turbulent open-channel BFS and slot flow have been covered in this chapter:

(1) A shear layer develops when a flow separates at a BFS, characterised by high turbulence intensities. The separated shear layer impinges the channel bed, at a point which is characterised by the highest turbulence intensities and Reynolds stresses. The production of turbulent energy ends at this point, and the turbulent flow begins to dissipate as it convects downstream.

(2) The point at which the shear layer impinges the channel bed, is also characterised by redevelopment of the streamwise mean velocity. The streamline between the separation point and this reattachment point, is know as the separation streamline, and the distance at which reattachment occurs from the BFS is known as the reattachment length.

(3) For fully-developed turbulent flow, the reattachment length is normally between 5-9 step heights downstream of the step.

(4) The reattachment length can be determined experimentally as the point where 50% of the surface flow moves upstream. This has been shown to be the same as the point of zero mean streamwise velocity at a small distance above the channel bed.

(5) In wide channels, a central 2-dimensional region exists which exhibits similar reattachment lengths. Like rectangular channel flow, the side-walls produce an increase in turbulence activity. This increases the growth rate of the shear layer, and hence, it impinges the channel bed at a shorter distance from the step (i.e. shorter reattachment length).

(6) The flow over forward facing steps experience a separation at a short distance upstream of the step. Although there is not much in the literature for this flow condition, the distance at which this occurs is somewhere between 1.2-1.5 step heights.

(7) There exists two main flow types over a slot. For a slot aspect ratio less than 5, a single recirculation vortex dominates the slot. When the slot aspect ratio increases to values greater than about 10, the flow develops much the same as that in the BFS flow configuration, characterised by a single recirculation cell with a separation streamline with it's associated reattachment length. It is unknown if the FFS has any effect on the reattachment length, although it has been speculated (Manson, 1994).

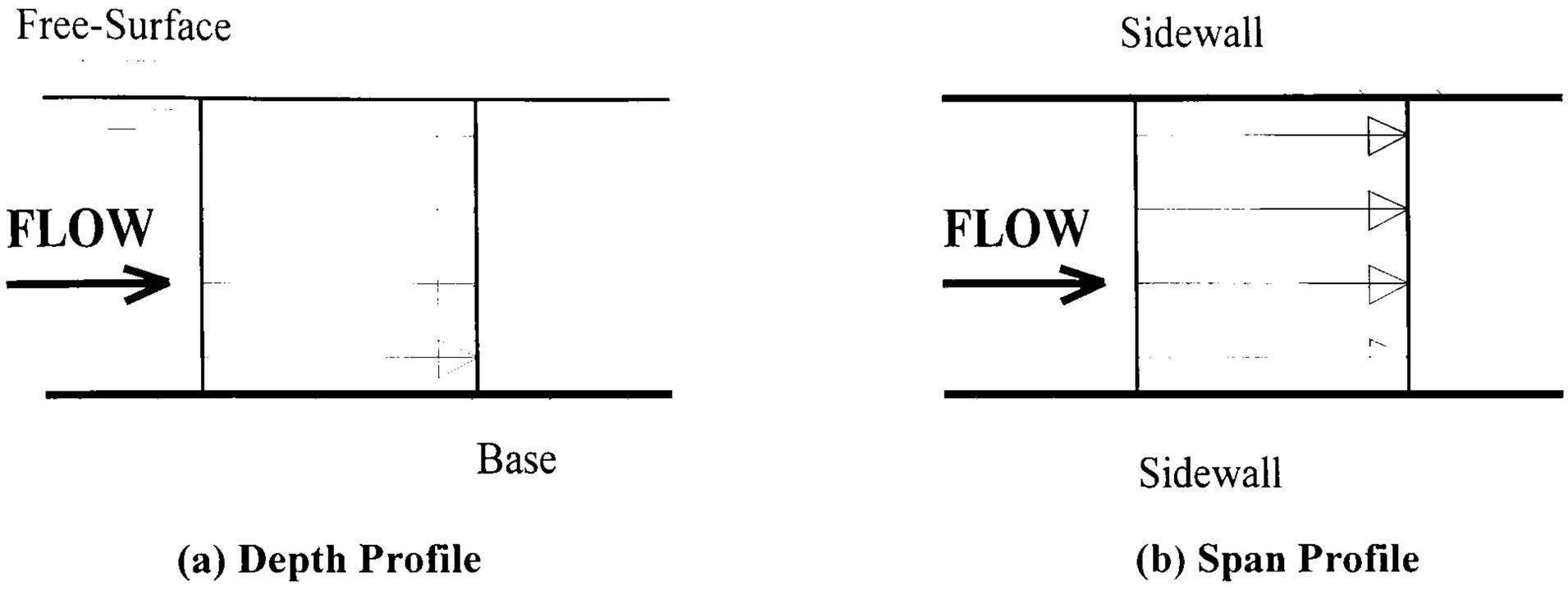

(a) Depth Profile **(b) Span Profile**

Figure 2.1 - Ideal Flow Conditions

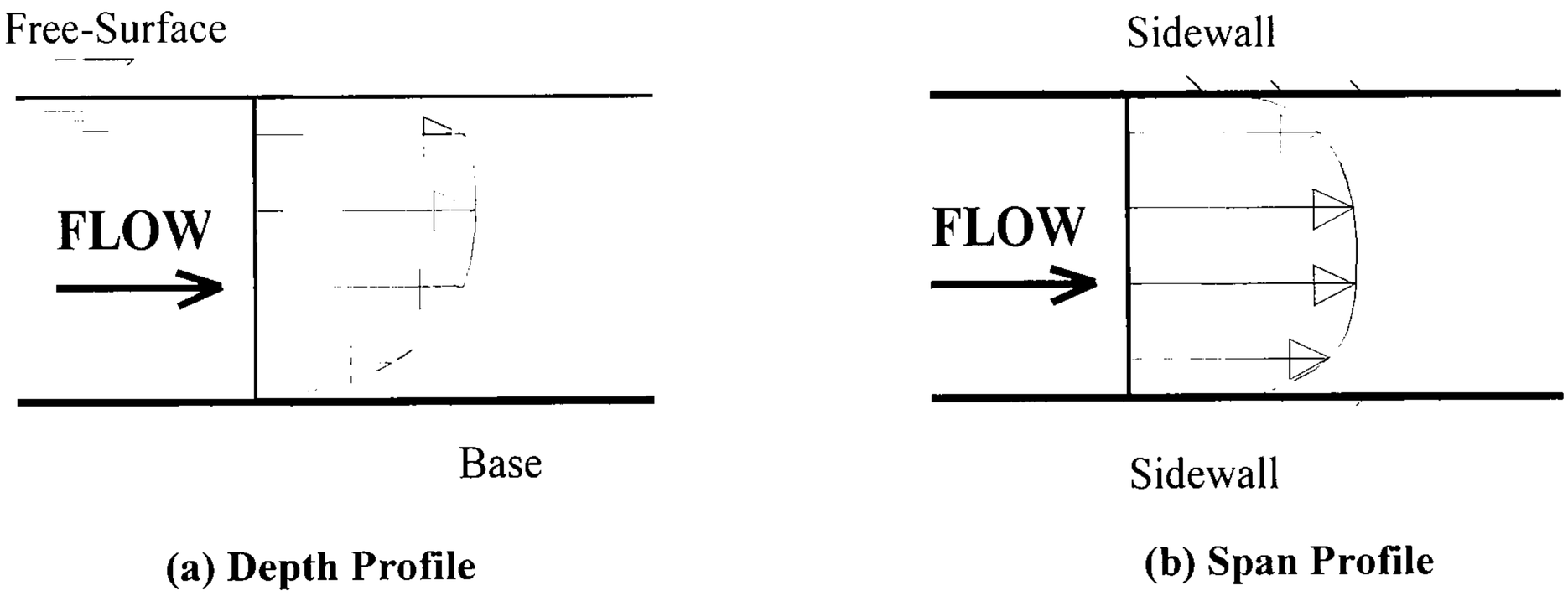

(a) Depth Profile **(b) Span Profile**

Figure 2.2 - Real Flow Conditions

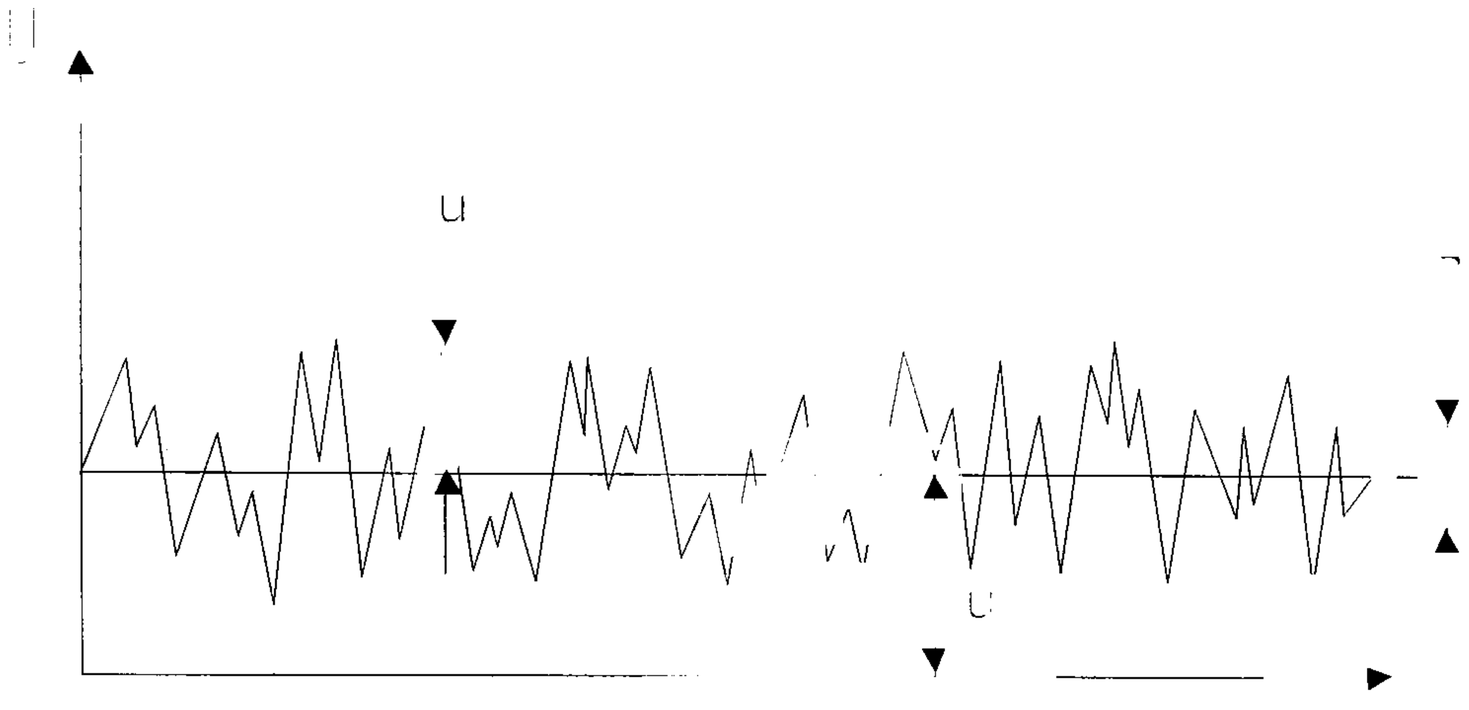

Figure 2.3 - Velocity Fluctuation Taken at a Point in Space

$$\sigma = \sqrt{\overline{u'^2}}$$

$$P(u') = \frac{1}{\sqrt{2\pi\sigma^2}} e^{-(U-u)^2/2\sigma^2}$$

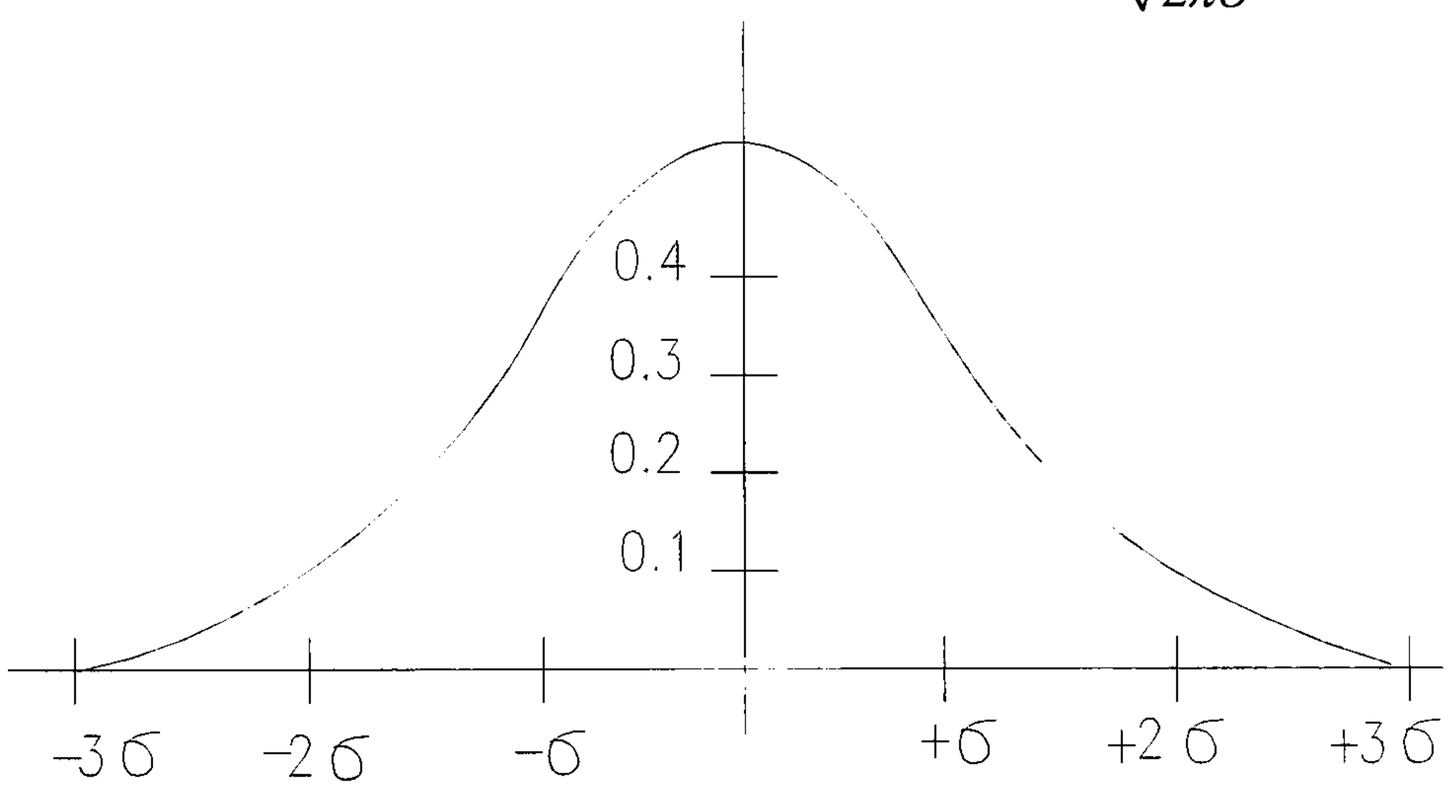

$(U-u) = u'$

Figure 2.4 - Typical Gaussian Probability Distribution Function

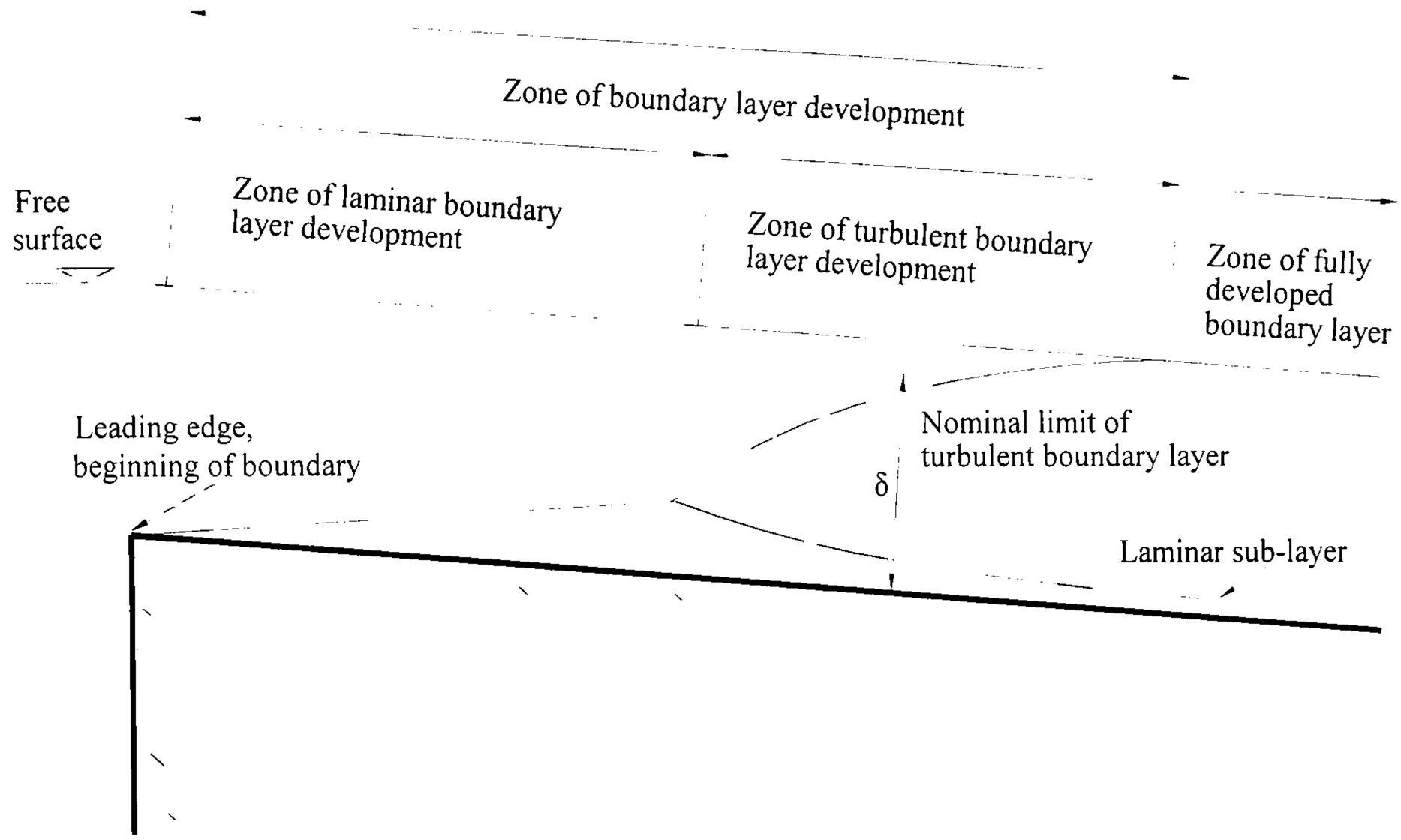

Figure 2.5 - Stages of Boundary Layer Development

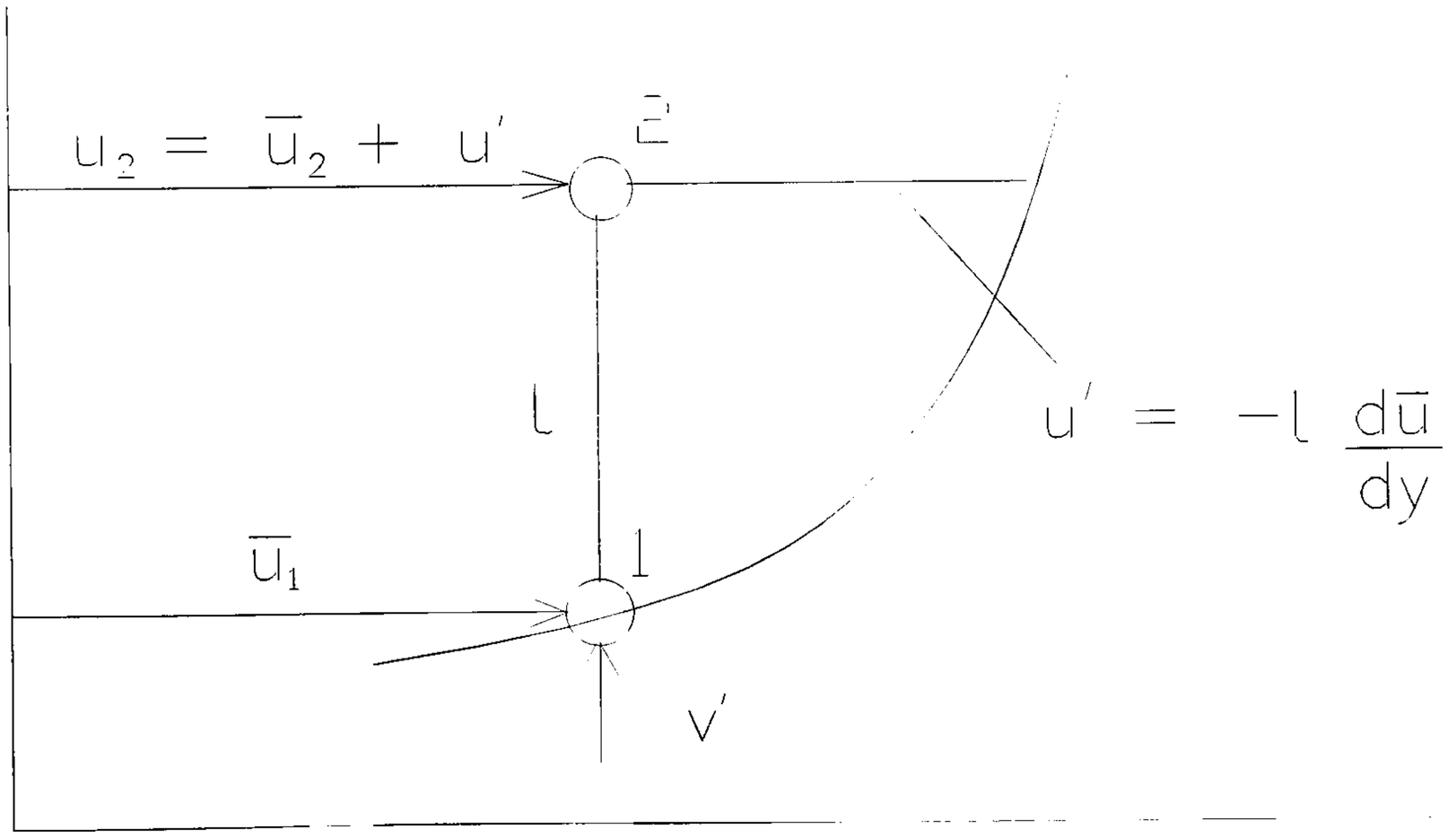

Figure 2.6 - Turbulent Mixing Length and Velocity Fluctuation

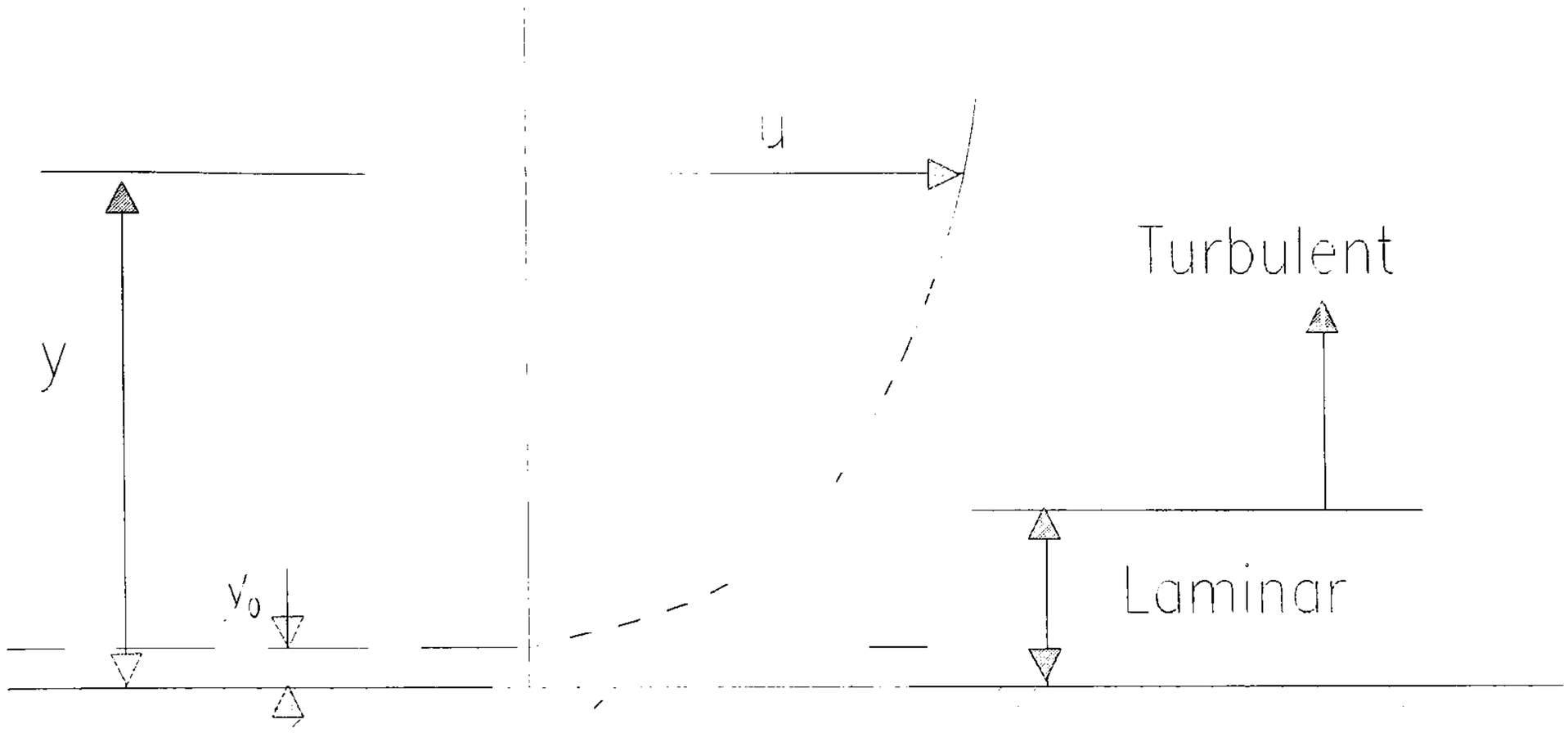

Figure 2.7 - Boundary Condition

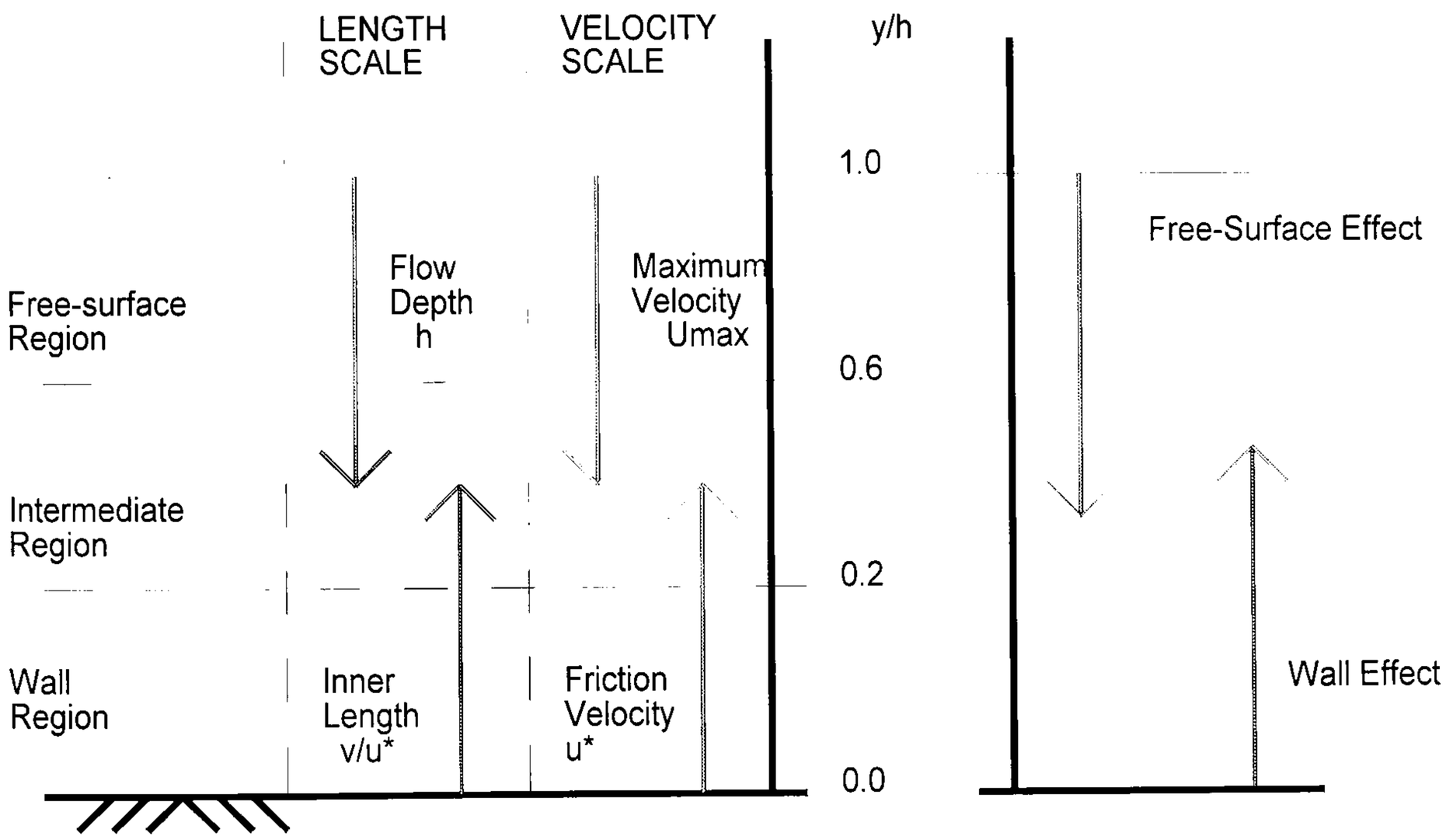

Figure 2.8 - Sub-Division of the Open-Channel Flow Field

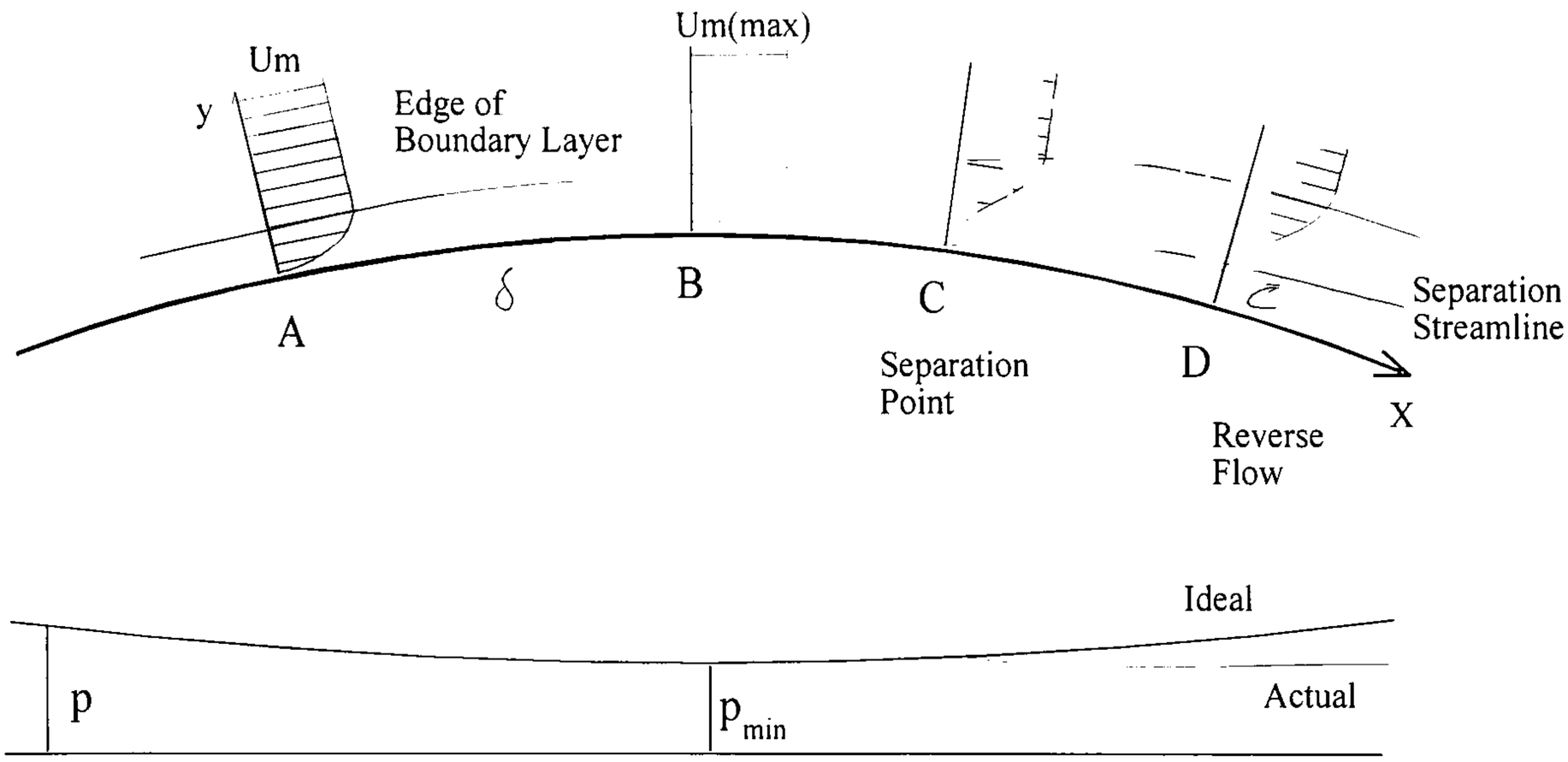

Figure 2.9 - Prandtl's Model of Separation

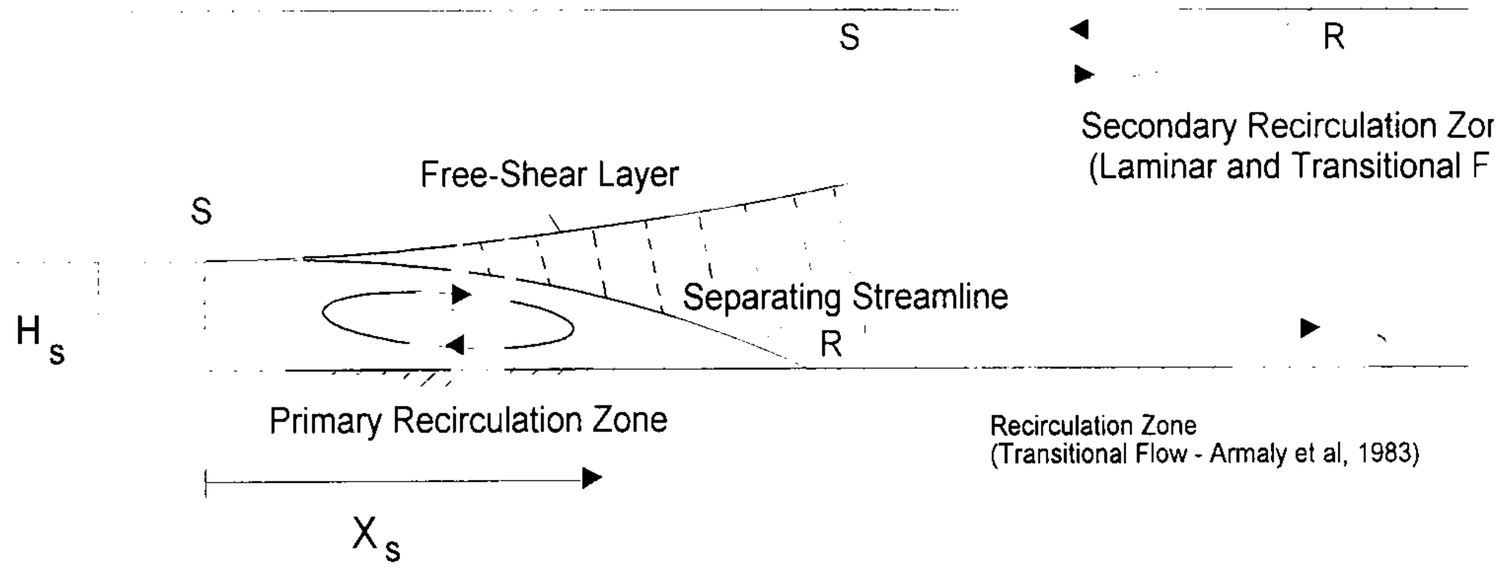

Figure 2.10 - Characteristics of BFS Flow in a Closed Duct (Armaly et al, 1983)

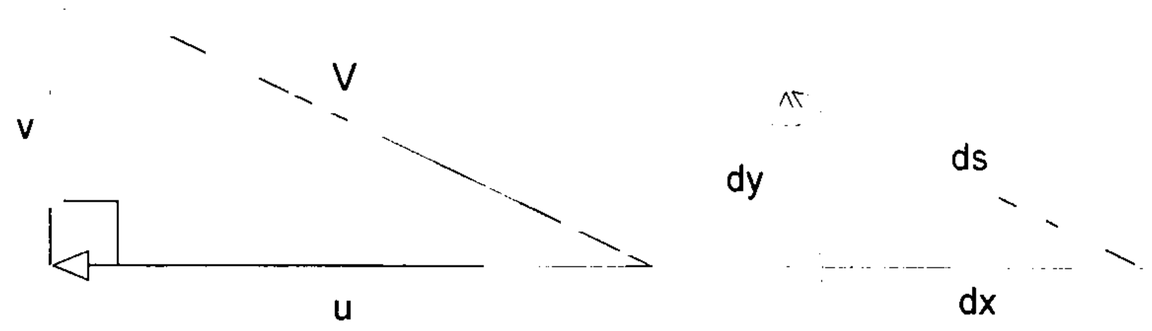

(a) Velocity and Displacement Components

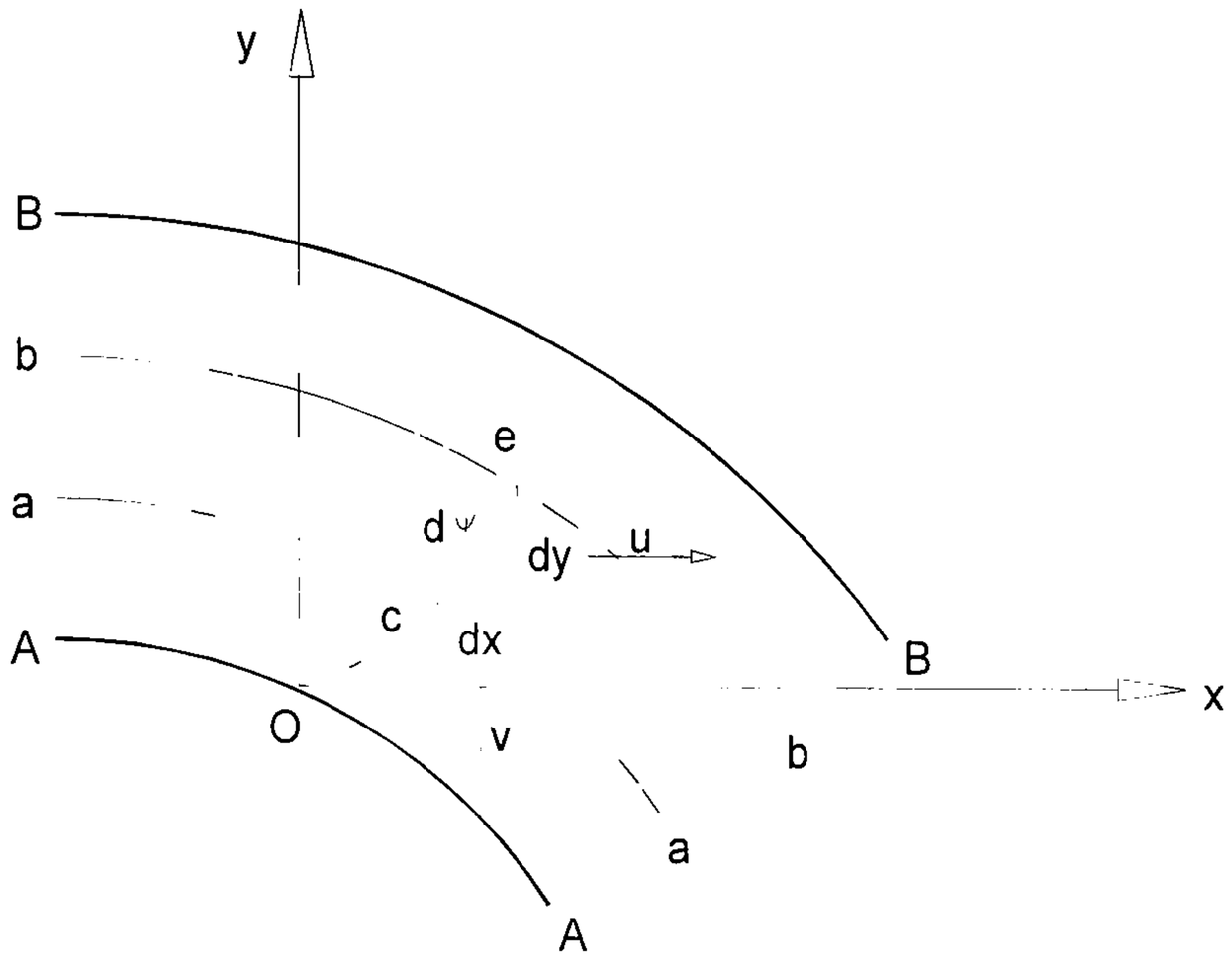

(b) The Stream Function

Figure 2.11 - Streamline Definition

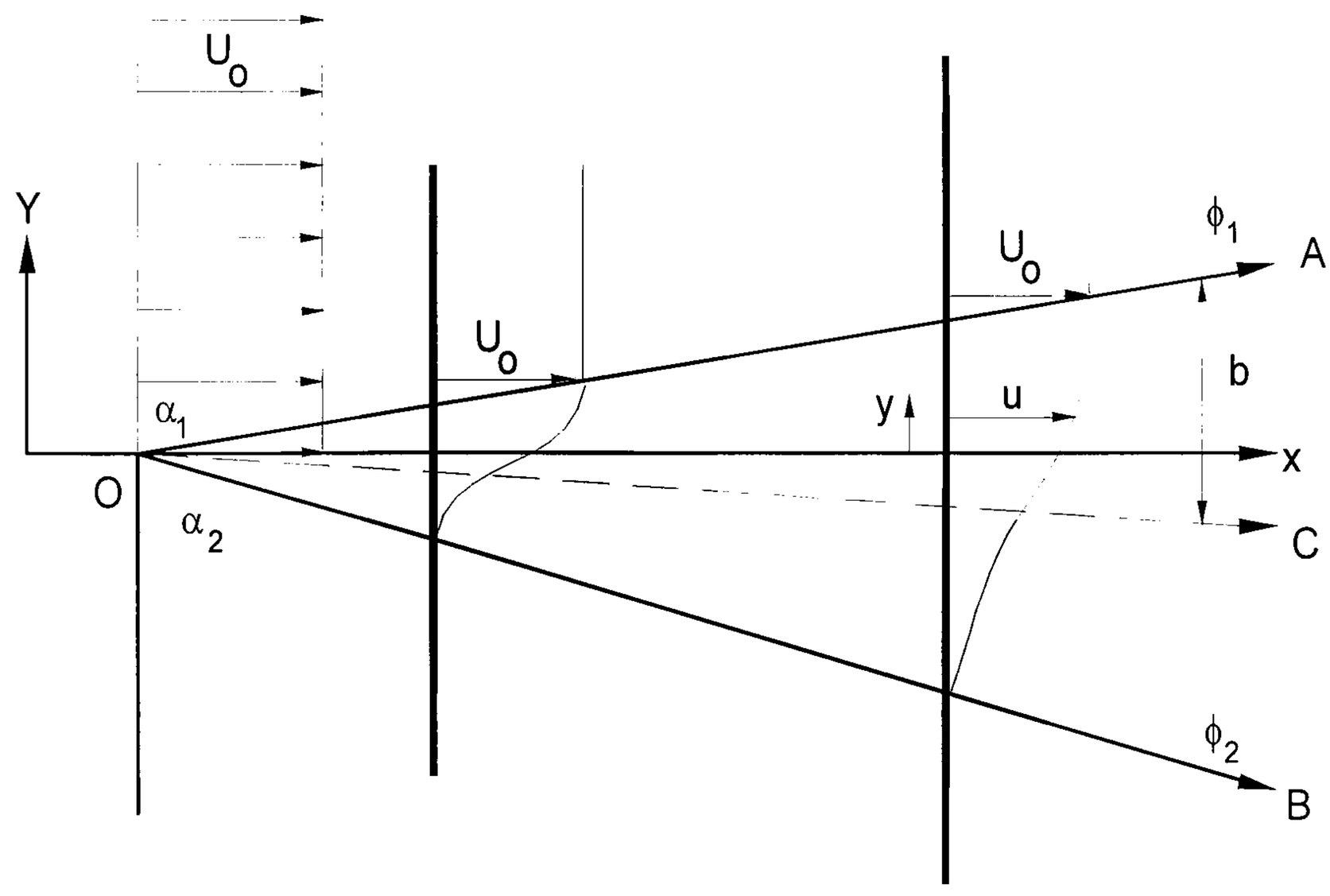

Figure 2.12 - Schematic Representation of a Plane Shear Layer

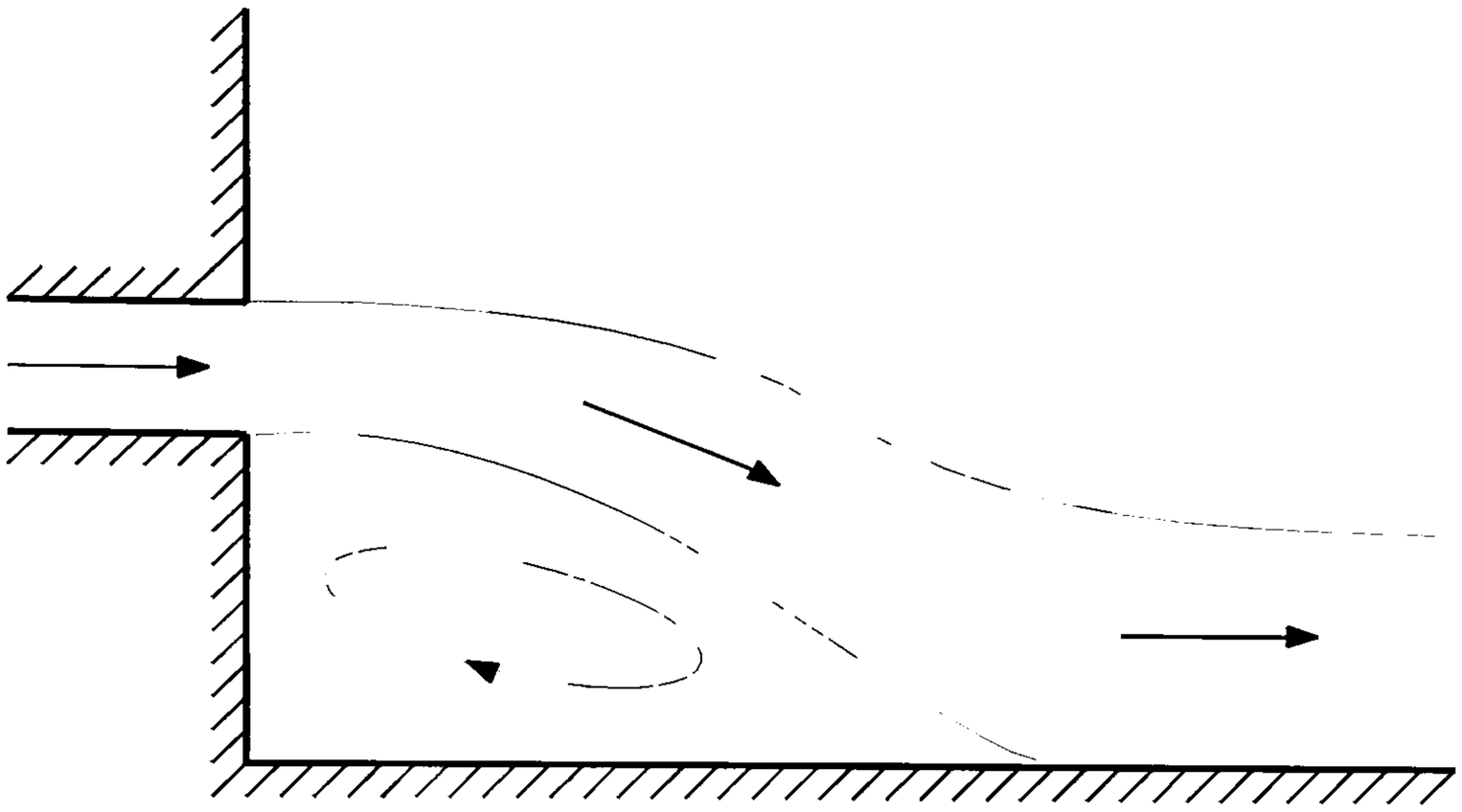

Figure 2.13 - Wall Impinging Jet (Coanda Effect)

(a) Slot Flow: Small Slot Aspect Ratio

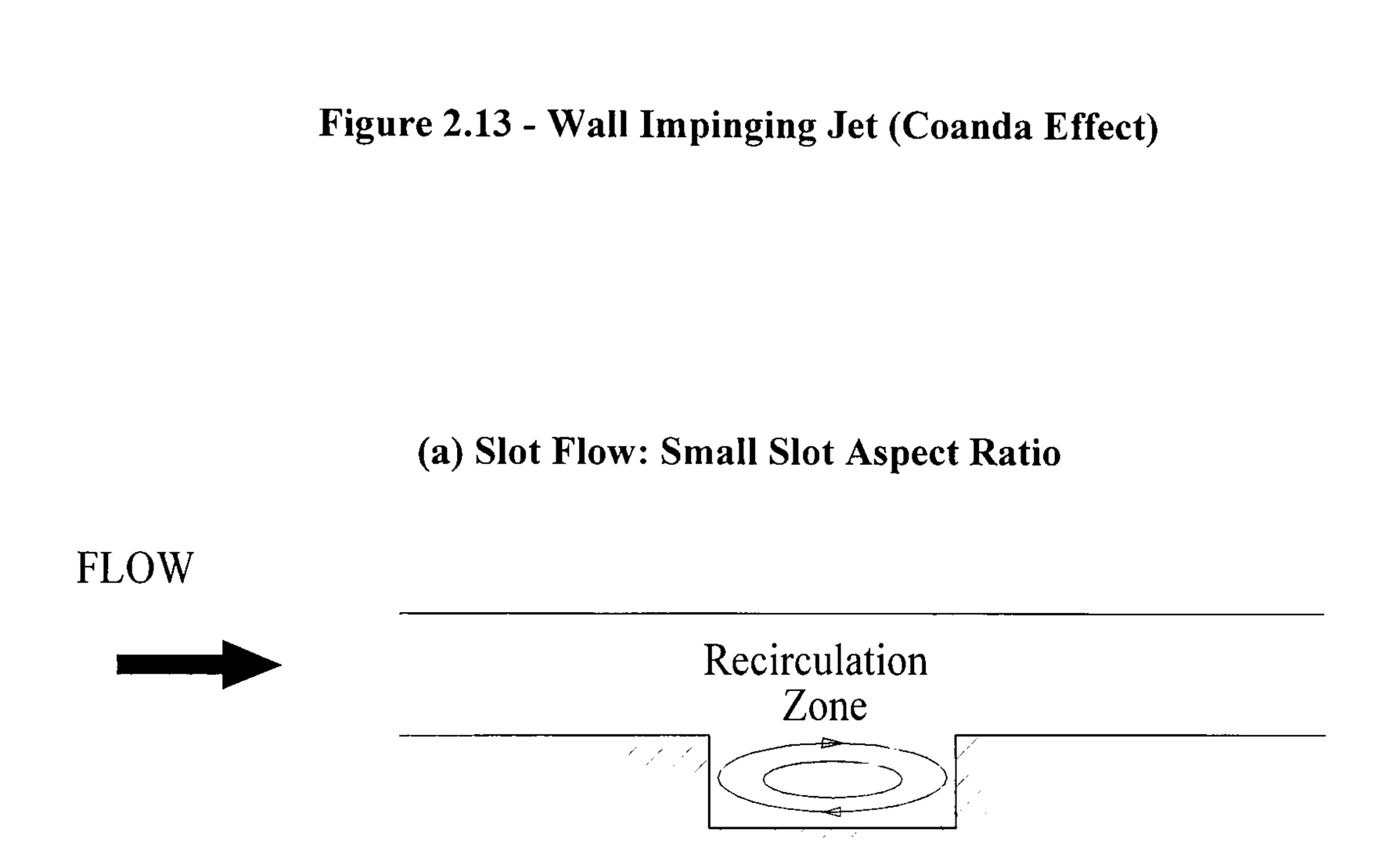

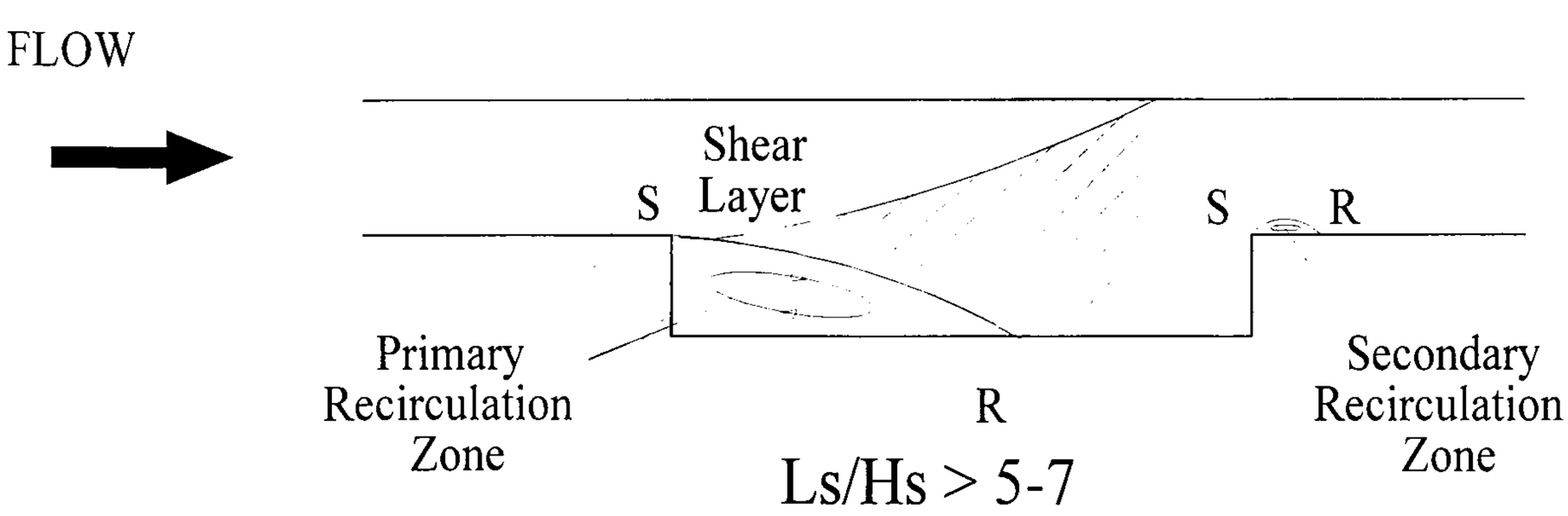

(b) Slot Flow: Large Slot Aspect Ratio

Figure 2.14 - Slot Flow Characteristics

CHAPTER 3

EXPERIMENTAL APPARATUS

3.1 INTRODUCTION

3.2 LDV SYSTEM

3.1.1 Introduction
3.2.2 FlowLite Integrated Laser-Optics Unit
3.2.3 Laser Beam Refraction Correction
3.2.4 Flow Velocity Analyser (FVA)
3.2.5 Back-up Software - Floware

3.3 LASER PROBE SUPPORT-TRAVERSE SYSTEM

3.3.1 Introduction
3.3.2 Probe Support-Traverse Criteria
3.3.3 Laser Probe Support-Traverse Design
3.3.4 Alterations for Main Investigation

3.4 EXISTING LABORATORY FLUME

3.4.1 Introduction
3.4.2 Flume Details
3.4.3 Slot Installation

3.5 MAIN FLUME DESIGN

3.5.1 Introduction
3.5.2 Flume Channel Details
3.5.3 Channel Support Frame
3.5.4 Main Support Frame
3.5.5 Downstream Tank
3.5.6 Upstream Tank
3.5.7 Flume Pump
3.5.8 Pipework
3.5.9 Gatevalves
3.5.10 Electronic Flowmeter
3.5.11 Depth Gauge

3.6 FLUID CONDITIONS

3.6.1 Water Source

3.6.2 Water Temperature

3.6.3 Water Quality

3.7 CONCLUDING REMARKS

3.7.1 Design Alterations

3.7.2 Leakages

3.7.3 Water Contamination

3.7.4 Conclusion

CHAPTER 3

EXPERIMENTAL APPARATUS

3.1 INTRODUCTION

The quality of the data acquired in this project were highly dependent on the measuring device used, the integrity of the experimental system and the correct experimental procedures. The ideal approach for ensuring that these factors were addressed was to establish exactly: What was to be measured; how it was going to be measured; and where in the flow field it would be measured?. It has already been established in chapter 2 that the mean velocity and turbulence characteristics of rectangular open-channel flow, backward-facing step flow and slot flow are of interest. The method of laser-Doppler velocimetry (LDV) was deemed suitable for the acquisition of the mean and fluctuating velocities within the flow field, due to its advantages of accuracy and non-interference of the flow. Finally, it had to be established where the results would be taken and under what experimental conditions. A recirculating water flume capable of producing the correct hydraulic conditions and its compatibility with the LDV system was therefore required. A flume which complied to these specifications was not readily available, and therefore had to be designed by the author and constructed within the department.

During the design and construction of the main flume, a preliminary investigation was undertaken in an existing teaching flume. The geometry of this existing flume restricted the hydraulic conditions and the full range of LDV measurements required for the objectives of the full study. However, it did allow a 2-component investigation of slot flow to be undertaken, providing the author with invaluable experience in LDV data acquisition, slot flow characteristics and an insight into the design requirements for the main flume.

This chapter describes the LDV system used in the study, the physical characteristics of the teaching flume and the design and construction of the main flume.

3.2 LDV SYSTEM

3.2.1 Introduction

A 1-component He-Ne back scatter laser system was purchased from Dantec Measurement Technology with backup software. The integrated system allows non-contact velocity measurements of liquids and gases, with menu driven software allowing easy configuration of LDV optics, electronics, data acquisition and processing. The system is called FlowLite and is composed of 3 main components (see plate 3.1), which are:

(i) Laser optics-unit (which comprises a laser and a probe connected by a fibre optic cable).
(ii) Flow velocity analyser signal processor (which converts the Doppler bursts to instantaneous velocities).
(iii) Floware (this is the application software, operated on a dedicated Hewlett-Packard 386 PC).

Accurate positioning of the laser probe was essential for this study, and therefore a mechanism was required which would support and facilitate the accurate adjustment of its position. To achieve this, a purpose built support-traverse was designed and constructed. The full system is now described in more detail.

3.2.2 FlowLite Integrated Laser-Optics Unit

The laser-optics unit comprises of a laser and a probe connected by a 5m fibre optic cable. The laser itself is a 1-component 10mW He-Ne (632.8 nm - Red) laser with built in frequency shifter for reversing flows. This laser is of type Class 3b, which according to 'Safety in Universities: Notes of guidance Part 2:1' (CVCP, 1992) requires the use of safety goggles, warning signs, external red light warning and door micro-switch to cut the power source of the laser. These safety requirements are illustrated in plates 3.2 and 3.3.

Using a fibre optic cable, the laser is connected to a probe thus allowing the laser to be easily moved during experimental work. The probe itself is 275mm long, has a diameter of 60mm and is made from lightweight aluminium. Two lenses were used in this study with focal lengths of 160mm and 400mm (in air).

Although 2 and 3-component laser systems exist allowing simultaneous acquisition of more than one velocity component, the repositioning of a 1-component laser system probe allows the acquisition of the three velocity measurements U, V and W (but not simultaneously). This can be achieved using the following procedure. When the probe is placed perpendicular to the streamwise and vertical direction of fluid flow (side-on), the U and V components of velocity can be measured on rotation of the probe through 90^{o}, and similarly when positioned perpendicular to the streamwise and spanwise direction of fluid flow (beneath), U and W can be measured, again readjusting through 90^{o}. Therefore, in this study it is a requirement that the laser beams have clear sight through the sidewall(s) and base of the flume. Figure 3.1 illustrates these laser positions.

3.2.3 Laser Beam Refraction Correction

Although the focal lengths of the lens used in the study have been specified as 160mm and 400mm (in air), it should be remembered that the focal length alters when changing from one medium to the next, in this case from air to perspex to water. To compensate for this change of medium, Snell's Law is used, which states:

$$\frac{\sin(\theta_i)}{\sin(\theta_r)} = \frac{N_r}{N_i} \qquad \textbf{Equation 3.1}$$

where i and r refer to the incident and refractive beams respectively, θ_i and θ_r are the angles of incidence and refraction respectively, and N_i and N_r are the refractive indices of the incident and refractive medium respectively. This change of refractive index alters the focal length, in that a change in position of the light source (probe position) will represent a different change in the position of the focal point (control volume position). The relationship between these changes can be obtained if the refractive index of each medium is known. Since the laser light merely passes through the perspex, the rate of change between source and focal point is unaffected, and therefore this can be neglected. When moving the location of the focal point, or control volume of the laser beams, the change in position of the light source, or laser probe is thus determined using the refractive index for air (a) and water (w), 1.00 and 1.33 respectively (Tennent, 1986).

Therefore: $\Delta x_a / \Delta x_w = N_a / N_w = 1/1.33 = 0.75$

$$\Rightarrow \quad \Delta x_w = 0.75 \,.\, \Delta x_a \qquad \textbf{Equation 3.2}$$

A complete derivation of this relationship is described in Appendix A. The relationships obtained from equation 3.1 and in Appendix A were verified experimentally.

When measuring the *V*-component of velocity, the laser beams are orientated perpendicular to the mean flow direction. The vertical movement of the control volume throughout the full flow depth is therefore restricted due to the obstruction of the lower and upper beams by the channel bed and free-water surface respectively. Appendix B illustrates this problem with calculations of the limitations imposed on movement in the vertical direction.

3.2.4 Flow Velocity Analyser (FVA)

Using six different band-pass filters ranging from 120kHz to 36MHz, the system can measure a large range of velocities (-66.6 m/s to 233.4 m/s). A frequency detector incorporating a phase detector, and a burst detector based on signal intensity, use analogue correlation to analyse the detected signals and determine the flow characteristics. Small signals swamped with noise can also be detected and the correlation process ensures correct estimation of the frequency. The FVA can analyse low signal-to-noise ratio signals and can resolve the velocity field with an accuracy that is more than sufficient for most uses.

A purpose made cable between the 40MHz input connector and the Bragg cell driver output ensures that there is correct signal propagation, even when the signal is weak. The covariance processor comes with a dedicated interface board that connects to the computer. All the settings and functions of the processor are controlled from the computer. The computer used in the study was a Hewlett-Packard 386-SX with a maths co-processor added for increased computational power.

3.2.5 Application Software - Floware

As part of the integrated system, a software package accompanied the laser and FVA. This package, called *Floware*, is an application program designed for analysing LDV signals. It is a user friendly menu driven package allowing control of the laser and FVA. It also possesses a processing and analysis module providing data files and graphical interpretation of results. The data obtained from a single traverse position includes:

(1) Mean and RMS velocities.

(2) Turbulence intensity.

(3) Velocity moments.

(4) Spectrum displays.

(5) Correlations.

(6) Skewness and flatness.

Appendix C contains a sample velocity and moment file with the corresponding histogram and time series.

For this study, the velocity and moment files were converted to text files and imported into Excel ver5.0 and Stanford Graphics ver3.0b for further analysis and graphical representation.

3.3 LASER PROBE SUPPORT-TRAVERSE SYSTEM

3.3.1 Introduction

The laser probe is approximately 275mm long with a diameter of 60mm, and weighs 1.0 kg. It is connected to the laser system by means of a fibre optic cable 5m long. The accurate positioning of this probe is critical to the data measurements, as small movements within the flow field may yield large differences in results. It was therefore imperative that the laser probe be held in a fixed position allowing the location of the control volume to be known relative to some fixed datum. Similarly, accurate movement of the control volume to various locations within the flow field had to be achieved with minimum effort.

In order to meet these criteria, a laser probe support-traverse system was required. There were three options considered regarding the type of system which would be adopted for the study. The first of these was the purpose built traverse system available from the laser manufacturer, Dantec Measurement Technology. The main advantages of this system were:

(i) Software driven - allowing unsupervised data acquisition.

(ii) Accurate control of movement and positioning to fractions of a millimetre.

Despite being automated, the amount of movement was limited and only one component of velocity could be measured without re-adjustment, therefore, frequent repositioning and adaption to various orientations would be required.

The next option was to design and build a manually operated support-traverse. This had the following advantages:

(i) Significantly lower cost.

(ii) Quick to construct, allowing data acquisition to commence sooner.

(iii) Designed to meet the specification of the study, in terms of compatibility with the flume(s).

(iv) Easy to maintain and alter when necessary.

As time and cost were major factors, it was decided to opt for the in-house manually operated traverse. A third option, based on an in-house automated system was also considered, but again time and cost led to this option being discarded.

3.3.2 Probe Support-Traverse Criteria

The criteria for the probe support-traverse was based on accuracy of movement, physical size, and compatibility with the flume(s). It should also be noted that the laser probe was very fragile, and excess movement and accidental knocks could disturb the internal optics.

At this stage it was clear that the system would have to support the probe firmly to minimise accidental movement and vibrational effects resulting from any physical contact or from the pump itself. The system would have to allow controlled movement of the probe laterally, longitudinally and vertically to a desired accuracy with minimum time and effort. For ease of relocation and change of orientation, the physical size, weight and limitation of movement of the support were considered. Again, based upon the known dimensions of the teaching flume and from estimation of the full-scale flume dimensions, the range of movement without relocation in each direction was considered. The only direction which the traverse should cover without repositioning was the vertical direction. Although the height of the teaching flume was 300mm, the range of depths used for data acquisition would be considerably less, both in the initial and main study. Choosing a minimal vertical range of 300mm would therefore ensure full compatibility between the flume and the support-traverse, especially for future studies. An

additional 200mm was incorporated to overcome any difference in height between the support-traverse and the support frame connected to the flume.

Lateral movement through the flow (i.e. in the spanwise direction), was limited to 100mm on the teaching flume, however, lateral movement in the main study was expected to exceed this. It must be remembered that the control volume occurs at either 160mm or 400mm from the front lens of the probe, depending on which lens is used (approximately 213mm and 533mm in water respectively), and therefore movement of the control volume between the sidewall and channel centreline must be accommodated. Since the refractive index for water is greater than air, the probe will move through a shorter distance than the control volume, this characteristic being considered advantageous. For the purpose of the preliminary study and from an estimate for the main flume at time of construction for the support-traverse, the range of movement laterally was given the range of 0-250mm (in air). Adjustment of the probe in the probe housing allowed an additional 150mm of movement laterally, thus exceeding the anticipated distance of 300mm to the channel centreline. As flow symmetry was expected to occur about the flume centreline (as confirmed in chapter 4), there was no requirement to relocate the traverse to the opposite side-wall. However, had this been necessary, both sidewalls were constructed from transparent perspex.

For the longitudinal (streamwise) direction, it seemed impractical to allow continuous movement along the entire length of the flume (4m for the teaching flume, and a maximum of 6m for the main flume) without repositioning of the support-traverse itself. Using a smaller length scale longitudinally would provide greater flexibility of movement and orientation if required. It was decided that a range of movement of 300-400mm would allow a sufficient amount of measurements to be taken prior to relocation.

Rotation of the laser probe through 90^{o} has already been discussed for the acquisition of different flow velocity components. To facilitate this, the probe housing was a cylindrical support-clamp which could be loosened easily to allow rotation of the probe. To provide support in the vertical alignment of the laser probe, the probe housing could be rotated through 90^{o}.

3.3.3 Laser Probe Support-Traverse Design

Adhering to the specifications and criteria for a laser probe support-traverse as mentioned above, a system was designed and built within the department. It was constructed mainly from mild

steel and involved a system of moveable components by means of bolt screws with turning handles. Figure 3.2 shows a schematic representation of this whilst Appendix D provides detailed drawings of this system. The constructed support-traverse can be seen in plate 3.4.

The support-traverse is composed of several main components. The first of these is the laser probe housing, which consists of a hollow cylindrical clamp. This clamp can be tightened to fix the probe in position in order to minimise accidental rotation and movement, and similarly loosened to facilitate rotation and movement when desired. This is connected to a vertical moving carriage which can be rotated to allow alignment of the probe in both the vertical and horizontal planes. A secondary support is installed when the probe is housed vertically. This secondary support is a small cylindrical cup which supports the conical shaped end of the probe.

The support-traverse facilitates movement of the laser probe vertically, longitudinally and laterally. Vertical movement within a range of 0-500mm and an accuracy of 0.05mm can be obtained. This is achieved by turning a manually operated calibrated screw bolt which in turn moves the probe carriage vertically. The lateral carriage can move through a range of 0-250mm with an accuracy of 0.05mm. An additional 150mm of movement can be obtained by sliding the laser probe in the probe housing-support. This movement is also controlled by a calibrated manual screw bolt. A second horizontal plate allows movement of the longitudinal carriage through a range of 0-400mm with the same degree of accuracy. This plate is supported on a fixed base plate which connects to the various frames connecting the support-traverse to the flume. To reposition the probe longitudinally, both the support frame and the support-traverse can be moved to any position along the length of the flume.

Movement of the control volume during data acquisition required a known datum to be established. This was achieved by measuring its location with reference to the sidewalls and the backward facing step. Verification of vertical location was obtained by positioning the control volume with respect to the channel bed.

The supporting frames were of different designs depending on which flume was used and the orientation of the probe support, see figure 3.3.

3.3.4 Alterations for Main Investigation

Although the support-traverse was originally designed for the initial study, it was used in the main investigation without any significant alterations. The only alterations being the fabrication of support frames and the secondary probe support for use when aligned vertically.

3.4 EXISTING LABORATORY FLUME

3.4.1 Introduction

It was anticipated that the design and construction of the main flume would take approximately 18 months. During this period an existing flume was used for an initial investigation. This was deemed suitable for a 2-component study owing to the clear side panels of the flume, thus allowing penetration of the laser light for U and V components of velocity. A study of open-channel slot flow was conducted for slot aspect ratios of 2, 5, 10, 15 and 20, with an additional set of results for a backward facing step. This was possible in this flume using a slot height ≤0.1m.

3.4.2 Flume Details

The flume was purchased previously for use as a teaching aid. It consists of a rectangular channel 4m long, 0.1m wide, and 0.3m deep. The base was composed of stainless steel with provision for teaching aids, such as weirs, to be attached by means of bolt holes. The sidewalls were constructed from clear glass plates extending throughout the length of the flume. The flume was stabilised by a surrounding frame composed from 40x40mm thick hollow rectangular sections. This frame was supported on a pivot at the upstream end of the flume and on a screw bolt located near the downstream end of the flume. A screw wheel operating this bolt allowed the slope of the flume to be adjusted, which was read directly from a calibrated gauge located on the screw wheel. The pivot and screw bolt were supported on a large base which was bolted to the laboratory floor for stability. The flume can be seen in plates 3.5 and 3.6, with dimensions and details illustrated in figure 3.4.

Water was recirculated through the flume by means of an impeller pump and 100mm diameter cast iron pipework. The pump was powered by a 2-phase electrical supply capable of pumping

20 l/s. Water was pumped from a downstream holding tank to an upstream supply tank, and the flowrate was regulated using a gatevalve located upstream of the pump. The flowrate was measured using an orifice plate connected to a mercury manometer. This was calculated using an empirical equation based on the manometer head difference:

$$Q = 3.235\sqrt{\Delta h} \qquad \textbf{Equation 3.3}$$

where,

Q - Flowrate (l/s)

Δh - Difference in manometer readings (cm)

The downstream tank served as a reservoir to store all the water when not in use and any excess fluid when in use. When in use, the discharge from the flume freely enters one end of the tank and the demand for the particular flowrate is pumped via a 100mm diameter outflow hole at the opposite end of the tank. To reduce swirl created by the jet of water discharging from the flume, a dividing plate was installed between the jet and the outflow of the tank. The tank had a volume of $2m^3$, and was fabricated using 3mm thick steel sheets and reinforced using a steel frame composed of 40x40mm steel hollow sections. The tank rested on the laboratory floor and was coated with a waterproof resin and a top layer of waterproof paint to prevent rusting.

The upstream tank was smaller in design and was attached to the flume. Similarly, this was also painted to prevent rusting. A mesh plate was installed in the upstream tank to reduce swirl created by the flow entering the tank. The width of the tank was slightly greater than the width of the flume and was therefore connected via a gradual transition.

Flow depth was controlled using a tailgate located at the extreme downstream end of the flume. This could be accurately moved to provide the required depth of flow. The depth was measured using a depth pointer gauge which was housed on a moveable carriage. This carriage could be moved manually along the entire length of the flume on stainless steel rails located along the top of the flume. The pointer gauge had an accuracy of 0.5mm and a range covering the full depth of the flume.

3.4.3 Slot Installation

For the investigation of open-channel slot flow, various slot configurations had to be introduced into the teaching flume. As a slot could not be cut into the original base of the flume, the only option was to raise the bed of the flume. This was achieved by the addition of blocks constructed from 10mm plastic sheets and inserted into the flume to produce a central slot region. The upstream block was 0.1m in height and 1.6m long, and was fixed into position using screws which connected to the original base of the flume. A series of downstream blocks were constructed, also of height 0.1m, and of varying length. These blocks were then temporarily inserted flush with the tailgate at the extreme downstream end of the flume. The space created between these two blocks created the 'slot' section. A variety of downstream blocks were used to alter the slot length, and hence the different aspect ratios were obtained. Removal of the downstream block created the condition of a backward-facing step. This system can be seen in figure 3.5. The blocks were constructed from 10mm thick plastic sheets, and were cut and screwed together to form the specified dimensions of the blocks.

This sudden increase of bed elevation at the upstream end of the flume caused disturbance of the flow as it discharged from the upstream tank into the flume. To reduce this disturbance propagating along the initial stretch of the flume, a contoured transition was inserted. This was achieved using a sheet of thin aluminium cut to the correct shape then bent into position, see figure 3.6.

An additional set of results were undertaken with a slot height of 25mm for aspect ratios of 5 and 10 for a collaborative study with the University of Glasgow (Pender et al, 1995). The new slot configuration for this study was achieved using smaller blocks.

3.5 MAIN FLUME DESIGN

3.5.1 Introduction

The requirements imposed on the design of the main flume were controlled by several factors. Firstly, the flume channel would have to be constructed from a transparent material to facilitate light penetration through both sidewalls and the channel bed. Secondly, the hydraulic conditions required would have a significant bearing on the dimensions of the flume. These conditions include the ability to produce fully developed turbulent flow with realistic Reynolds numbers

(3000-50000) that are typical in river flows. In addition, the flume would have to allow different slot geometries and scales to be investigated.

The size, time and cost of construction were also important factors in the design. Limited floor space of 9.3x8.5m in the laboratory meant that the total length of the apparatus was restricted to less than 9.3m. The speed of construction was also considered, as time was a limiting factor for the entire project. Finally, the apparatus had to be financed within a set budget.

Although the hydraulic conditions required could be obtained at different scales, especially within a range of flume sizes possible in the limited space available, the advantages and disadvantages with large and small flumes had to be considered. The problems associated with a small flume included:

(1) an increased sensitivity to the accuracy of the instrumentation, especially the positioning of the laser control volume;
(2) a higher tolerance of accuracy in the design and construction;
(3) a reduced range of the measurement field, especially with data acquisition of the vertical velocity component, V (as discussed in section 3.2.3 and Appendix B); and,
(4) an increased sensitivity to perturbations of the system, such as vibration from the pump, movement of the laser probe and accidental contact.

Similarly, a large flume has the following problems associated with its design and construction:

(1) a longer period of construction, thereby reducing the time available for data acquisition;
(2) an increased time for data acquisition, associated with the larger scale of movement of the instrumentation; and,
(3) an increased cost for construction materials.

Bearing these factors in mind, the general concept of the flume was considered. In general, a recirculating water flume with clear glass, or perspex side panels and base would be supported on a steel structural frame with slope adjustment capabilities. With the facilities available and the limited laboratory space, flow would be created using a recirculating system with the inflow and outflow tanks being an integrated part of the system. Different slot flow geometries and scales would also have to be accommodated in the design.

As a point of reference, the hydraulic conditions used in the initial study were adopted as a basis for the size requirements for the main flume design. Another aid to determine the dimensions of the flume was the requirement that full development of the turbulent boundary layer was dependent on satisfying L/y_o>60-100, where L is the longitudinal distance and y_o is the flow depth. Also, in order to eradicate sidewall contamination, the aspect ratio B/y_o should be greater than 6, where B is the channel width. It is evident from these requirements, that the flow depth, y_o, is a key parameter in the flume design. Using the normal flow depth, y_o=0.1m, from the initial study, then L and B would be 6m and 0.6m respectively.

To obtain slot flow, a slot had to be incorporated into the flume. This was based on a sudden increase in depth (of height, H_s) followed by a sudden reduction in depth (of H_s) at some point further downstream. As the slot would have to occur in the central region of the flume, the length required to produce fully developed turbulent flow would therefore be reduced considerably. Due to the limited length of the flume, it was decided that a reduction in flow depth, y_o, was a suitable solution to this problem. To facilitate large slot aspect ratios, and at the same time ensure correct slot inlet conditions, the design depth was reduced by 50%. Therefore, locating the slot 3m downstream would fulfil the development of the turbulent boundary layer prior to entering the slot region. Using y_o=0.05m as a characteristic length, the step height, H_s, was similarly chosen as this value. Adopting these values, the depth of flow in the slot region was therefore, $y_s=y_o+H_s$. By maintaining the slot width as 0.6m, a slot depth of 0.1m satisfied the requirement that the channel width, B, was greater or equal to 6 times the slot depth.

Based on this design approach, the following flume dimensions and hydraulic conditions were confirmed (shown schematically in figure 3.7).

(1) The flume design length, L, was chosen as 6m, since this was the maximum channel length which could be constructed in the limited laboratory space.

(2) The flume design height, H, was set at 0.3m, therefore allowing greater flow depths to be used in future studies using the flume.

(3) The design width, B, was set at a value of 0.6m in order to comply with the requirement that $B \geq 6y_s$.

(4) The step height (as per design), H_{sd}, was set at 0.1m. The channel depth therefore increased from 0.3m to 0.4m in the slot section. Slot lengths and slot heights could be reduced by inserting clear perspex blocks in the slot region.

(5) Based on an anticipated upstream flow depth, y_o=0.05m, the upstream length of flume, L_{us} was chosen as 3.0m in order to satisfy the requirement of $L \geq 60y_o$ for boundary layer development.

(6) The slot Length, L_S was set at 2m in order to accommodate large slot aspect ratios (L_S/H_{sd}>20).

(7) The experimental step height, H_s, was set at 0.05m. The design depth of the slot was reduced from 0.1m to 0.05m by inserting a clear perspex block in the slot. This increased the range of slot aspect ratios and allowed both the upstream flow depth and slot depth to be adopted as a suitable characteristic length.

(8) The downstream length of flume, L_{ds}, was the remaining length of flume given by L-(L_{us}+L_s). The initial design value of this was therefore 6-(3+2)=1m, however, this increased in length when reducing the slot aspect ratio. The secondary recirculation zone experienced immediately beyond the slot (FFS) was of interest, however, the flow conditions beyond 15-20H_s of this was of little interest. Therefore, the remaining 1m (20H_s) was deemed a suitable minimum length for the downstream section of the flume.

Using clear perspex, a channel of length 6m, depth of 0.3m and a width of 0.6m was constructed, with a removable centre section allowing different bed forms to be installed. The original bed form was a slot section 0.1m deep and 2m long located 3m from the start of the flume. Detailed drawings of the constructed flume can be seen in Appendix E.

Flow was created in the flume using a pump and UPVC pipework to transfer water from a downstream holding tank to an upstream tank. As the head of water increased in this upstream tank, it spilled into the flume via a gradual transition. Water then discharged from the end of the flume back into the downstream tank where it was recirculated back through the system. The flowrate was measured by an electromagnetic flowmeter and controlled using a gatevalve located between the pump and upstream tank.

Typical Reynolds numbers found in rivers and open-channel flow investigations range from 3000<Re<50000. The flowrate required from the pump was determined by considering various flow depths over this range of Reynolds numbers. From figure 3.8, it can be seen that as the depth of flow increases, very high flow rates are required for the higher Reynolds numbers. It seemed reasonable that a pump with a maximum delivery of approximately $0.04m^3/s$ (40l/s) would provide a suitable range of Reynolds numbers for the anticipated experimental depths.

The flume was supported on a steel frame which could be adjusted in height to allow change of slope. Flow depth was controlled using a sluice gate at the downstream end of the flume, and was measured using a depth pointer gauge. Different slot depths, aspect ratios and bed formations could be achieved by inserting fabricated perspex blocks into the slot section.

Construction of the flume took 12 months, with several months spent thereafter making minor alterations and installing additional components. These included support frames for the laser probe support, mesh filters for cleaning the water, additional perspex blocks and a turbulence diffuser in the upstream tank. Plates 3.7-3.21 illustrate various features of the flume.

A more detailed report of the flume design and construction method now follows.

3.5.2 Flume Channel Details

Sheets of clear perspex material, $9m^2$ and 10mm thick, were purchased from a local supplier. Different sheet thicknesses were available from the supplier, however, 10mm thick sheets were deemed to be of sufficient strength and stability for the flume construction. Prior to purchase, a sample section was tested for compatibility with the laser, primarily to ensure that the laser light passed through the material without distortion. This material was chosen in preference to glass since perspex is easier to cut and handle, is more durable, and was also cheaper. Its main disadvantage however, is its susceptibility to scratching due to wear and tear, which could subsequently distort the penetration of the laser. Minor scratching of the perspex did occur during this study, however, this was not severe enough to be detrimental to the acquisition of data by LDV measurements.

The flume channel sidewalls and base were cut from the perspex sheets using a standard electric saw. When assembled they formed the flume channel, see figure 3.9. It was decided that the channel would be composed of three sections, namely: an upstream section; slot (centre) section;

and a downstream section. These three sections were connected together forming a channel 6m in length, 0.6m wide, and 0.3m deep in the main (upper) channel and 0.4m deep in the slot section.

All the cut sections were connected using a combination of screws and silica gel. The latter providing additional strength and a water-tight bond. Screw connections were made at intervals of approximately 0.2m. To provide additional support, 10x10x1mm angle steel sections were used externally along the seems. These angle sections were connected to the perspex using silica gel. A silica bond was preferred to glue as it was not permanent and therefore easier to remove and maintain. It was also feared that some compounds of glue could potentially react with the perspex material.

3.5.3 Channel Support Frame

To provide additional stability, especially to prevent bulging and warping of the perspex panels, a steel frame was used to support the channel, see figure 3.9. Hollow rectangular steel sections 40x40x2mm were purchased in 8m lengths from a local supplier then cut and welded together to form the frame. The channel was then supported in this frame. To provide stability, the angle sections used for the channel seams were tac-welded to the frame. Weather seal foam and silica gel were also used at the interface between the frame components and the perspex channel. This frame was constructed in 3 parts as with the channel, i.e. upstream, centre and downstream sections, and bolted together with flanged connections. This was to allow the centre section to be removed and replaced by different channel geometries, extending the use of the flume for future investigations.

The frame is of simple lattice design with longitudinal, vertical and spanwise members. In the slot section, the spanwise supports were skewed to increase the overall access of the laser probe from beneath the flume.

Prior to inserting the flume channel into the support frame, all the steel sections were coated with a waterproof paint to prevent rusting.

3.5.4 Main Support Frame

To elevate the flume to a workable level and allow slope adjustment, a main support frame was constructed from rolled steel sections, the details of which are shown schematically in figure 3.9, and in greater detail in Appendix E.

The main support was provided by two longitudinal beams and connecting spanwise members, supported by 3 pairs of vertical legs resting on the laboratory floor. Once this frame had been erected, the flume was lowered and bolted into position. All members were painted with waterproof paint to prevent rusting. Plates 3.7-3.8 illustrate the integration of these components to produce the flume channel.

The legs used to support the frame consisted of 80x80x2mm hollow rectangular sections. Steel plates were welded across the bottom of these legs, each plate being been pre-drilled with a threaded 12mm diameter hole. Threaded bolts 12mm in diameter and 90mm long with a fixed hexagonal nut were welded perpendicular to the centre of steel discs of diameter 80mm. These components were then screwed into the threaded hole at the base of each leg, and subsequently used to alter the height of the flume. These discs rested on anti-vibration pads of size 100x100mm composing of a 5mm thick steel upper plate and 15mm rubber lower pad. These pads rested on the concrete floor of the laboratory, see plate 3.9.

The legs located at the upstream and downstream ends of the frame provided the main support, whilst the centre pair of legs were used for additional support. The slope of the flume could be changed by adjusting the height of the upstream or downstream legs.

3.5.5 Downstream Tank

Water was stored in a purpose built reservoir and recirculated through the system. Two suitable options were available for the location of this reservoir, namely upstream or downstream of the flume inlet. With reference to the teaching flume design, it was decided that a downstream tank would be used to store enough water to allow maximum flow rate conditions, see plate 3.10 and figure 3.10.

Based on the maximum flowrate expected in the main investigation (40l/s), and the maximum flow depth of the flume, a tank was designed to cater for the extreme volume of water these

conditions present. The tank had a volume of $2m^3$ and was constructed from 3mm thick steel sheets. These sheets were pre-cut by the supplier and welded together in the laboratory and coated initially with a layer of epoxy paint followed by an additional layer of water proof paint to prevent rusting. The dimensions of this tank were restricted by the remaining length of the laboratory after the flume and upstream tank (section 3.5.6) had been accounted for.

The jet discharge from the flume entered one end of the downstream tank. The outlet of this tank was a 300mm diameter hole located on a side panel at the opposite end of the tank. On the outside of this outlet was the pipework (see section 3.5.8) leading to the pump. On the inside of this outlet a right angled pipe-bend was inserted so that the inlet faced the base of the flume. This pipe-bend came to within 50mm of the tank base and was used to ensure that pump suction could take place even when the flow depth was below the outlet hole, see plate 3.11 and figure 3.10.

When the flowrate was large, the water discharging from the flume created highly turbulent conditions in the tank, causing large amounts of swirl and air entrainment in the water. To reduce this swirl, a dividing plate was installed in the tank close to the discharge area of the flume. This confined the swirl within a section of the tank, remote from the outlet pipe leading to the pump, see plate 3.12. Owing to the size of the flume, a steel frame was constructed around the tank to prevent bulging and excess strain on the welded connections.

3.5.6 Upstream Tank

The teaching flume used in the initial study had a small upstream tank attached to the flume inlet. However, the volume of water required in the main study would be much larger, requiring a larger tank. It was therefore decided that the tank would rest on the laboratory floor with an inlet located at the same level as the pipework, see plate 3.13.

The tank was constructed using the same steel sheeting used in the downstream tank (see figure 3.11). Once again, these sheets were pre-cut by the supplier and welded together in the laboratory. A frame was also incorporated into the design of the tank for additional stability and strength. An inlet hole 250mm in diameter was cut in a lower panel to accommodate the pipework which supplied the water. Inside the tank, the inlet pipe branched into a T-connection with right angled bends orientated to direct the flow to the base of the tank. This was to reduce the pressure created by a single jet and to reduce swirl. To further reduce swirl and excessive

turbulence from entering the flume, a diffuser was installed approximately half-way up the tank. This diffuser was a 3mm thick aluminium plate of same dimensions as the tank cross-section, and was supported on four steel legs at the mid-depth of the tank. Holes 5mm in diameter were drilled at 15mm spacings in a grid format across the surface area, see plate 3.14.

The tank width was greater than the width of the flume, thereby a gradual transitional section was used to reduce the width of the tank to fit the flume. A similar transition was used for the connection of the tank to the base of the flume, whereby a gradual connection reduced turbulence created from the transition from vertical flow to horizontal flow, see plate 3.15.

The connection of the tank to the flume was complicated, as the upstream tank would be stationary whilst the flume would be moved vertically in order to change the slope of the flume bed. This ruled out a rigid connection due to the stresses which would be created. To overcome this problem, a connection composed of a rubber strip 1.3m long, 150mm wide and 2mm thick, was bolted to both the flume and upstream tank creating a flexible connection 50mm wide, see plate 3.16. Silica gel was used to ensure that the bonds were water-tight. The gap produced by this connection was covered using aluminium sheets cut to size and integrated into the transition from the tank to the flume.

As with the downstream tank, the upstream tank was coated with a water-proof epoxy paint and an additional water-proof paint for protection against rusting.

3.5.7 Flume Pump

To facilitate a large range of hydraulic conditions generated within the flume, it was established that a suitable maximum flowrate was approximately 40l/s. A centrifugal in-line pump was purchased capable of delivering this flowrate, see plate 3.17.

The inlet diameter of the pump was 300mm, whilst the outlet diameter was 250mm. The pump was powered by a two-phase electrical supply and operated by a simple on/off switch box. To prevent movement of the pump, it was bolted to the concrete floor of the laboratory.

3.5.8 Pipework

UPVC pipes were used to connect the pump to the upstream and downstream tanks. A layout of the pipework can be seen in plate 3.18.

All connections required within the pipework e.g. to pump, tanks, flowmeter and gatevalves, were achieved using flanged connections, again the details for these can be seen in plate 3.18. The gatevalves and flowmeter were supported on the laboratory floor, and therefore doubled as a support for the weight of the pipework.

3.5.9 Gatevalves

To regulate the flow produced by the pump, a gatevalve was inserted in the pipework between the pump and the upstream tank. This cast-iron gatevalve was operated manually using a screw wheel.

A similar gatevalve was inserted in the pipework between the flowmeter (see section 3.5.10) and the downstream tank. The only difference between these two gatevalves was the larger inlet-outlet diameters required for connections to the pipework. This second gatevalve was installed purely for the purpose of maintenance requirements to the pump or flowmeter.

Both gatevalves rested on purpose built supports made from excess 40x40x2mm rolled steel sections. These were supported on the laboratory floor and ensured that the gatevalves remained in-line with the pipework, see plate 3.19.

3.5.10 Electronic Flowmeter

To reduce time taken using conventional flow-rate measurement methods, such as orifice plates and venturi meters, an electronic flowmeter was purchased.

The flowmeter was supported on a steel frame similar to those used for the gatevalves and was powered using a standard 12v wall socket. An LCD display on the flowmeter provided constant updates of the flowrate (l/s) at 1 second intervals, accurate to 0.0001 l/s, see plate 3.20. A manufacturers certificate of calibration is given in Annex F.

3.5.11 Depth Gauge

The depth pointer gauge used in the initial study was adapted for use in the main study. The gauge comprised of an adjustable steel scale rule supported on a steel frame. On the initial flume, this frame was moved manually to the required position along steel rails located on top of the flume. Using this same method, circular steel rails were connected to the top of the flume. As this flume was wider than the initial flume, an additional frame was constructed to support the gauge, see plate 3.21. These frames allowed the gauge to move both longitudinally and laterally throughout the channel. To increase the accuracy of the steel scale rule, a micrometer accurate to 0.05mm was incorporated into the gauge.

The accuracy of this gauge was also dependent on the level of the steel rails supported along the top of the flume. The rails were levelled using a standard spirit level when the flume was horizontal, and were adjusted using the screw bolts which connected the rails to the flume.

The flow depth was then measured as the difference in readings between the channel bed and the free-surface. The gauge was used primarily to ensure normal flow conditions prevailed prior to data acquisition.

3.6 FLUID CONDITIONS

3.6.1 Water Source

The flume systems described in this project (i.e. both teaching and main flume) used a pump to recirculate a stored reservoir of water between the downstream tank, the upstream tank and the flume. The downstream tank, which served as this reservoir, was filled using ordinary tap-water piped from a nearby supply (with drain), located approximately 10m from the flume. Transfer of water from the supply to the tank was achieved using a hose-pipe. The tank was emptied using an immersible pump to transfer water from the tank to the drain.

3.6.2 Water Temperature

A wide range of flow depths and velocities were used in this project, particularly in the investigations using the main flume (see chapter 4 and 5). These variations result in a change of

Reynolds number (equation 2.7). The calculation of this non-dimensionalised parameter is not only dependent on a characteristic length (e.g. flow depth, y) and velocity, u, but also the fluid density, ρ, and coefficient of dynamic viscosity, μ. In order to achieve the desired flow conditions, both y and u were altered, however, the values of ρ and μ were kept constant. These parameters were kept constant by adopting the NBS (National Bureau of Standards) datum μ (20°C)=1002.0 μ Pa s (Kestin et al, 1978). Therefore, by maintaining a water temperature, T, of 20°C:

$$\rho = 998.2336 \text{ kg/m}^3 \qquad \mu = 1002.0\ \mu\text{Pa s} \qquad \nu = 1.0039 \text{ mm}^2/\text{s}.$$

For changes in temperature, Kestin et al (1978) used this standard to develop an empirical equation for the viscosity ratios over the temperature range $0°C \le t \le 40°C$:

$$\log\left\{\frac{\mu(t)}{\mu(20°C)}\right\} = \frac{20-t}{t+96}\left\{1.2364 - 1.37\text{x}10^{-3}(20-t) + 5.7\text{x}10^{-6}(20-t)^2\right\}$$

Equation 3.4

During the acquisition of data in the present investigation, the water temperature rose above 20°C in the summer months, and dropped below this value in the winter months. The water temperature also increased during long periods of continuous use. To compensate for these temperature changes, hot or cold water was added where appropriate, and in some extreme cases, data acquisition was postponed due to overheating.

The temperature was measured regularly, depending on the time of year, using a standard mercury thermometer. In general, the temperature was checked hourly and was maintained in the region $18°C \le t \le 22°C$. This range was deemed practical and suitable as a lower range would be difficult to maintain and the viscosity change was in an acceptable limit. Table 3.1 indicates variations in the viscosities and density for different temperatures:

Table 3.1 - Viscosity/Temperature Variation (Kestin et al, 1978)

Temp. °C	Density ρ, kg/m^3	Viscosity μ, μ Pa s	Kinematic Viscosity ν, mm^2/s
15	999.1286	1138.4	1.1393
20	998.2336	1002.0	1.0039
25	997.0751	890.2	0.8928

According to equation 3.4, the variation in kinematic viscosity, ν, within the temperature range $18^{o}C \leq t \leq 22^{o}C$ does not exceed 5.4% of $\nu(20^{o}C)$.

3.6.3 Water Quality

Ordinary tap-water was used in this study, as there was no evidence in the literature to suggest that the properties of tap-water differed significantly from pure or distilled water. In addition, the latter would be difficult to obtain. Although particle seeding can aid the data sampling rate of LDV measurements, this was deemed impractical since the water was changed on a regular basis, and the tap-water inherently contained small particles.

3.7 CONCLUDING REMARKS

3.7.1 Design Alterations

Throughout the course of the study, there were several adjustments to the design and some maintenance required in order to increase or maintain the integrity of the flume. A major design alteration was the addition of a jack system to adjust the slope of the flume. Excess use of the turning bolts at the base of the legs stripped the thread from the bolts and therefore an alternative method was adopted to alter the height of the flume. A standard car jack, installed at the upstream leg brace proved to be a reliable method of adjusting the slope of the flume (see plate 3.22).

3.7.2 Leakages

Prior to the flume being used, it was anticipated that some leakage might occur. Initially, there were large areas of leakage from the connections of the perspex panels, however, these were overcome by upgrading the silica bond. During the course of the study, leakage problems did persist. However, at no time was this excessive or detrimental to the data acquisition process. The process of upgrading the silica bond took approximately 48 hours, between drying the flume, making the alteration, and allowing the silica to dry.

There were no leakage problems from either of the tanks or the pipework during the course of this project.

3.7.3 Water Contamination

The integrated design of flume, tanks, pipework etc. was aimed at creating a system whereby rust and water renewal would be kept to a minimum. Internal rusting of the gatevalves did occur which subsequently aided data acquisition as a form of particle seeding. Excess rust was at times problematic, reducing the penetration and strength of the laser beams in the flow field. When the water contamination became excessive, the water was renewed using the process described in section 3.6.1. In this way, the water was kept at a suitable quality for LDV measurements.

3.7.4 Conclusion

In general, all the components used in the study proved to be effective. The probe support-traverse was originally designed for use in the initial study, however, simple alterations allowed it to be used in the main study. The range of movement the support-traverse permitted proved to be sufficient, with only the longitudinal direction requiring the support-traverse to be repositioned.

The alterations to the teaching flume allowed it to generate slot flows. Installation of the blocks to produce the various flow conditions and aspect ratios was quick and simple and allowed the flume to be returned to its initial state.

Using the design concepts of the teaching flume, the main flume was designed and constructed. Many problems associated with the construction of such a flume greatly depended on the accuracy of construction and the degree of workmanship. The success of the flume confirmed that these were of the highest standard and much gratitude and praise is given to Mr. John Callaghan of the Civil and Transportation Engineering Department at Napier University for undertaking the construction of this flume. Assessment of the quality of the flume is given in Chapter 4.

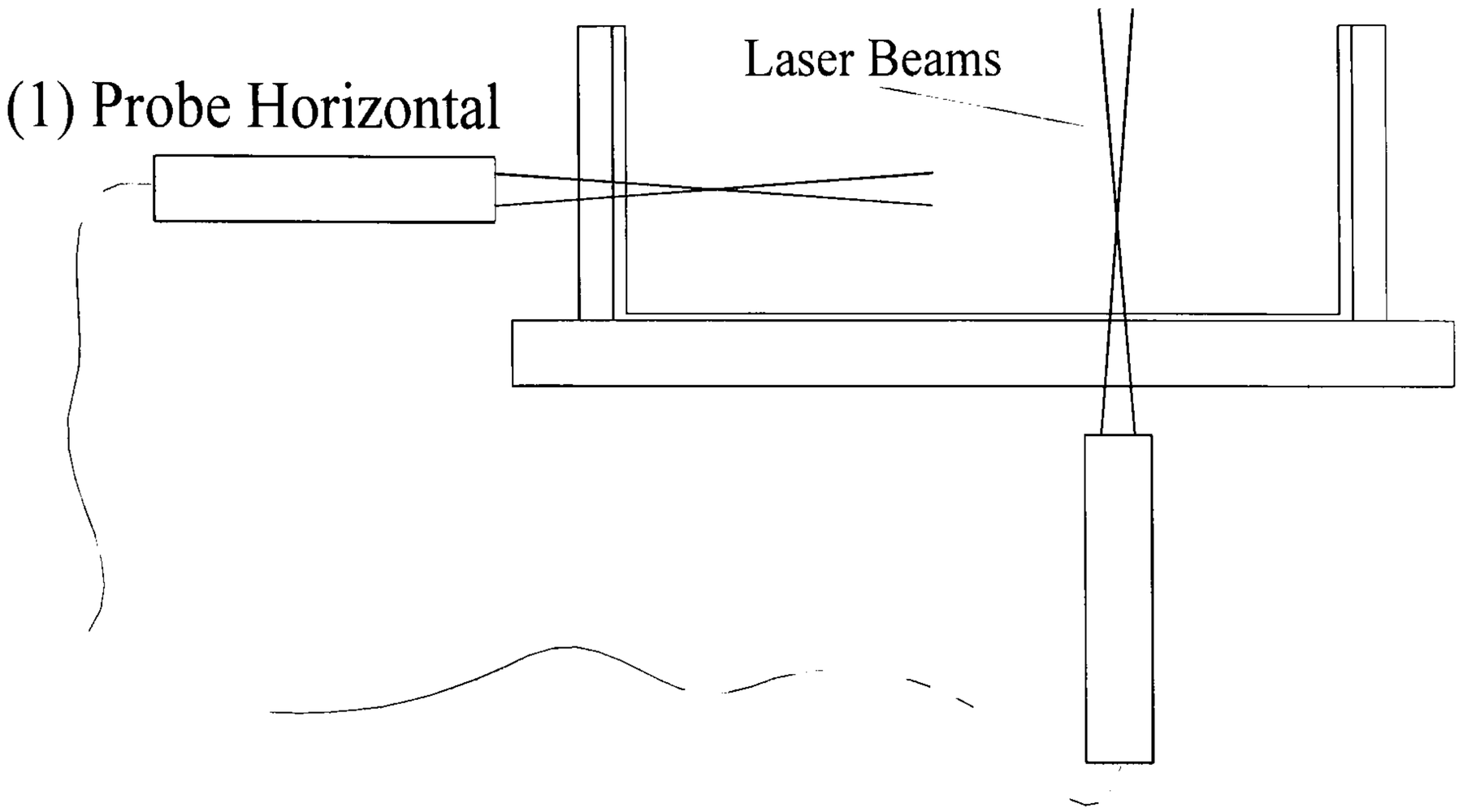

(a) Laser-Probe Location

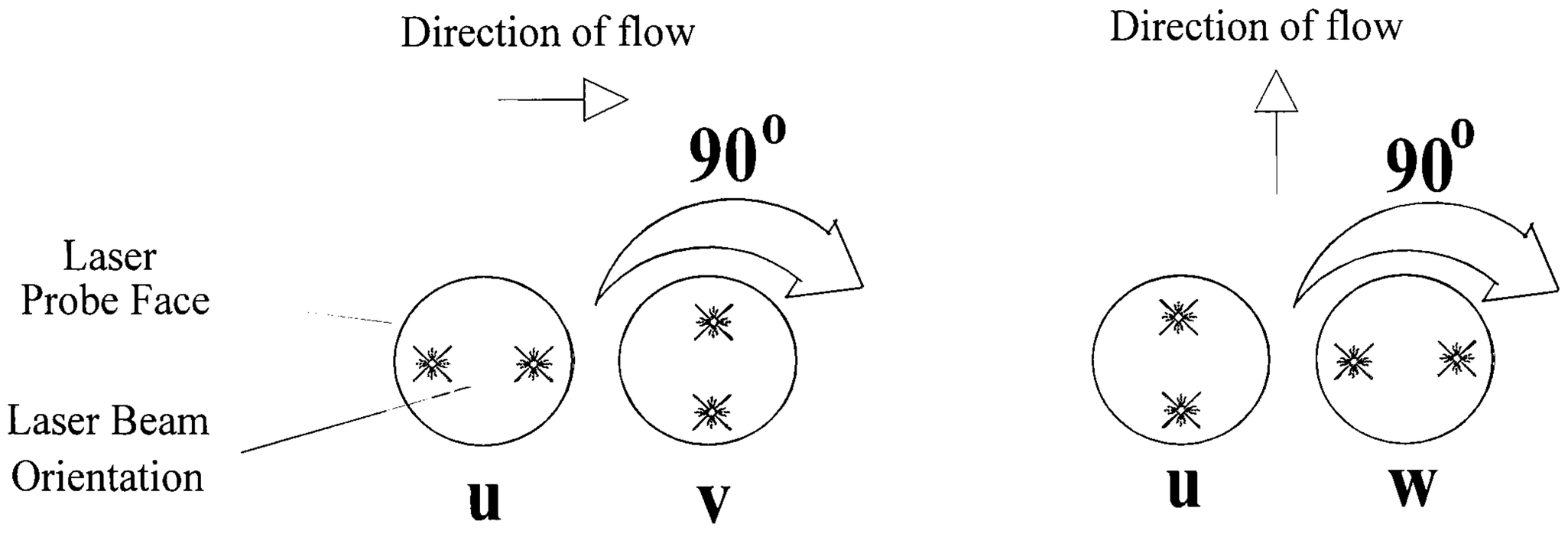

(b) Laser-Probe Orientation

Figure 3.1 - Laser-Probe Location and Orientation for 3-Component Data Acquisition

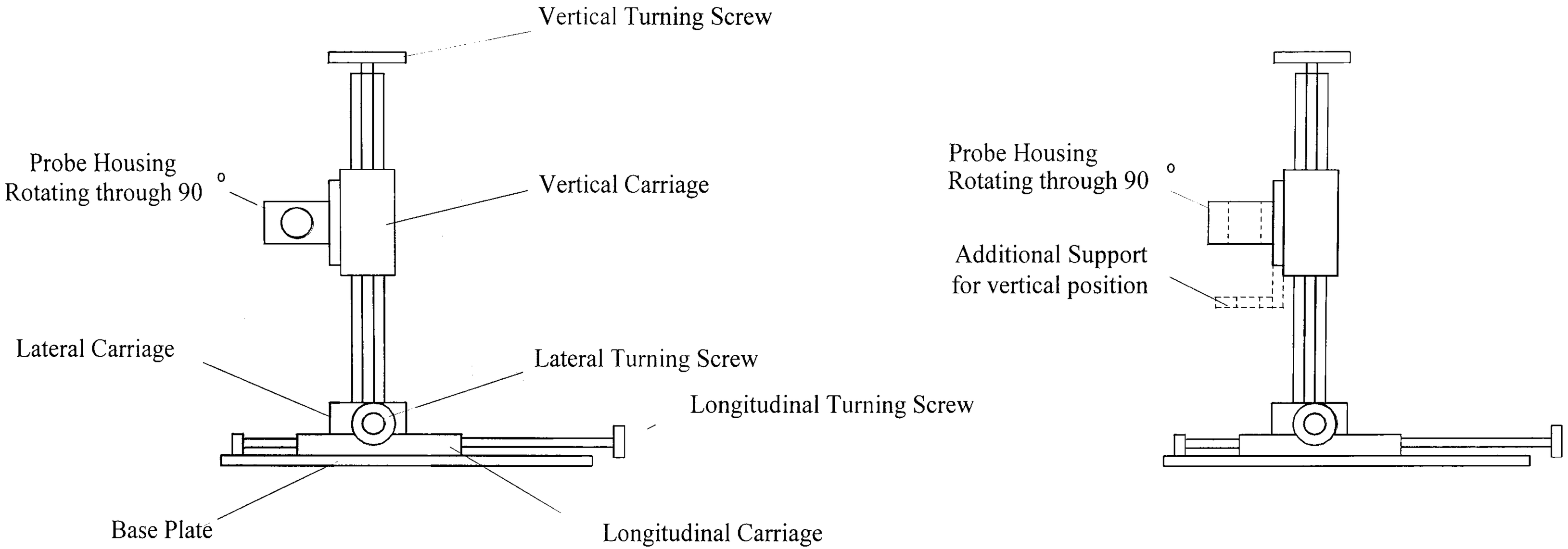

Figure 3.2 - Schematic Drawing of Laser Probe Support-Traverse

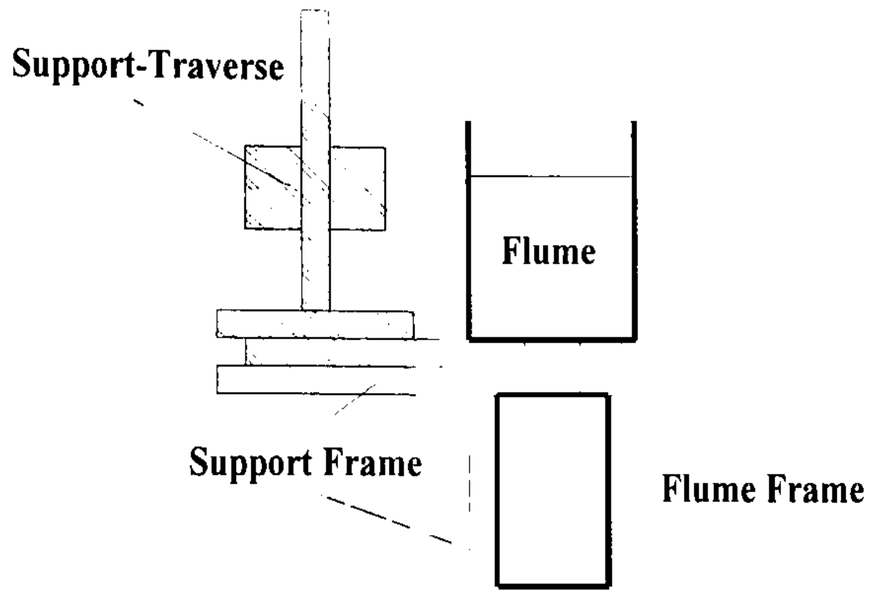

(a) Teaching Flume - U and V Position

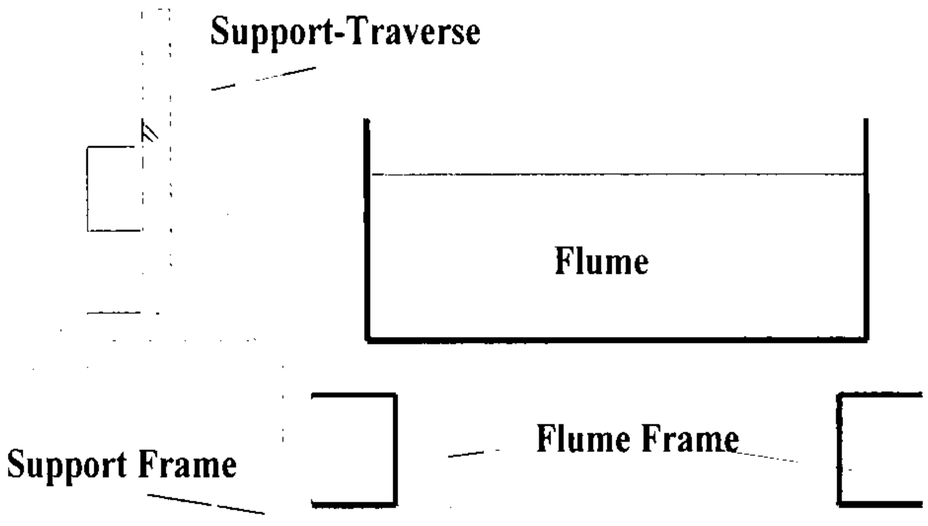

(b) Main Flume - U and V Position

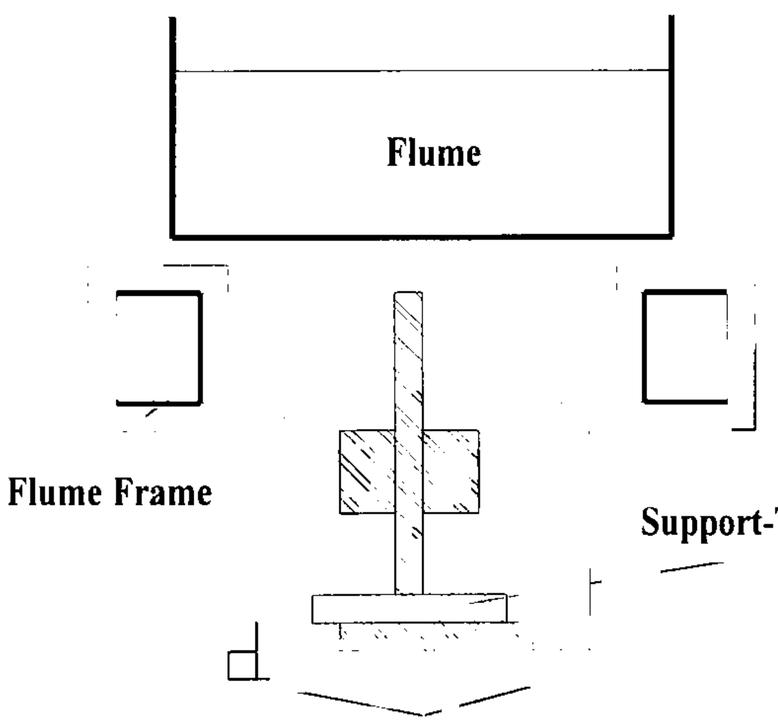

(c) Main Flume - U and W Position

Figure 3.3 - Support-Traverse Support Frames

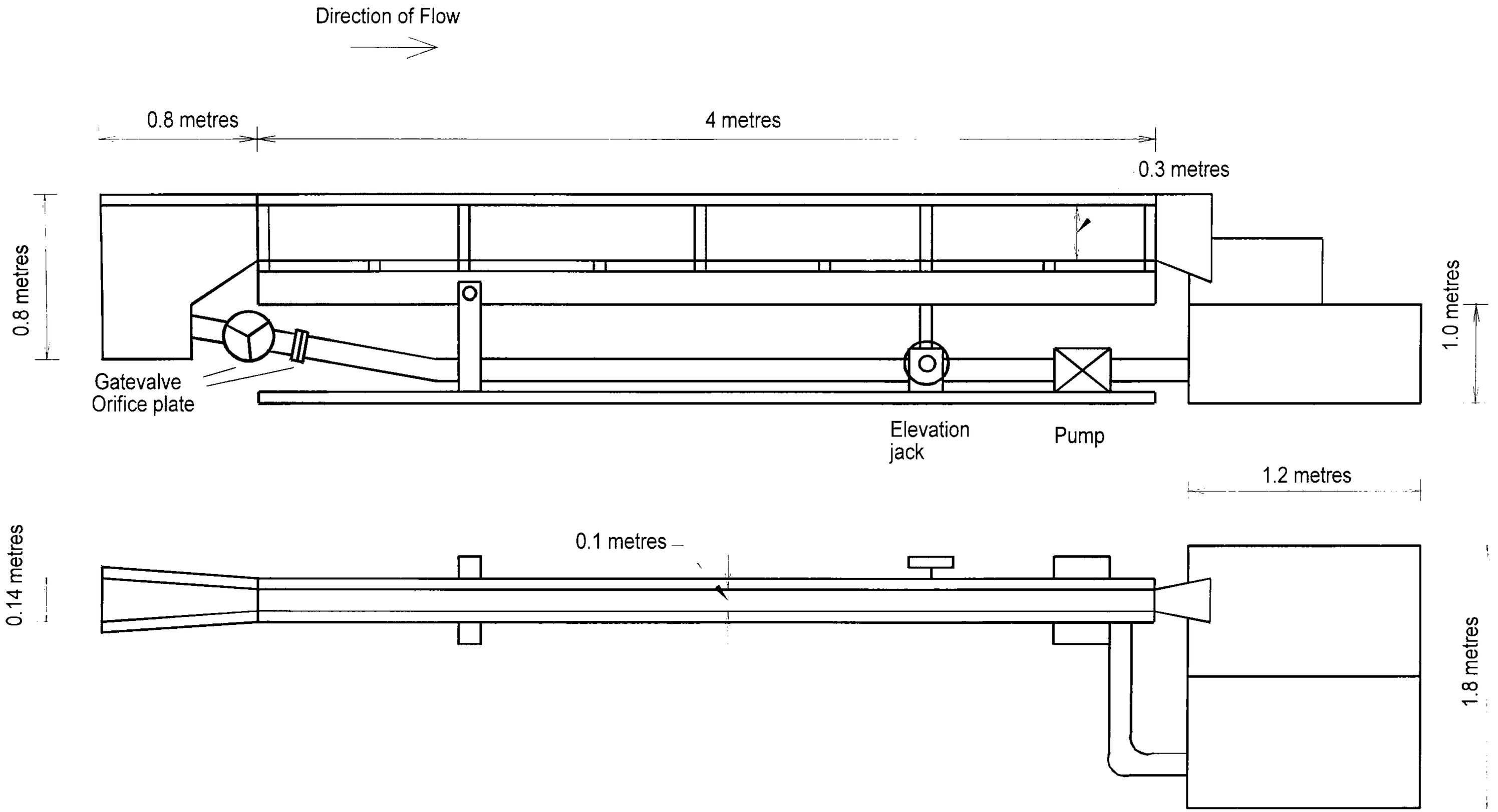

NB - Not to scale

Figure 3.4 - Teaching Flume Details

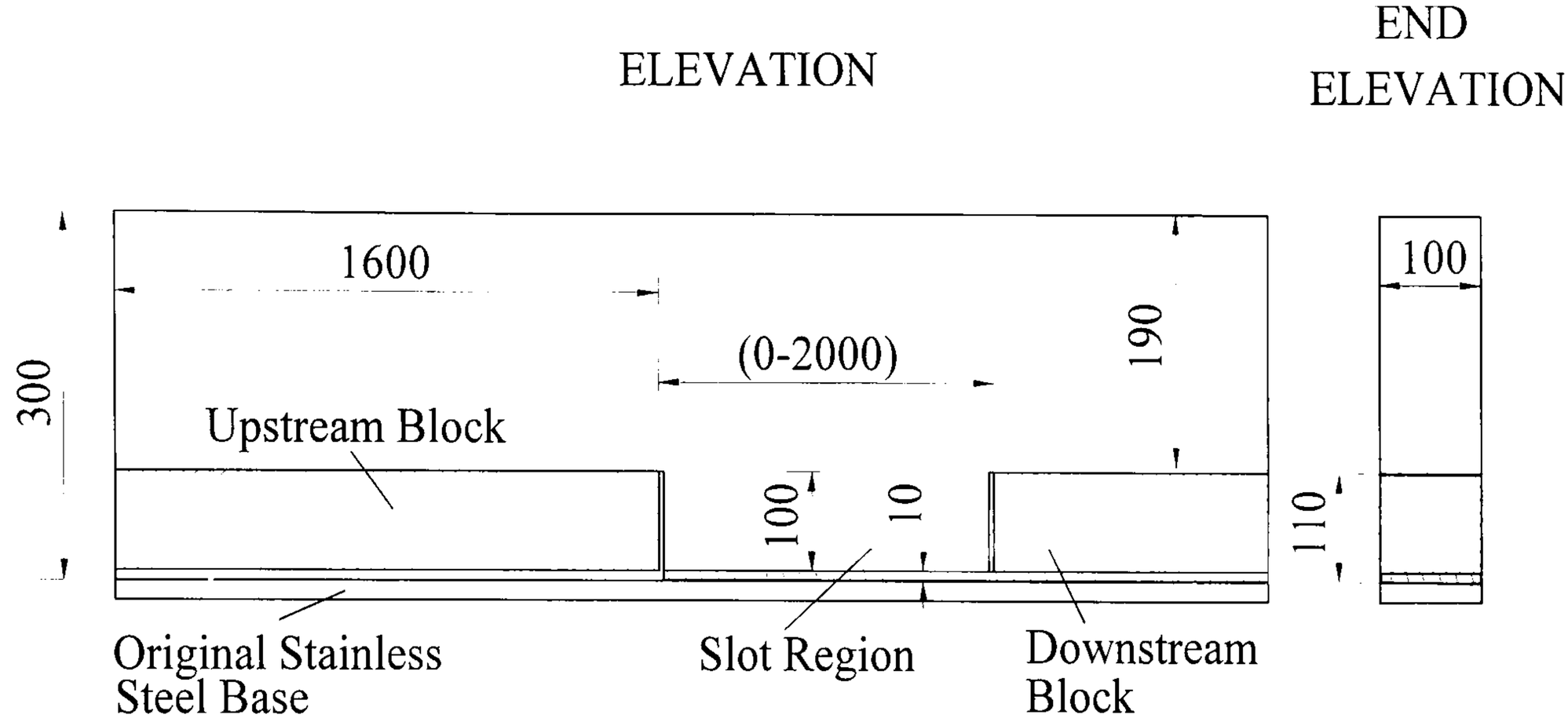

Figure 3.5 - Slot Installation on Teaching Flume

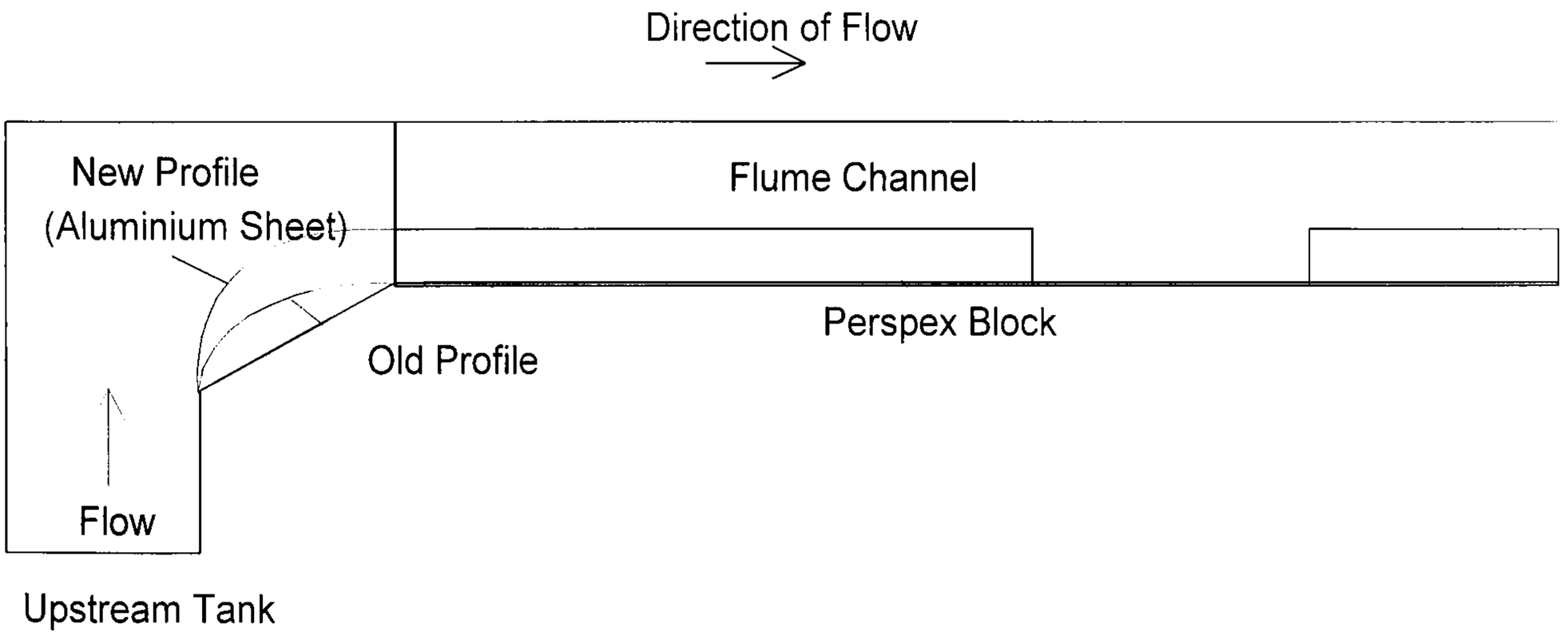

Figure 3.6 - Schematic Diagram of Flow Transition from Upstream Tank to Flume Channel in Teaching Flume

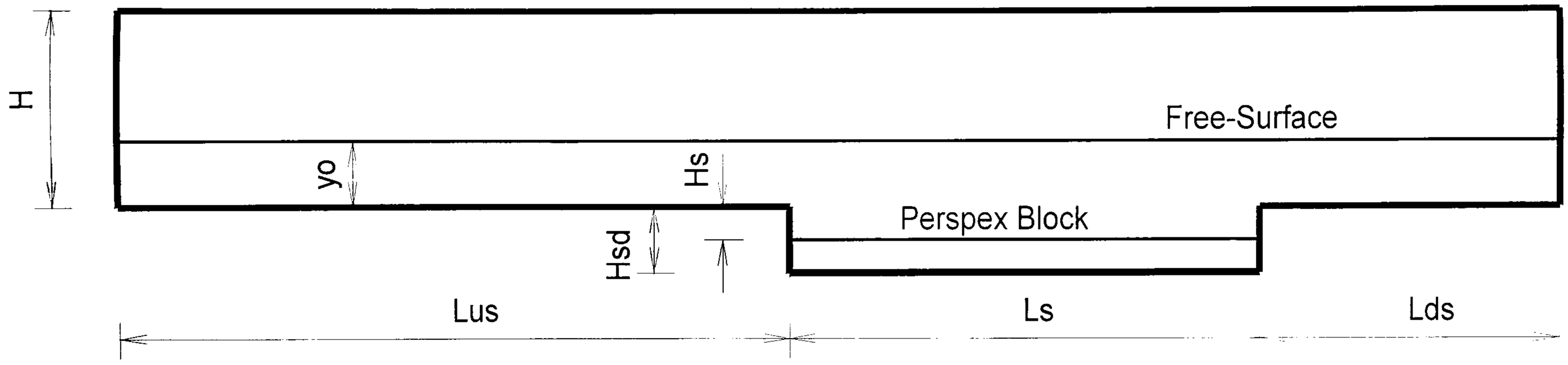

END ELEVATION

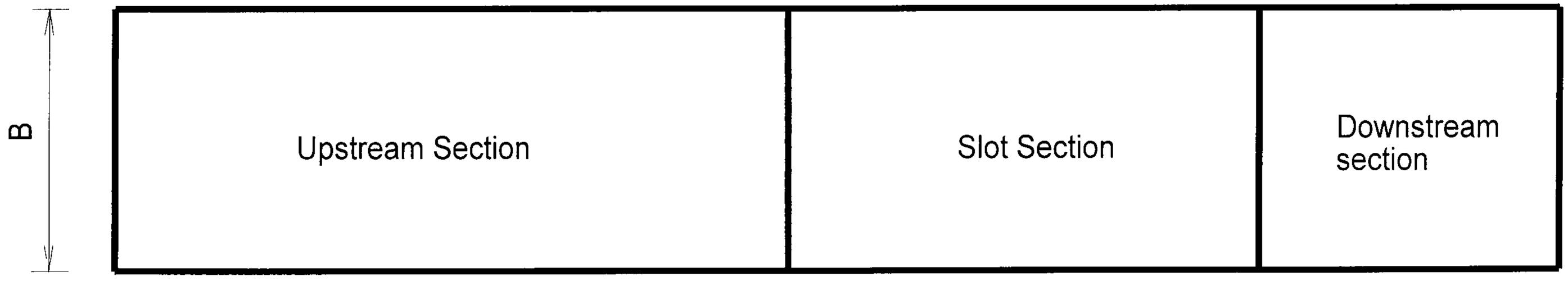

PLAN

Figure 3.7 - Schematic Layout of Main Flume

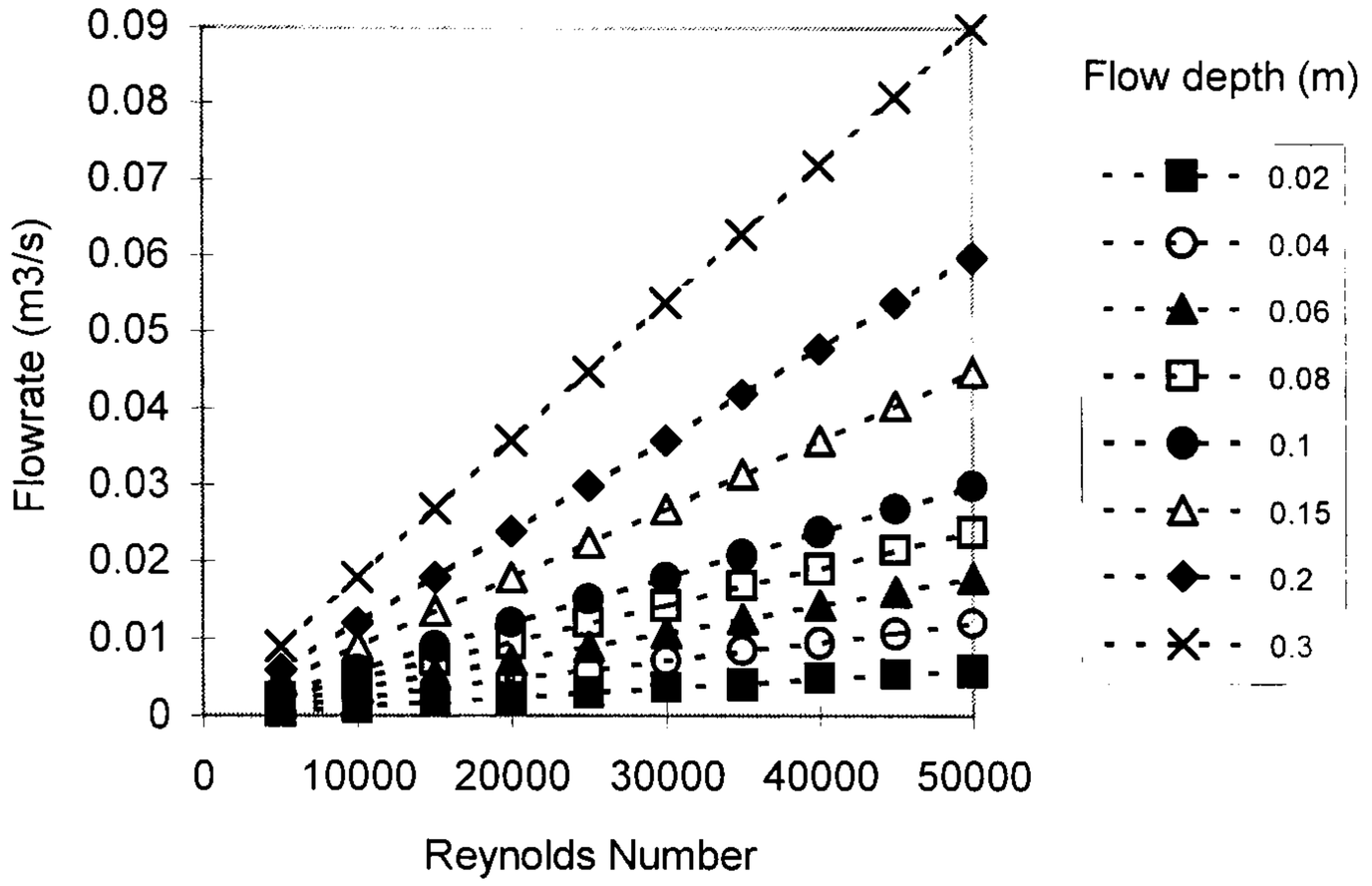

Figure 3.8 - Flowrate vs Reynolds Number for Various Flow Depths

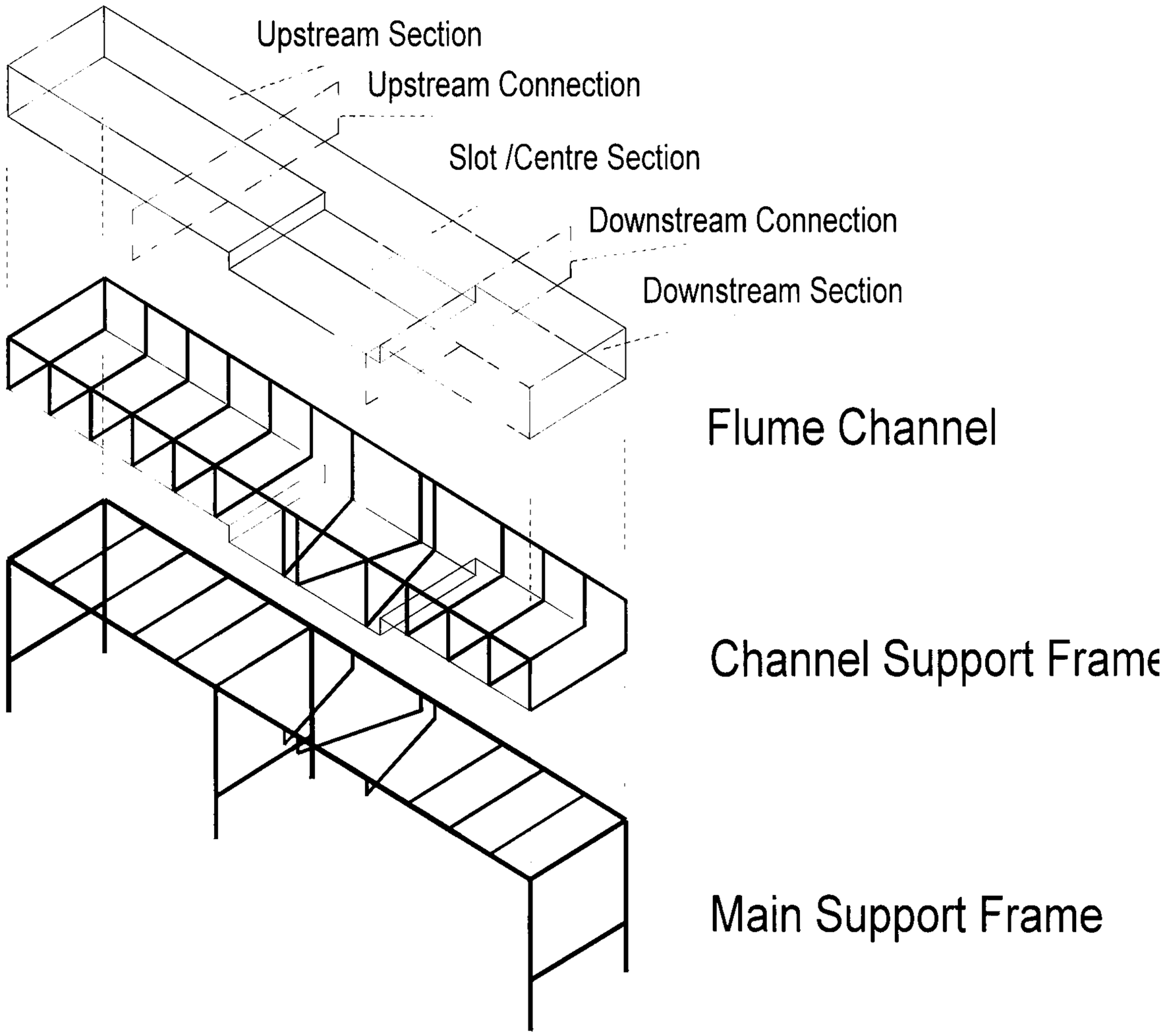

Figure 3.9 - Schematic Representation of Main Flume Components

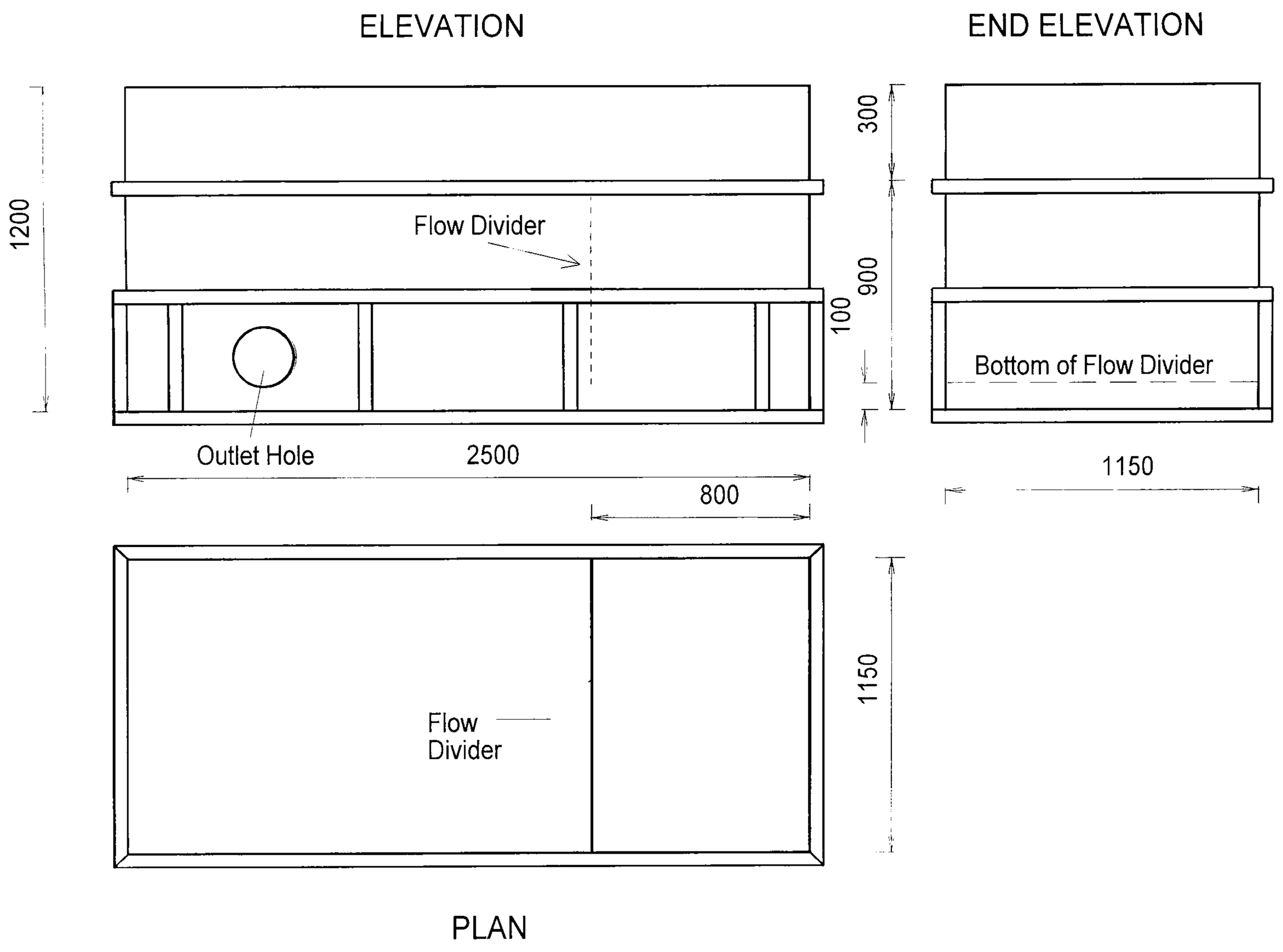

Figure 3.10 - Downstream Tank Details

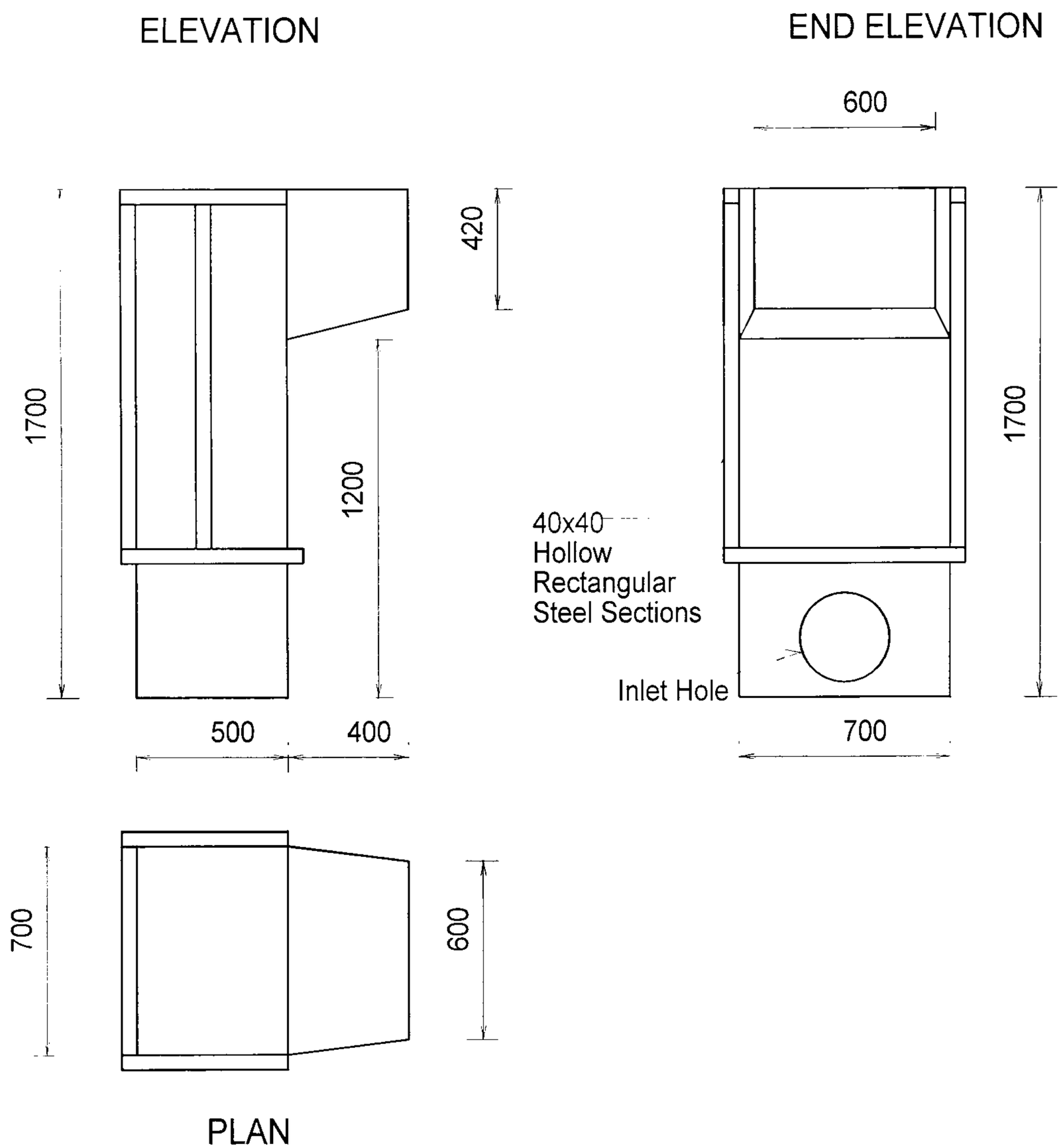

Figure 3.11 - Upstream Tank details

Plate 3.1 – FlowLite System: Comprising of a Flow Velocity Analyser, Laser-Optics Unit and Computer Software

Plate 3.2 – Warning Signs and Red Light on Laboratory Door

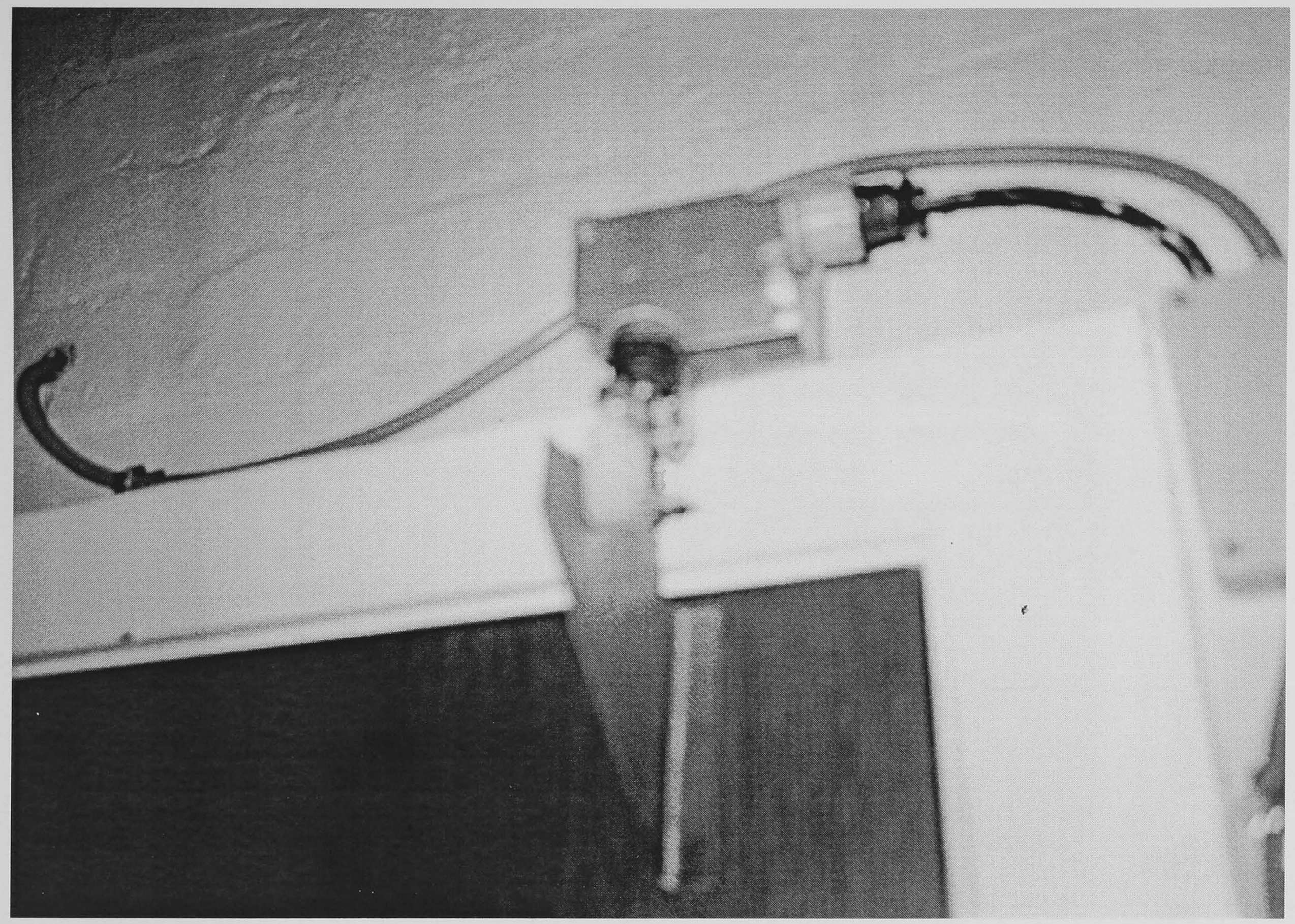

Plate 3.3 – Laboratory Door Micro-Switch

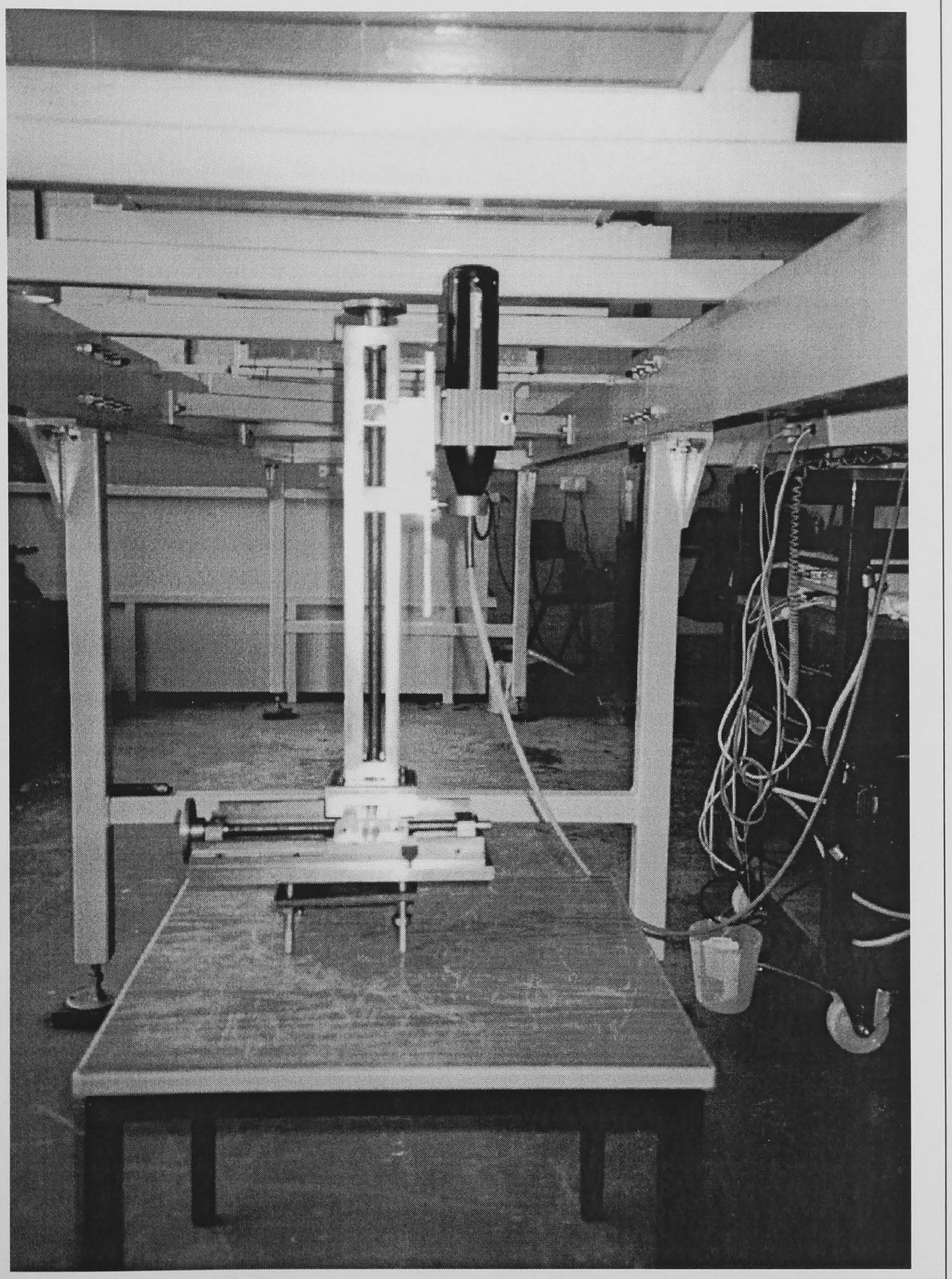

Plate 3.4 – Laser Support-Traverse (with Probe in Vertical Position)

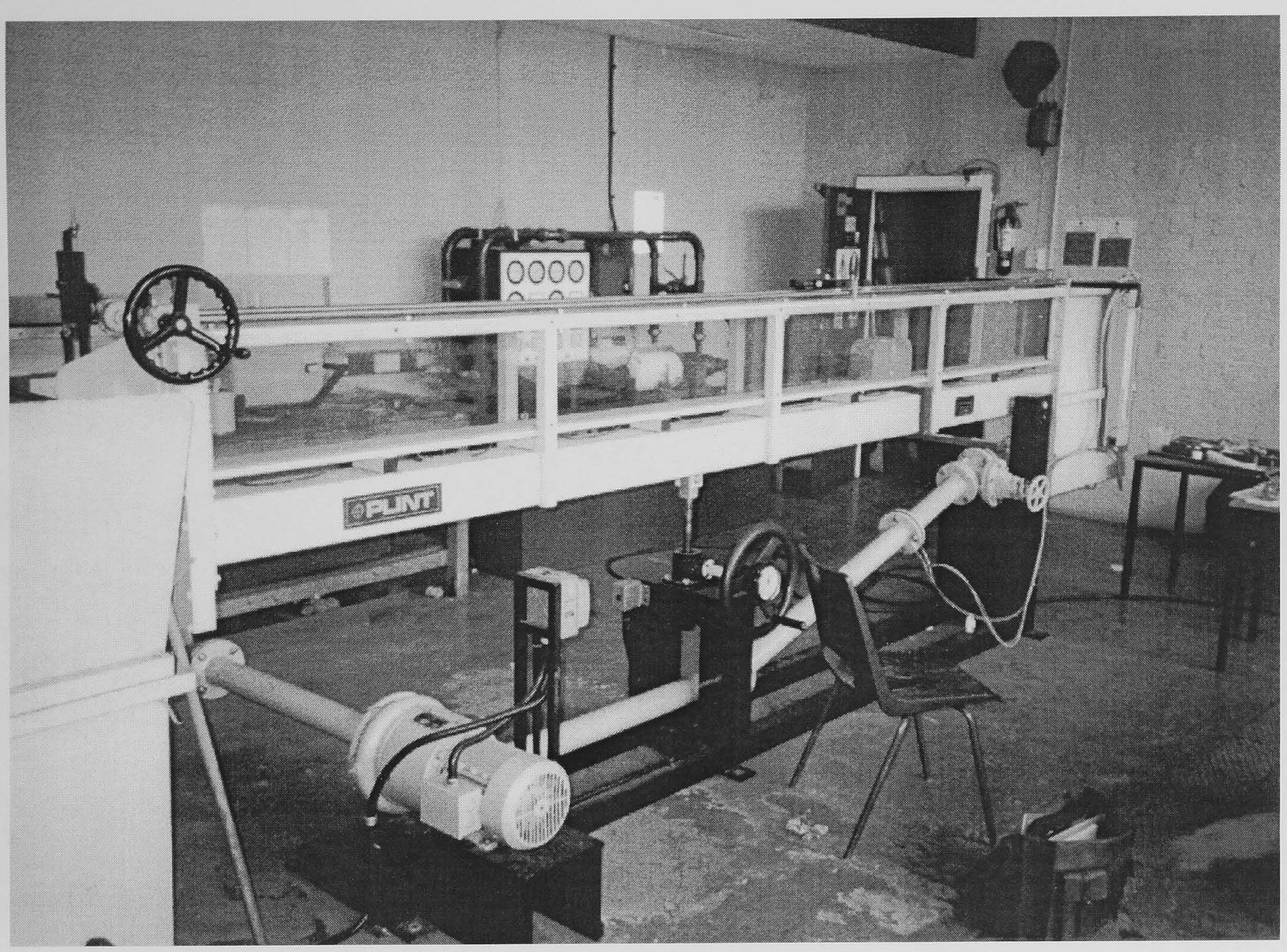

Plate 3.5 – Laboratory Flume (General View 1)

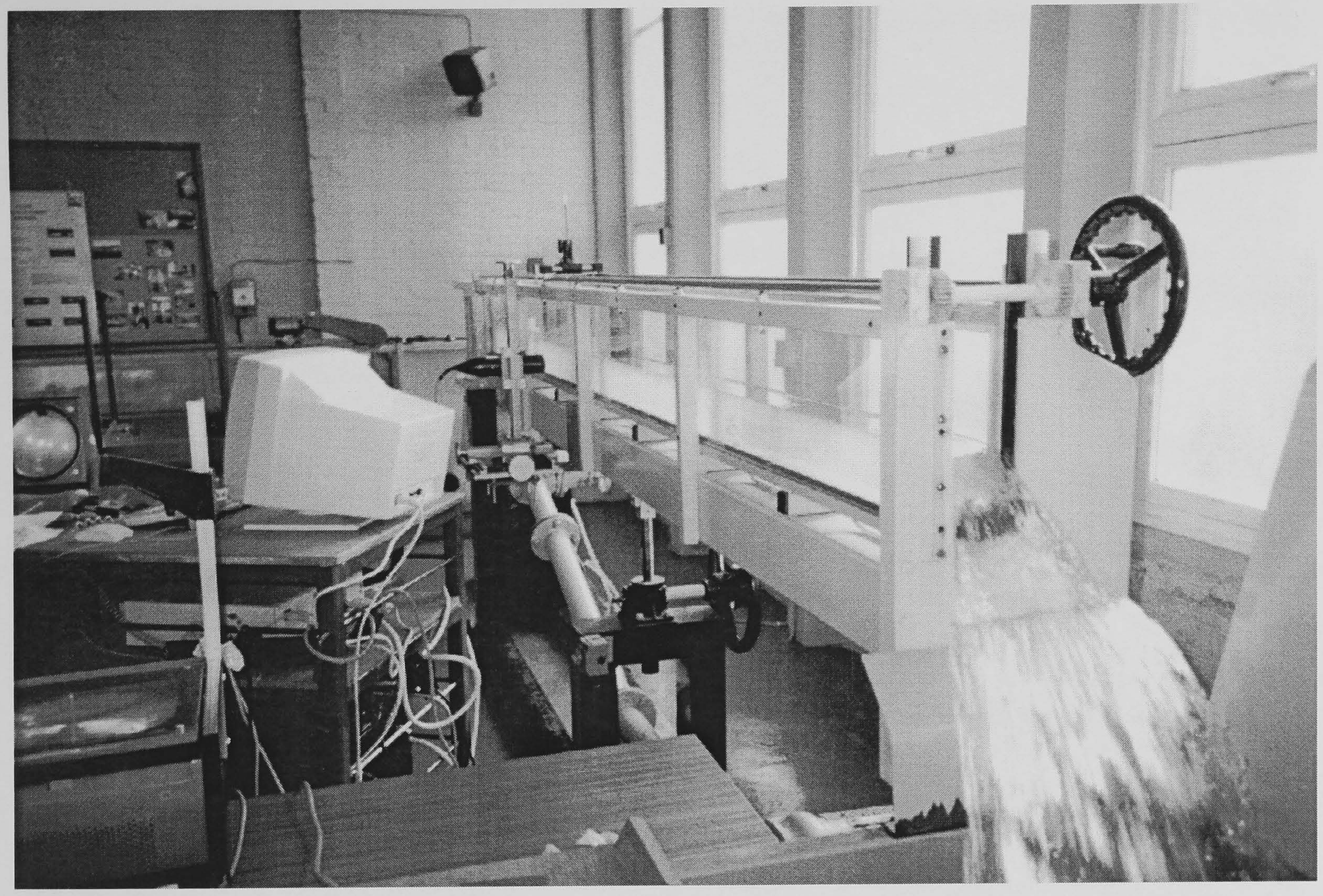

Plate 3.6 – Laboratory Flume (General View 2)

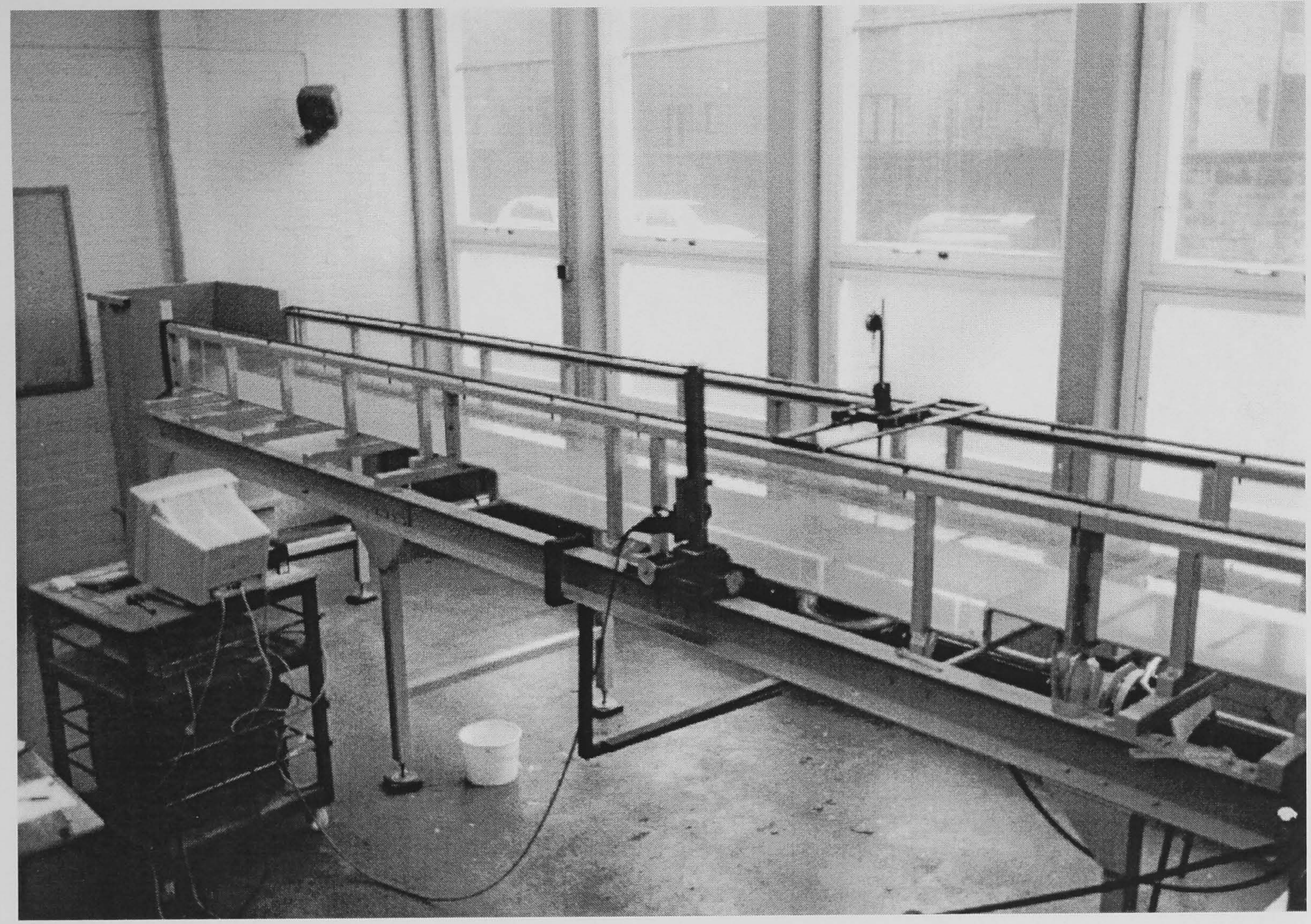

Plate 3.7 – Main Flume (General View 1)

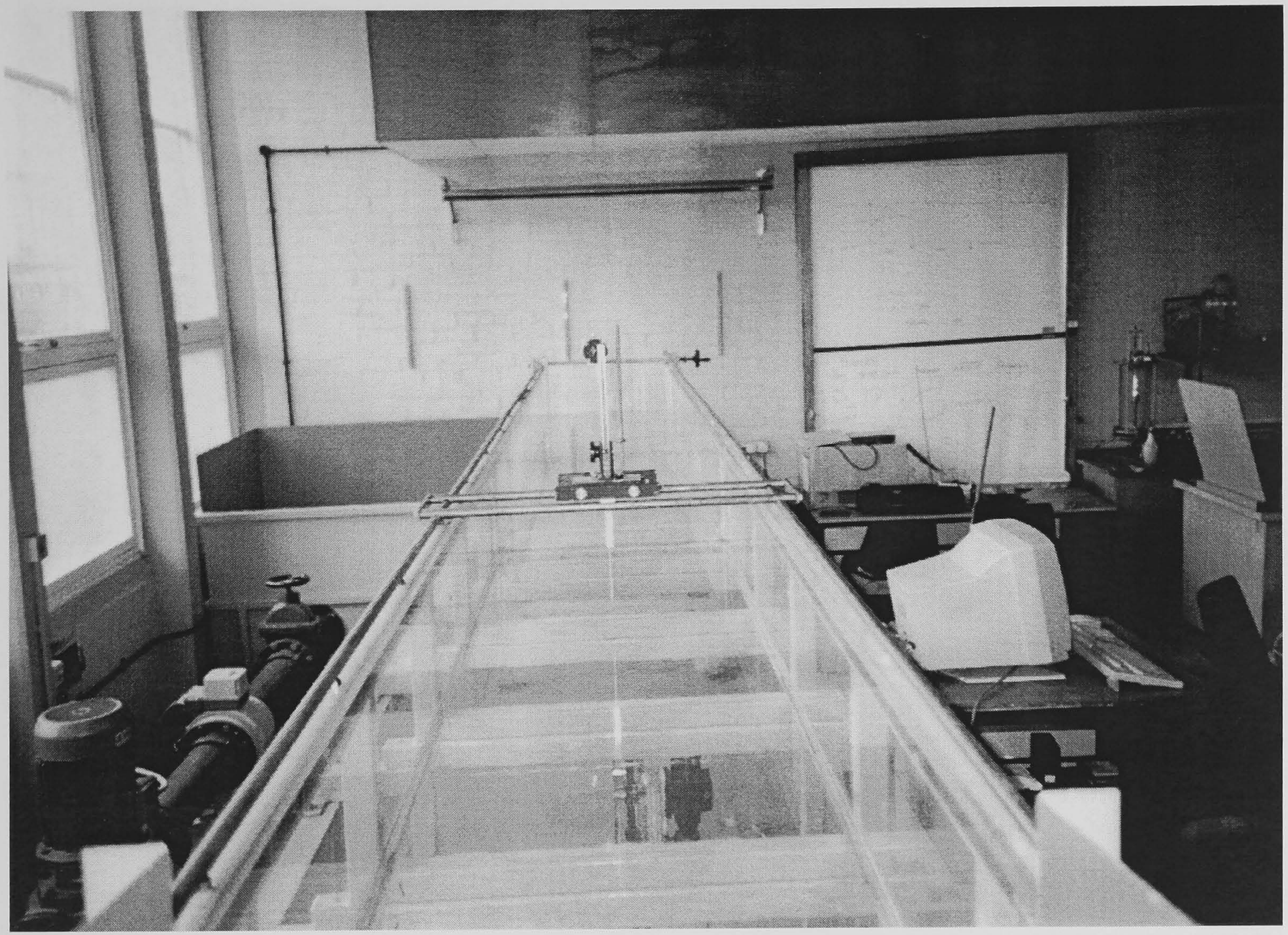

Plate 3.8 – Main Flume (Looking Along Channel)

Plate 3.9 – Vibrational Pads: Used on Main Flume Support Legs

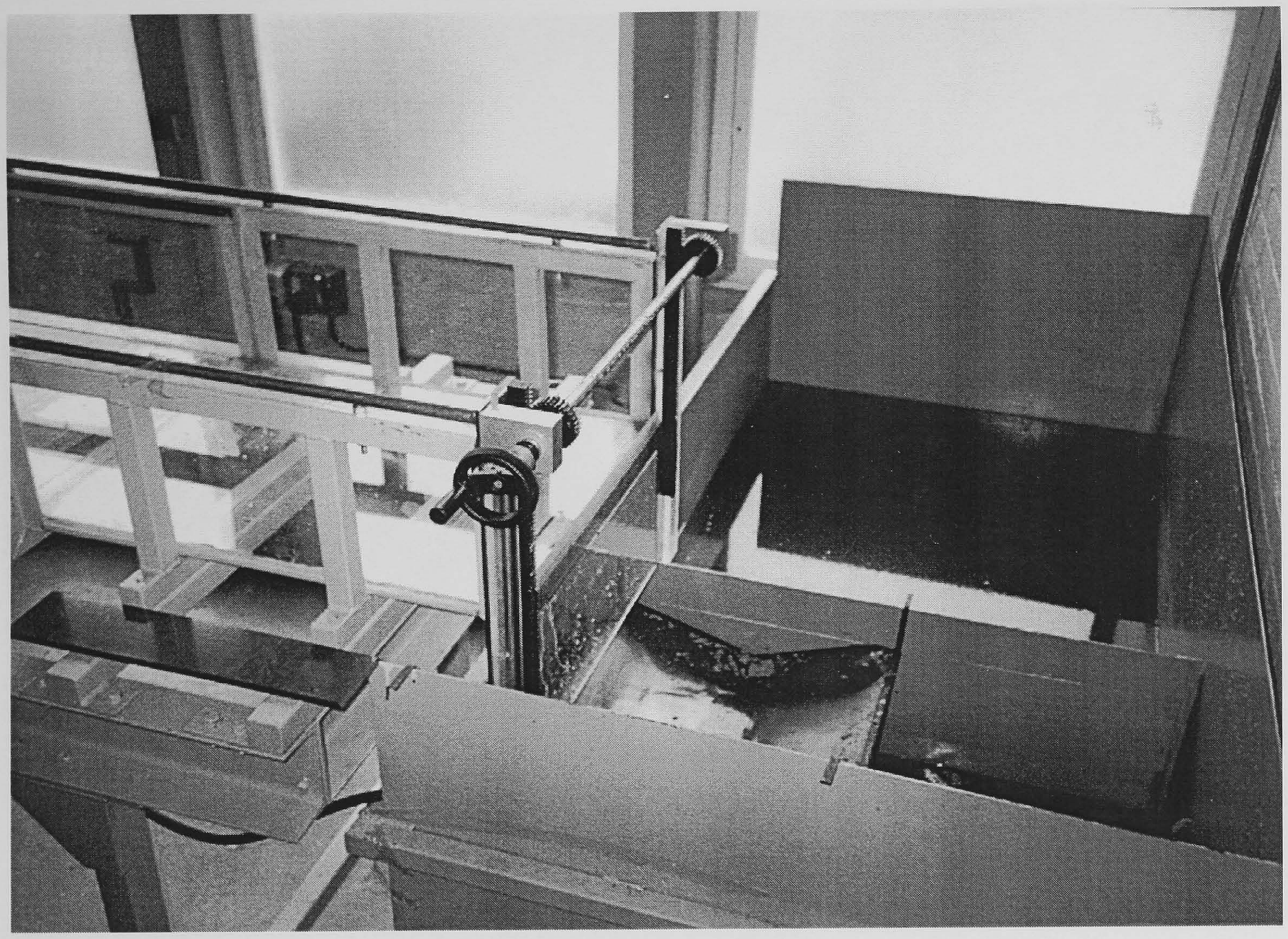

Plate 3.10 – Downstream Tank (General View)

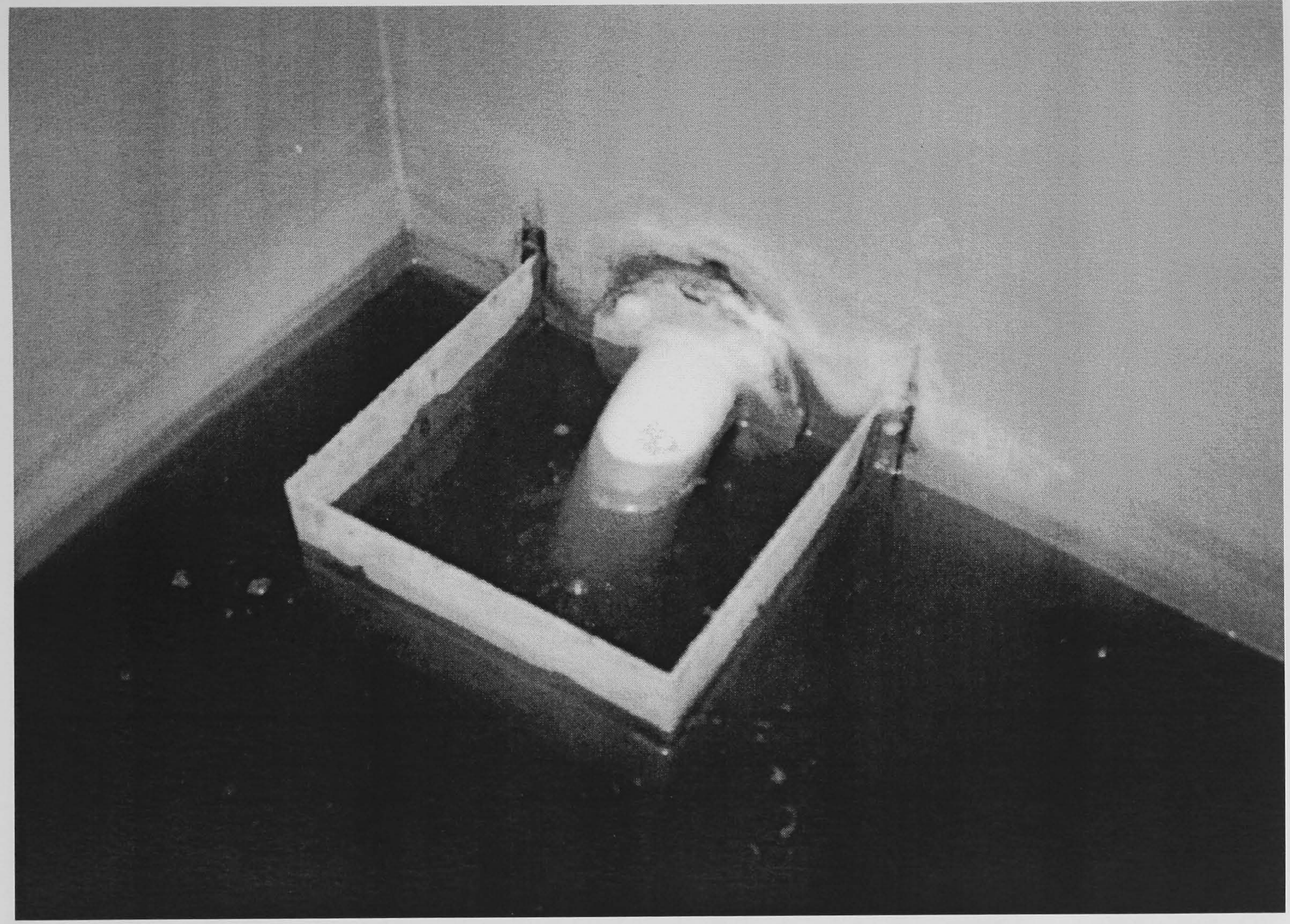

Plate 3.11 – Downstream Tank (Outlet Pipe)

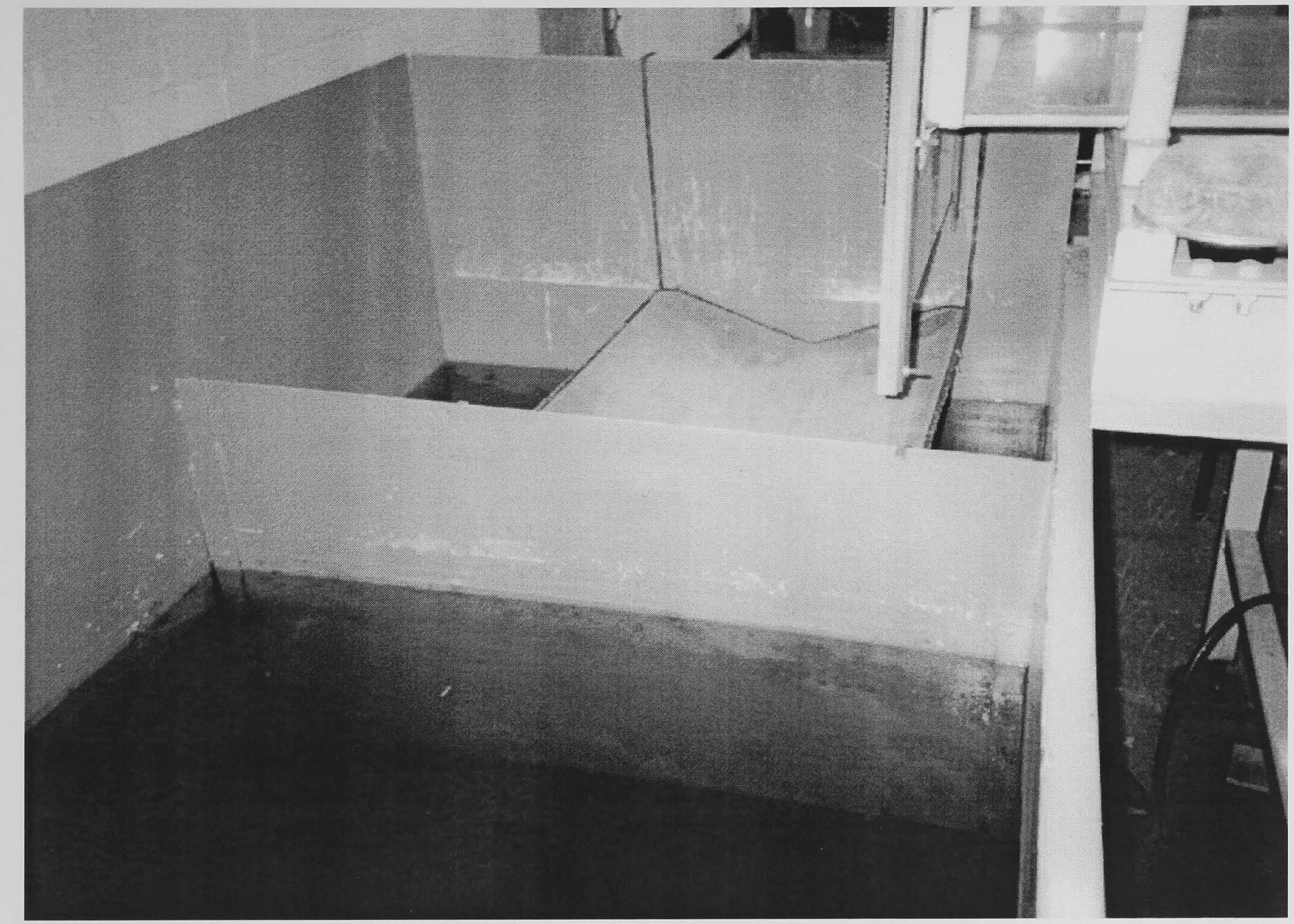

Plate 3.12 – Downstream Tank (Dividing Plate, with Mesh Filter in background)

Plate 3.13 – Upstream Tank (General View)

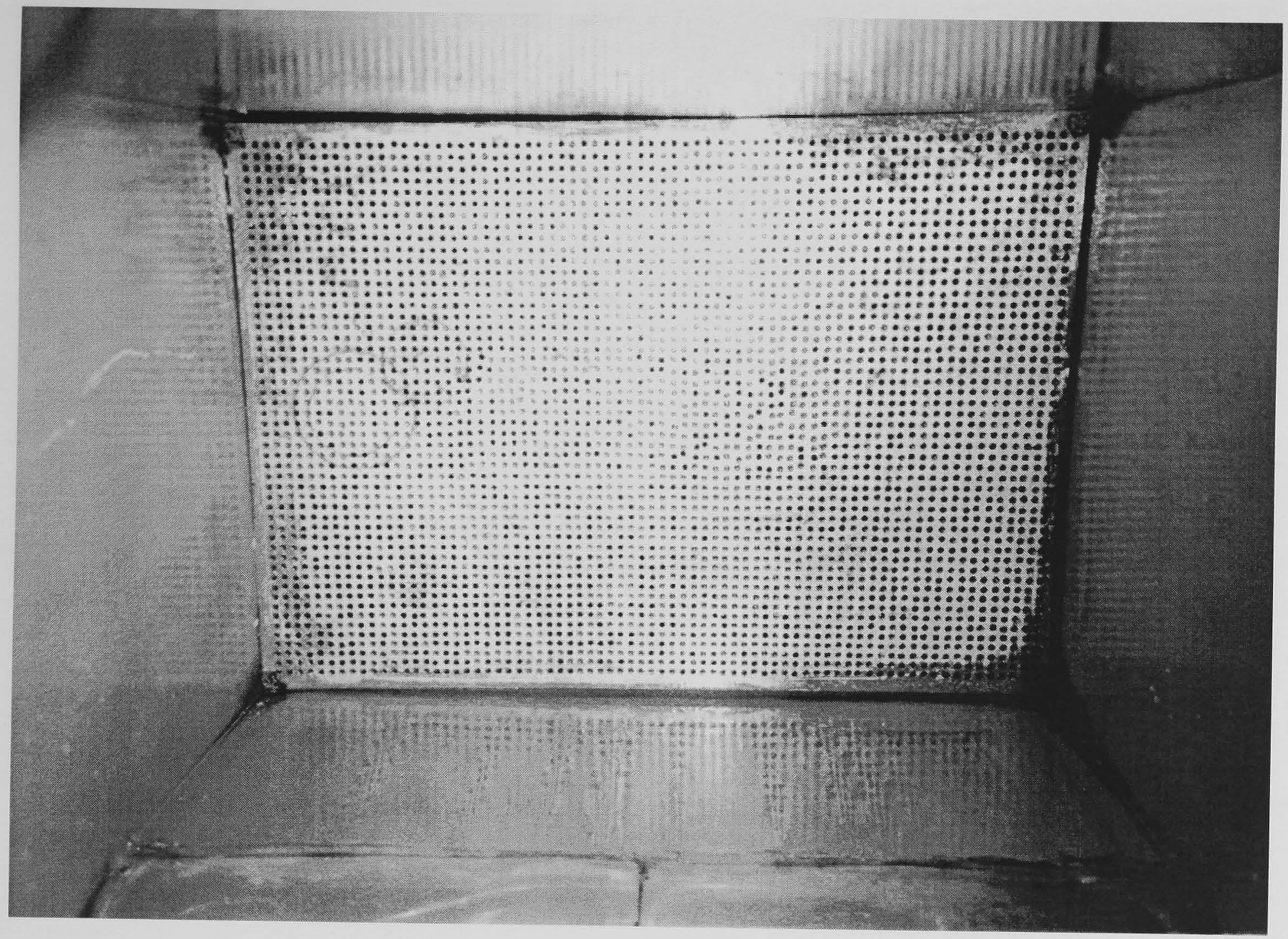

Plate 3.14 – Upstream Tank (Turbulence Diffuser)

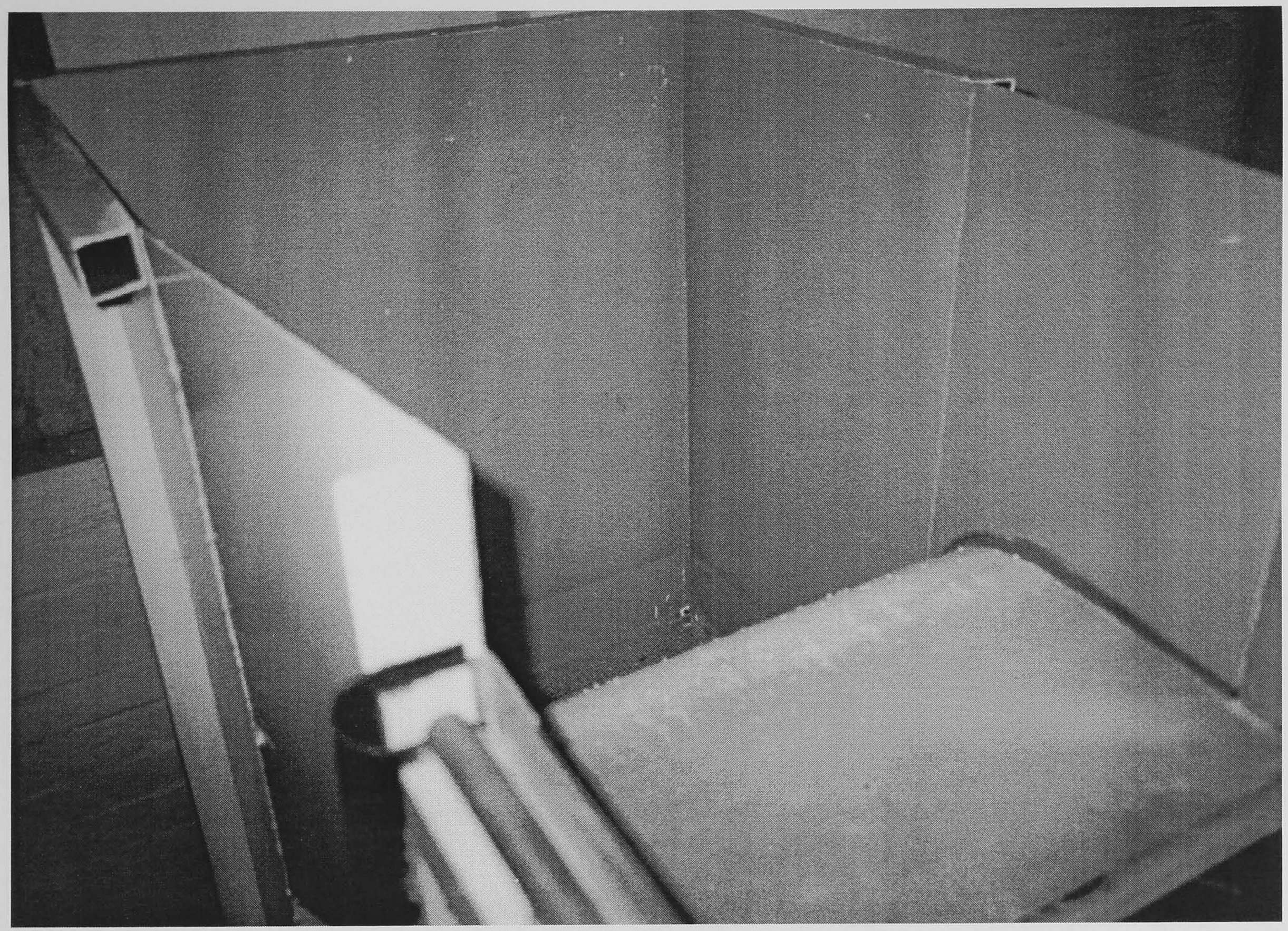

Plate 3.15 – Upstream Tank (Vertical and Horizontal Transitions)

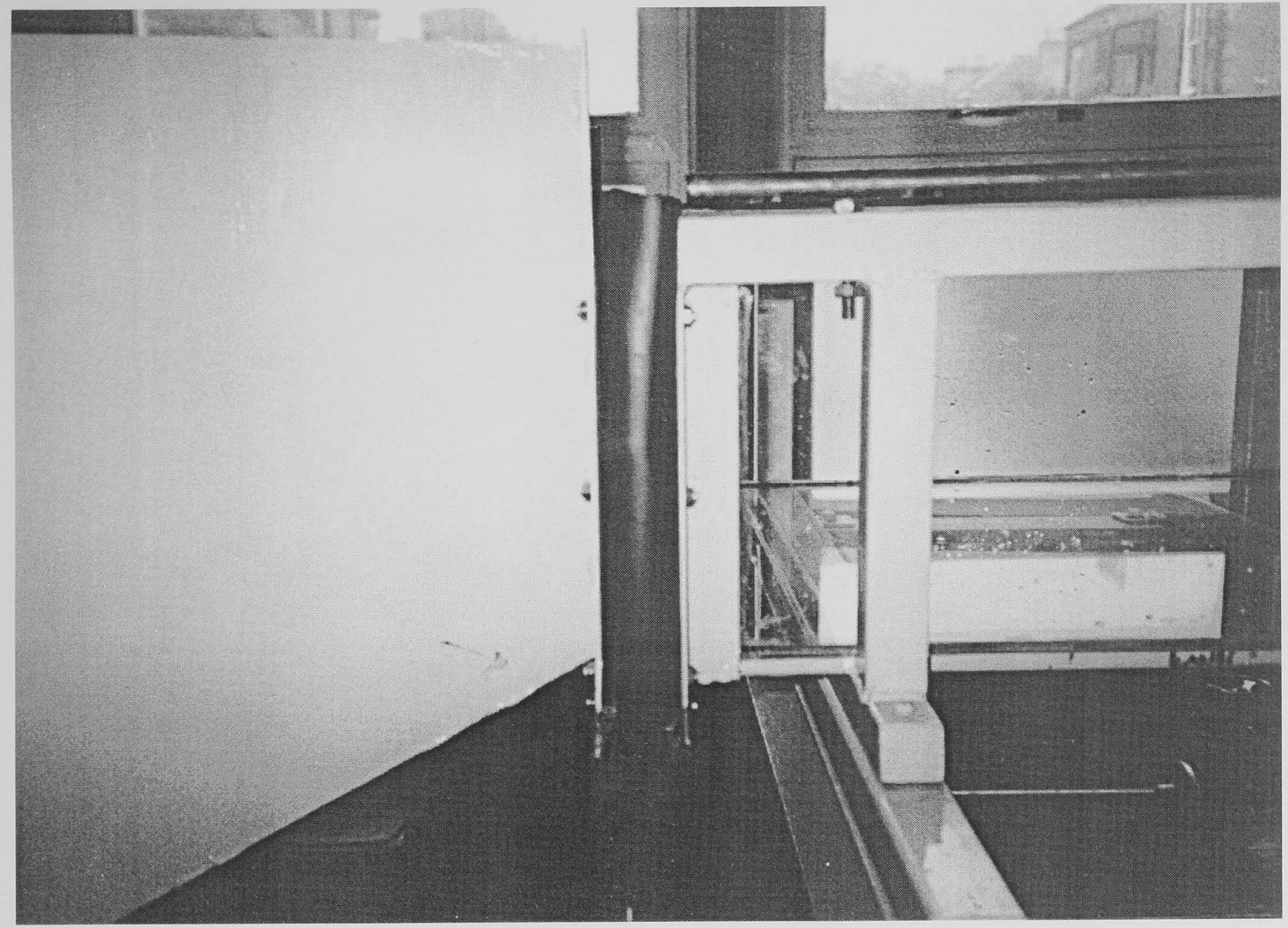

Plate 3.16 – Upstream Tank (Tank-Flume Connection)

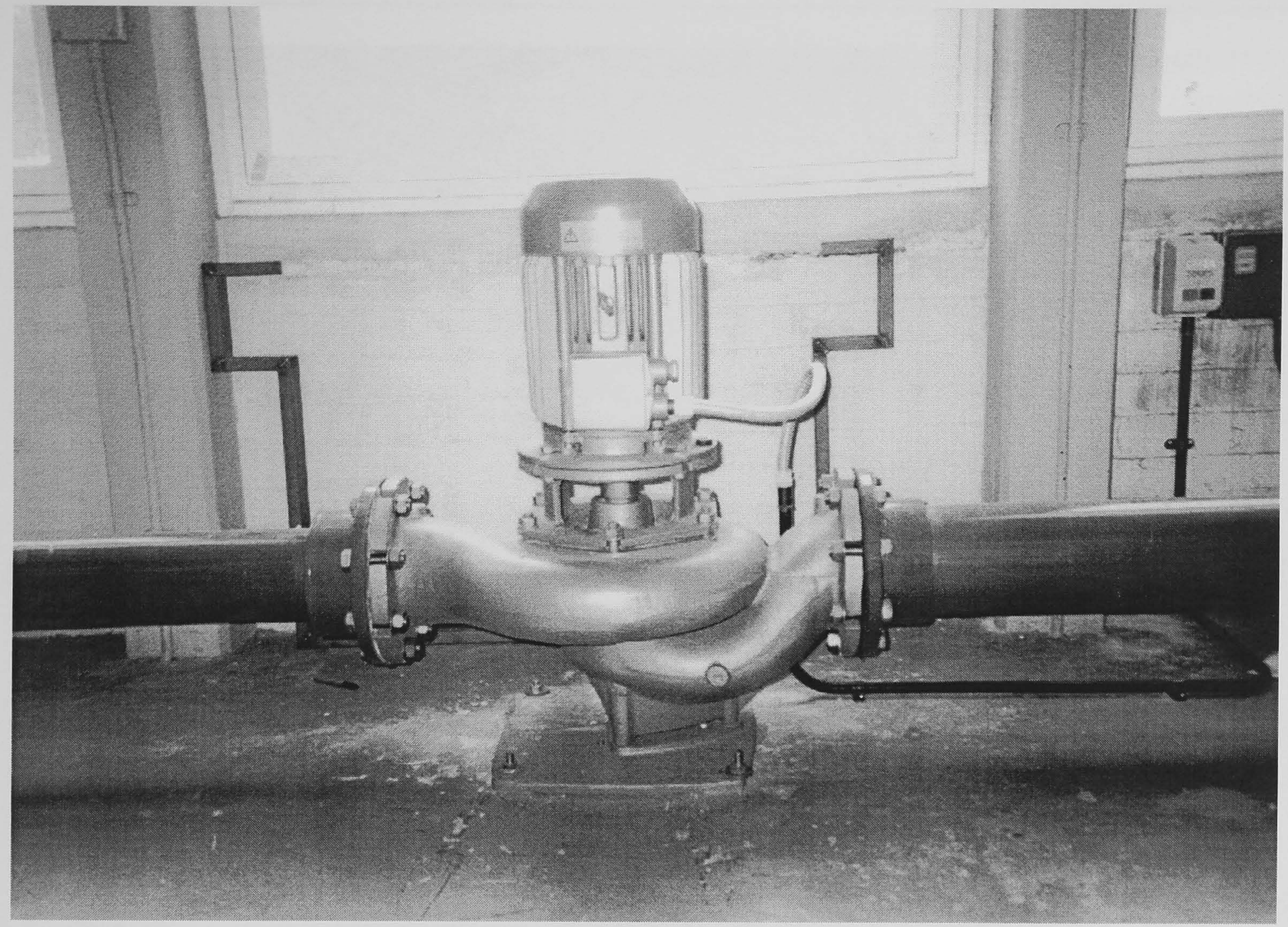

Plate 3.17 – Main Flume Pump (Two-Phase Electrical Supply with On/Off Switch on Wall)

Plate 3.18 – Pipework Layout Used in Main Flume

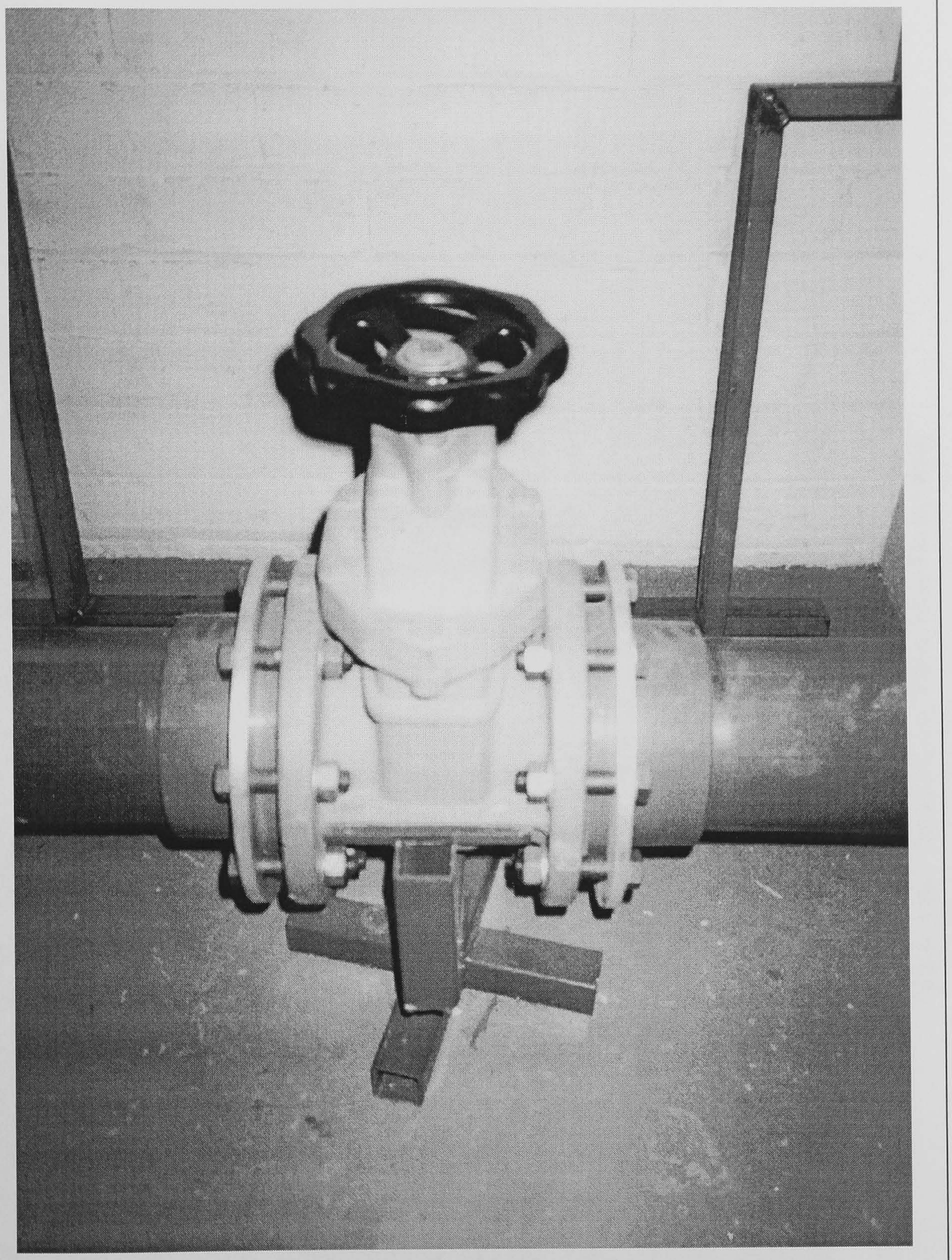

Plate 3.19 – Gatevalve Used in Main Flume

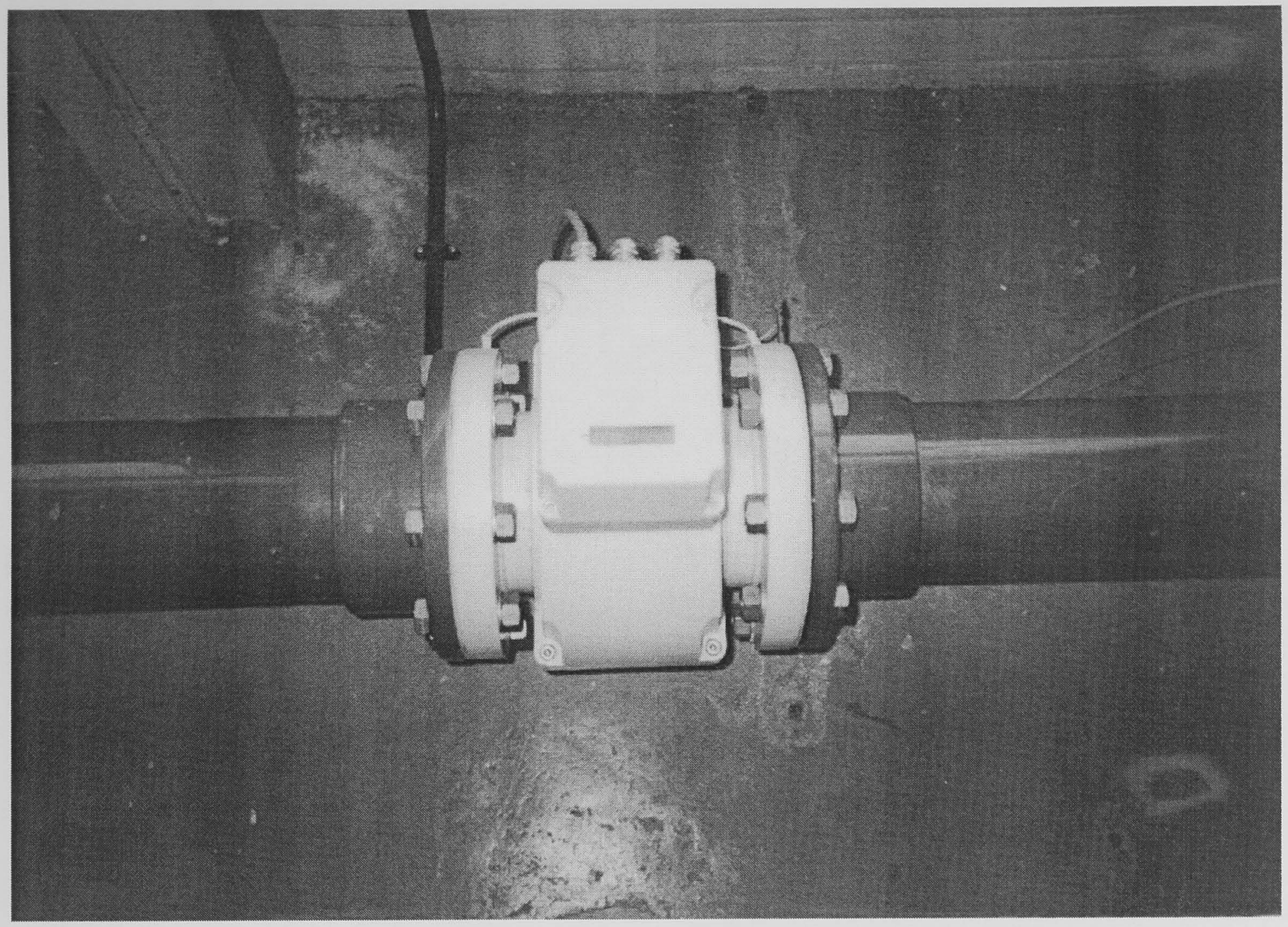

Plate 3.20 – Main Flume Electronic Flowmeter

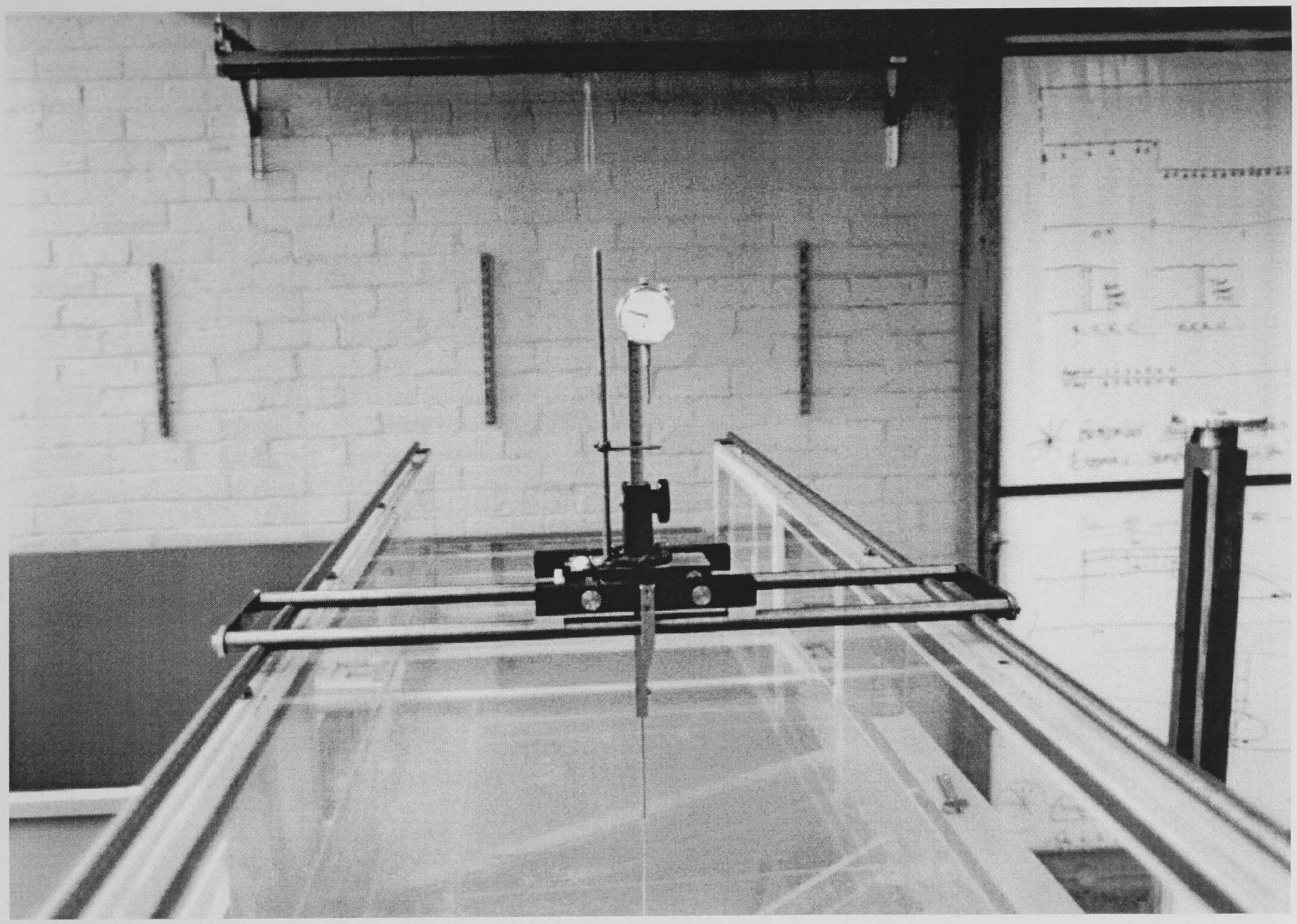

Plate 3.21 – Depth Gauge Used in Main Flume

Plate 3.22 – Jack System for Channel Slope Adjustment

CHAPTER 4

INITIAL STUDY & MAIN FLUME CALIBRATION

4.1 INTRODUCTION

4.2 INITIAL STUDY

4.2.1 Introduction
4.2.2 Physical Set-Up
4.2.3 Hydraulic Conditions
4.2.4 Flow Field Limits of Observation
4.2.5 Flow Field Discretization
4.2.6 LDV Sampling Rate

4.3 INITIAL STUDY - RESULTS

4.3.1 Introduction
4.3.2 Slot Aspect Ratio - 2
4.3.3 Slot Aspect Ratio - 5
4.3.4 Slot Aspect Ratio - 10
4.3.5 Slot Aspect Ratio - 15
4.3.6 Backward Facing Step

4.4 MAIN FLUME

4.4.1 Introduction
4.4.2 Flume Bed Elevations
4.4.3 Flume Sidewall Spacing, Vertical Alignment and Smoothness
4.4.4 Flume Centreline

4.5 DATA VALIDATION

4.5.1 Introduction
4.5.2 Minimum Number of Samples
4.5.3 Laser Beam Rotation

CHAPTER 4

INITIAL STUDY & MAIN FLUME CALIBRATION

4.1 INTRODUCTION

During the design and construction of the main flume, an initial study was undertaken using the teaching flume as detailed in section 3.4. This study aimed at providing the following:

(i) Familiarisation with the laser-Doppler velocimetry (LDV) system and data acquisition methodology.
(ii) An insight into the flow characteristics of rectangular open-channel flow.
(iii) An insight into the flow characteristics of open-channel slot flow.
(iv) A basis for the design of the main flume and recommendations for the main study.

The initial study was successful in its aim, providing the author with the required knowledge to undertake a 3-dimensional analysis of open-channel slot flow. It was evident from this study that many factors influenced the quality of data obtained using the method of LDV, such as, the location of the control volume in the flow-field, the quality of the water, the type of flow, and the controlling parameters governing the LDV system. To overcome the problems highlighted in the initial study, and from an understanding of the principle of LDV measurements, a series of conditions were established to improve and maintain a high degree of integrity of data acquisition.

The main flume was also used for an investigation of rectangular open-channel flow. This served the following purposes:

(i) To investigate the flow characteristics which develop under different hydraulic conditions.

(ii) To assess the integrity of the LDV measurements.

(iii) To establish accurate experimental methods.

4.2 INITIAL STUDY

4.2.1 Introduction

The purpose of the initial study was to investigate some known characteristics of open-channel slot flow, especially flow separation and its associated recirculation zone, reattachment point and shear layer development. The study was limited to a 2-component analysis, with the acquisition of mean and fluctuating velocity components in the vertical and longitudinal directions, i.e. u, u', v and v' respectively. This limitation was caused by the solid base of the flume which did not allow penetration of the laser, thereby limiting access of the laser to the sidewalls only.

Another physical restriction was the low flume breadth to depth ratio of 0.333. The relatively small width of the flume caused sidewall contamination at practical depths of flow. Although a low depth would eradicate sidewall contamination, it would be impractical with the LDV system. This was due to the restriction of the laser beam at the channel bed and free-surface, as described in section 3.4.

Despite these restrictions, a study was undertaken to establish the general flow characteristics which develop in open-channel slot flow. Instantaneous point velocities were measured throughout the flow field for a series of aspect ratios, A_s, defined as slot length/slot height. The author felt, however, that a detailed investigation at this stage would both be time consuming and have limited application. Therefore, the investigation at this stage concentrated on only one set of flow conditions, i.e. constant Reynolds number, flow depth and slot height.

This initial investigation also gave an insight into the taking of LDV measurements, highlighting the need to establish the correct set-up parameters of the system and the requirements to maintain a high degree of integrity with the measurement techniques.

4.2.2 Physical Set-Up

Adjustments to the teaching flume were required for its use in this initial study. The main adjustment being the addition of perspex blocks to create a series of slots of height, H_S with

various lengths (see section 3.4). The slot aspect ratios, A_S, created using these blocks were 2, 5, 10 and 15. Also investigated was a BFS, achieved by omitting a downstream block.

These aspect ratios were chosen as they allowed a wide range of slot flow characteristics to develop. With a low A_S such as 2, the slot is filled by a single recirculating cell. Increasing the A_S to 5 illustrates the flow characteristics prior to flow reattachment within the slot. With flow reattachment likely to occur between A_S=5-10, using an A_S=10 would illustrate reattached flow close to a FFS. Increasing to A_S=15 allows the flow to develop beyond reattachment prior to the sudden contraction at the FFS. Finally, the use of a BFS allowed rectangular open-channel flow conditions to develop without the influence of a FFS.

4.2.3 Hydraulic Conditions

With the physical conditions of the channel established, the hydraulic conditions were then considered. It was decided that a main channel depth, y_o, of 0.1m (i.e. similar to the slot depth) would be used. Flow depths which would eradicate sidewall contamination would be impractical in this flume, as described in section 3.4, and therefore it was accepted that such a problem was an inherent factor in this investigation.

Although a range of Reynolds numbers from 0-50000 could be achieved in this flume, time restrictions limited this to a single set of flow conditions. According to French (1994), the use of the hydraulic radius as the characteristic length for calculating Re is suited more to narrow channels. Using the hydraulic radius, a Reynolds number of 10000 was chosen. It was anticipated that this would generate a mean velocity similar to those used in the main investigation. It was also observed that Reynolds numbers greater than this created a wavy distortion of the free-surface, thus making measurements in this part of the flow difficult.

The data acquisition was time consuming, taking several days to complete one full sweep of the flow field for each aspect ratio. The consequence of this was the interruption of the flow conditions due to repeated stopping and starting of the flume for each block of data measurements. This caused minor changes in the flow rate each time, and therefore adjustment of the gate-valve was generally required to re-establish the required flowrate. Once the flow depth was re-established at 0.1m, several inlet profiles were taken and compared to flow profiles taken from the initial flow rate. This process was repeated until the flowrate was within 98% of the original flow condition. This method allowed an accurate assessment of the flow rate to be

made in a relatively quick time, and proved to be more accurate than using the mercury manometer installed on the flume (see section 3.4.2).

4.2.4 Flow Field Limits of Observation

The first stage in the discretization of the flow field was to determine the limits of observation. For this experiment, only the centreline flow field was considered, therefore limiting the number of sweeps to one per aspect ratio. Although the slot region was the main area of interest, limiting the study to this region would have ignored the effects of the flow over the FFS. The range of measurements were extended beyond the FFS to increase the scope of the study, facilitating an investigation of the flow characteristics in the immediate area of the FFS and its recovery to normal open-channel flow conditions. The downstream limit of observation was selected as 700mm beyond the slot, or $7H_s$.

Similarly, the flow upstream of the slot is also of interest, as it provides the inlet and normal open-channel flow conditions. It may also highlight any upstream influence the slot may have on the flow. There is however a limitation imposed by the overall length of the flume, and the time restraint for data acquisition. With this is mind, the upstream limit of observation was chosen as 500mm upstream of the slot, or $5H_s$.

4.2.5 Flow Field Discretization

To provide a picture of the flowfield (i.e. mean velocities and turbulence intensities), the U and V velocity time series were sampled at a number of discrete points within the ranges given above. The velocity samples were taken on a grid, the discretisation of which was considered in detail prior to data acquisition.

Due to time limitations, a dense discretization of the flowfield would be impractical. The flow in the slot is the principal area of interest, and therefore requires the greatest attention. Since the flow depth in the slot was 200mm throughout this study, a constant number of vertical sampling points was used. These points are defined in terms of the incremental change in height, Δy, which is equal to the slot depth, y_S, divided by the number of points in the profile. Selecting a high number of points would be time consuming, while selecting a low number of points will potentially overlook the detail of the flow characteristics being investigated. By trial and error

using different discretisations, a suitable number of points for the vertical traverse was chosen as 20, thereby, the incremental change in height between points is given by:

$$\Delta y = y_S/20 = 200/20 = 10\text{mm}$$

To achieve this, the first point was at a depth of 5mm i.e. ($0.5\Delta y$), and the last point was at a depth of 195mm i.e. ($200\text{-}0.5\Delta y$).

A similar approach was adopted for the longitudinal incremental change, Δx. Consideration was given to the fact that the length of the slot, L_S, varied for each aspect ratio. Using a constant Δx would mean the number of vertical profiles would increase as the slot length increases, alternatively, a constant number of profiles could be established, meaning that Δx would be different for each aspect ratio. It was decided that since both methods had advantages and disadvantages, depending on the aspect ratio, a mixture of both would be used. To maintain the number of vertical profiles to 20 (for As=2, 5 and 10), the longitudinal increment, Δx, was equal to $L_S/20$. For As=15 and the BFS configuration, the Δx for A_S=10 was maintained. In most cases, this produced a grid of 400 defined sample points within the slot domain.

For both the upstream and downstream regions of the flow, Δy remained the same i.e. 10mm, allowing points in the main channel profiles to tie in horizontally with the slot profiles. It was anticipated that the upstream section of the flow required less longitudinal measurements. In general, profiles were taken at increments of Δx=50mm in this region. A similar approach was adopted for the downstream section, with more detail provided immediately downstream of the FFS.

4.2.6 LDV Sampling Rate

The validity of the data from each measurement point is highly dependent on the sampling frequency and the number of samples taken. It was evident that the sampling frequency was affected by the location of the control volume within the flow field and the clarity of the water itself. In general, the sampling rate varied between 40-100hz throughout this investigation. In certain areas where the velocity was low, such as the upstream corner of the slot, the sampling rate dropped to as low as 10hz. On average, these sampling rates were maintained at each traverse point for 60 seconds, resulting in approximately 2000-6000 samples in the faster flow regions, and reducing to approximately 500-1000 in the slower regions.

Although particle seeding of the water can improve the sampling rate, it was not introduced into the flow during this investigation. It was observed, however, that rust particles caused by the erosion of the cast iron pipework improved the sampling rate, although excessive discoloration was detrimental as this greatly reduced the penetration of the laser into the flow.

4.3 INITIAL STUDY - RESULTS

4.3.1 Introduction

A series of results were taken for aspect ratios of 2, 5, 10, 15 and a BFS configuration. The slot height, H_s, remained constant at 100mm, with an upper channel flow depth, y_o, also of 100mm. A Reynolds number of 10000 was used for each aspect ratio, and the velocity profiles were obtained along the centreline on a defined mesh as described in section 4.2.4.

Both the horizontal and vertical components of velocity were determined independently. The sampling rate varied throughout the flow field, but generally, 3000 samples were taken over a period of 60 seconds at each point. This allowed both the time-averaged velocities, u and v, and the instantaneous velocities, u' and v', to be analysed and represented graphically throughout the flow domain.

The time averaged values, both u and v, were used to plot the flow velocity vectors. The sign notation used regards flow in the longitudinal downstream direction as positive, and in the vertical direction, positive flow is in the upwards direction from the channel bed to the free-surface. For graphical presentation, both the horizontal and vertical axes have been non-dimensionalised using H_s. The vectors have been normalised using u_{max}, which represents the maximum streamwise velocity in the upstream channel section. The y-axis is scaled greater than the x-axis to provide a clearer illustration of the flow, therefore the v-component is consequently exaggerated.

The instantaneous velocities, u' and v', were converted to turbulent kinetic energy (TKE) using equation 4.1.

$$k = \frac{1}{2} . \rho . (\overline{u'^2} + \overline{v'^2})$$

Equation 4.1

where, k = TKE per unit volume,

$\overline{u'^2}$ and $\overline{v'^2}$ = mean squares of the longitudinal and vertical velocity fluctuations respectively.

Filled contour plots of the normalised values, k/k_{up}, have been used to indicate the intensity of TKE, where k_{up} is the maximum upstream value of TKE.

The hydraulic conditions for the initial investigation are presented in table 4.1.

Table 4.1 - Hydraulic Conditions for Initial Investigation

Upstream depth, y_o (m)	Slot height, H_S (m)	Flowrate, Q (m^3s^{-1})	Mean upstream velocity, u_o (ms^{-1})	Reynolds number, Re	Froude number, F	Slope, S
0.100	0.100	2.900×10^{-3}	0.290	10000	0.293	1×10^{-5}

4.3.2 Slot Aspect Ratio - 2

The 2-component velocity vector plot for this aspect ratio is given in figure 4.1(a). It can be seen that the main feature is a single recirculating eddy which fills the slot. This eddy rotates due to the action of the faster moving main flow shearing across the fluid contained in the slot. The upstream corner of the slot contains an almost stagnant region of flow, whilst the downstream corner contains fast moving flow generated by the sudden downward deflection of the flow against the FFS. The maximum recirculating velocity in the slot, u_{Rmax}, has a value of $0.4u_o$, where u_o is the mean upstream longitudinal velocity. The centre of the recirculating eddy can be clearly seen with its associated low velocities. There is no evidence of a secondary recirculation zone over the FFS (see figure 2.16). It is unclear if the spatial scale of point measurements has failed to detect this.

The TKE of the flow can be seen in figure 4.2(a). Prior to entering the slot, the flow exhibits the characteristic behaviour for a turbulent boundary layer in open-channel flow. The turbulence intensity in the upstream channel is zero at the channel bed and increases rapidly away from the laminar sub-layer due to the friction between the flow and the channel bed. This region of high

turbulence intensity reaches a maximum, k_{up}, still close to the channel bed, and decreases gradually through the flow until the free-surface is reached.

As the flow enters the slot, the interaction of the main channel flow and the fluid in the slot produces a free-shear layer, as illustrated by the high TKE values. The turbulence generated along this shear layer can be seen to migrate beyond the FFS, where the maximum turbulence levels can be seen to occur just before the FFS. The maximum TKE in the slot region, k_{max}, has a value of $10k_{up}$.

The area of near stagnation at the upstream corner of the slot has TKE values as low as $0.1k_{up}$. There is negative flow along the base of the slot with TKE values reaching $0.3k_{up}$, whilst the centre of the recirculating eddy has values as low as $0.1k_{up}$.

There is no evidence from the TKE values that increased turbulent activity occurs over the FFS, which suggests that there is no development of a secondary recirculation zone.

4.3.3 Slot Aspect Ratio - 5

The vector plot for this aspect ratio (figure 4.1b) indicates that the main feature in this slot is still a recirculating eddy. This time however, the eddy does not completely fill the slot, due to the main flow intruding into the slot as it progresses downstream along the separation streamline, see section 2.5.2. The centre of the recirculating region can again be identified, as can a small region of essentially stagnant flow in the upstream corner of the slot. Within the recirculation region, values of $u_{Rmax}=0.35u_o$ can be observed. As the flow exits the slot, the velocity increases due to an upward deflection of the flow over the FFS. This same flow then experiences an additional acceleration as it merges with the faster moving main channel flow. A velocity vector with a relatively large vertical component can be identified at the edge of the FFS. This vector has a magnitude of $0.9u_o$, with the vertical component, v, contributing a value of $0.25u$ to this value. Although a secondary recirculating region is not apparent at this scale, the high TKE values in this region may be attributed to the development of a secondary shear layer, see figure 4.2(b).

It was observed from the free-surface profile that the depth increased gradually over the slot, with a sudden decrease in the nominal depth as the flow passed over the FFS. This produced a wavy distortion at the free-surface for some distance downstream of the slot. The reduction in depth over the FFS created a region of faster moving flow, with velocities reaching $1.25u_o$. From both

the mean velocities and the TKE, there was no evidence that the flow returned to normal open-channel flow conditions within the limits of observation, i.e. 6*Hs* downstream of the FFS.

The increased length of this slot results in a longer separation streamline, resulting in a greater length of shear within the slot, which subsequently increases the amount of TKE generated. The rate of generation of turbulence is greater than its dissipation all along this separation streamline, and therefore the turbulence intensity increases with distance. When the shear layer impacts onto the FFS, much of the flow deflects downwards into the recirculating region, and therefore accounts for the large zone of high TKE observed.

The values of TKE observed in the upstream corner of the slot were comparable to those found in the previous example, with values as low as $0.1k_{up}$. Within the slot, the value of k_{max} was of the order 25-30k_{up}. At the FFS, TKE values as high as $58k_{up}$ were observed, which are expected to be attributed to the development of a secondary recirculation zone and its associated shear layer.

4.3.4 Slot Aspect Ratio - 10

The velocity vectors for the aspect ratio of 10 are presented in figure 4.1(c). One of the main features in this slot is a recirculation cell bounded by the separation streamline and the upstream corner of the slot. This separation streamline can be seen to reattach at a length of approximately 7-8*Hs*. The primary recirculation zone is clearly defined by the velocity vectors, characterised by its centre and the strong reverse flows along the slot bed, with values of u_{Rmax}=0.26u_o. An area of essentially stagnant water can again be observed at the bottom upstream corner of the slot.

As the flow proceeds downstream, it encounters the FFS and deflects upwards and over the step, as can be seen by the large velocity vectors at the top of the FFS. The largest velocity vector in this region has a value equal to 1.1u_o, with the vertical component again accounting for 0.25u of this value. The maximum horizontal velocity occurring over the step however, is 1.26u_o, which can be attributed to the acceleration of the velocity due to a reduction in flow depth as it passes over the step.

The TKE plot is presented in figure 4.2(c). Since the flow conditions are unaltered, the upstream TKE, k_{up}, is again comparable with the previous investigations. Unlike the previous examples, the primary recirculation zone within the slot is fully developed. Associated with this is a reattaching separation streamline, where maximum shearing occurs between the recirculating

flow and the faster moving main flow. This is evident from the high TKE values which can be seen in the slot. Since reattachment of the flow occurs near the end of the slot, the slower velocities associated with reattachment and the slow velocities which occur in the downstream corner of the slot create a combined zone of low velocity. This has the effect of containing these high TKE values within this region. This can be seen in figure 4.2(c) where high TKE values remain at some distance away from the point of flow reattachment. The value of k_{max} is approximately $55k_{up}$.

The flow over the FFS creates a secondary recirculation zone producing a small zone of high TKE with values reaching $53k_{up}$. It should be noted however, that these values are not solely attributed to that of the secondary free-shear layer, but are combined with the migrating TKE generated within the slot, as can be seen by the TKE plot.

4.3.5 Slot Aspect Ratio - 15

The vector plot for this slot is given in figure 4.1(d). The main flow characteristic within the slot is a single recirculation cell, similar to that observed for an aspect ratio of 10. Reattachment of the flow occurs at a distance of 7-8Hs, with u_{Rmax} values of $0.25u_o$, which is similar to that for A_s=10. In this case, the flow begins to develop into normal open-channel flow due to the increased distance between the reattachment point and the FFS. This produces an increase in the flow-rate within the slot, i.e. at y<100mm, and therefore a larger mass flow is deflected up and over the FFS than for smaller aspect ratios, indicated by the large velocity vector at the FFS. This vector has a value of $1.25u_o$, with an increased vertical component contribution of $0.4u$ of this value. The large deflection of the flow over the FFS produces an unsteady fluctuation of the free-surface at and beyond the FFS. Horizontal velocities as high as $1.28u_o$ are experienced in this unsteady zone due to the resulting reduction in flow depth.

The TKE values are illustrated in figure 4.2(d), where the full development of the free-shear layer and its dissipation within the slot can be seen. The TKE values upstream are again similar to those of the other slots. The maximum TKE in the slot, k_{max}, is approximately $25k_{up}$, which is less than that experienced for As=10. The high TKE values can be seen to dissipate as they progress along the slot, however, the distribution of these values is worth noting. The region of high TKE stretches furthest downstream at a height of $0.8Hs$ above the slot floor. This could be attributed to the larger longitudinal velocities and the maximum TKE values, including k_{max}, occurring at this height, which will therefore persist longer as the flow migrates downstream.

At the FFS, the maximum TKE observed has a value of $170k_{up}$. This value seems particularly high, and may be a rogue result, however, several values of the order $80k_{up}$ were also observed. Beyond this area of high TKE activity, the turbulence can be seen to dissipate as the flow progresses downstream.

4.3.6 Backward Facing Step

This configuration allows the flow to develop at an expanded depth ratio of 2. Figure 4.1(e) illustrates the mean velocity vector plot, which highlights the expected recirculation region. Maximum velocities of $0.26u_o$ are observed in the recirculation region, which are similar to those observed for the other slot bed reattachment cases, i.e. A_s=10 and 15. The reattachment length can be seen to occur at approximately 7-8Hs. As the flow migrates downstream, it recovers from the perturbation induced by the sudden expansion and appears to recover towards a normal open-channel velocity distribution.

The TKE plot can be seen in figure 4.2(e). The main feature is the shear layer, which develops without any adverse effects of a forward facing step. The maximum TKE produced by the shear layer, k_{max}, has a value in the region of $50k_{up}$. Also worth noting is that TKE values of $20k_{up}$ are observed in the flow at a distance of $15Hs$ from the BFS.

4.4 MAIN FLUME

4.4.1 Introduction

The design criteria for the main flume has been outlined in section 3.5. Prior to slot flow measurements in this flume, a series of initial tests were undertaken, primarily to ensure that the flume met these design criteria. This involved a detailed survey of the channel bed and sidewalls using an automatic level for the channel bed, and a spirit level and a theodolite for measuring angle deviation of the sidewalls.

Initial data acquisition focused on the LDV system and the integrity of the data it measured. This involved an analysis of the system parameters, the data sampling rate, and the correct alignment of the laser beams. Once these were established, an investigation into rectangular open-channel

flow was undertaken. This was an extensive study allowing comparison of experimental data and theoretical relationships for open-channel flow.

4.4.2 Flume Bed Elevations

Due to the sensitivity of the flow, the flume channel should provide a smooth uniform surface to minimise detrimental effects from unwanted changes in bed elevation. To assess the smoothness of the channel bed and to determine the presence of any irregularities, a detailed traverse of bed elevations was undertaken.

The bed elevations were measured using a surveying level and a 300mm steel scale rule. This scale rule was held perpendicular to the flume bed and readings were obtained using the surveying level. Prior to using the level for bed elevations, a standard two-peg test was undertaken to ensure the level was in working condition and fit for use.

The surveying level was positioned and levelled in clear sight of the entire length of the flume. The four corner legs of the flume were then measured and adjusted until they were equal. This provided a datum to work from and ensured that the flume frame was horizontal during the investigation.

The flume was marked into a grid of 58x7 points: 58 points at 100mm spacings longitudinally (two sets of levels were taken at each step, one representing the upper channel height and the other the base of the slot); and 7 points laterally also at 100mm spacings (this includes points at the base of both sidewalls). Levels were then taken at each of these points enabling a 3-dimensional plot of the flume bed to be produced. The readings taken at each of the four corners, already known to be the same, were adopted as the datum level. All the measured heights were then compared to this datum.

The flume bed was divided into an upstream section, a slot section, and a downstream section. A plot of the levels in each of these sections is illustrated in figures 4.3a-4.5a. These levels were plotted onto a 3-dimensional surface plot to illustrate the overall geometry of the flume bed, see figures 4.3b-4.5b.

To assess the degree of smoothness, the standard deviation from the mean of each of these sections were calculated, see table 4.2.

Table 4.2 - Statistical Data for Flume Bed Levels

Section	Length of section (m)	Standard Deviation (mm)
1-Upstream	2.7	0.3434
2-Slot	2.0	0.2235
3-Downstream	1.0	0.2621

It can be seen that the standard deviation is very small for all three sections, indicating that the mean level has been calculated from a series of consistently good measurements.

The shape of the channel bed can be seen from the measured levels. The tilt of the flume both vertically and laterally can be adjusted using the screw bolts on the base of each corner leg, with the centre pair of legs being used for additional support of the flume. From the levels measured and on inspection of the surface plots (figures 4-3b-4.5b), the general shape and slope of the channel can be seen. It should be noted that these plots are not to scale and the vertical axis is greatly exaggerated. The initial stretch of the upstream section displays a smooth surface with a slight tilt over the span. The points plotted in figure 4.3(a) suggest that this tilt is no more than 0.8mm across the width of the flume and could be compensated by adjusting the height of one of the upstream legs. This value is relatively small and is not likely to have a significant bearing on the flow. The middle and latter stretch of this section displays a more uneven surface. A visual inspection of this area indicates that this is attributed to a slight vertical misalignment at the connection between the centre and upstream sections of the flume. The mean change in height between the points either side of this connection is approximately 0.3mm. In general, this section displays a level surface with nearly all the centreline values lying on the mean level. The surface appears to be twisted, evident from the change in elevations between each sidewall. However, this was overcome by fine adjustment of the central support legs.

The surface plot of the downstream section, see figure 4.5(b), displays the smoothest section, with very little deviation along the surface. This surface also appears to be horizontal throughout the spanwise direction. It can be observed that a small ridge occurs laterally at the longitudinal distance of 5000mm, which is attributed to the connection between the slot and downstream sections of the flume. The difference in elevation is less than that observed in the upstream section, and once again, the error is considered negligible.

In general the surface is relatively smooth, with only the area around the connection between the upstream and slot section displaying a noticeable error, and this is considered to have little influence on the flow. There was a small lateral tilt in the upstream half of the flume, however, this was overcome by adjusting the height of the central support legs of the flume. It is worth noting that when altering the channel slope, the upstream (or downstream) pair of legs should be adjusted by the same amount to minimise differential levels across the span. Also, the central legs are vital in maintaining the integrity of the slope, and they should be adjusted accordingly when altering the channel slope.

Areas along the flume bed with very small deviation from the mean were identified for use when adjusting the channel slope. All adjustments to the slope of the flume during the study were measured using the change in elevation between these points. Using these same points as a datum, the levels taken in the slot were subtracted from these in order to establish the mean depth of the slot. This yielded a mean slot depth, H_S, of 99.6mm, which represents an error of approximately -0.4% from the desired 100mm design depth.

Another method to confirm the slot depth, H_S, was to compare the heights between the main (upper) channel section and the slot region at the transition, i.e. at locations 2700mm and 4700mm. These values are given in table 4.3.

Table 4.3 - Slot Height, H_S, Established From Change in Height at Slot Transition

Spanwise Position	0	100	200	300	400	500	600	Average H_S (mm)
2700u	148.8	148.9	149	149	149	149.1	149	
2700l	249.3	249.4	249.3	249.3	249.3	249.2	249.1	
Δ =	100.5	100.5	100.3	100.3	100.3	100.1	100.1	100.3
4700u	150.8	151	151.2	151.3	151.3	151.3	151.1	
4700l	251.5	251.5	251.5	251.5	251.4	251.4	251.3	
Δ =	100.7	100.6	100.6	100.2	100.1	100.1	100.2	100.3

u - denotes upper section, l - denotes lower section

It was evident from the results that the slot depth at the transition between the upper channel and the slot was very close to the design depth of 100mm, with an error of +0.3% at both the upstream and downstream transitions. Combining these errors suggests that the slot was deeper

at the transitions, and less at its centre. Visual examination of the slot base made this more apparent, where it appeared that the base bulged upwards in the centre of the slot section. This was likely to be caused by stresses applied on the base section created during construction. It was observed that this error was overcome by applying a slight pressure to the slot base, which conveniently occured when the channel was full of water. Random levels were taken to confirm this, and similarly, use of a submersible spirit level indicated that the base of the slot flattens under the weight of water. This effect cannot be over-compensated producing a sag, since the flattened base connects with the cross-beams of the supporting frame.

4.4.3 Flume Sidewall Spacing, Vertical Alignment and Smoothness

The flume width was obtained by measuring the mean distance between the two sidewalls using a 650mm steel scale rule with an attached micrometer (sensitive to 0.1mm). Each sidewall was discretised into a grid of 58 longitudinal stations at 100mm intervals, and four points vertically at 100mm intervals (with five points in the slot region).

The results of this investigation are summarised below:

Average width of flume, $\overline{B} = 600.8\text{mm}$

Standard deviation, $\sigma = 0.5\text{mm}$

The average width of the flume, $\overline{B}$, was found to be very close to the design width of 600mm. This value deviates from the design value by only 0.8mm, which represents an error of only 0.13%, which is considered to be insignificant at the scales used in this study. The width of the flume is therefore accepted as 600mm. The standard deviation is likewise very small, indicating that the average width has been calculated using consistently good values.

The smoothness and vertical alignment of the sidewalls were achieved using a standard spirit level. By changing the orientation of the level and its location, an idea of the smoothness and vertical alignment was obtained. Although no calculations were taken, this method proved reliable, and illustrated that there were no areas of concern on either sidewall, even at the connection between the flume sections. Visual inspection of the sidewalls also indicated that there were no significant areas of concern.

4.4.4 Flume Centreline

Although the location of the centreline at any point along the length of the flume could be found visually and by simple measurement using a scale rule, both with an acceptable degree of accuracy, it was considered that a defined centreline be established prior to data acquisition. This would allow rapid location of the centreline during repositioning of the control volume, and importantly, it would assist in the orientation of the laser beams when measuring the longitudinal velocity when the laser probe is vertically aligned beneath the flume, see figure 3.3(c).

Two methods were considered for establishing a centreline. The first method was to simply measure the half-width of the channel at various points using a scale rule. The second method involved using a theodolite at one end of the flume, and adjusting its position until similar angles between known stations on either side of the flume were equal. The centreline could then be drawn along the line defined by the vertical cross-hair of the theodolite, see figure 4.6.

Using the theodolite method, the flume centreline was established and was marked on the underside of the flume at various points using a fine permanent pen. To establish the correct orientation of the laser beams, various points were also etched on the laboratory ceiling using a pencil. This facility proved to be useful during data acquisition.

4.5 DATA VALIDATION

4.5.1 Introduction

It was evident from the initial study that the procedure of data acquisition and the quality of data should be assessed. Primarily, this would ensure that a minimum length of record is obtained at a suitable sampling frequency, and that correct movement and alignment of the laser system is achieved.

The sampling frequency is the rate at which instantaneous velocity events are recorded each second. The higher the sampling frequency, the more sensitive the instrumentation is to the scales of velocity occurring at that point. Nezu and Nakagawa (1993a) describe a method to obtain the maximum response frequency, f_{max}, based upon the microscale length of turbulence, l,

and the maximum wave-number, k_{max}, beyond which the signal is noise rather than a contribution to the measurement. If L_x is the macroscale of turbulence, the dimensionless wave number $L_x.k_{max}$ should be at least 100 in order to analyse the spectral range down to the viscous sub-range. In the outer region of the flow, L_x scales with the flow depth, y_o, therefore, f_{max} can be evaluated as follows:

$$f_{max} = k_{max}.u/(2\pi) \geq 100.u/(2\pi L_x) \approx (50/\pi).(u/y_0) \qquad \textbf{Equation 4.2}$$

where u is the mean longitudinal velocity at a point in the flow, and:

$$l = 1/k_{max} \leq L_x/100 \approx y_o/100 \qquad \textbf{Equation 4.3}$$

To allow for the elimination of data aliasing, the minimum sampling frequency, f_{min}, of data processing should be chosen so as to satisfy the condition, $f_{min} > 2.f_{max}$.

The next stage was to identify the minimum number of samples required to calculate an accurate mean velocity, u, and mean fluctuating component, u'_{RMS}. As these are time averaged values, they will be more accurate if measured over a longer sample time. The true value of these cannot be established. However, within a practical period of time a suitable approximation can be obtained. A criterion must therefore be introduced in order to establish a suitable cut-off time, or number of samples. This is a practical measure and will save both data acquisition time and computer time.

Using f_{min} as the minimum sample rate, then any point measurement taken over a long period of time should produce an accurate u and u'_{RMS}. Where N is the total number of data samples, the comparison of the velocity components at time intervals from 0 to $\Delta t_{0\rightarrow N}$ will allow a suitable cut-off time to be assessed. Raichlen (1967) adopted this method in a study of turbulence measurements in open-channel flow using hot-film anemometry. In general, Raichlen observed that the mean velocity, $u_{\Delta t}$, approximated u_T long before the $u'_{RMS\Delta t}$ approximated u'_{RMST}. A minimum sampling time, T, was established whereby the $u'_{RMS\Delta t}$ was within 2% of the u'_{RMST}, where the time T was 100 seconds. Since $u_{\Delta t}$ approximated u_T before u'_{RMS}, then $u_{\Delta t}$ was within 2% of u_T prior to this minimum sampling time. From a series of investigations, with a sampling rate of 100Hz, Raichlen (1967) established 50secs as the minimum sampling time, but recommended that this value be increased to 80secs, i.e. an increase of 60%.

4.5.2 Minimum Number of Samples

Using the method described above, the minimum sampling frequency, f_{min}, was used for a series of point velocities to obtain a minimum cut-off time (or minimum number of samples). The sampling frequency and number of samples are related as follows:

$$f = N / T \qquad \textbf{Equation 4.4}$$

where, N = number of samples

T = sample time (secs)

Point measurements were taken from a flow of depth 0.05m, with a mean velocity, u_o, of 0.35m/s. Using equation 4.2, and satisfying $f_{min} > 2.f_{\max}$, 6000 samples were taken at each point location with a sampling rate of 0.2kHz.

Figures 4.7 and 4.8 show the mean values of u and u'_{RMS} respectively over the duration of the sample record. It should be noted that these plots only show the record for the first 3000 samples, as this highlights the unsteady nature of the trace at the beginning of the record. It can also be seen that the traces approach a constant by N=3000. Both figures show traces at various depths throughout the velocity profile. From figure 4.7, it can be seen that the localised mean velocity is lower at the bottom of the channel, and increases with depth to higher velocities close to the free-surface, as would be expected in open-channel flow. The most distinguishing feature from this plot is the trace for y/d=0.02, which, unlike the other traces, this increases from a low velocity of approximately 0.25m/s to an almost constant velocity of 0.32m/s half-way through the time series. This is likely to be caused by the increased turbulent nature of the flow just above the channel bed, creating large fluctuations in the velocity, and therefore taking longer to establish a mean value. This is evident when compared to the same trace in figure 4.8, which indicates that a longer period is required for u'_{RMS} to reach a constant value. The remaining traces illustrate the trend expected for this type of flow, where the area of greatest turbulence intensity occurs close to the channel bed, with a reduction in turbulence towards the free-surface.

The next stage of the analysis was to determine a cut-off time. This was based on the method used by Raichlen (1967), whereby the trace was analysed to establish at what time u and u'_{RMS} settle to a consistent value which deviates less than 2% of values obtained from a long-term record. In order to do this, the time series would be taken over a long time period, whereby the end mean value for both u and u'_{RMS} could be used in comparison to the rest of the trace. This

mean was obtained from an abnormally long duration of record. Figure 4.9 illustrates this method schematically.

A series of point measurements were taken whereby u and u'_{RMS} were obtained for each record. Intermediate values of u and u'_{RMS} were then calculated throughout the time series. Where N is a large sample, the u and u'_{RMS} values were calculated for the intermediate periods of 2.5%, 10%, 25%, 50% and 75% of N. The difference between these values and those obtained for 100%N (i.e. the long-term value of u and u'_{RMS}) were then compared to establish where in the time series the percentage difference deviated less than 2% of the respective long term value. The eight different flow cases used in this study have a range of sampling frequencies and mean velocities. Tables 4.4 and 4.5 illustrate the flow conditions used in this analysis and the subsequent findings for u and u'_{RMS} respectively.

Table 4.4 - Data Validation Analysis - Mean Velocity, *u*

		Samples	Long-term	2% u	Percentage deviation after:				
Case	f (Hz)	N	u	deviation	2.5% N	10% N	25% N	50% N	75% N
1	90	10000	0.29637	0.005927	4.496913	1.978945	0.40743	0.108817	0.222695
2	85	10000	0.12286	0.002457	0.549699	1.463131	2.564135	2.355235	1.369744
3	80	10000	0.172762	0.003455	7.509175	4.337398	3.136082	0.978126	0.41699
4	29	4000	0.179627	0.003593	1.185458	0.683245	0.566773	0.125354	0.089916
5	74	10000	0.379945	0.007599	1.137641	2.355963	1.723655	0.784915	0.291097
6	121	10000	0.338868	0.006777	10.13017	6.447319	1.204499	1.170441	1.316949
7	2	8000	0.059666	0.001193	1.410242	0.457391	0.076013	0.126115	0.115875
8	300	25500	0.055269	0.001105	0.928188	4.948977	2.760379	0.575361	0.330809

Table 4.5 - Data Validation Analysis - Root Mean Square Velocity, *u'*

		Samples	Long-term	2% u'	Percentage deviation after:				
Case	f (Hz)	N	u'	deviation	2.5% N	10% N	25% N	50% N	75% N
1	90	10000	0.01382	0.000276	6.837916	8.140376	2.116498	1.465268	0.227931
2	85	10000	0.020466	0.000409	3.887588	6.251574	2.585045	1.112595	0.93627
3	80	10000	0.01481	0.000296	16.88475	0.628408	1.077563	2.073525	1.303878
4	29	4000	0.011082	0.000222	21.32085	3.322408	7.242148	2.8314	0.944314
5	74	10000	0.034667	0.000693	17.67508	12.42647	9.466926	2.150588	0.678291
6	121	10000	0.039595	0.000792	18.0144	1.538019	2.753522	0.826602	0.798851
7	2	8000	0.005097	0.000102	3.217324	2.901225	0.893913	0.974113	0.876065
8	300	25500	0.005308	0.000106	22.10578	5.05487	12.08449	4.0817	1.606476

Figure 4.10 illustrates the mean velocities, u, derived at each intermediate point in the time series for the eight different cases. Depending on the sampling rate, and the duration of the record, the time at which this 'suitable' mean is obtained will vary. Using Case 3 in table 4.4 as a typical example, where the sampling rate is 80Hz, and the number of samples is 10,000 taken over a period of 125 secs, then a mean velocity which differs consistently less than 2% of the long-term value occurs after 60 secs, or 5000 samples. In some of the cases shown, the mean velocity is seen to deviate further from the mean after a greater number of samples have been used. An example of this can be seen in Case 2, where the mean calculated at $0.025N$ differs less than the preceding mean values. This illustrates the requirement to obtain a sufficient length of record and that there is no guarantee that a 'suitable' mean velocity will occur in a short period of time.

The analysis of the u'_{RMS} trace, figure 4.11, shows that a suitable u'_{RMS} is obtained within a limited time period. However, in most cases this occurs later in the time series than for u, at approximately $0.5N$. This finding is similar to that observed by Raichlen, whereby the u'_{RMS} settled to a suitable value after a greater duration of record.

These methods have been restricted to only one direction of fluid flow. Using equation 4.2 to establish f_{max} for vertical and lateral velocities would not be viable, since the mean vertical velocity is approximately zero, and, the theoretical mean lateral velocity in a 2-dimensional flow is zero. Therefore, by using equation 4.2, the calculated f_{max} for both these components would be very low or zero. Yet it has been shown that the relationship between their respective turbulence intensities are such that $u' > w' > v'$, where the ratios of w' and v' to u' are 0.7 and 0.55 respectively (Nezu and Nakagawa, 1993b). It is therefore assumed that owing to this relationship between the turbulence intensities, the minimum sampling frequency, f_{min}, established for the longitudinal velocity would be a suitable sampling frequency for the vertical and lateral components.

The number of samples required to establish a suitable mean and root mean square for both V and W could be established in a similar manner to that for U. Figures 4.12 - 4.14 show traces of the mean and turbulent components of velocity for U, V and W at the same point in a flow, where the sampling frequency used throughout was calculated using u in equation 4.2. From these figures it can be seen that both the mean and root mean square components approach a constant value (<2%) well within the range of samples taken.

4.5.3 Laser-Beam Rotation

An important factor for ensuring that accurate data measurements were obtained was the correct position and alignment of the laser beams. Using the laser probe support-traverse system as discussed in section 3.3, the laser control volume can be accurately positioned within the flow field. Prior to data acquisition, the plane of the laser-beams must first be correctly aligned. Depending which velocity component is required, the laser-beam plane must be either parallel or tangential to the direction of flow. For different hydraulic conditions, the slope of the flume will change in order to obtain uniform flow, therefore, the laser-beam plane will have to adjust accordingly.

The main flume uses a crude system for adjusting the slope, however, accurate measurement of the slope can be made using a surveying level and scale rule. During uniform flow conditions, the measured angle of the flume can be used to align the laser probe. This was achieved initially by levelling the probe support-traverse system using a spirit level, whereupon the probe was rotated to suit the slope of the flume (see figure 4.15). A graduated scale in degrees etched on the probe housing was used to measure this. However, the differences in the angle of the flume used in this study were so small (between 0-1°) that it was difficult to set these angles accurately. A simpler method was adopted during actual data acquisition. This involved adjusting the height and rotation of the laser probe until both beams intersected the free-surface of the flow (or the channel bed). Accurate rotation through 90° was undertaken if required, depending on the nature of the velocity component being measured. To verify this simpler method, point velocities were obtained using both methods, from which it was concluded that no appreciable difference occurred in the results. To further validate this method, measurements were taken for small successive changes in rotation in order to investigate the extent at which an appreciable change in velocity occurred. It was found that a difference in reading only occurred when it was visually apparent that the laser-beams were out of the plane of the flow.

Several simplistic procedures were employed to ensure that the orientation of the probe was correct. Consider first the vertical alignment of the probe. Figure 4.16 illustrates a schematic representation of the probe aligned so that the laser beams are perpendicular to the sidewall (or *in-plane*). The term *out of plane* refers to the condition where the beams are not perpendicular. When the laser beams strike the first sidewall, they produce a reflection, one for each beam. The light which refracts into the flume then strikes the second sidewall, which also produces a double reflection. The reflected light from the second sidewall has enough intensity to produce yet another double reflection on the first sidewall. This creates a series of reflections, which can be

viewed together with respect to the source light, which is used as the datum. If the probe is in-plane, the reflections will appear linear, however, if the probe is out of plane, the reflections will occur at different heights. This process was found to be extremely sensitive to very small changes in the vertical alignment.

The same concept was applied to the horizontal alignment (figure 4.17). In this case, a set of symmetrical reflections around the vertical centreline of the probe will appear if the probe is in-plane. If the probe is out of plane, the reflections will appear skewed around the vertical centreline.

4.6 RECTANGULAR OPEN-CHANNEL FLOW

4.6.1 Introduction

The first stage of data acquisition in the main flume consisted of an investigation of the flow characteristics which develop in rectangular open-channel flow. This served to confirm the validity of existing velocity and turbulence distribution models for open-channel flow and the two-dimensionality of the cross-sectional velocity distribution. The first investigation, Series A, was used to examine the vertical distribution of streamwise velocity and turbulence intensity (T.I.) at various Reynolds numbers and flow depths. The profiles were all taken at the flume centreline at a location 3.5m downstream of the flume inlet. The boundary layer thickness was determined and compared to the seventh-power law which describes the boundary layer velocity profile in turbulent open-channel flow (see section 2.2.2). The full depth velocity profiles and turbulence intensities were also analysed and compared respectively to the law of the wall and the T.I. models proposed by Nezu (1977). The second study, Series B, comprised of a detailed investigation aimed at determining the two-dimensionality of the flow across the span of the flume. This study was also used to verify the log-law, the T.I. models and the boundary layer velocity profile.

Throughout the acquisition of the data, the sampling rate and duration of sample were established and maintained in accordance with section 4.4.

4.6.2 Series A: Initial Open-Channel Flow Investigation

4.6.2.1 Flow Conditions

Nine different sets of hydraulic conditions were used in Series A. These are detailed in table 4.6. Flow depths ranging from 0.060-0.164m and Reynolds numbers between 1600-55600 were investigated. The actual flowrate, Q_{act} (m^3/s), was initially measured using the electronic flowmeter, which provides a mean flowrate across the flume width (equation 4.6). However, the local flowrate, Q_{loc} was used, which, in wide channels, represents the flow rate (m^3/s) per unit width within the central region of the channel (equation 4.7). The Reynolds number was calculated using equation 2.7, and the Froude number using equation 4.8.

$$Q_{act} = \int_0^h \int_0^B u(y,z)dydz \qquad \textbf{Equation 4.6}$$

$$Q_{loc} = \int_0^h u(y)dy \qquad \textbf{Equation 4.7}$$

where, y - vertical location (m)

z - lateral location (m)

B - channel width (m),

h - flow depth (m),

u – local mean velocity taken throughout depth (m/s).

$$\mathrm{F} = \frac{u}{\sqrt{g.l}} \qquad \textbf{Equation 4.8}$$

where, F - Froude number,

g - gravity (9.81m/s)

l - a characteristic length (in this case the flow depth, h, is used).

Table 4.6 - Series A: Hydraulic Conditions

Series: A	Flow Depth, h (m)	B/h	u_o (m/s)	Q_{loc}	Re	F	Hyd Rad, R	Slope ($x10^{-3}$)	u^*_1	u^*_2	% Diff $(u^*_2-u^*_1)/u^*_2$
1	0.068	8.8	0.023	0.001	1591	0.029	0.010	0.003	0.0017	0.0015	14.139
2	0.148	4.1	0.187	0.017	27750	0.156	0.554	0.017	0.0096	0.0090	7.397
3	0.164	3.7	0.084	0.008	13808	0.066	0.107	0.017	0.0042	0.0043	2.894
4	0.092	6.5	0.243	0.013	22328	0.256	0.070	0.210	0.0120	0.0118	2.493
5	0.100	6.0	0.261	0.016	26120	0.264	0.075	0.230	0.0130	0.0127	2.268
6	0.080	7.5	0.179	0.009	14288	0.202	0.063	0.140	0.0093	0.0090	3.584
7	0.060	10.0	0.390	0.014	23430	0.509	0.050	0.780	0.0196	0.0188	4.042
8	0.060	10.0	0.166	0.006	9930	0.216	0.050	0.170	0.0091	0.0086	6.181
9	0.088	6.8	0.632	0.033	55580	0.680	0.068	1.650	0.0332	0.0325	2.082

u^*_1 - Friction velocity calculated from channel slope

u^*_2 - Friction velocity obtained from log-law

4.6.2.2 Friction Velocity

In order to compare the experimental velocity results with the semi-empirical log-law and T.I. models, the friction velocity, $u*$, for the flow has to be evaluated. The requirement of this parameter and the methods used to determine its value has been covered in section 2.2.4. Only two methods were available to find $u*$ in this study. The first of these is the method using equation 2.27, which relies on the accurate measurement of the channel slope, S_o.

The channel slope, S_o, was measured using the change in elevation between two known points along the length of the flume:

$$S_o = (h'_2-h'_1)/L = \Delta h'/L \qquad \textbf{Equation 4.9}$$

Where, h'_1 and h'_2 are two bed elevations separated by a distance L.

The main problem with this system is that $\Delta h'$ is very small, and therefore an accurate means of obtaining this value is required. One method was the use of a surveying level to take readings from a levelling staff, positioned on the channel bed. Another method to obtain $\Delta h'$ was based on taking still water levels. This was achieved by filling the flume to a suitable level and measuring

two water depths a distance L apart using the water depth gauge. The results from both of these techniques were found to give comparable values where the slope of the flume was large, i.e. S_o>0.001. However, discrepancies occurred when S_o<0.001 due to the limited accuracy of the measuring devices.

The friction velocity can also be determined using the log-law relationship (equation 2.26). This requires adjusting the value of u_* until the experimental curve is a best fit to the curve defined by the log-law equation. This method has been widely used in open-channel flow studies, especially when the friction velocity cannot be measured accurately by other means.

The most accurate method of determining the friction velocity is from the Reynolds stress distribution, however, it has been shown that the two methods described above can have an accuracy within 5% of this method when using accurate LDA measurements (Nezu and Rodi, 1986). As the Reynolds stresses were not obtained in the current investigation, the friction velocity was obtained using the two methods described above, both of which are given in table 4.6. Both values of friction velocity can be seen to agree well with one another. Only Case 1 shows a large discrepancy between the values, however, this difference is exaggerated due to the relatively low values of the friction velocity.

4.6.2.3 Series A: Velocity Profiles

The vertical velocity profiles for each of the series are plotted in figures 4.18-4.26. These show the velocity distributions of streamwise velocity through the depth for each case. Table 4.7 contains information regarding notable features observed from these plots, these being:

(1) The velocity rapidly increases from zero at the channel bed to a value, u_1, which approximates to 0.75-0.85u_o at a depth, y_1, equal to 0.02-0.06y/h. This corresponds to the viscous sub-layer ($0<Y^+<8$) which forms the initial region of the inner layer as described in section 2.3.1.

(2) The velocity then increases at a less rapid rate to a value approximately equal to u_o, which generally occurs at a depth, y_2, equal to 0.3y/h. The region of flow from the channel bed to this value is comparable to the 'inner region' of open channel flow (Sarma et al, 1983, and Xinyu et al, 1995).

(3) In general, u_{max}, or values very close to u_{max}, occur in the flow between a height of 0.7-1.0y/h. This agrees with the definition of the free-surface region ($0.6<y/h<1.0$), where the velocity scale is u_{max}.

Table 4.7 - Velocity and Depth Data for Series A: Cases 1-9

Case	u_o	u_1	u_1/u_o	y_1/h	y_2/h	u_{max}	u_{max}/u_o	y_{max}/h
1	0.023	-	-	-	0.360	0.028	1.200	1.000
2	0.180	0.150	0.800	0.050	0.350	0.210	1.100	0.880
3	0.080	0.070	0.860	0.060	0.220	0.096	1.140	0.950
4	0.240	0.200	0.830	0.070	0.330	0.270	1.130	0.800
5	0.260	-	-	-	0.240	0.300	1.150	0.660
6	0.170	0.130	0.770	0.030	0.250	0.190	1.050	0.700
7	0.390	0.300	0.770	0.030	0.300	0.430	1.100	0.750
8	0.160	0.120	0.750	0.030	0.270	0.180	1.120	1.000
9	0.630	0.430	0.680	0.030	0.250	0.680	1.080	0.700

Note: u_1, y_1 - see (1) above
y_2 - see (2) above

4.6.2.4 Series A: Turbulence Intensities

The turbulence intensities for Series A are also presented on figures 4.18-4.26. The first stage of the analysis was to examine the relationship between the relative turbulence intensity, u'/u_o, and depth, y, where u' represents u'_{RMS}. It can be seen in these figures that there is a definite relationship, whereby the relative turbulence intensity is at a maximum close to the channel bed, which reduces towards the free-surface. A summary of the turbulence intensity results for Series A is presented in table 4.8.

Table 4.8 - Summary of Relative Turbulence Intensities for Series A: Cases 1-9

Case	u_o	u'_{max}/u_o	y_{max}/h	u'_{min}/u_o	y_{min}/h
1	0.023	0.184	0.132	0.0520	0.603
2	0.187	0.110	0.051	0.0392	0.844
3	0.084	0.116	0.076	0.0541	0.838
4	0.243	0.096	0.110	0.0487	0.848
5	0.261	0.123	0.099	0.0436	1.000
6	0.170	0.114	0.075	0.0506	0.780
7	0.390	0.117	0.033	0.0448	0.830
8	0.160	0.113	0.100	0.0465	1.000
9	0.630	0.135	0.023	0.0490	0.930
Mean		0.12	0.09	0.0477	0.84

Very close to the channel bed, within the viscous sub-layer, the turbulence intensity is very small since the viscous influence is dominant. This rapidly increases to a maximum value which occurs within the inner layer ($0<y/h<0.2$) at a depth of approximately $y/h=0.1$ from the channel bed. It can also be seen that this maximum turbulence intensity, u'_{max}, has a value in the range $0.1\text{-}0.15u_o$. The sudden increase in turbulence intensity from the channel bed to the maximum value is not clear in these figures, as the incremental change in depth, Δy, is not sensitive enough to illustrate this region of flow in detail. As the depth increases, there is a decrease in the relative turbulence intensity which reaches a minimum value, u'_{min}, somewhere between $0.8\text{-}1.0y/h$ from the channel bed. It has been suggested that this is caused by the damping of the turbulence by the free-surface. In all the cases, this minimum value is approximately $0.05u_o$.

4.6.2.5 Series A: Boundary Layer Velocity Profiles

The boundary layer velocity profiles were plotted for each flow case. This was achieved using the empirically derived seventh-power law (see section 2.2.2). The first stage using this method was to establish the boundary layer thickness, δ, defined as the depth where the local velocity, u, is equal to $0.99U_S$, where U_S is the free-stream velocity. The free-stream velocity is defined as the mean velocity of the fluid outwith the boundary layer. In turbulent open-channel flow, the velocity profile close to the wall and the free-surface is not fully-understood, and therefore U_S becomes difficult to define (Munson et al, 1990). In the current investigation, the velocity increases rapidly from the channel bed, whereupon this rate of increase reduces and the velocity gradient du/dy approaches zero. It will be assumed that the velocity at $du/dy\approx 0$ represents the free-stream velocity, U_S. Therefore, the boundary layer thickness,δ, can be defined as the

distance between the channel bed and the point where the velocity, u, first becomes equal to $0.99U_S$. In some cases du becomes negative, however, in all the cases, there is a rapid decline in du/dy at a depth in the region y/h=0.3-0.5. This can be seen visually from the mean velocity profiles (figures 4.18-4.26). Using δ and U_S to non-dimensionalise the flow depth and local velocity respectively, the velocity profiles satisfying $y/\delta \leq 1$ were plotted.

Figures 4.27-4.35 show the boundary layer velocity profiles for each case in Series A. In each example, the actual velocity profile is compared to the distribution described by the seventh-power law. Although some curves compare better than others, there is no hydraulic condition which can be attributed to these better fits. The closest match between the actual results and the empirical values appear in cases 9, 8, 4 and 3, which have R_e numbers of 55580, 9930, 22328 and 13808 respectively. With the exception of Case 1, these include the two extreme values and typical intermediate values of Re numbers used in this study. Cases 5 and 7 have the greatest deviation between the two sets of curves, however, it can be seen that this difference is relatively small.

Case 1 is the exception in this series of results. It can be seen to have lower velocities than those described by the seventh-power law. One obvious observation from the hydraulic conditions is that this case has by far the lowest Re number, at 1591. This value could easily be described as being in the lower transitional region of fluid flow. In figure 4.27, a Blasius profile for laminar flow has also been included. Although the experimental curve does not map onto either of the empirical curves, it matches the Blasius profile better than the seventh-power law for turbulent flow.

4.6.2.6 Series A: Law of the Wall Analysis

The velocity profiles were converted to law of the wall plots of U^+ versus LOG Y^+, figures 4.36-4.44. These plots include the semi-empirical relationships described by the log-law (equation 2.26), denoted by the line U^+, and the modified log-law equation using Coles wake function (equation 2.28) denoted by the line U^+(Coles).

Although in some cases the number of points are few, the results are in good agreement with the log-law for the inner region ($y/h<0.2$) and similarly for Coles' wake function in the outer region ($y/h>0.2$). Unfortunately, due to the nature of the logarithmic relationship, the points are

increasingly condensed as Y+ increases. This shows the log-law and velocity defect-law portion of the profile clearly, however, fewer points exist in the linear region ($U^+=Y^+$).

4.6.2.7 Series A: Turbulence Intensity Model

Nezu's (1977) function for the streamwise turbulence intensity (equation 2.36), and the modified constants for this equation proposed by Nezu and Rodi (1986), were compared to the experimental turbulence intensities for Cases 1-9. Figure 4.45 illustrates the curves for both sets of constants and for Cases 1-9.

The depth profile discretisation makes it difficult to examine the flow in the near wall region, which can be described by a damping function extension to the TI model (see equation 2.40). Case 1 contains points within this range and, as can be seen in figure 4.46, the points agree with the curve described by equation 2.40.

In figure 4.45, nearly all the points in the outer-region are well described by the semi-empirical curve irrespective of their Reynolds number and Froude number. The experimental values of u'/u^* up to a depth of $0.3y/h$ are slightly greater than those from the semi-empirical curve, and in the region $0.4<y/h<0.8$ the values dip below the curve values. In the latter region, $0.8<y/h<1.0$, the values again fit well with the curves. In most of the cases, the experimental values of u'/u^* in the wall region are greater than that described by the function, however, when we introduce the damping function, equation 2.40, we can see that a much better fit occurs (figure 4.46).

4.6.3 Series B: Spanwise Velocity Distribution

4.6.3.1 Series B: Flow Conditions

A series of investigations were undertaken to examine the spanwise velocity distribution. This was done primarily to determine the 2-dimensionality of the flow in the flume. In addition to the longitudinal velocity components, u and u', the vertical and spanwise velocity components were also obtained, i.e. v, v', w and w'.

In this series, three sets of results were taken at a location 3m downstream of the flume inlet. Due to flow symmetry, only one half of the span, between the centreline and one sidewall, was

measured in detail. To prove flow symmetry however, confirmative profiles were obtained in the opposite half of the span. Table 4.9 gives a summary of the hydraulic conditions used in this investigation.

Table 4.9 - Hydraulic Conditions: Series B1, B2, B3

Series	h	B/h	u_o	Q_o (m^3/s)	Re	F	u^*_1 slope	u^*_2 log	S_o ($x10^{-3}$)	% Diff $(u^*_2-u^*_1)/u^*_2$
B1	0.032	18.75	0.199	0.00381	6360	0.35	0.0130	0.0120	0.60	8.30
B2	0.050	12.00	0.270	0.00810	13500	0.39	0.0138	0.0145	0.45	4.80
B3	0.100	6.00	0.254	0.01521	25400	0.26	0.0150	0.0132	0.30	13.60

4.6.3.2 Series B1: Velocity Profiles

Case B1 consisted of a series of velocity profiles for a flow depth of 32mm. The incremental change in depth of point measurements was 1mm. Using the depth as the characteristic length, profiles were taken from the centreline towards the sidewall at incremental changes equal to the characteristic length. All three components of velocity were obtained for analysis of the turbulence intensities.

Figure 4.47 illustrates a reduced set of mean-velocity profiles for clarity, corresponding to the centreline (z/h=0) and the three spanwise distances, z/h=4, 6 and 7 from the centreline. These profiles represent the mid-region of the channel and the initial profiles which are affected by sidewall contamination. Since the ratio B/h is approximately 20, a large central area of the cross-section is expected to produce two-dimensional flow. It can be seen from the results that the profiles corresponding to z/h=0, 4 and 6 illustrate this region with similar velocity profiles, whilst z/h=7 displays a reduction in velocity, which can be attributed to sidewall effects.

The boundary layer velocity profiles are illustrated in figure 4.48. It can be seen quite clearly that all four boundary layer profiles are displaced to the left of the profile described by the seventh-power law, particularly in the region y/h<0.5. It is possible that the low Reynolds number is responsible for this, as this value could be described as being in the transitional range. The profiles for z/h=0, 4 and 6 are similar, with z/h=7 displaying a reduction in velocity, again, this being attributed to sidewall effects.

The friction velocity obtained from the log-law, $u*_2$, was obtained for the centre-line profile and used for the rest of the profiles in this series. This value was similar for all the mid-region profiles, however, the value of $u*_2$ for the near wall profile was found to be lower. It was decided that the centreline value of $u*_2$ would be used throughout for comparison. The log-law profiles for this series can be seen in figure 4.49, which indicate that the experimental curves have a similar gradient to the log-law profile, particularly in the central-region. The profile z/h=7, which is furthest from the centreline, maintains a log-law profile but with lower velocities.

It is evident from this set of results that the central region produces similar mean velocity profiles. This region accounts for approximately two-thirds of the channel width.

4.6.3.3 Series B1: Turbulence Intensities

The streamwise turbulence intensities, u'/u_o, for this series of flows can be seen in figure 4.47. The profiles for z/h=0, 4 and 6 produce similar values of turbulence intensity, however, the profile for z/h=7 displays a reduction in the turbulence intensity.

All three components of velocity were acquired during this investigation. The experimental turbulence intensities were plotted together with the semi-empirical models describing the outer-region of the flow (see figures 4.50-4.52). In figure 4.50, the profiles for z/h=0, 4 and 6 are well described by the modified equation for TI. Although most of the points in these profiles occur in the outer-region, some points do exist in the inner-region, y/h<0.2, as shown by the TI function which includes the damping function. It can be seen that most of the profiles follow the shape of this curve, although there is a large scatter between each profile. Both the profiles for v' and w' are well described by their respective TI curves using the modified constants.

The general trend of the profiles for each velocity component are well described by their respective TI models. The main difference between the general shape of the profiles can be seen in the inner-region, y/h<0.2, whereby the curves for the streamwise component, u', increase in value in this region, whereas v' fits the TI curve and w' decreases slightly.

4.6.4 Series B2: Spanwise Velocity Distribution

A series of vertical profiles were taken along the span of the flume at a location 3.5m from the inlet, with a nominal flow depth of 50mm. Profiles were taken throughout one-half of the cross-section at 20mm spacings from the centreline to the sidewall, with each profile containing 10 points. Another set of profiles were obtained from the other half of the span at 60mm spacings from the centreline to the sidewall, with each profile containing 20 points.

Although 15 profiles were taken on one side of the channel and six for the other, much of the analysis in this section concentrates on the corresponding profiles either side of the centreline. Table 4.10 summarises the details of the profiles used in this part of the study.

Table 4.10 - Profile Spanwise Location: Series B2

Case	**1**	2	3	**4**	5	6	**7**	8	9	**10**	11	12	**13**	14	**15**
Number points	**10**	10	10	**10**	10	10	**10**	10	10	**10**	10	10	**10**	10	**10**
Spanwise Locn from centreline, z	**0**	20	40	**60**	80	100	**120**	140	160	**180**	200	220	**240**	260	**280**
Case	**16**	**17**	**18**	**19**	**20**	**21**		1(c)	2(c)	3(c)	4(c)				
Number points	**20**	**20**	**20**	**20**	**20**	**20**		10	10	10	10				
Spanwise Locn from centreline, z	**0**	**-60**	**-120**	**-180**	**-240**	**-280**		0	20	40	60				

Note: Cases in bold used for detailed analysis
The case numbers with (c) are confirmatory profiles in the central region

4.6.4.1 Series B2: Velocity Profiles

The velocity distributions of corresponding profiles with respect to distance either side of the centreline are presented in figures 4.53-4.58. Although these figures compare paired profiles, the centreline profile has also been included to allow comparison with the centreline measurements.

Figure 4.53 gives two profiles taken at the centreline, where as expected the profiles are similar. The same can be said for figures 4.54 and 4.55, where the paired profiles are not only identical to each other, but also match the centreline profile. The first sign of deviation from the centreline profile occurs in figure 4.56. The profiles in figure 4.57 show a slight decrease in velocity from the centreline profile, while the profiles in figure 4.58 show a marked decrease in velocity. This

gradual decrease can be attributed to sidewall effects, which can be seen to have greater bearing as the profiles approach the sidewall.

Most of the curves display a similar shape, characterised by a rapid increase in velocity from the channel bed to a height of $y/h \approx 0.2$, whereupon the velocity gradually increases to a maximum value close to the free-surface. The shape of the profiles close to the side-walls however, increase to a maximum velocity at a height approximate to mid-depth before decreasing in velocity towards the free-surface. This feature has been documented in the literature and is referred to as *dip* (see section 2.3 and section 4.6.4.2 below).

4.6.4.2 Series B2: Cross-Sectional Average Velocity and Dip

The depth-averaged velocity, u_o, of each profile is illustrated in figure 4.59. It can be seen quite clearly from this plot that a mid-region of relatively consistent velocities exists, which can be defined as the middle two-thirds of the full channel cross-section. Towards the sidewalls, the mean velocity can be seen to decrease as expected.

In an attempt to further classify a central region, the *dip* effect in each profile was examined. To illustrate *dip*, the depth at which the maximum velocity, u_{max}, occurs in each profile has been plotted, figure 4.60. For most of the cross-section of the flume, u_{max} occurs close to the free-surface. It must be remembered that the change in depth between successive points in the profiles is quite large, and therefore this produces the constant depth of most of the points observed in the figure. Also, the first two points which drop on the left-hand side of the plot, appear to more severe than what exists in reality. Indeed, these velocities which represent the maximum are only slightly larger than the values occurring nearer the free-surface, this can be verified by their respective velocity profile plots. In general, the effect of *dip* is only apparent in the region very close to the sidewalls. For the mid-span region, $z/B=0.6$, there is no doubt that u_{max} occurs very close to the free-surface. As the sidewall is approached, a range of high velocities exists in the upper region of the profile, making the exact location of u_{max} somewhat ambiguous. However, very close to the sidewall, the depth of u_{max} does decrease, as can be seen in the velocity profiles.

4.6.4.3 Series B2: Log-Law Velocity Profiles

The log-law profiles for this investigation are shown in figures 4.61-4.62. Figure 4.61 illustrates profiles 1, 4, 7, 10, 13 and 15. Profiles 1, 4, 7 and 10 fit the line defined by the log-law in the central-region, and Coles' wake function in the outer-region. Profiles 13 and 15 have a log-law distribution, but the velocities are lower than the previous cases. Towards the free-surface, profile 15 can be seen to fall away from the log-law line quite sharply as a result of edge effects.

Figure 4.62 illustrates the more detailed profiles 16-21. These profiles follow the same pattern as those observed on the opposite side of the channel centreline. Profiles 16, 17 and 18 follow the log-law and wake function profiles accurately. It can be seen that profiles 19 and 20 show signs of sidewall contamination, while profile 21, which is closest to the sidewall, initially maintains a log-law profile, however, as the curve approaches the free-surface, the velocities can be seen to fall away from this relationship.

4.6.4.4 Series B2: Turbulence Intensity Profiles

The streamwise turbulence intensities for this series can be seen in figures 4.63 and 4.64. Figure 4.63 features the profiles for Cases 1, 4, 7, 10, 13 and 15. Although there is a noticeable deviation from the semi-empirical curve, Cases 1, 4 and 7 are well described by it in the outer-region of the profiles. Cases 10 and 13 are also well described by this relationship, however, there is an increase in the amount of deviation. The points for Case 15 show a marked decrease in intensities in the inner-region and an increase in the free-surface region.

Figure 4.64 features the profiles for Cases 16 to 21. In this series of profiles, most of the results are well described by the semi-empirical T.I. relationships in the outer-region, with the exception of Case 21, which is the closest to the sidewall.

4.6.5 Series B3: Spanwise Velocity Distribution

In this study, the nominal flow depth was increased to 0.1m, thereby reducing the breadth/depth ratio to 6. Profiles were obtained throughout the span similar to those for B2, as described in table 4.8, with the exception that Cases 16-21 have only 10 points throughout the depth.

4.6.5.1 Series B3: Cross-Sectional Average Velocity

The mean velocity, u_o, for each lateral position was calculated from the velocity profiles and is illustrated in figure 4.65. This shows a symmetrical distribution of the mean velocities about the flume centreline, with a distinct region of similar values confined to the central third of the flume. Again symmetry is observed with these values. As the sidewall is approached, the values suddenly decrease at a distance of approximately 50mm from the wall, or $0.083B$.

4.6.5.2 Series B3: Log-Law Velocity Profiles

The log-law profiles for series B3 are shown in figures 4.66 and 4.67 for the corresponding profiles in each half-section of the flume. Both sets of profiles display a similar relationship, whereby the central profiles, Cases 1 and 4, and their corresponding opposites 16 and 17, are well described by the velocity defect law. It was evident from the lateral mean velocity distribution that this central region is limited to these profiles, and that a reduction in mean velocity occurs beyond these. This is also evident from the log-law velocity plots, where the subsequent profiles have decreased velocities throughout the depth. In both figures, the near sidewall profiles (Case 15 and Case 21) both have a notable reduction in their velocities, nevertheless, both profiles appear to be similar to one another, indicating a good degree of symmetry in the channel.

4.6.5.3 Series B3: Turbulence Intensity Profiles

The streamwise turbulence intensities, u'/u^*, are presented in figures 4.68 and 4.69 for the corresponding profiles in each half of the channel. Also given are the turbulence intensities for the vertical and lateral turbulence intensities, v'/u^* and w'/u^* from one half of the channel in figures 4.70 and 4.71 respectively.

The streamwise turbulence intensities appear to be well described by the TI models in the outer-region of the flow for most of the cases. Again, the inner-region and free-surface region of the profiles do deviate from the TI models. The only profiles which display a large scatter are those for the near wall profiles, Cases 15 and 21, where again each profile displays values which are similar throughout the depth.

Figure 4.70 illustrates the vertical turbulence intensities for Cases 1, 4, 7, 10, 13 and 15. These profiles appear to be very well described by the curve using the modified set of constants proposed by Nezu and Rodi (1986). The central profiles fit this relationship better than those closer to the sidewall, however, there is good consistency between all the profiles.

Figure 4.71 illustrates the lateral turbulence intensities for Cases 1, 4, 7, 10, 13 and 15. Nezu (1977) proposed constants for the w' model, however, the work conducted by Nezu and Rodi (1986) only concluded a modified set of constants for u' and v'. Figure 4.71 includes two model curves, one based on the initial set of constants by Nezu (1977), and a second curve with the constants D_W=1.59 and C_W= 0.75 proposed by the author. Cases 1, 4, 7 and 10 can be described fairly accurately by this proposed modification to the TI model, particularly in the outer-region. Initial signs of deviation occur in Case 13, particularly as the free-surface is approached. An even greater deviation occurs for the near sidewall profile (Case 15), where the turbulence intensity increases as the free-surface is approached.

4.7 CONCLUDING REMARKS

4.7.1 Introduction

This chapter includes much of the preparation and initial data acquisition necessary to continue the next phase of the investigation. The knowledge gained from this work has provided confidence in the equipment and apparatus used in the project, and has established various criteria and experimental methods for use in the study. The results from the initial investigation compare favourably with existing models and relationships describing turbulent open-channel flow.

4.7.2 Initial Study - Conclusions

The purpose of the initial study was to provide an insight into slot flow and to gain experience on the use of the LDV system. Despite limitations imposed by the dimensions of the teaching flume, a useful preliminary investigation of slot flow was undertaken.

Due to time constraints, the initial study was limited to a single set of hydraulic conditions. However, measurements were obtained from 4 different aspect ratios, namely 2, 5, 10 and 15, and from a BFS. This provided information on the different flow characteristics which develop under these different aspect ratios, and in addition it allowed comparison between shared characteristics. Although much of this information is already known, it has also provided more detailed information pertinent to the main study. This work is also documented in Keogh and Addison (1996a).

The following points were observed from the results:

(1) For a slot aspect ratio A_s=2, a recirculating eddy completely fills the slot. This eddy is still the dominant feature for the larger aspect ratio of A_s=5, however, a separation streamline can be seen to develop which intrudes into the slot. For both of these aspect ratios, there was no evidence of a secondary recirculation zone at the FFS. However, the flow over the FFS does have large local velocities, particularly for A_s=5, suggesting that an undetected recirculation zone may exist.

(2) At increased aspect ratios, $A_s \geq 10$, the main feature observed was the primary recirculation zone with its associated separation streamline. This streamline reattaches to the base of the slot at a distance of x/H_s=7-8. Beyond flow reattachment, the velocity profile begins to re-establish normal open-channel flow characteristics. As the flow approaches the end of the slot, it deflects over the sudden contraction created by the FFS producing a smaller secondary recirculation zone. Although the spatial resolution of the measurements did not clearly indicate this using the velocity vectors, the turbulence intensities did indicate the development of a new turbulent shear layer (see below).

(3) The maximum velocities within the recirculation cells, u_{Rmax}, were identified. These were found to be higher for the lower aspect ratios, where values of $0.4u_o$ and $0.35u_o$ were observed for A_s=2 and 5 respectively. For the cases where flow reattachment on the channel bed occurred, i.e. $A_s \geq 10$ (including the BFS), a similar value of approximately $0.25u_o$ was observed.

(4) The shear layer within slots of $A_s \geq 10$ can be seen to reach maximum TKE values along the separation streamline. For A_s=15, the plume of high TKE begins to dissipate towards the end of the slot, where it can be seen that a new smaller shear layer of even higher TKE is generated at the top of the FFS.

(5) For $A_s \leq 5$, the shear layer is characterised by a region of high turbulent energy which develops along the separation streamline and grows as it migrates downstream. For an aspect ratio, $A_s=5$, the maximum TKE is significantly higher than for $A_s=2$ due to the increased length of the separation streamline. It was observed that the rate of turbulence generation was greater than its rate of dissipation in this region. This causes an accumulation of TKE along the separation streamline, evident from the high TKE values observed. In the case for $A_s=5$, the low velocities which develop in the centre of the recirculation zone are coupled with the low velocities which occur in the upstream corner of the slot. This appears to entrain the high TKE which deflects down the FFS. There is also evidence of high TKE values developing over the FFS for $A_s=5$, owing to the increased deflecting of flow over the FFS, however, much of the turbulence detected in this region originated from the slot shear layer.

(6) Downstream of the slot, the recovery of the flow back to normal flow conditions depends on the extent of the perturbation to the flow caused by the slot. For $A_s \leq 5$, the flow recovers within several slot heights downstream of the FFS, however, when the $A_s \geq 10$, the turbulence generated at the secondary recirculation zone was still detected at the limit of measurement (i.e. x/H_s=6-7 downstream of the FFS).

(7) The BFS configuration displayed similar flow characteristics to those observed for $A_s \geq 10$. The length of reattachment of the separation streamline was similar at 7-8H_s. The shear layer was seen to develop fully and dissipate as the flow progressed downstream. Although a central core of high TKE was observed, the migrating plume of high TKE extends over the full depth of the flow. This is in contrast to that for the $A_s=15$ slot, where the plume narrowed towards the FFS due to the deflection of the flow over the FFS.

4.7.3 Main Flume Calibration

The main flume was constructed during the initial investigation. Initial tests on the completed flume were undertaken to determine its ability to provide suitable flows and to highlight any modifications prior to continuation of data acquisition. Some of these tests have been documented in this chapter. The reason for undertaking these tests was to assess the geometrical properties of the flume, in particular any deviation from the design value and any unforeseen properties which may affect the nature of the flow.

The following points were observed from a detailed survey of the channel:

(1) The smoothness of the channel bed was investigated by means of accurate elevations with the use of a surveying level. It was concluded from this survey that the channel bed was sufficiently smooth, evident from the low standard deviation in the channel bed elevations.

(2) The only areas of real concern were found to be at the flume connections. In both cases there was a slight vertical misalignment between the sections, however, this displacement was less than 0.3mm, which would have no effect on the flow at the scales being used in this study.

(3) The slot depth was also investigated, where it was observed that the slot base bulged at the centre. This was possibly caused by stresses induced during construction. Although this bulge only created a difference in depth of less than 1mm within the slot, it was found that the weight of water in the slot overcame this, giving a slot of uniform depth.

(4) The sidewall spacing was also measured to establish the mean width of the flume and to identify any areas which deviate significantly from this. A grid was superimposed onto each sidewall, whereby the distance between similar points either side of the flume was measured using a scale rule with a fitted micrometer. The average width, $\overline{B}$, was calculated using all these points and was found to be 600.8mm with a standard deviation of 0.5mm. The sidewall width is therefore very close to the design value, and the standard deviation suggests that the mean was obtained from consistently similar widths.

4.7.4 Data Validation - Conclusions

During the initial investigation, it was observed that the LDV system was sensitive to various properties of the flow, such as velocity, location within the flow field, clarity of the water, and depth of laser penetration within the flow. This was overcome by changes to the system parameters and accurate movement of the control volume. There was also a requirement to establish a minimum sampling frequency which was sensitive enough to measure the smallest magnitude of velocity fluctuation. In conjunction with this, the minimum number of samples for

each point measurement was required to obtain statistical properties of the time series, such as u and u'_{RMS}.

The following data validation points were observed:

(1) Using functions proposed by Nezu and Nakagawa (1993) (see equations 4.3 and 4.4), the minimum sampling frequency for a flow could be found. This depended on the flow depth and the mean velocity, whereby a new minimum frequency could be established for different flow types and regions of flow .

(2) Raichlen (1967) adopted a statistical method to establish the minimum sample time. This served two main purposes:

(a) To reduce data processing of excessive time series.

(b) To ensure that the calculated values of u and u'_{RMS} are representative of the actual flow values.

The method was based upon analysis of the u and u'_{RMS} throughout the time series. A suitable cut-off time was established when both components consistently deviated less than 2% of a value obtained from an excessively long record.

This method was used successfully to obtain the minimum sample time. The results varied depending on the location of the flow measurement and on the Reynolds number of the flow. It was observed that u'_{RMS} took longer than u to achieve its cut-off time, and therefore, this became the deciding factor when obtaining the minimum length of record, a feature also observed by Raichlen (1967).

4.7.5 Open-Channel Flow - Conclusions

An attempt was made to compare some universal flow characteristics, semi-empirical relationships and theoretical equations to some experimental open-channel flow results taken in the main flume. The purpose of this was to verify these characteristics and relationships, thereby giving confidence in the apparatus and the measurement, processing and analysis techniques.

The following points were observed from this investigation:

(1) The friction velocity, $u*$, was difficult to determine accurately. The method to obtain this by measurement was highly sensitive to the accurate measurement of the channel slope. An alternative method of obtaining $u*$ was by trial and error using the log-law equation, assuming that the log-law is a valid theory. By comparing both methods, it was observed that the values in most cases were within 5% of each other.

(2) The boundary layer profile can be described by the seventh-power law for open-channel flow. For investigations where the flow was in the turbulent region, the experimental boundary layer compared favourably with the seventh-power law. In some cases where the Reynolds number was in the transitional range, the boundary layer profile was also compared to the Blasius profile for laminar flow. It could be seen that the experimental (transitional) boundary layer profile lay somewhere between these two profiles. Deviation from the seventh-power law was observed in profiles close to the sidewalls due to the reduction in velocity which is attributed to sidewall contamination.

(3) The log-law is used to describe the inner-region of flow, defined as $0<y/h<0.2$, and the velocity defect law describes the outer-region, defined as $0.2<y/h<1.0$. Experimental results have been plotted against these semi-empirical relationships. Profiles around the flume centreline which are not influenced by sidewall contamination agree well with these relationships. As the sidewall influence increases, the log-law still describes the inner region of flow, however, as the experimental curves approach the free-surface, the velocities fall rapidly away from the velocity defect law curve. This is attributed to the phenomena known as *dip*, whereby the maximum velocity occurs further below the free-surface for the flow near a sidewall.

(4) Nezu (1977) proposed universal functions to describe the turbulence intensity in the outer region of flow. These were later modified by Nezu and Rodi (1986). A damping function was also introduced to describe the TI in the inner-region of longitudinal flow. Experimental turbulence intensity profiles were compared to these functions. Although most of the profiles did not contain points in the inner-region of flow, some cases are presented which compare well with this inner-region function. For the outer-region, the experimental results are similarly well described by the outer-region function, particularly with the modified constants. This was observed for $u'/u*$, $v'/u*$ and $w'/u*$. In the literature, there was no set of modified constants for $w'/u*$, however, the results

compare well with the initial constants given by Nezu (1977). The results obtained by the author suggest a more accurate set of constants for this TI component of D_W=1.59 and C_W= 0.75.

(5) Profiles were taken throughout the width of the channel to identify the limits and effects of sidewall contamination. Velocity profiles in the central region have higher velocities than those close to the sidewalls. The maximum velocity occurs at, or very close to the free-surface in the central region, whereas, profiles close to the sidewalls have their maximum velocity lower in the profile.

(6) Profiles of TI across the span of the flume indicate that a central region does exist. Sidewall influence on the TI appeared to be localised within a relatively small distance, b/h=0.5, from the wall.

(7) From the three detailed investigations of the flow across the width of the flume, the central region can be described as the region which is not affected by sidewall contamination, and where flow characteristics such as mean velocity and turbulence intensity are similar, irrespective of their lateral location. If B is the actual channel width, b_S the width influenced by sidewall contamination (from both sidewalls), and h is the flow depth, then the following was observed from the results:

Table 4.11 - Sidewall Contamination Aspect Ratios

Series	h (mm)	B/h	b_S/h
B1	32	18.75	6.75
B2	50	12	4.8
B3	100	6	4.8

It can be seen in all three cases that the ratio b_S/h is less than B/h, and therefore the difference between these two values represents the extent of the central region of the channel. The results for the ratio b_S/h are similar, suggesting that the sidewall influence scales with approximately 5-7 times the flow depth. These findings, albeit from a small sample of results, compare favourably with the literature.

(8) From the three full width investigations, it was also observed that good flow symmetry existed about the flume centreline.

Figure 4.1 - Initial Investigation: Mean Velocity Vector Plots

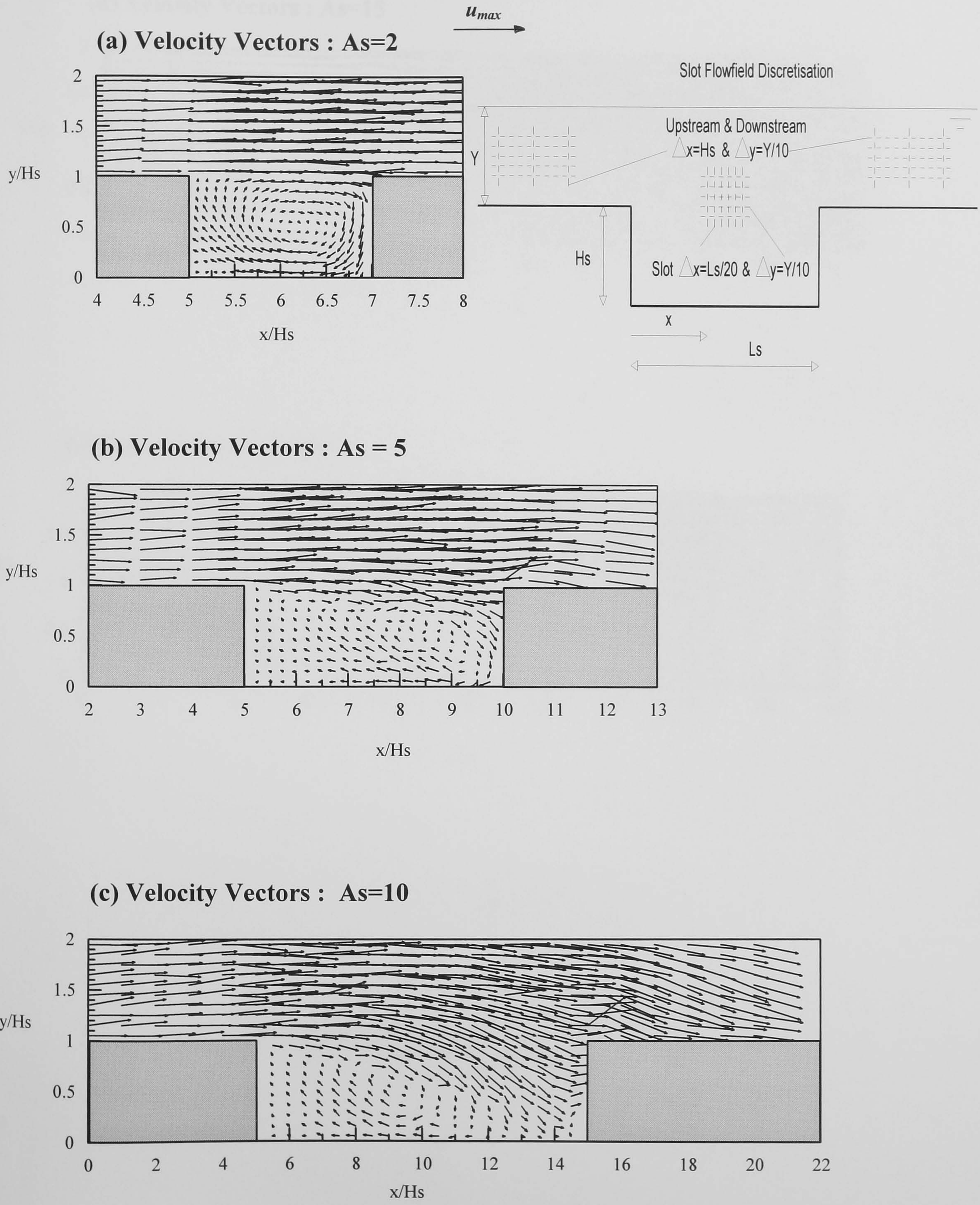

(d) Velocity Vectors : As=15

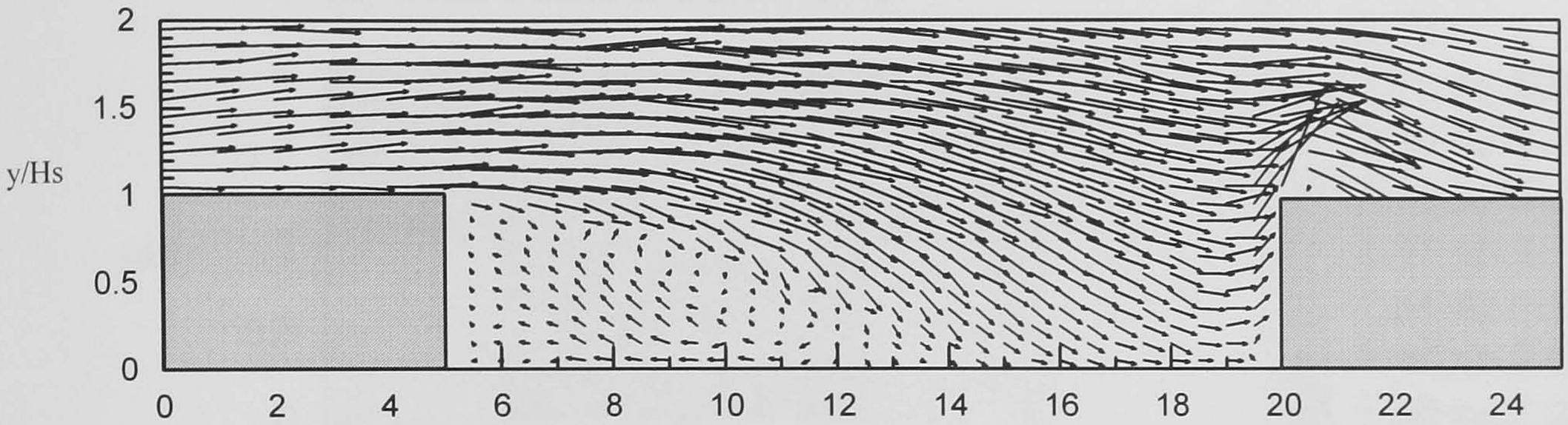

(e) Velocity Vectors : BFS

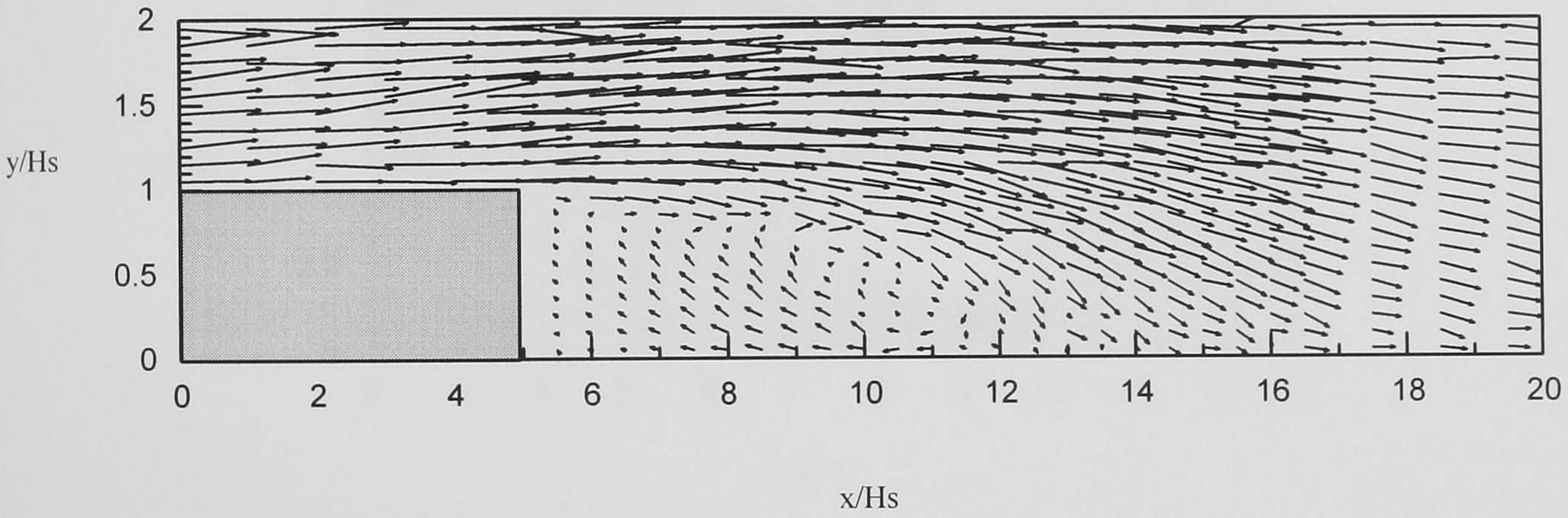

Figure 4.2 - Initial Investigation: TKE Contour Plots

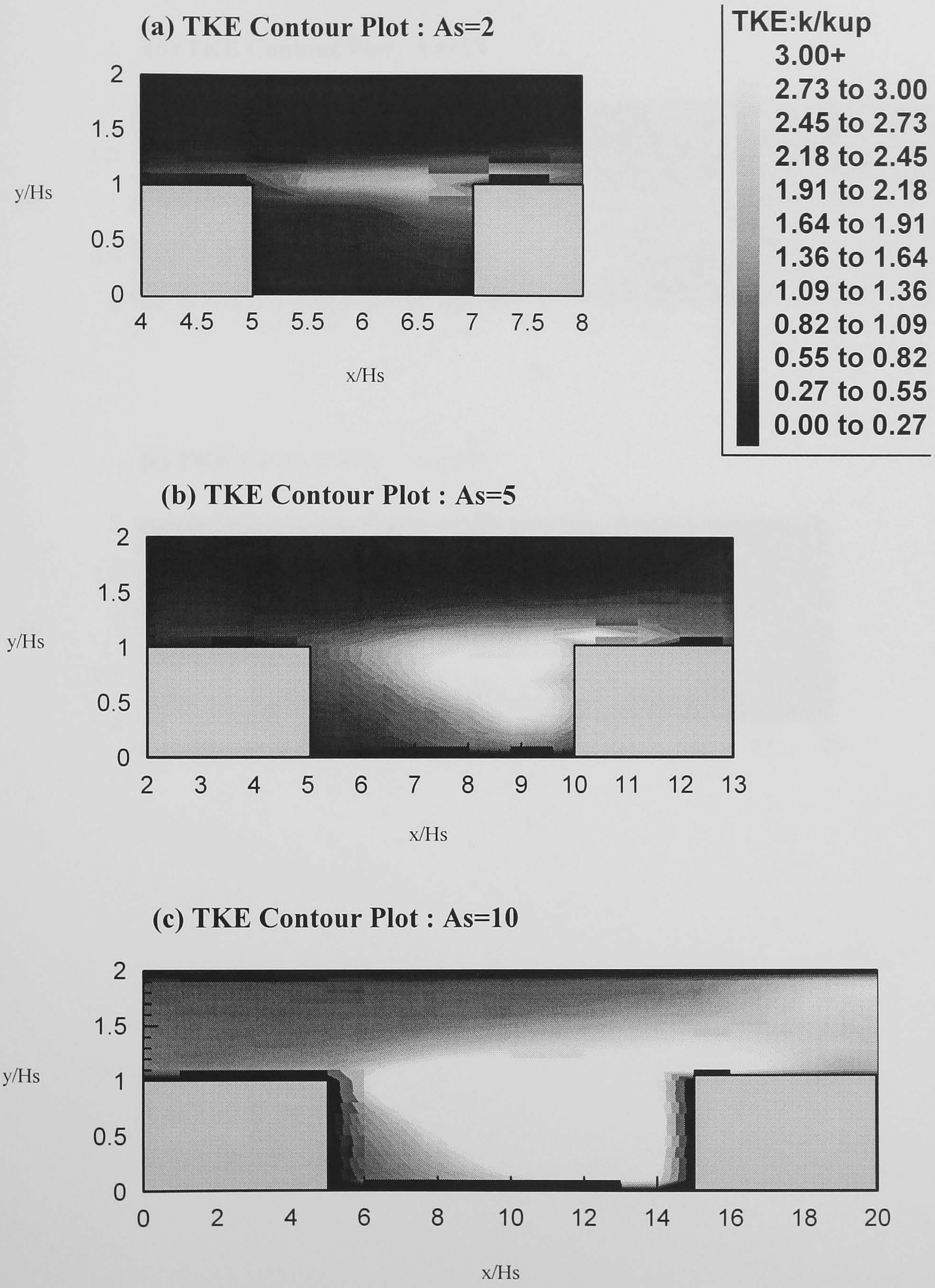

(d) TKE Contour Plot : As=15

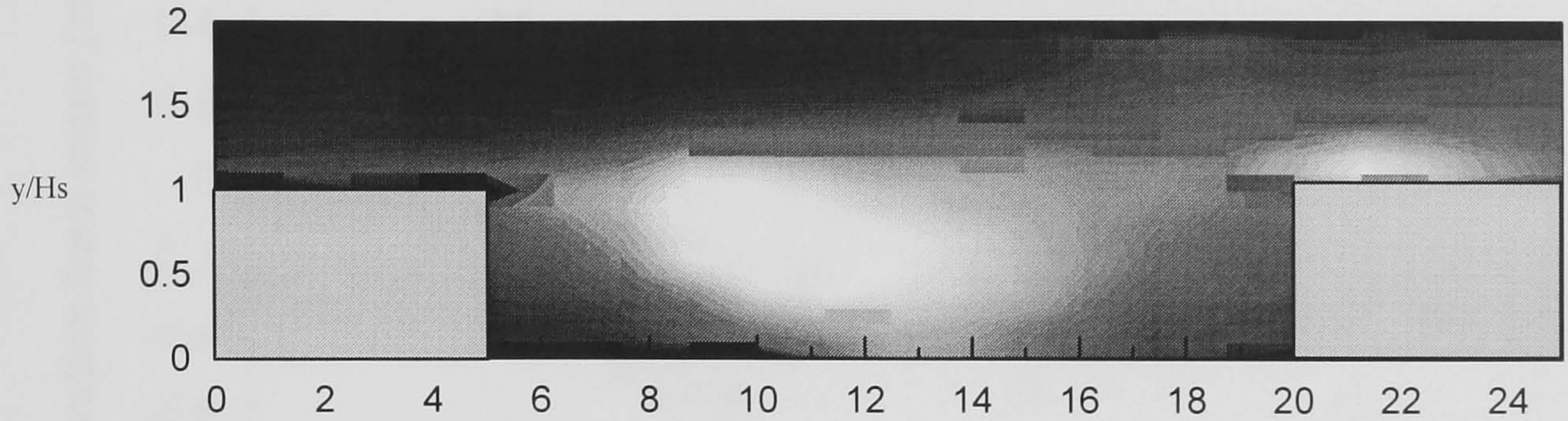

(e) TKE Contour Plot : As=BFS

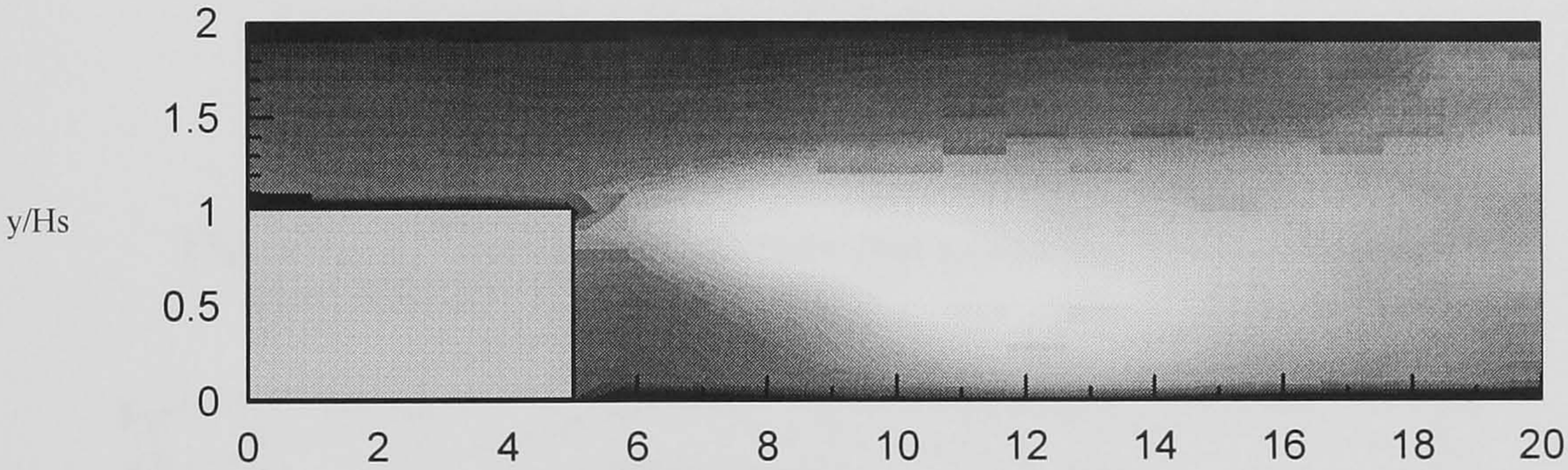

Figure 4.3 (a) - Flume Bed Elevations: Upstream Section (1)

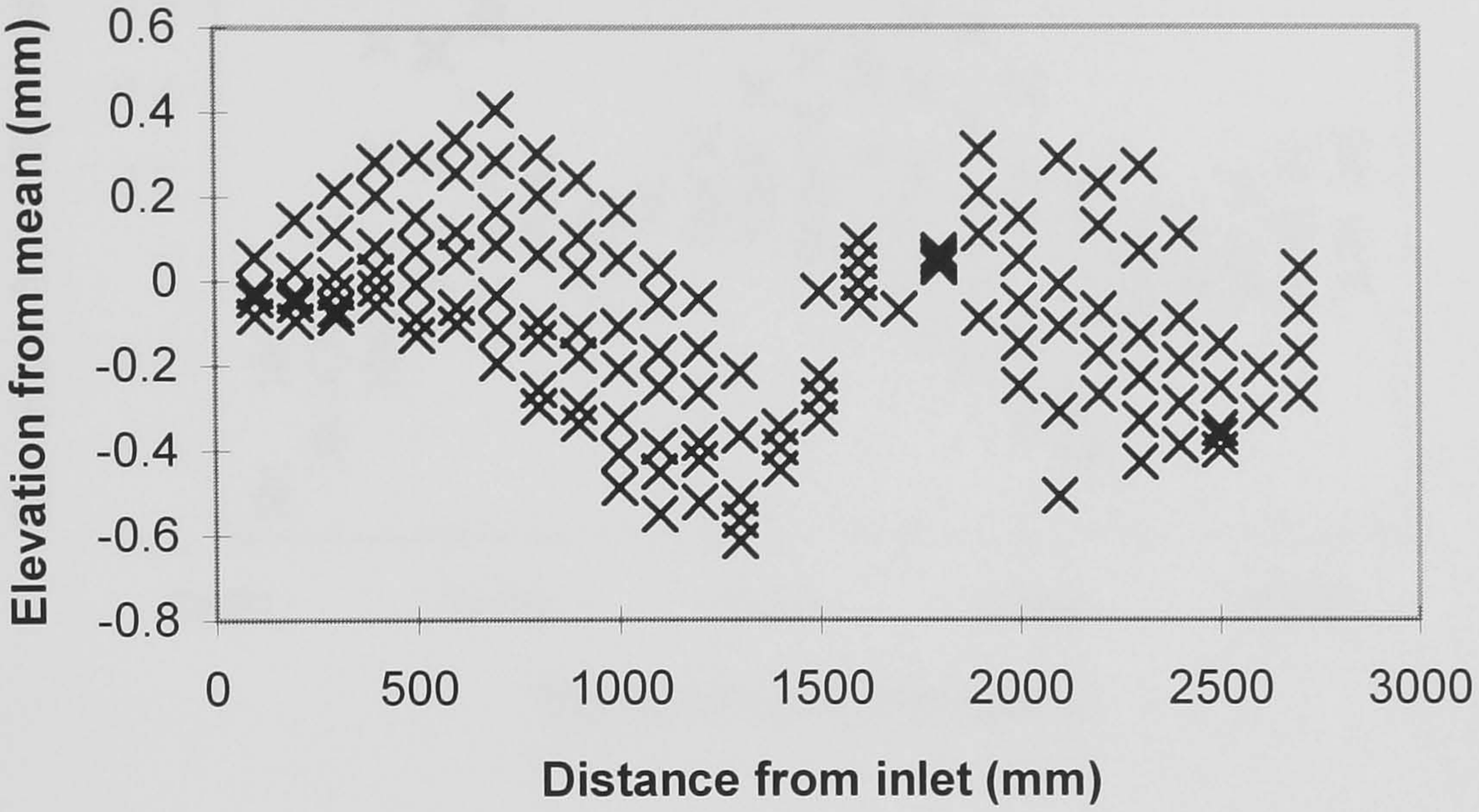

Figure 4.3 (b) - Surface Plot of Flume Bed Elevations: Upstream Section (1)

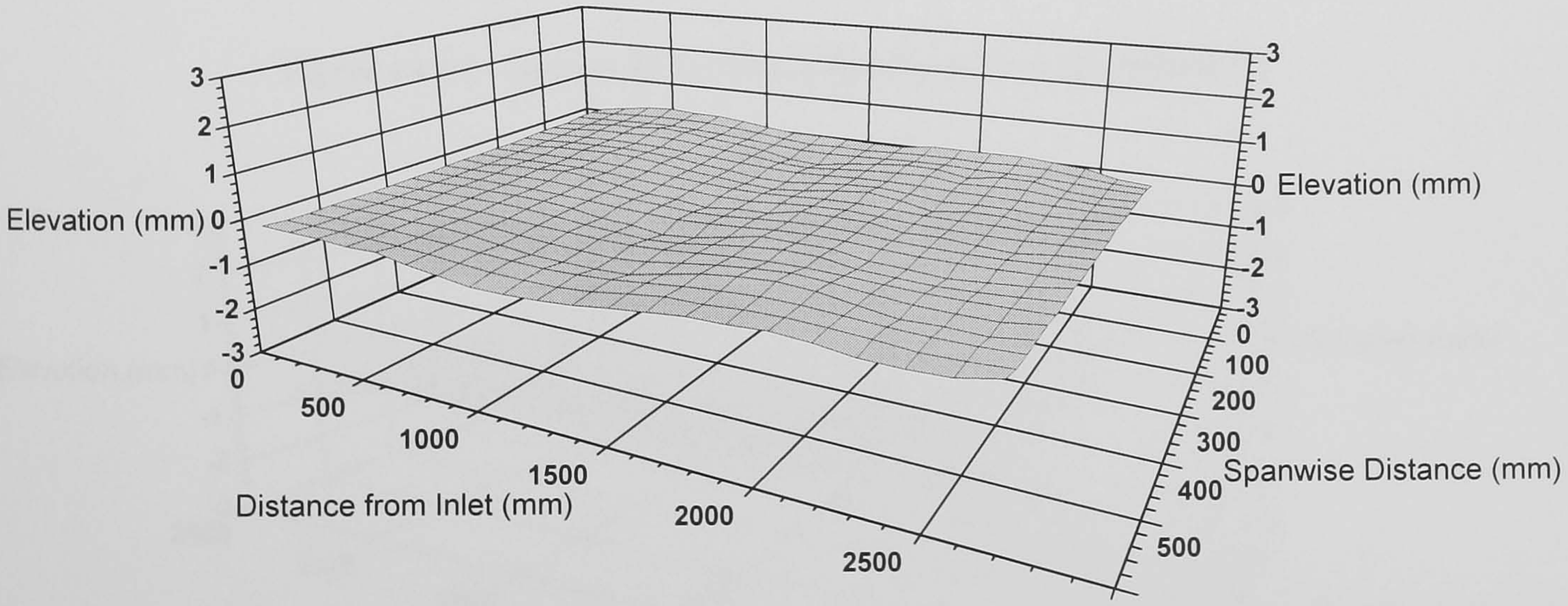

Figure 4.4 (a) - Flume Bed Elevations: Slot Section (2)

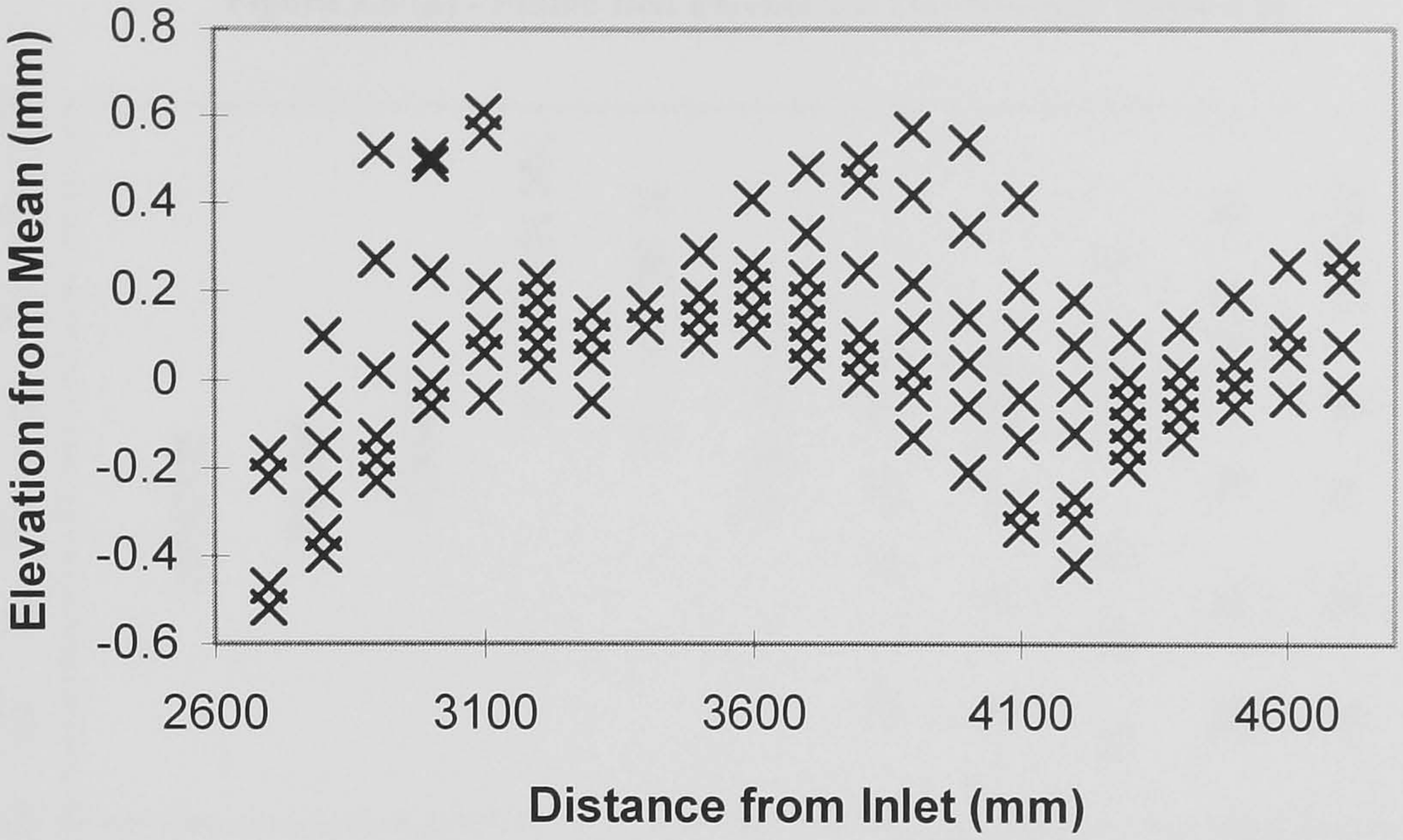

Figure 4.4 (b) - Surface Plot of Flume Bed Elevations: Slot Section (2)

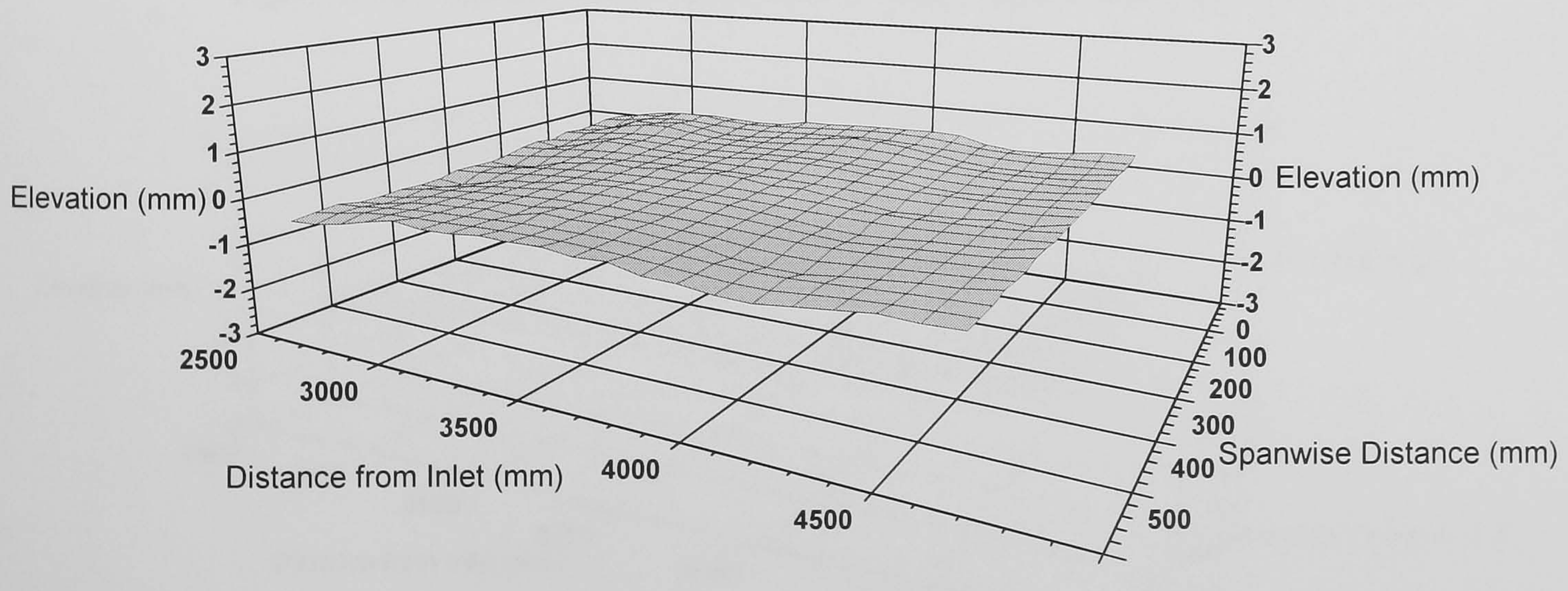

Figure 4.5 (a) - Flume Bed Elevations: Downstream Section (3)

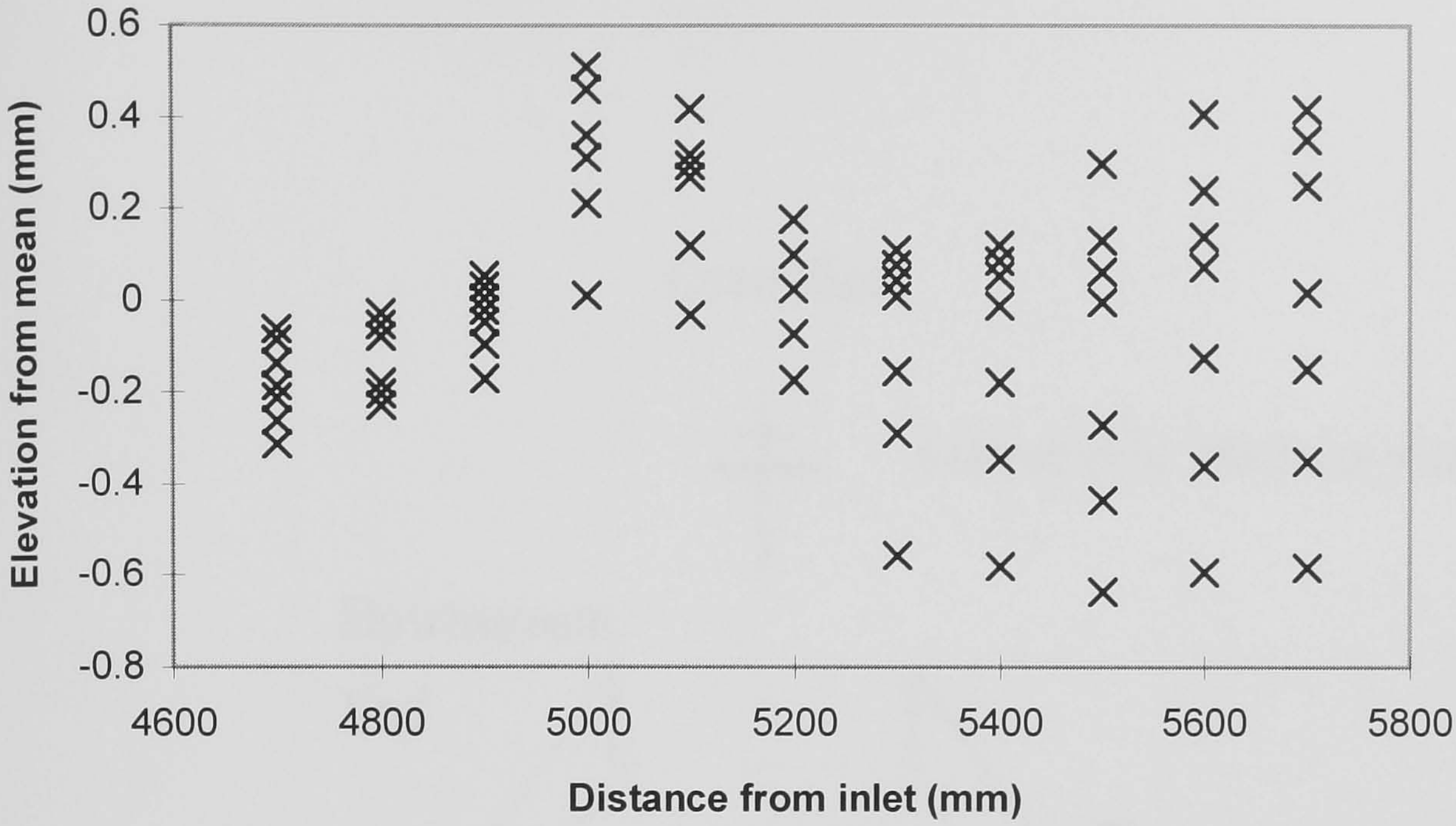

Figure 4.5 (b) - Surface Plot of Flume Bed Elevations: Downstream Section (3)

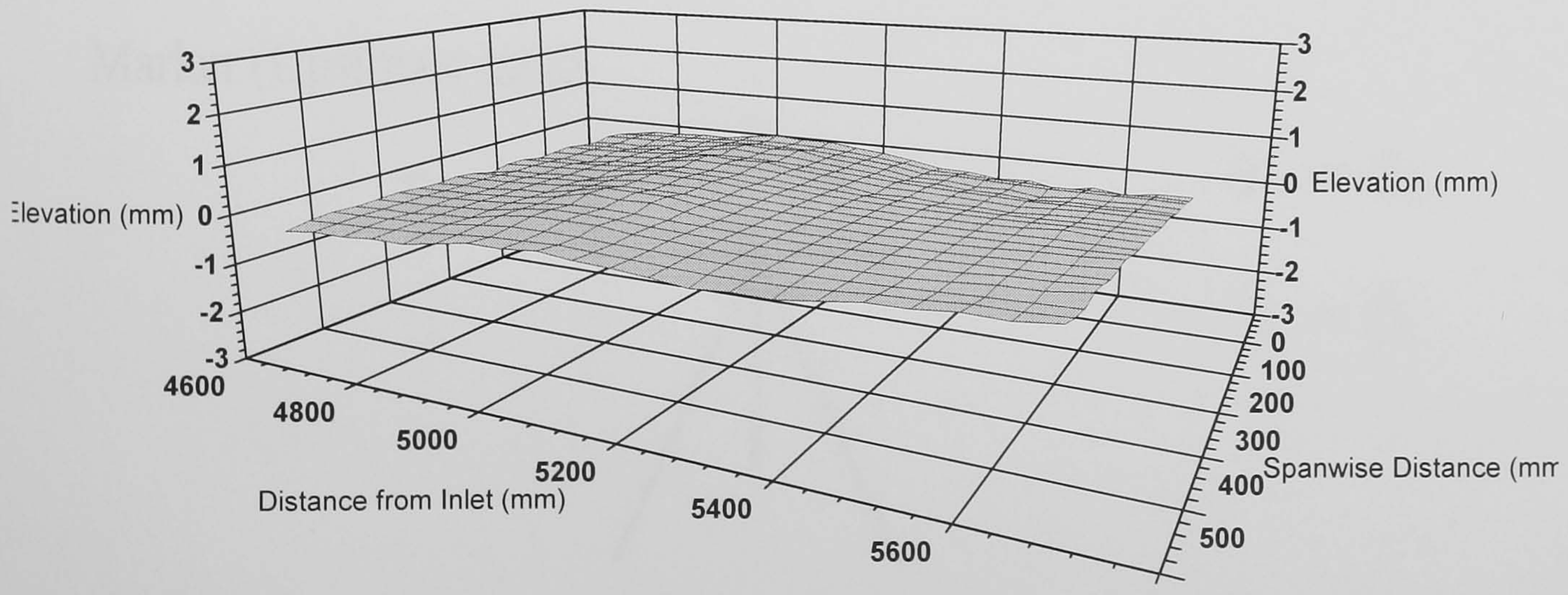

Figure 4.6 - Centreline Location on Main Flume

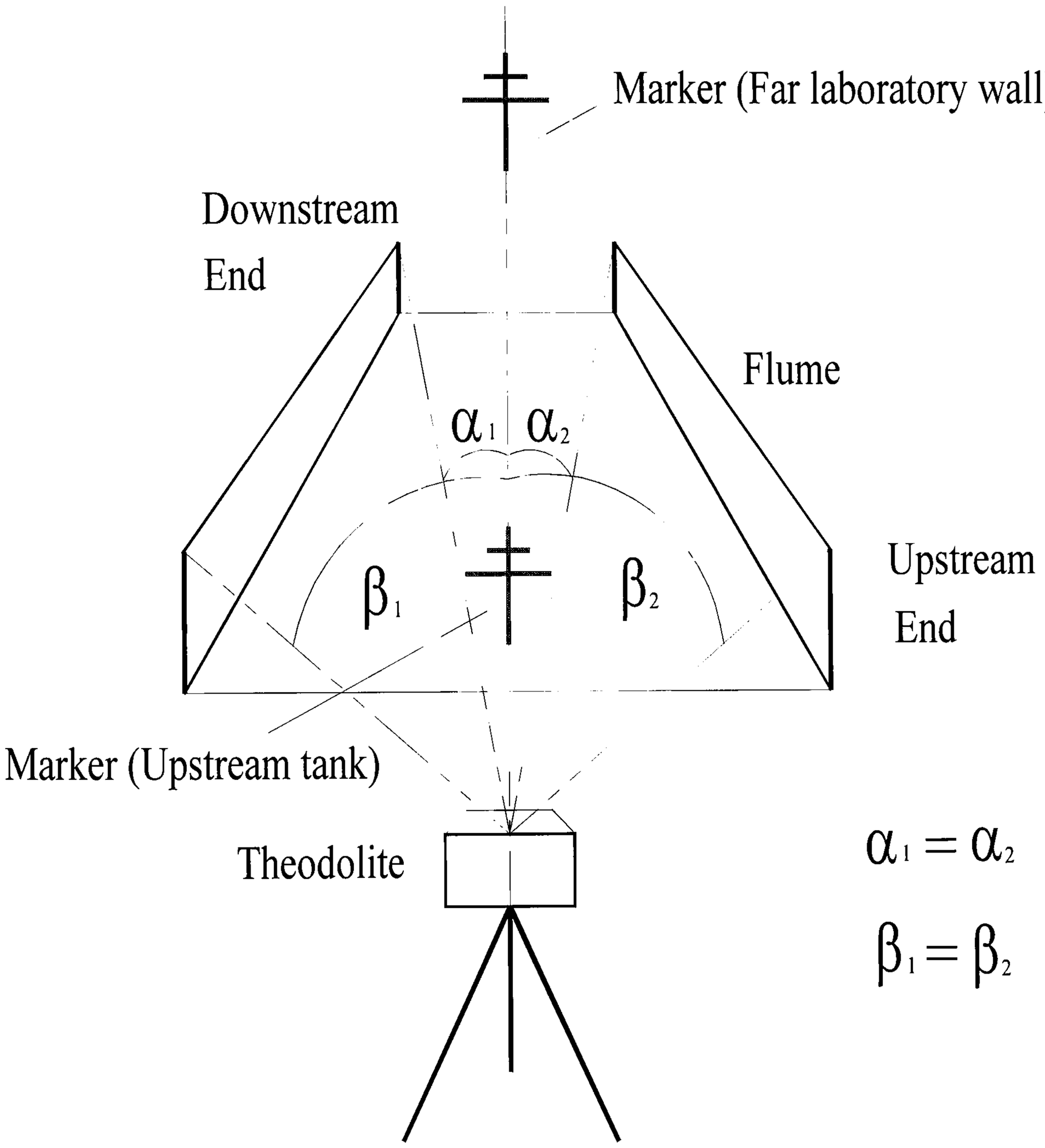

Figure 4.7 - Data Sample Validation - Mean Velocity

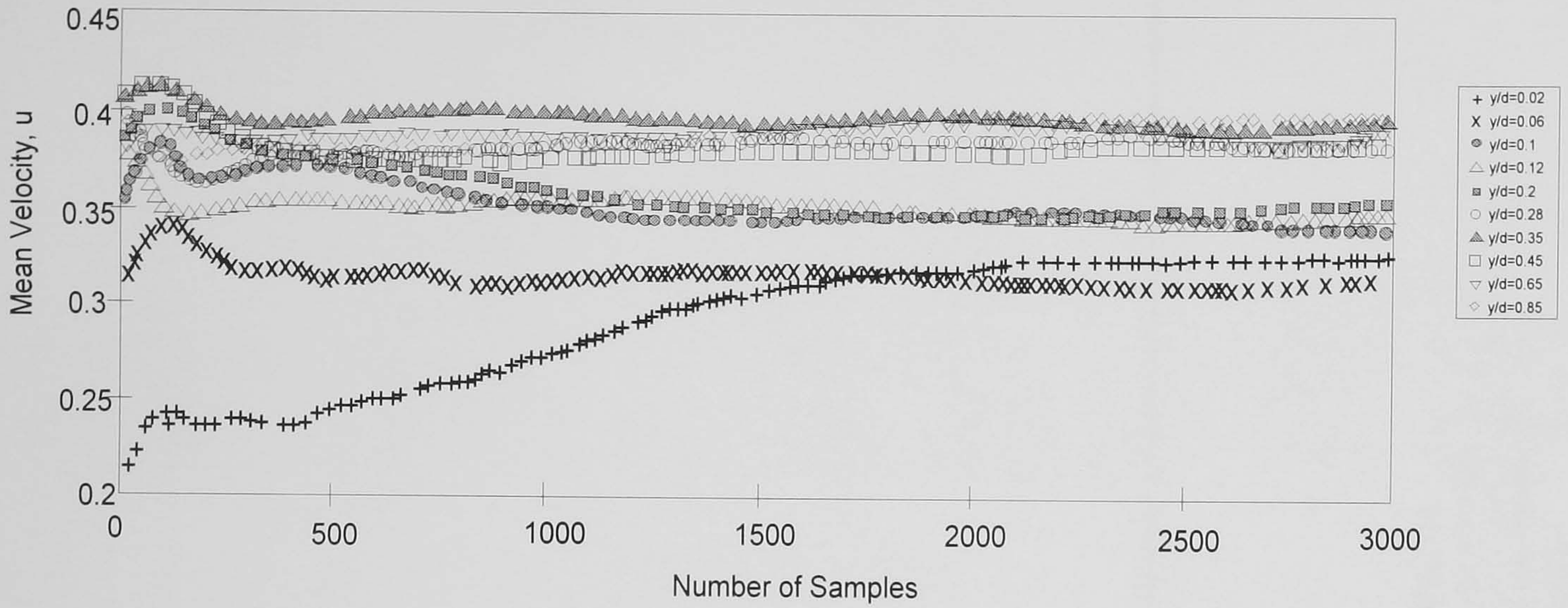

Figure 4.8 - Data Sample Validation - u'rms

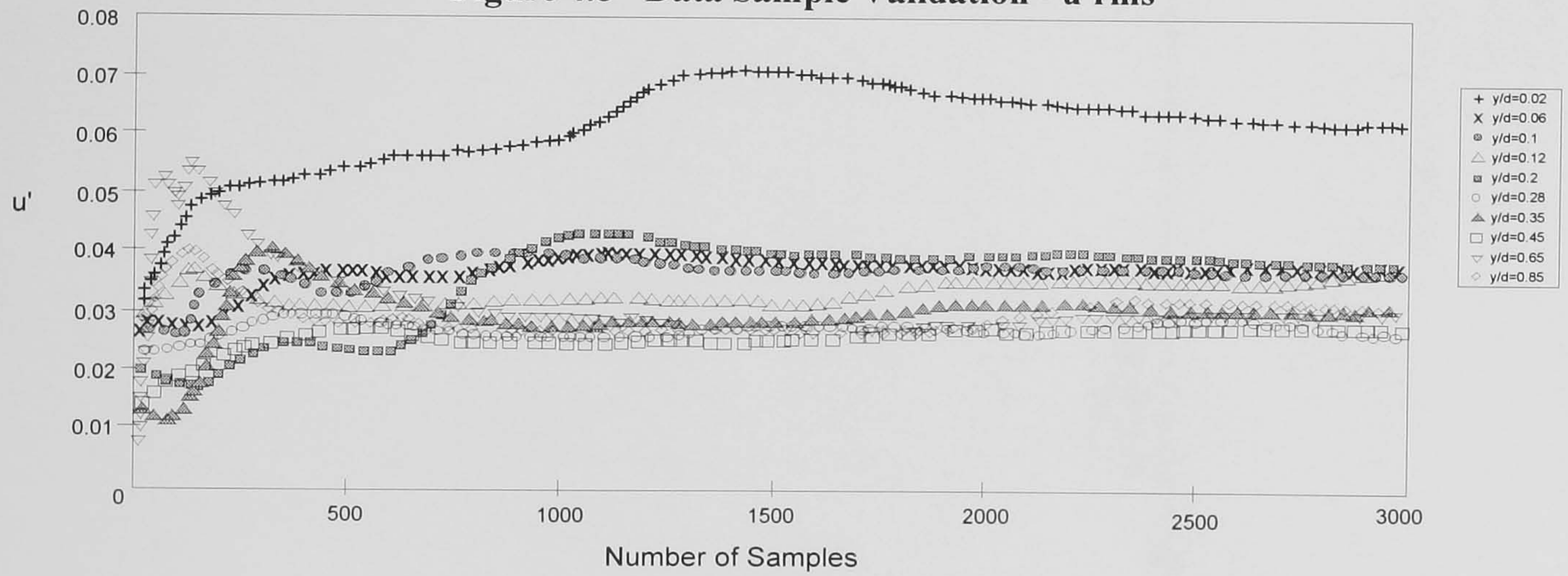

Figure 4.9 - Schematic Representation of Trace Cut-Off Time

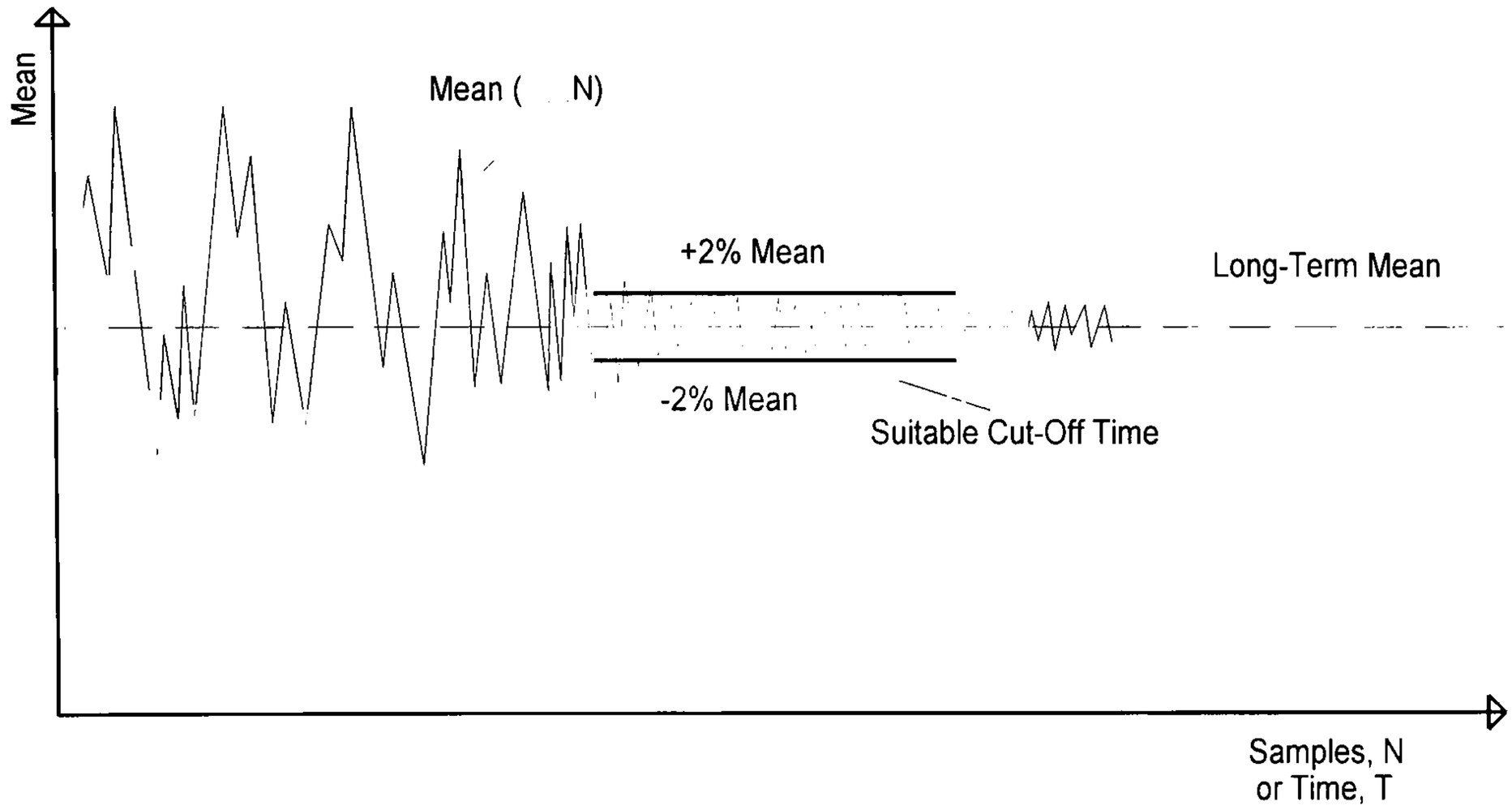

Figure 4.10 - Data Validation Analysis - Mean Velocity

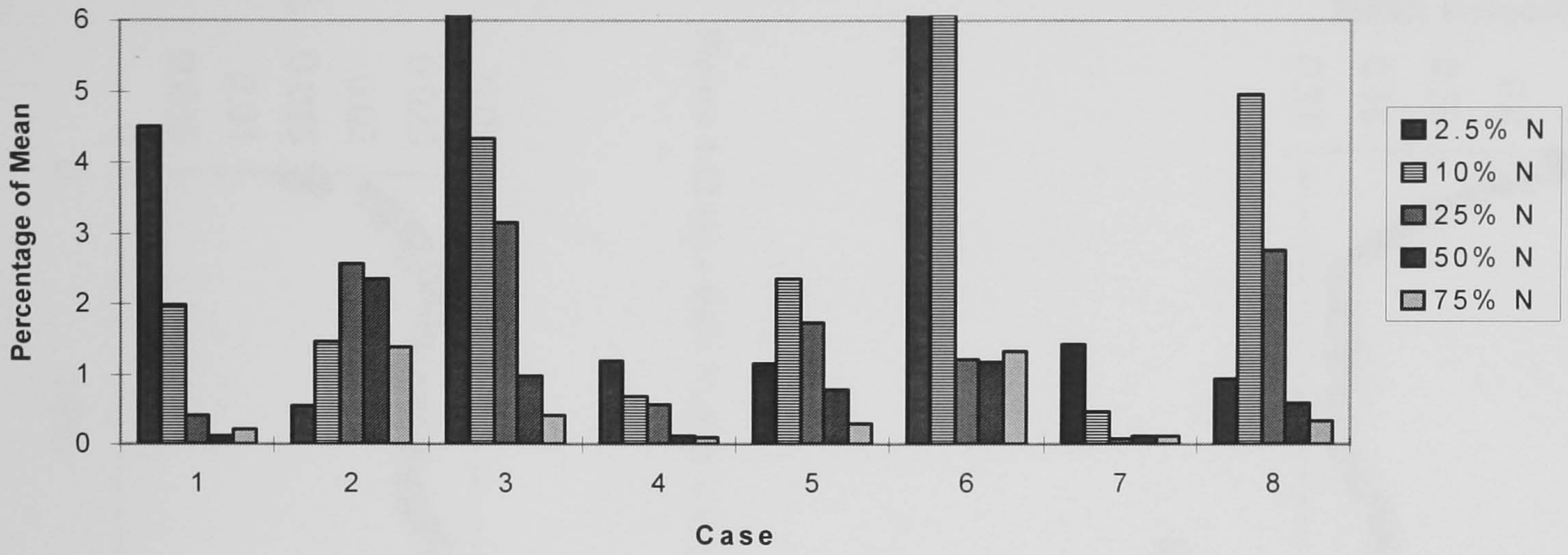

Figure 4.11 - Data Validation Analysis - Root Mean Square Velocity

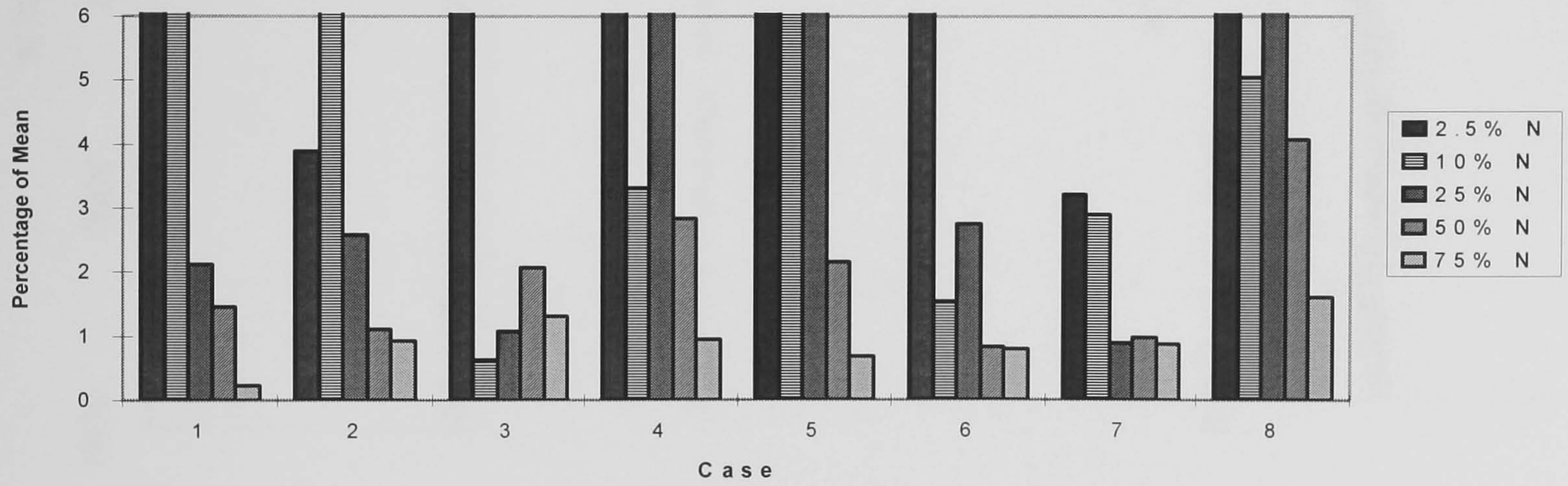

Figure 4.12 (a) - Data Validation: U-component - Mean Velocity, u

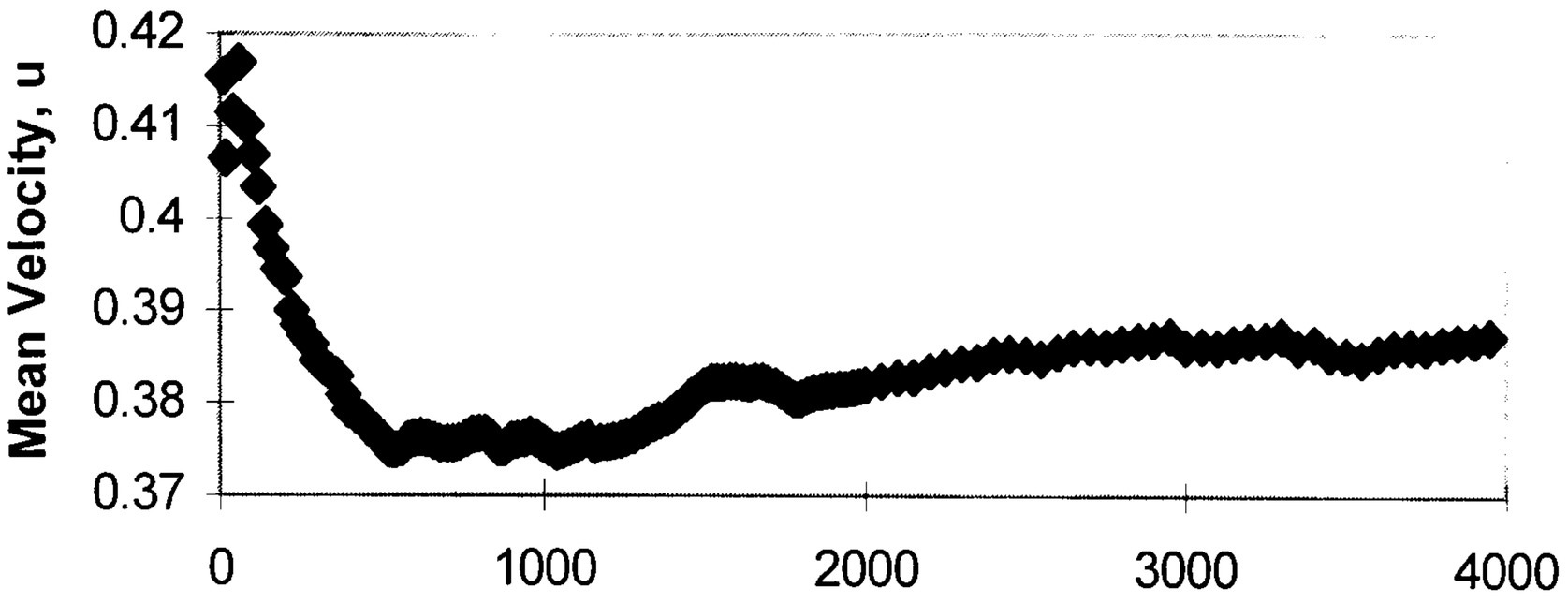

Figure 4.12 (b) - Data Validation: U-component - Fluctuating Velocity, u'

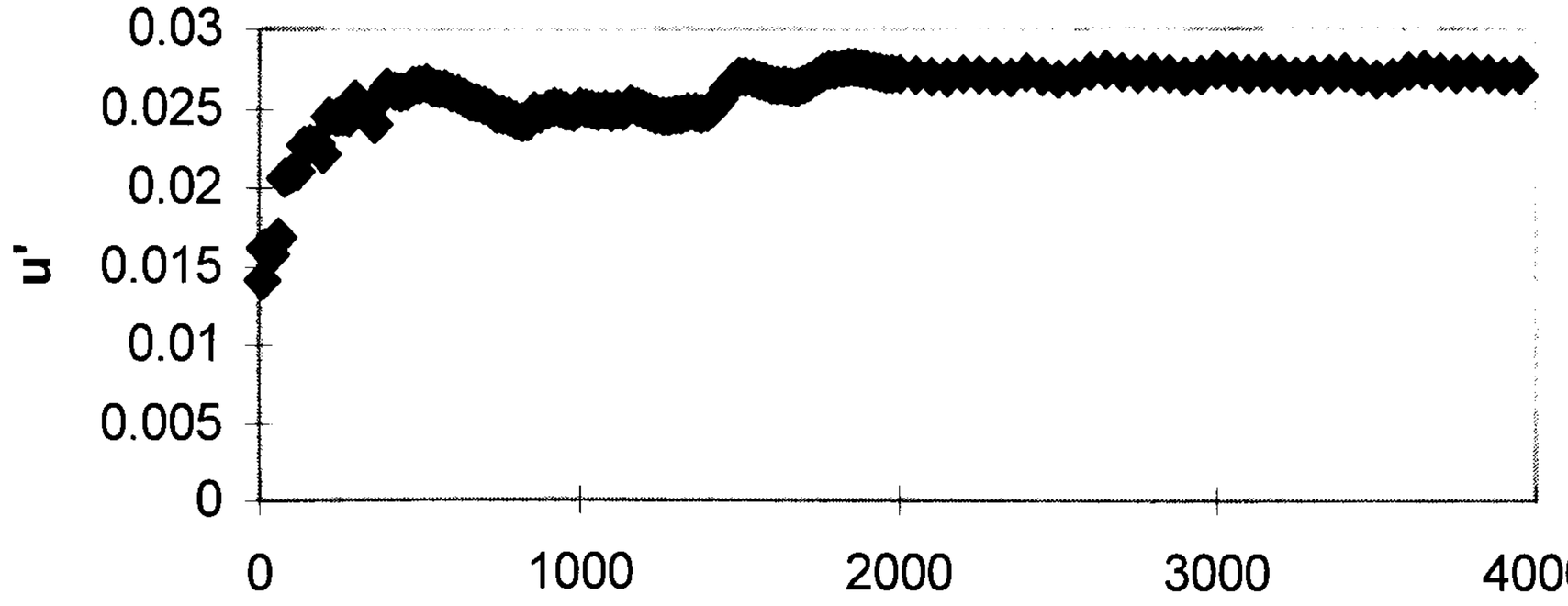

Figure 4.13 (a) - Data Validation: V-component - Mean Velocity, v

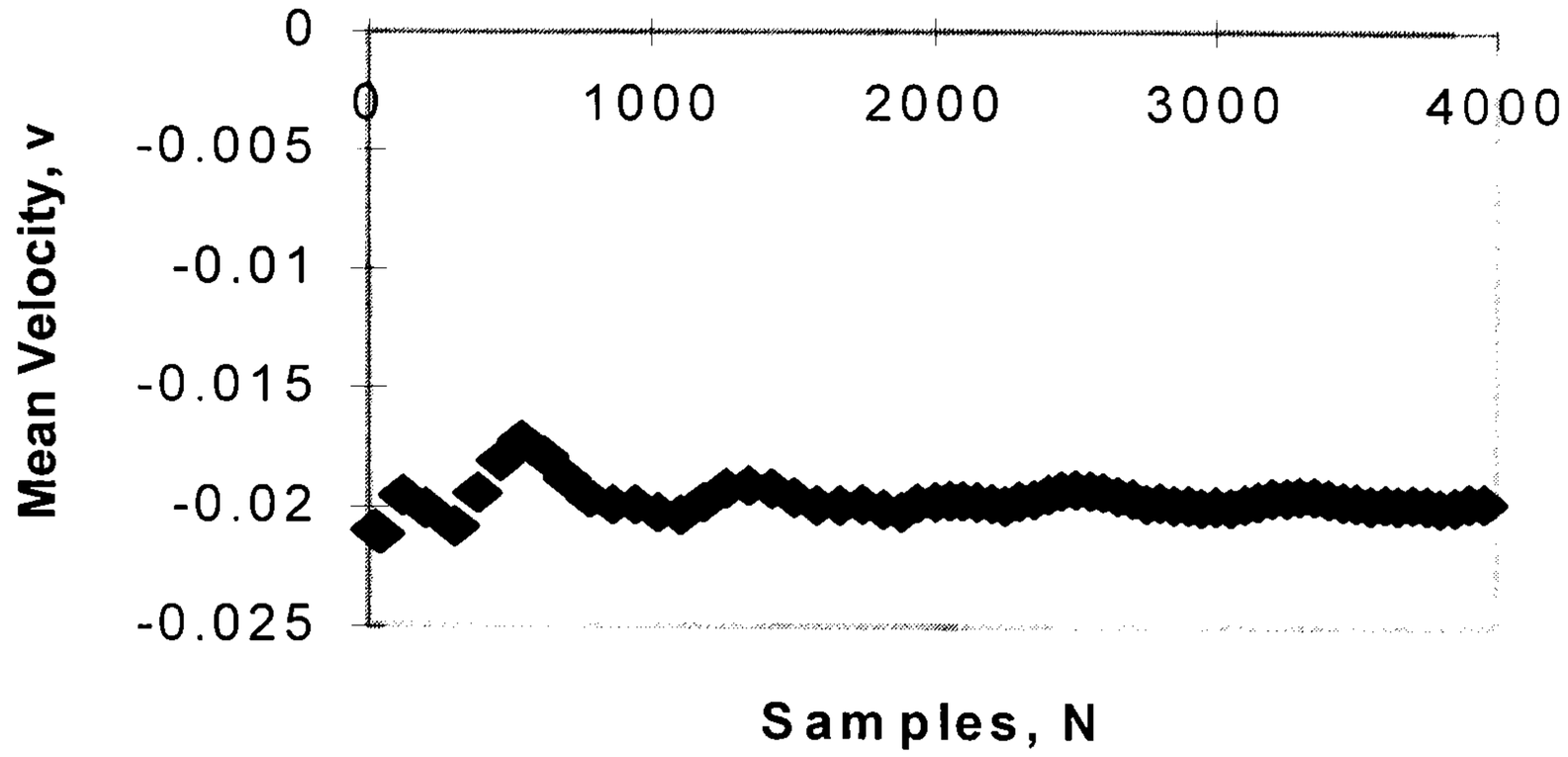

Figure 4.13 (b) - Data Validation: V-component - Fluctuating Velocity, v'

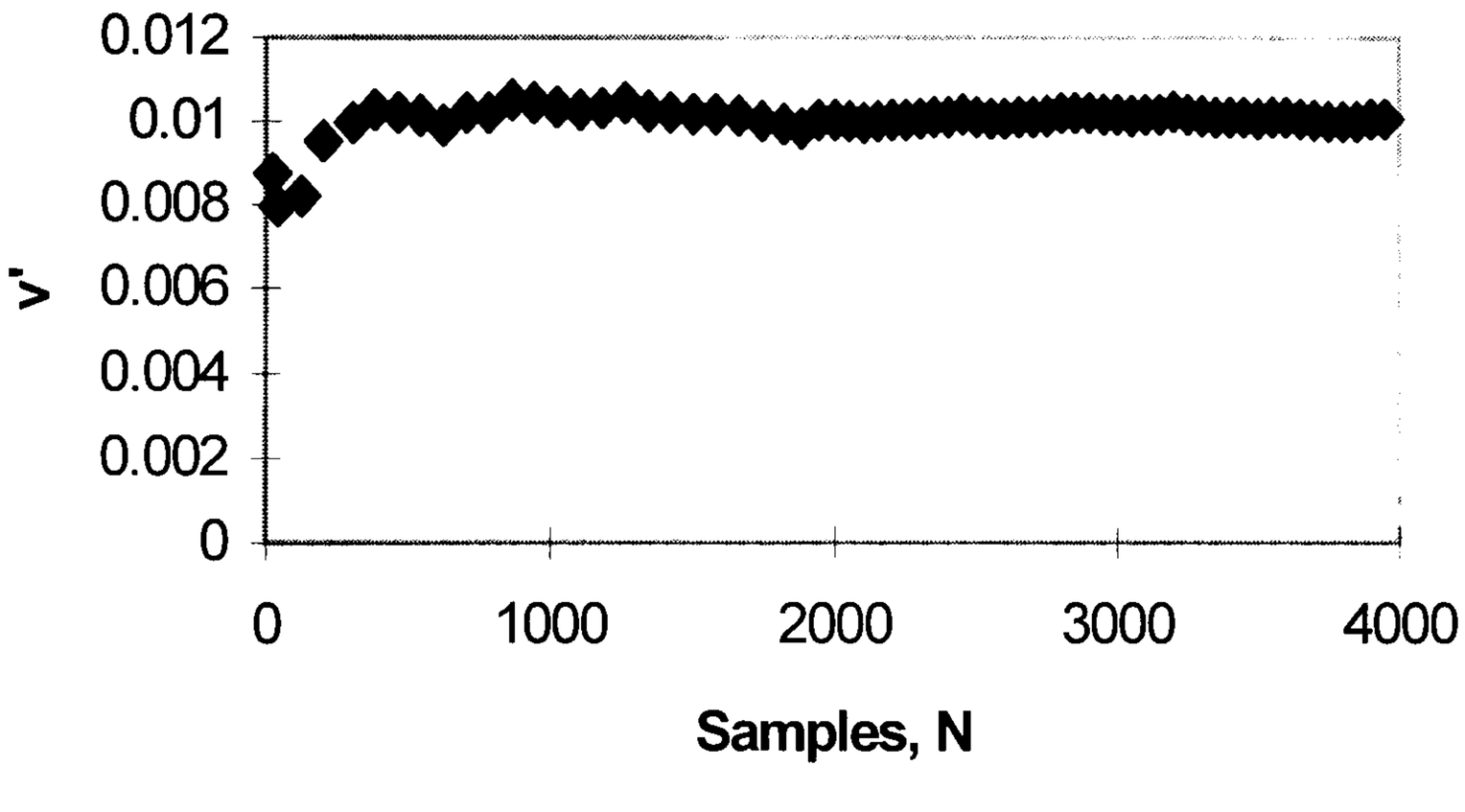

Figure 4.14 (a) - Data Validation: W-component - Mean Velocity, w

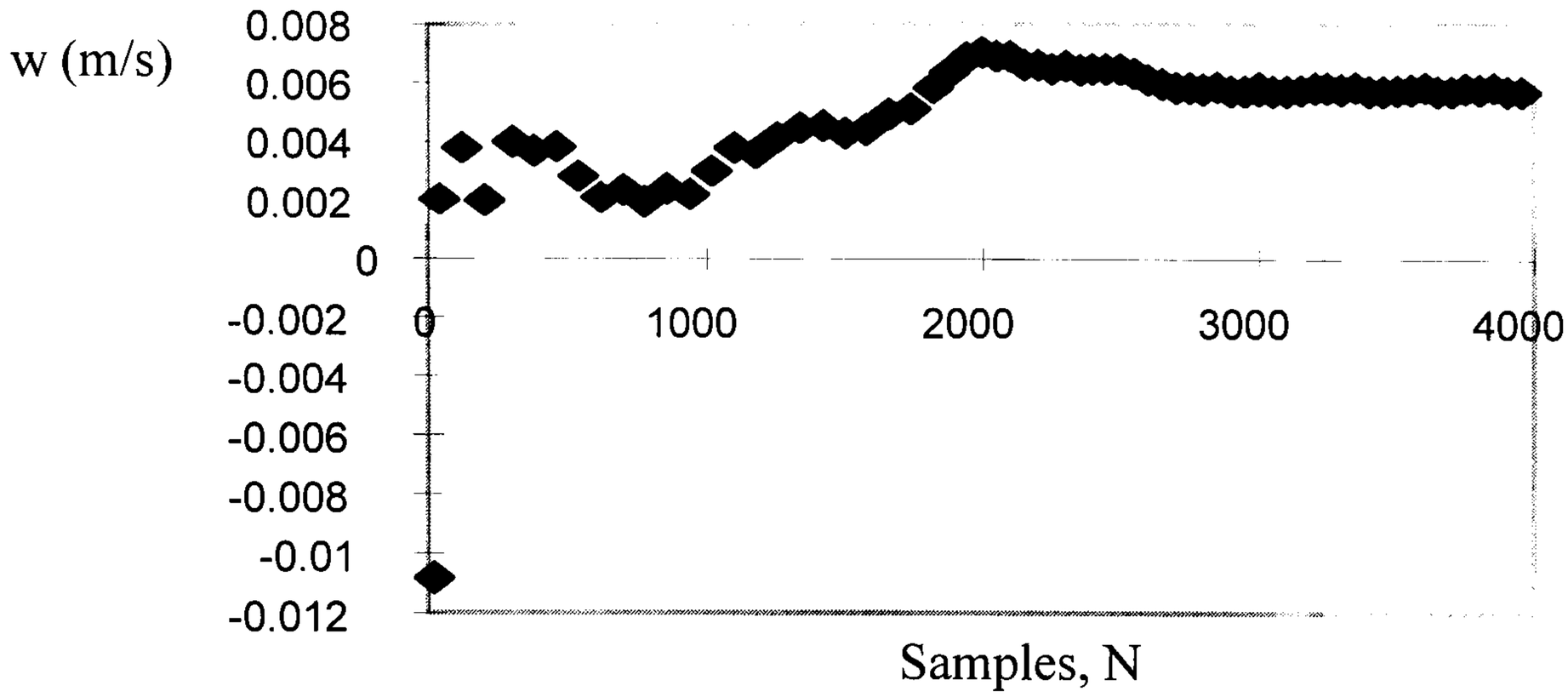

Figure 4.14 (b) - Data Validation: W-component - Fluctuating Velocity, w'

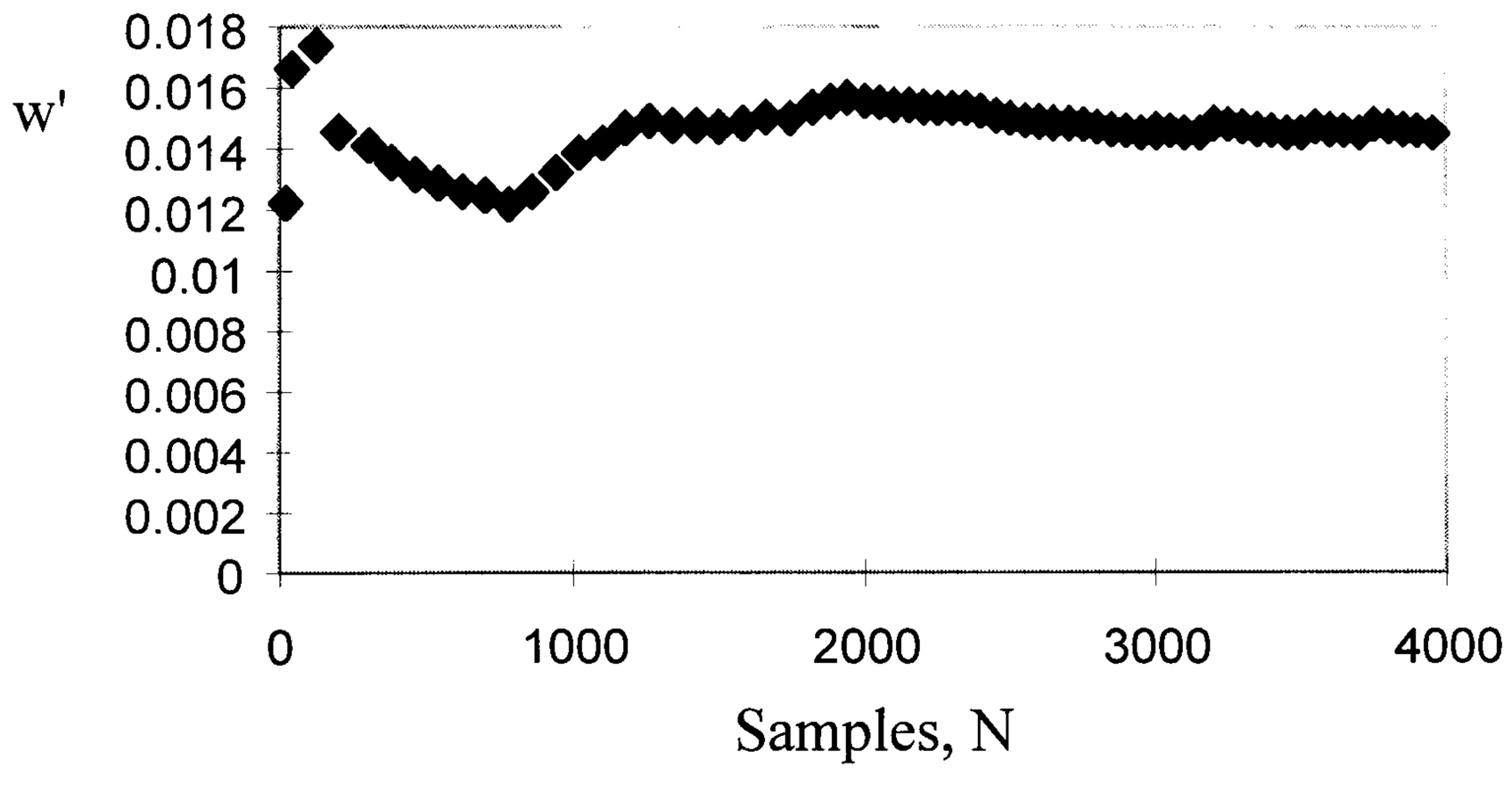

Figure 4.15 - Probe Rotation with Respect to Channel Slope

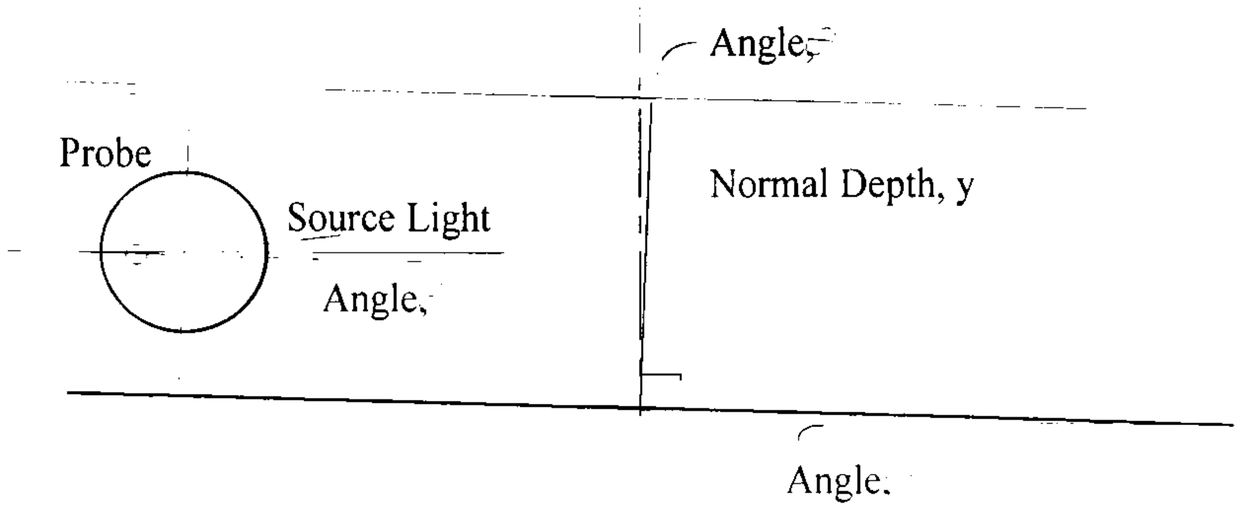

Figure 4.16 - Schematic Representation of Probe Vertical Alignment

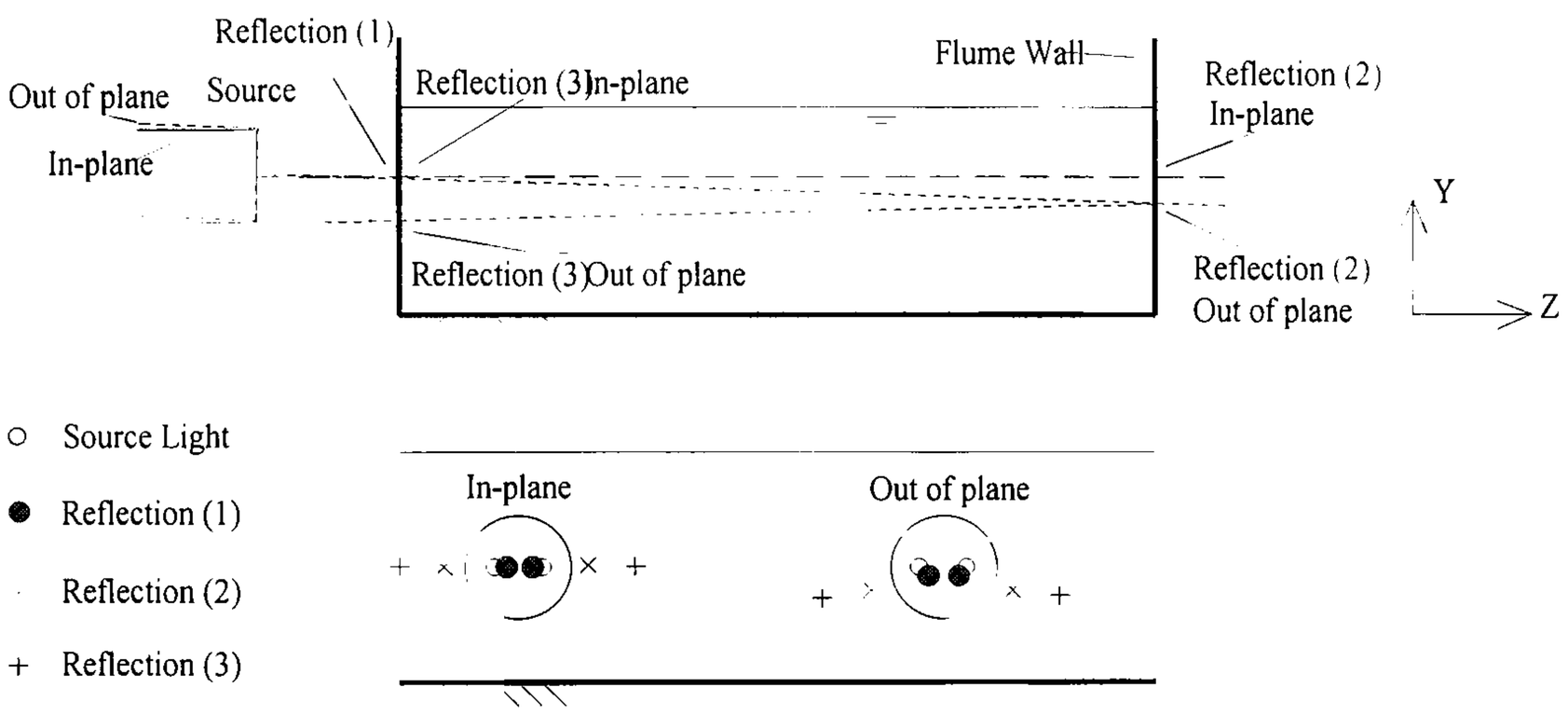

Figure 4.17 - Schematic Representation of Probe Horizontal Alignment

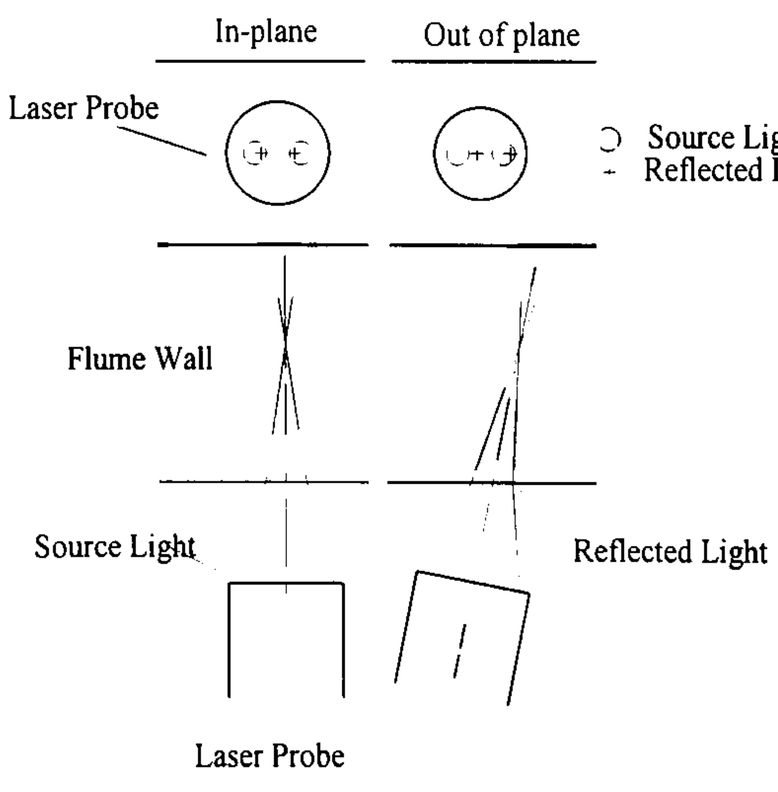

Figure 4.18 - Series A: Mean Velocity and Turbulence Intensity Distribution - Case 1

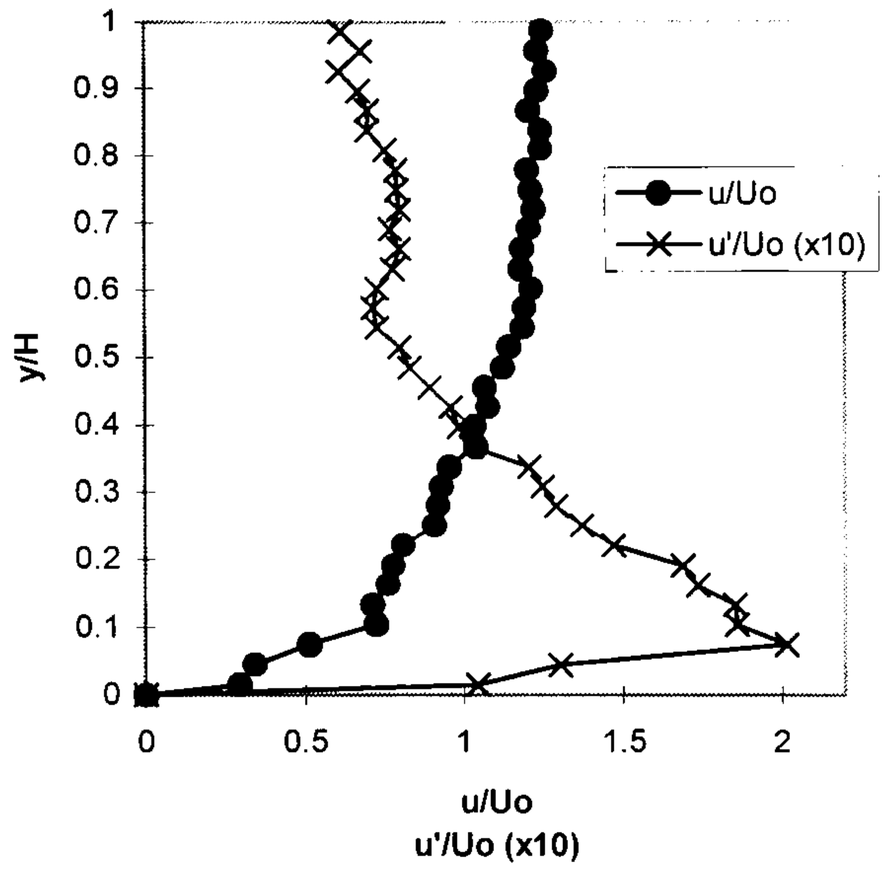

Figure 4.19 - Series A: Mean Velocity and Turbulence Intensity Distribution - Case 2

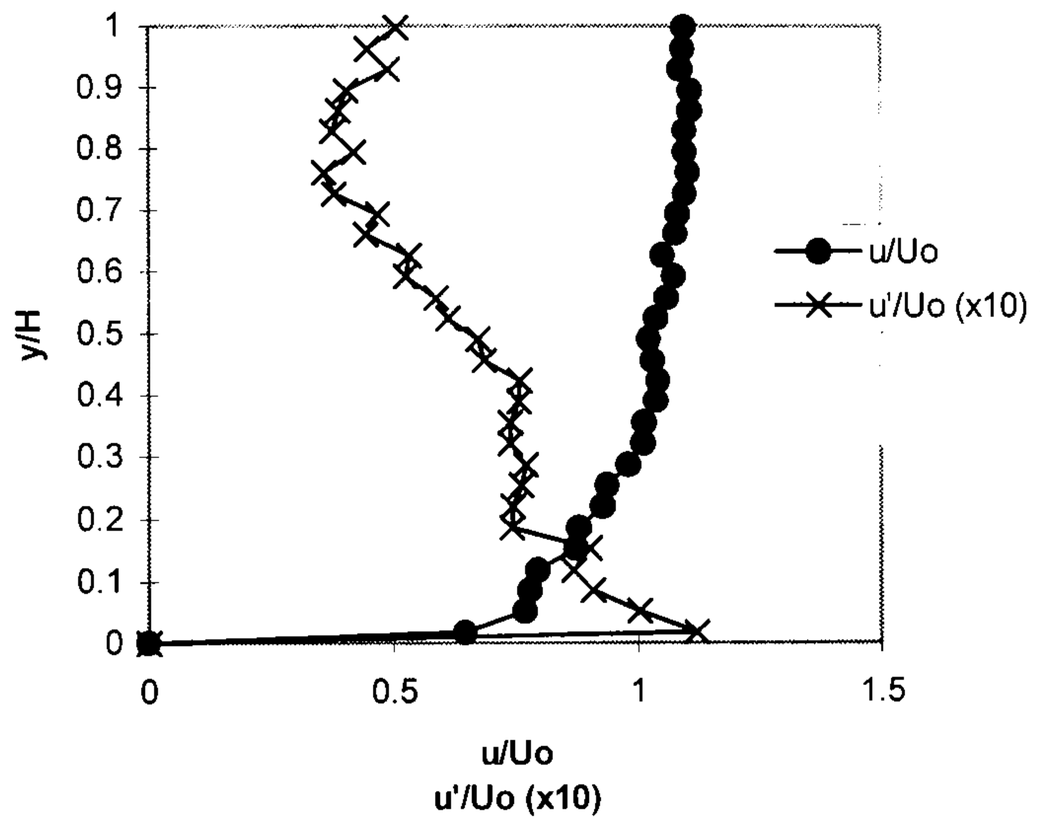

Figure 4.20 - Series A: Mean Velocity and Turbulence Intensity Distribution - Case 3

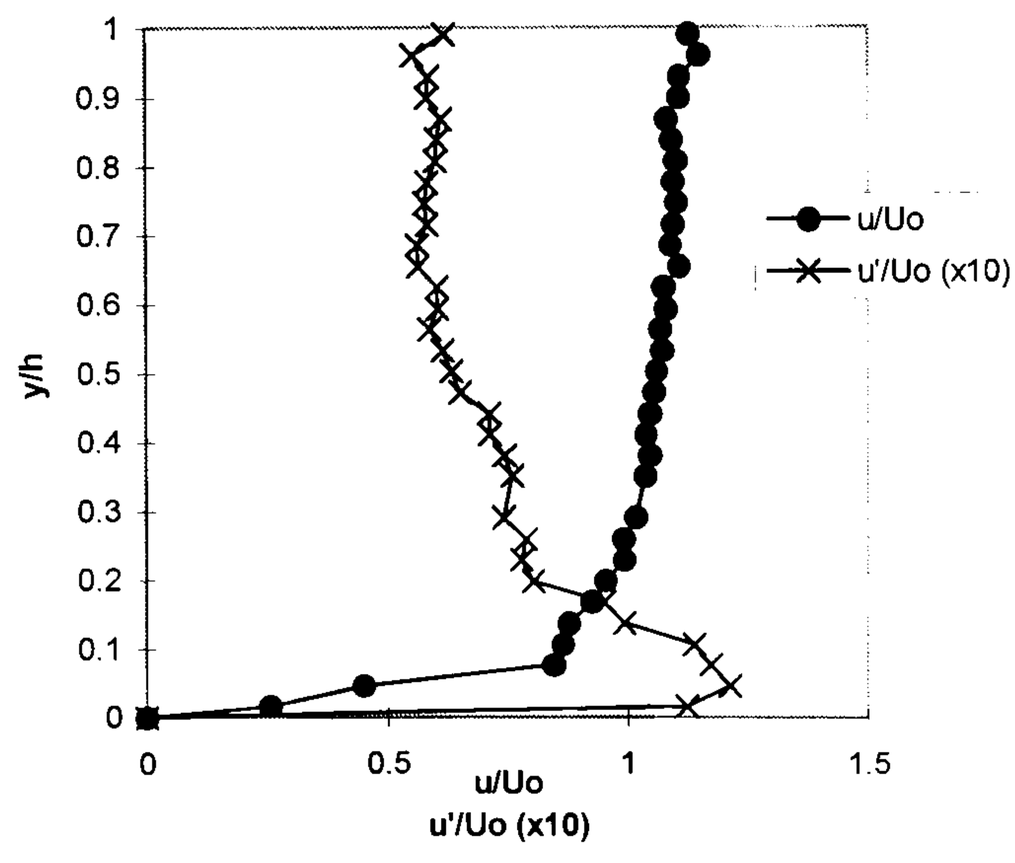

Figure 4.21 - Series A: Mean Velocity and Turbulence Intensity Distribution - Case 4

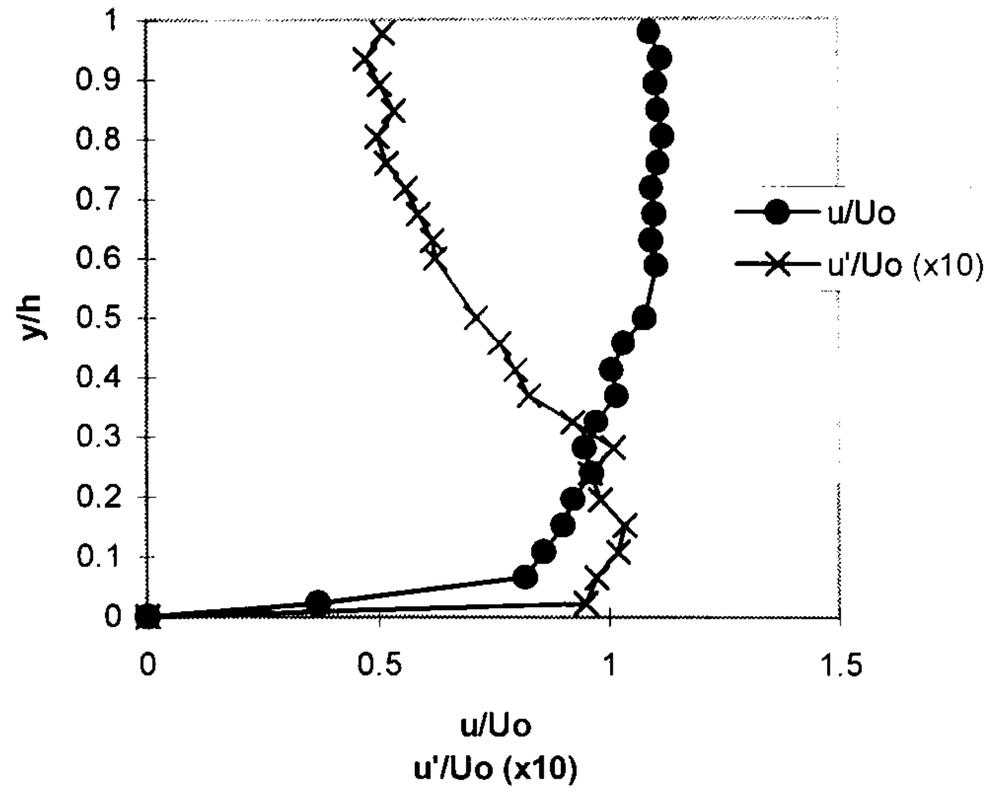

Figure 4.22 - Series A: Mean Velocity and Turbulence Intensity Distribution - Case 5

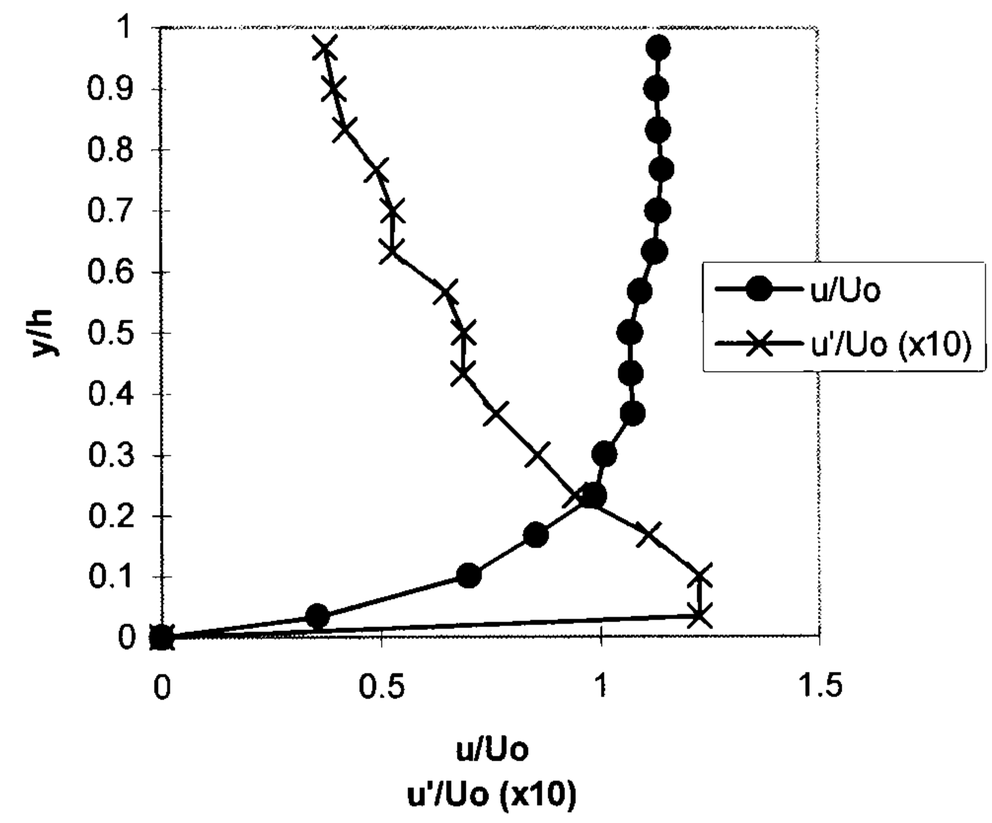

Figure 4.23 - Series A: Mean Velocity and Turbulence Intensity Distribution - Case 6

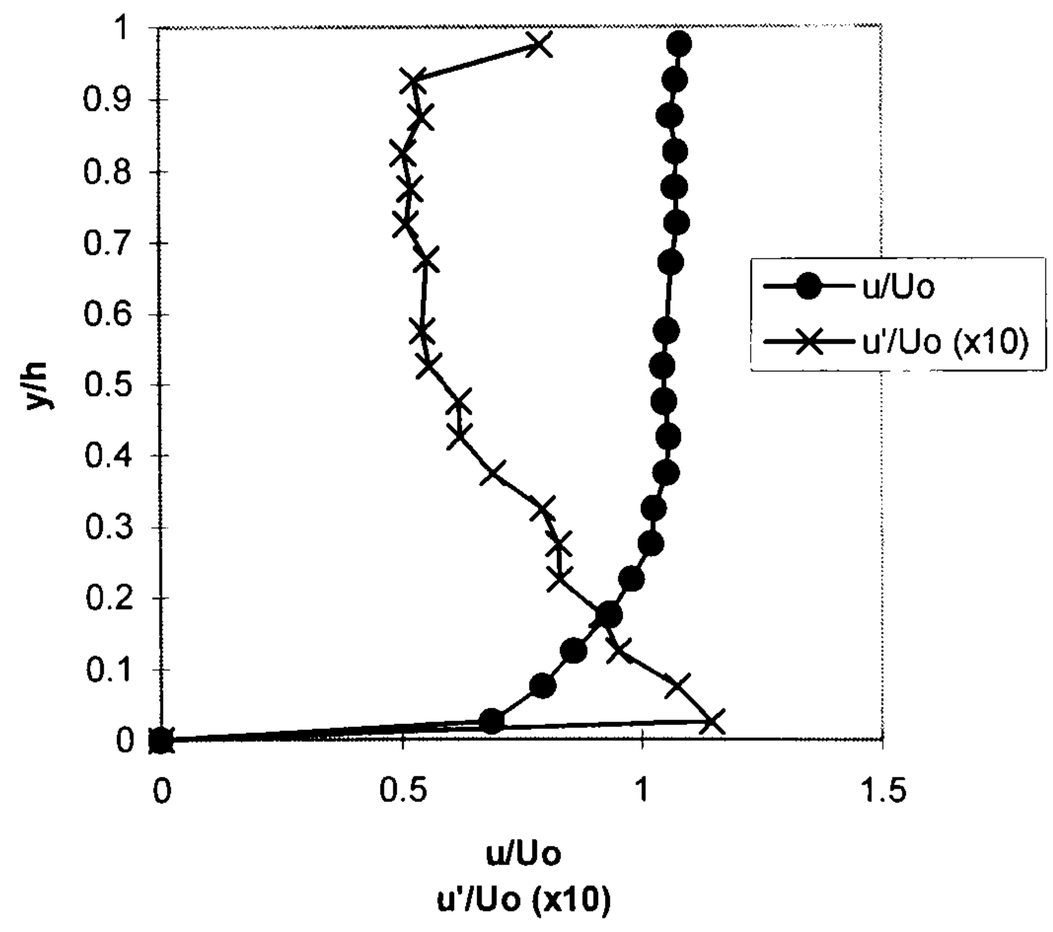

Figure 4.24 - Series A: Mean Velocity and Turbulence Intensity Distribution - Case 7

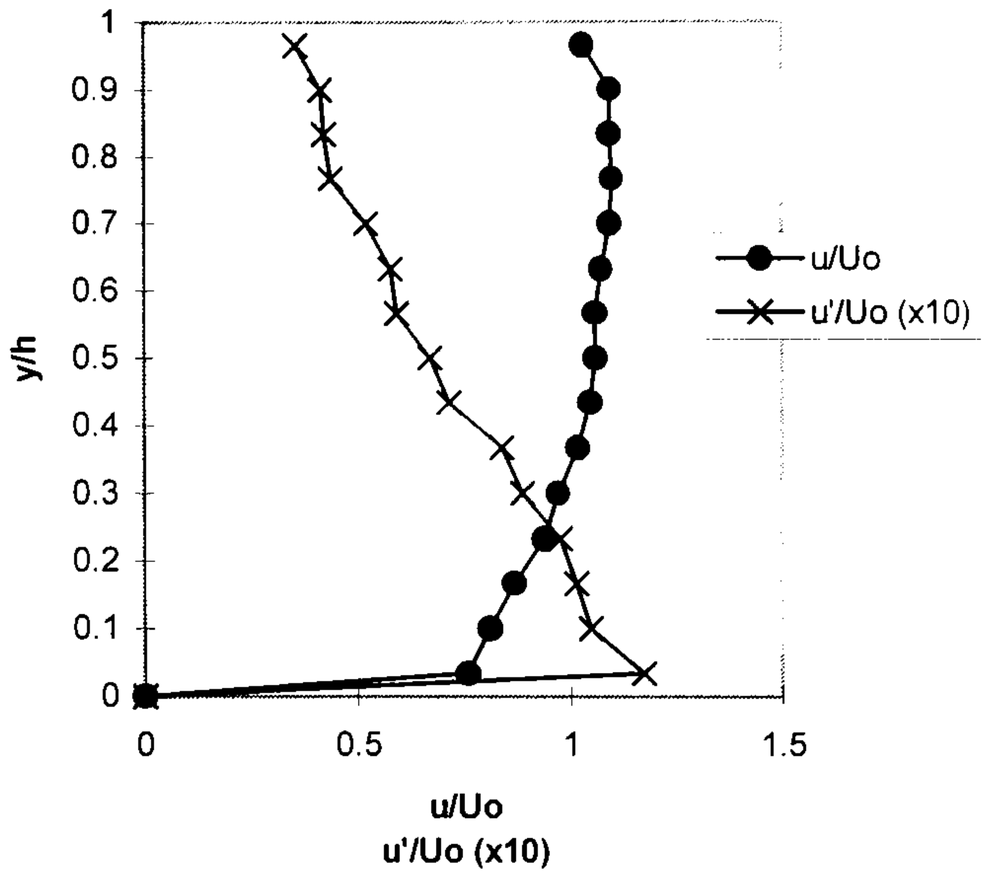

Figure 4.25 - Series A: Mean Velocity and Turbulence Intensity Distribution - Case 8

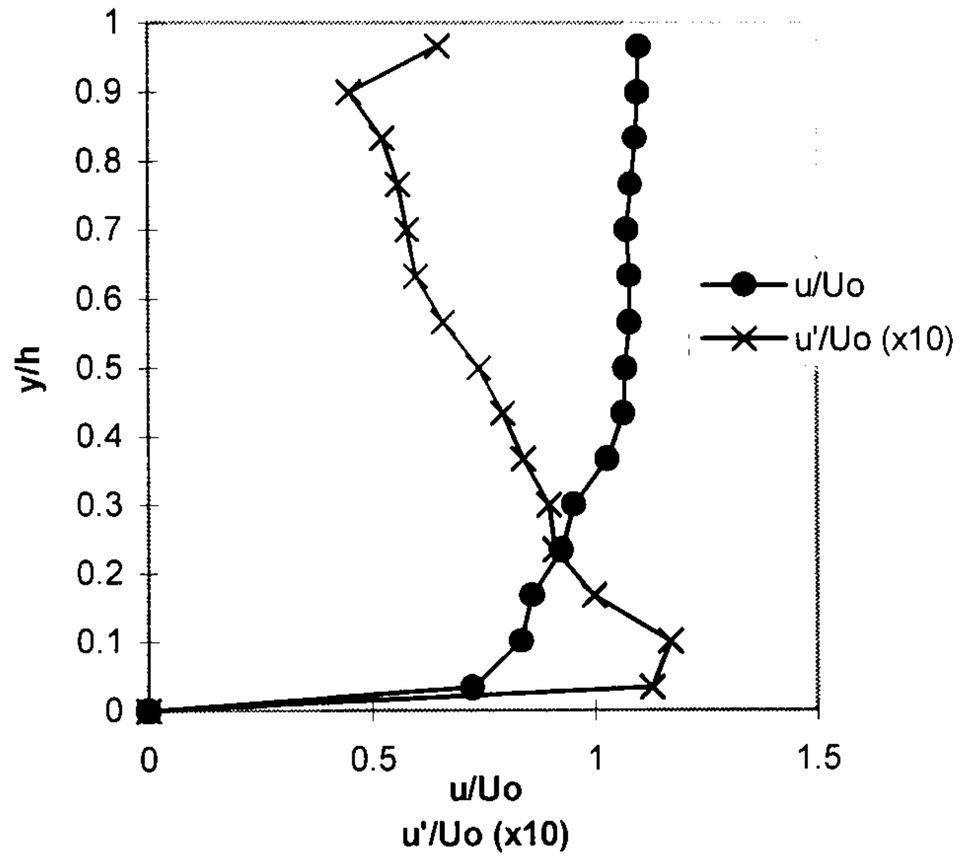

Figure 4.26 - Series A: Mean Velocity and Turbulence Intensity Distribution - Case 9

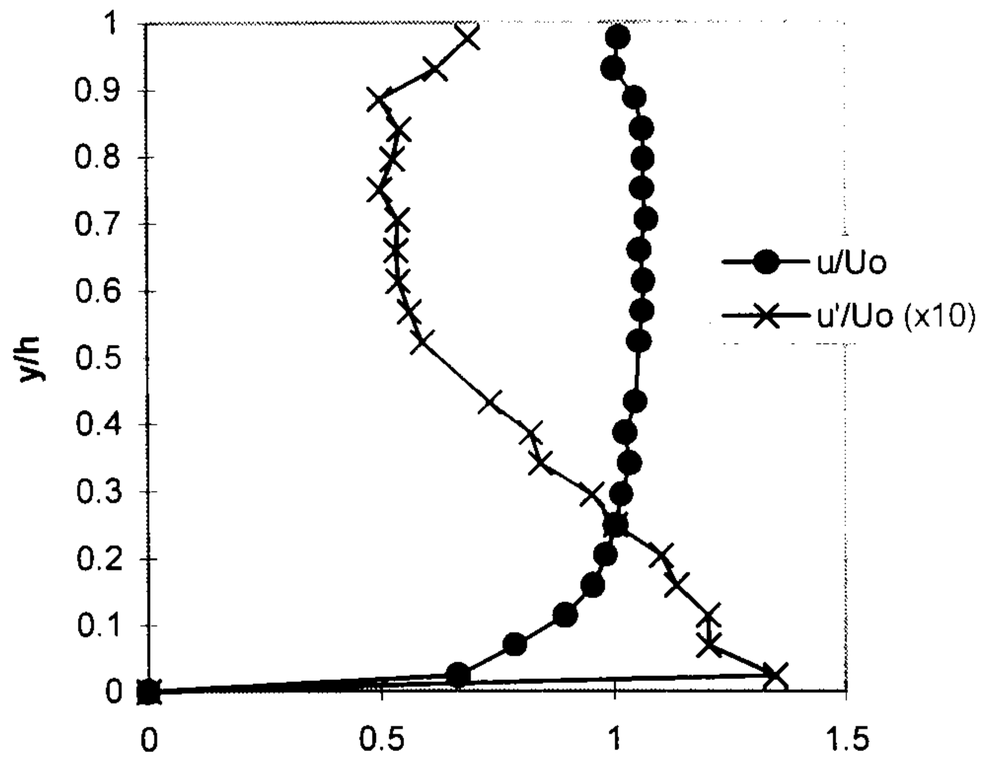

Figure 4.27 - Series A: Boundary Layer Velocity Profile Case 1

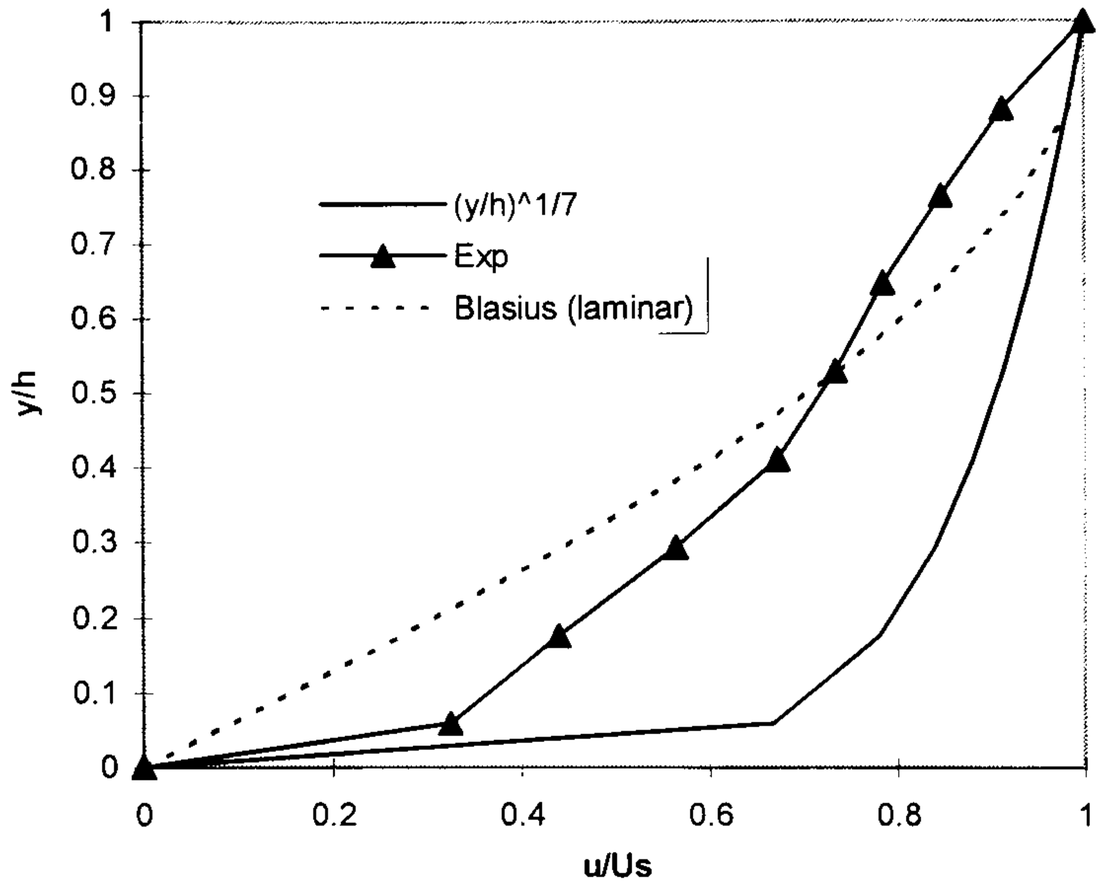

Figure 4.28 - Series A: Boundary Layer Velocity Profile Case 2

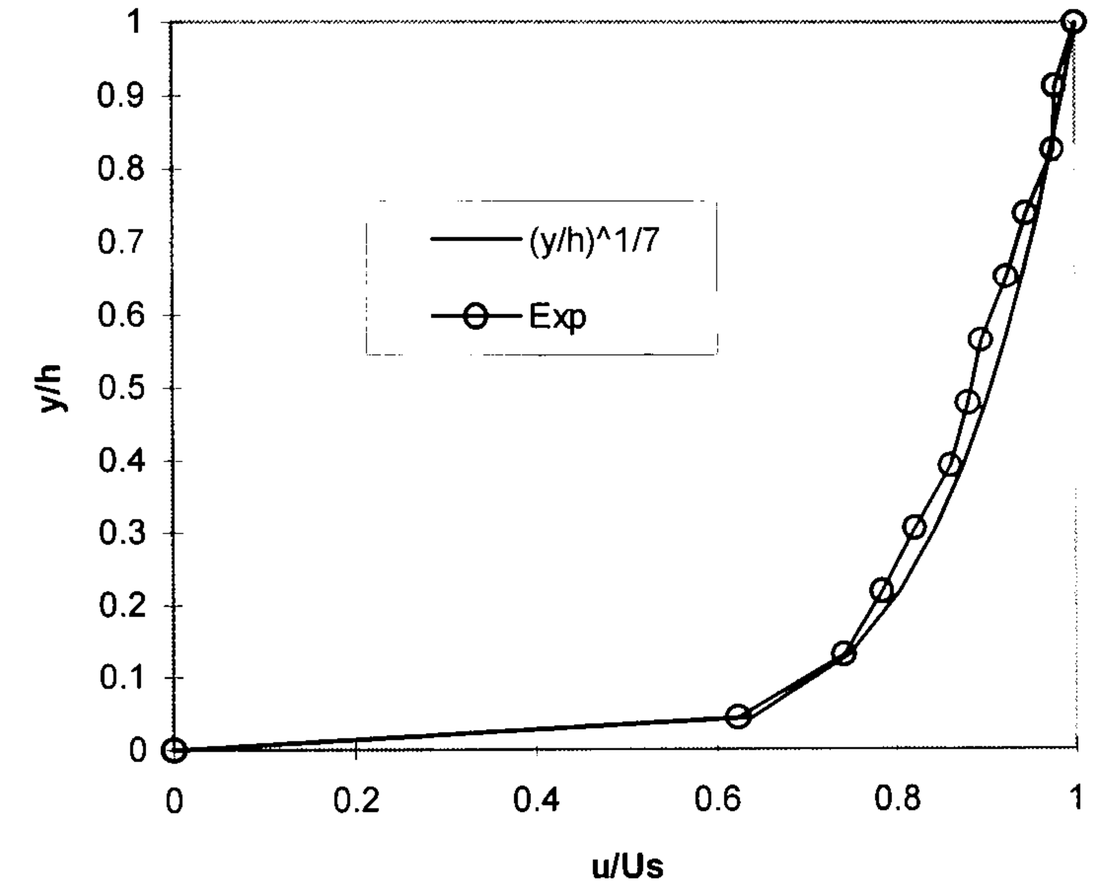

Figure 4.29 - Series A: Boundary Layer Velocity Profile Case 3

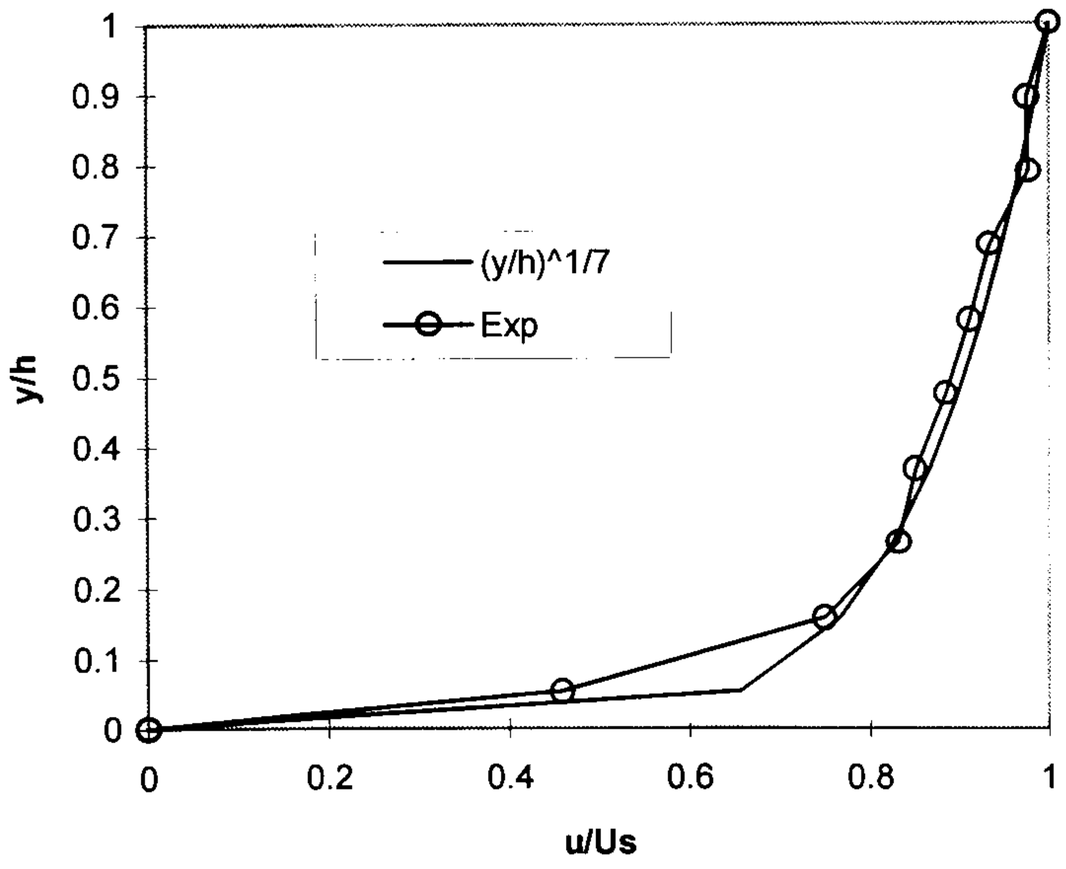

Figure 4.30 - Series A: Boundary Layer Velocity Profile Case 4

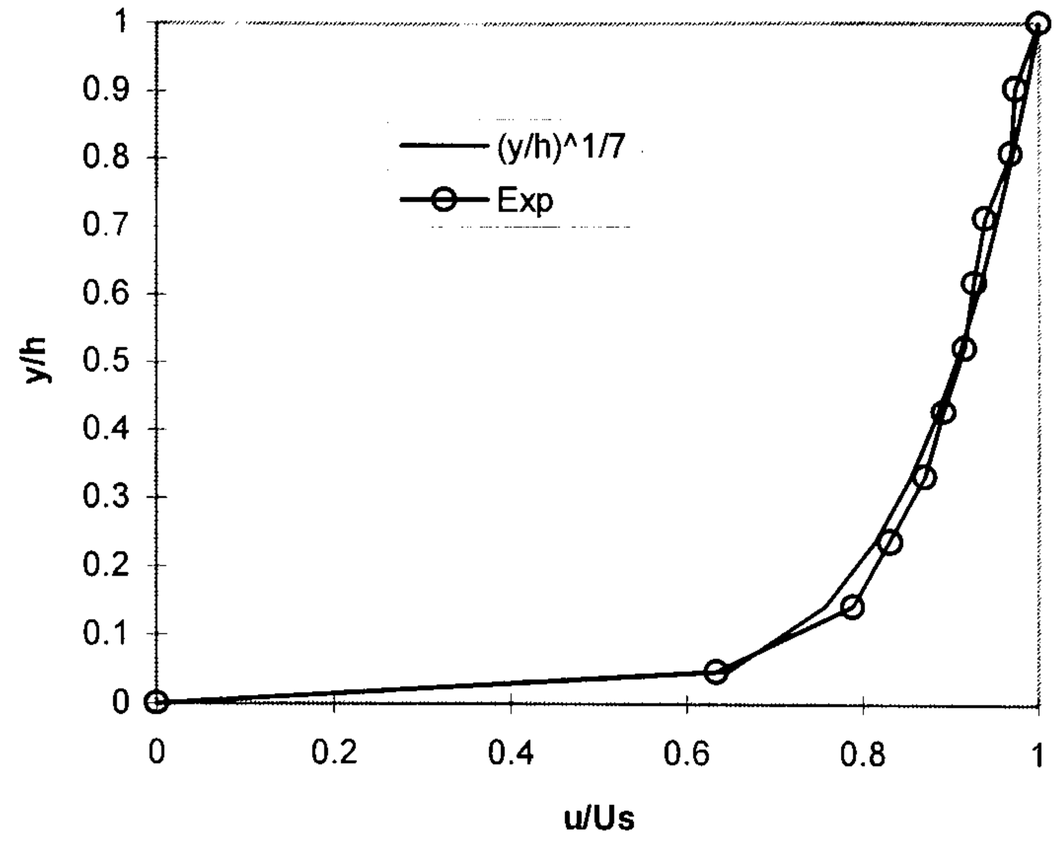

Figure 4.31 - Series A: Boundary Layer Velocity Profile Case 5

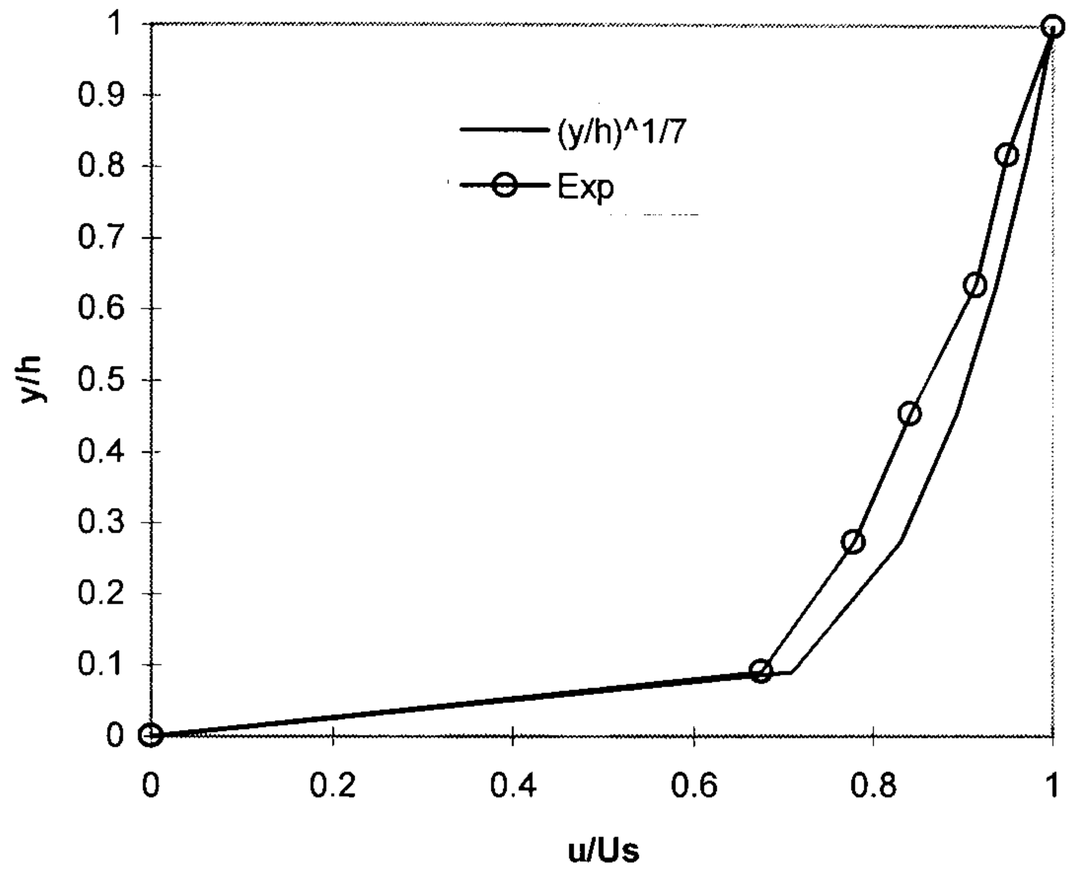

Figure 4.32 - Series A: Boundary Layer Velocity Profile Case 6

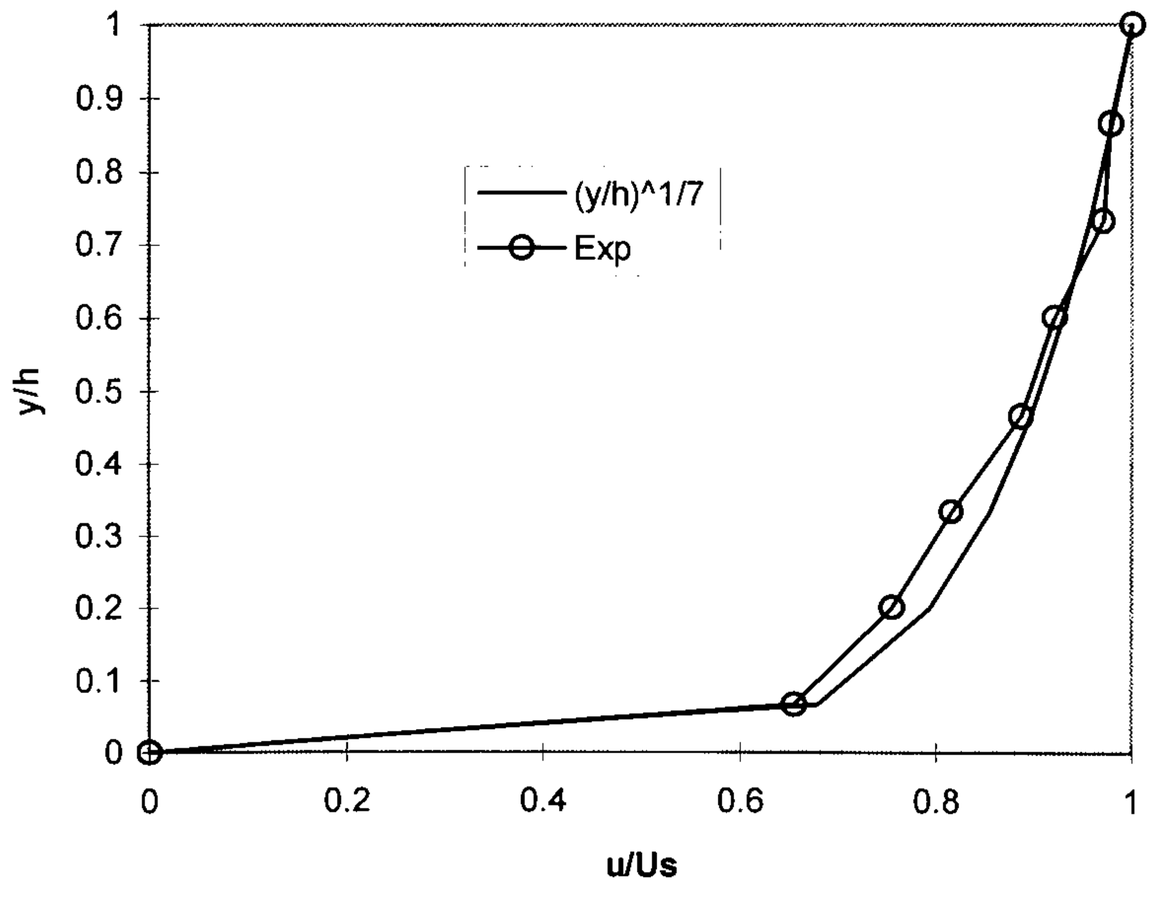

Figure 4.33 - Series A: Boundary Layer Velocity Profile Case 7

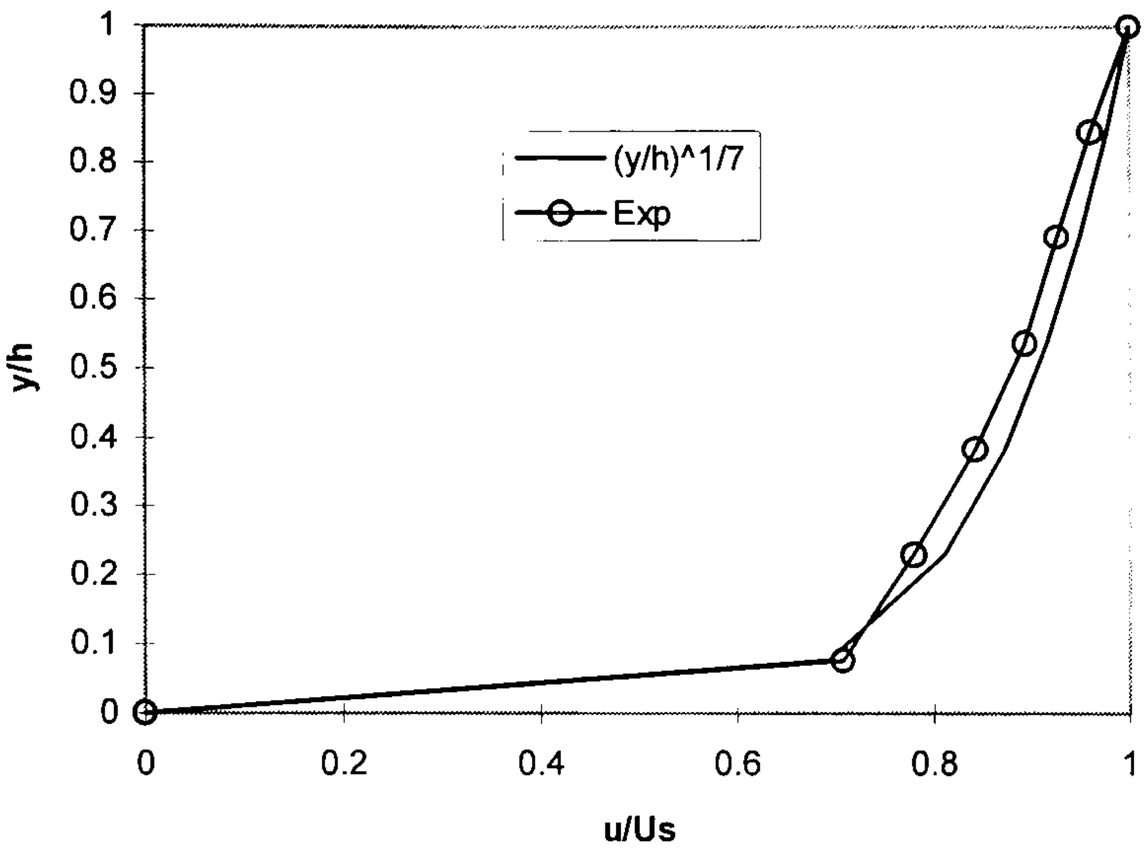

Figure 4.34 - Series A: Boundary Layer Velocity Profile Case 8

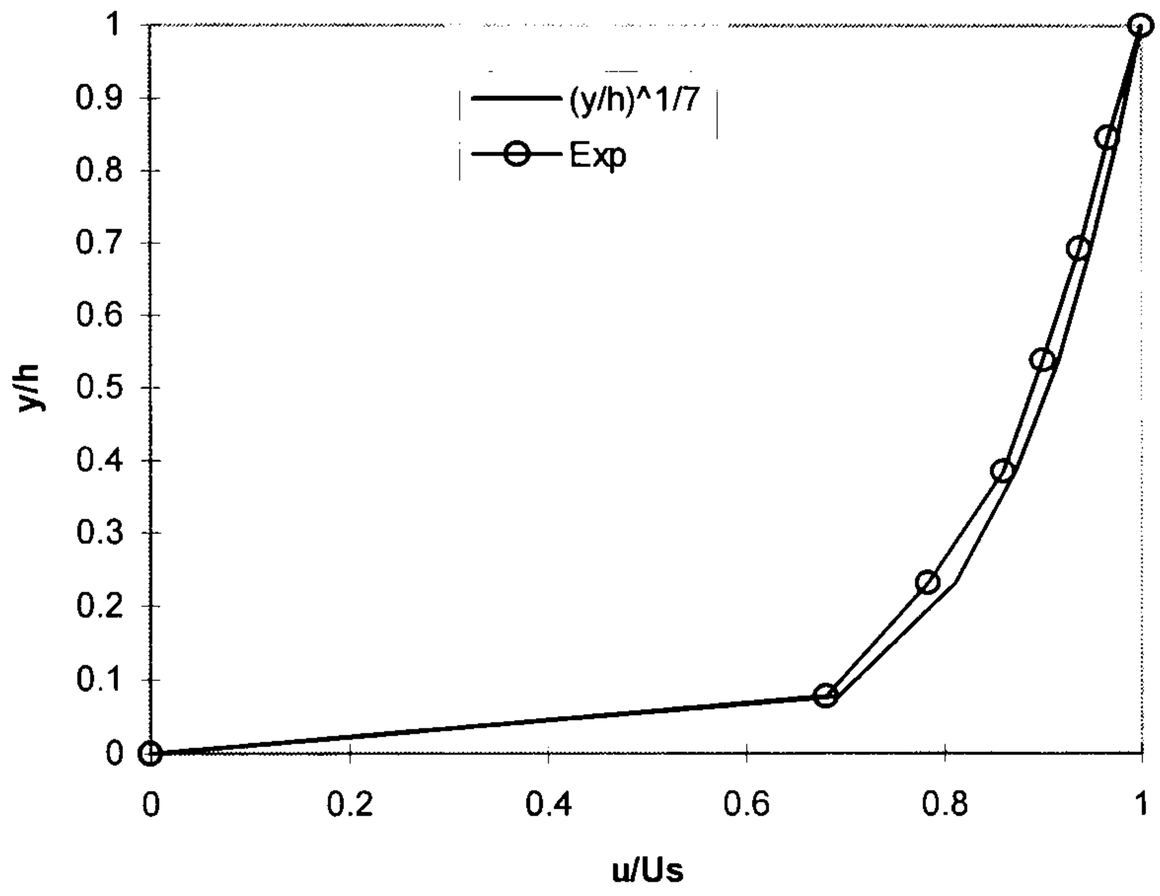

Figure 4.35 - Series A: Boundary Layer Velocity Profile Case 9

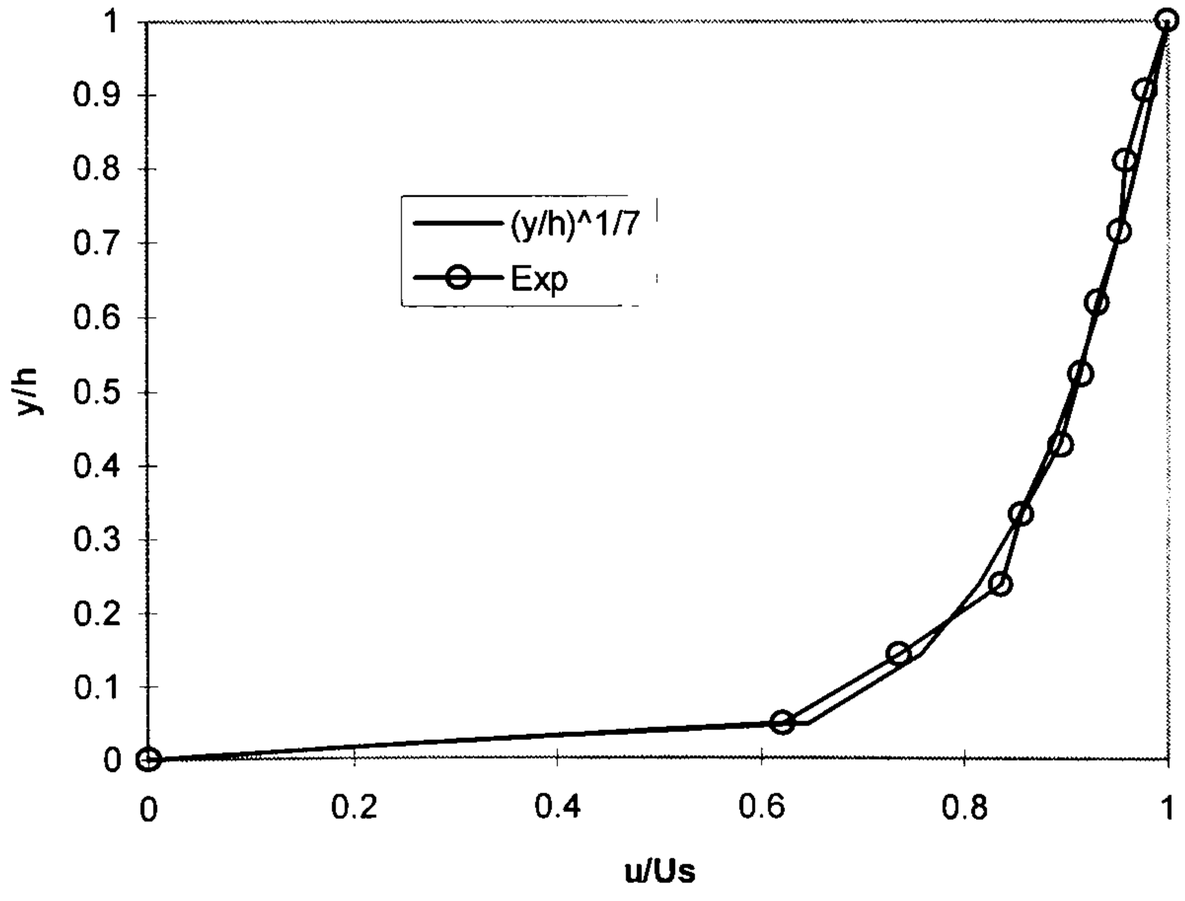

Figure 4.36 - Series A: Mean Log-Law Velocity Profile - Case 1

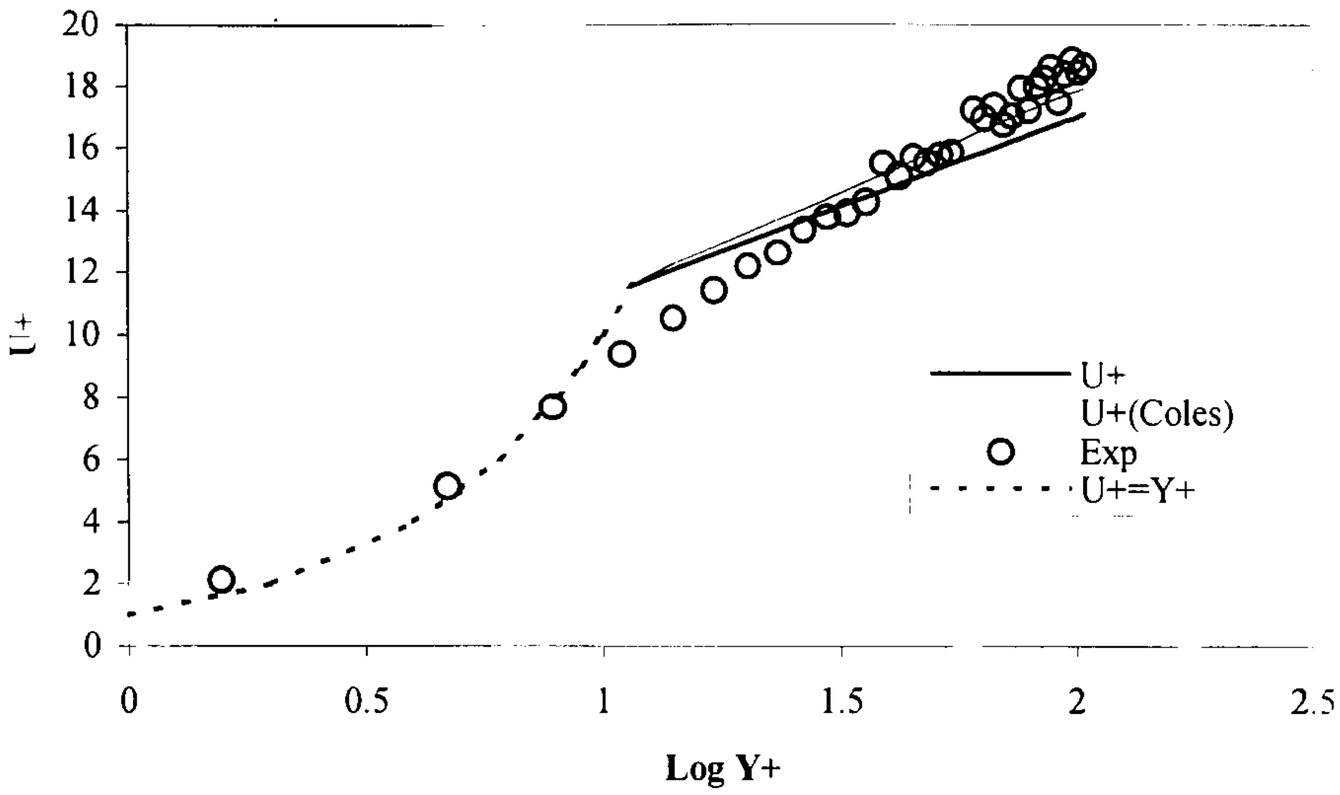

Figure 4.37 - Series A: Mean Log-Law Velocity Profile - Case 2

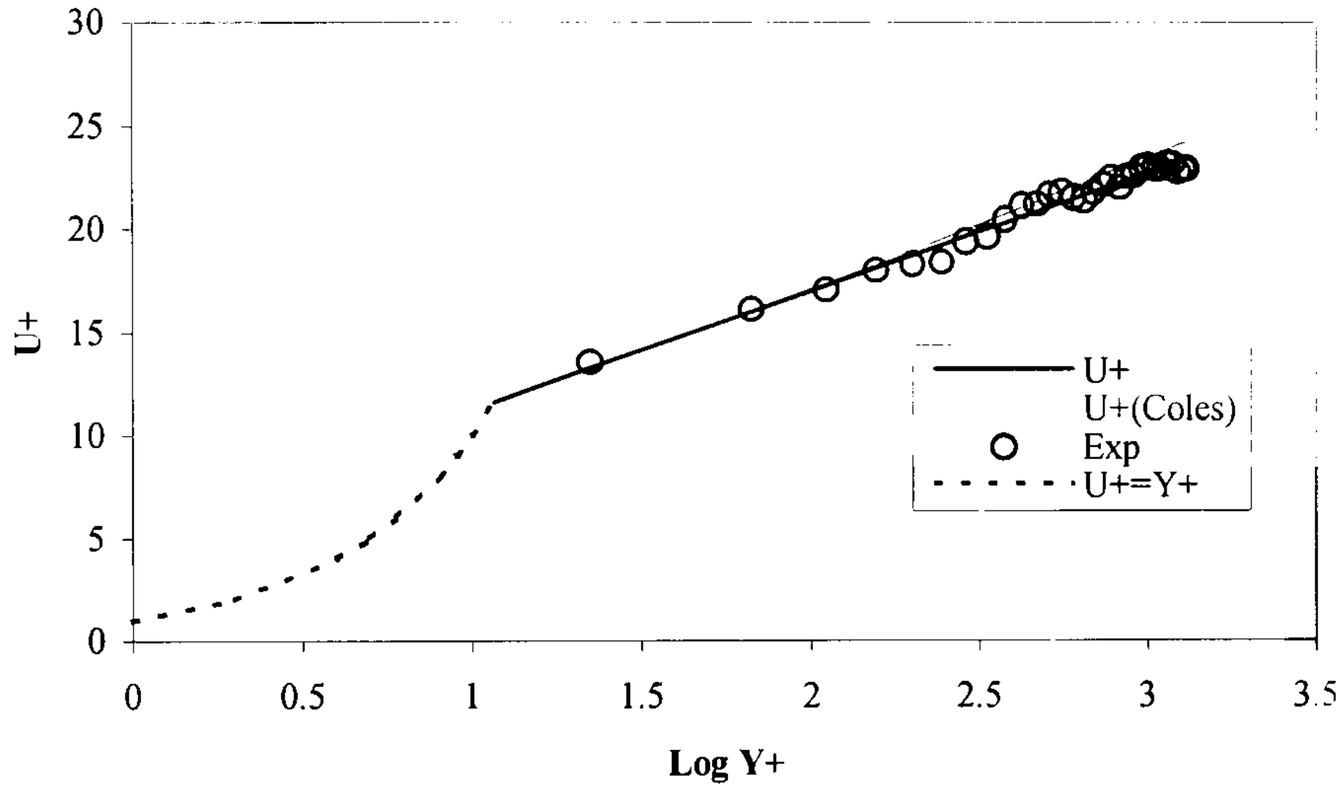

Figure 4.38 - Series A: Mean Log-Law Velocity Profile - Case 3

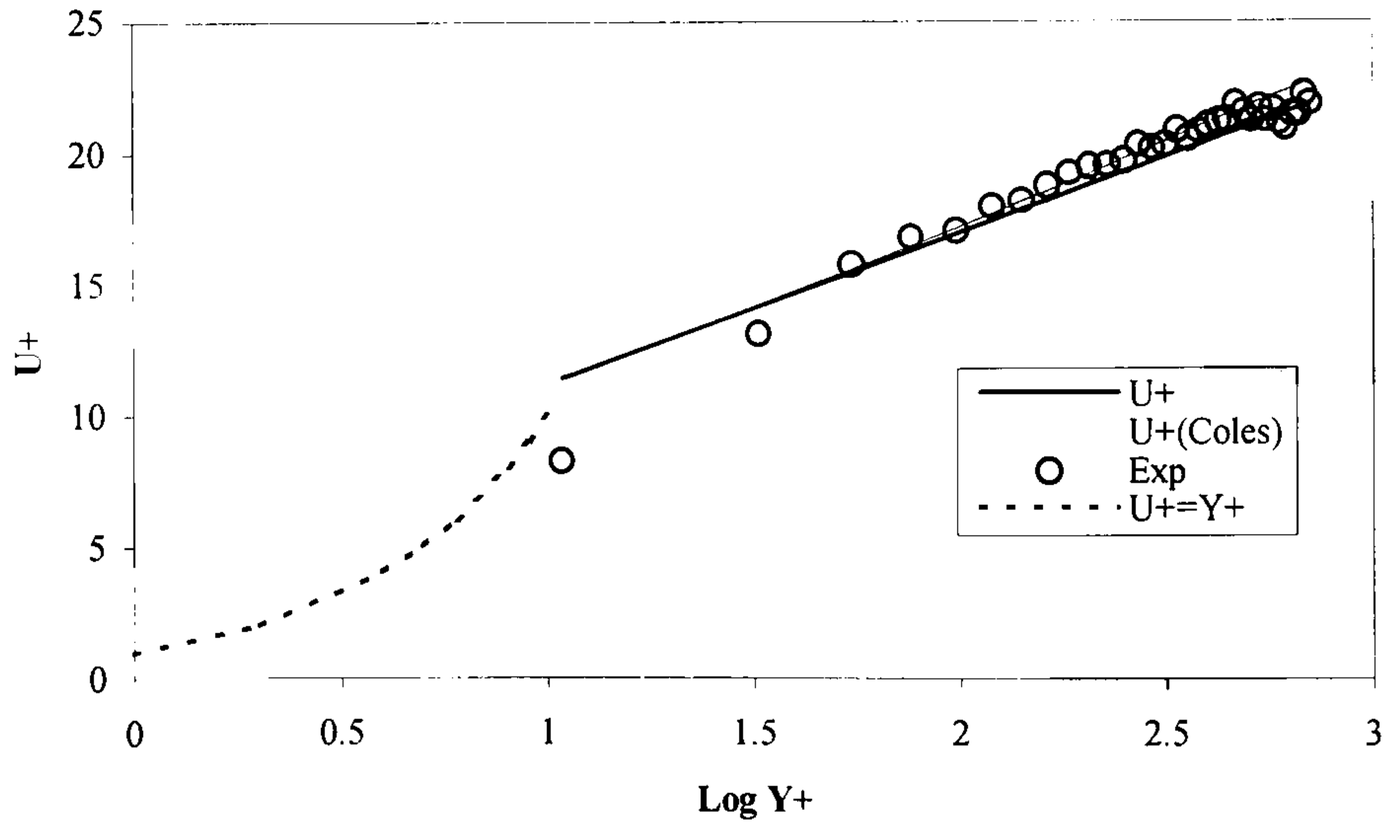

Figure 4.39 - Series A: Mean Log-Law Velocity Profile - Case 4

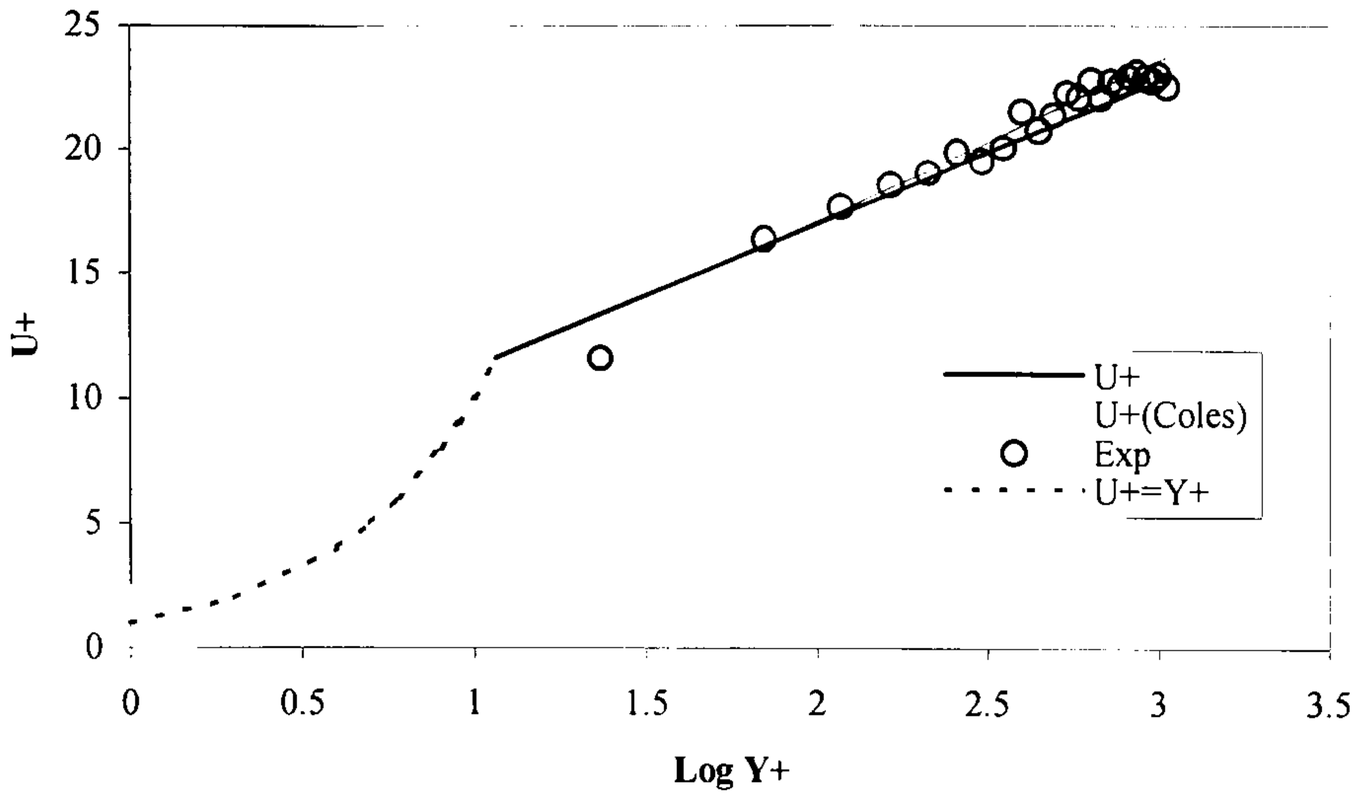

Figure 4.40 - Series A: Mean Log-Law Velocity Profile - Case 5

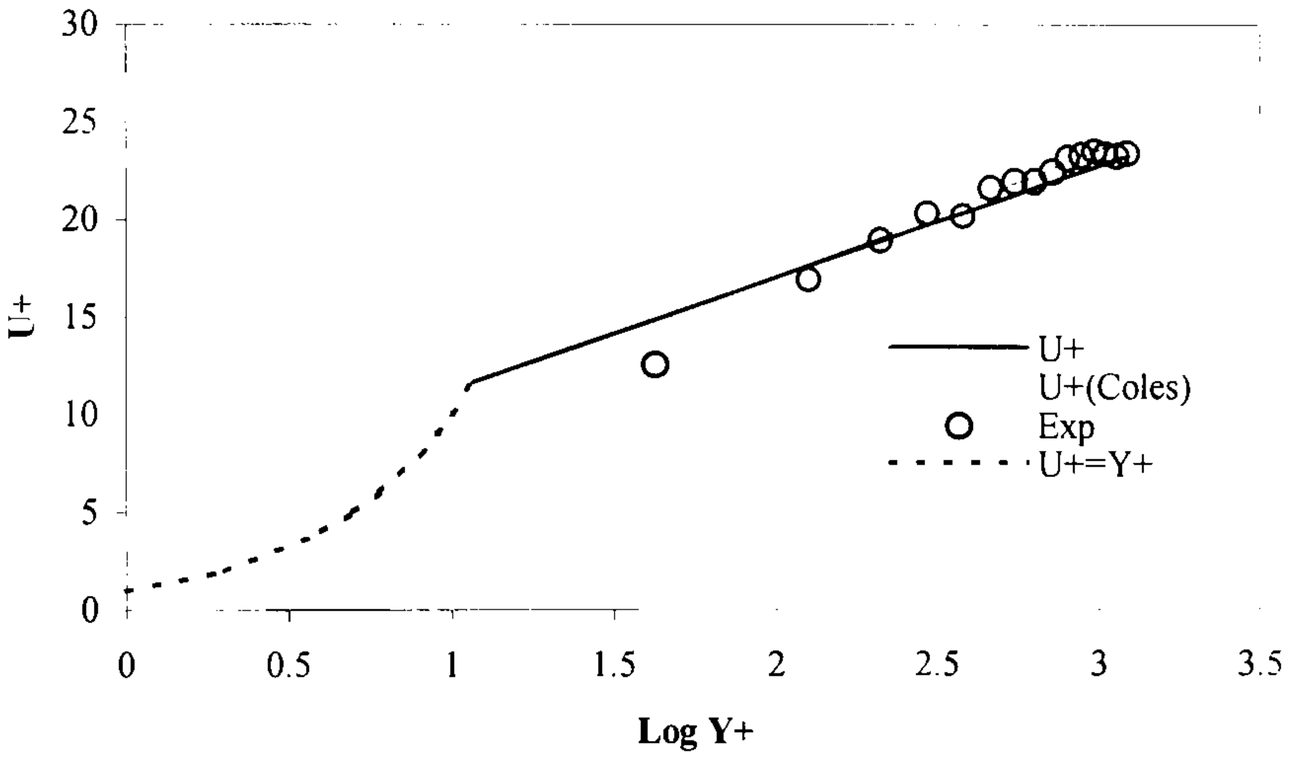

Figure 4.41 - Series A: Mean Log-Law Velocity Profile - Case 6

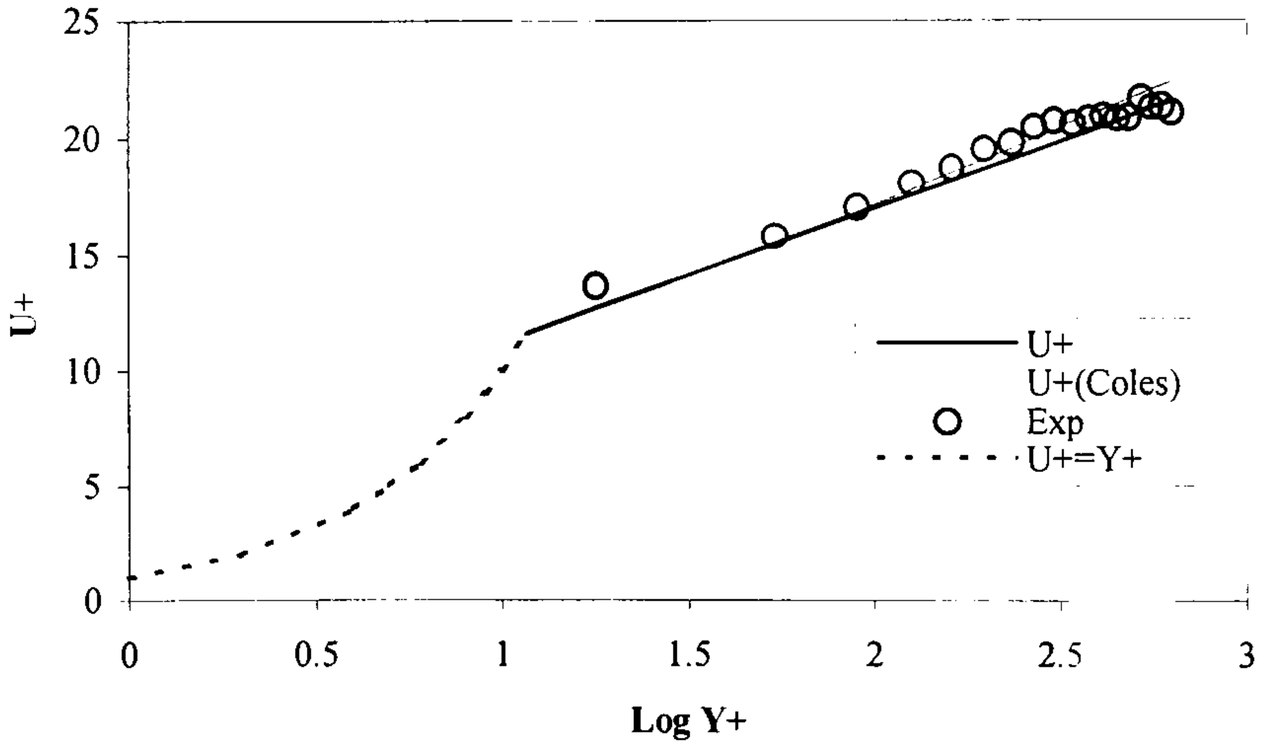

Figure 4.42 - Series A: Mean Log-Law Velocity Profile - Case 7

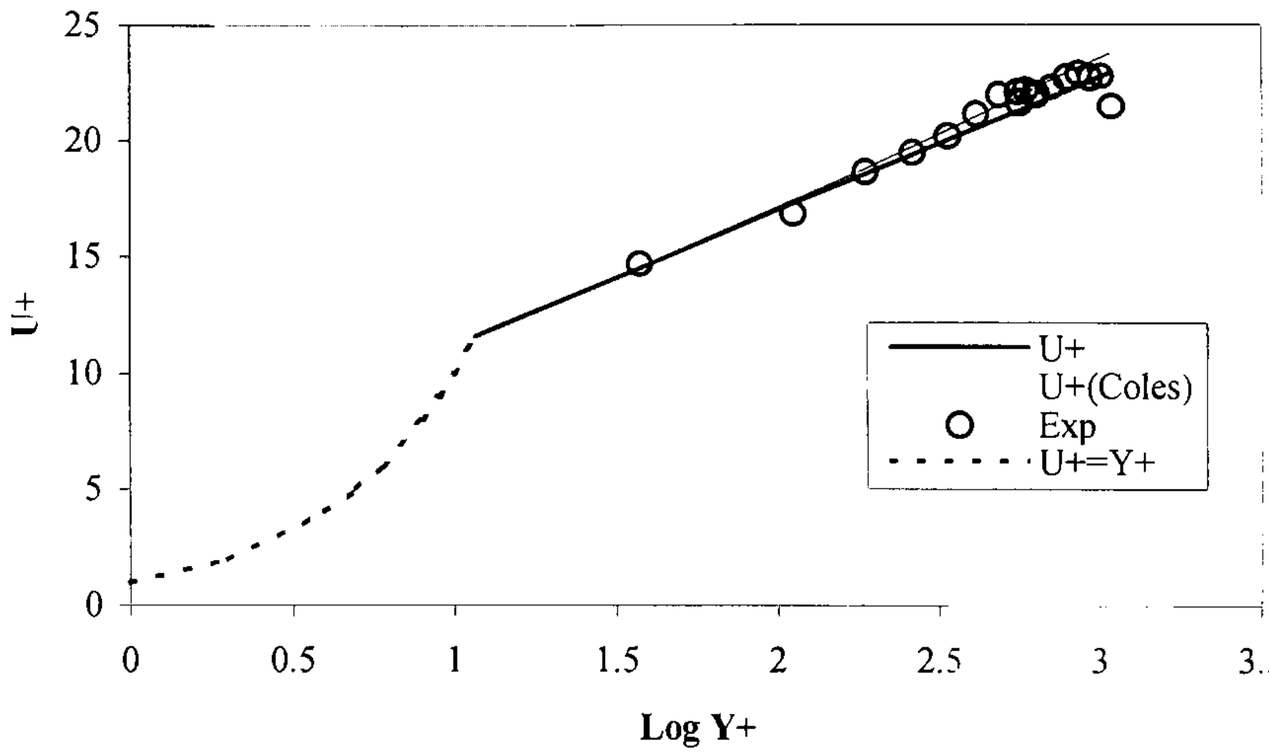

Figure 4.43 - Series A: Mean Log-Law Velocity Profile - Case 8

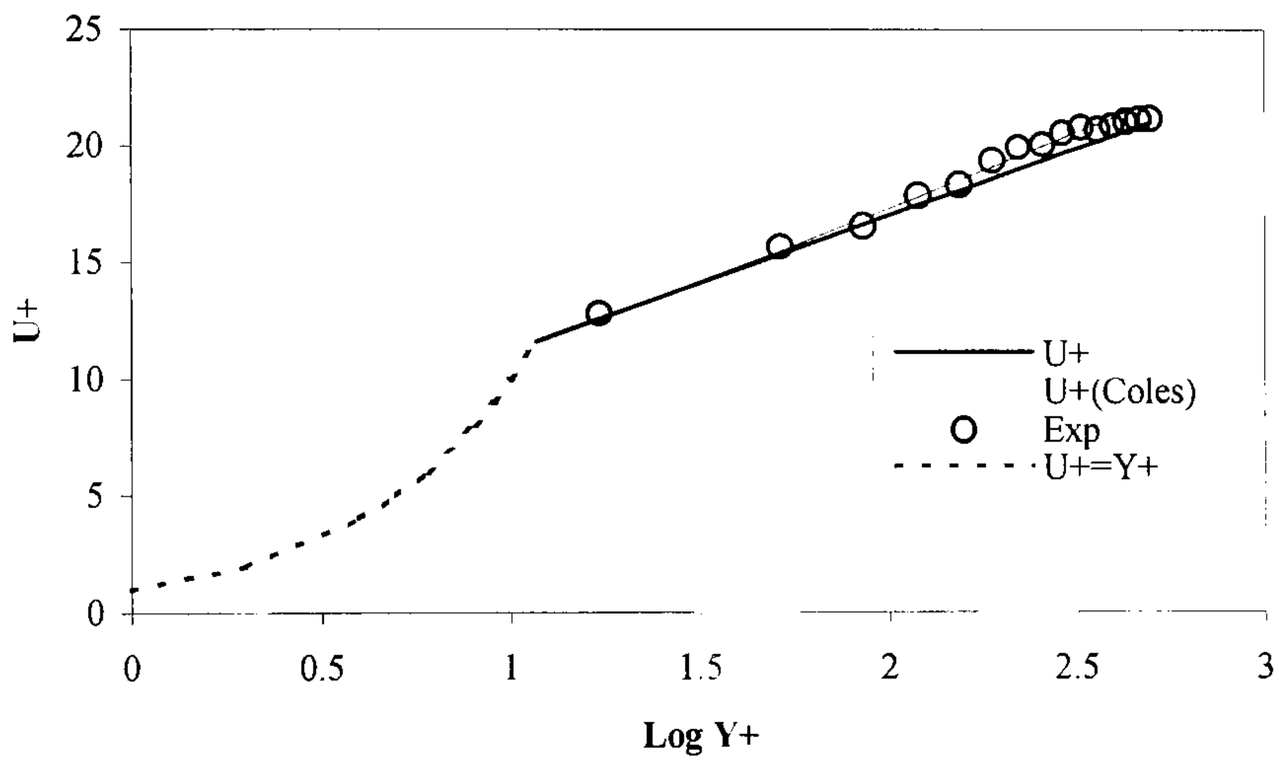

Figure 4.44 - Series A: Mean Log-Law Velocity Profile - Case 9

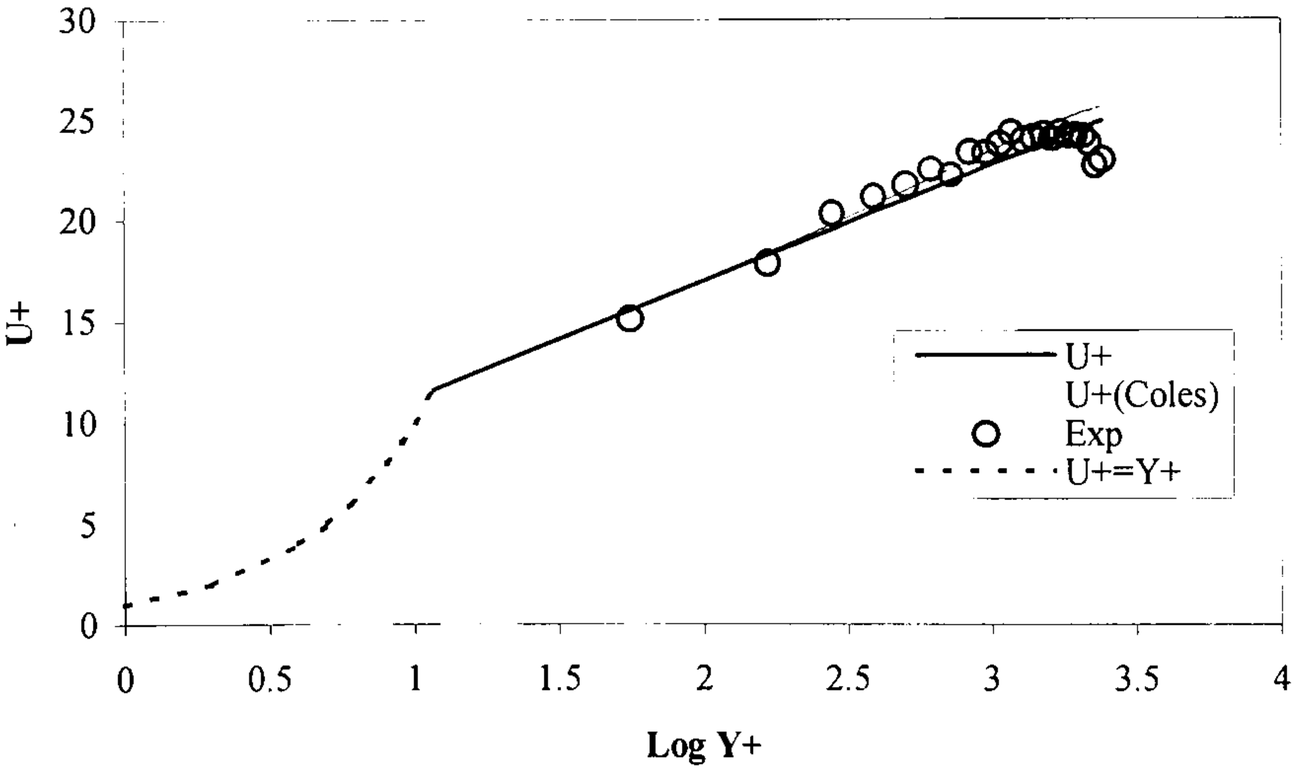

Figure 4.45 - Series A: Turbulence Intensity, u'/u* in Outer-Region: Cases 1-9

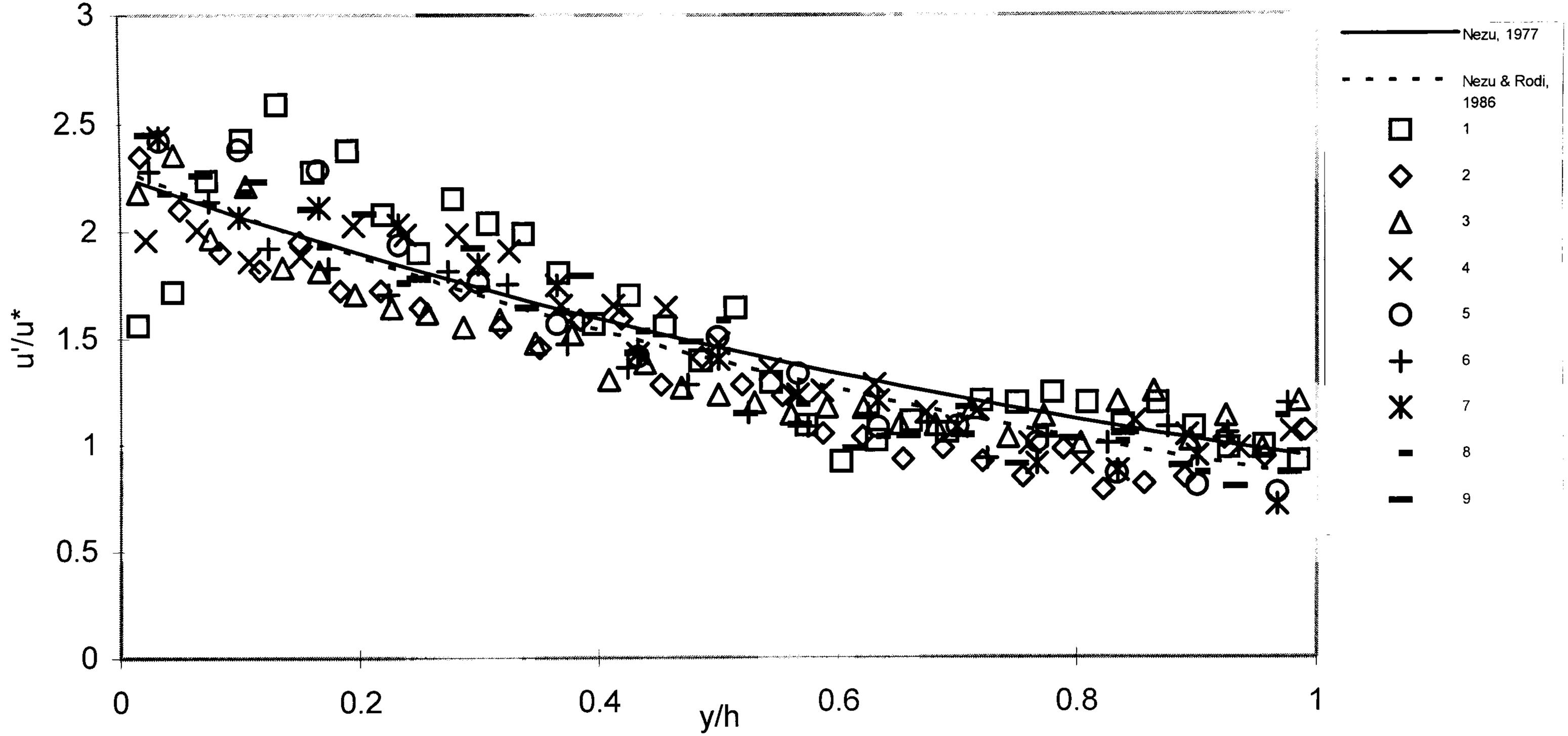

Figure 4.46 - Series A: Turbulence Intensity, u'/u*, in the Wall Region: Case 1

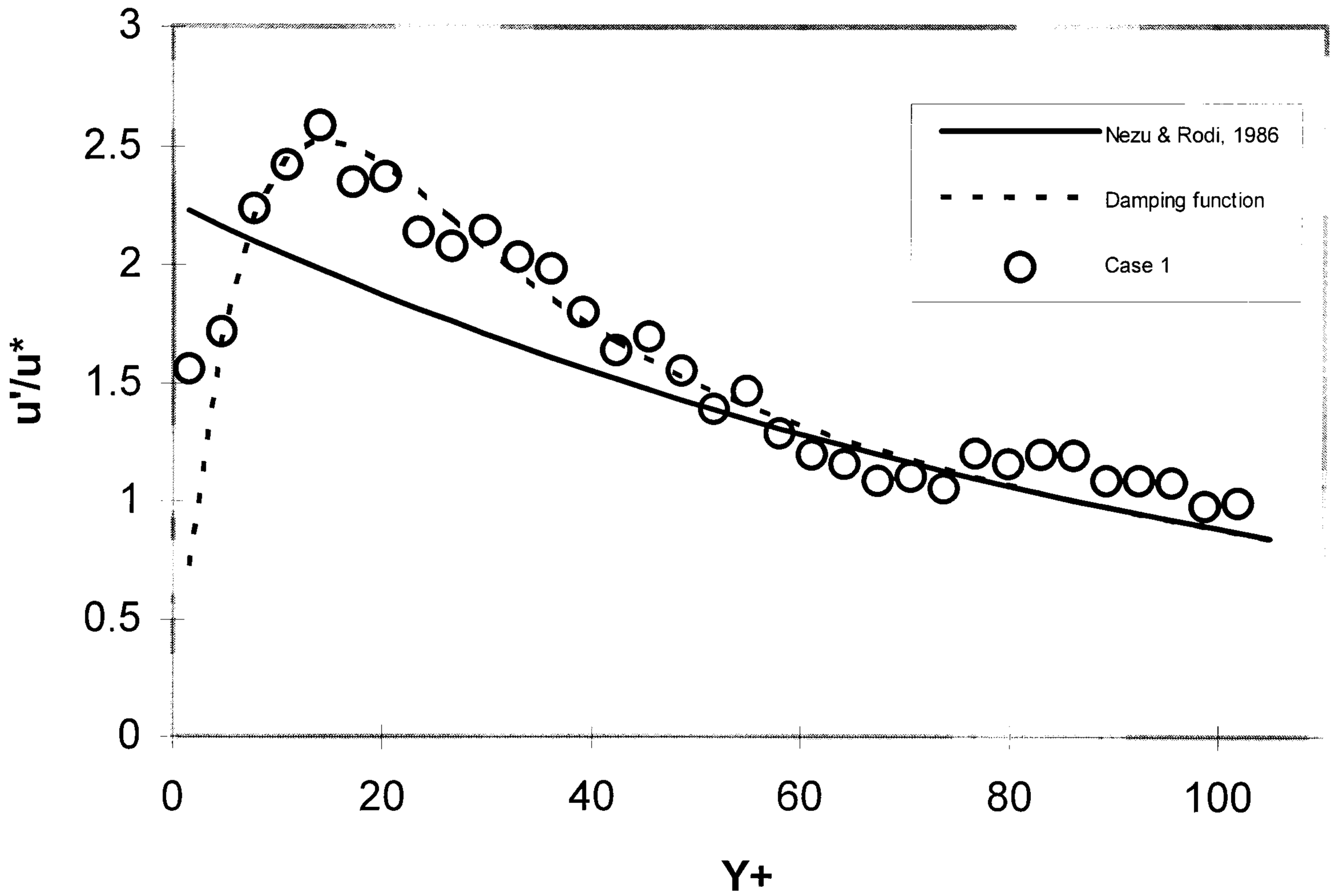

Figure 4.47 - Series B1: Mean Velocity Profiles and Turbulence Intensities

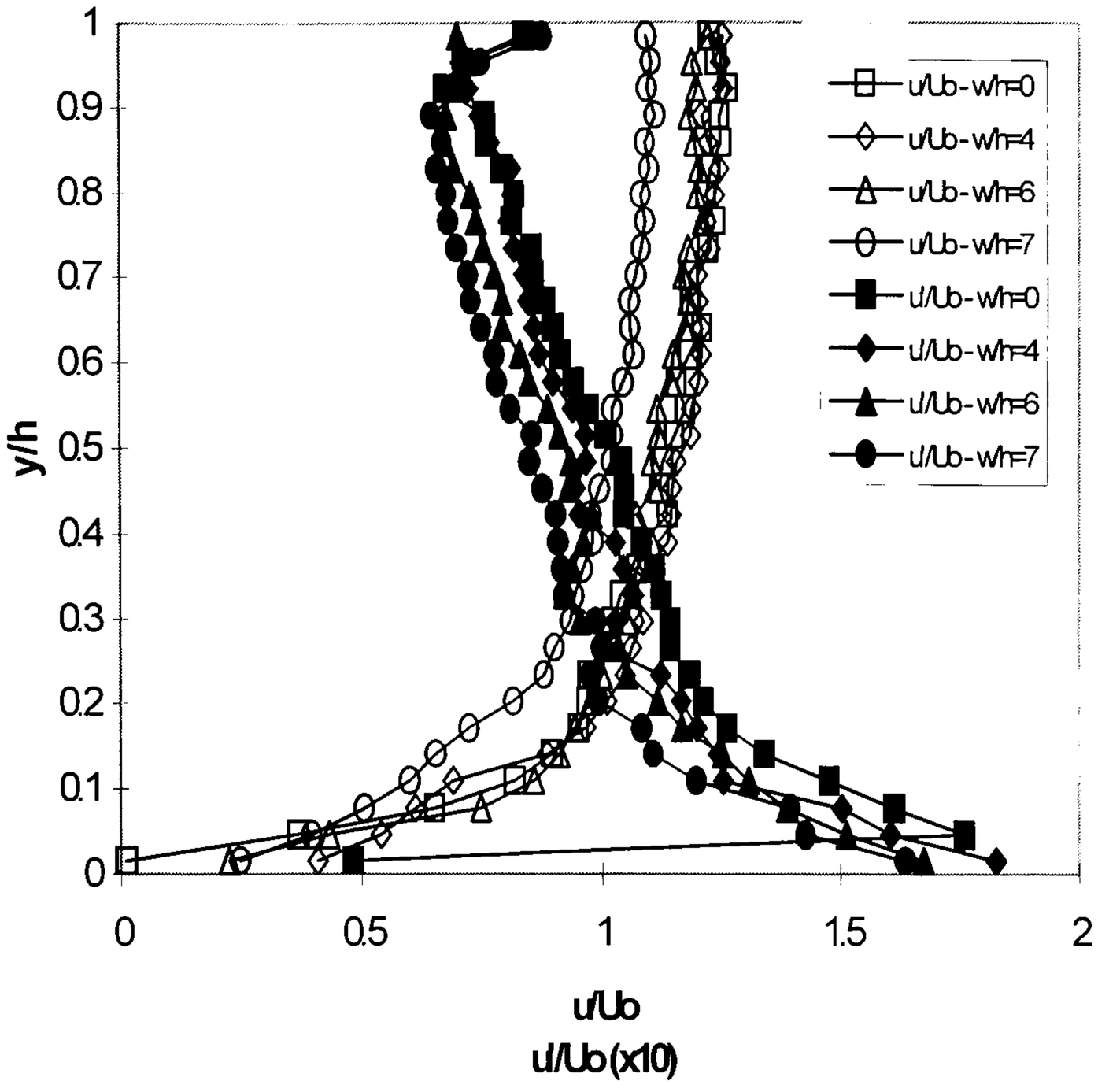

Figure 4.48 - Series B1: Boundary Layer Velocity Profiles

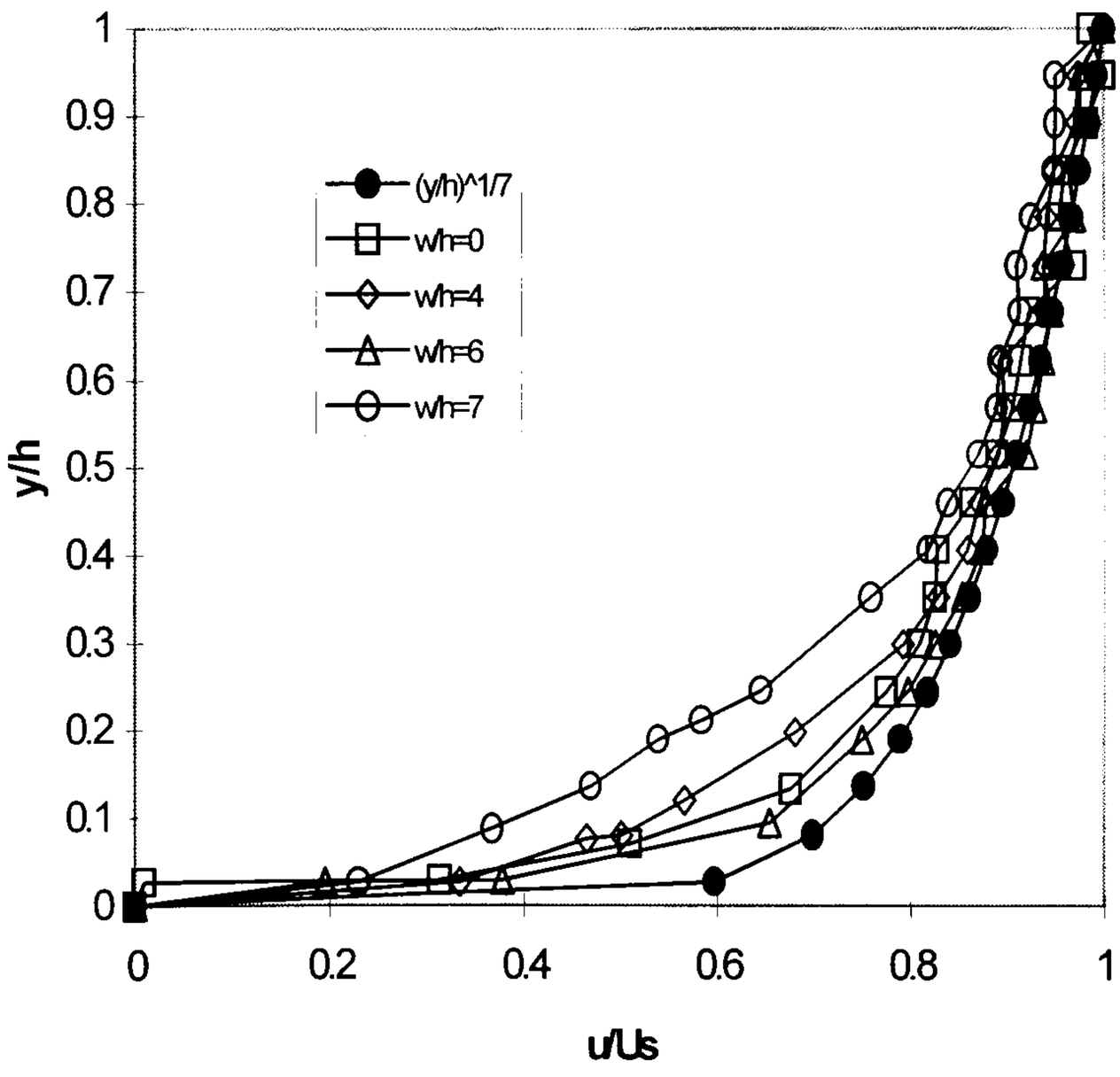

Figure 4.49 - Series B1: Mean Log-Law Velocity Profile

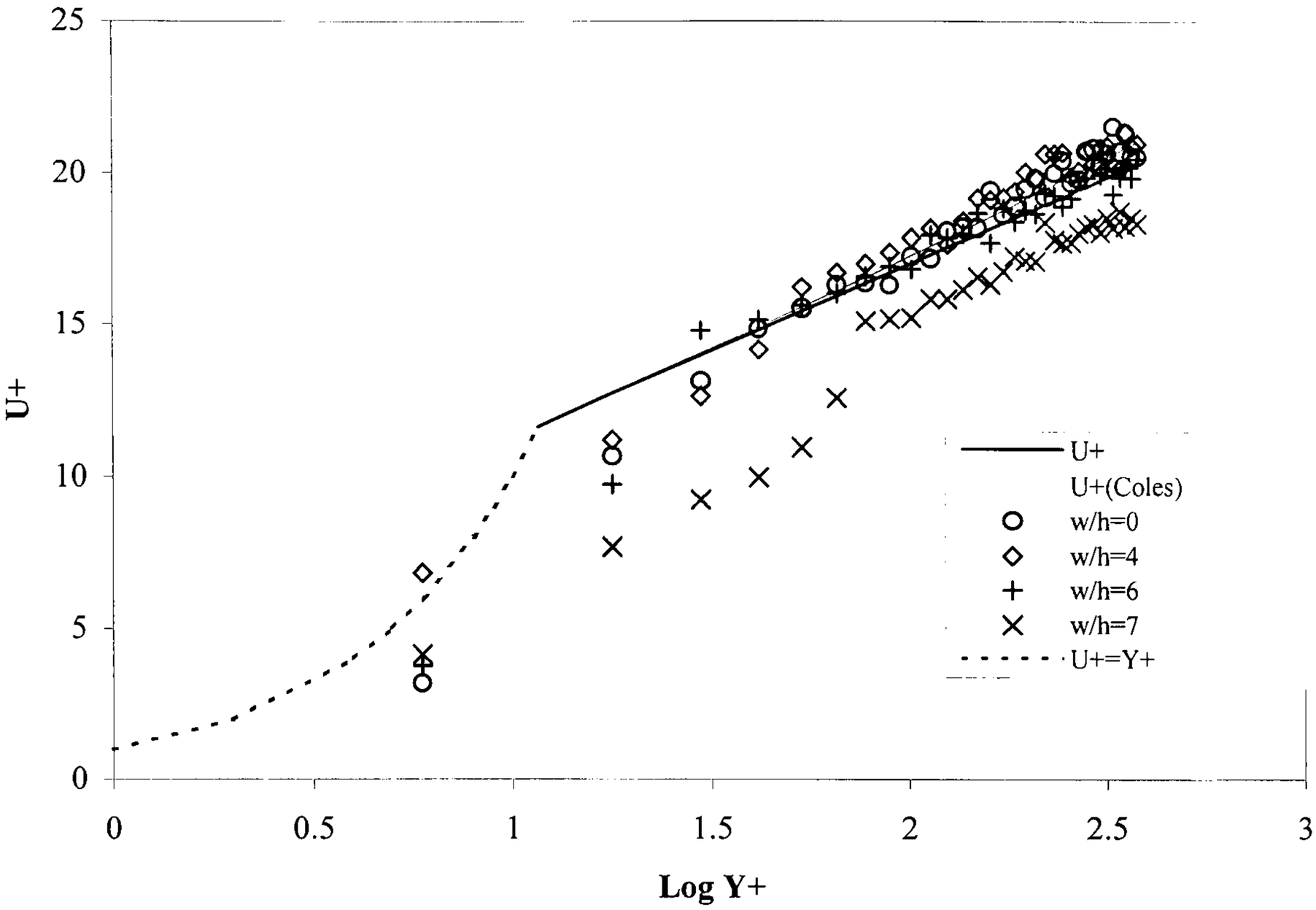

Figure 4.50 - Series B1: Turbulence Intensity, u'/u*

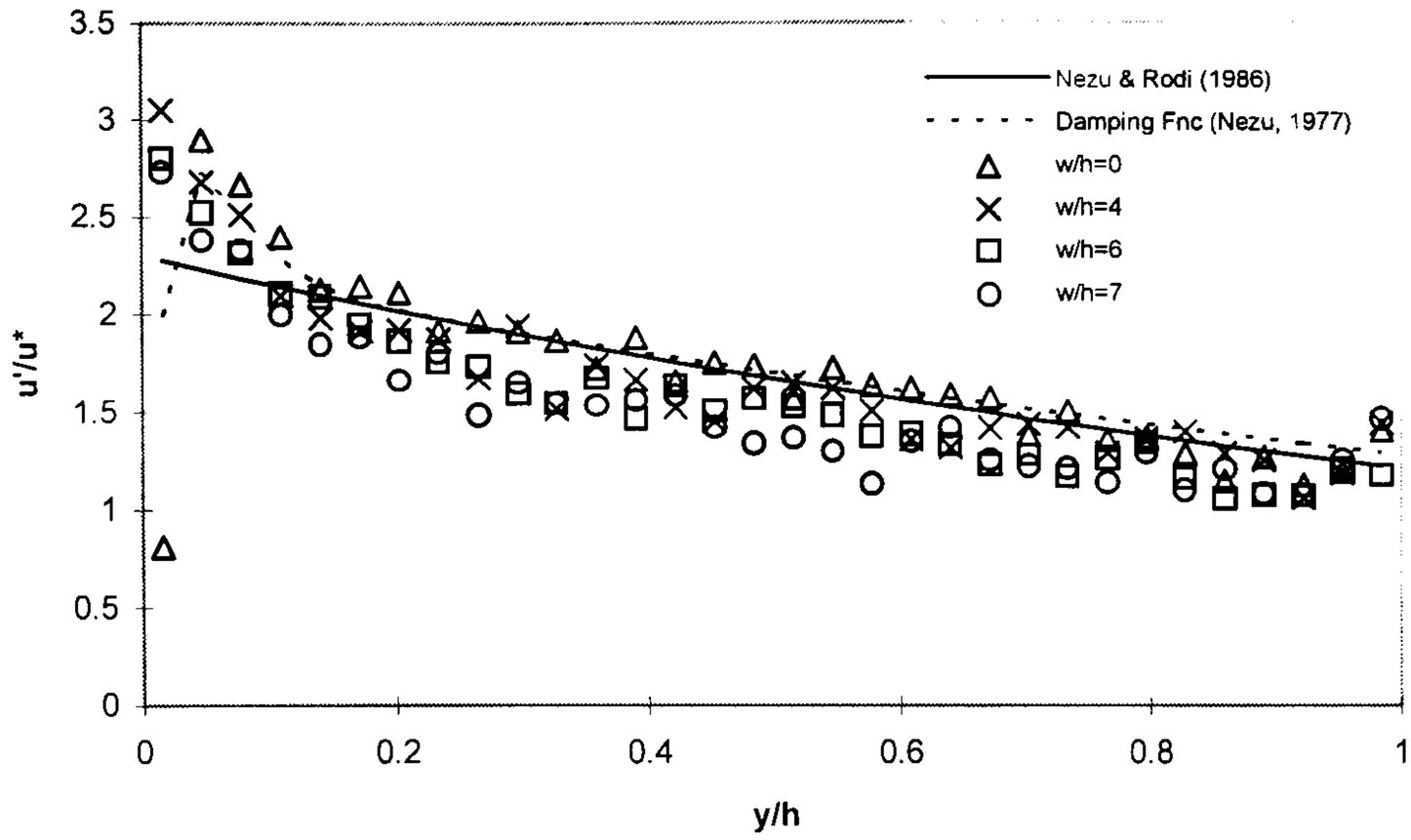

Figure 4.51 - Series B1: Turbulence Intensity, v'/u*

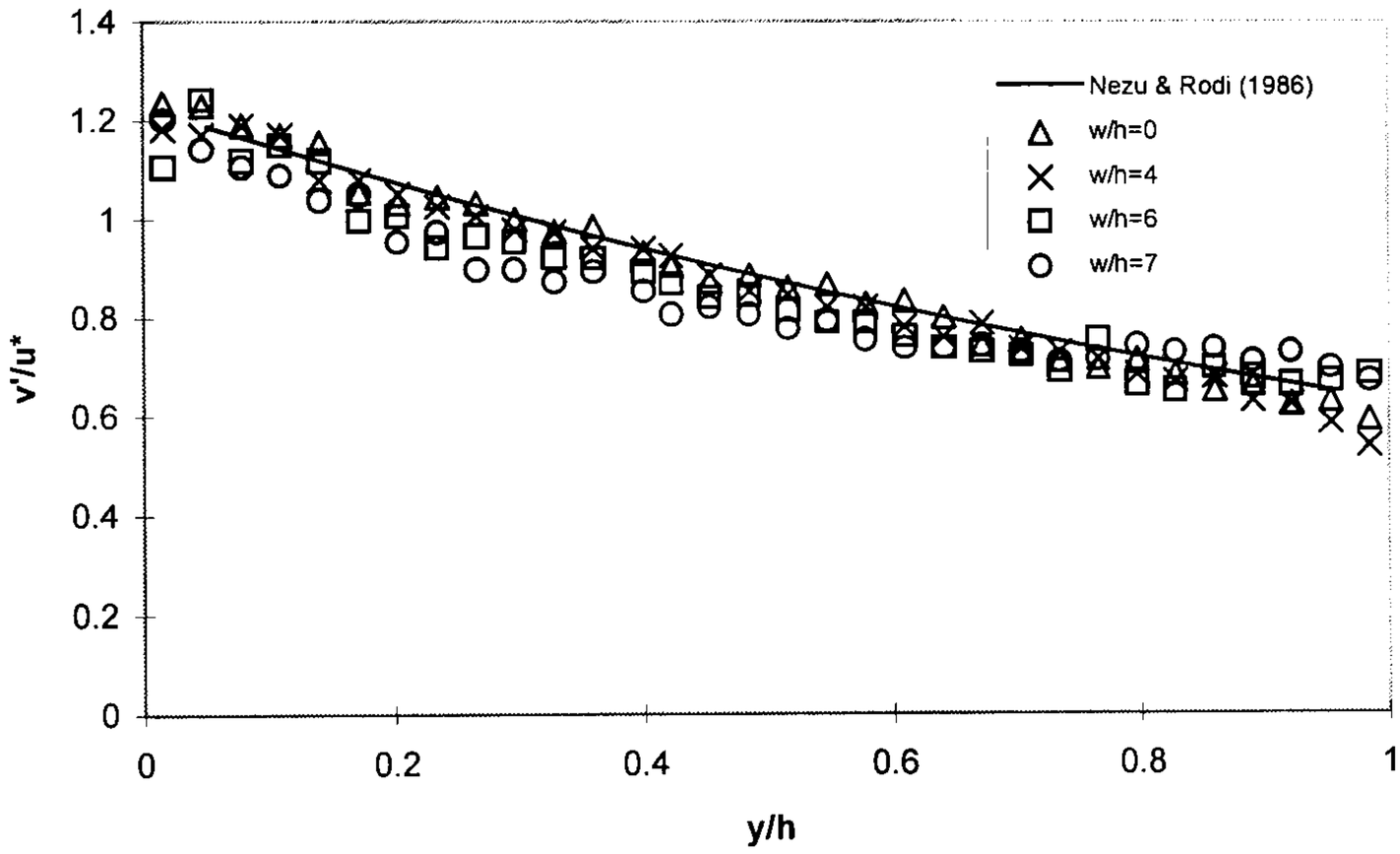

Figure 4.52 - Series B1: Turbulence Intensity, w'/u*

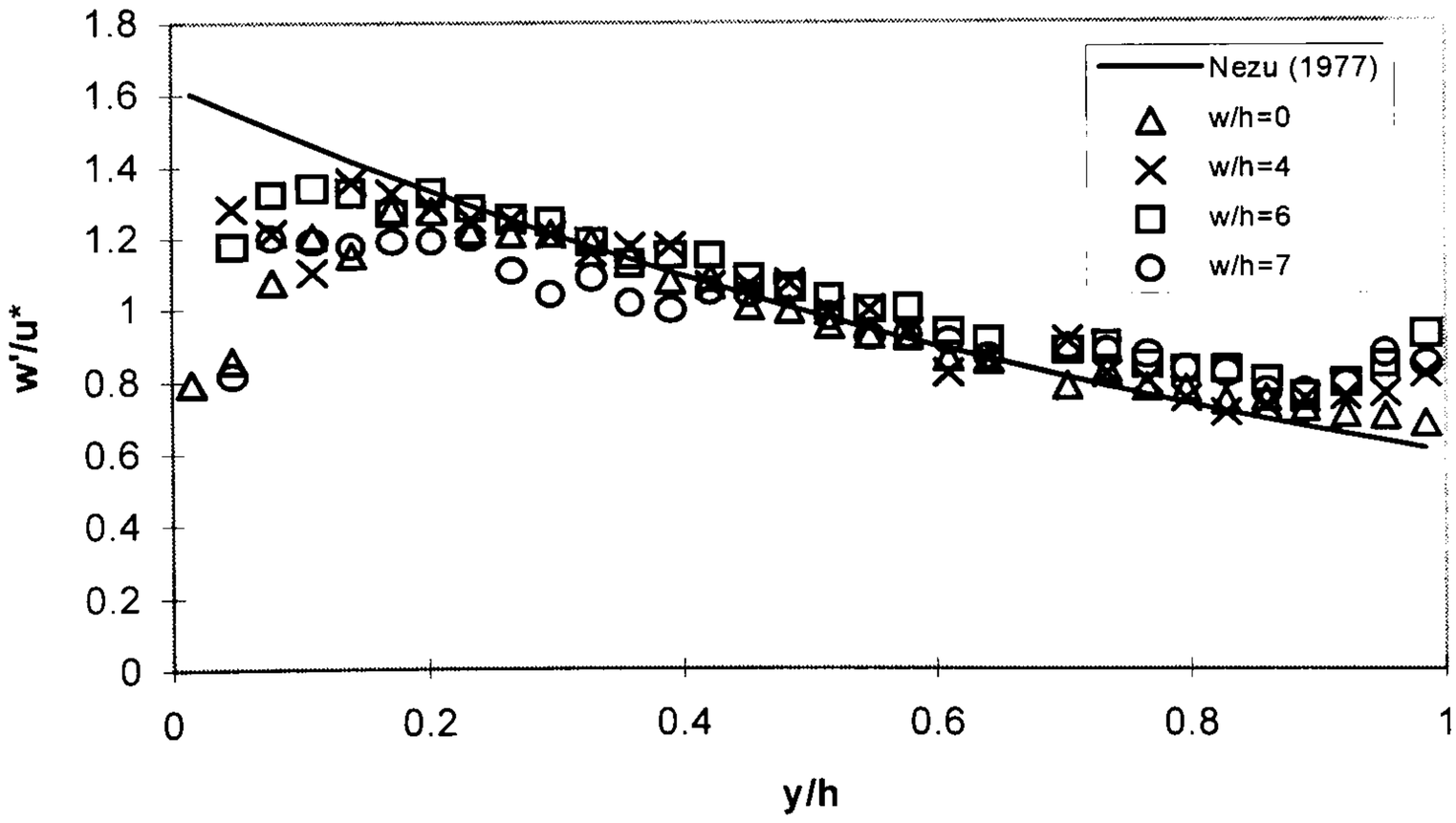

Figure 4.53 - Series B2: Velocity Profiles - Case 1, 16 (Centreline)

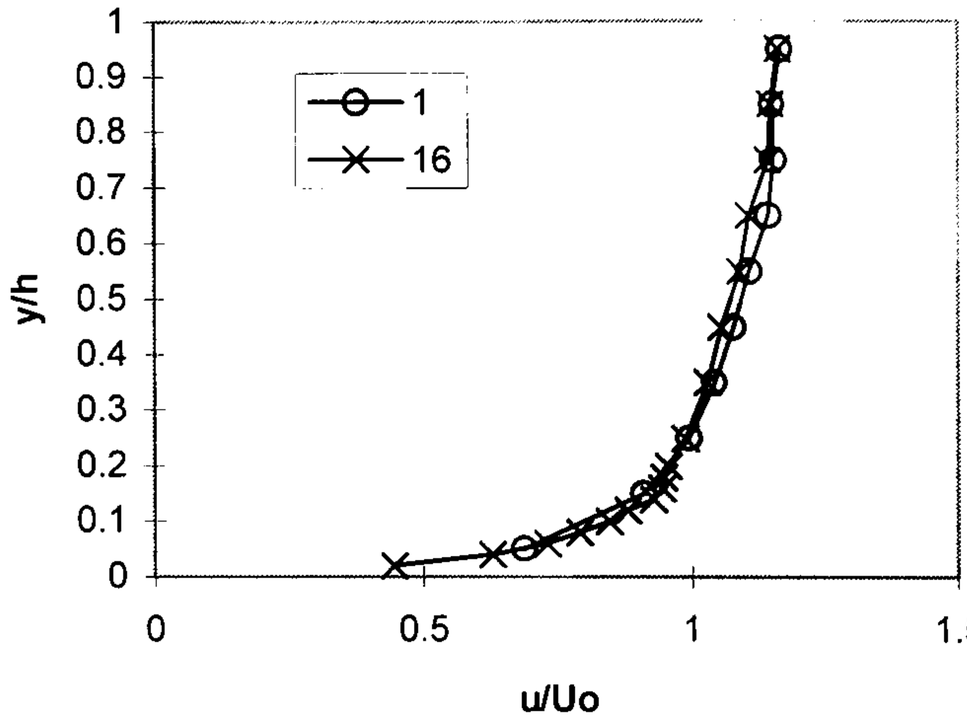

Figure 4.54 - Series B2: Velocity Profiles - Case 4, 17

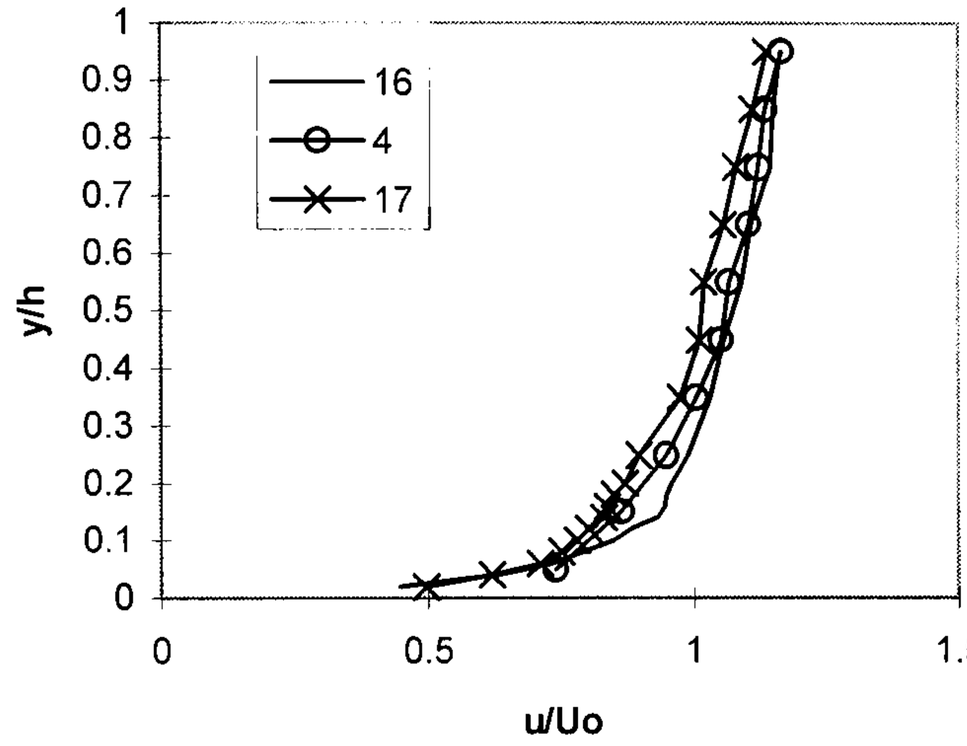

Figure 4.55 - Series B2: Velocity Profiles - Case 7, 18

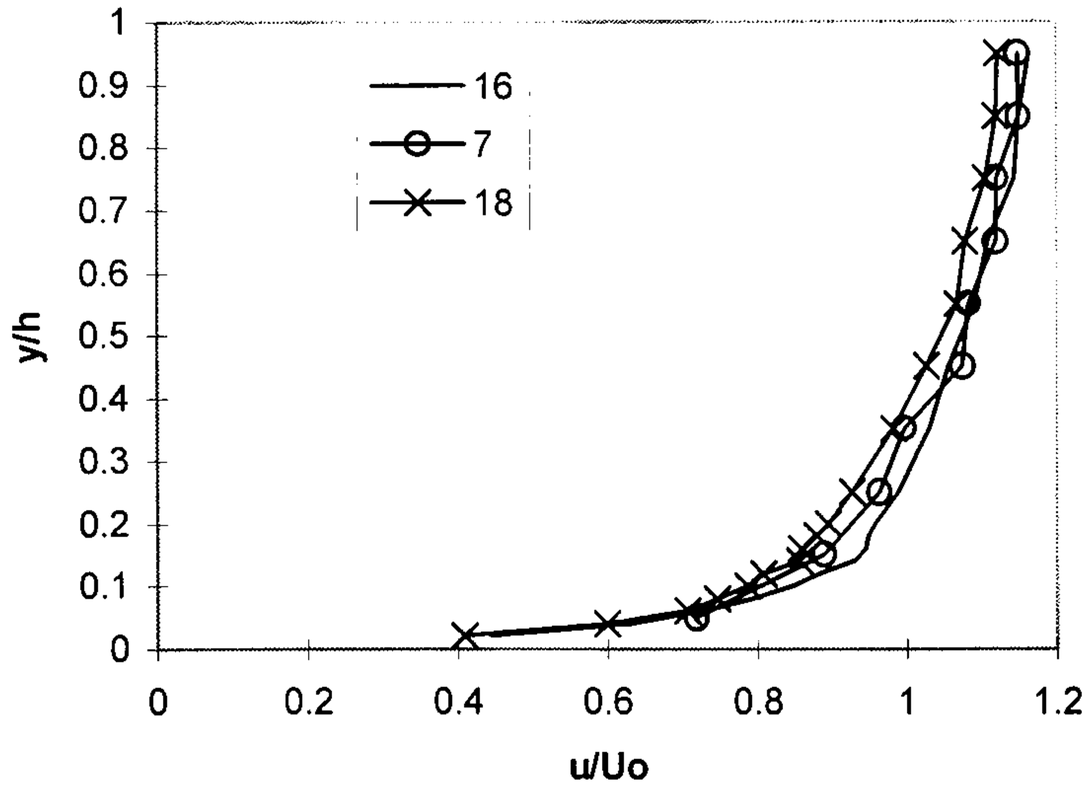

Figure 4.56 - Series B2: Velocity Profiles - Case 10, 19

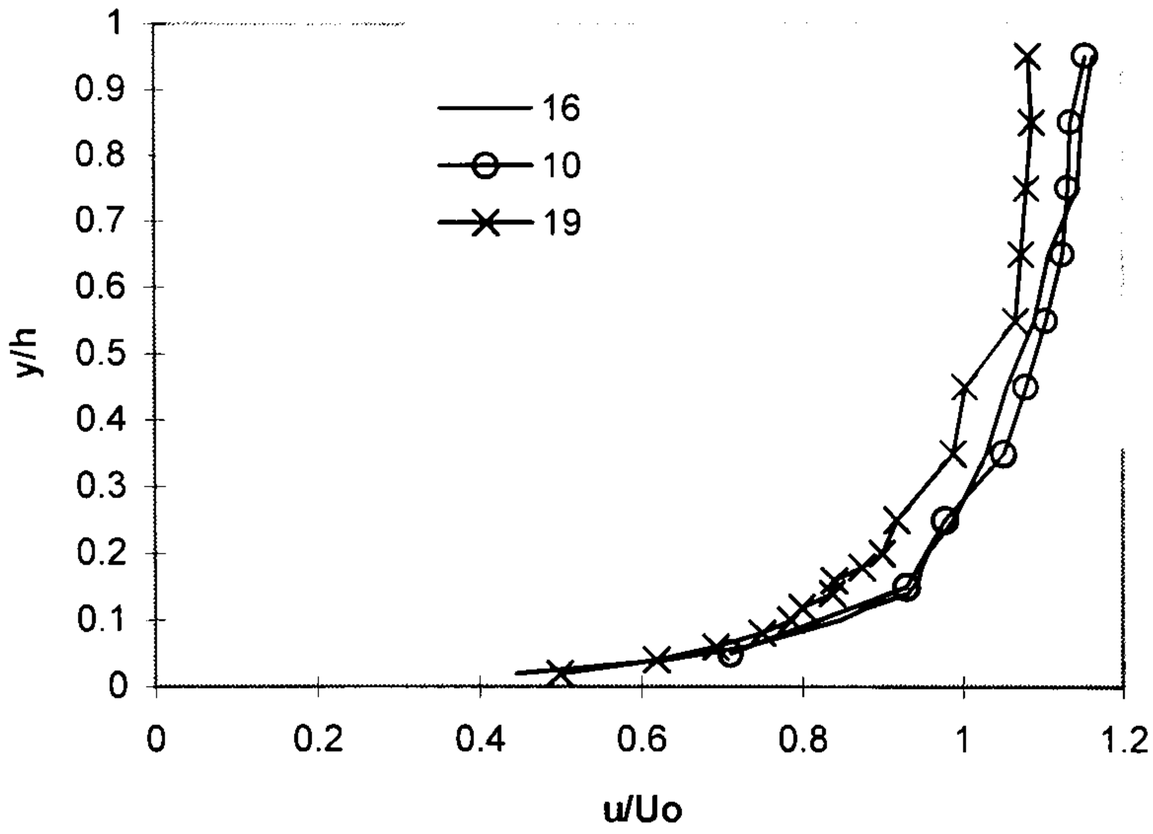

Figure 4.57 - Series B2: Velocity Profiles - Case 13, 20

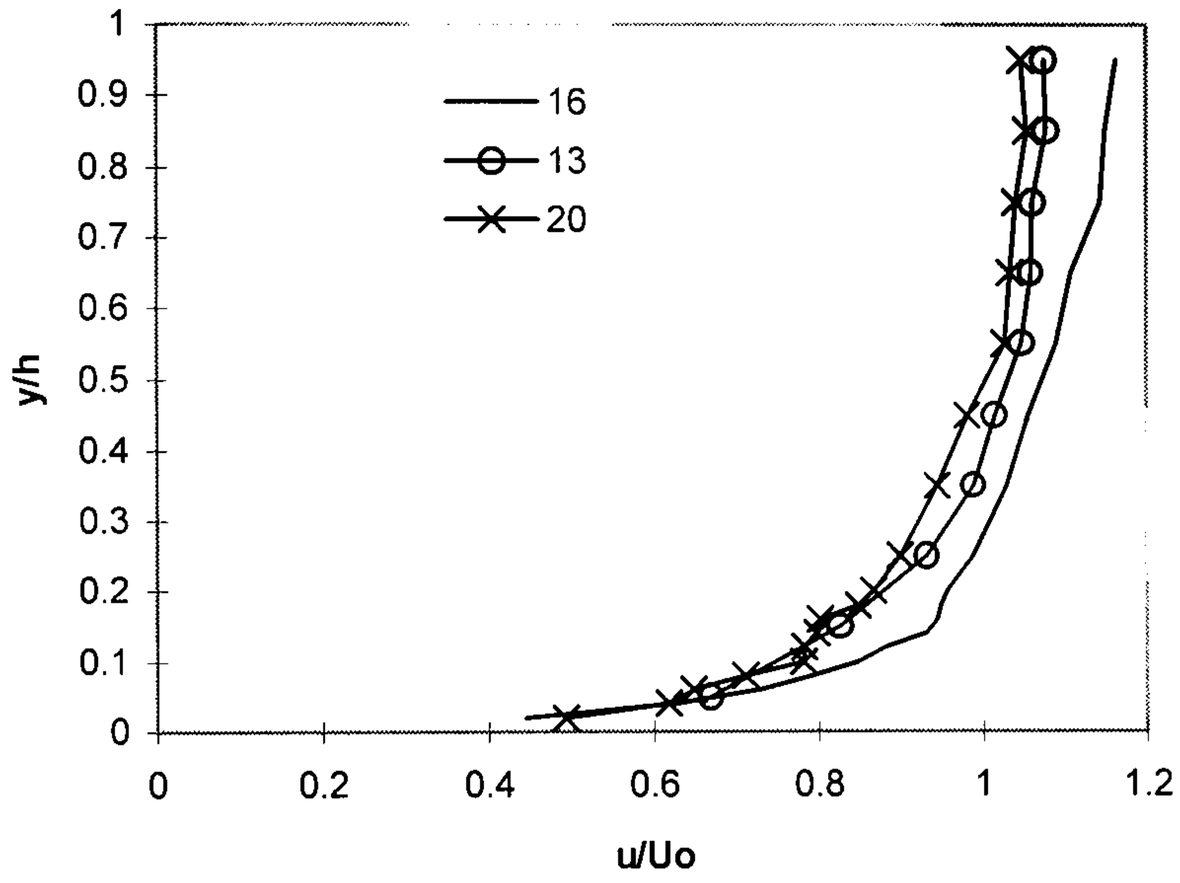

Figure 4.58 - Series B2: Velocity Profiles - Case 15, 21

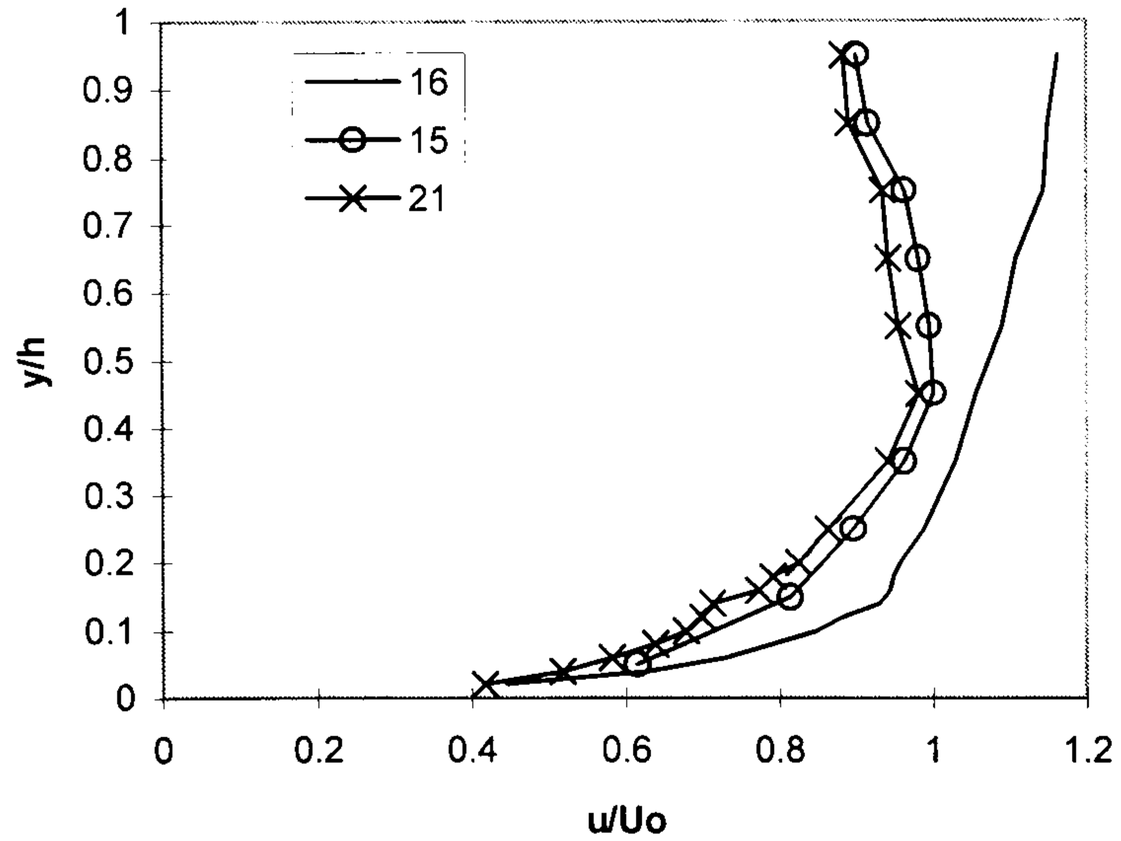

Figure 4.59 - Series B2: Spanwise Distribution of Depth-Averaged Velocity, u_o

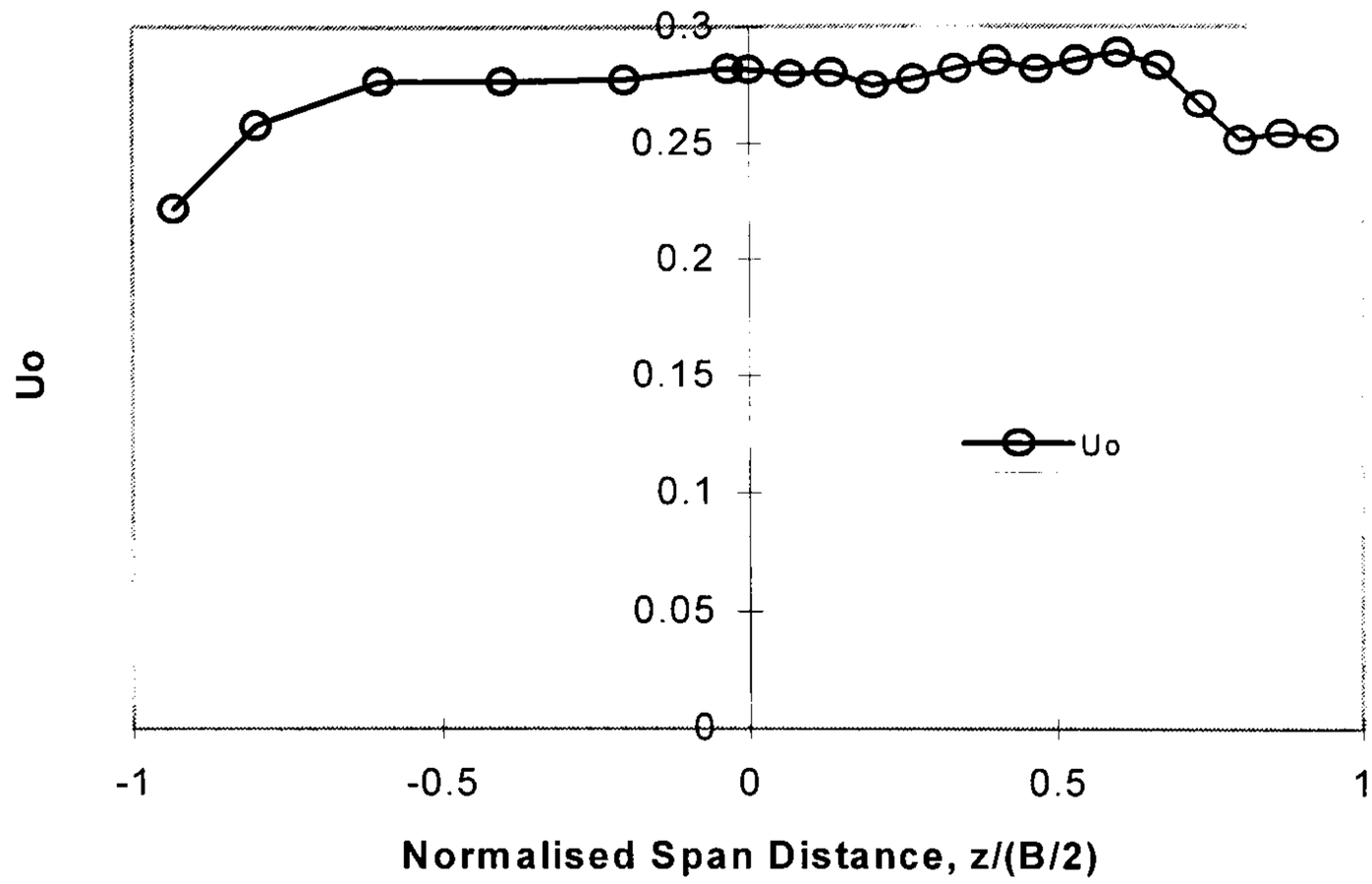

Figure 4.60 - Series B2: Spanwise Distribution of Dip (Depth of u_{max})

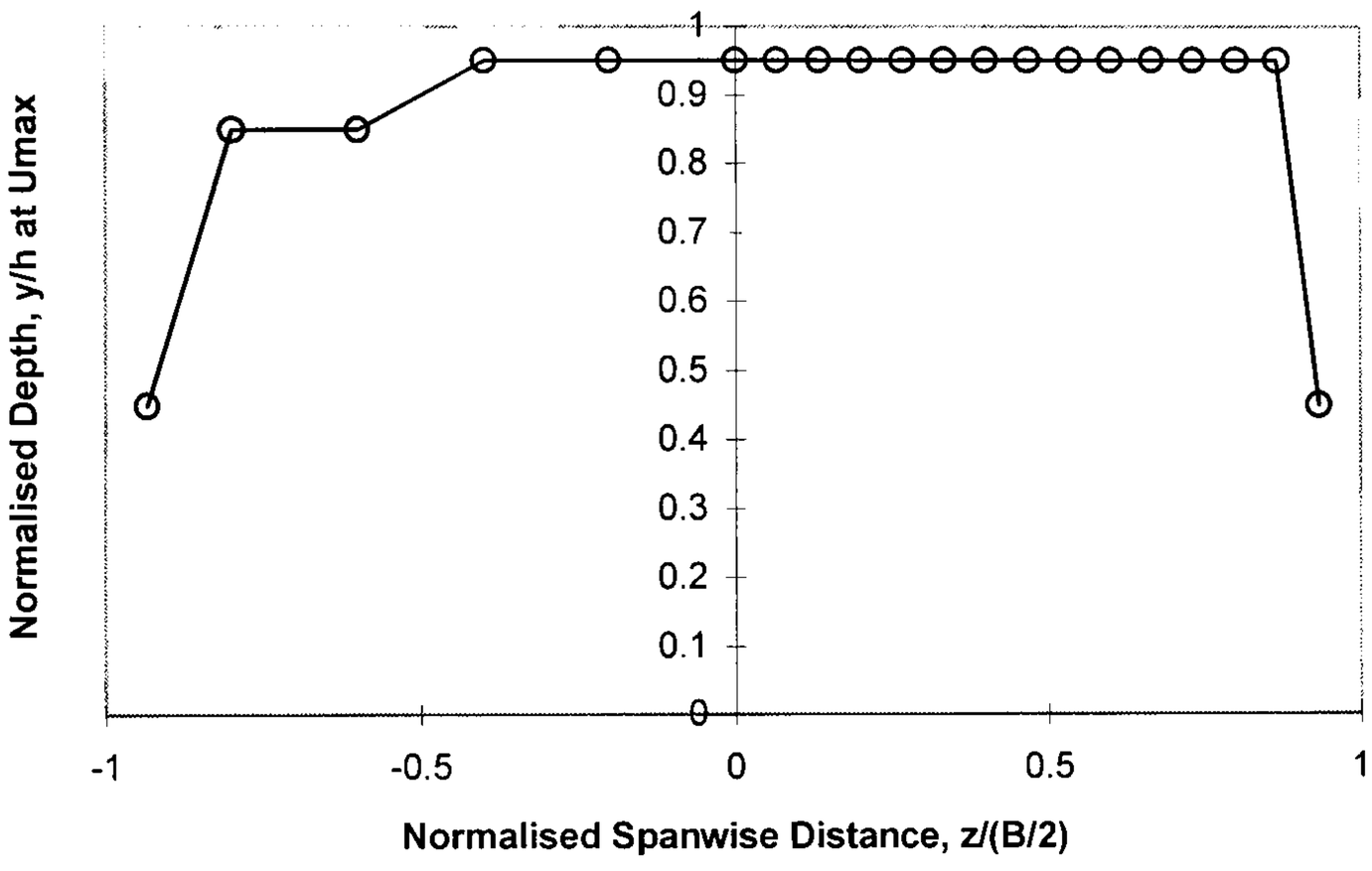

Figure 4.61 - Series B2: Mean Log-Law Velocity Profiles (1,4,7,10,13,15)

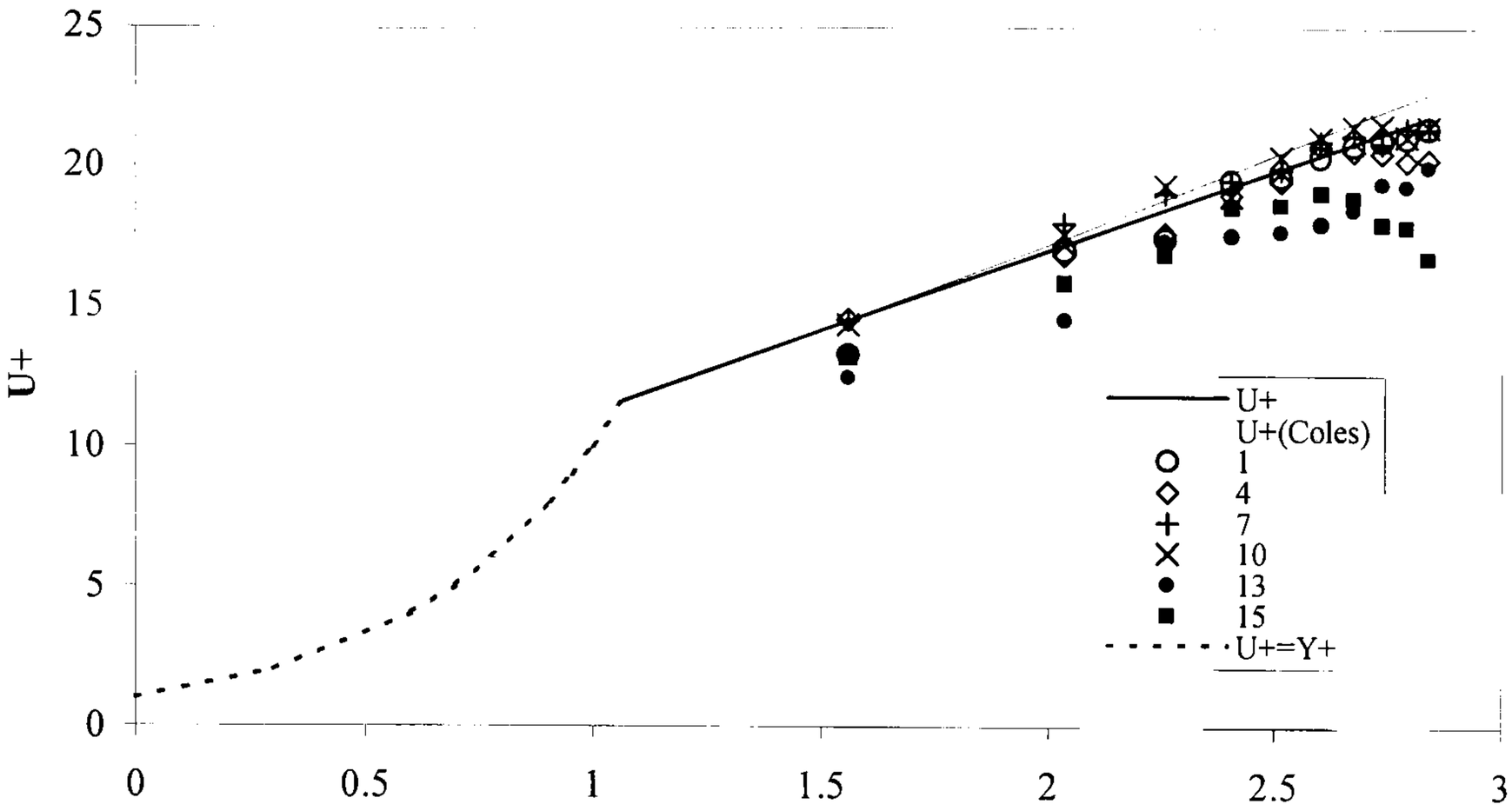

Figure 4.62 - Series B2: Mean Log-Law Velocity Profiles (16-21)

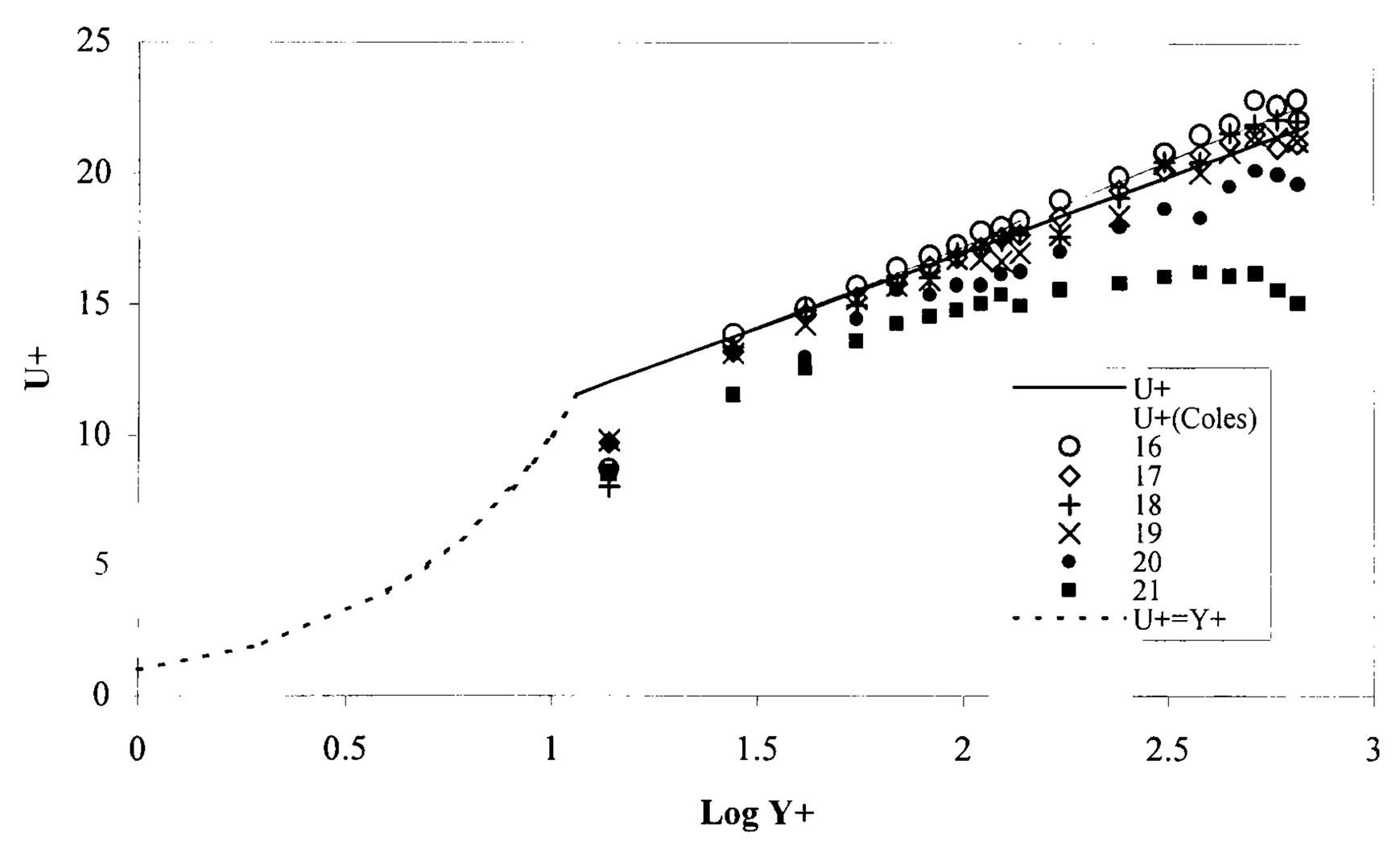

Figure 4.63 - Series B2: Turbulence Intensity, *u'/u
Cases 1, 4, 7, 10, 13, 15**

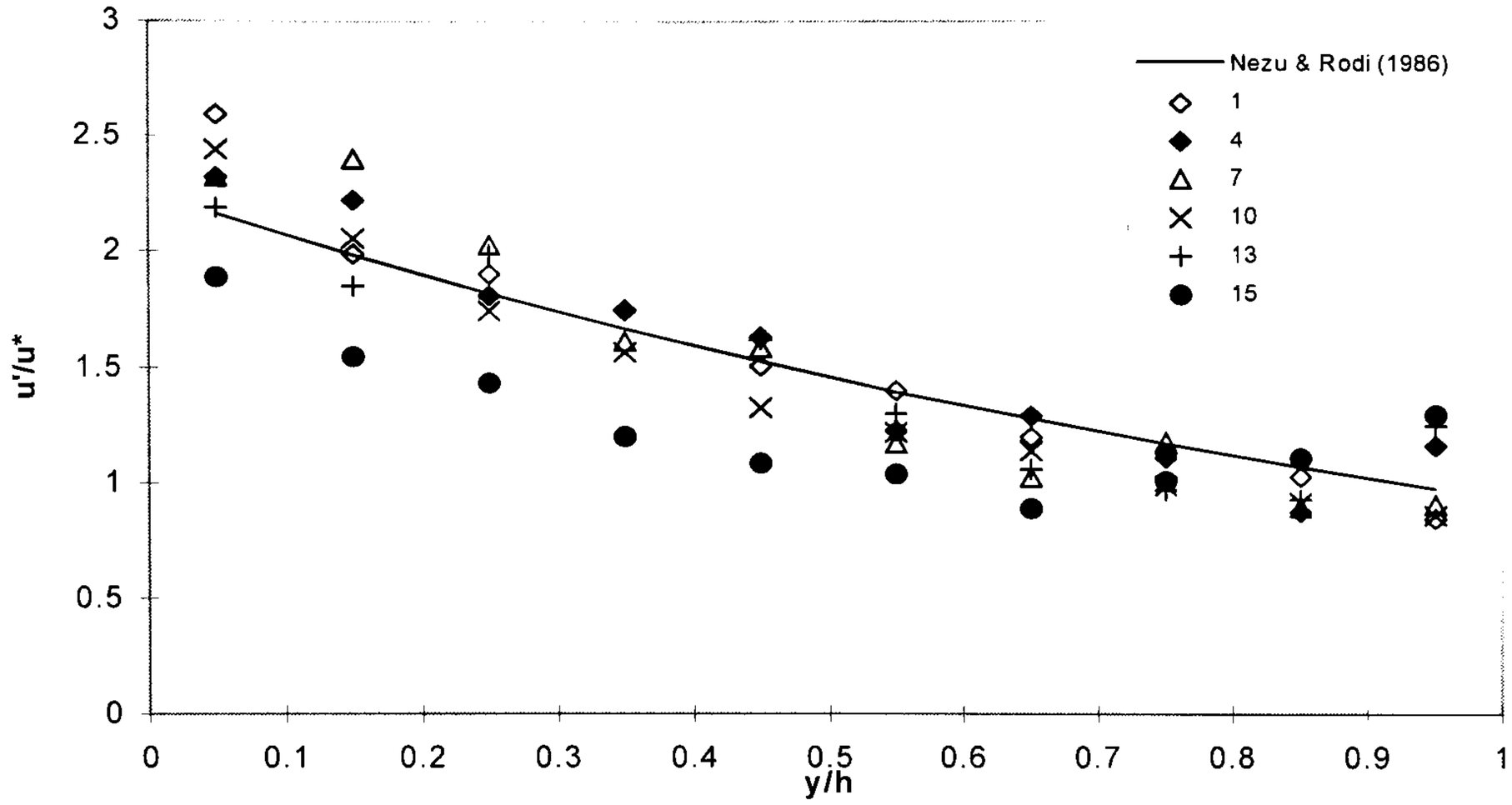

Figure 4.64 - Series B2: Turbulence Intensity, *u'/u
Cases 16-21**

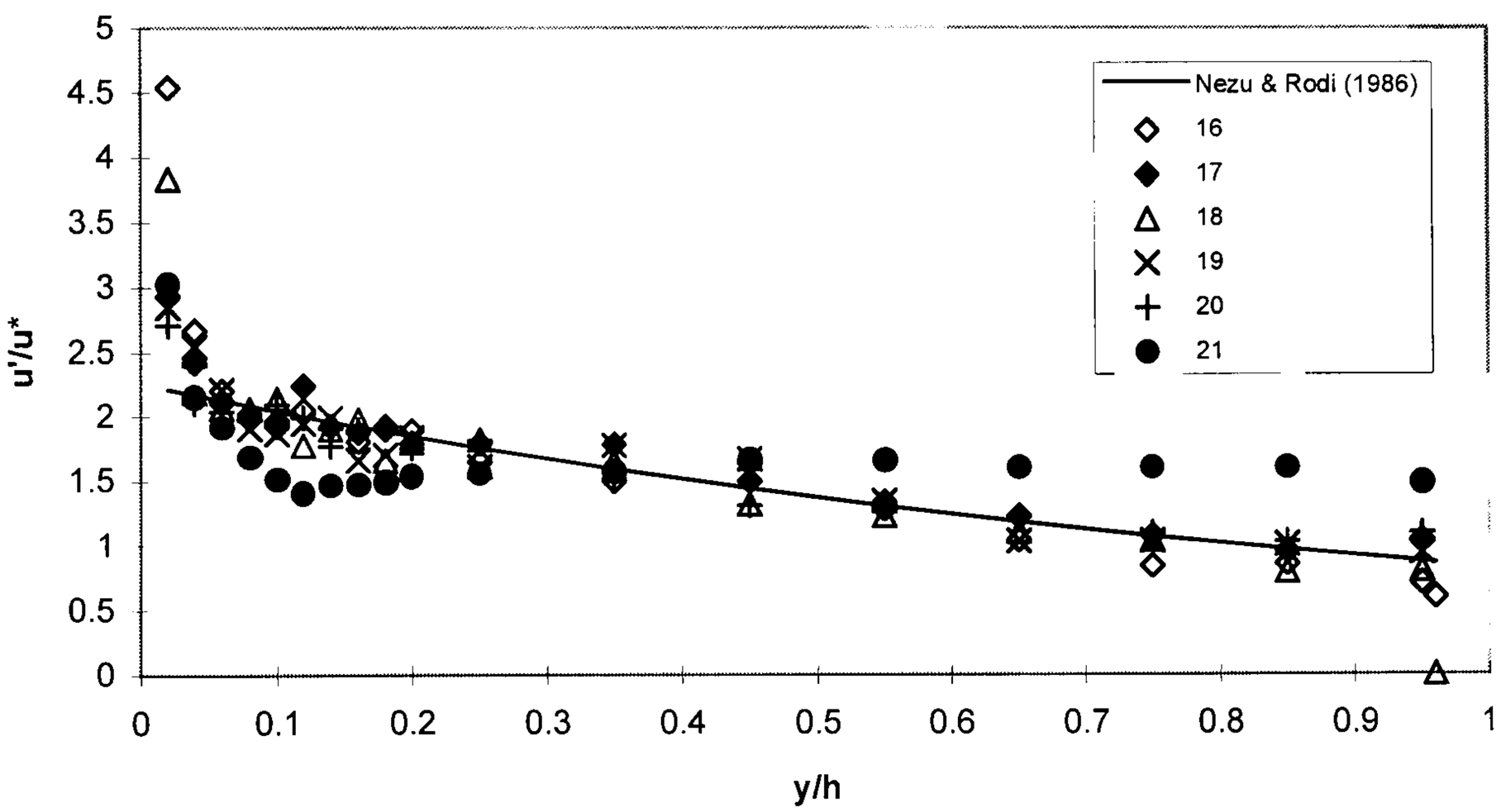

Figure 4.65 - Series B3: Spanwise Distribution of Depth Averaged Velocity, u_o

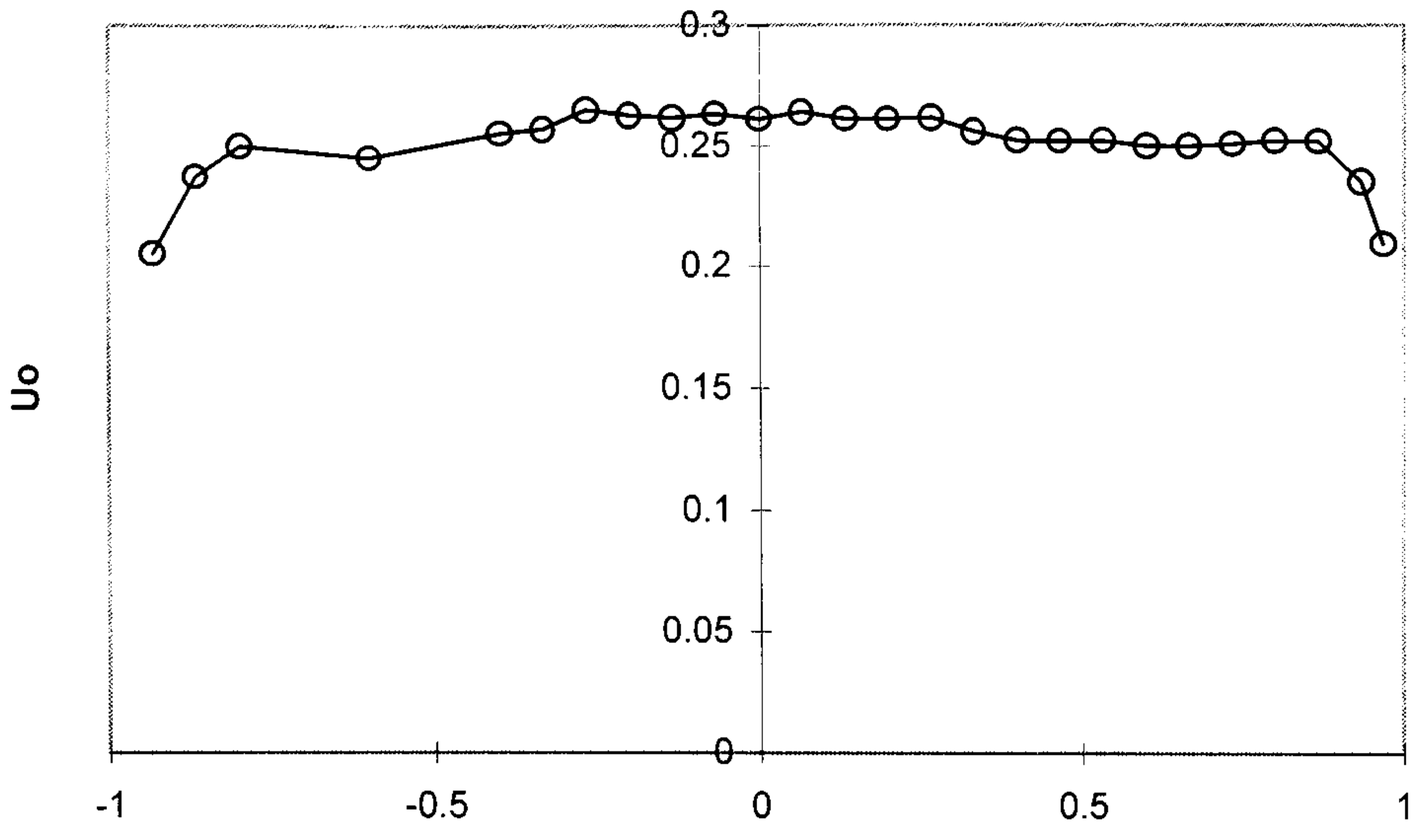

Figure 4.66 - Series B3: Mean Log-Law Velocity Profiles
Cases 1, 4, 7, 10, 13, 15

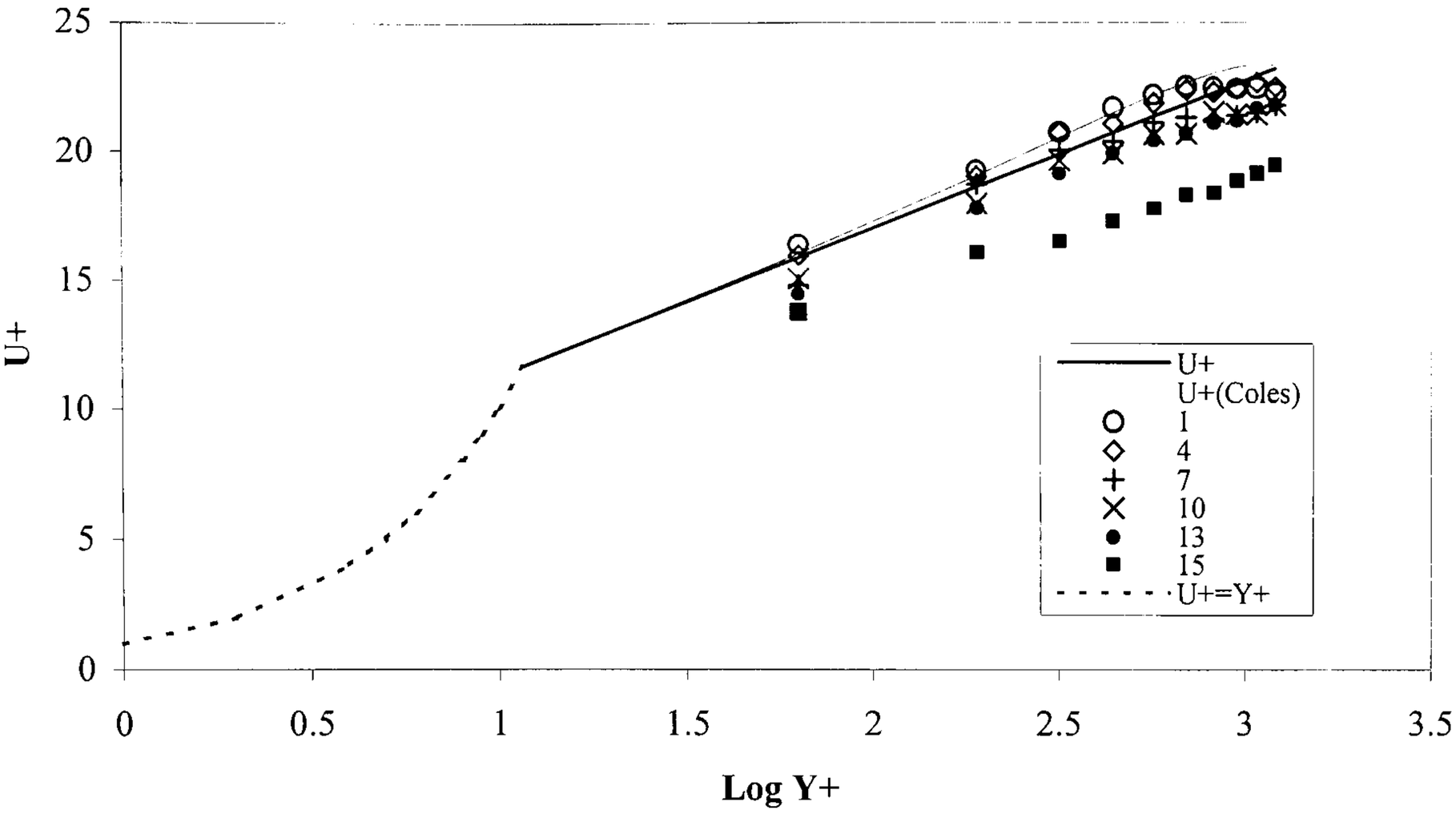

Figure 4.67 - Series B3: Mean Log-Law Velocity Profiles
Cases 16-21

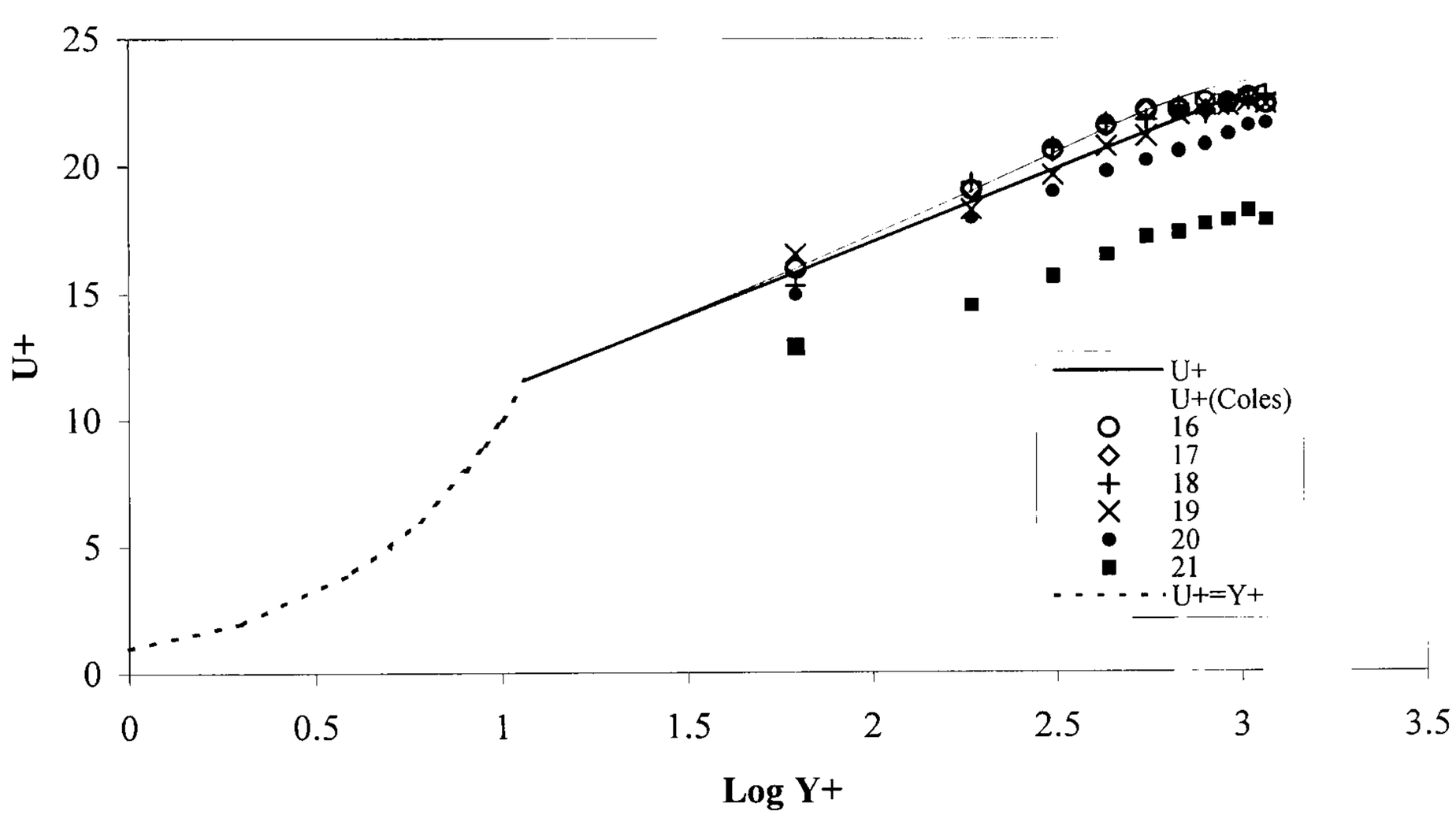

Figure 4.68 - Series B3: Turbulence Intensity, *u'/u
Cases 1, 4, 7, 10, 13, 15**

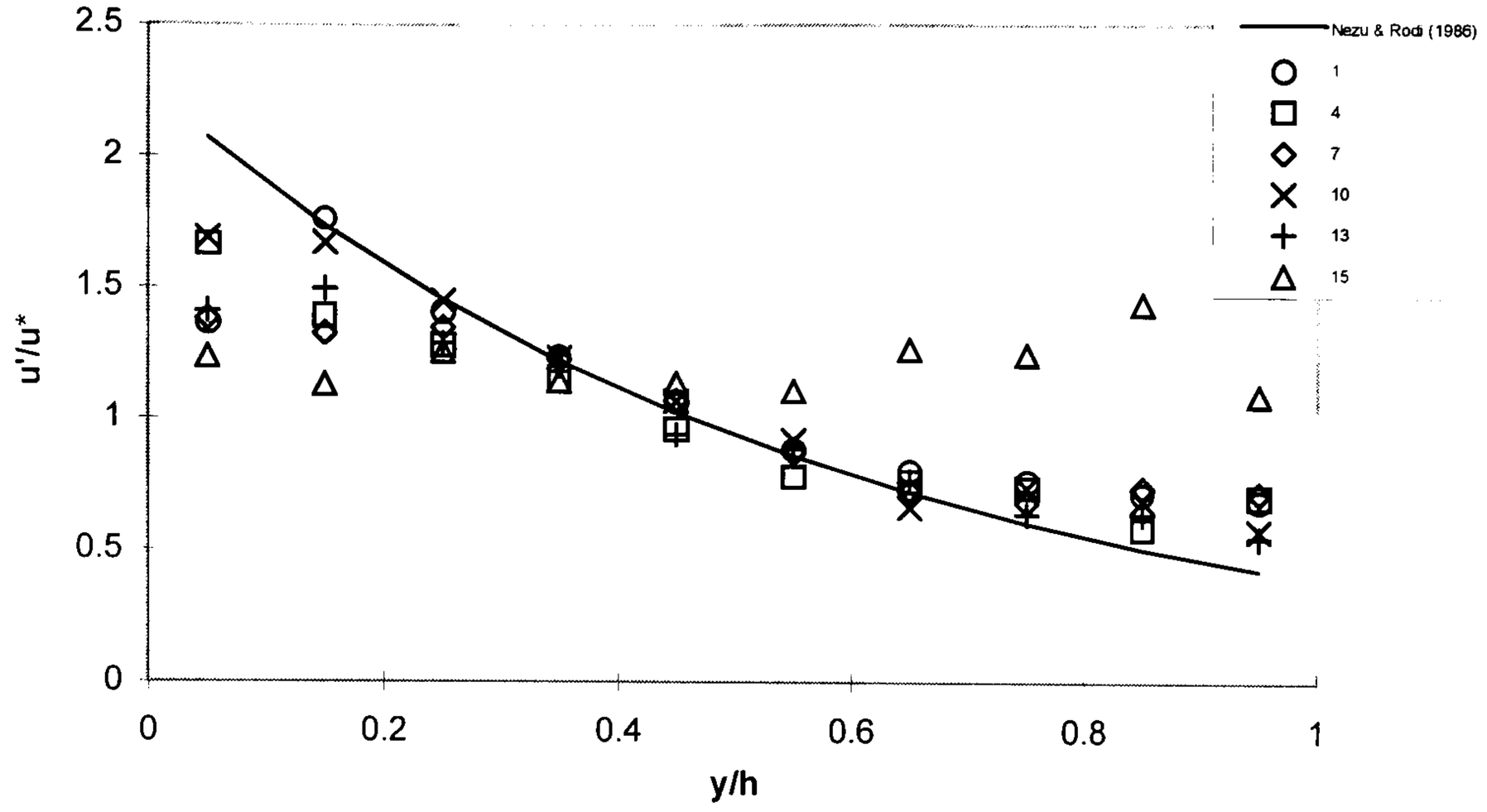

Figure 4.69 - Series B3: Turbulence Intensity, *u'/u
Cases 16-21**

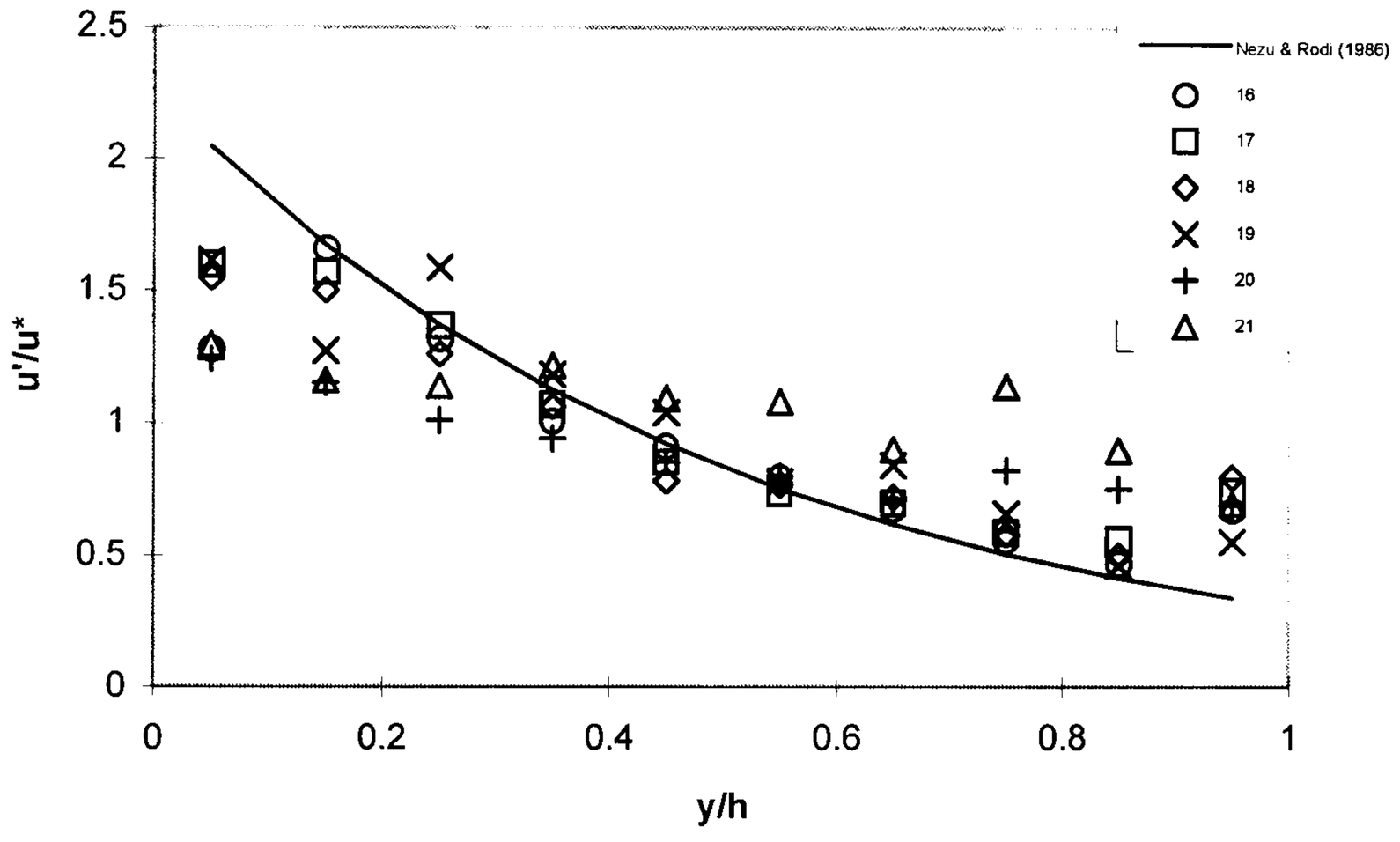

Figure 4.70 - Series B3: Turbulence Intensity, *v'/u
Cases 1, 4, 7, 10, 13, 15

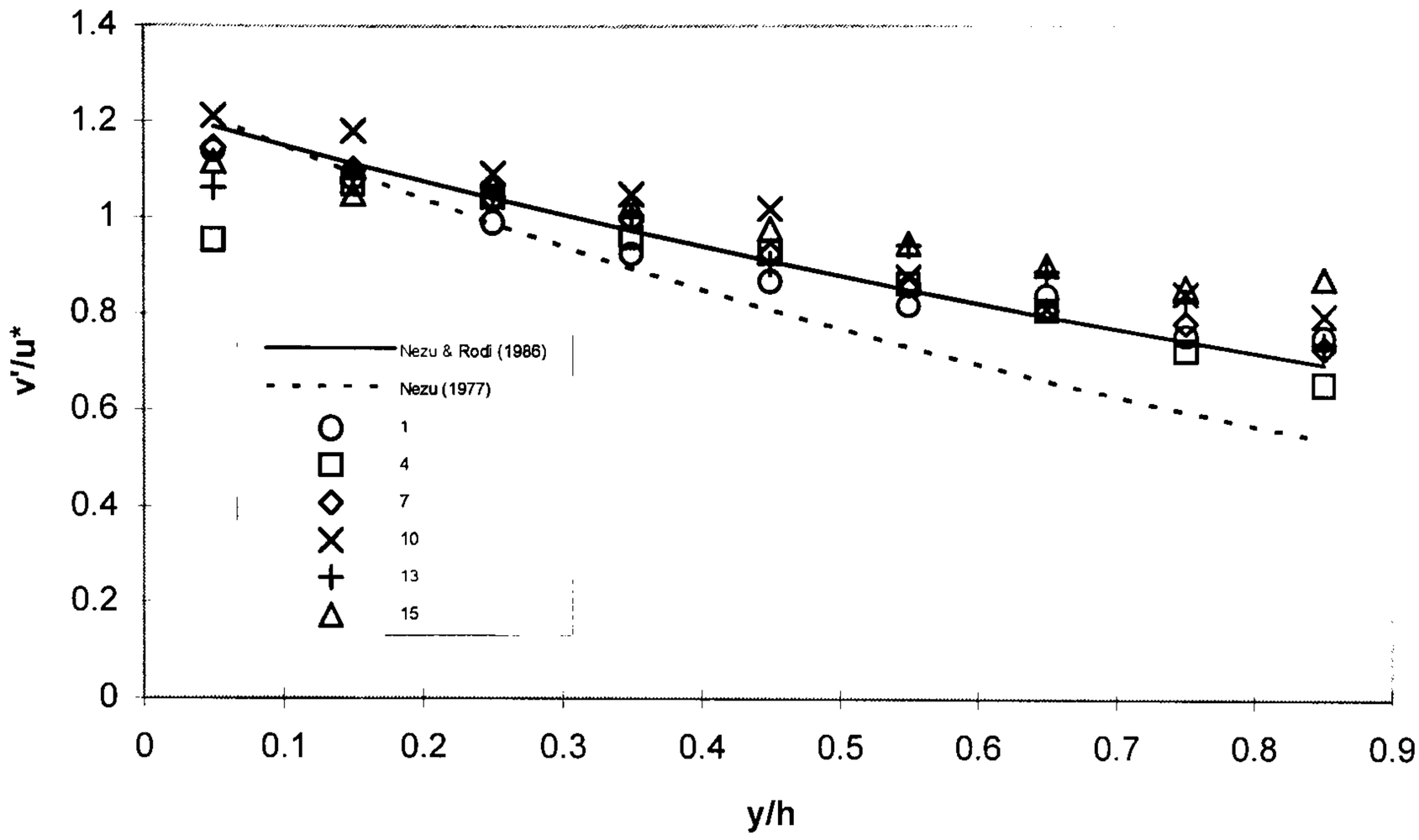

Figure 4.71 - Series B3: Turbulence Intensity, *w'/u
Cases 1, 4, 7, 10, 13, 15

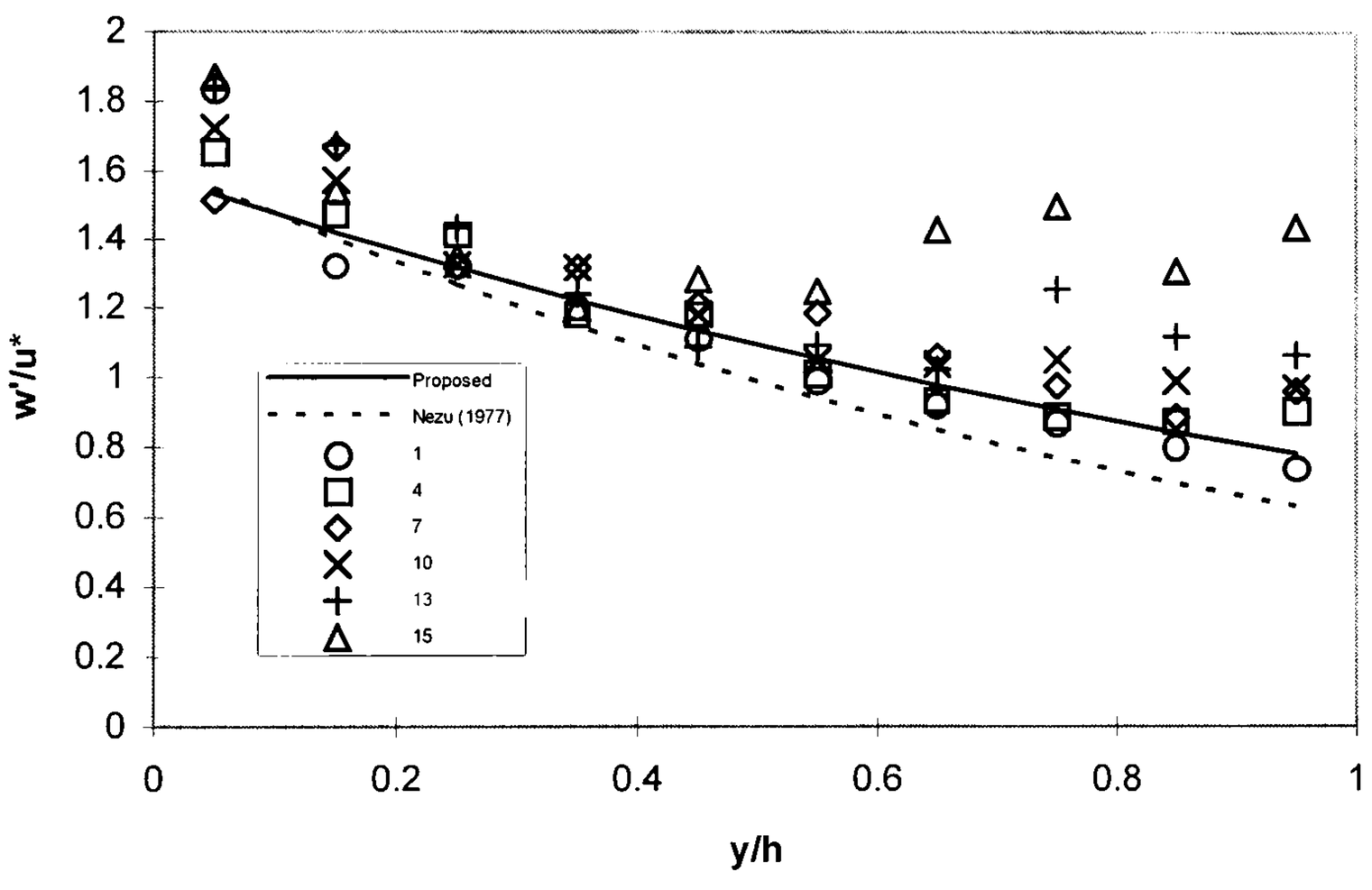

CHAPTER 5

MAIN SLOT FLOW INVESTIGATION

5.1 INTRODUCTION

5.2 REATTACHMENT LENGTH INVESTIGATION

5.2.1 Introduction
5.2.2 Experimental Set-Up and Flow Conditions
5.2.3 $R_L$vs Re: Constant Flow Depth, y_o
5.2.4 $R_L$vs Re: Constant Slot Aspect Ratio, A_s
5.2.5 Maximum Reattachment Lengths
5.2.6 Spanwise Distribution of Reattachment Length
5.2.7 Spanwise Reattachment Length: Results

5.3 FLUME SET-UP AND FLOW CONDITIONS FOR MAIN INVESTIGATION

5.3.1 Introduction
5.3.2 Slot Height: H_S
5.3.3 Upstream Flow Depth, y_o, and Reynolds Number Selection
5.3.4 Slot Aspect Ratios, A_s
5.3.5 Flow Field Limits of Observation
5.3.6 Flow Field Discretization
5.3.7 LDV Sampling Rate and Number of Samples

5.4 MAIN INVESTIGATION: MEAN VELOCITY CHARACTERISTICS

5.4.1 Introduction
5.4.2 2-Component Velocity Vector Plots
5.4.2.1 Velocity Vectors - BFS
5.4.2.2 Velocity Vectors - As=15
5.4.2.3 Velocity Vectors - As=10
5.4.2.4 Velocity Vectors - As=5
5.4.3 Mean Non-Dimensional Velocity Profiles Downstream of a BFS
5.4.4 Mean Non-Dimensional Streamlines of u_m
5.4.4.1 Flow Mass Deflected Upstream at Reattachment
5.4.4.2 Flow Mass Deflected into Slot

CHAPTER 5

SLOT FLOW INVESTIGATION

5.1 INTRODUCTION

The initial slot flow investigation was limited to a single set of hydraulic conditions measuring only two velocity components, namely U and V. Although this proved useful as an insight into slot flow behaviour, a more detailed investigation was required. To overcome the physical limitations imposed by the experimental apparatus, a purpose built flume which could support the acquisition of all three components of velocity was constructed (Chapter 3).

In this chapter, the experimental results obtained from an investigation of open-channel slot flow characteristics using this purpose built flume are presented. The following points summarise the content of this chapter:

(1) An investigation was undertaken to establish the influences that both the oncoming flow depth, y_o, and Reynolds number have on the reattachment length, R_L, downstream of a backward-facing step (BFS). This investigation was broadened to include slot flows of varying aspect ratio, A_s, in order to examine the possible influence the forward-facing step (FFS) has on the reattachment length.

(2) The literature has shown that the flow downstream of a BFS can result in 3-dimensional flow patterns if the slot width to flow depth ratio is not sufficiently large. Using different flow depths and Reynolds numbers, spanwise measurements of the reattachment length were obtained to establish a central 2-dimensional region free from sidewall contamination.

(3) The experimental parameters and hydraulic conditions had to be determined prior to the data acquisition. The investigation of reattachment length was used to aid in this selection process.

(4) The results for the 3-component slot flow investigation are presented in this chapter. The following flow characteristics obtained from the mean velocity measurements are discussed:

(a) The general flow characteristics are shown in the form of 2-dimensional vector plots, similar to that presented in the initial investigation. This illustrates the primary recirculation zone and its associated characteristics such as reattachment length and maximum recirculating velocities. The mean velocity characteristics which develop at the FFS can also be examined from these results.

(b) The mean non-dimensional streamlines of the longitudinal velocity component are presented. This information highlights the characteristics of the separating streamline, including the reattachment point. A universal expression for the separating streamline is also examined.

(c) The shear layer development has also been examined. Expressions are given for the outer and inner boundaries of the shear layer, and for the shear layer thickness.

(d) The velocity profiles in the recirculation region are compared to empirically derived formulae. Existing Gaussian forms for recirculating flow are presented in addition to a modified expression which accounts for the downstream location of the profile.

(e) The recovery of the mean longitudinal flow beyond reattachment to the thin-shear layer state is also presented.

(5) The turbulence characteristics of the flow are presented as contour plots of the total (three-component) turbulent kinetic energy (TKE). In addition to the total TKE, the individual component TKE plots are also given. These plots indicate the shape and intensity of the turbulence which is generated in the shear layer immediately downstream of the BFS, and the dissipation of this with longitudinal distance. The turbulence generated over the FFS is also examined.

(6) Previous investigations of the flow downstream of a BFS have generally been limited to a 2-component analysis, namely U and V. In order to include the third component, W, particularly w', an assumed value derived from the other two components has generally been used. With the measurement of this component in the current investigation, the validity of this assumption is examined.

(7) The 3-component turbulence intensities which develop not only in the recirculation region but also downstream of reattachment are presented. The latter was investigated in order to establish the turbulence characteristics during the recovery of the flow to the thin-shear layer state.

5.2 REATTACHMENT LENGTH INVESTIGATION

5.2.1 Introduction

One of the main features of a step induced separated flow is the streamline which develops between the separation and reattachment points. This is known as the separation streamline, and is characterised by the development of high turbulent activity between the slow moving fluid in the recirculation zone and the faster moving main channel flow. The location and length of this streamline is highly dependent on R_L since the separation point is fixed at the top of the BFS. It was therefore decided that an extensive investigation on the location of R_L would be undertaken using different slot geometries and hydraulic conditions. From the literature, it was evident that both the oncoming flow depth to slot height ratio, y_o/H_s, and the Reynolds number influence the reattachment length (Abbot and Kline, 1962; Eaton and Johnston, 1981; and, Armaly et al, 1983). Therefore, the influence of these were examined in this investigation.

It has been discussed in chapter 2 that the reattachment length could be regarded as a property of the shear layer, and hence, conditions affecting the shear layer will subsequently affect the reattachment length, such as initial turbulence intensity levels and sidewall contamination. These influences can be neglected when the initial flow conditions are based upon a fully developed turbulent flow in a smooth rectangular channel of infinite length and width. Therefore the laboratory flow conditions which approximate these features need to be evaluated.

For turbulent flow, the reattachment length increases with Reynolds number until it reaches a maximum length, R_{Lmax}. As the Reynolds number continues to increase, R_L decreases until it reaches a constant value, despite further increases in Re. An exact relationship between R_L and Re is not presented in the literature, with many of the previous investigations being confined to a limited set of flow conditions. As an approximate summation of this relationship, the initially low reattachment lengths are in the region of 3-4H_S for 2000<Re<4000. The value of R_{Lmax}=7-9H_S for Re=6000-10000, with the stable region of R_L =4-6H_S for Re>40000 (Armaly et al, 1983; Nakagawa and Nezu, 1987)

To examine this relationship further, an investigation was undertaken using a BFS flow at various Reynolds numbers. The study was expanded to include various upstream flow depths, y_o, and the insertion of a FFS at varying distances downstream of the BFS.

It was decided that in order to change the aspect ratio of the slots, the slot height, H_S, would be kept constant and the slot length would change. This was achieved by inserting various perspex blocks of known lengths.

The slot height, H_S, was maintained at 50mm throughout the investigation. This was deemed suitable as the resulting slot depths would generally produce 2-dimensional flow, based on the findings presented in chapter 4 for the ratio of channel width to flow depth. In order to achieve this, a block 50mm deep was fixed into the slot section of the flume, see section 3.5.

Aspect ratios were based on the initial study, however, as aspect ratios of 2 and 5 would not yield reattachment points along the slot bed, they were omitted from this part of the investigation. The A_s values used were therefore 10, 12.5, 15, 20 and 40. The latter value was considered to be of sufficient slot length to be considered as a BFS, particularly since the area of interest within the flow field is immediately downstream of the BFS. This case is therefore referred to as a BFS.

Different hydraulic conditions were imposed by varying the upstream flow depth, y_o, and the Reynolds number. These were limited to the physical depth of the flume and the maximum flow rate generated by the pump.

5.2.2 Experimental Set-Up and Flow Conditions

Using a slot height, H_S, of 50mm, flows with varying depths and Reynolds numbers were generated over slots with aspect ratios of 10, 12.5, 15, 20 and a BFS. The laser was orientated vertically beneath the flume and the beams aligned to measure the streamwise velocity component, U. The control volume of the laser beams was positioned 2.5mm above the channel bed. This height provided a mean velocity close to the channel bed which was outwith the influence of the laminar sub-layer. Longitudinal movement of the laser control volume was achieved accurately using the longitudinal turning wheel on the support-traverse.

The reattachment length is defined as the point where the separated shear layer reattaches to the channel bed. Three methods have been used to determine this reattachment point in the

literature. The first method is to obtain the point where the time-averaged streamwise velocity component very close to the surface is equal to zero. The second method is to establish where 50% of the surface flow moves upstream, i.e. negative velocity. The third method which could not be used at this stage requires the use of streamlines, see section 5.4.5. These methods can be combined to achieve a mean reattachment point, however, Ötügen (1991) adopted the first two techniques and observed that during long observations, both methods gave the same reattachment point.

The method adopted in the current investigation was to initially establish an approximate region of reattachment. This was achieved by moving the control volume along the base of the slot until the time-averaged mean velocity changed from a positive to a negative value (or vice versa) on a successive movement. Point velocities over a long time duration where then obtained at incremental longitudinal locations, thereby giving a series of positive and negative mean velocities.

In general, several points were taken at longitudinal increments of $\Delta x/Hs$=0.4-0.8. These mean velocities were then plotted against their normalised location, x/Hs, from the BFS. It was observed that the resulting relationship between velocity and distance in the vicinity of reattachment was linear. Using a linear best fit of these points, the reattachment length can be obtained, see equation 5.1.

$$\frac{x}{H_s} = mu + R_L \qquad \textbf{Equation 5.1}$$

where, x/H_s = normalised longitudinal distance from the BFS,

m = gradient of line,

u = mean longitudinal velocity, and,

R_L = reattachment length.

To illustrate this method, an example profile of R_L vs Re for a BFS with a flow depth of y_o/H_s=1 is given in figure 5.1(a). The reattachment lengths given in figure 5.1(a) were each determined from plots of u vs x/Hs, which are shown in figures 5.1(b)-(j). These figures illustrate the linear relationship between u vs x/Hs near the reattachment point. The equation of this linear relationship is indicated on these figures, however, it should be noted that this equation is in the notation, $y=mx+c$.

Due to the high turbulent activity and low mean velocities which exist in this region of flow, the sampling frequency expression (equation 4.2) could not be used to determine the

minimum sampling frequency. This was overcome by using a higher sampling frequency than that defined using the mean upstream velocity, u_o. Similarly, the duration of each sample record was much longer. This was necessary since the sampling frequency varied greatly between successive points. Random checks, particularly in extreme conditions, were made to validate the trace statistics using the methods described in section 4.5.3.

The normalised depths investigated in this part of the study varied between y_o/Hs=0.6 and 2.0. In general, depth increments of $\Delta y_o/Hs$=0.2 were used.

For each value of y_o, a wide range of Reynolds numbers were investigated, however, this range was limited by the ability of the flume to produce high Reynolds numbers. Low Reynolds numbers were easy to obtain, irrespective of the flow depth or aspect ratio. Since turbulent flow conditions were required, Reynolds numbers below 3500 were not investigated. In open-channel flows, even where there is no change in the channel geometry, the free-surface tends to become wavy and unstable at high Reynolds numbers. When this occurred in the present study, it became difficult to determine if the flow condition was uniform, and hence Reynolds numbers above this were not investigated. This generally occurred at high Froude numbers, close to the onset of super-critical conditions, i.e. for values just less than unity.

5.2.3 R_L vs Re: Constant Flow Depth

Figures 5.2 (a)-(g) presents plots of R_L vs Re. Each figure represents this relationship for a different upstream depth, y_o/Hs. where each profile represents the reattachment lengths for a specified aspect ratio. Table 5.1 indicates the maximum reattachment lengths, R_{Lmax}, and their corresponding Reynolds number for each of the profiles given in figures 5.2 (a)-(g).

Table 5.1 - Maximum Reattachment Length (R_{Lmax}) vs Reynolds Number (Re)

A_s	BFS		20		15		12.5		10	
y_o/H_s	R_{Lmax}	Re	R_{Lmax}	Re	R_{Lmax}	Re	R_{Lmax}	Re	R_{Lmax}	Re
2			7.3	32000					7.0	31000
1.6	7.5	16000							7.8	20000
1.4			7.4	18000	7.4	18000	7.4	18000	7.8	18000
1.2	8.1	17500							-	-
1.0	8.9	13000	8.6	14000	8.3	17500	7.7	17500	8.0	22500
0.8	8.8	12000	8.8	11000	8.9	13000				
0.6	8.6	10000	8.6	10000			8.6	12500		

NB: Blank sections represent combinations which were not investigated
'-' denotes combinations investigated but no reattachment length observed

In general, the shape of the profiles are similar to that observed by Armaly et al (1983). At low Reynolds numbers, R_L is also low, however, as Re increases so does R_L, increasing to a maximum, R_{Lmax}. As Re is increased above the point of R_{Lmax}, R_L decreases. This continues until R_L stabilises at a minimum value.

At the largest depth ratio, y_o/H_S=2, see figure 5.2 (a), the shape of the profiles are similar irrespective of aspect ratio, in this case a large and small aspect ratio are presented. Within the range of Reynolds numbers taken, the reattachment lengths observed are within the range $5.5<R_L<7.3$, where R_{Lmax} occurs at a Reynolds number of approximately 32000.

As the flow depth is decreased to y_o/H_S=1.6, figure 5.2 (b), the profiles are again similar irrespective of the aspect ratio, with reattachment lengths in the range of $6<R_L<7.8$, where R_{Lmax} occurs at a lower Reynolds number of approximately 20000.

Figure 5.2 (c) illustrates the profiles for a depth ratio, y_o/H_S=1.4. Although a large range of Reynolds numbers are presented, a reduced range of reattachment lengths, $6.7<R_L<7.4$ are associated with these. The profile for A_S=10 differs from the other profiles. Although similar in shape, the reattachment lengths correspond to lower Reynolds numbers, therefore, the profile appears to be displaced below the other profiles. This profile has a slightly greater R_{Lmax} of 7.8 which occurs at Re=18000. This downward displacement is very little, and may be attributed to slight changes in the hydraulic conditions, however, irrespective of this difference, the reattachment lengths are greater and worth noting at this stage.

Decreasing the depth ratio again, figure 5.2 (d) illustrates the profiles for y_o/H_S=1.2. The profiles are similar in shape, with reattachment lengths in the range $6.8<R_L<8.1$. For the BFS profile, R_{Lmax} occurs at Re=17500, however, it can be seen that in the profile for A_s=10 that a blank section exists between $7000 \leq Re \leq 16000$, where no reattachment lengths are given. Although flows with Reynolds numbers within this range were investigated, a reattachment point could not be obtained. This will be discussed later.

Figure 5.2 (e) illustrates the profiles for y_o/H_S=1.0. The previous depth ratios produced similar sets of profiles for the different aspect ratios, however, the profiles within this depth ratio differ. For the BFS profile, the reattachment lengths can be found in the range $7<R_L<9$ where R_{Lmax}=8.9 corresponding to an Re=13000. The smallest aspect ratio, A_s=10, has reattachment lengths in the range $7<R_L<8$, where R_{Lmax}=8 which corresponds to Re=22500. The profiles for the BFS and A_s=10 illustrate the two extremes from this set of profiles. The remaining profiles display an affiliation to either one of these two extremes. The profile for A_s=20 is similar to the profile for the BFS, whilst the profile for A_s=12.5 is almost identical to

A_s=10. The profile for A_s=15 lies between these two sets, however. its shape and location is linked closer to the smaller aspect ratios.

As the depth ratio decreases to y_o/H_S=0.8, see figure 5.2(f), the profiles for the different aspect ratios become similar again. At this same depth for A_s=10 however, no reattachment points could be found. For the profiles presented, the reattachment lengths are within the range $6.5<R_L<9$, and R_{Lmax} corresponds to Re=13000.

At the smallest depth ratio of y_o/Hs=0.6, see figure 5.2 (g), no reattachment lengths could be found for A_s=10. At this flow depth, it can be seen that the maximum Reynolds number obtained was approximately 14000. Values of Re above this were not possible to create due to distortion of the free-surface. The reattachment lengths observed are within the range $7.3<R_L<8.5$, where R_{Lmax} occurs at approximately Re=10000-13000.

5.2.4 R_L vs Re: Constant Slot Aspect Ratio, A_s

Using the same data from the plots in figures 5.2 (a)-(g), figures 5.3 (a)-(e) represent the relationship between different flow depths for a given aspect ratio. For the BFS case, figure 5.3 (a), depths ranging from $0.6\leq y_o/H_s\leq 1.6$ are presented giving reattachment lengths ranging between $6<R_L<9$. The lower reattachment lengths belong to the high and low Reynolds numbers, whilst a central region of Reynolds numbers provide higher reattachment lengths. Another key observation is the increase in reattachment length as the depth ratio reduces, however, this trend stabilises at the lower flow depths, $y_o/H_s<1.0$.

A reduction in slot length to A_s=20 produces a similar distribution to the BFS. Figure 5.3(b) illustrates this slot length with depth profiles ranging between $0.6\leq y_o/H_s\leq 2.0$. Reattachment lengths in the range $5.5<R_L<8.5$ are observed where once again, the lower reattachment lengths are attributed to the high and low Reynolds numbers, with higher reattachment lengths observed in a central band of Reynolds numbers. In this case however, this central region has a greater range than that for the BFS, where R_{Lmax} occurs at higher Reynolds numbers for the larger depth ratios. Another similarity with the previous case is the increase in reattachment length as the depth y_o/H_s reduces, again stabilising at the lower flow depths, $y_o/H_s<1.0$.

Figure 5.3 (c) illustrates the profiles for depths in the range $0.8\leq y_o/H_s\leq 1.4$ for an aspect ratio of 15. The main feature from this figure is the increase in R_L as y_o/H_s reduces. When the

aspect ratio is reduced slightly to A_s=12.5, the profiles retain a similar shape and distribution to that observed for A_s=15, see figure 5.3 (d).

Figure 5.3 (e) shows the final set of profiles where A_s=10. The range of reattachment lengths from these profiles are between $5.7<R_L<8$. The depths used for this aspect ratio are in the range $1.0\leq y_o/H_s\leq 2$. Once again, the larger depth ratios produce smaller reattachment lengths.

5.2.5 Maximum Reattachment Lengths

The distribution of the maximum reattachment lengths and the Reynolds numbers at which they occur is now considered. Table 5.1 gives the R_{Lmax} and its corresponding Reynolds number for all of the flow depths and aspect ratios investigated. A plot of the R_{Lmax} vs y_o/H_s is also given in figure 5.4 (a). It can be seen that for all the aspect ratios, with the exception of A_s=10, that a similar distribution of R_{Lmax} vs y_o/H_S occurs. The location of R_{Lmax} increases as the depth ratio reduces. In the case of the BFS and A_s=20, i.e. where the aspect ratio is large, a cut-off depth occurs between y_o/H_S=0.8-1.0 after which there is a decrease in R_{Lmax}. However, in other cases there is no evidence of this cut-off since reattachment lengths for lower depths were not obtained. The profile for A_s=15 is similar to that for A_s=20, however there is no evidence that R_{Lmax} decreases at the lower depths.

The exception to this trend is the profile for A_s=10. The reattachment lengths are similar for the higher flow depths which represent the lower reattachment lengths, however, as the depth decreases, the reattachment length stabilises at a longitudinal distance of $x/H_S\approx 8.0$.

In a further attempt to establish a relationship between the results, the Reynolds number at which these maximum reattachment lengths occur have been plotted (figure 5.4b). It is clear from this set of curves, with the exception of A_s=10, that as the depth increases, so does the Reynolds number of R_{Lmax}. Whilst for most of the points in the profile for A_s=10 this relationship holds, there is an initially high Reynolds number at the lower depth, y_o/H_s=1.0.

5.2.6 Spanwise Distribution of Reattachment Length

The spanwise distribution of the reattachment length in open channel BFS flow is documented in the literature. Investigations of the spanwise distribution of the reattachment length have shown that in wide-channels, a central 2-dimensional region exists, whereby the reattachment length is constant across this region (De Brederode and Bradshaw, 1972;

Berbee and Ellzey, 1989; and, Ötügen and Muckenthaler, 1992). The increased turbulence activity near the sidewalls promotes the growth of the shear layer thickness, and hence the reattachment length is less at the sidewalls. To determine the conditions which produce a central 2-dimensional region of similar reattachment lengths, a series of different flow conditions were investigated.

This study was undertaken with a BFS only configuration with depths of y_o/H_s=0.6, 0.8, 1.0 and 2.0. Points were taken from the centreline to each of the sidewalls in order to verify flow symmetry, however, a greater concentration of results were taken over one-half of the channel.

There were approximately five different runs for each flow depth, with each run having a different Reynolds number. These Reynolds numbers ranged between a low value of approximately Re=6000 to the highest attainable value which supported uniform flow conditions.

5.2.7 Spanwise Reattachment Length: Results

The results for the spanwise reattachment length investigation are presented in figure 5.5 (a)-(d). Each figure represents a different flow depth ratio, y_o/H_S, with a series of profiles of the spanwise reattachment lengths for various Reynolds numbers. Reattachment lengths were taken along the channel width at increments of Δz=30mm, which corresponds to a non-dimensional value of z/B=0.05, where B is the full channel width.

Figure 5.5 (a) illustrates the results for a flow depth of, y_o/Hs=2. Reynolds numbers ranging between 8333<Re<40333 were used in this investigation yielding reattachment lengths of $5.5<R_L<7.1$. This compares with the reattachment lengths in figure 5.2 (a) for the same flow conditions. The Reynolds number for R_{Lmax} also occurs at the same value of Re=30000.

It can be seen that for all the profiles the reattachment length is consistent across most of the channel, with closer inspection indicating that there is a reduction in R_L in the vicinity of the sidewalls. This reduction is approximately x/H_S=0.5 and occurs at a distance of z/H_S=1-1.5 from the sidewall.

Figure 5.5 (b) gives profiles of R_L vs Re for the reduced flow depth of y_o/H_s=1. In this case, a maximum reattachment length of 8.5 occurs at Re=17500. Comparison of this value to the earlier results in figure 5.2 (e) indicates the same R_{Lmax} and Re. Nearly all the profiles

display reattachment lengths similar to their centreline value throughout most of the span, however, there is a rapid decrease in R_L close to the sidewalls. Again, this reduction is of the order of x/H_S=0.5 and occurs over a distance of z/H_S=1-1.5 from the sidewall. The exception to this trend occurs in the profile for Re=23833, the highest Re investigated. The R_L remains constant in a central region corresponding to 0.66B, however, at a distance of approximately z/H_S=2 from the sidewall, there is a rapid decrease in the R_L from 8.5 to 7.5.

Figure 5.5 (c) shows the R_L vs Re for y_o/H_S=0.8, illustrating three profiles for the range 6000<Re<14900. At the channel centreline, the R_{Lmax}=8.7 for a value of Re=14900. The corresponding profile in figure 5.2 (f) has a similar maximum R_{Lmax} of 8.6 for the same Re. The spanwise distribution profiles indicate that only the profile for Re=14900, which again, is the highest Re investigated, has notably reduced reattachment lengths close to the sidewalls. In this case, the R_L reduces from approximately 8.7 to 6.2, however, this reduction occurs at the increased distance of z/H_S=4 from the sidewall. This is attributed to the increase in shear layer growth which develops due to the combination of higher shear layer turbulence and the complex 3-dimensional effects which occur at the sidewall. The spanwise distribution for the lower Reynolds numbers are relatively consistent across the channel width.

Figure 5.5 (d) gives the profiles for the final depth ratio of y_o/H_S=0.6. For the profile corresponding to Re=14833, the centreline R_L=8 which is similar to that observed for the same Re in figure 5.2 (g). Similarly, the centreline R_{Lmax} for Re=10167 in both figures are the same. The spanwise distribution for this flow depth ratio illustrates a constant R_L for Re=6583, however, the profiles for both Re=14833 and 10167 illustrate a central region of constant R_L, before reducing from approximately 8.5 to 7.5 at a distance of z/H_S=3 from the sidewall.

5.3 FLUME SET-UP AND FLOW CONDITIONS FOR MAIN INVESTIGATION

5.3.1 Introduction

One of the main reasons for undertaking the reattachment length investigation was to assist in choosing both the hydraulic and physical parameters for the main 3-component velocity investigation. These parameters were as follows:

(a) Slot height, *Hs*;

(b) Upstream flow depth, y_o;

(c) Reynolds numbers, Re;

(d) Slot aspect ratios, A_S;

(e) Limits of observation (upstream and downstream boundaries);

(f) Mesh discretization;

(g) Velocity characteristic requirements; and,

(h) Time limitations.

These will each be addressed in turn, thereby building a complete picture of the methodology and requirements of the investigation.

5.3.2 Slot Height: H_S

In order to reduce the number of variables in the investigation, thereby simplifying the variations in flow conditions, several parameters had to be fixed. The R_L investigation used a fixed value of H_S=0.05m. As this slot height achieved its aim in generating a central 2-dimensional region of flow, at suitable flow depths, it was therefore adopted as the step height for the main investigation. Although the definition of narrow and wide channels depends on the ratio between channel width and the upstream flow depth, B/y_o, the depth of flow in the slot region, $y_s=y_o+H_S$, must also be considered.

5.3.3 Upstream Flow Depth, y_o, and Reynolds Number Selection

It was evident that both the Reynolds number and upstream flow depth have a significant bearing on the reattachment length. This investigation used a large combination of these parameters, however, this would be difficult to re-create for the main investigation. Therefore, several options were considered for scaling down the number of flow combinations. These options were as follows:

(1) **Constant y_o, various Re:**

Using a single flow depth, a selection of Reynolds numbers could be extracted from the reattachment length investigation. These Reynolds numbers would reflect the different characteristics observed from the R_L profile.

(2) **Constant Re, various y_o:**

A constant Re corresponding to a common feature could be used, for example, the Re corresponding to R_{Lmax}. Unfortunately, the R_L profiles suggest that this may be difficult, since many of the common features occur at different Reynolds numbers.

(3) **Various conditions pertaining to Key Features:**

Although this would allow certain flow characteristics to be examined more closely, the main disadvantages with this system is the selection criteria, the limitation of the results and the difficulty in correlating the findings.

It was decided that the first option would be the simplest to implement. Although the results would be limited to a single flow depth, the findings would be representative, since no fundamental change to this flow type occurs with a change in depth (Nakagawa and Nezu, 1987). The next step was to ascertain the value of y_o and the set of Reynolds numbers to be used. Using figures 5.2 (a)-(g), the individual flow depths were each considered. All the flow depths produced similar profiles for each of the different aspect ratios with the exception of y/Hs=1.0. At this flow depth, the reattachment lengths could be grouped as either being influenced by the FFS, i.e. $As \leq 15$, or not. It was observed that the reattachment length profiles increased as y_o/Hs decreased. When $y_o/Hs \leq 1.0$, the reattachment length profiles stabilised. Closer inspection of the profiles for y_o/Hs=1.0 (figure 5.2e), revealed the following points:

(a) For $A_s > 15$, R_{Lmax} occurs at Re≈14000. This Reynolds number corresponds to the low Re, low R_L portion of the profile for $A_s \leq 15$.

(b) For A_s=10, R_{Lmax} occurs at Re≈23000. This Reynolds number also corresponds to the high Re, low R_L portion of the profiles for $A_s \geq 15$.

(c) The profile for A_s=15, which has characteristics pertinent to both the large and low aspect ratios, has its R_{Lmax} occurring at Re≈18,500. Although the profile for A_s=12.5 is similar to A_s=10, it also has its R_{Lmax} occurring at Re≈18,500.

From this set of observations, it can be seen that Reynolds numbers of 14000, 18500 and 23000 are the Reynolds numbers which correspond to R_{Lmax} throughout the range of aspect ratios. In addition to this, these Reynolds numbers also correspond to other important features of the R_L profiles. It can be seen that a pattern exists within this set of numbers, whereby the Re increases by increments of approximately 4500.

It was therefore decided to adopt a flow depth of y_o/H_s=1.0, as this corresponds to the most influential flow depth observed from the R_L investigation. The Reynolds numbers, 14000, 18500 and 23000 were used as they represent the R_{Lmax} values for A_s<15, A_s=15 and A_s>15

respectively. These Reynolds numbers were used in all the aspect ratios and not just to the one pertinent to the maximum reattachment length.

5.3.4 Slot Aspect Ratios, A_s

The slot aspect ratios to be used in the main investigation were determined primarily using the findings from the R_L investigation. There was no doubt that a BFS had to be investigated, as this would serve as an index case for comparison with the slot configurations. In order to assess the influence of a FFS close to reattachment, an aspect ratio of A_s=10 was used. Due to the similarity of the reattachment lengths observed when A_s=12.5, it was decided that there was no requirement to use this aspect ratio in the main investigation. It was observed that certain Reynolds numbers for A_s=15 gave reattachment lengths similar to those for larger aspect ratios, while others were more representative of lower aspect ratios. The ambiguous nature of the flow field at this aspect ratio made it an ideal condition for further investigation.

All the above aspect ratios will produce reattachment of the flow along the slot bed, however, the main investigation was not limited to this feature. The initial investigation used smaller aspect ratios of 2 and 5 to investigate the flow condition of a recirculating eddy with no reattachment on the channel bed. Although similarities between these two aspect ratios existed, the flow characteristics for A_s=5 were closer to those observed for larger aspect ratios where reattachment did occur on the channel bed. An aspect ratio of 5 was therefore used in the main investigation in order to represent this condition.

The slot aspect ratios chosen were therefore, A_s=5, 10, 15 and a BFS. A constant depth, y_o/H_s=1.0, and three different Reynolds numbers, Re=14000, 18500 and 23000 were used for each A_s, therefore providing twelve different flow cases.

5.3.5 Flow Field Limits of Observation

The rectangular open-channel investigation described in section 4.6 illustrated the 2-dimensional nature of the flow in the central region of the channel. The spanwise distribution of R_L was an extension of this characteristic in order to establish a suitable slot flow depth, y_s, whereby the sidewall influence would not affect the mid-channel flow. It was observed that for all Re at a depth of y_o/Hs=1.0 there existed a large central region unaffected by sidewall contamination. Since a central region of 2-dimensional flow exists, then only one longitudinal sweep along the channel centreline was required.

Although the slot flow field is the main area of interest, the flow conditions both upstream and downstream of the slot are also of interest. The upstream limit of observation was chosen as 1000mm (or $20H_S$) upstream of the slot. This was deemed a suitable distance to allow the upstream flow conditions to be investigated without influence from the slot. The downstream limit of observation was primarily influenced by the available distance between the end of the slot and the end of the flume. Despite this, the station x/Hs=33 from the BFS was generally used as the downstream limit of observation, therefore, the number of profiles downstream of the FFS varied between aspect ratios.

5.3.6 Flow Field Discretization

The flow field within the slot is the principal region of investigation and therefore it requires the greatest attention. Since the slot flow depth, y_S, was maintained at a constant value of 100mm, or $2H_S$, a constant number of vertical sampling points was used. These points are defined in terms of the incremental change in height, Δy, which is equal to the slot depth, y_S, divided by the number of points in the profile. Selecting a high number of points would be time consuming, whilst selecting a low number of points will potentially overlook the detail of the flow characteristics being investigated. It was decided to adopt a discretization similar to that used in the initial investigation. This was based upon the vertical profile being constructed from 20 individual point measurements, therefore:

$$\Delta y = y_S/20 = 100/20 = 5\text{mm, or } 0.1H_S$$

To achieve this, the first point was at a depth of 2.5mm i.e. ($0.5\Delta y$), and the last point was at a depth of 97.5mm i.e. ($200\text{-}0.5\Delta y$).

For the longitudinal incremental change, Δx, the method used in the initial investigation was adopted. Consideration was given to the fact that the slot length varied for each aspect ratio. This meant that a constant Δx would give an increased number of vertical profiles as the slot length increased, alternatively, the number of profiles could be kept constant resulting in a different Δx for each aspect ratio. It was decided that since both methods had advantages and disadvantages, depending on the aspect ratio, that a combination of both would be used. In general, the value of Δx for the BFS, A_S=15, and A_S=10 was 25mm, or $0.5H_S$, and for A_S=5 the value of Δx was 12.5mm, or $0.25H_S$.

For both the upstream and downstream regions of the flow, Δy remained the same i.e. 5mm, allowing points in the profiles to tie in horizontally with the slot profiles. It was established that there was no requirement for the same detail of measurements in the upstream section, and therefore profiles were generally taken at longitudinal increments of 50mm (or H_s). A similar approach was adopted for the downstream section, with more detail provided immediately downstream of the FFS.

5.3.7 LDV Sampling Rate and Number of Samples

A method of establishing the data sampling frequency is given in section 4.5.3, however, this method is restricted to the larger velocities such as those experienced in the streamwise direction. A method of defining the correct number of samples in each record has also been introduced in section 4.5.3 which is applicable to all scales and components of velocity expected in this investigation.

The validity of the data from each point measurement is highly dependent on the sampling frequency and the number of samples taken. At this stage there was no formal criteria in setting these conditions. However, it was evident that they were highly dependent on the flow conditions, in particular the location of the control volume within the flow field and the clarity of the water itself. In general the sampling rate varied between 40-100hz throughout this investigation. Certain areas where the velocity was low, such as the upstream corner of the slot, the sampling rate dropped to as low as 10hz. On average, these sampling rates were maintained at each traverse point for 60 seconds, resulting in approximately 2000-6000 samples in the faster flow regions, and reducing to approximately 500-1000 in the slower regions.

5.4 MAIN STUDY: MEAN VELOCITY CHARACTERISTICS

5.4.1 Introduction

The previous sections outlined the physical conditions imposed by the flume geometry and the hydraulic conditions of the flow which will be applied to the main study. The procedure for data acquisition and data processing have also been given. This section describes the results obtained from the main investigation coupled with analysis of these results.

As outlined in the main introduction of this chapter, much of the analysis focuses on the mean velocity characteristics, as this property provides more detail and is more widely discussed in the literature, providing comparative methods and analysis techniques. The turbulence characteristics of the flow are also presented, however, the omission of the Reynolds stresses from this investigation, due to equipment limitations and time restrictions. meant that some turbulent features could not be investigated. This section focuses on the mean velocity characteristics, and section 5.5 deals with the turbulence characteristics.

Twelve cases were investigated using the experimental conditions previously documented. Table 5.2 summarises the hydraulic conditions imposed. It should be noted that the design values of Re were not accurately achieved, however, the values attained are considered to be within an acceptable limit of these design values.

Table 5.2 - Hydraulic Conditions for Main Investigation

Case	u_o (ms^{-1}) upstream value	Q_o (m^3s^{-1}) per unit width	Re (actual)	Froude number	u_{max} (ms^{-1}) upstream	Slope S ($x10^{-4}$)
BFS-1	0.286	0.014	14300	0.408	0.322	0.660
BFS-2	0.379	0.019	18950	0.541	0.421	1.340
BFS-3	0.462	0.023	23100	0.660	0.536	1.810
15-1	0.285	0.014	14250	0.407	0.323	0.680
15-2	0.378	0.019	18900	0.540	0.429	1.410
15-3	0.462	0.023	23100	0.660	0.540	1.890
10-1	0.281	0.014	14050	0.401	0.314	0.630
10-2	0.378	0.019	18900	0.540	0.421	1.360
10-3	0.456	0.023	22800	0.651	0.540	1.780
5-1	0.268	0.013	13400	0.383	0.308	0.610
5-2	0.375	0.019	18750	0.535	0.413	1.290
5-3	0.461	0.023	23100	0.660	0.525	1.850

NB: Values calculated with respect to the local mean velocity at channel centreline.

5.4.2 2-Component Velocity Vector Plots

For each of the flow conditions, the 2-component velocity vector plots (for u and v) have been constructed, see figures 5.6-5.9 (a)-(c).

For presentation purposes, these plots illustrate the main area of interest, i.e. the flow immediately downstream of the BFS. The vectors have been normalised using u_{max}, which represents the maximum streamwise velocity in the upstream channel section for that flow

condition, see table 5.2. The y-axis is scaled greater than the x-axis to provide a clearer illustration of the flow, therefore the v-component is consequently exaggerated.

5.4.2.1 Velocity Vectors - BFS

The main feature observed in all three cases is the single recirculating region immediately downstream of the BFS, see figure 5.6 (a)-(c). The zero streamline, ψ=0, also called the separating streamline, has been superimposed on each figure to illustrate the boundaries of the recirculation region and to verify the reattachment point. The reattachment lengths obtained in this way (table 5.3) are compared to the results from the reattachment length investigation. It can be seen that these values, denoted as $R_{L(s)}$, are slightly less than those obtained in the reattachment study, however, this difference is no more than 4%.

Another characteristic which can be obtained from this region of flow is the maximum (negative) velocity in the recirculation region, u_{Rmax}. This was measured in a similar investigation by Jasem (1990), where it was observed that values of u_{Rmax}/u_o varied between 0.1-0.3, with the lower values attributed to larger slot aspect ratios. The location of these maximum recirculating velocities were at a distance of approximately x/H_s=5 from the BFS. The present results indicate that u_{Rmax}/u_o varies between 0.21-0.28, and are located at a distance of approximately x/H_S=3.5-4 downstream of the BFS at a height of y/H_S=0.05 from the channel bed.

The region in the upstream corner of the slot is characterised by very low velocities, but could not be considered as being stagnant. It is possible that a smaller secondary recirculation exists in this corner, driven by the flow from the primary recirculation zone, however this was not determined due to the low spatial resolution of the measurements.

5.4.2.2 Velocity Vectors - As=15

The following cases now consider slot flows. The velocity vector plots for A_S=15 are presented in figure 5.7 (a)-(c). These plots show the key feature of a recirculation zone in the slot. The centre of this recirculation zone can be clearly seen, as can the magnitude and direction of the vectors close to the channel bed. The $R_{L(s)}$ values again compare favourably with the R_L values, where $0.96<R_{L(s)}/R_L<1.16$.

The maximum (negative) recirculating velocities, u_{Rmax}/u_o, range between 0.23-0.27, which are also comparable to those observed for the BFS. The longitudinal location of these values are again in the central region of the recirculation zone, x/H_s=3-4, and their vertical location from the channel bed is also similar at y/H_s=0.05-0.15.

An additional area of interest is the flow which deflect upwards and over the FFS. This produces a small region of almost stagnant flow in the downstream corner of the slot, however, the scale of measurement does not show this region clearly. The extent of this smaller recirculation zone within the slot appears to be limited to a length of x/H_s=1.5 upstream of the FFS and to a very small depth, y/H_s<0.15. The flow at the top of the FFS produces a secondary recirculation zone, however, as with the initial investigation (section 4.4) the scale of measurements does not show this in detail. The plot for case 15-2 does show a velocity vector at the top of the FFS of low magnitude which is attributed to the secondary recirculation zone, however, in general this zone is not well represented in these results.

The velocity vector profile which corresponds to the flow at the edge of the FFS, i.e. x/H_s=15 and y/H_s=1.05, indicates a large increase of velocity, particularly in the vertical direction. The components of the velocity vector located at the edge of the FFS are given in table 5.3.

5.4.2.3 Velocity Vectors - As=10

The three cases for A_s=10 once again show a recirculation zone with reattachment on the slot bed, see figure 5.8 (a)-(c). The reattachment length can again be identified using both the velocity vectors close to the channel bed and the superimposed separation streamline. The $R_{L(s)}$ values in these cases are once again comparable to the R_L values from the reattachment length investigation with values ranging between $0.99<R_{L(s)}/R_L<1.03$, see table 5.3.

The velocity vectors close to the channel bed between the reattachment point and the FFS remain very low with no definite direction. This occurs due to a combination of the low velocities which occur near flow reattachment and the low velocities associated with the recirculation zone in the downstream corner. When the FFS is further downstream, the flow develops a new boundary layer after reattachment whereupon the velocities close to the channel bed increase as the boundary layer develops downstream. At some point downstream the flow then deflects over the FFS, however, in this case the flow is forced to deflect at an earlier stage prior to the development of the new boundary layer. Less flow is therefore transferred from the upper channel section into the slot, evident from the streamline plots (see section 5.4.5) and hence the velocity of the flow in this region is less. The

presence of the FFS so close to reattachment reduces the velocity close to the channel bed, therefore distorting the longitudinal velocity gradient, *du/dx*. The separation streamline is forced to develop faster and hence a lower reattachment length occurs. This is discussed in more detail in section 5.4.5.

The maximum (negative) recirculating velocities range between u_{Rmax}/u_o=0.22-0.26, at a location of x/H_s=4 and y/H_s=0.05-0.15. These being comparable to the previous cases.

The velocity components over the FFS are also similar to those observed previously, where the vertical component is significantly higher than anywhere else in the flow field.

5.4.2.4 Velocity Vectors - As=5

This aspect ratio was investigated in an attempt to establish whether similarities exist between slots which support flow reattachment along the channel bed and those which do not. The vector plots for the three cases (figures 5.9 a-c) show a recirculating cell which does not reattach along the slot floor. The separating streamline can be seen to impact onto the FFS, where the velocity vectors can also be seen to diverge either upwards and over the FFS, or downwards into the slot.

The maximum (negative) recirculating velocities, u_{Rmax}/u_o for these cases give larger values ranging between 0.34-0.36. The velocity vectors indicate that some flow deflects up and over the FFS whilst the remainder is recirculated back into the slot. These maximum recirculating velocities are located at x/H_s=4, the same distance from the BFS as that observed in the previous aspect ratios, however, in these cases they are very close to the FFS, suggesting that the flow deflected down the FFS influences these. Their vertical location from the channel bed is also similar to the previous examples at y/H_s=0.05-0.15.

In general, the recirculating flow characteristics are similar for the cases where the separation streamline attaches to the slot bed. The values of u_{Rmax}/u_o are similar irrespective of the slot aspect ratio and Reynolds number, with values ranging between 0.21-0.28. The large velocity vector which can be observed over the FFS can also be seen to have a similar value, irrespective of aspect ratio and Reynolds number for the slots which exhibit reattached flow within the slot.

Table 5.3 - Reattachment Length, R_L, and Maximum Recirculation Velocities, u_{Rmax} for Slot Flows

Case	u_O	u_{Rmax}	u_{Rmax}/u_O	x/H_S (u_{Rmax})	y/H_S (u_{Rmax})	u_F/u_O	v_F/u_O	$R_{L(S)}$	R_L	$R_{L(S)}/R_L$
BFS 1	0.286	-0.060	-0.211	4	0.05	-	-	8.6	8.9	0.97
BFS 2	0.379	-0.091	-0.241	4	0.05	-	-	7.9	8.2	0.96
BFS 3	0.462	-0.130	-0.282	3.5	0.05	-	-	8.0	7.8	1.03
15-1	0.285	-0.078	-0.273	3	0.15	0.765	0.600	8.5	7.3	1.16
15-2	0.378	-0.089	-0.236	4	0.15	0.728	0.317	7.8	8.3	0.96
15-3	0.462	-0.116	-0.251	4	0.05	0.734	0.779	8.5	7.9	1.08
10-1	0.281	-0.064	-0.226	4	0.15	0.875	0.544	7.4	7.2	1.03
10-2	0.378	-0.091	-0.241	4	0.05	0.611	0.505	7.6	7.7	0.99
10-3	0.456	-0.117	-0.257	4	0.05	0.855	0.450	8.2	8	1.02
5-1	0.268	-0.091	-0.340	3.25	0.15	0.713	0.463	-	-	-
5-2	0.375	-0.128	-0.341	4.25	0.05	0.717	0.328	-	-	-
5-3	0.462	-0.167	-0.361	4.25	0.05	0.933	0.537	-	-	-

NB: (-) Not applicable.
Subscript *F* denotes FFS.

A more detailed discussion of the mean flow characteristics in the downstream region of a BFS is given below. This also includes the region beyond reattachment for the BFS cases, and the FFS regions of the slot flow cases.

5.4.3 Mean Non-Dimensional Velocity Profiles

Figures 5.10-5.13 contain velocity profiles of u/u_{max} in the region between $0 \leq x/H_s \leq 10$, with the exception of $A_s=5$ which only includes the slot region, $0 \leq x/H_s \leq 5$.

The figures display profiles typical of that observed in a shear layer, where the velocity gradient, *du/dy*, for each profile is 'nearly' constant within the boundaries of the newly developed shear layer. The boundaries of the shear layer are defined in section 5.4.7. It has been established that the velocity profile in the upstream section has a log-law profile, however, the profiles in the expanded region deviate from this and coincide well with a Gaussian distribution, as will be discussed later. The distance over which *du/dy* is constant within each profile can be seen to increase with x/H_S. At reattachment, a nearly constant velocity gradient, *du/dy*, extends throughout the flow depth.

5.4.4 Mean Non-Dimensional Streamlines of u_m

The mean non-dimensional streamlines throughout the flow field were calculated for each flow case. The streamline plots can be seen in figures 5.14-5.17 (a)-(c), which show the streamfunctions, ψ, non-dimensionalised by $(u_{max}.H_s)$. The use of streamlines in flow analysis and the method used to calculate them are discussed in more detail in section 2.5.3.

In general, these streamlines indicate the recirculation region, bounded by the streamline, ψ=0, and the upstream corner of the slot. A selection of streamlines have been included to illustrate the flow field, including the maximum streamfunction observed in the recirculation region.

For the cases which include a FFS, the general streamline characteristics can be seen as they deflect up and over the FFS. These do not show the small recirculating region at the base of the FFS or the recirculating cell at the top of the FFS. This is again due to the spatial resolution of the flow measurements missing this detail.

The streamlines throughout the upper channel depth at x/H_s=0 are packed closer than that observed further downstream at and beyond reattachment. It is also worth noting that the streamlines above the line of zero velocity in the recirculation zone are more closely spaced than those below, indicating a more rapid change in the velocity gradient.

5.4.4.1 Mass Flow Deflected Upstream at Reattachment

A feature of this flow type documented in the literature is the mass flow rate deflected into the recirculation cell at the point of flow reattachment (Etheridge and Kemp, 1978). The first step was to determine the mass flow rate generated in the new shear layer at the point of reattachment. This was achieved by obtaining the non-dimensionalised streamline, $\psi/(u_{max}H_s)$, which corresponds to the depth of the upper boundary of the shear layer, y_{OB}/H_s, at reattachment, which will be denoted as q_{shear}. The next stage is to determine the maximum mass flow rate in the recirculation cell, denoted as q_r. Therefore the ratio q_r/q_{shear} corresponds to the fraction of the mass-flow rate in the shear layer which deflects at reattachment into the recirculation zone.

This method was applied to the current data and the results are documented in table 5.4. Results are also presented for As=5, since the same method can be applied by using the

downstream location of the FFS to represent flow reattachment. The definition and location of the shear layer boundaries are given in section 5.4.6.

Table 5.4 - Characteristic Streamfunctions in Recirculation Cell and at Reattachment

Case	Mass flow rate in recirculation region, q_r	Depth of outer boundary at reattach, y_{OB}/Hs	Mass flow rate in shear layer, q_{shear}	Ratio q_r/q_{shear}
BFS-1	0.09	2.00	1.00	0.09
BFS-2	0.11	2.00	1.00	0.11
BFS-3	0.12	2.00	1.00	0.12
15-1	0.13	2.00	1.00	0.13
15-2	0.10	2.00	1.00	0.10
15-3	0.11	2.00	1.00	0.11
10-1	0.08	2.00	1.00	0.08
10-2	0.09	2.00	1.00	0.09
10-3	0.09	2.00	1.00	0.09
5-1	0.12	1.50	0.47	0.26
5-2	0.13	1.50	0.47	0.28
5-3	0.12	1.50	0.47	0.26

In the cases where flow reattachment occurs on the slot bed, the outer boundary of the shear layer extends to the free-surface. Since the outer boundary reaches the free-surface at a longitudinal distance prior to flow reattachment, the shear layer has therefore extended throughout the full flow depth. The ratio q_r/q_{shear} is consistent for these cases where it can be seen that approximately 10% of the new shear layer is deflected upstream at reattachment. In the single investigation by Etheridge and Kemp (1978), they observed that one-sixth of the flow was deflected into the recirculation zone at reattachment. This larger proportion appears to be caused by a reduction in the depth of the outer boundary of the shear layer at reattachment, resulting in a lower mass-flow rate in the new shear layer.

In the cases where A_s=5, the depth of the outer boundary is much less, corresponding to a lower mass flow rate in the shear layer. Despite this, the ratio q_r/q_{shear} has a larger value of 0.26 which indicates that over one-quarter of this thinner shear layer is deflected down the FFS into the slot.

5.4.4.2 Flow Mass Deflected into Slot

The effect of the FFS close to reattachment has been discussed for A_s=10 (section 5.4.2.3). It was observed that the small recirculation cell at the base of the FFS and the flow near reattachment combine to produce a larger region of low velocity. This reduction of flow velocity prevents the downstream migration of the reattachment length, which subsequently reduces the size of the primary recirculation cell. The streamline plots (figures 5.14-5.17) also illustrate the characteristics of the flow between reattachment and the end of the slot. As the aspect ratio decreases, the flow mass deflected below the height of the step can be seen to decrease.

To quantify this, the maximum flow deflected into the region $y_O/H_s \leq 1.0$ was calculated. Using the BFS cases as an index, the streamline corresponding to $y_O/H_s=1.0$ at a large distance downstream of reattachment will represent the normal flow mass below this depth without the influence of a FFS. The maximum streamline at this depth for the slot configurations will therefore represent the flow mass deflected into the slot region. If Q_{slot} represents the normalised flow rate in the expanded region, then q_{slot} represents the flow mass deflected below the step height. Figure 5.18 illustrates the values of q_{slot} for each of the cases investigated. A linear relationship can be seen for the slot configurations, whereby q_{slot} increases as the aspect ratio increases. Assuming that this linear relationship continues, the aspect ratio which corresponds to the BFS can be estimated at A_s=20-25.

5.4.5 An Expression for the Separating Streamline, ψ=0

It has been established that the streamfunction, ψ=0, plays an important role in defining a recirculation region. It is therefore important for further analysis to model this phenomena. Jasem (1990) gives an expression for the shape of this streamline in a BFS flow:

$$y = H_s\sqrt{1-(x/R_L)^2} \qquad \textbf{Equation 5.2}$$

where, $y = y/Hs$,

$x = x/Hs$,

R_L = Reattachment length.

Figures 5.19-5.21(a)-(c) compare this elliptical curve (denoted as 'sep str (fnc)'), with the experimental separation streamlines (denoted as 'sep str (exp)'). These figures show good

agreement between the two curves, and therefore this expression is representative of the separation streamline in the present investigation.

5.4.6 Shear Layer Development

Using the assumption that the velocity gradient *du/dy* is nearly constant within the shear layer for any longitudinal distance x/H_S, the shear layer thickness can then be defined as the distance between the inner and outer boundaries of this region of constant velocity gradient. Where u_O is the mean longitudinal upstream velocity, these boundaries can be described as the curves which connect the points where u/u_O=1, for the outer boundary, and u/u_O=0 for the inner boundary. Figure 5.22 shows a schematic representation of the shear layer containing the terms used in this part of the investigation.

From plane mixing layer theory, these boundaries have a linear relationship, where each deviates from the point of separation at angles of α_1=4.8° and α_2 =9.5° for the outer and inner boundaries respectively. Ötügen et al (1992) also defines the shear layer thickness by equation 2.5.2, which assumes that the velocity profile through the depth for any location, x/H_S, has a constant velocity gradient, *du/dy*.

The boundaries of the shear layer were calculated using the interpolation technique given in equation 5.3, and depicted in figure 5.23:

If,

$$\frac{(x_t - x_1)}{(x_2 - x_1)} = \frac{(y_t - y_1)}{(y_2 - y_1)} \qquad \textbf{Equation 5.3(a)}$$

therefore,

$$y_t = \left[\frac{(x_t - x_1)}{(x_2 - x_1)}.(y_2 - y_1)\right] + y_1 \qquad \textbf{Equation 5.3(b)}$$

where, y_t - is the target value,

x_t - is the known x co-ordinate for y_t, in this case, u=0 and $u=u_O$,

(x_1,y_1), (x_2, y_2) - are known points.

This procedure was performed throughout the shear layer development region, $0 \le x/Hs \le R_L$. The resulting shear layer boundaries for each group of aspect ratios are given in figures 5.24 (a)-(d), where each figure gives the inner and outer boundaries of the shear layers for each aspect ratio.

5.4.6.1 Outer Boundary of Shear Layer

Figure 5.24 (a)-(d) illustrates the developing shear layers and their respective boundaries for all the cases. By definition from plane mixing theory, the outer boundary begins at the point of flow separation, however, with this flow type, the velocity profile at the BFS, x/H_s=0, has a log-profile, where the mean velocity, u_o, does not occur at y=0, but at a height, h_o, from the channel bed (see figure 5.22). In reality, the shear layer will develop at the point of flow separation, and will therefore not affect u_o until the shear layer migrates through the vertical distance, h_o, which defines the height where u_o occurs. The results indicate a slower growth of the outer boundary over an initial distance of x/H_s=3. As the shear layer continues to grow due to the entrainment of the surrounding fluid, the flow beyond h_o is influenced and the outer boundary appears to expand at an increased rate.

In the region between flow separation and reattachment there is a transition in the mean velocity from the larger upstream value, u_o, to the lower mean velocity of the expanded region, u_s (figure 5.22). Therefore, the development of the outer boundary will continue as long as the original flow region maintains a minimum velocity of u_o.

The outer boundaries for A_s=15 and 10 are similar to each other, however, the outer boundary for these cases approach the free-surface earlier than the BFS cases, implying that the shear layer grows more rapidly. As the boundaries approach the free-surface, there is a rapid increase in their growth, which suggests a sudden decrease in u_{max} towards u_o.

The outer boundaries for A_s=5 show a similar growth rate over the smaller distance $0 \leq x/Hs \leq 5$. Near the end of the slot, the rate of growth decreases and it appears that the boundary begins to recede in depth. This could be attributed to an increase in velocity as the flow accelerates over the FFS, causing the depth of u_o to reduce back towards its original depth.

5.4.6.2 Inner Boundary of Shear Layer

The inner boundary of the shear layer can also be seen in figures 5.24(a)-(d). By definition from plane mixing layer theory, the inner boundary will develop from the point of separation, as can be seen in the figures.

From the results, the development of this inner boundary is similar, irrespective of the aspect ratio. Close observation after flow separation indicates an initial rapid growth of this

boundary into the slot region. The growth rate reduces to a more stable value after approximately one step height downstream of separation. This may be explained by the large velocity gradient which exists in this region, subsequently increasing the shearing stress between the two flows, and therefore increasing the rate of flow entrainment into the slot. In addition to this, the recirculating flow which moves up the BFS will recirculate back into the shear layer, thereby creating an additional positive flow velocity which will subsequently reduce the depth where u=0.

As the inner-boundary moves closer to the slot bed, there is an increase in its growth as it attaches to the slot bed at the point of flow reattachment. This is caused by the rapid deceleration of the streamwise velocity close to reattachment as it changes from a negative to a positive velocity, and hence the depth of u=0 will also reduce. This is explained by the Coanda effect, whereby the shear layer boundary struggles to entrain flow due to the presence of the channel bed, which forces the entrained flow upstream away from the shear layer (section 2.5.6).

5.4.6.3 Universal Shear Layer Boundaries - Angle of Deviation

From plane turbulent shear layer theory, the outer and inner boundaries develop linearly from the point of separation at angles, α_1 and α_2 respectively, where experiments have determined these values as α_1=4.8^o and α_2 =9.5^o (Rajaratnam, 1976). The current flow cannot be considered as simple as a plane turbulent shear layer, since the inlet flow has a log-law profile and the presence of the channel bed and recirculating flow complicates this flow type. However, in order to identify the applicability of this shear layer theory, the angles at which these boundaries depart from the point of flow separation were determined.

Owing to the non-linear development of these boundaries, these angles have been determined from the line of best fit which connects the points creating the boundary. Table 5.5 summarises the values calculated for these angles.

In table 5.5, the overall mean angle for each boundary excludes the results from A_s=5, as this case is clearly different from the other aspect ratios. The mean angle measured for the outer boundary was α_1=4.59^o, which is similar to the value of 4.8^o for a plane mixing layer. However, the mean angle for the inner boundary was α_2=4.96^o, which is considerably less than the value of 9.5^o for plane mixing layers.

Table 5.5 - Shear Layer Boundary Angles of Deviation from Point of Flow Separation

Case	α_1	α_2	Case	α_1	α_2	Case	α_1	α_2	Case	α_1	α_2
BFS-1	4.34	5.1	15-1	5.65	4.42	10-1	4.65	5.32	5-1	2.59	5.76
BFS-2	4.73	5.1	15-2	3.99	4.6	10-2	4.83	5.11	5-2	2.8	4.8
BFS-3	3.64	4.27	15-3	5.5	5.16	10-3	3.97	5.58	5-3	3.85	5.82
BFS Mean	4.23	4.82	15	5.05	4.73	10	4.48	5.34	**As=5**	**3.08**	**5.46**
Mean (not As=5)	**4.59**	**4.96**									

NB: All values in degrees, where α_1 positive above horizontal plane, and α_2 positive below horizontal plane.

The results may be better interpreted as plane compound mixing layers, where the stagnant fluid in the expanded region for a plane mixing layer is replaced by a fluid of velocity, u_1, where $u_1<u_o$. Owing to this new velocity component, the angle α_2 may reduce to as much as 1^o as u_1 approaches u_o (Rajaratnam, 1976). In plane mixing layer theory the expansion of the flow is considered as infinite and therefore it does not consider the presence of a recirculation cell. Therefore, the recirculated flow which feeds around the BFS and back into the downstream direction can be treated as this additional velocity component, u_1.

The mean value of α_1 for A_s=5 has a lower value of 3.08^o. Although the deviation of this boundary is similar to the other cases over the initial development of the shear layer, the cessation of shear layer growth towards the end of the slot reduces α_1. The inner boundary angle, α_2, is similar in value to those observed for the other aspect ratios.

5.4.6.4 A Universal Function for Shear Layer Boundaries

Due to the similarity of the boundary angles for each aspect ratio, an attempt was made to develop a universal function to represent them. The previous section which discussed the angle of deviation of the boundaries assumed a linear relationship, however the results indicate a more complex relationship. Despite their non-linear characteristics, an empirically derived equation has been proposed by Jasem (1990) for the inner boundary of the shear layer. The following two sections represent an attempt to better describe these boundaries.

5.4.6.5 Outer Boundary Universal Function

The outer boundary of the shear layer for each case displayed a great deal of similarity with little deviation observed between the extreme conditions. Due to this, the boundary can be expressed by a single universal equation which relies on only two parameters, the distance, x, and the initial depth of the mean velocity, h_o, at x/H_s=0.

The empirically derived function is represented graphically in figure 5.25 and it takes the form:

$$\frac{y}{H_s} = \frac{h_o}{y_o} e^{0.032(\frac{x}{H_s}^{1.3})}$$

Equation 5.4

where, y_O - is the upstream flow depth,

h_O - initial depth of u_O at x/H_s=0.

This equation is therefore valid in the region $0<x/H_s<R_L$, however, at this stage there is no evidence that it holds for greater flow depths.

5.4.6.6 Inner Boundary Universal Function

The inner boundary of the shear layer for each of the aspect ratios, also gave similar profiles, however, the boundaries differed in length owing to their dependency on the reattachment length, see figure 5.24(a)-(c). From this set of results, it can be seen that the shape of the inner boundary is similar to the curved profile of the streamfunction, ψ=0, as can be seen in figures 5.19-5.21. The shape of this streamfunction is described by equation 5.2, which therefore served as the basis for an expression for the inner boundary. The following expression gave the best fit with the experimental data:

$$\frac{y}{H_s} = H_s\sqrt{0.6(1-\frac{x}{H_s R_L})}$$

Equation 5.5a

This equation compares favourably with the experimental results between $1.5<x/H_s<R_L$ as can be seen in figures 5.26-5.28(a)-(c). In order to include the initial stage of the profile, an additional expression has been introduced. The region which this curve affects is limited to the rapid expansion of the shear layer inner boundary between $0<x/H_s<1.5$, and it takes the linear form:

$$y/H_s=1-(0.25x/H_s)$$ **Equation 5.5b**

From figures 5.26-5.28(a)-(c), it can be seen that these two expressions combine to give a suitable approximation of the inner boundary of the shear layer.

5.4.6.7 Shear Layer Thickness, δ_S

The shear layer thickness, δ_S, was found by taking the difference in height between the outer boundary, u/u_o=1, and the inner boundary, u/u_o=0. Figure 5.29 illustrates the profiles obtained from the experimental results for δ_S plotted against x/H_S. Although there is some scatter between the curves, there is still a reasonable degree of similarity between them. The differences observed between these curves is attributed to the initial thickness of the shear layer at separation, however the rate of growth of these shear layers is similar in all the cases.

The following expression gave a best fit curve from the experimental data:

$$y_o=h_o e^{0.17x} \qquad \textbf{Equation 5.6}$$

For clarity, a single curve using h_o=0.45 has been plotted on figure 5.29. It can be seen that the shape of this curve is similar to the trend observed from the experimental curves, where δ_S increases exponentially with longitudinal distance.

The shear layer thickness was also determined using the assumption that the velocity gradient, du/dy, within the shear layer is constant and applies to the region between u=0 and $u=u_O$, see section 2.5.2. This can be seen visually from the mean longitudinal streamwise velocity profiles in figures 5.10-5.13(a-c), where the central portion of these profiles have a velocity gradient which is nearly constant, and therefore, the extent of this constant velocity gradient describes the shear layer. This method was adopted by Ötügen et al (1992), where the local maximum of mean velocity gradient was used. The problem associated with this method is that the velocity gradient is not constant across the shear layer, where low gradients exist at the outer region and increase in value towards the inflexion point in the centre of the shear layer. Therefore, the use of the maximum velocity gradient will underestimate the shear layer thickness.

In figure 5.30, the shear layer thicknesses obtained using the velocity gradient method are compared to a curve using the previous method (as used in figure 5.29 for h_o=0.45). It can be seen that the values of δ_S using the velocity gradient method are less than those observed using the shear layer boundary method, particularly as the longitudinal distance increases. In addition to the lower shear layer thicknesses, there is also a larger scatter between the different cases which cannot be attributed to any specific characteristic of that flow type. Also, the growth of the shear layer is different between the results, with some cases increasing, decreasing or constant throughout the longitudinal distance.

The investigation by Ötügen et al (1992) concluded that the development of the shear layer thickness was not linear, and that the thickness increased with longitudinal distance, as observed in the current investigation.

5.4.7 Velocity Profiles in the Recirculation Region

The mean velocity distribution in a mixing layer has been shown experimentally to have a Gaussian distribution (Rajaratnam, 1976). An expression for this distribution is described as follows:

$$\tilde{U} = \exp(-0.693\eta^2)$$

Equation 5.7

where $\tilde{U}$ is related to the experimental results by the non-dimensionalised form:

$$\tilde{U} \equiv \frac{u_{max} - u}{u_{max} - u_{min}}$$

Equation 5.8

where, u_{max} - is the maximum velocity at any cross-section, x,

u_{min} - is the minimum velocity at any cross-section,

u - is the streamwise velocity at depth y from the channel bed,

η - is the non-dimensionalised depth, given by

$$\eta \equiv \frac{y - y_{min}}{b_{0.5}}$$

Equation 5.9

where, y_{min} - is the depth of u_{min}, and,

$b_{0.5}$ - is the half-width, described as,

$$b_{0.5} = \frac{y_{max} - y_{min}}{2}$$

Equation 5.10

where, y_{max} - is the depth of u_{max}.

This expression was initially derived from experimental results for plane turbulent jets, however, the same expression was used for the velocity downstream of a BFS by Nakagawa and Nezu (1987). In their investigation, the expression was used to describe the velocity

distribution not only between flow separation and reattachment, $0 \leq x/Hs \leq R_L$, but also for an extended downstream distance of $R_L \leq x/Hs \leq 18$. For the flow downstream of reattachment, the minimum velocity becomes a positive value, $u_{min} > 0$. Due to the development of a new sub-boundary layer, this was taken as the velocity at the edge of this layer, therefore, $y_{min} = \delta$.

Nakagawa and Nezu (1987) found that their experimental results coincided well with the Gaussian distribution, particularly as the profiles approached the reattachment point. After reattachment, a new sub-boundary layer was formed, and consequently the half-width, $b_{0.5}$, reduces gradually downstream. As the downstream distance increased, it was also observed that the velocity distribution began to deviate from the Gaussian distribution.

This method was applied to the BFS cases, as these provided the required downstream distance without the interference of a FFS. Another variation on the Gaussian distribution has been applied to the other cases and is discussed later.

The results for this investigation are presented in figures 5.31-5.33. Each figure gives a separate graph illustrating the velocity profiles upstream of reattachment and another for the velocity profiles downstream of reattachment between $R_L \leq x/Hs \leq 30$ for each case. The profiles in the region $x/Hs \leq R_L$ are considered first. Whilst most of the profiles could be described by a Gaussian distribution of some form, it appears that this distribution changes with longitudinal distance, x/Hs. The velocities in the profile closest to the BFS show little change in magnitude both at the lower and higher depths, with a rapid change in magnitude in the central depth region. This is attributed to the fact that the higher and lower depths are unaffected by the new shear layer whilst a relatively small band in the centre are affected. As the profiles move further downstream, and the shear layer spreads through the depth, the Gaussian distribution flattens out. Another observation is that the Gaussian distribution tends to overestimate the velocity distribution at larger flow depths, this can also be seen in the results by Nakagawa and Nezu (1987).

The results for $x/H_s > R_L$ show that the experimental curves coincide well with the Gaussian distribution, particularly for the profiles close to reattachment. As the longitudinal distance increases, the profiles can be seen to become flatter than the Gaussian distribution, a feature also observed by Nakagawa and Nezu (1987).

Another variation on the Gaussian distribution was used by Jasem (1990) for the flow downstream of a BFS. This expression takes the form:

$$\tilde{U} \equiv (1+t)e^{-t}$$

Equation 5.11

where,
$$t = 1.67(y / y_b)^{2.5}$$ **Equation 5.12**

The experimental values are related to this expression in the following non-dimensional form:

$$\widetilde{U} \equiv \frac{u - u_{\min}}{u_{\max} - u_{\min}}$$ **Equation 5.13**

where, u - is the streamwise velocity,

y - depth from the free surface,

y_b - normalising depth, defined as the depth measured down from the free-surface where:

$$u = (u_{max} + u_{min})/2$$ **Equation 5.14**

Figures 5.34-5.37 illustrates this distribution for all the cases, including the results for the A_s=5. Also, in an attempt to determine the universality of this expression, the BFS flow from the initial investigation was also used, see section 4.3.6.

The results indicate a good correlation with little scatter between the distribution of equation 5.11) and the experimental velocity profiles. As the longitudinal distance from the BFS increases, the profiles can be seen to change about a point of inflexion at approximately y/y_b=1. Equation 5.11 coincides better with the profiles located in the mid-region of the recirculation zone, i.e. x/H_s=3-4.

To account for the longitudinal location of the velocity profile within the recirculation region, a new power term was introduced by the author to equation 5.11.

$$t = 1.67(y / y_b)^{c}$$ **Equation 5.15**

where,

$$c = \frac{5}{\sqrt{x / H_s}}$$ **Equation 5.16**

Adopting this updated version of the universal velocity profile, individual plots were constructed for x/H_s=1, 3, 5 and 7, for each of the BFS cases. From figure 5.38, it can be

seen that the updated Gaussian distribution coincides better for the profiles at their respective longitudinal distance.

It can be concluded that the expression used by Jasem (1990), equation 5.11, provides a mean representation of the velocity profiles throughout the recirculation zone, where at some point in the flow, approximately x/H_s=3-5, the expression best describes the experimental results. A modified expression has been given, equation 5.15 and 5.16, which accounts for the location of the velocity profile within the recirculation zone. This expression is more accurate throughout the flow depth, particularly for the profiles closer to the BFS. It would appear that this over-estimates the velocities close to the channel bed, but only in the region approaching flow reattachment.

5.4.8 Velocity Profiles Downstream of Reattachment

So far, the analysis of the mean velocity has concentrated in the region from the point of flow separation to the point of flow reattachment. The flow beyond reattachment is now considered.

The literature provides documentation on the interest both on the immediate response to the perturbation and in the relaxation back to the thin-shear layer state. Bradshaw and Wong (1972) conducted a detailed investigation on the response of the flow beyond the separation region induced by a BFS. It was concluded from this investigation that the key parameter influencing the relaxation of the flow back to the thin-shear layer state was the fraction of the shear layer mass flow that is deflected upstream at reattachment. If this fraction is appreciable, the large eddies in the shear layer are torn in half, producing a turbulence structure which is different to that found in any conventional shear flow. Analysis of the mean velocity downstream of reattachment concluded that the law of the wall formulation was inapplicable within a distance of at least 30 times the shear layer thickness at reattachment.

Nakagawa and Nezu (1987) used the Gaussian distribution (equation 5.7) to analyse the velocity profiles beyond reattachment. This same method has also been applied to the current investigation, and is detailed in section 5.4.7. In their investigation Nakagawa and Nezu (1987) were limited to a distance of x/H_s=18 downstream of the BFS, where it was observed that the profiles began to deviate from the Gaussian distribution at this distance. The current measurements extend to a distance of x/H_s=33.

Nakagawa and Nezu (1987) also made an attempt to apply their data to the log-law curve. However, due to the limited longitudinal distance of their results, they were only able to confirm that the flow close to the boundary began to develop towards the law of the wall for depths up to $y/H_s<0.28$.

The BFS cases were plotted against the log-law distribution, figures 5.39 (a)-(c). These results clearly indicate a transition towards a log-law profile in the distance from $x/H_s=15$ to $x/H_s=27$. In all three cases however, it is not until $x/H_s=27$ where the velocity profile could be adequately described by the log-law.

5.5 MAIN INVESTIGATION: TURBULENCE CHARACTERISTICS

5.5.1 Introduction

The turbulence characteristics which develop in the shear layer of the expanded flow region will now be discussed. This turbulence is measured directly as the fluctuating velocity component in the longitudinal, vertical and lateral direction (namely u', v' and w') at each point measurement. These are converted to their respective root-mean square (RMS) values, which for brevity will subsequently be referred to as u', v' and w'.

In order to illustrate the turbulence characteristics of the flow, the data is presented in two formats. The first of these is in the form of the turbulent kinetic energy (TKE) balance of the flow. The total TKE is calculated from equation 5.17, which is an extension of equation 4.1 now including the lateral component, w'.

$$k = \frac{1}{2}\rho(u'^2+v'^2+w'^2) \qquad \textbf{Equation 5.17}$$

where, k - TKE/unit volume

ρ - density of fluid, kg/m^3

The turbulence characteristics which develop downstream of a BFS have been widely documented in the literature. However, as with most investigations on BFS flow, these tend to limit their coverage to measuring only u' and v'. Whenever these investigations require the lateral component, w', generally for turbulent energy balance analysis, the following assumption is made (Etheridge and Kemp, 1978; Driver and Seegmiller, 1985; Nakagawa and Nezu, 1987):

$$w'^2 = \frac{(u'^2 + v'^2)}{2}$$ **Equation 5.18**

therefore,

$$k = 3\rho\frac{\left(u'^2 + v'^2\right)}{4}$$ **Equation 5.19**

Plots of TKE have been produced for each velocity component and for the total as defined in equation 5.17. Each set of TKE results have been normalised by its respective value of u_{max}^2. Figures 5.40-5.55 illustrate both the expanded flow region (or slot region), and the downstream region (which includes the secondary shear layer developed by the FFS).

5.5.2 General Observations from the Turbulent Kinetic Energy Plots

Figures 5.40-5.43 clearly show the development of the turbulent free shear layer in the expanded flow region downstream of the BFS. The shear layer is characterised by the plume of high TKE values, beginning at the point of flow separation at the BFS and developing along the separation streamline. Although generated in the vicinity of the separation streamline, these high values continue to exist as they are transported downstream. This plume gradually dissipates as it progresses downstream, with the highest turbulence levels remaining at the mid-depth, approximately y/Hs=1.0, and reducing in intensity towards the free-surface and channel bed. Further evidence of this can be seen from the turbulence intensity profiles in figures 5.56-5.67.

The cases which include a FFS show an additional smaller region of turbulence development at the top of the FFS. Depending on the aspect ratio of the slot, the FFS can also deflect turbulent flow from the original shear layer back into the slot.

Figure 5.44 (a)-(c) illustrates the total TKE generated in the three As=15 cases. Due to the relatively large distance between the shear layer development region and the FFS, the core of high turbulent activity has dissipated sufficiently enough not to be greatly influenced by the presence of the FFS. As the flow depth contracts at the FFS, the secondary recirculation zone at the top of the FFS is clearly visible by the presence of increased turbulent activity. The secondary shear layer associated with this is smaller, however, the turbulence produced within this small zone can be seen to have a large level of intensity. The individual components of TKE for each of these cases can also be seen in figures 5.45-5.47 (a)-(c).

The influence of the FFS on the original shear layer turbulence becomes more apparent in the A_s=10 cases, see figure 5.48-5.51 (a)-(c). The high levels of turbulence spread further along the slot compared to the longer aspect ratios. This may be attributed to the shear layer impacting the FFS with larger turbulence intensities, whereupon a large amount of this turbulence is recirculated back into the slot becoming localised in the small recirculating zone which occurs at the base of the FFS. The increased turbulence which occurs close to the FFS can also be seen in the turbulence intensity profiles for these cases, figures 5.62-64 (a-c).

At the reduced aspect ratio of *As*=5, see figures 5.52-5.55, this concentration of turbulent flow within the slot region can be seen. Similarly, the turbulence intensity profiles (see figures 5.65-5.67) indicate these higher values for $y/Hs<1.0$, especially the profiles close to the FFS.

5.5.3 Turbulence Intensities

In order to investigate the universal nature of the results, and in keeping with the previous analysis on the mean velocity characteristics, the RMS values have been non-dimensionalised by the maximum upstream longitudinal velocity, u_{max}. The turbulence intensity profiles u'/u_{max}, v'/u_{max} and w'/u_{max}, are given for all the cases investigated in figures 5.56-5.67. Table 5.6 summarises the turbulence intensities observed in the key areas of the flowfield.

In table 5.6, the mean value of the maximum upstream turbulence intensity is used. As the upstream region of the flow is not affected by the slot, the normalised results should be consistent. The foot of table 5.6 contains the mean values of turbulence intensity for each component and a ratio of these values with respect to u'. These ratios compare favourably with the ratios for $u':v':w'$, presented by Nezu and Nakagawa (1993b) for open-channel flow, see section 4.6.

The maximum turbulence intensities observed in the slot region are also given in table 5.6. These values have been obtained from within the core of the shear layer. At the bottom of table 5.6, the mean value of each column is presented. These mean results are a good representation of all the cases, indicating that the ratio of the component turbulence intensities are consistent irrespective of aspect ratio or Reynolds number. The location of these values within the shear layer are also consistent, where they can be observed in the region bounded by $5.5 \leq x/H_s \leq 7$ and $0.65 \leq y/H_s \leq 0.95$.

Table 5.6 - Summary of Component Turbulence Intensities

Case	u_{max}	Max Upstream values			Max Slot Values			Max FFS values			Mean $0 \leq x/Hs \leq 10$		
		u'/u_{max}	v'/u_{max}	w'/u_{max}	u'/u_{max}	v'/u_{max}	w'/u_{max}	u'/u_{max}	v'/u_{max}	w'/u_{max}	u'/u_{max}	v'/u_{max}	w'/u_{max}
BFS-1	0.322	0.109	0.047	0.065	0.196	0.102	0.158	-	-	-	0.121	0.072	0.090
BFS-2	0.421	0.100	0.045	0.069	0.209	0.119	0.131	-	-	-	0.131	0.080	0.105
BFS-3	0.536	0.099	0.049	0.063	0.224	0.136	0.183	-	-	-	0.147	0.084	0.112
15-1	0.323	0.111	0.046	0.067	0.192	0.124	0.170	0.288	0.183	0.300	0.113	0.076	0.093
15-2	0.429	0.103	0.043	0.065	0.228	0.152	0.186	0.303	0.145	0.308	0.133	0.078	0.103
15-3	0.540	0.106	0.044	0.065	0.224	0.131	0.176	0.389	0.176	0.259	0.137	0.079	0.106
10-1	0.314	0.096	0.054	0.065	0.204	0.137	0.162	0.382	0.194	0.312	0.126	0.081	0.094
10-2	0.421	0.100	0.045	0.069	0.223	0.147	0.197	0.356	0.204	0.316	0.142	0.084	0.109
10-3	0.540	0.115	0.043	0.063	0.217	0.156	0.204	0.307	0.176	0.257	0.145	0.085	0.111
5-1	0.308	0.097	0.040	0.065	0.237	0.153	0.214	0.231	0.195	0.227	-	-	-
5-2	0.413	0.111	0.044	0.065	0.232	0.157	0.208	0.337	0.184	0.240	-	-	-
5-3	0.525	0.101	0.048	0.067	0.267	0.192	0.295	0.343	0.248	0.229	-	-	-
Mean		0.104	0.046	0.066	0.213	0.134	0.174	0.326	0.189	0.272	0.133	0.080	0.103
Ratio wrt u'		1	0.44	0.63	1	0.63	0.82	1	0.58	0.83	1	0.60	0.77

The turbulence intensities for As=5 are greater than those obtained from the larger aspect ratios. The location of the maximum turbulence intensities is consistent in all three cases, x/Hs=4.75 and y/Hs=0.85. It would therefore appear that the FFS creates greater turbulence intensities within the slot. This would appear to be caused by the blocking of the development of the shear layer by the FFS, resulting in the recirculation of highly turbulent flow back into the slot.

For all twelve cases investigated, the maximum turbulence intensities occur in the vicinity of y/H_s=1.0 for u'/u_{max} and w'/u_{max}. The peak values for v'/u_{max} occur nearer y/H_s=0.5 at reattachment, whereupon this depth increases beyond reattachment. It is worth noting that these peak values are not attributed to a single location, but tend to occur at mid-depth throughout most of the flow field bounded by $0 \leq x/H_s \leq 10$. Reference to the TKE plots illustrates that this central plume of high turbulent activity begins to dissipate beyond this distance, $x/H_s > 10$.

5.5.4 Ratio of Component Turbulent Intensities

Irrespective of the location in the flow field, the relationship between the turbulent intensities at any point can be seen to give $u' > w' > v'$. The normalised ratios with respect to u' are given in table 5.6. These ratios are based upon the results from single point measurements, however, table 5.6 also includes the mean turbulent intensity in the region bounded by

$0 \leq x/H_s \leq 10$ and $0 \leq y/H_s \leq 2$. This region was chosen as it contains the plume of high turbulent activity developed by the shear layer, and therefore the applicability of the point measurements can be made to this mean value. Using these mean values, the ratio of $u':v':w'$ was found to be 1:0.6:0.77. The value of w'/u' obtained from the method using u' and v' (equation 5.19) is 0.8, indicating that this method produces a reasonable estimate of this component.

For the upstream region, $x/H_s<0$, the normalised ratios of the maximum turbulence intensities are 1:0.44:0.63. This region is unaffected by the slot, and therefore this ratio should be similar to those obtained from rectangular open-channel flow. Using the universal turbulence intensity functions proposed by Nezu (1977), this ratio becomes 1:0.55:0.71 (section 2.4). Since the maximum turbulence intensity occurs in the near wall region, $y^+<50$, then making use of the modified constants proposed by Nezu and Rodi (1986) for u' and v' (section 2.4.1) and in the present investigation for w' (section 4.6.5.3) a more comparable ratio of 1:0.42:0.6 is obtained. The ratio of w'/u' obtained from u' and v' (equation 5.19) is overestimated at 0.72.

The maximum turbulence intensities in the new shear layer give normalised ratios of 1:0.63:0.82 (table 5.6), which indicates an increased ratio for both v'/u' and w'/u' compared to the upstream maximum turbulence intensities. The estimated value of w'/u' from equation 5.19 gives a similar ratio of 0.82.

Normalised ratios for the maximum turbulence intensities in the secondary shear layer (at the top of the FFS) are 1:0.58:0.83. Using equation 5.19, the estimated value for w'/u' is 0.79.

The change which each turbulent intensity undergoes between these areas of interest is now considered. The maximum value of u'/u_{max} obtained in the new shear layer is approximately twice the maximum value observed in the upstream section, whilst an even greater value of 3.13 times the upstream value is observed in the secondary shear layer at the FFS. The vertical turbulence intensity v'/u_{max} displays the largest increase of 3 and 4.1 times the upstream value for the primary and secondary shear layers respectively. A similar increase is observed for the maximum shear layer values of w'/u_{max}, with 2.6 and 4.1 times the upstream value for the primary and secondary shear layers respectively. This clearly indicates that the secondary shear layer generated by the FFS has larger turbulent intensities than those generated within the primary shear layer.

The above observations did not include the results for As=5. The maximum turbulent intensities in the slot region for this aspect ratio are greater than those for the larger aspect

ratios, where increases of 2.2, 3.6 and 3.2 times the upstream maximum were observed for u'/u_{max}, v'/u_{max} and w'/u_{max} respectively. This indicates that despite having a reduced length of shear layer development, this aspect ratio boasts greater turbulence intensities within the slot. This could be attributed to the recirculation of some of the shear layer as it splits at the FFS.

5.5.5 Turbulence Intensities Downstream of Reattachment

With the development of a new sub-boundary layer at the reattachment point, the flow will begin to relax towards the thin-shear layer state. This will commence from the channel bed, increasing through the depth with downstream distance from the reattachment point.

Selected velocity profiles downstream of reattachment were examined in section 5.4.5.3. The purpose of this was to investigate the distance required for the streamwise velocity profile to return to the law of wall distribution. It was observed in the three BFS cases that the velocity profile appeared to fit the log-law relationship after a distance of x/H_s=27 from the BFS.

As an extension to this investigation, it was decided to analyse the turbulence intensity profiles for the same longitudinal stations of x/H_s=15, 21, 27, 30 and 33 downstream of the BFS. The turbulence intensities u', v' and w' were compared to the universal turbulence intensity distributions using equations 2.35-2.37, with the modified set of constants, see figures 5.68-5.70.

The profiles for u'/u^* can be seen in figures 5.68 (a)-(c). These figures show that the turbulence intensity does not attain the universal turbulence intensity profile within the distances measured. As distance from the reattachment point increases, the u'/u^* profiles can be seen to approach the universal profile both in shape and intensity. This change can be seen to develop from the channel bed, owing to the development of the new thin-shear layer, whilst the high turbulent intensities developed from the free-shear layer still persist towards the free-surface. The subsequent profiles show a transition between this high turbulent profile towards the universal profile values, but fails to show a good match within the available distance. From the trend which can be observed, it could be expected that given an additional distance of approximately x/H_s=6 the experimental profiles would match the universal profile.

Figure 5.69 (a)-(c) illustrates the profiles for v'/u^* downstream of reattachment. Although these profiles do not match the universal profile, even at the furthest station, x/H_s=33, it can

be seen that their intensity and shape do approach this profile, but not as well as u'/u^*. The experimental profiles retain higher turbulent intensities at mid-depth, suggesting that damping of v'/u^* occurs at both the free-surface and the channel bed.

The final set of turbulence intensities, w'/u^*, can be seen in figure 5.70 (a)-(c). These profiles display a similar characteristic to the u'/u^* profiles, where there is a notable transition of shape and intensity towards the universal profile as downstream distance increases. Similarly, this transition occurs from the channel bed working through the depth as downstream distance increases. As with u'/u^*, it is expected that the w'/u^* profiles will match the universal profile after given a further downstream distance of approximately x/H_s=6.

5.6 CONCLUSIONS

The following points may be concluded from the results presented in this chapter:

(1) Separated flow was induced at a BFS in order to measure the length of flow reattachment, R_L, defined as the point where the mean streamwise velocity, u, is equal to zero. This was measured at a height of y_o/Hs=0.05 above the slot floor. The point of zero mean velocity, u=0, cannot be found directly, and was therefore interpolated from a series of successive points where the flow direction changed. It was observed that the streamwise velocity in the vicinity of the reattachment length at this depth changed linearly.

(2) Profiles of R_L were obtained over a range of Reynolds numbers and flow depths. This procedure was used for flows with the following aspect ratios, A_s=10, 12.5, 15, 20 and a BFS. The profiles of R_L vs Re displayed the same characteristic, whereby an increase in Reynolds number from an initially low value resulted in an increase in R_L. This continued until a maximum reattachment length, R_{Lmax}, was obtained. A subsequent increase in Re creates a reduction in reattachment length, eventually reaching a constant value at higher Reynolds numbers. Details of this work can be found in Keogh and Addison (1996b).

(3) It was observed that for depths of y_o/H_S>1.0, the reattachment lengths decreased as the depth ratio increased. However, for depths of y_o/H_S<1.0, the reattachment lengths remained similar to those obtained for y/H_S=1.0.

(4) The only aspect ratio which produced similar profiles throughout the full range of depth ratios to the BFS configuration was the largest aspect ratio of 20. For lower aspect ratios, notably A_s=10, it was evident that the FFS influenced the longer reattachment lengths, particularly those for lower depth ratios which boast greater reattachment lengths. There is also evidence that the FFS affects the reattachment lengths for A_s=12.5, and in the lower flow depths for A_s=15.

(5) The profiles of R_L vs Re at high depth ratios, i.e. y_o/Hs>1.0, are similar irrespective of the slot aspect ratio.

(6) For the BFS and A_s=20, reattachment lengths varied between $5.5<R_L<9$. Although fewer depths were investigated for A_s=15, reattachment lengths as high as 9 were observed.

(7) For A_s=12.5 and A_s=10, a noticeable decrease in reattachment length is observed for the low flow depths. It appears that the FFS limits the length of reattachment to $R_L<8$ when the FFS is introduced within 2-4 step heights downstream of reattachment. This is most evident from the reduced reattachment lengths of $5.5<R_L<8$ observed for A_s=10.

(8) The spanwise distribution of reattachment length downstream of a BFS was investigated. A combination of depths ranging between $0.6<y/H_S<2.0$ and Reynolds numbers of 6000<Re<40333 were used in this study. It was observed that for each flow condition, a central region of constant reattachment length was obtained, however, a reduction in reattachment length was observed close to the sidewalls. The effects of sidewall contamination was greater for larger Reynolds numbers.

(9) In the recirculation region downstream of a BFS, the normalised maximum (negative) recirculating velocity, u_{Rmax}/u_o, has been shown to range between 0.21-0.28. These were located at a normalised distance of approximately x/H_S=3.5-4 from the BFS, and at a height of y/H_S=0.05 from the channel bed.

(10) When the slot was filled by a recirculation eddy, as for the low aspect ratio A_s=5, greater normalised recirculation velocities of u_{Rmax}/u_o=0.35 were observed. This increase in velocity may be attributed to the sudden recirculation of flow as it deflects down the FFS.

(11) A smaller recirculation zone was observed at the base of the FFS. This recirculation zone is documented in the literature concerning flow over a FFS. Unfortunately, the scale of the measurements did not detect this region in great detail. However, it was observed to be limited to a distance of x/H_S=1 upstream of the FFS. The velocities in this region are relatively low, and hence detailed measurements were not conducted for this investigation.

(12) It was observed during the reattachment length investigation that the FFS influenced the reattachment length when A_s<15. This could be attributed to a combination of the low velocities which occur in the region of flow reattachment and the low velocities which occur at the smaller recirculation zone at the base of the FFS. This creates a larger region of low velocity along the slot bed causing the main flow in the slot to commence its deflection over the FFS at an earlier stage. This has the effect of reducing the reattachment length, particularly at lower Reynolds numbers where the flow has less momentum to overcome this effect.

(13) The flow deflecting over the FFS creates a recirculating zone immediately downstream of the FFS. Once again the scale of measurements used in this investigation failed to provide an accurate illustration of this and its associated velocities.

(14) When the aspect ratio does not support flow reattachment along the slot bed, it was observed that flow reattachment can occur on the vertical face of the FFS (as in the cases for A_s=5). This is evident from both the velocity vector plots which illustrate a change in the vertical direction of the flow, and from the streamline ψ=0 which could be seen to reattach at the vertical face of the FFS.

(15) In the cases where flow reattachment occurred along the slot bed, the mass-flow of the shear layer which deflects upstream at reattachment was found to be 10%. The shear layer was also observed to have influenced the full depth of flow at reattachment. This mass-flow increased to 27% for *As*=5, owing to the redirection of the flow back into the slot by the FFS.

(16) The mass flow which deflects below y/H_S=1.0 in the slot region was investigated. This mass flow, denoted as q_{slot}, was able to quantify the flow between reattachment and the FFS. A linear relationship was observed between q_{slot} and slot length, where q_{slot} increased to a maximum observed at A_S>20-25.

(17) The separating streamline (for slot bed reattachment cases) was confirmed to follow an elliptical curve defined by equation 5.2.

(18) The shear layer boundaries were determined for all cases. This indicated that the outer boundary development was consistent for all the cases where $As \geq 10$, and similarly for the inner boundary in all the cases. One of the main observations was that the outer boundary could not be truly considered as having its origin at the point of flow separation, but at an initial depth, h_o, which corresponds to the thin-shear layer depth of the upstream flow.

(19) The angles α_1 and α_2 which define the deviation from the point of separation for the outer and inner boundaries of the shear layer were investigated. For the outer boundary, the current investigation gave a value of $\alpha_1=4.6^o$, which is not dissimilar to the value of $\alpha_1=4.8^o$ obtained from plane and compound turbulent shear layer theory. The angle of the inner boundary from plane turbulent shear layer theory was found to have a value of $\alpha_2=9.5^o$, whilst for compound shear layers this can reduce to $\alpha_2=1^o$, depending on the ratio u_1/u_o, where u_1 represents a forced downstream velocity in the expanded flow region (Rajaratnam, 1976). The experimental value of α_2 was subsequently found to be 4.96^o, and therefore, this reduction from $\alpha_2=9.5^o$ may be attributed to the recirculating velocity around the BFS acting as a forced velocity, u_1.

(20) The angles α_1 and α_2 assume a linear relationship for the outer and inner boundaries of the shear layer respectively. However, it was observed that the relationship between depth and downstream distance was more complex in nature, whereby the shear layer rate of growth increased with longitudinal distance. A set of general expressions were derived to describe the shape of these boundaries (equations 5.4-5.6).

(21) The development of the shear layer thickness was also considered. This was found by obtaining the difference in height between the inner and outer boundaries (equations 5.4-5.6). The growth was found to be non-linear, and using these equations, the relationship can be described as exponential. A method based on the assumption that the velocity gradient *du/dy* is nearly constant in a shear layer was adopted by Ötügen et al (1992) to measure the shear layer thickness. This method was applied to the current investigation, however, the resulting shear layer thickness was less than that obtained from the previous method. Also, this method produced a large scatter between the different flow cases. It has been shown that the velocity

distribution in the shear layer has a Gaussian form (see below), and therefore, the use of the local maximum of mean velocity gradient is not fully representative of the velocity gradient.

(22) The streamwise velocity distribution downstream of a BFS has been shown to have a Gaussian form. It was observed that there were good similarities between the results and the Gaussian equations, however, the distribution of the experimental results were influenced by their longitudinal location, which the existing Gaussian distributions did not cater for. A modified Gaussian equation was therefore developed which considered longitudinal location, and was therefore more accurate in describing the flow distribution, equation 5.16-5.17.

(23) The Gaussian distribution was also found to be representative of the flow over the distance $R_L<x/Hs<21$, a finding also observed in a similar investigation by Nakagawa and Nezu (1987).

(24) The distance taken for a flow downstream of a strong perturbation, such as the flow over a BFS, to recover to the thin shear layer state is documented in the literature (Bradshaw and Wong, 1972; Nakagawa and Nezu, 1987). Vertical profiles downstream of reattachment were plotted against the log-law distribution for the BFS cases. It was observed that the experimental results matched the log-law after a distance of $x/Hs=27$ from the BFS.

(25) The maximum turbulence intensities observed in the slot shear layer were approximately 2-3 times greater than the maximum values observed in the upstream section prior to flow separation. The maximum turbulence intensities in the slot shear layer could generally be found along a vertical line defined by the depth $y/Hs=1.0$, and longitudinally in the region $5.5<x/Hs<7.0$. With respect to u', the normalised ratios of the maximum turbulent intensities found in the shear layer were 1:0.63:0.88 for $u':v':w'$.

(26) The shear layer generated at the top of the FFS was smaller in size than the shear layer in the slot, however, the magnitude of the turbulence intensities were greater, with values between 3 and 4 times the initial upstream maximum values. The ratio of the turbulence intensities in the FFS shear layer were 1:0.58:0.83 for $u':v':w'$.

(27) It was observed that for a smaller aspect ratio of 5, the recirculation zone exhibits greater turbulence intensities than that of larger aspect ratios. This may be attributed to the recirculation of highly turbulent flow back into the slot.

(28) The turbulence intensities downstream of reattachment for the BFS cases were investigated. This revealed that although the mean velocity appeared to have a log-law distribution within the limits of observation, the turbulence intensities did not match the universal turbulence intensity profiles within these limits. Both u' and w' gave similar trends and did approach the universal profile, where it was estimated that this would be achieved by $x/Hs \approx 40$. However, the shape and magnitude of v' did not approach the universal profile within the downstream range considered, and hence it is assumed that it would take longer to match the universal profile.

(30) It was observed throughout that the turbulence intensities satisfied $u'>w'>v'$. In addition, the assumption used by many investigators that $w'=(u'+v')/2$ appeared to be generally acceptable, especially in the slot and FFS shear layers.

For the upstream channel section, which applies to rectangular open-channel flow, the value of w' could be described more accurately by the following expression:

$$w'=(u'+2v')/3$$

Figure 5.1 (a) - Reattachment Length vs Reynolds Number for a BFS, y/Hs=1

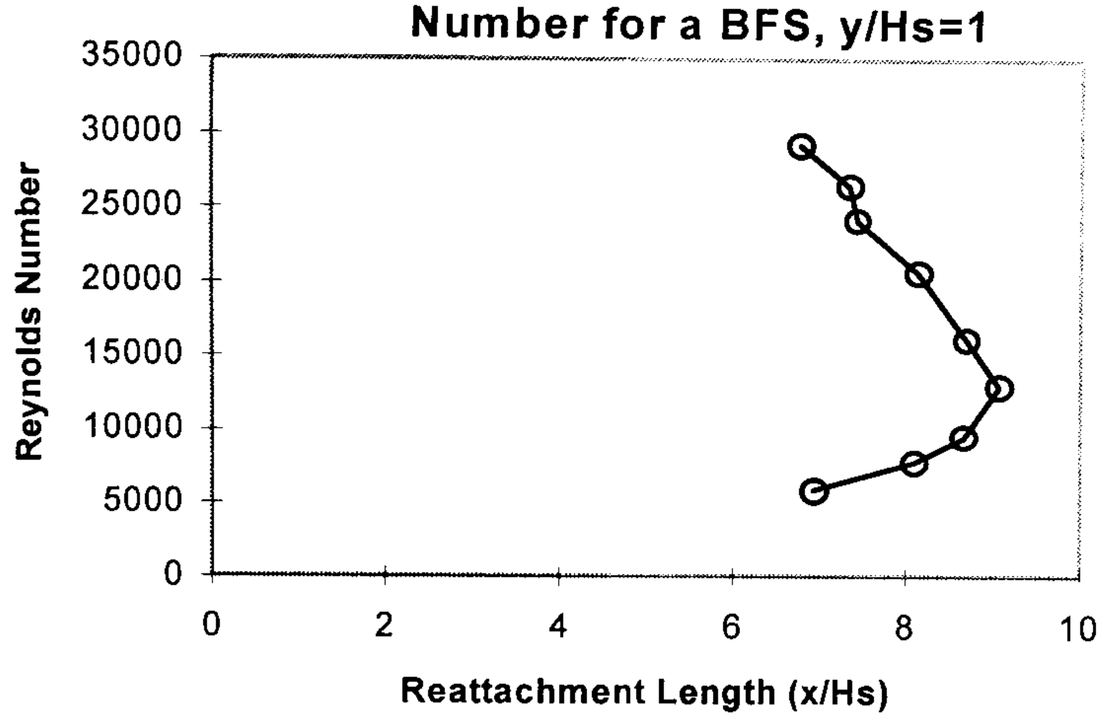

Figure 5.1 (b) - Reattachment Length: Re = 29167

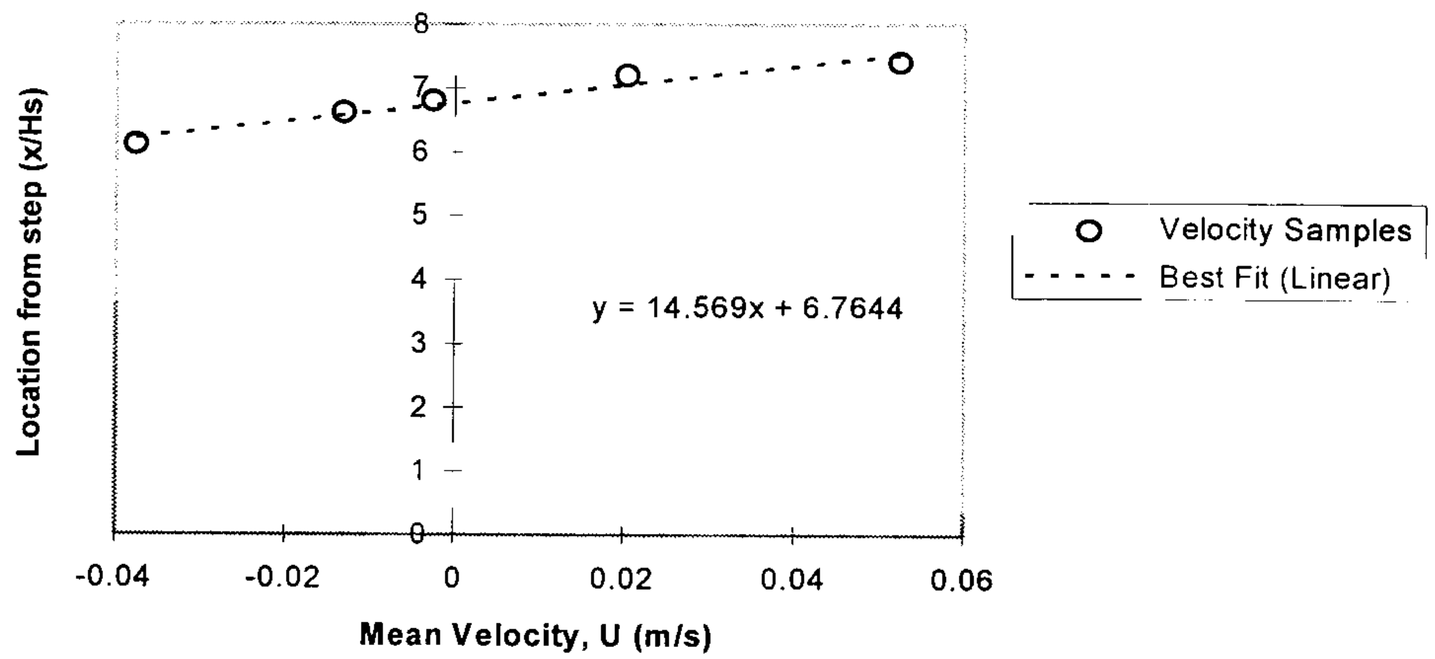

Figure 5.1 (c) - Reattachment Length: Re = 26367

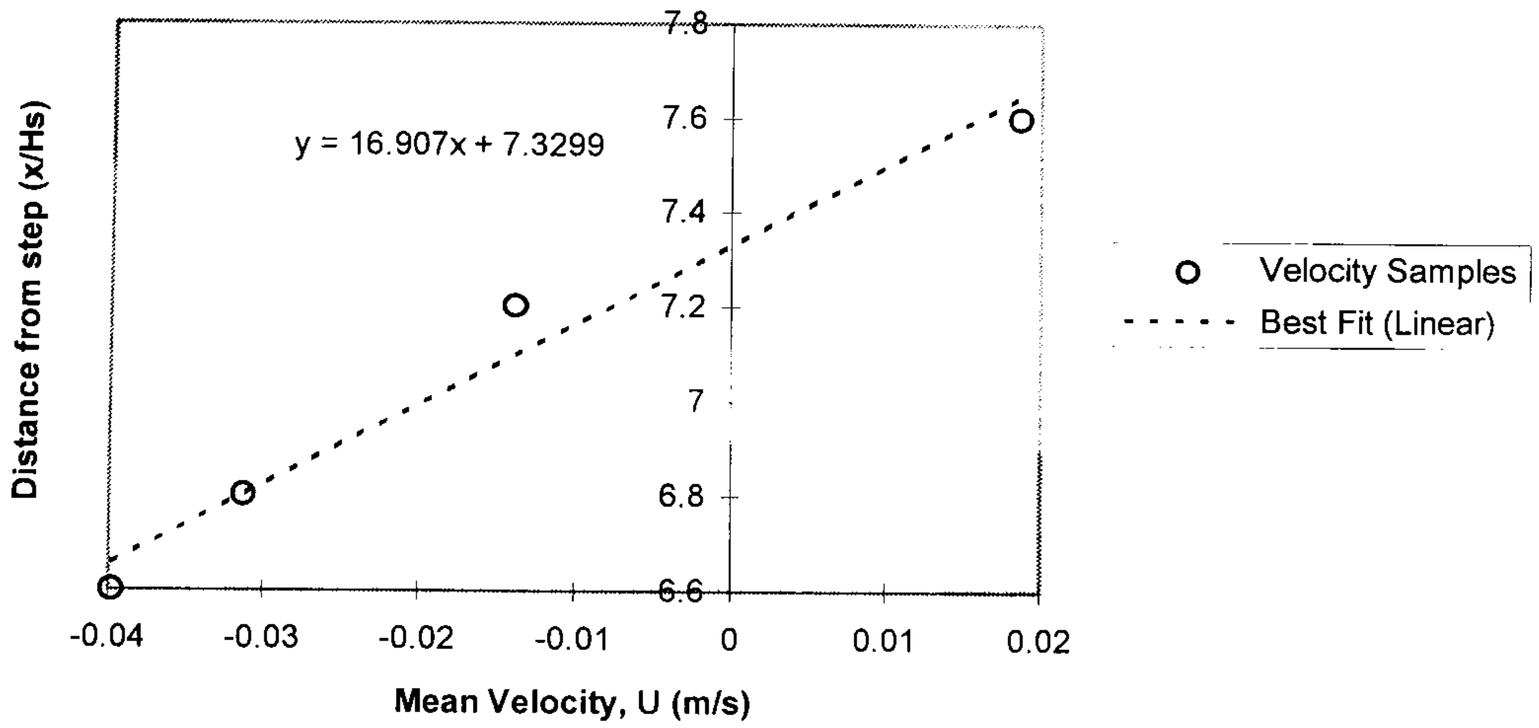

Figure 5.1 (d) - Reattachment Length: Re = 24050

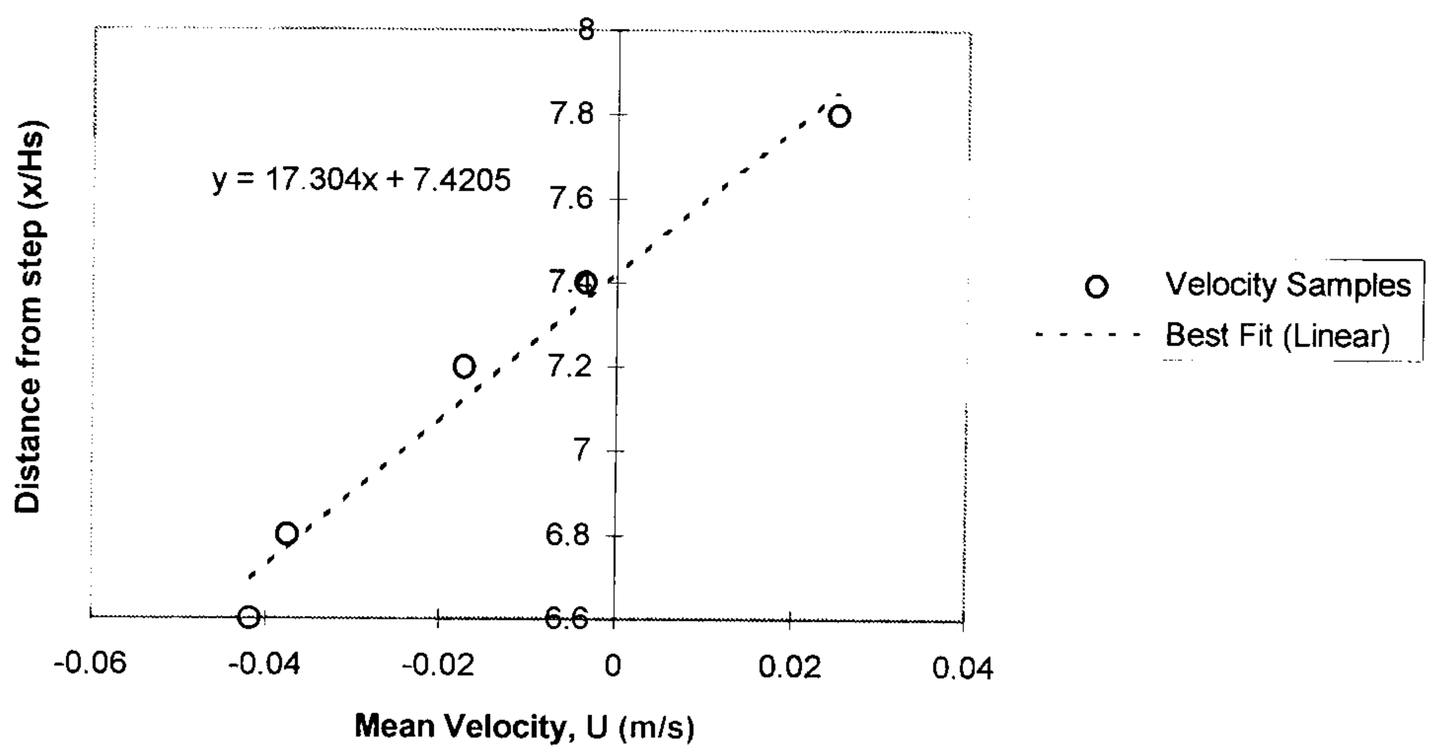

Figure 5.1 (e) - Reattachment Length: Re=20567

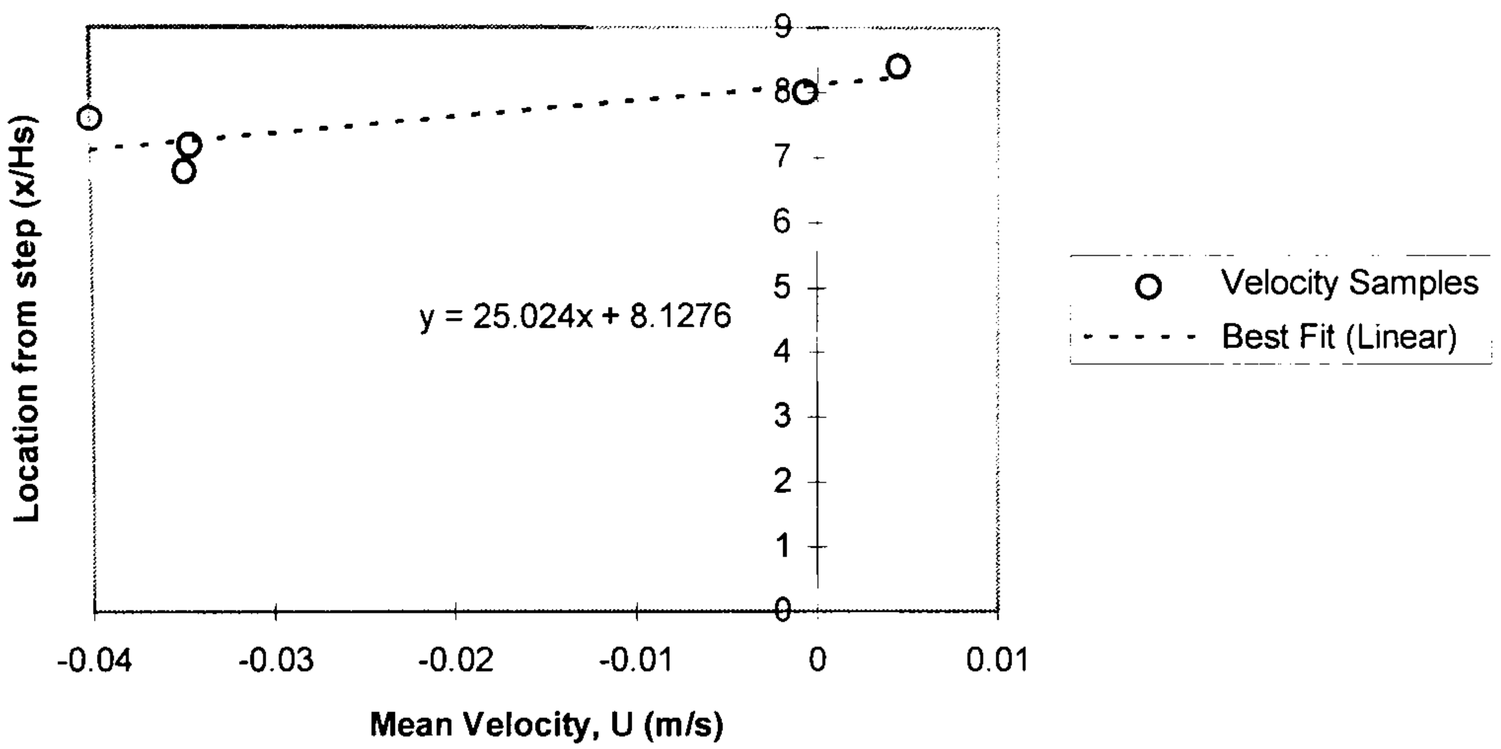

Figure 5.1 (f) - Reattachment Length: Re =16000

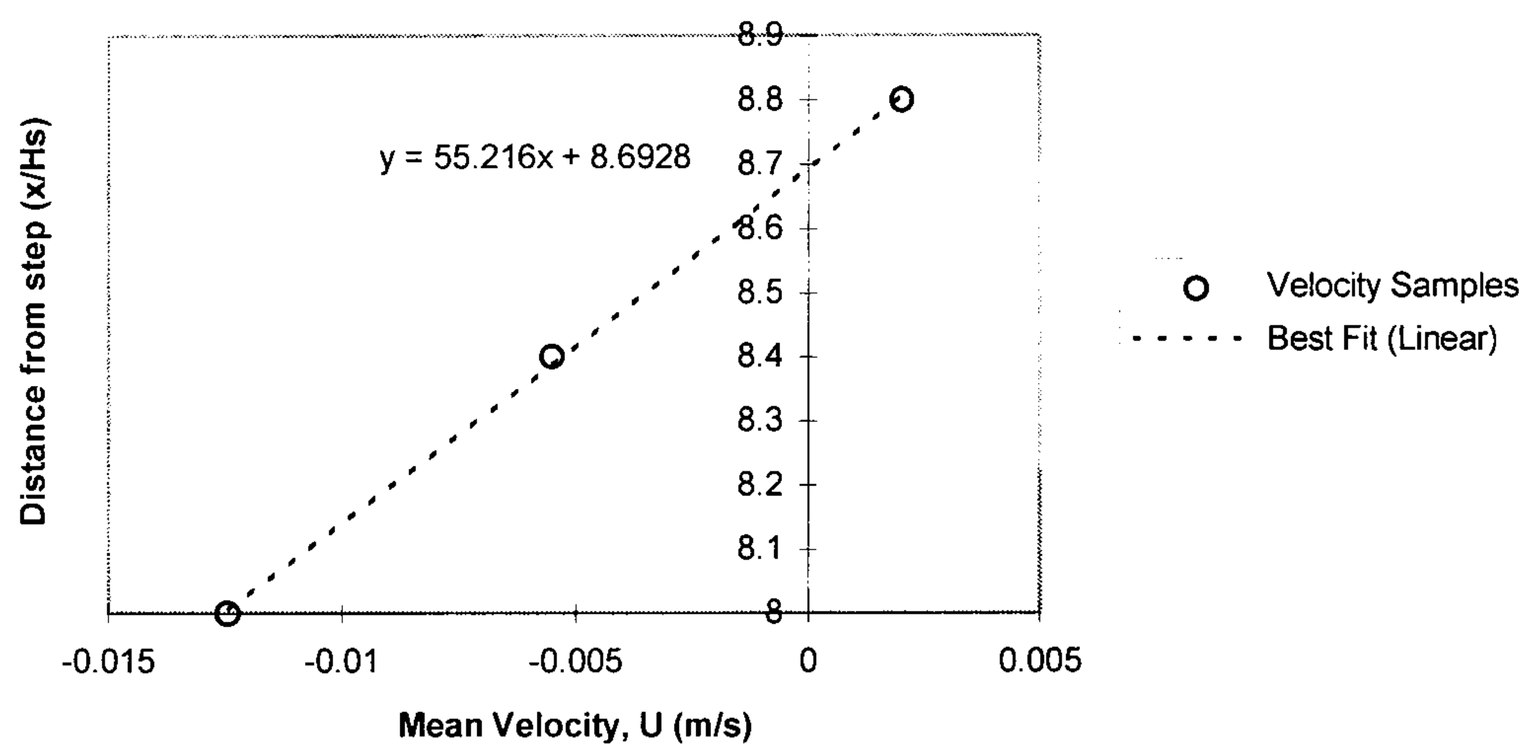

Figure 5.1 (g) - Reattachment Length: Re = 12867

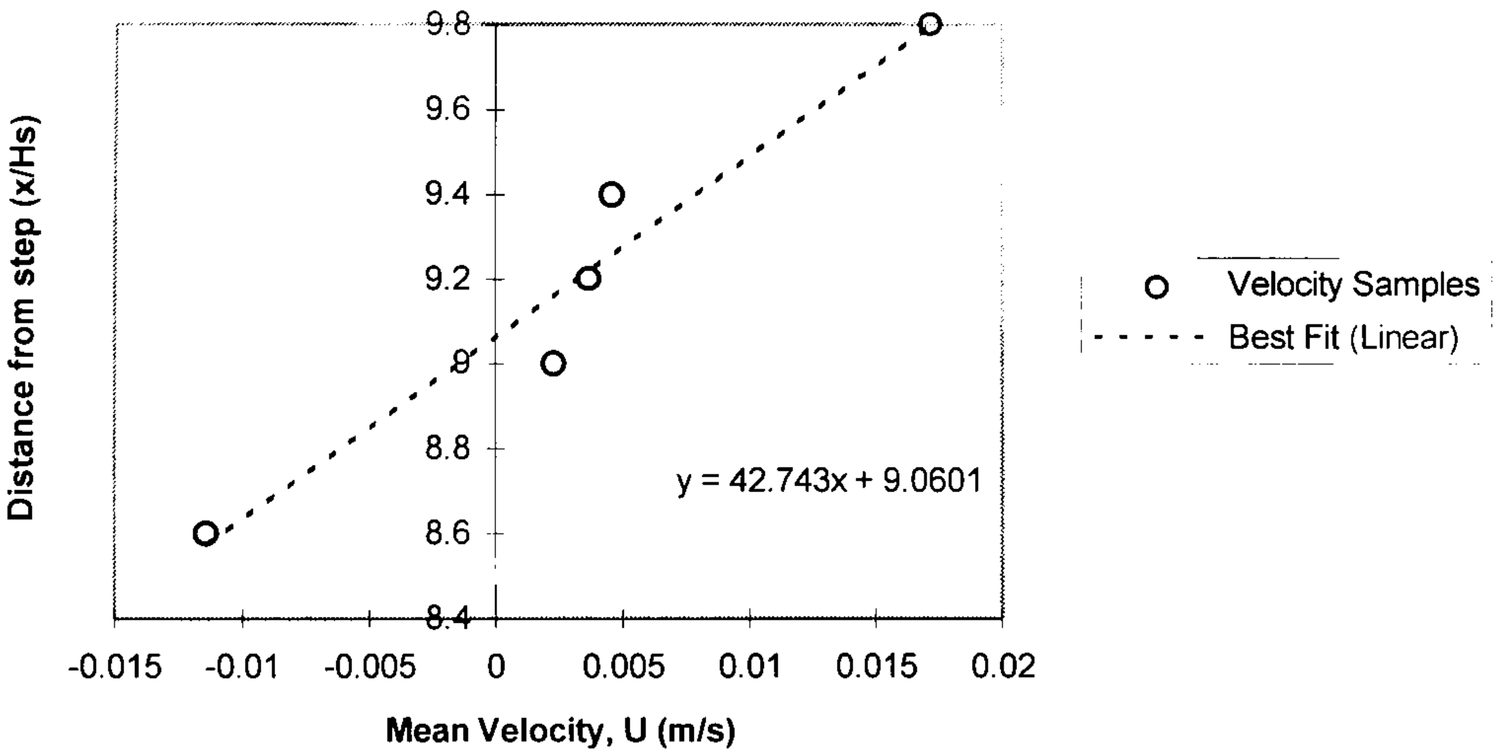

Figure 5.1 (h) - Reattachment Length: Re = 9433

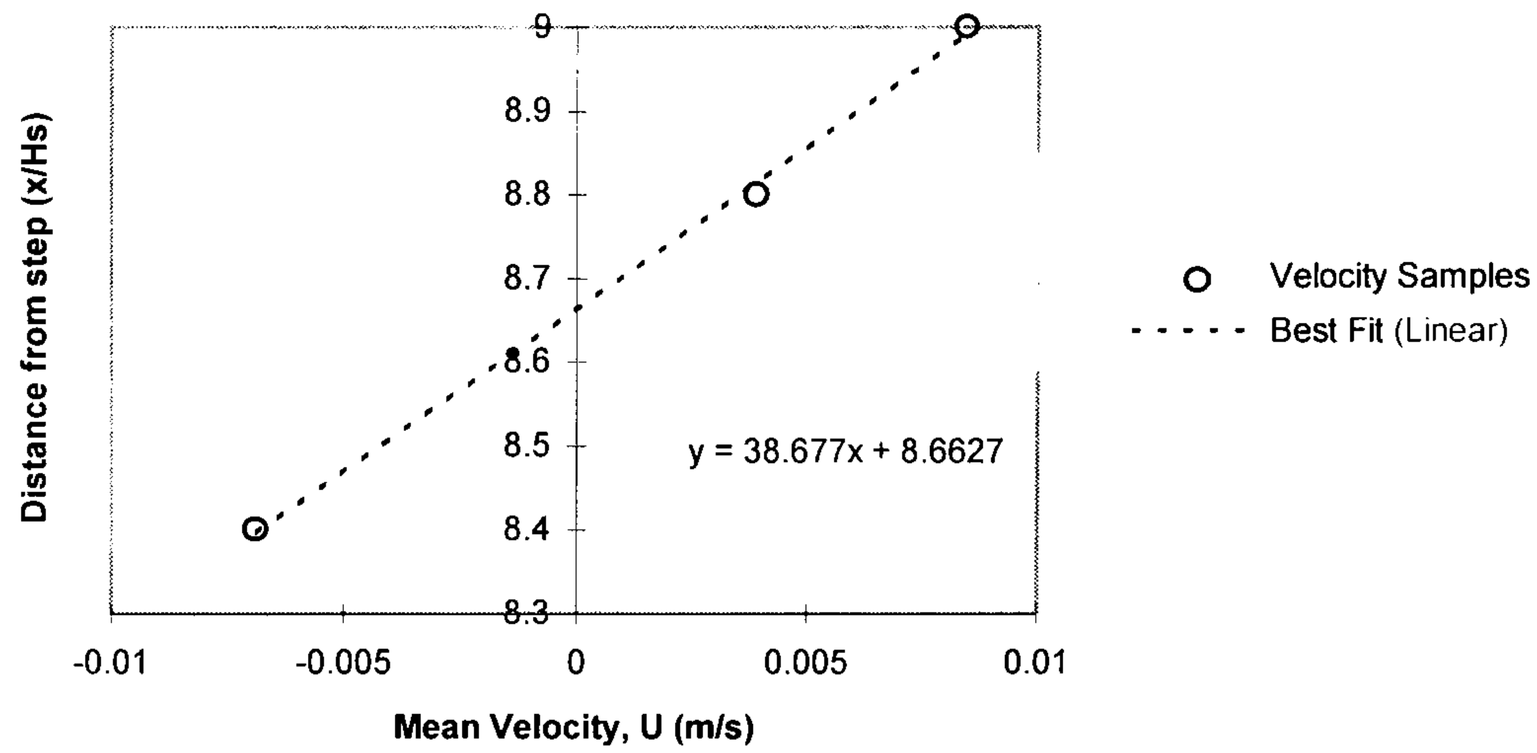

Figure 5.1 (i) - Reattachment Length: Re = 7750

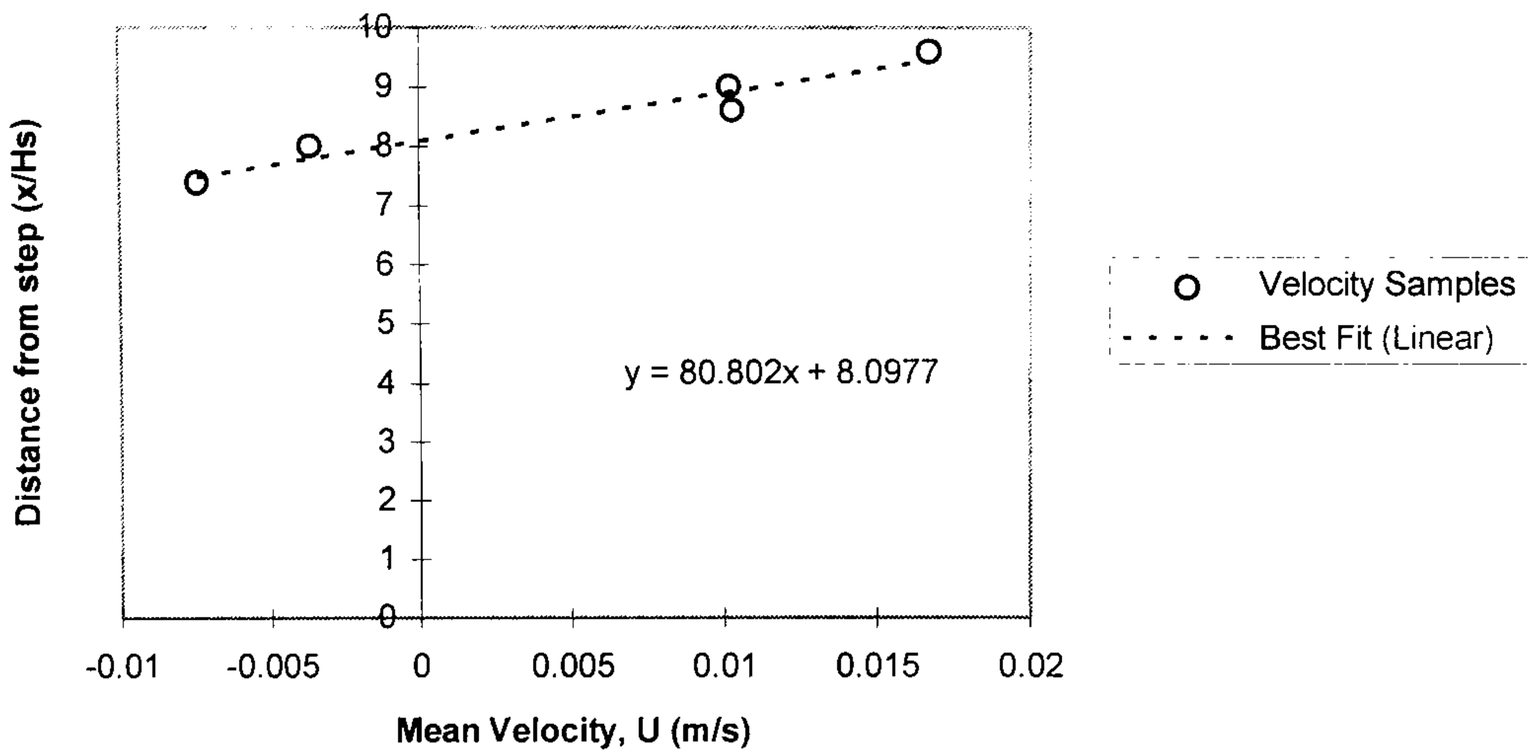

Figure 5.1 (j) - Reattachment Length: Re = 5833

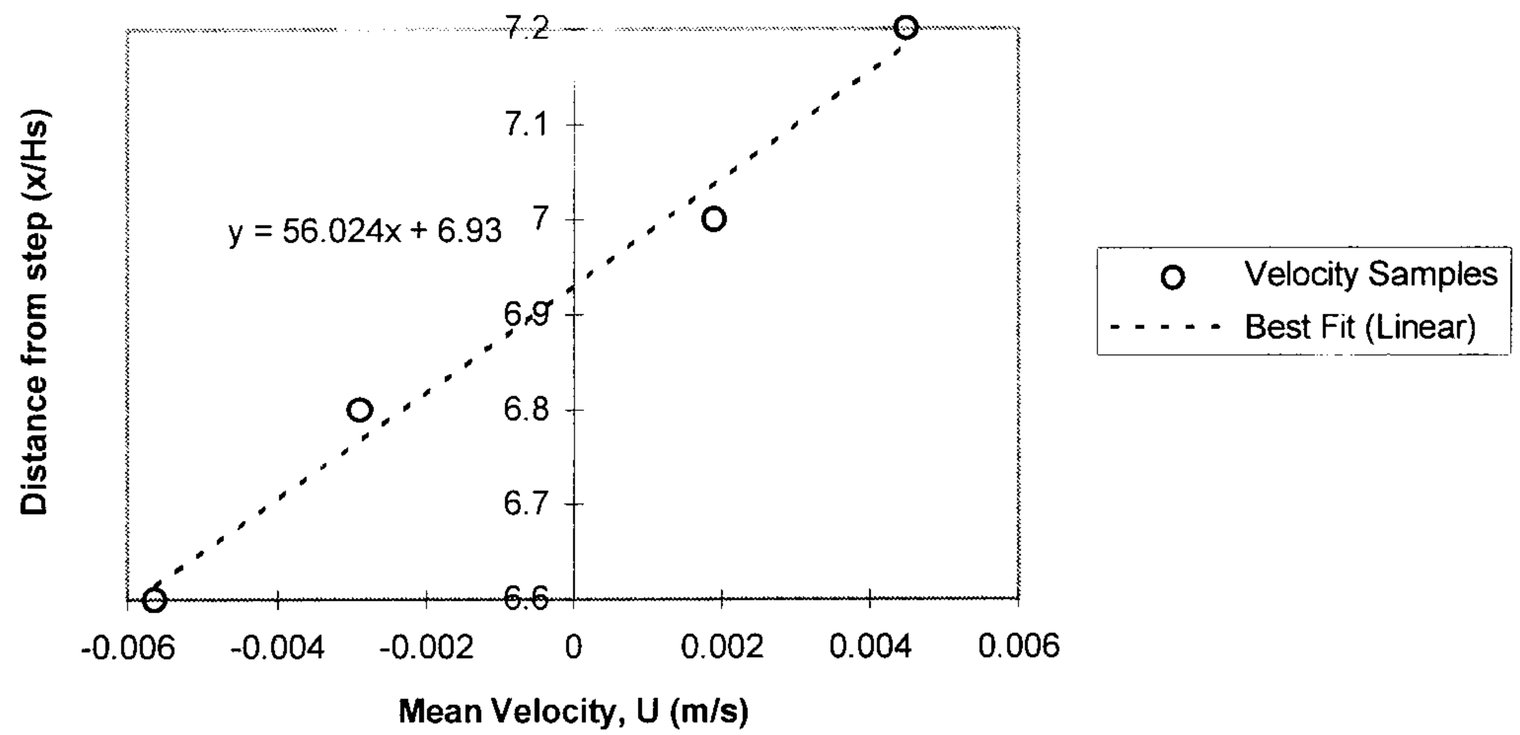

Figure 5.2(a) - Reattachment Length vs Reynolds Number: y/H_s=2

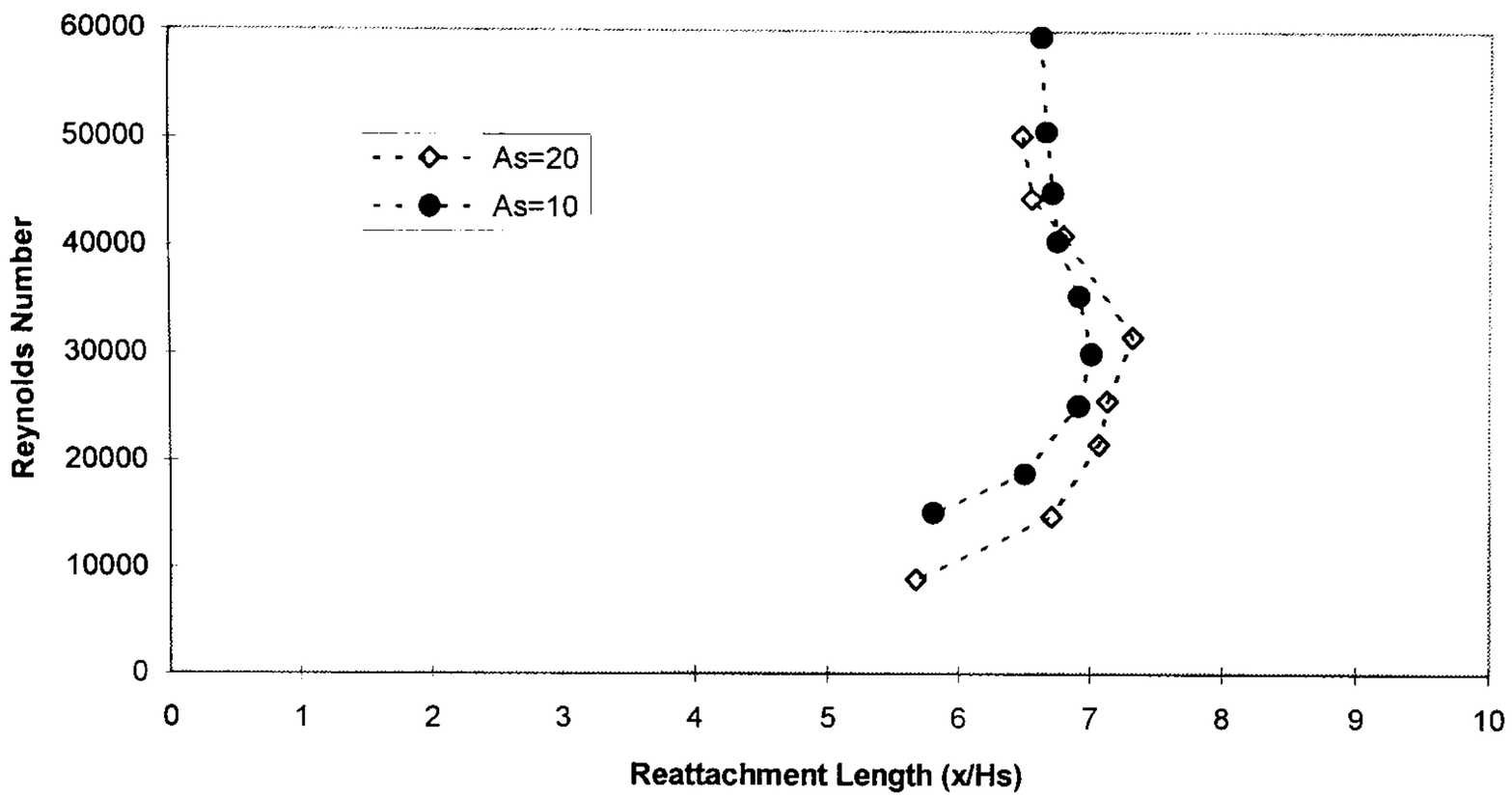

Figure 5.2(b) - Reattachment Length vs Reynolds Number: y/H_s=1.6

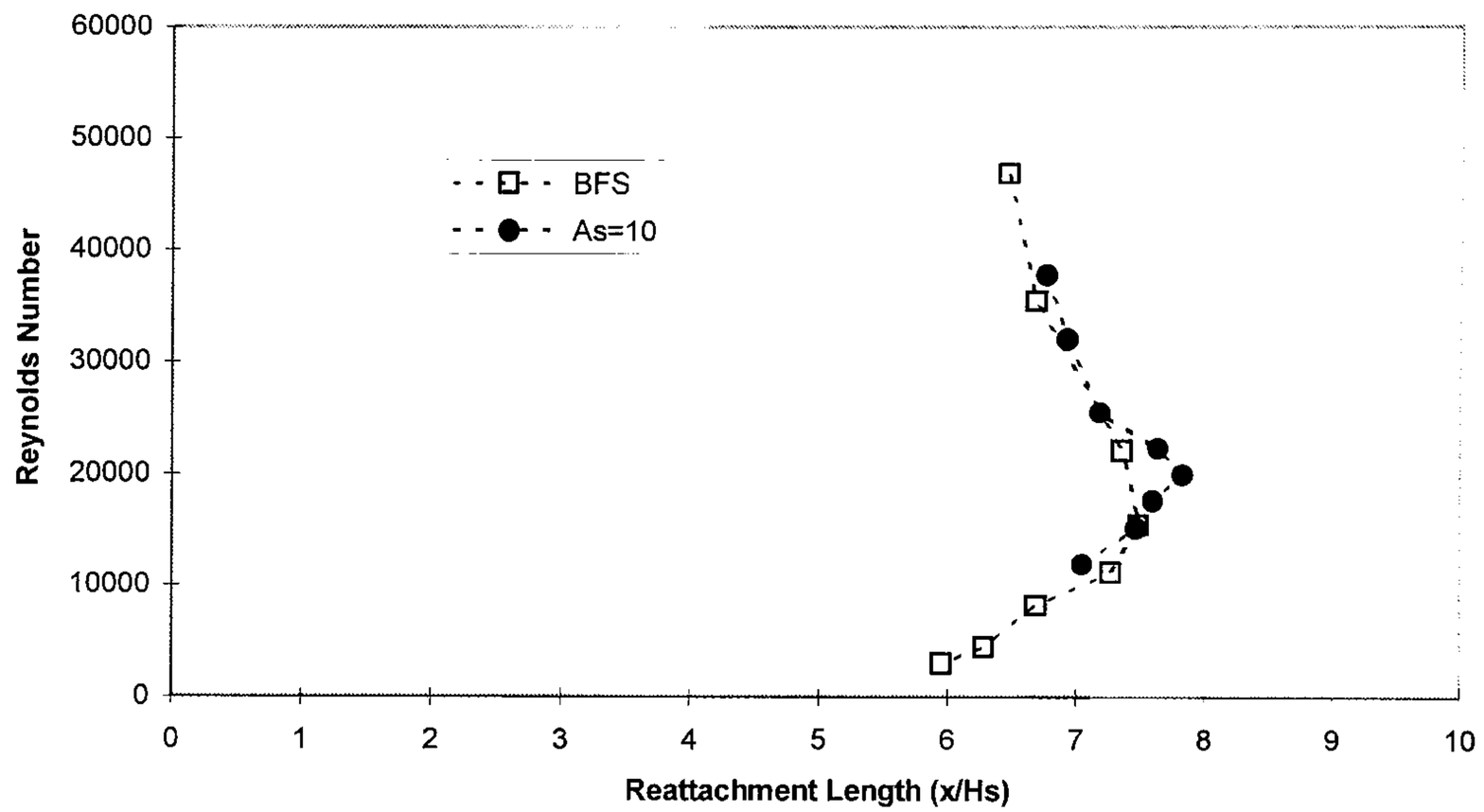

Figure 5.2(c) - Reattachment Length vs Reynolds Number: y/H_s=1.4

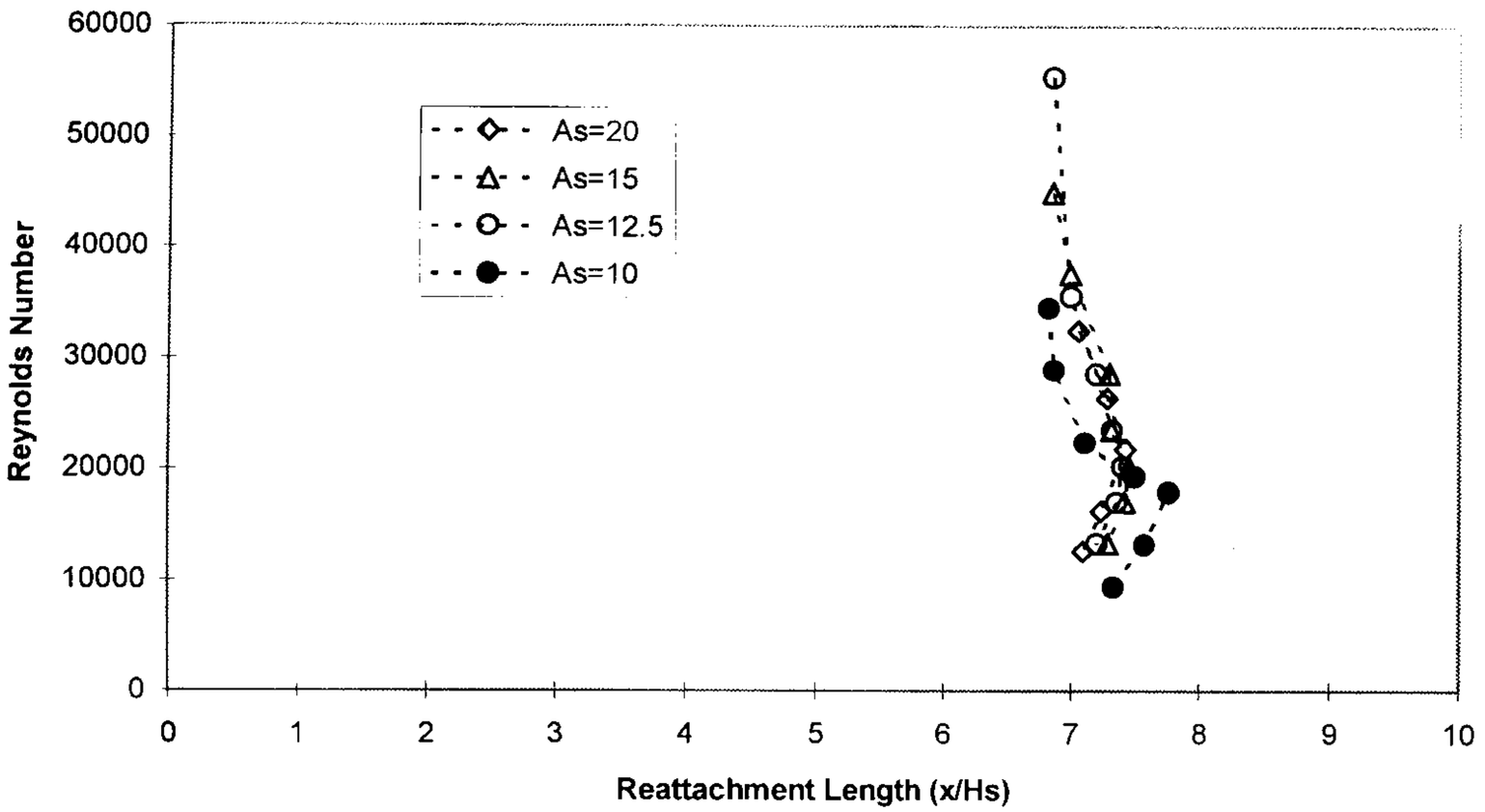

Figure 5.2(d) - Reattachment Length vs Reynolds Number: y/H_s=1.2

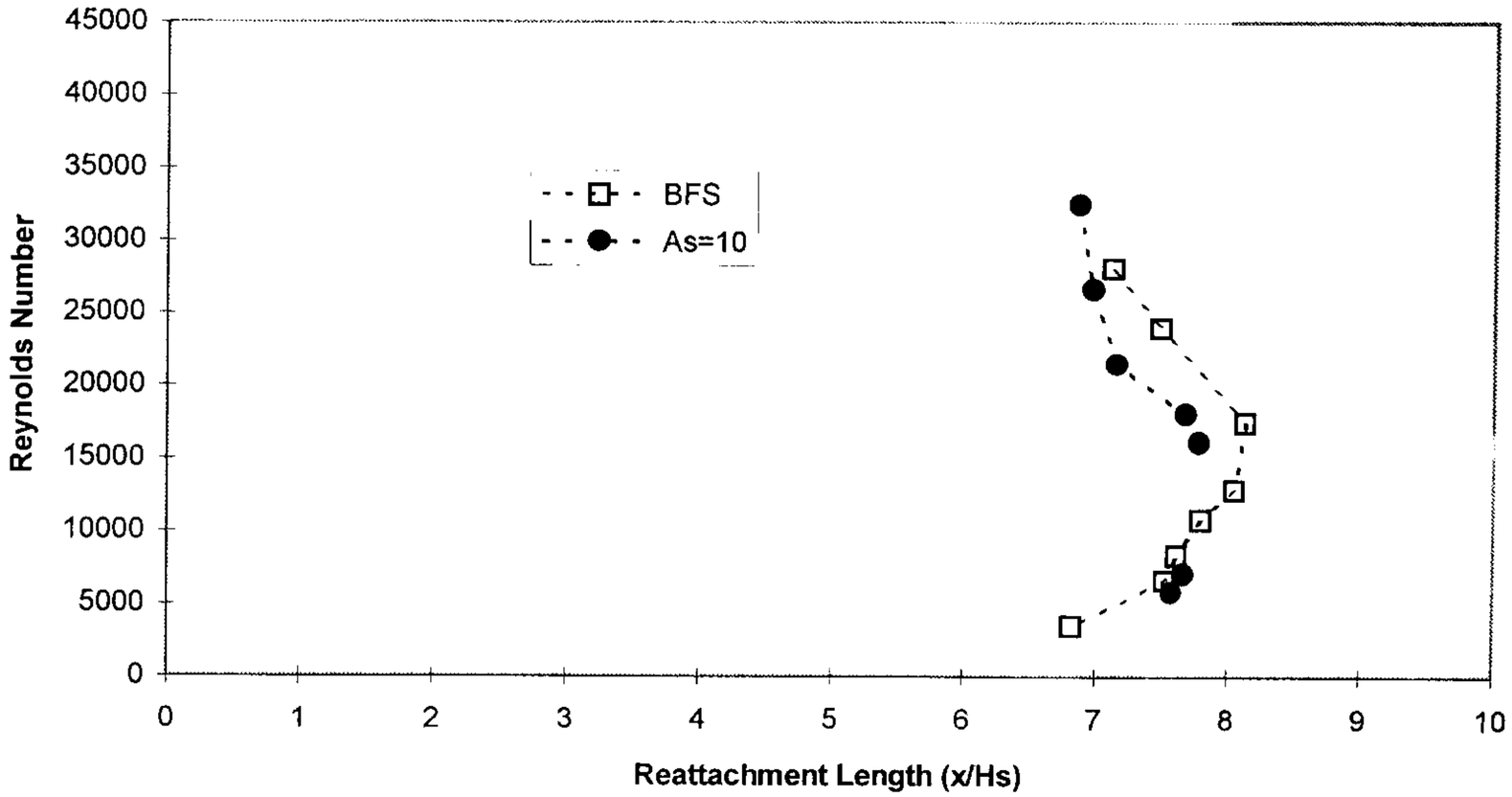

Figure 5.2(e) - Reattachment Length vs Reynolds Number: y/H_s=1.0

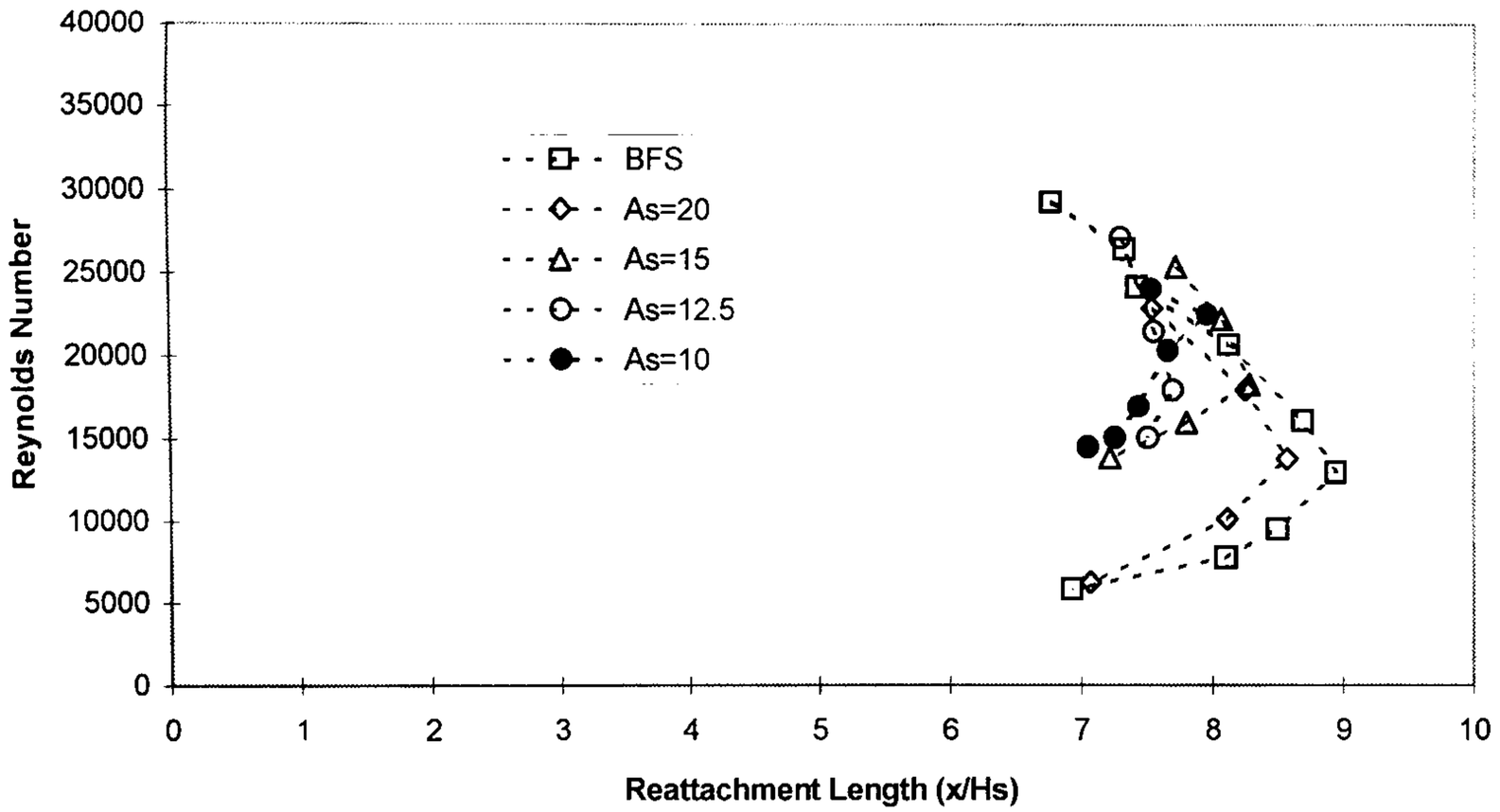

Figure 5.2(f) - Reattachment Length vs Reynolds Number: y/H_s=0.8

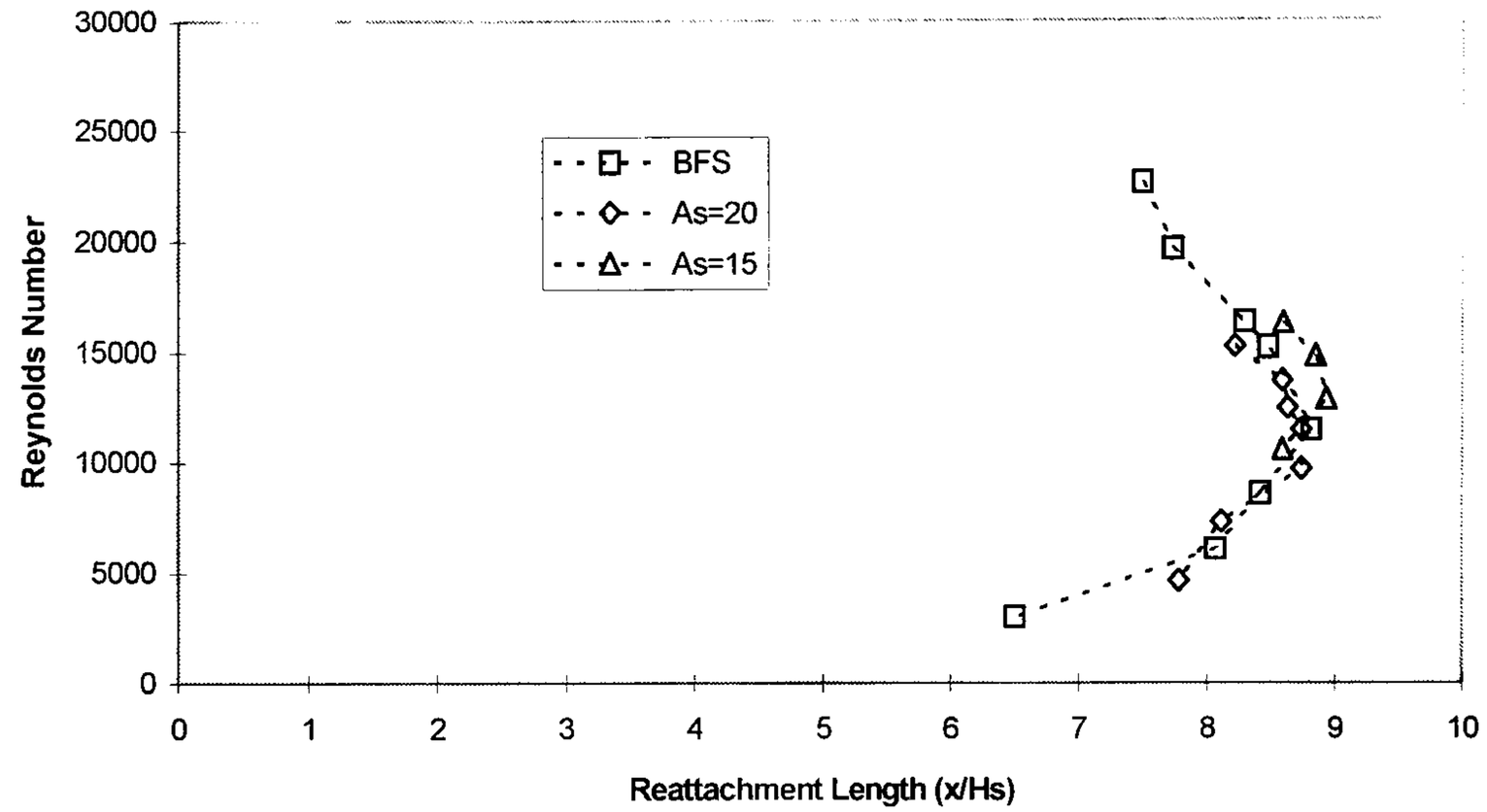

Figure 5.2(g) - Reattachment Length vs Reynolds Number: y/H_s=0.6

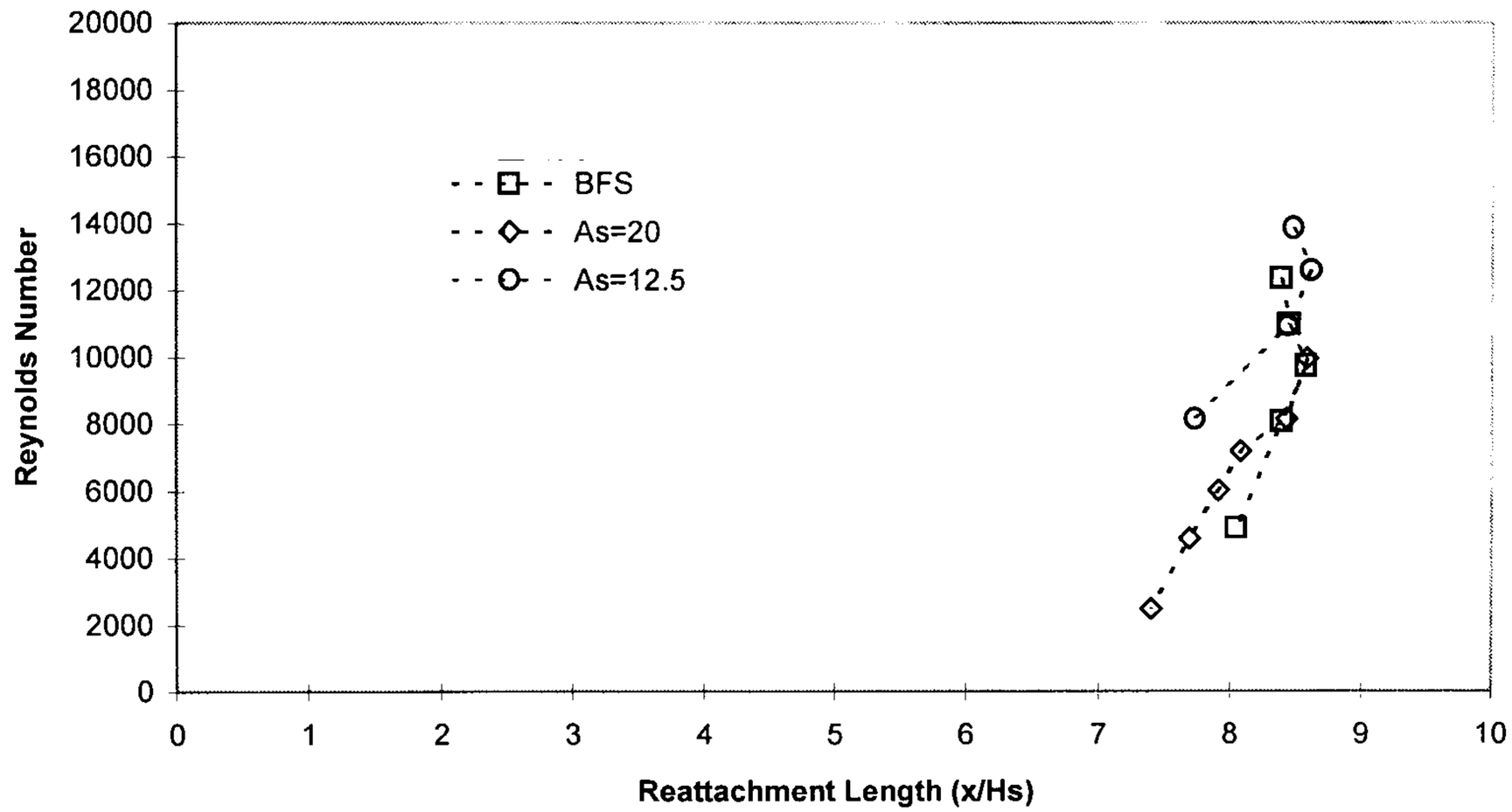

Figure 5.3(a) - Reattachment Length vs Reynolds Number: BFS

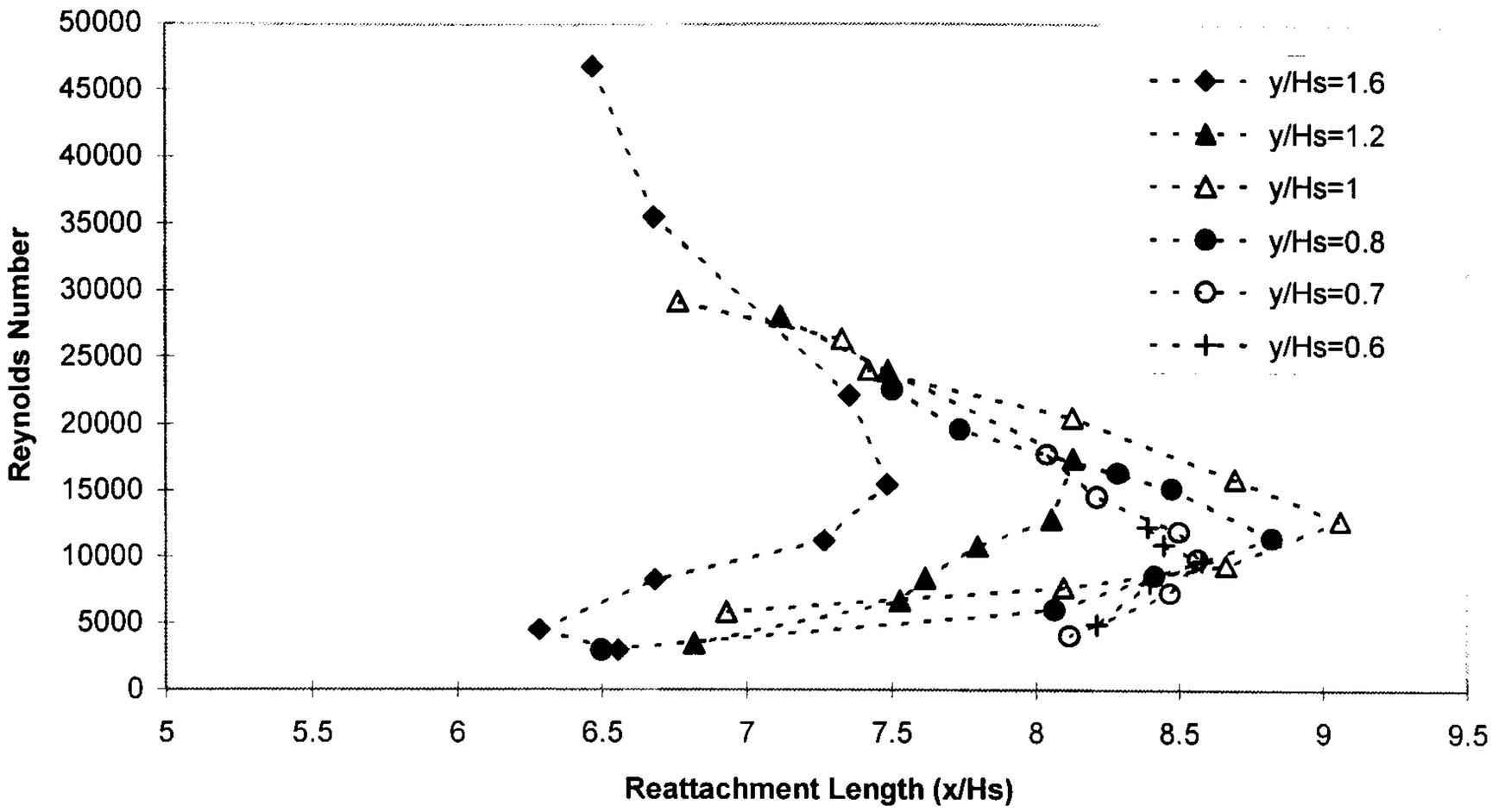

Figure 5.3(b) - Reattachment Length vs Reynolds Number: As=20

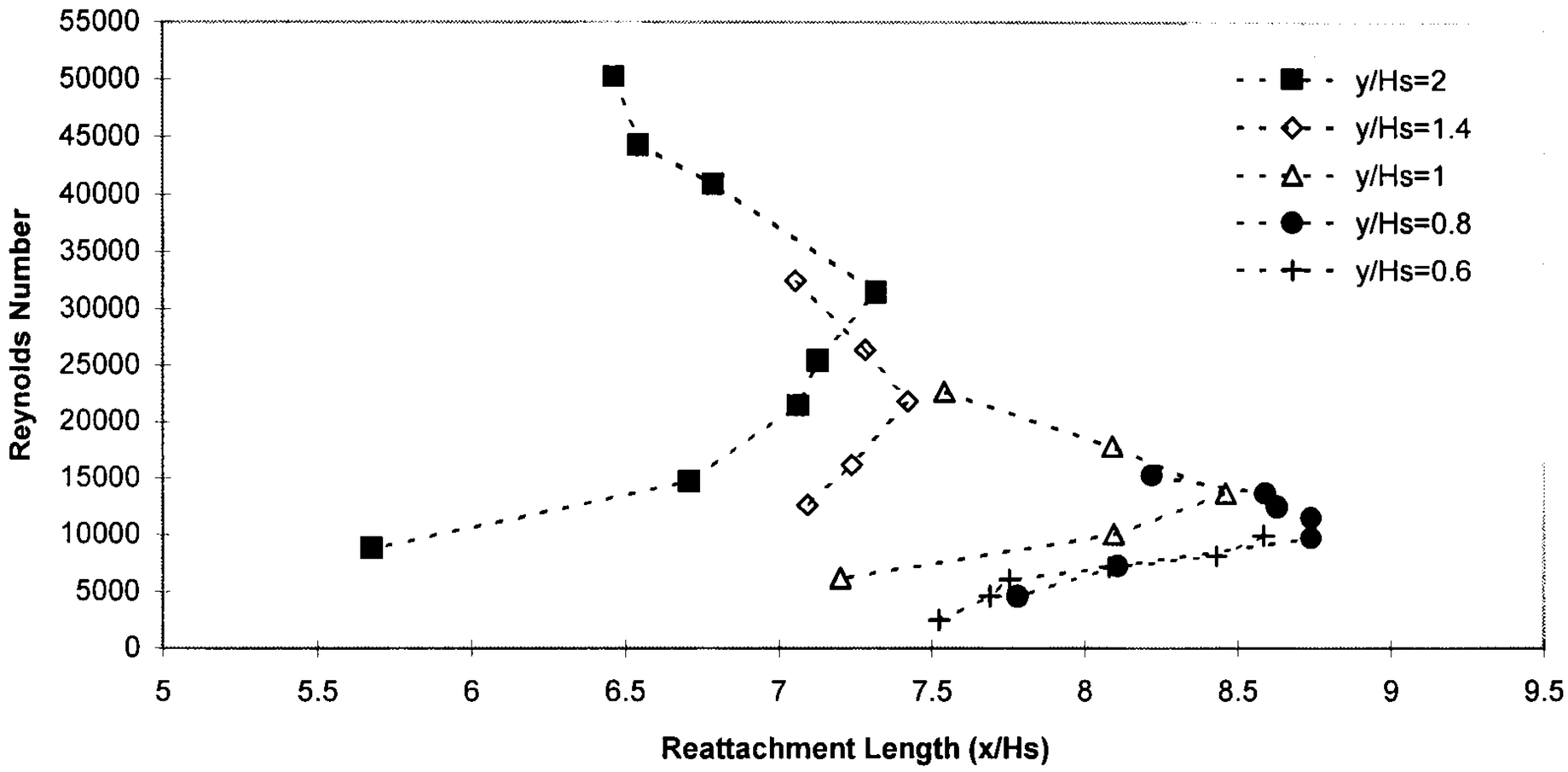

Figure 5.3(c) - Reattachment Length vs Reynolds Number: As=15

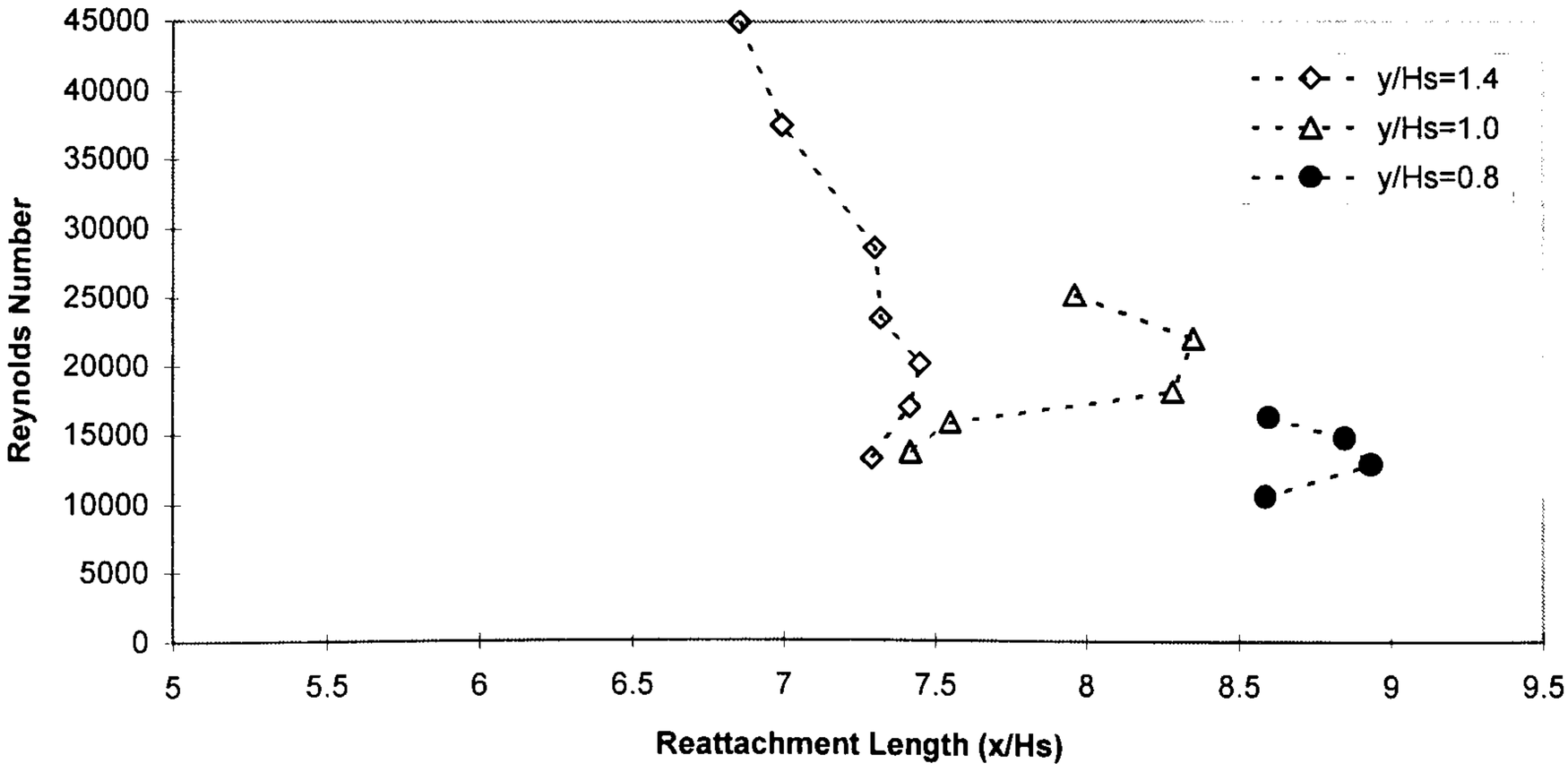

Figure 5.3(d) - Reattachment Length vs Reynolds Number: As=12.5

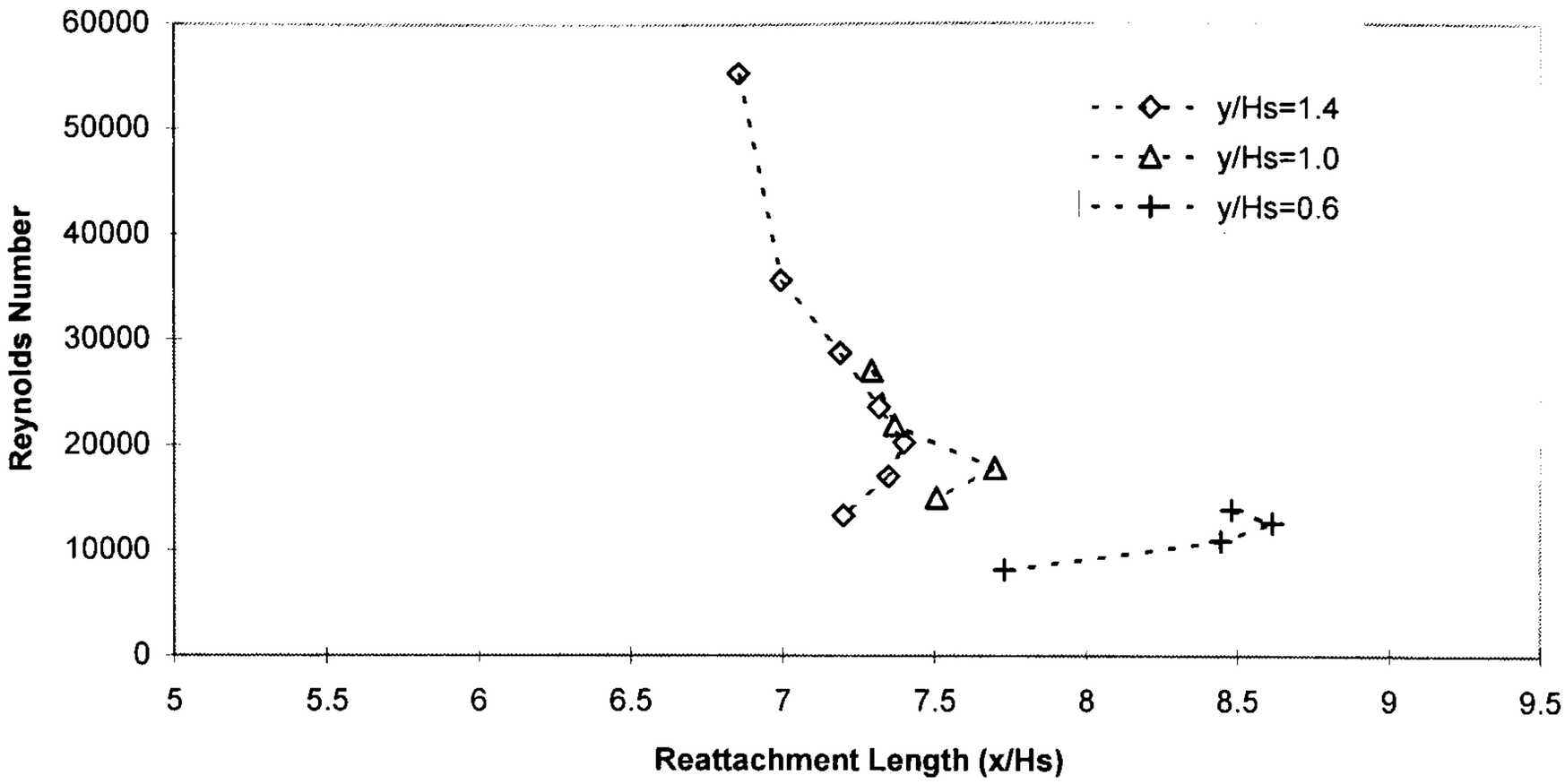

Figure 5.3(e) - Reattachment Length vs Reynolds Number: As=10

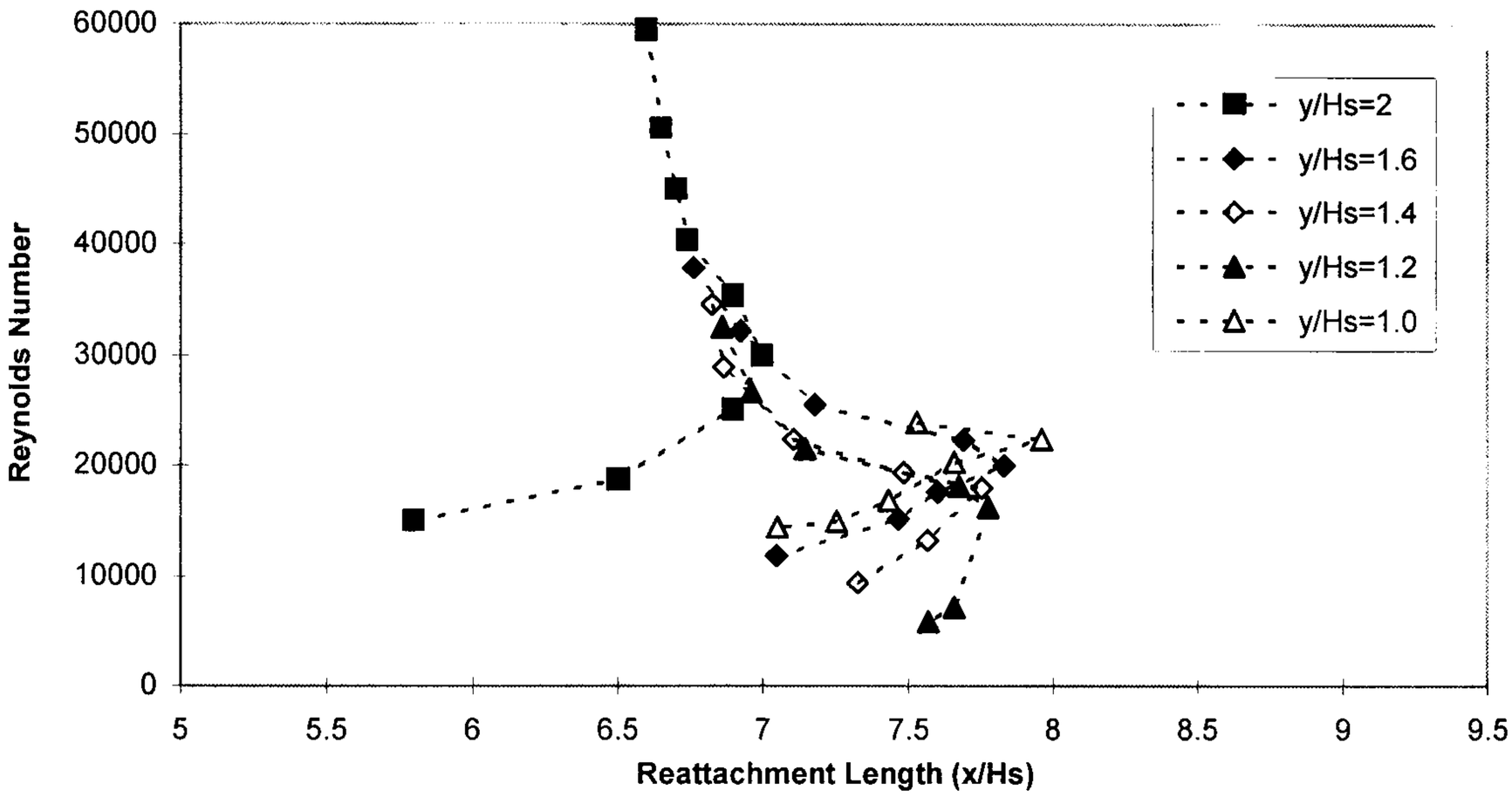

Figure 5.4(a) - R_{Lmax} vs y/H_S for Different Aspect Ratios

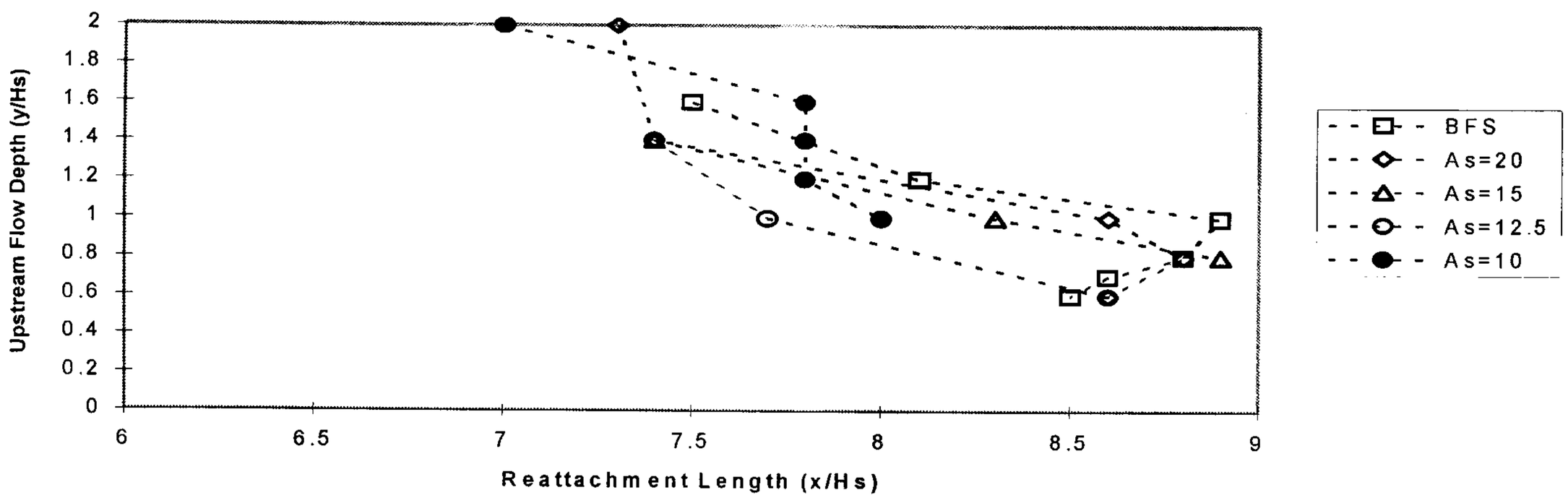

Figure 5.4(b) - Reynolds Number at R_{Lmax} vs y/H_S for Different Aspect Ratios

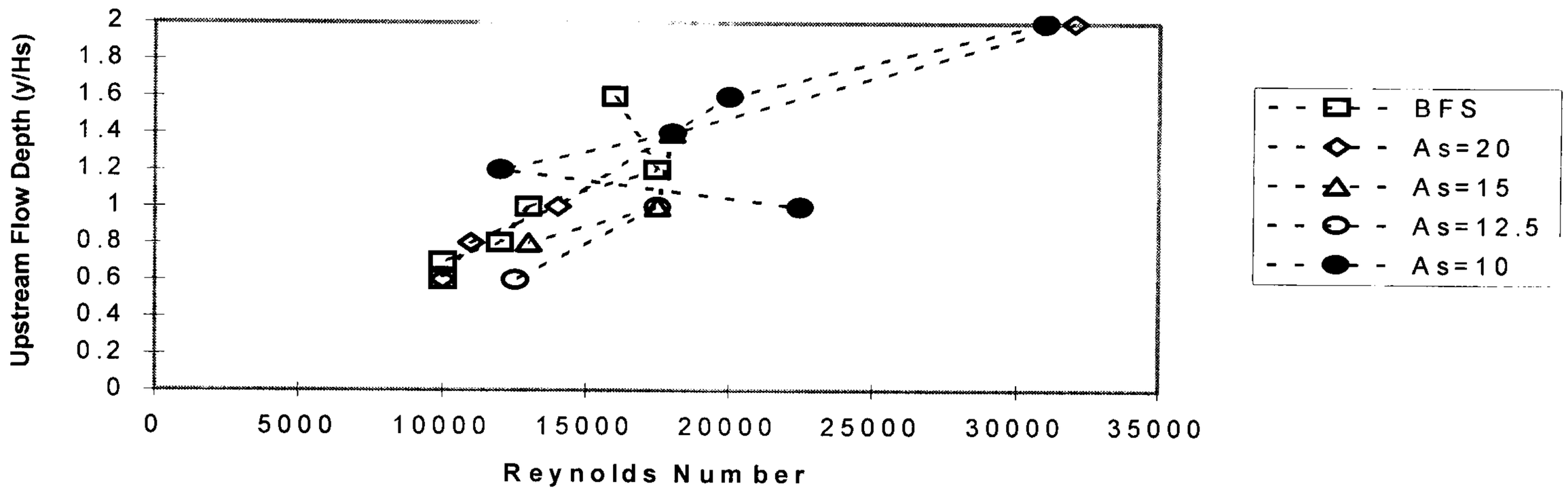

Figure 5.5 (a) - Spanwise Distribution of R_L vs Re: *y/Hs*=2

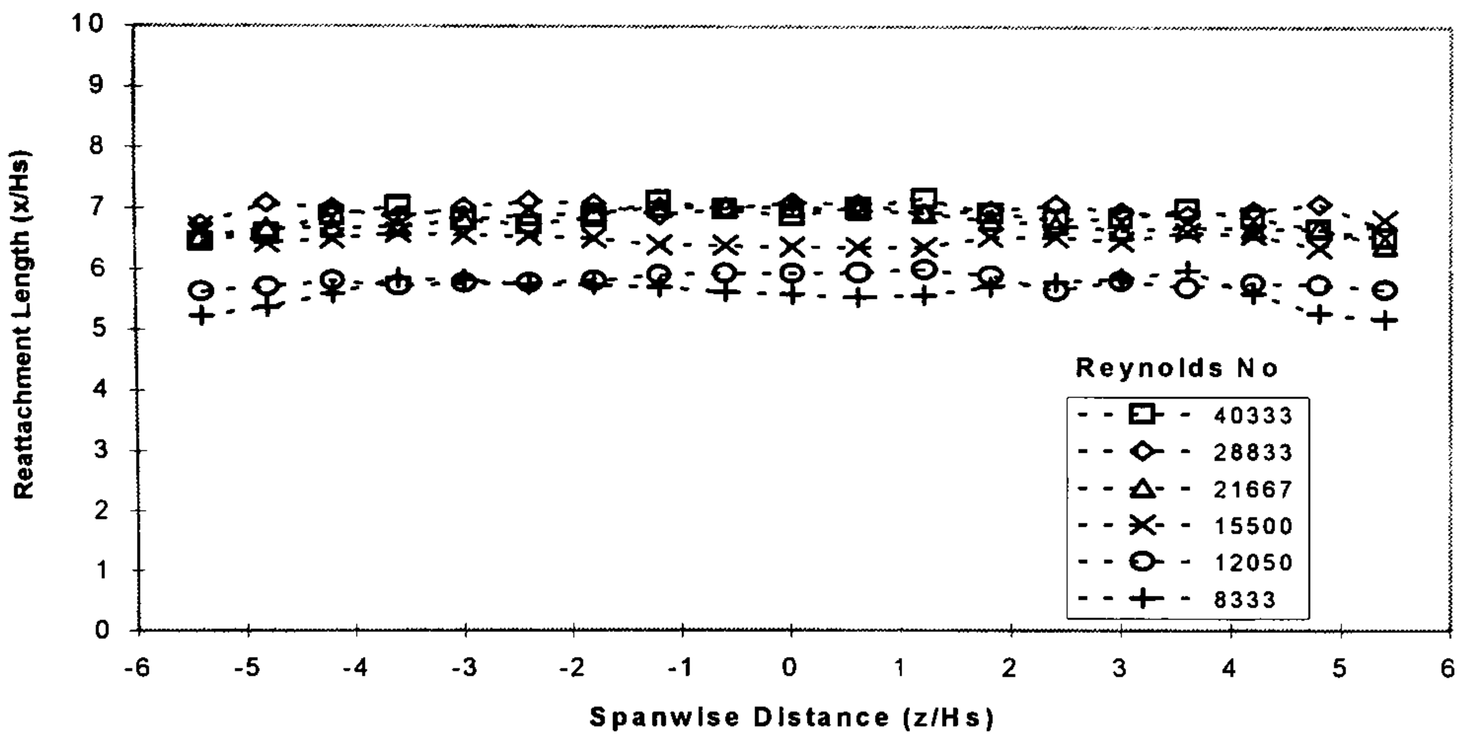

Figure 5.5 (b) - Spanwise Distribution of R_L vs Re: *y/Hs*=1.0

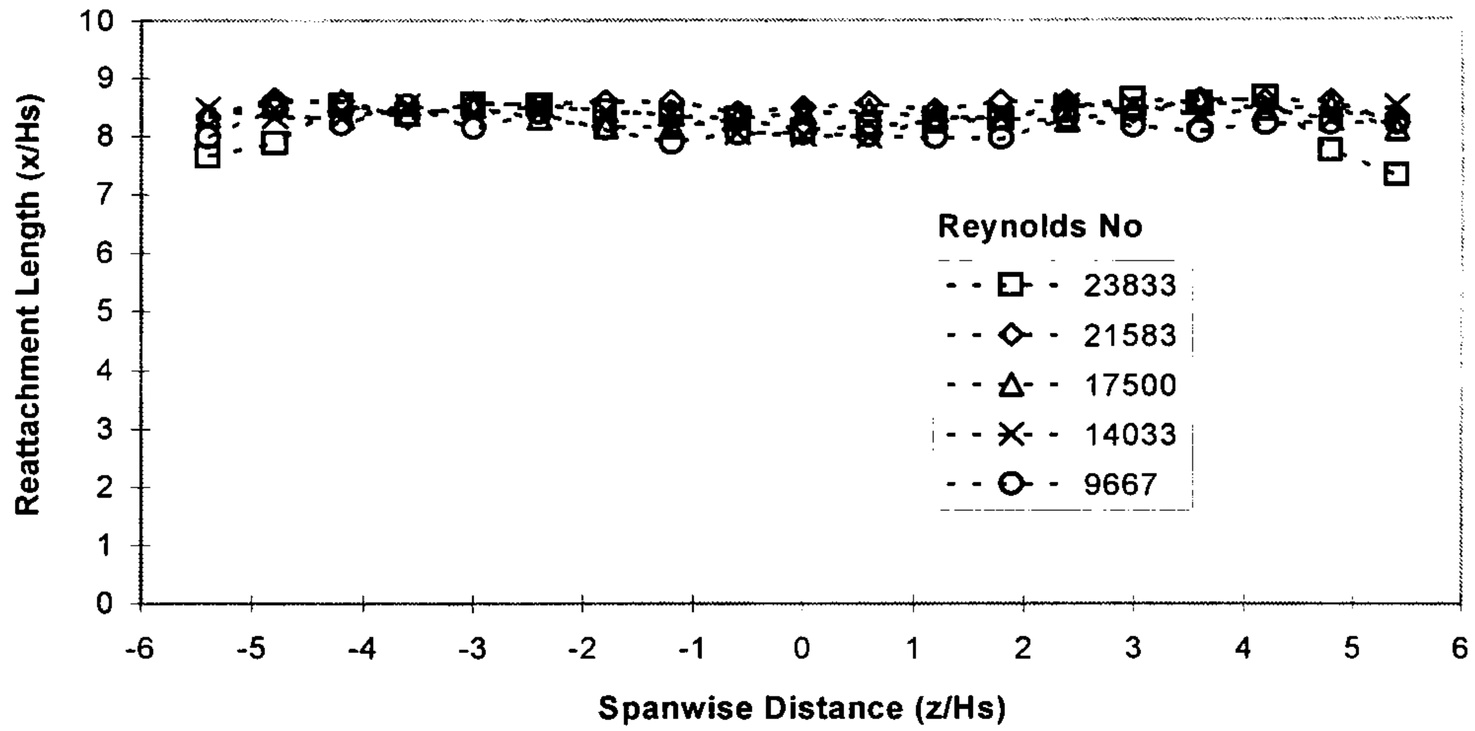

Figure 5.5 (c) - Spanwise Distribution of R_L vs Re: *y/Hs*=0.8

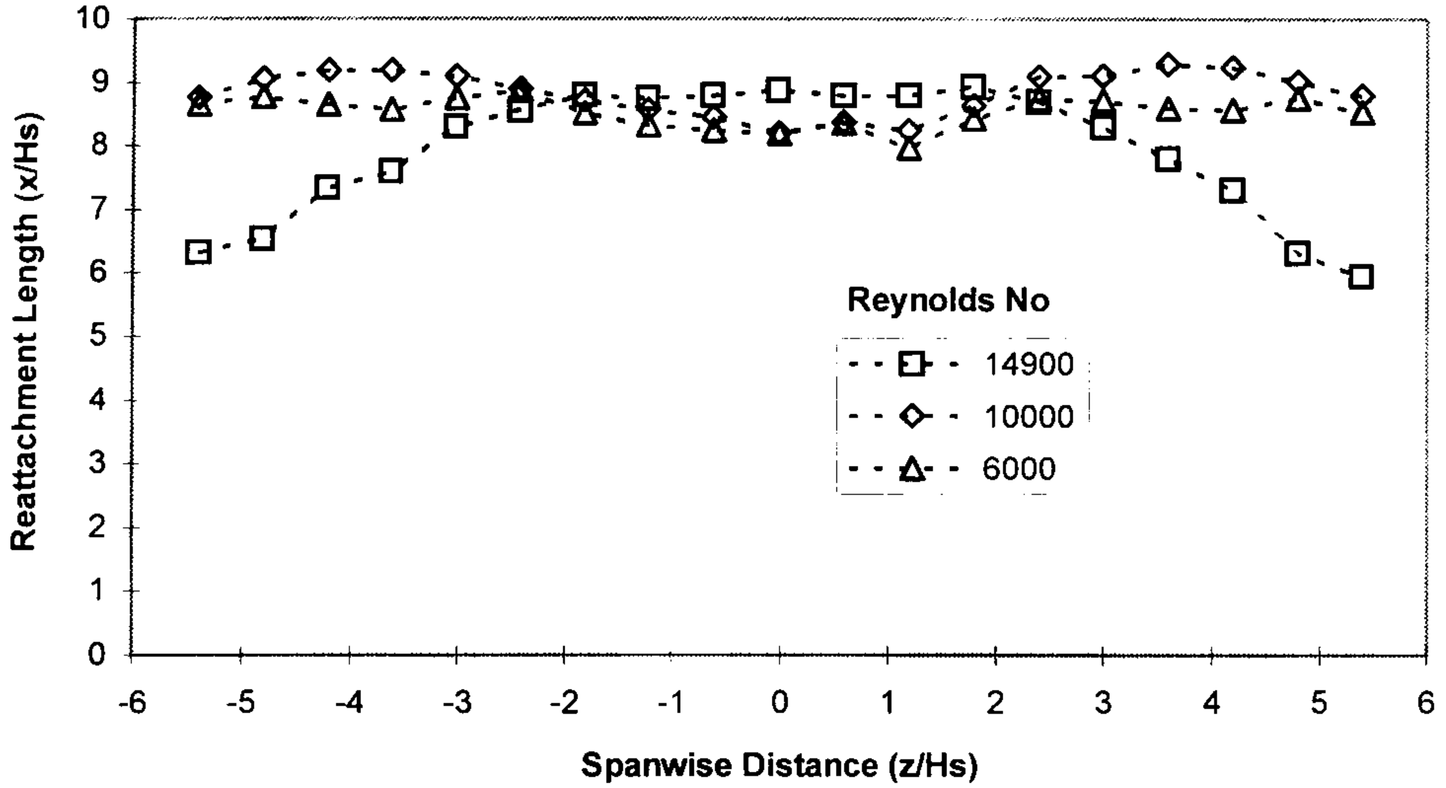

Figure 5.5 (d) - Spanwise Distribution of R_L vs Re: *y/Hs*=0.6

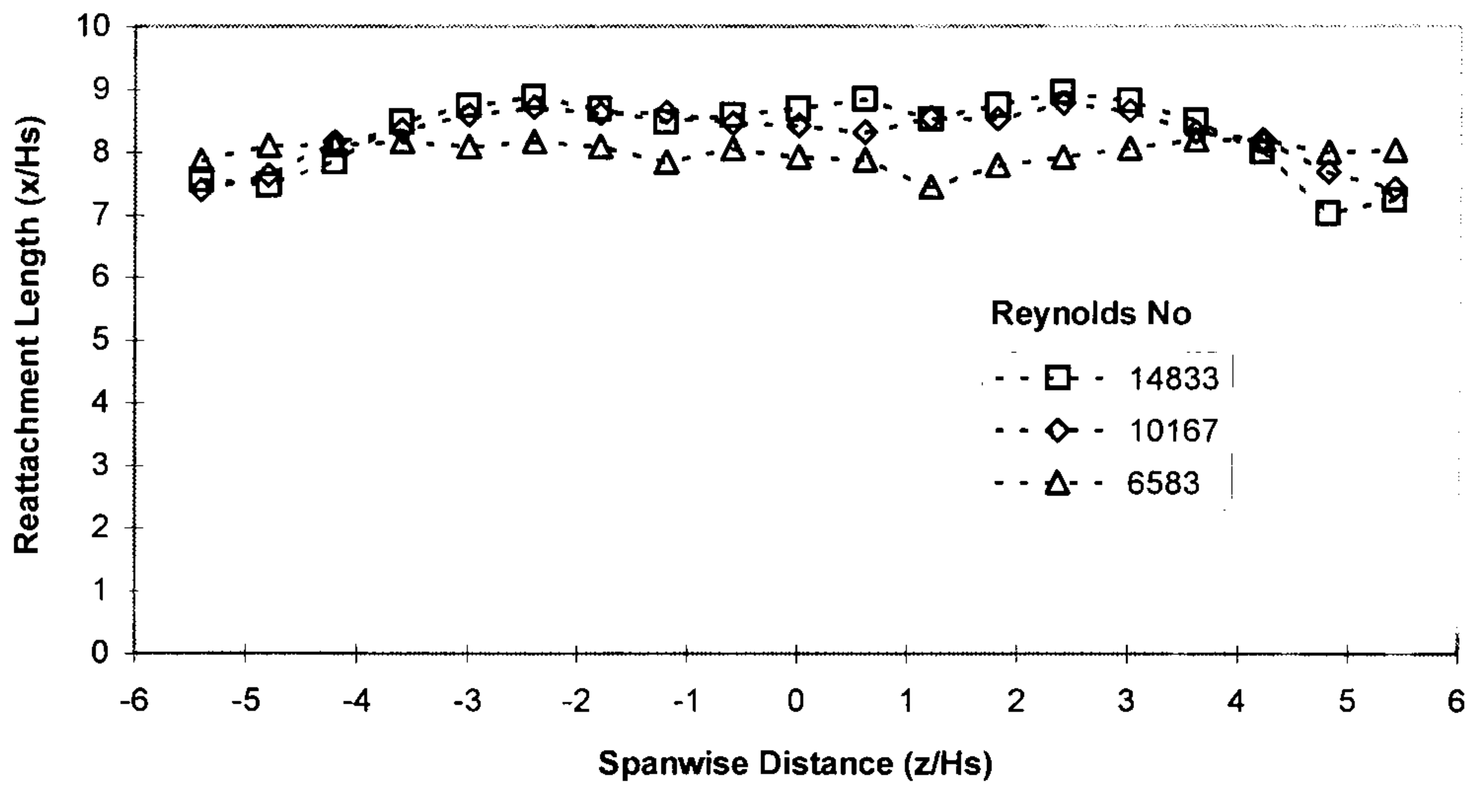

Figure 5.6 (a) - 2-Component Velocity Vector: BFS-1

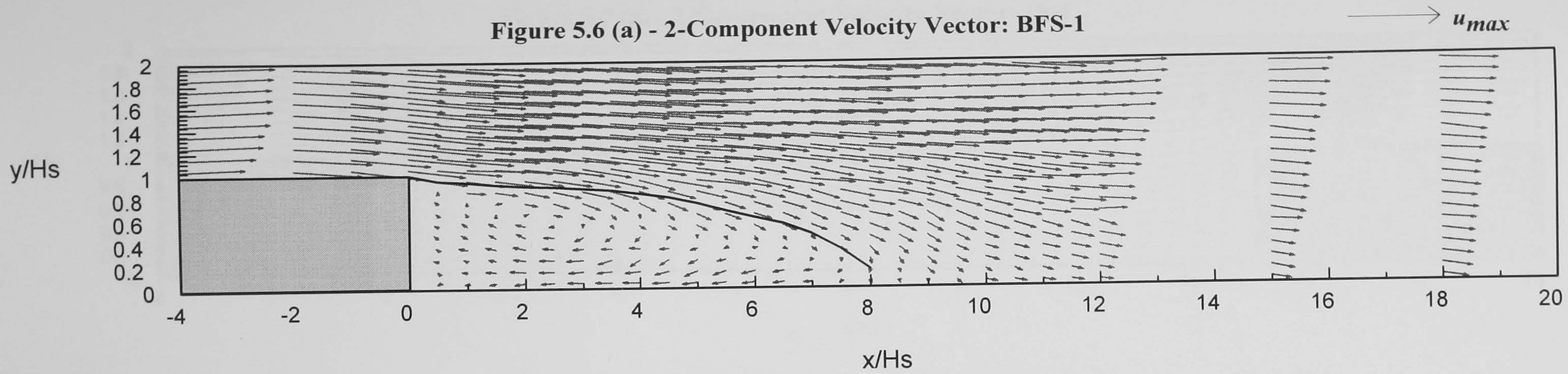

Figure 5.6 (b) - 2-Component Velocity Vector: BFS-2

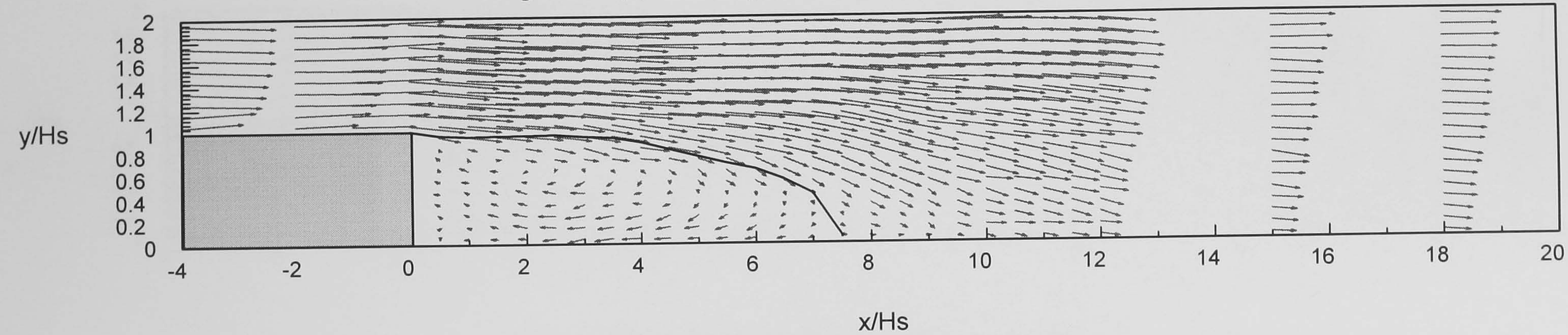

Figure 5.6 (c) - 2-Component Velocity Vector: BFS-3

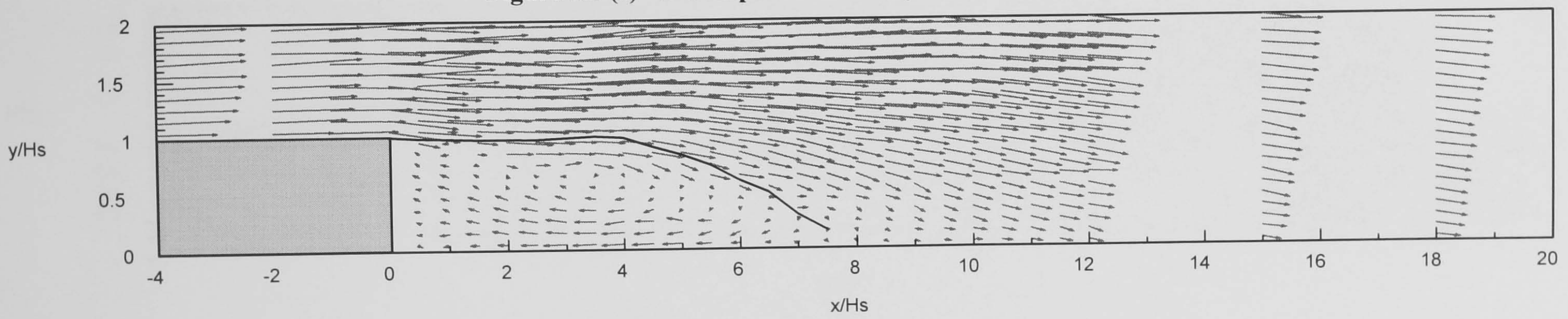

Figure 5.7 (a) - 2-Component Velocity Vector: 15-1

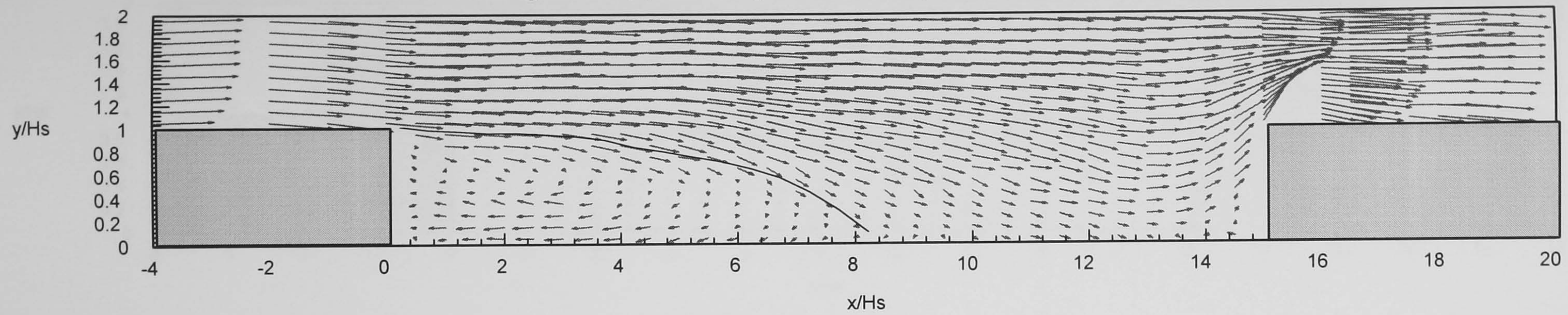

Figure 5.7 (b) - 2-Component Velocity Vector: 15-2

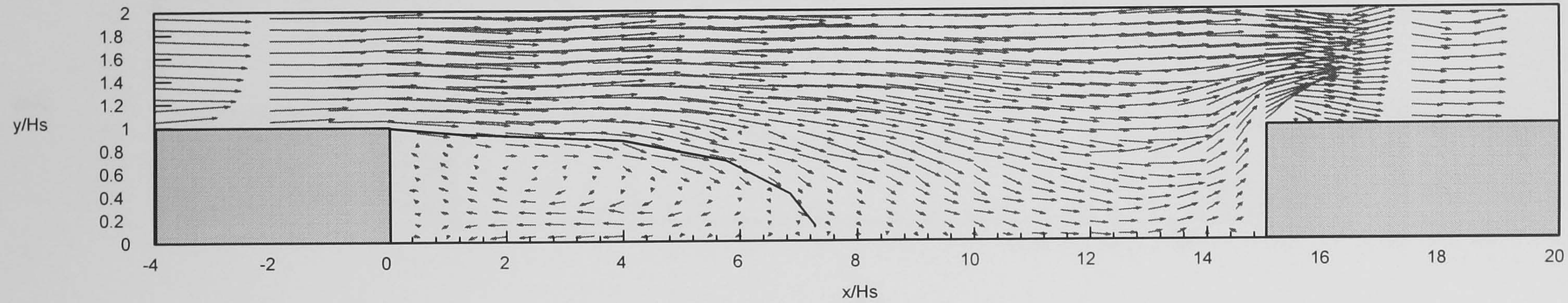

Figure 5.7 (c) - 2-Component Velocity Vector: 15-3

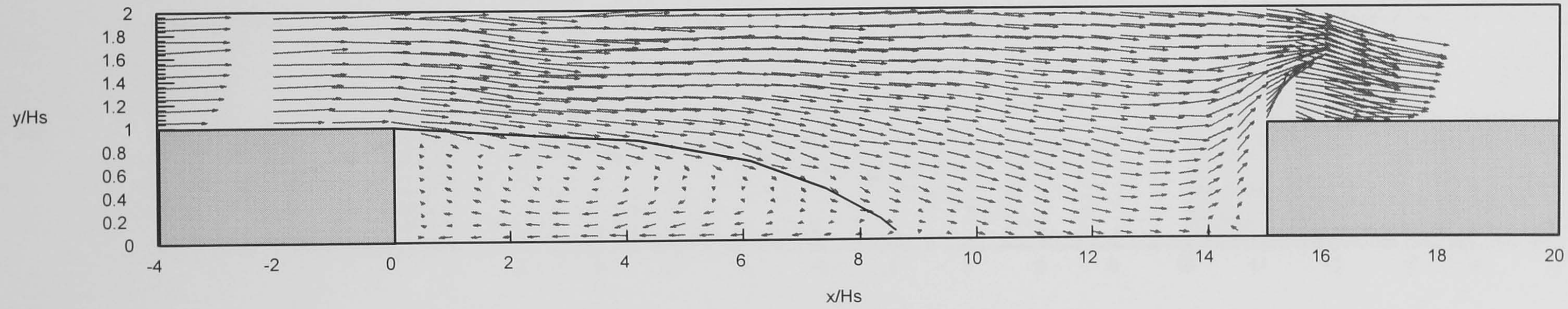

Figure 5.8 (a) - 2-Component Velocity Vector: 10-1

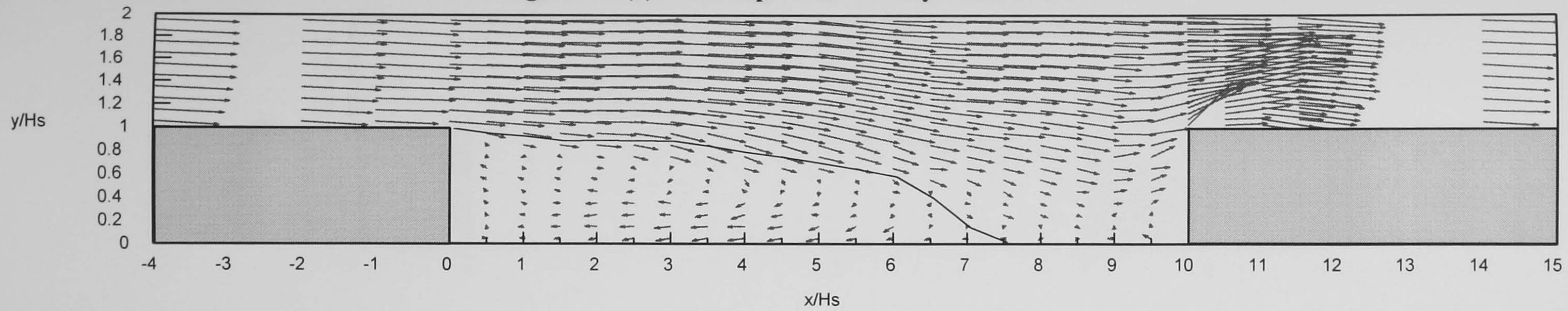

Figure 5.8 (b) - 2-Component Velocity Vector: 10-2

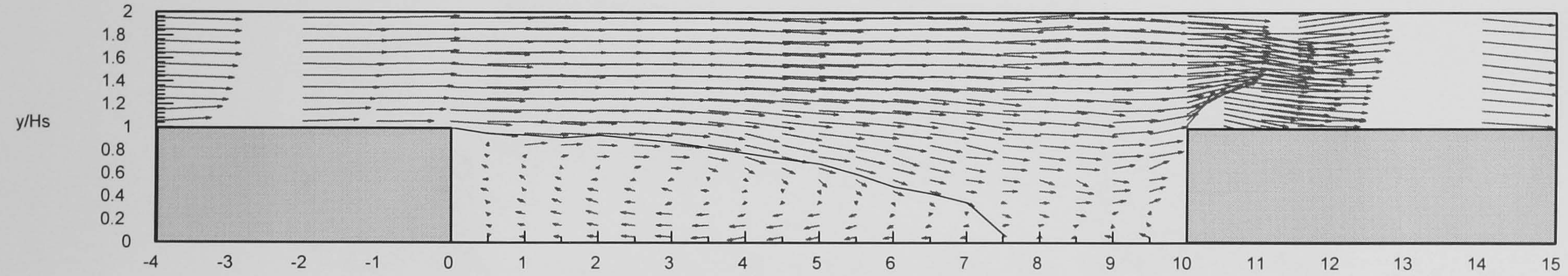

Figure 5.8 (c) - 2-Component Velocity Vector: 10-3

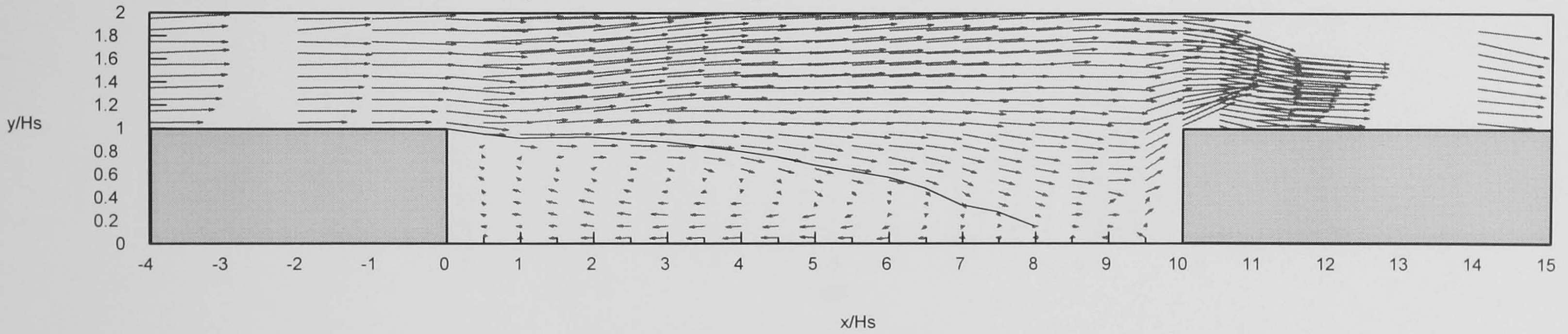

Figure 5.9 (a) - 2-Component Velocity Vector: 5-1

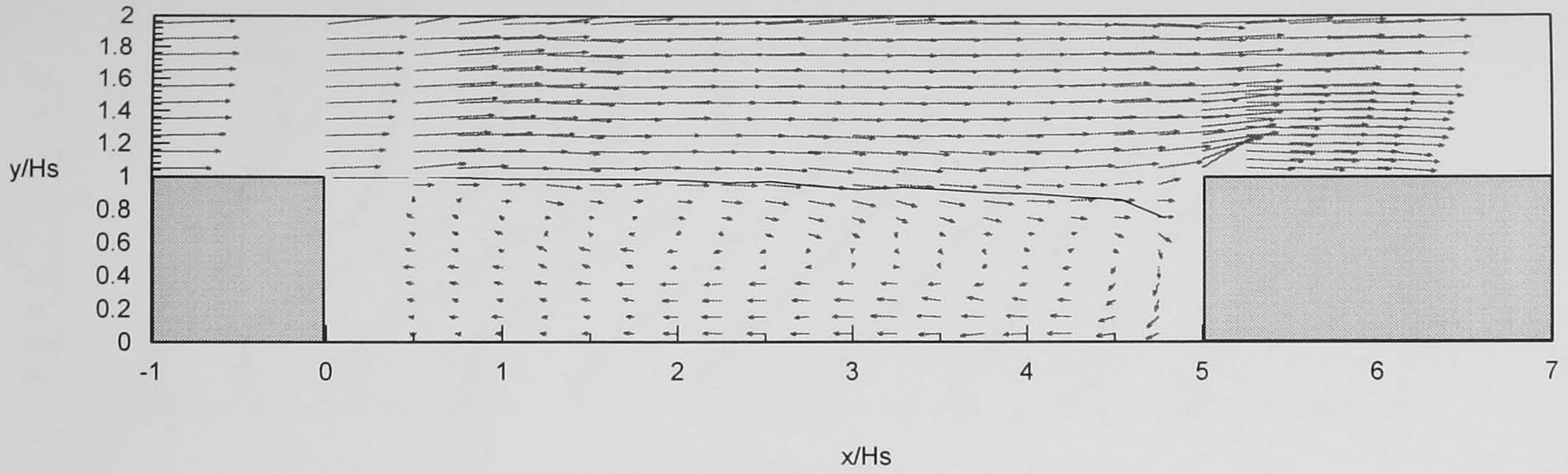

Figure 5.9 (b) - 2-Component Velocity Vector: 5-2

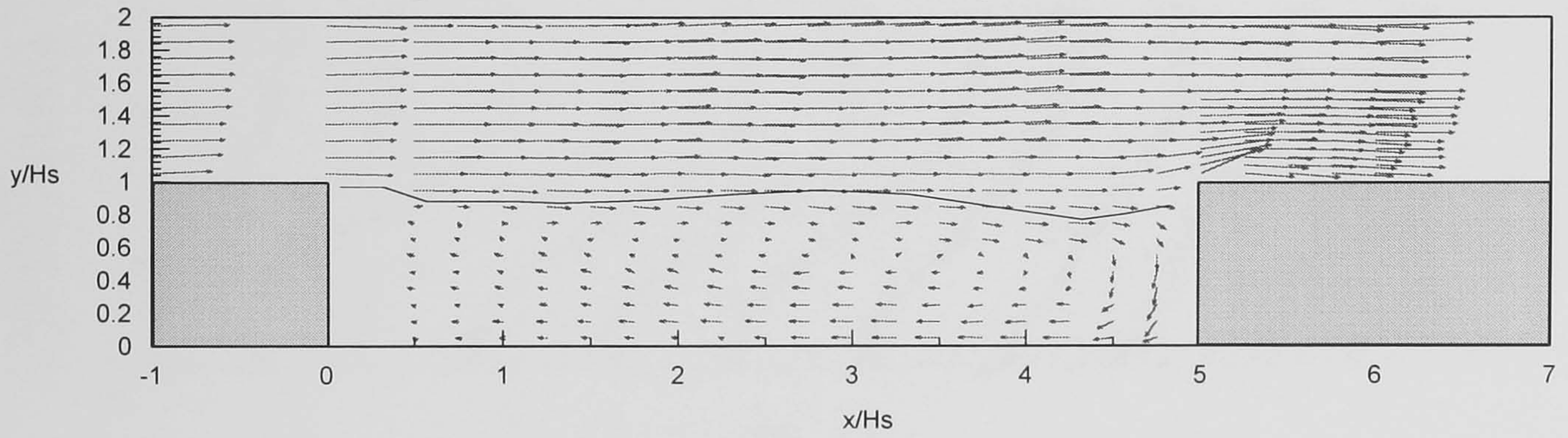

Figure 5.9 (c) - 2-Component Velocity Vector: 5-3

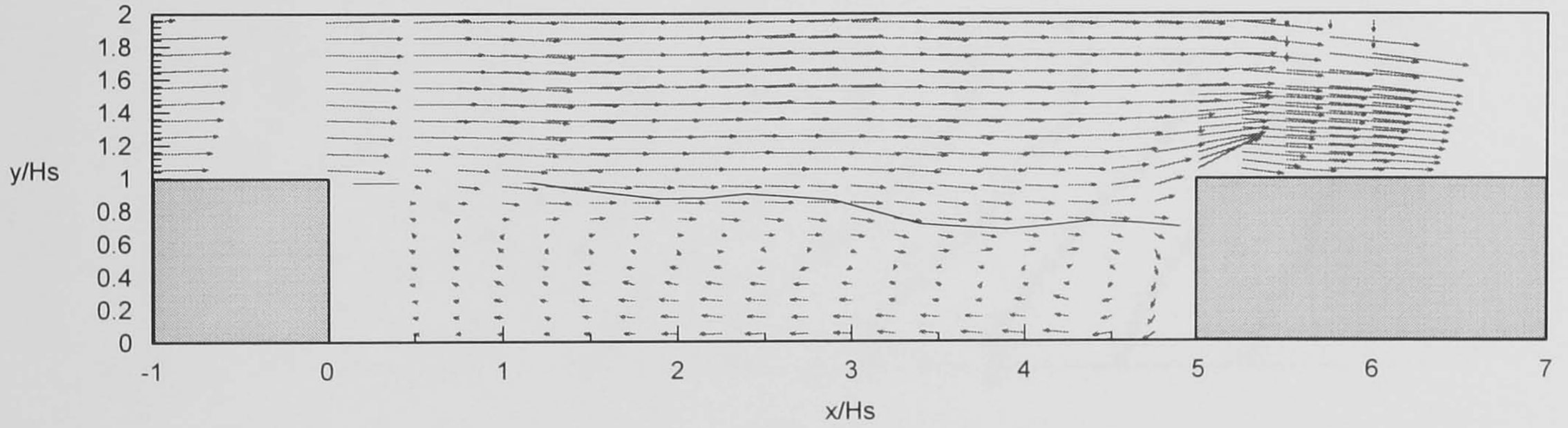

Figure 5.10(a) - Selected Velocity Profiles in Recirculation Zone: BFS - 1

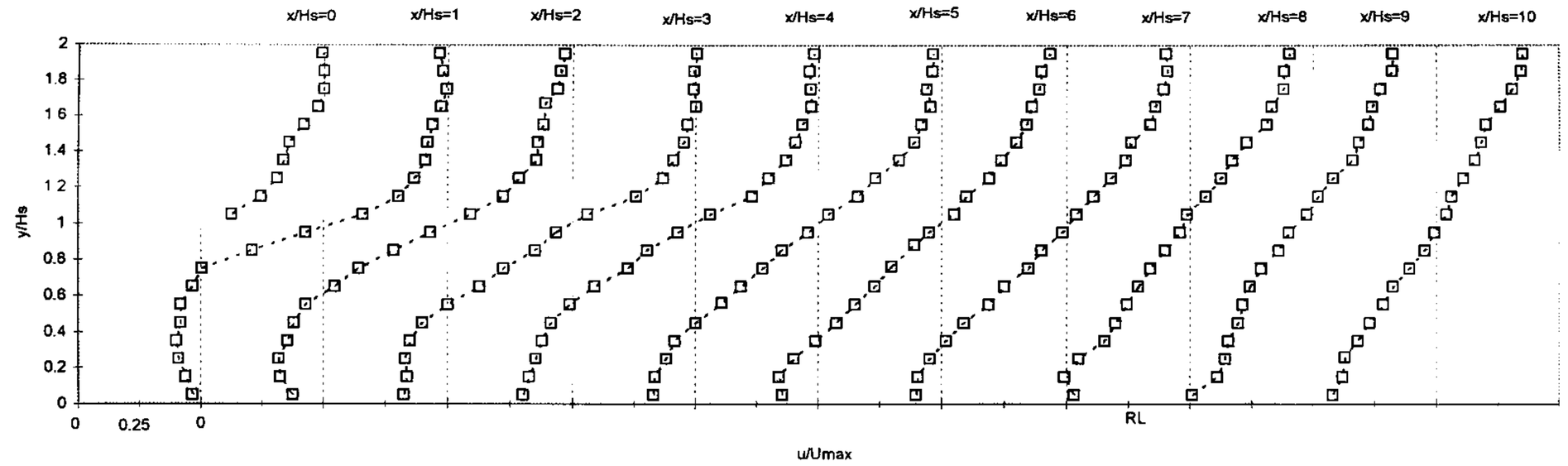

Figure 5.10(b) - Selected Velocity Profiles in Recirculation Zone: BFS - 2

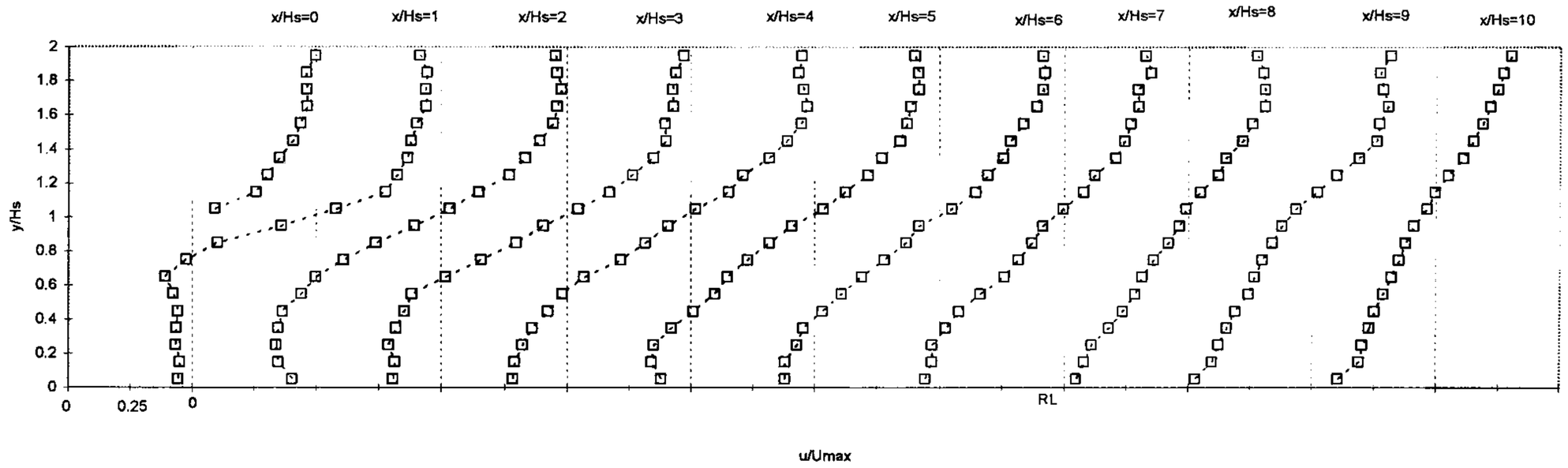

Figure 5.10(c) - Selected Velocity Profiles in Recirculation Zone: BFS - 3

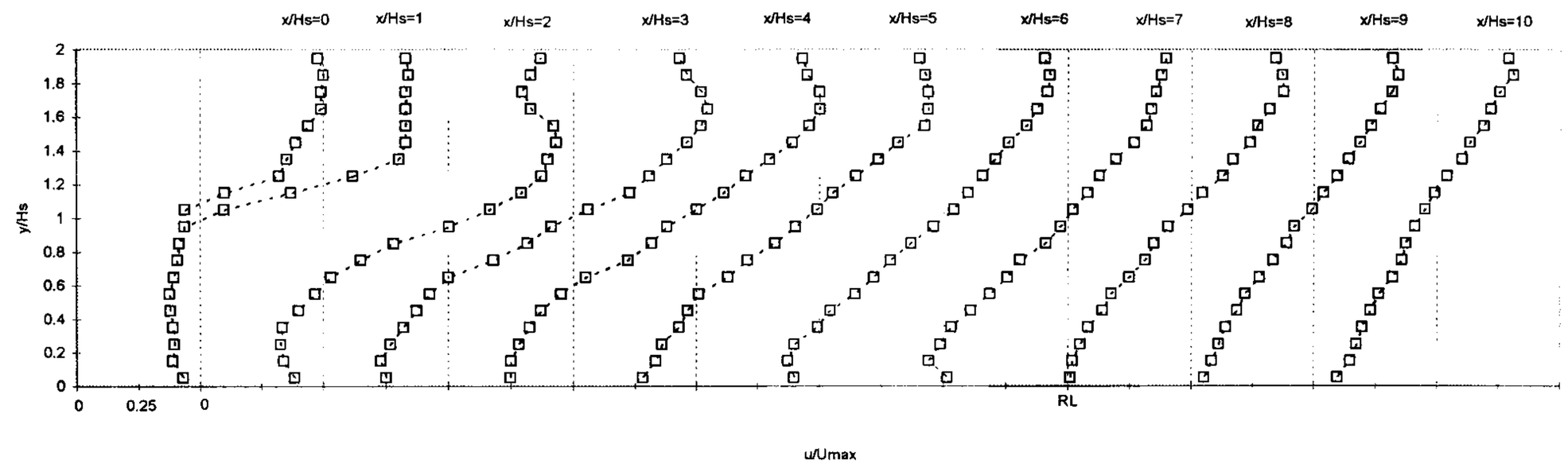

Figure 5.11(a) - Selected Velocity Profiles in Recirculation Zone: 15-1

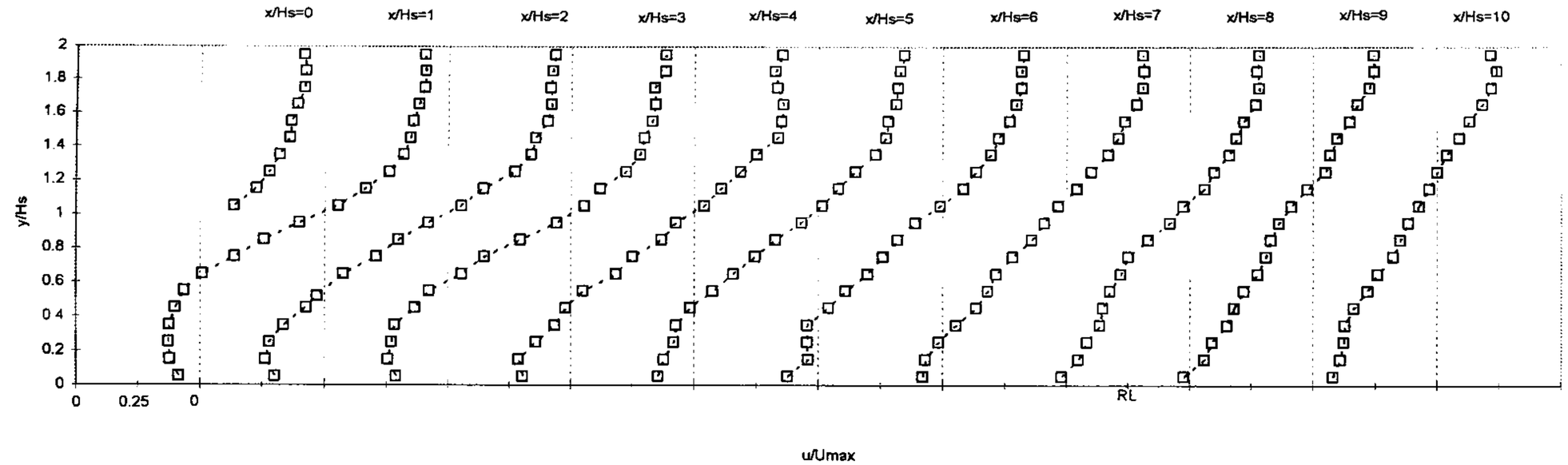

Figure 5.11(b) - Selected Velocity Profiles in Recirculation Zone: 15-2

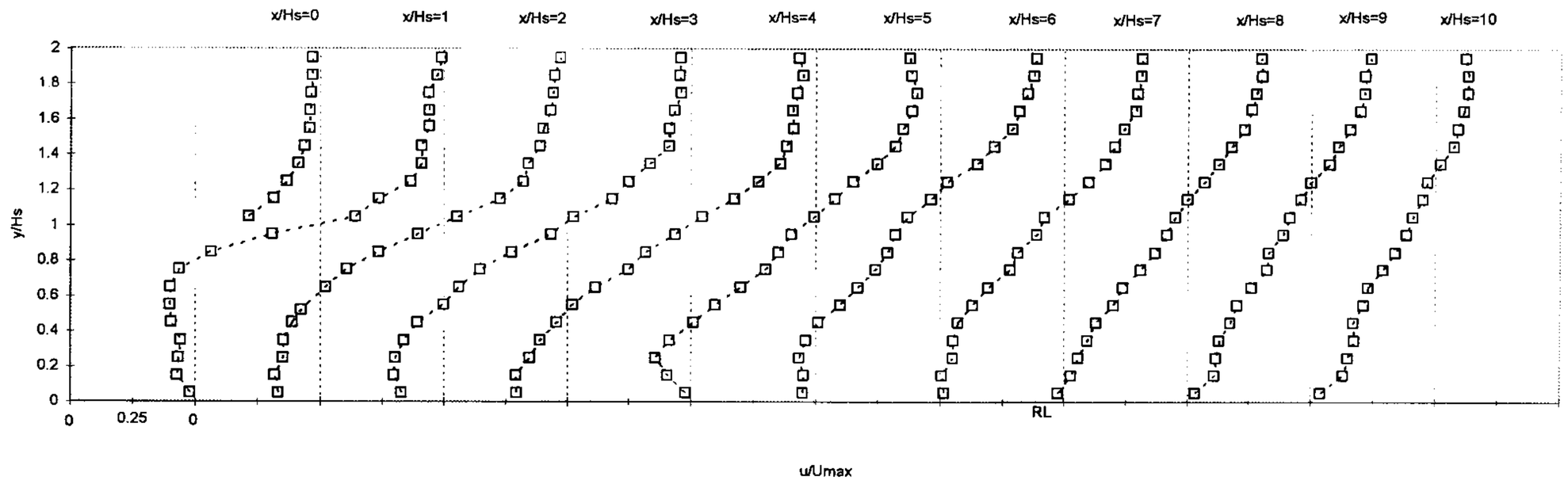

Figure 5.11(c) - Selected Velocity Profiles in Recirculation Zone: 15-3

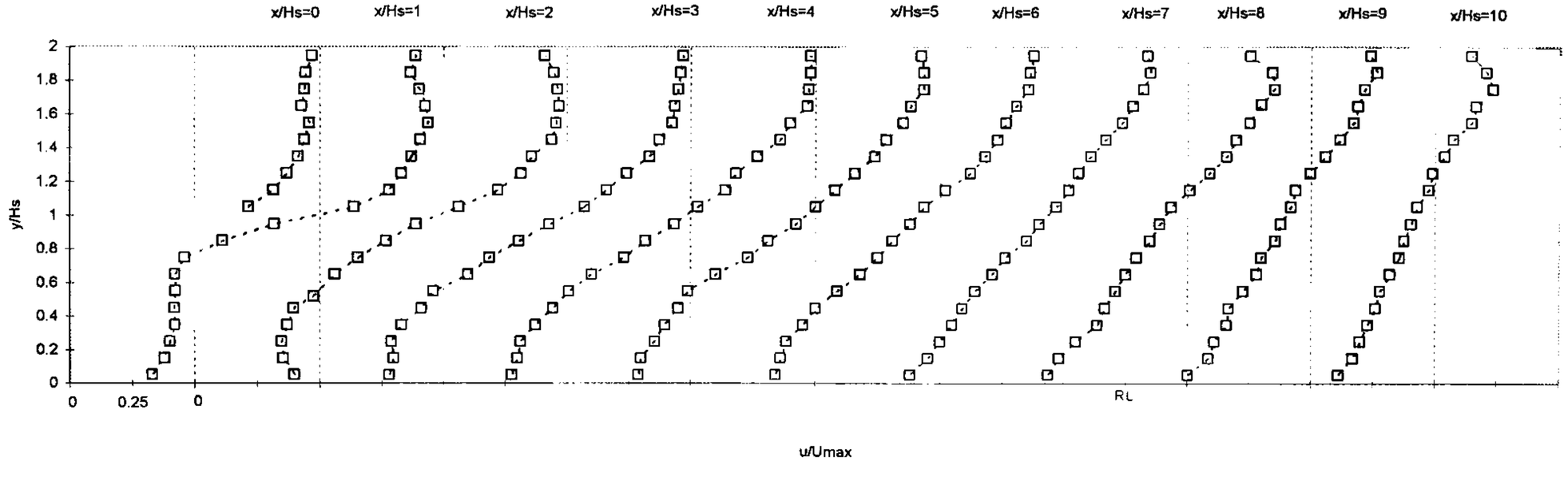

Figure 5.12(a) - Selected Velocity Profiles in Recirculation Zone: 10-1

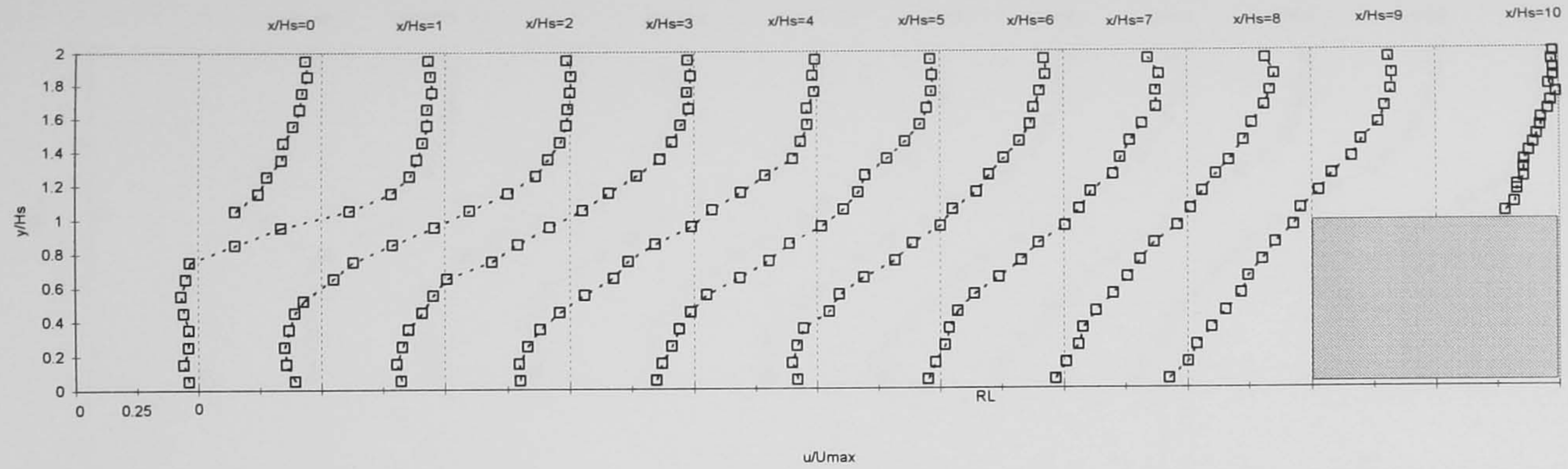

Figure 5.12(b) - Selected Velocity Profiles in Recirculation Zone: 10-2

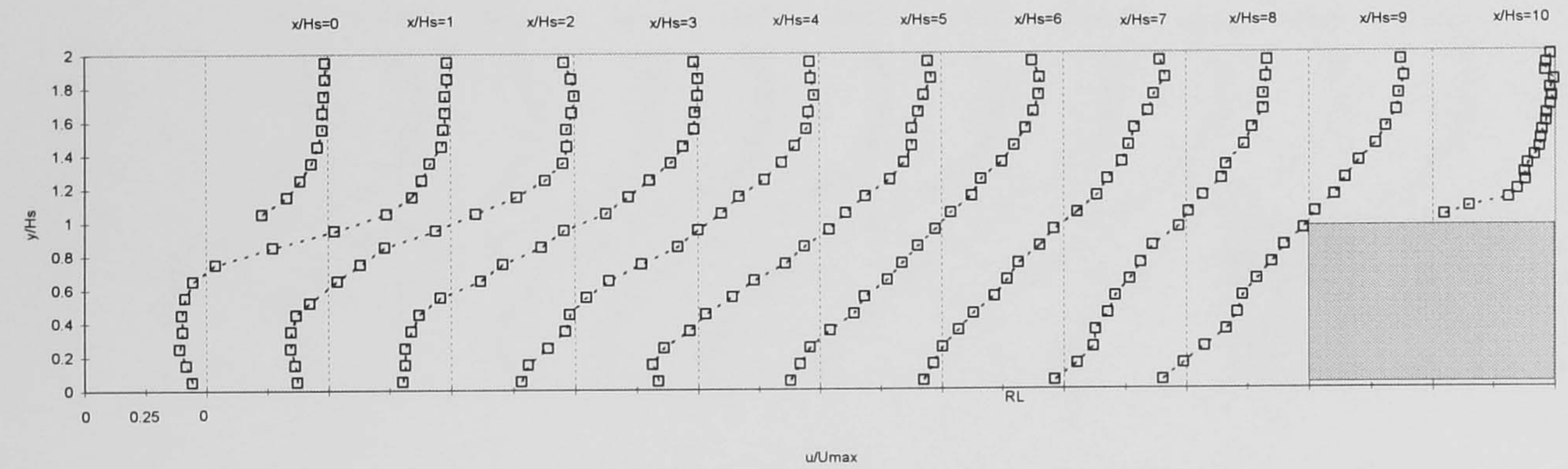

Figure 5.12(c) - Selected Velocity Profiles in Recirculation Zone: 10-3

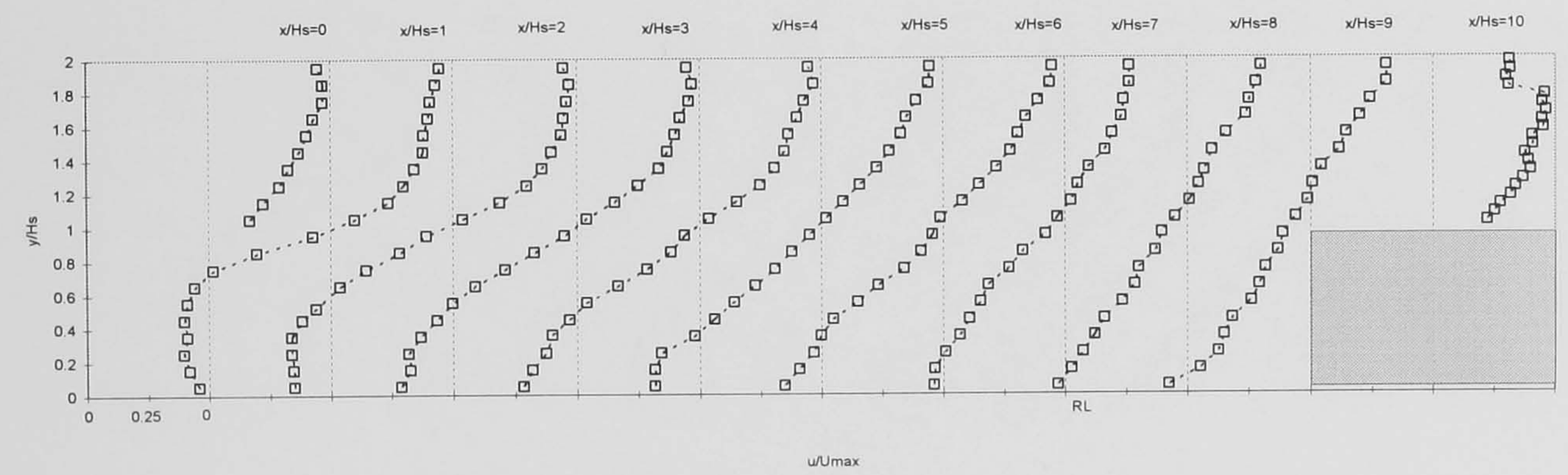

Figure 5.13(a) - Selected Velocity Profiles in Recirculation Zone: 5-1

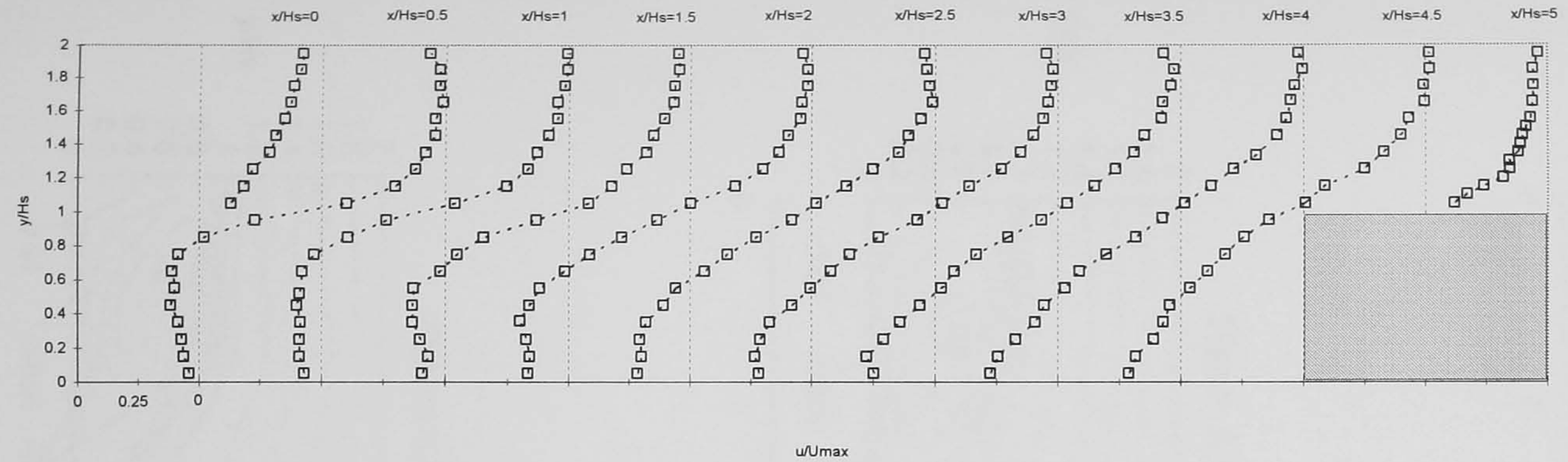

Figure 5.13(b) - Selected Velocity Profiles in Recirculation Zone: 5-2

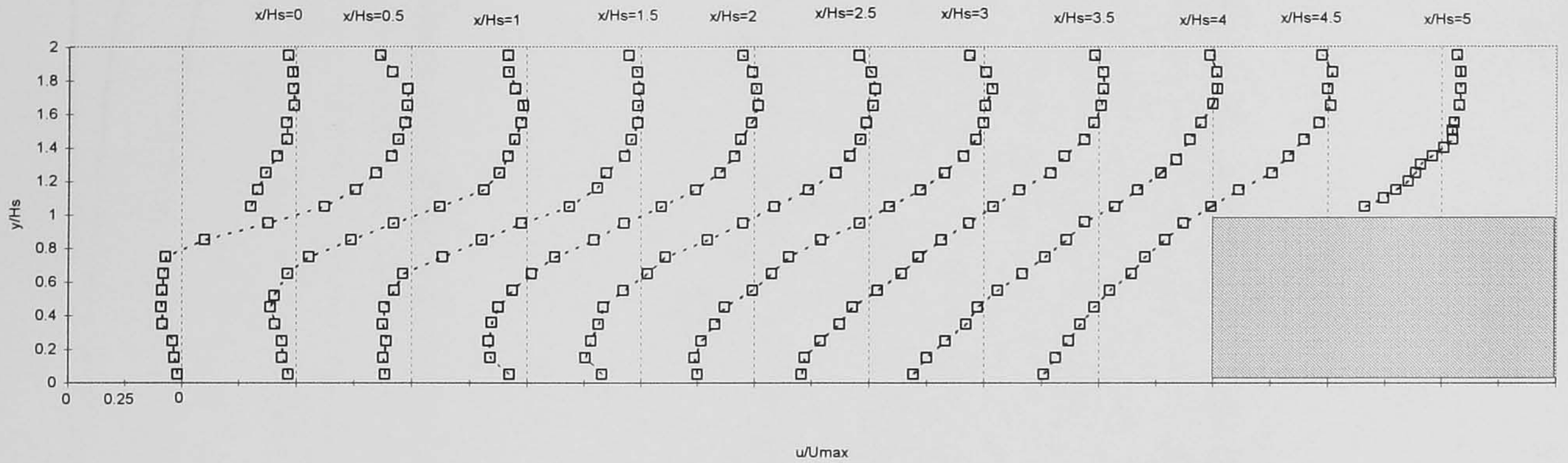

Figure 5.13(c) - Selected Velocity Profiles in Recirculation Zone: 5-3

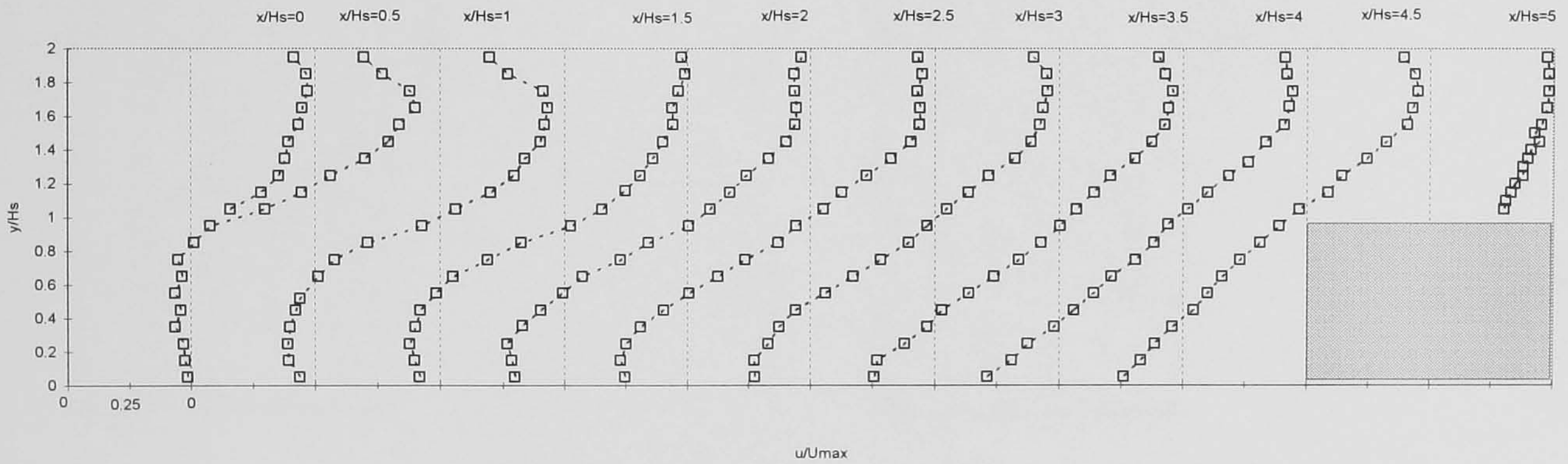

Figure 5.14(a) - Mean Non-Dimensional Streamlines: BFS-1

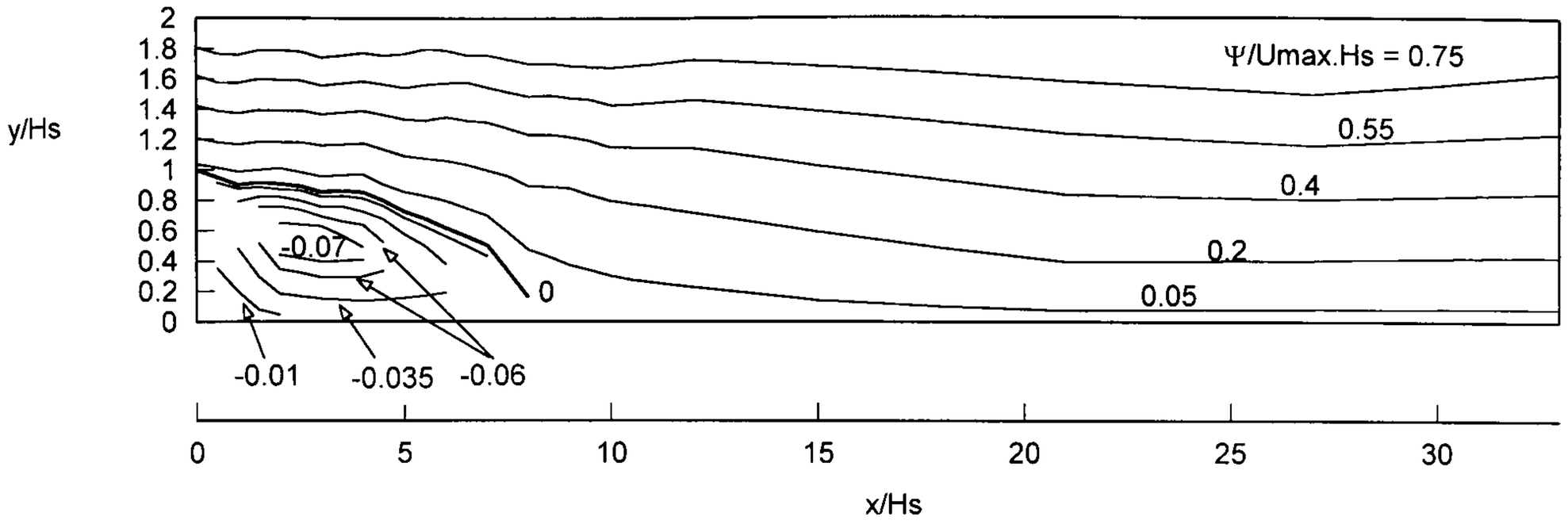

Figure 5.14(b) - Mean Non-Dimensional Streamlines: BFS-2

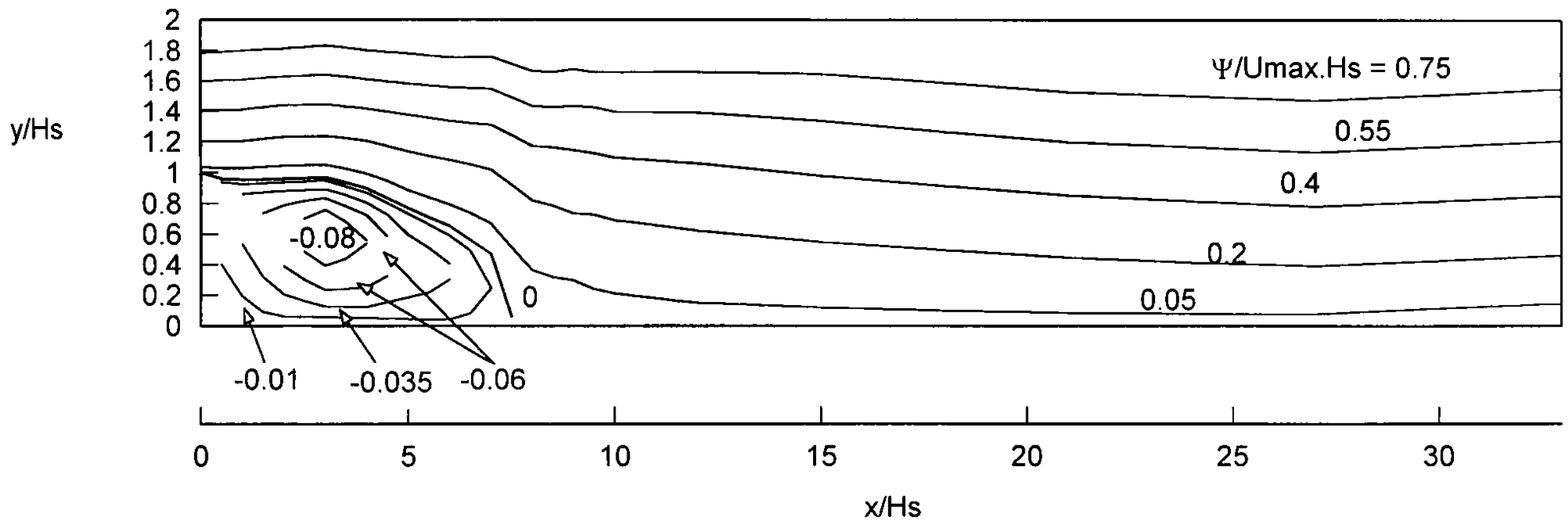

Figure 5.14(c) - Mean Non-Dimensional Streamlines: BFS-3

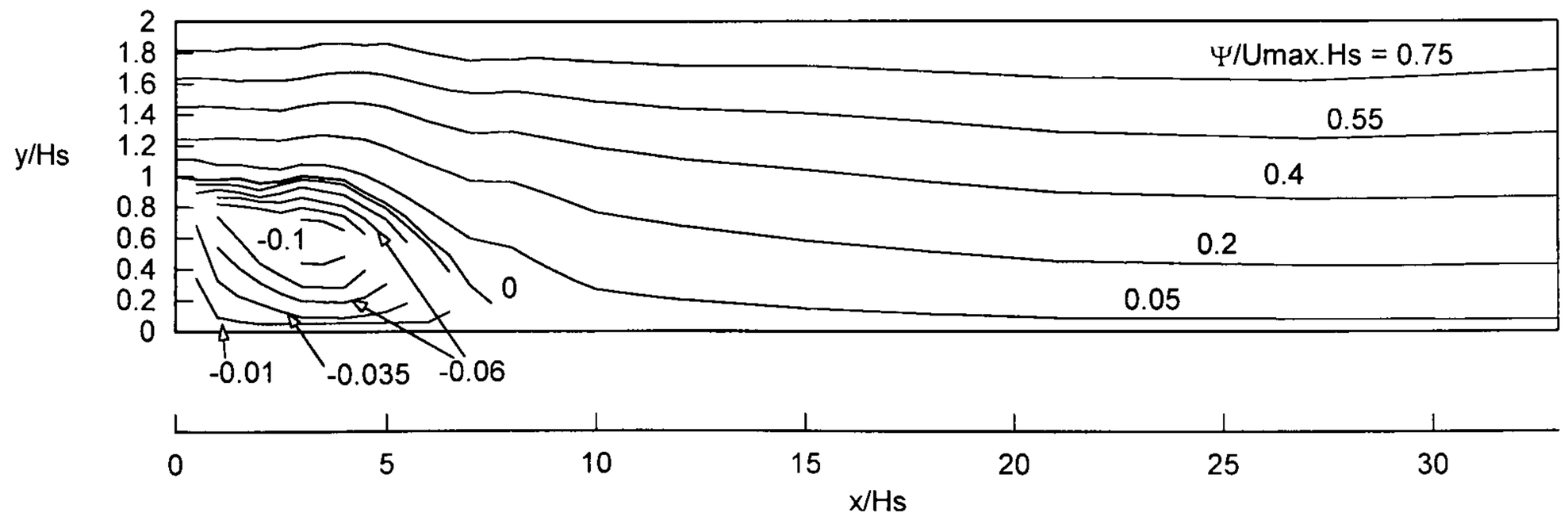

Figure 5.15(a) - Mean Non-Dimensional Streamlines: 15-1

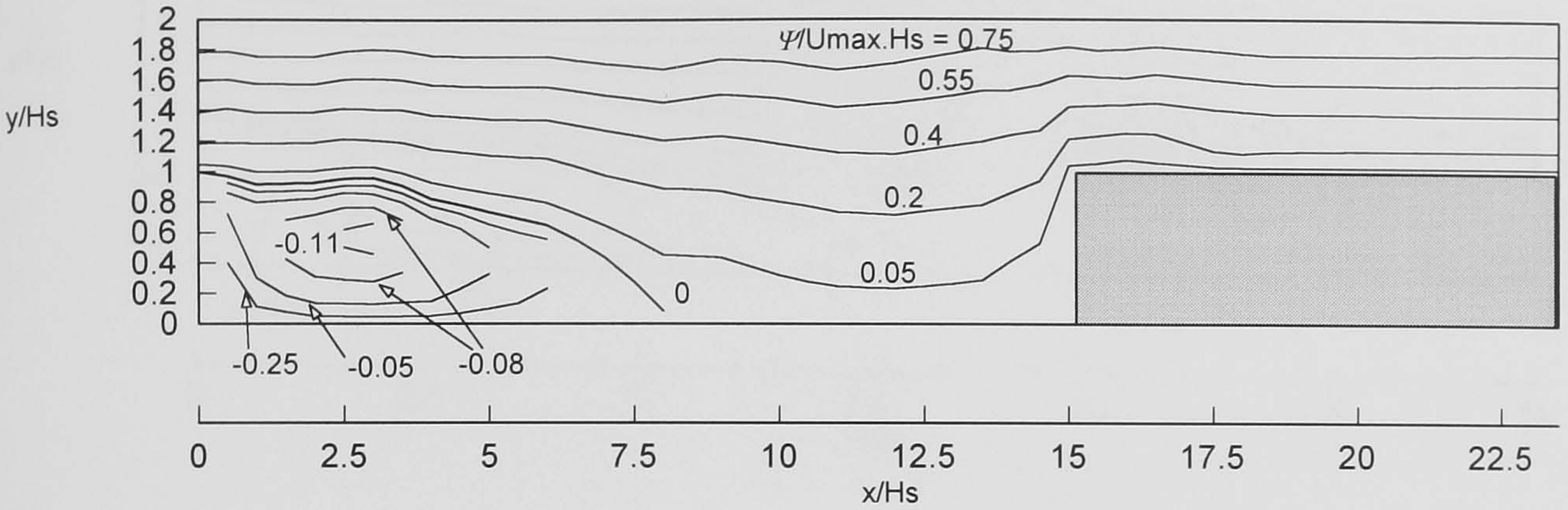

Figure 5.15(b) - Mean Non-Dimensional Streamlines: 15-2

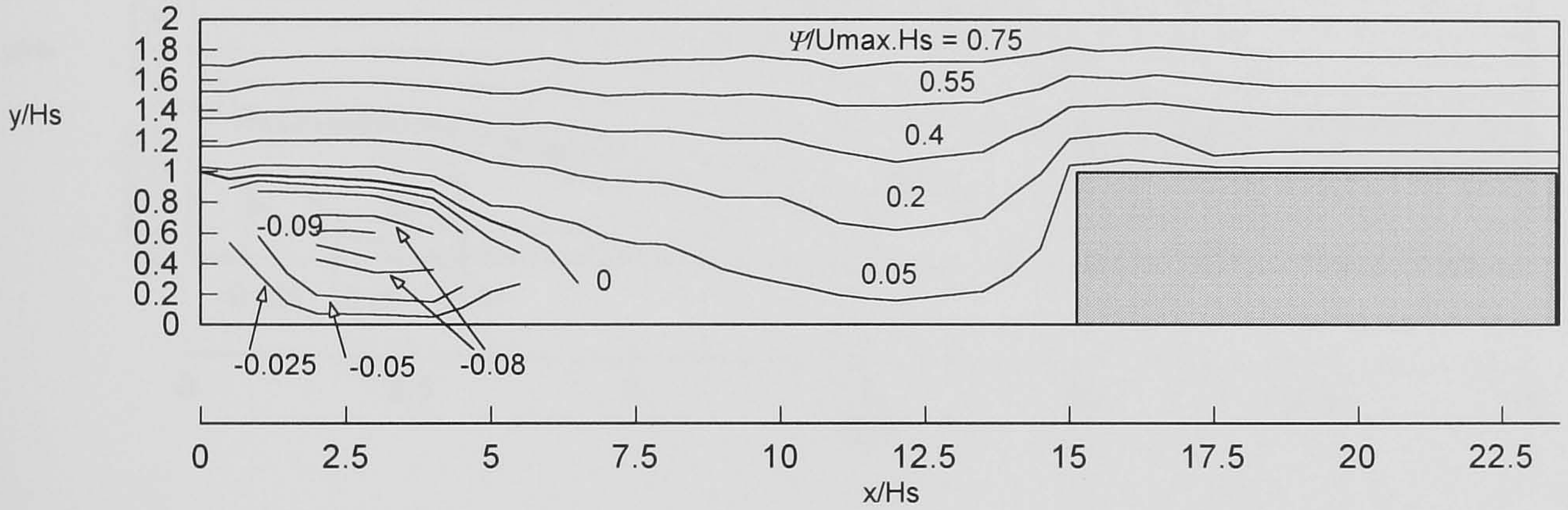

Figure 5.15(c) - Mean Non-Dimensional Streamlines: 15-3

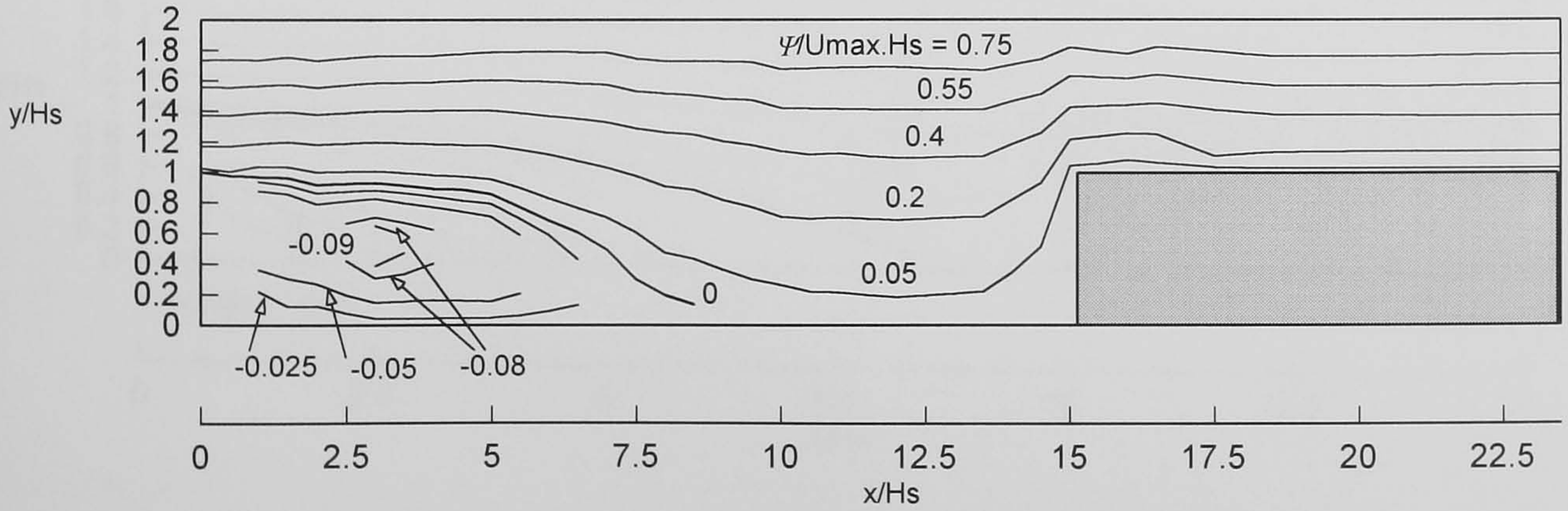

Figure 5.16(a) - Mean Non-Dimensional Streamlines: 10-1

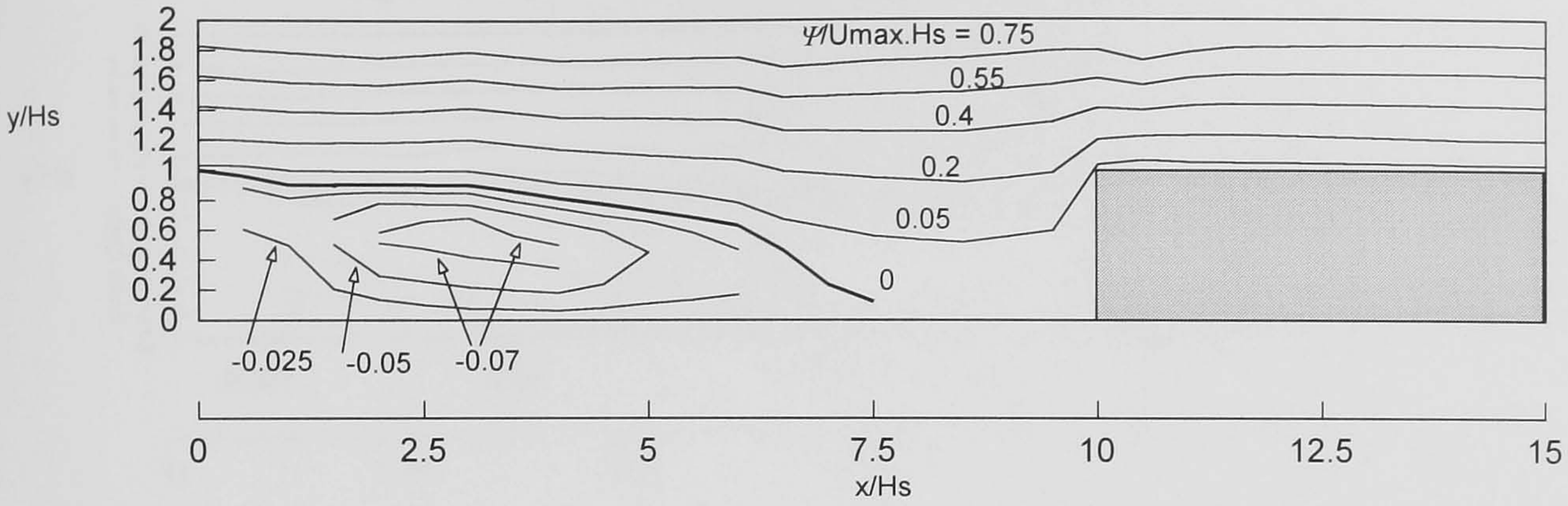

Figure 5.16(b) - Mean Non-Dimensional Streamlines: 10-2

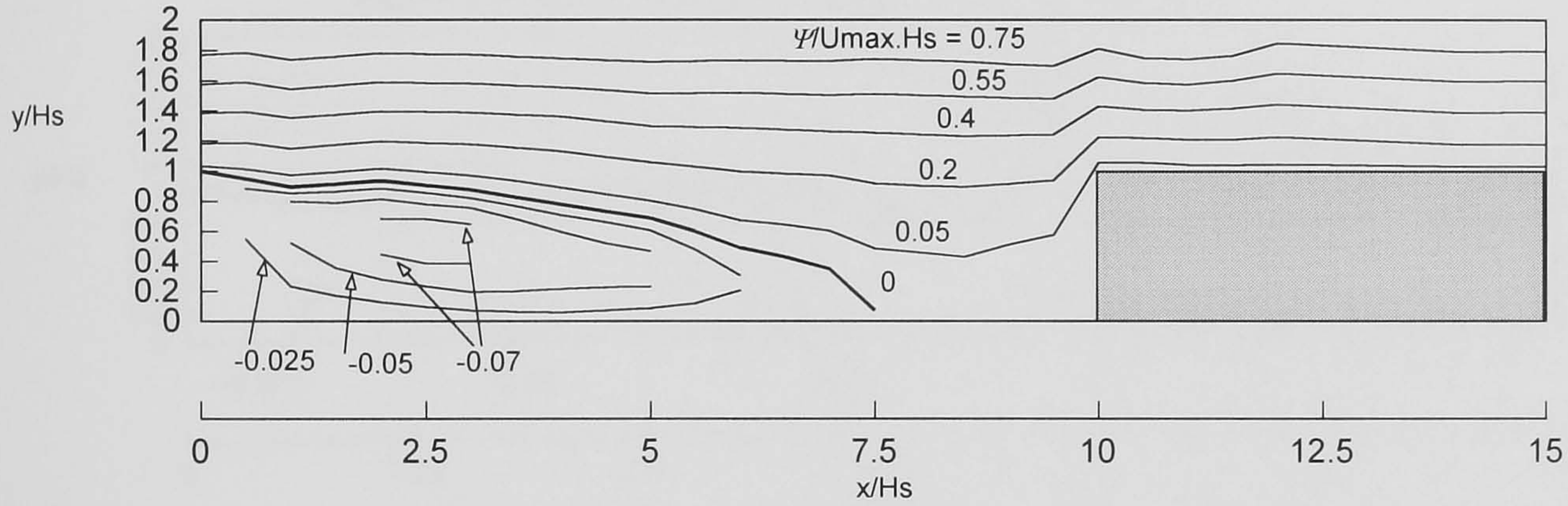

Figure 5.16(c) - Mean Non-Dimensional Streamlines: 10-3

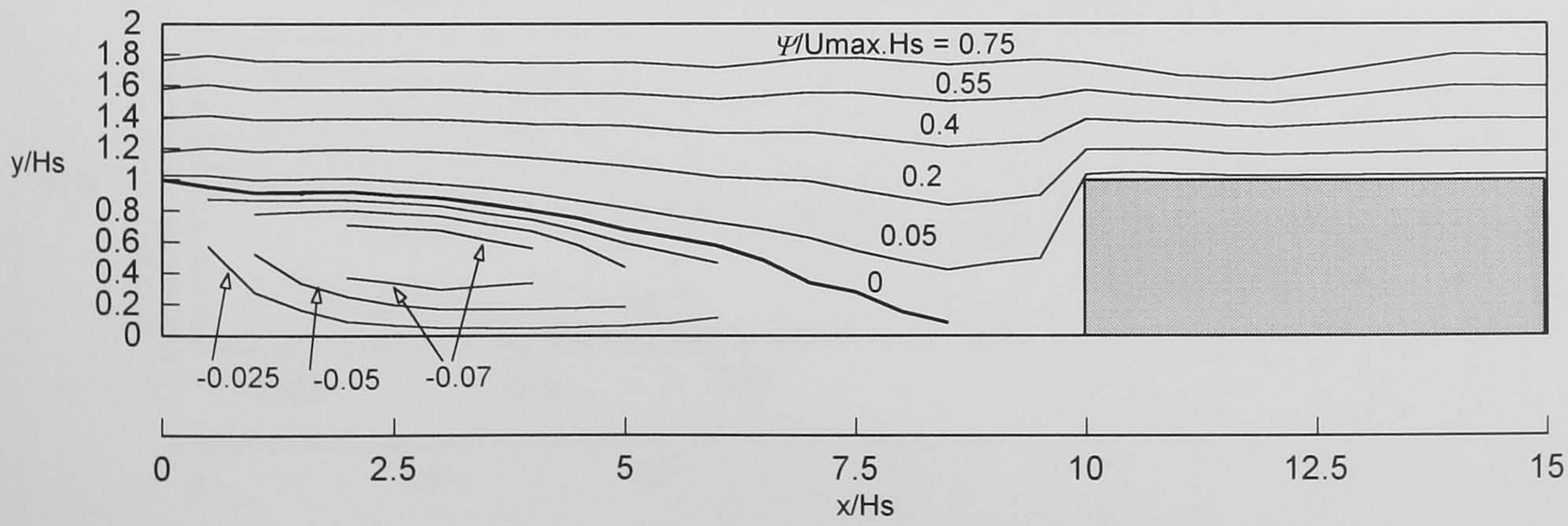

Figure 5.17(a) - Mean Non-Dimensional Streamlines: 5-1

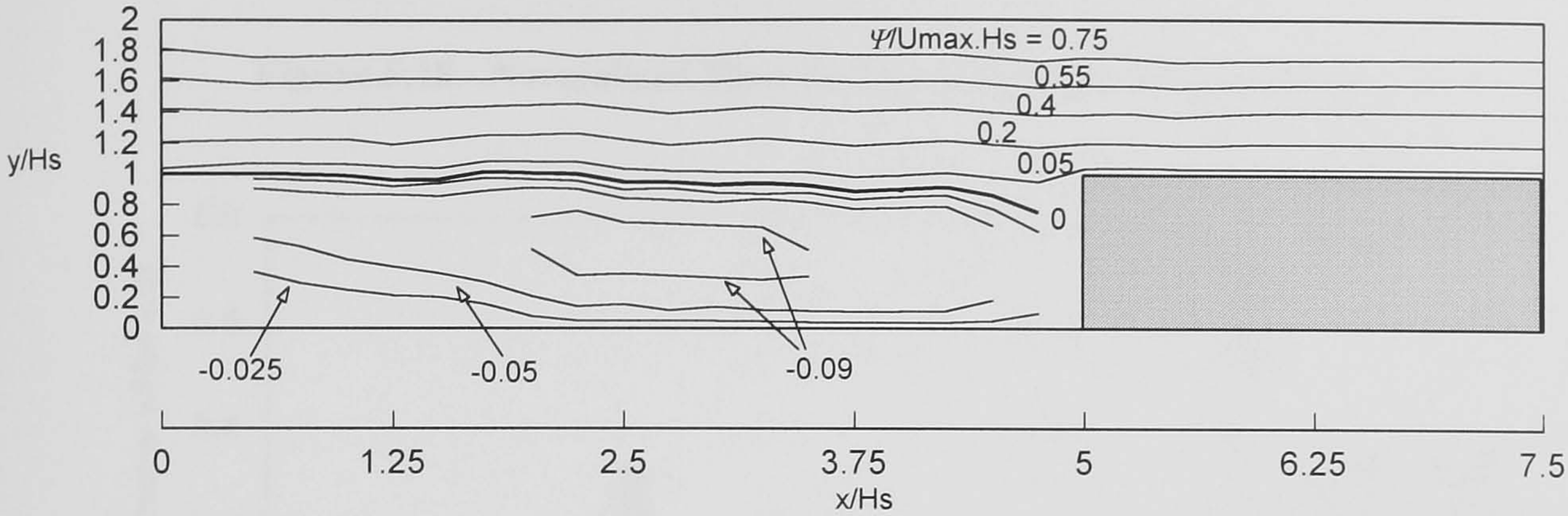

Figure 5.17(b) - Mean Non-Dimensional Streamlines: 5-2

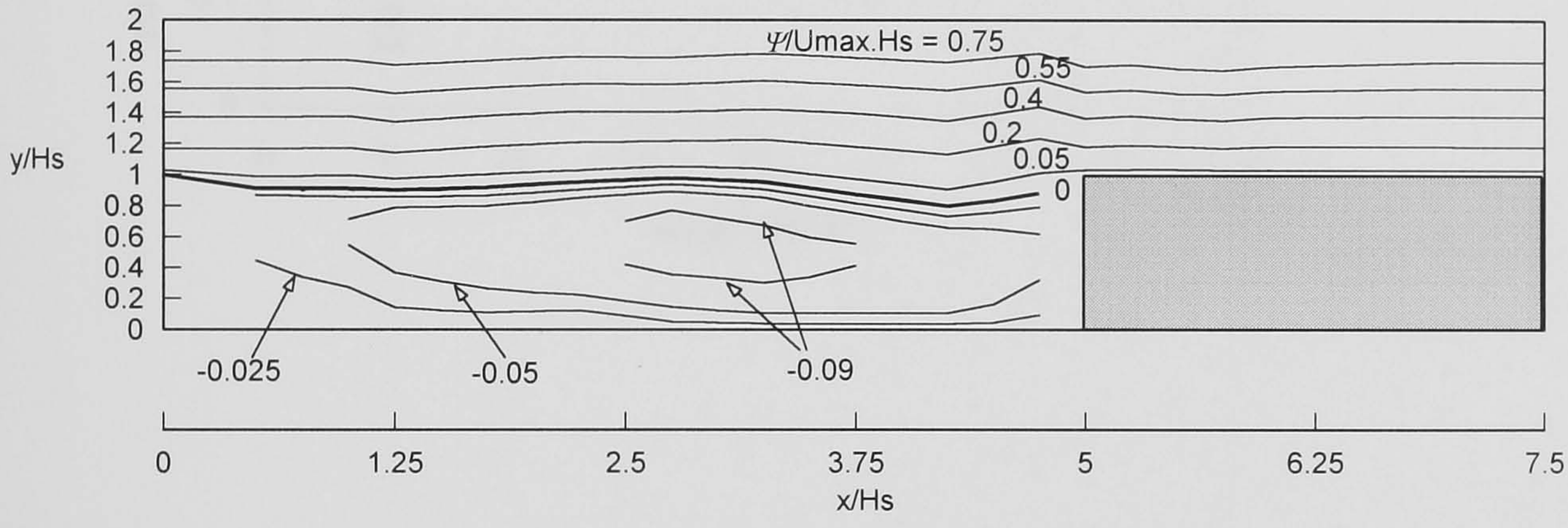

Figure 5.17(c) - Mean Non-Dimensional Streamlines: 5-3

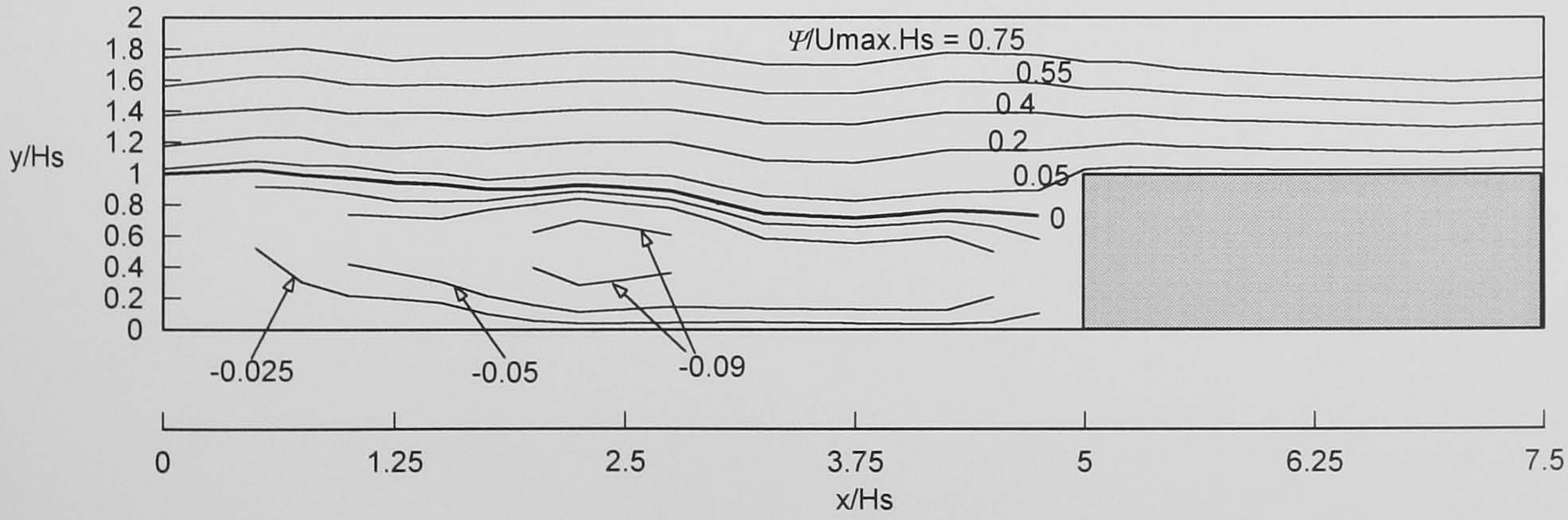

Figure 5.18 - Normalised Flow Deflected into Slot ($Q_{slot} \leq y_o/H_s$)

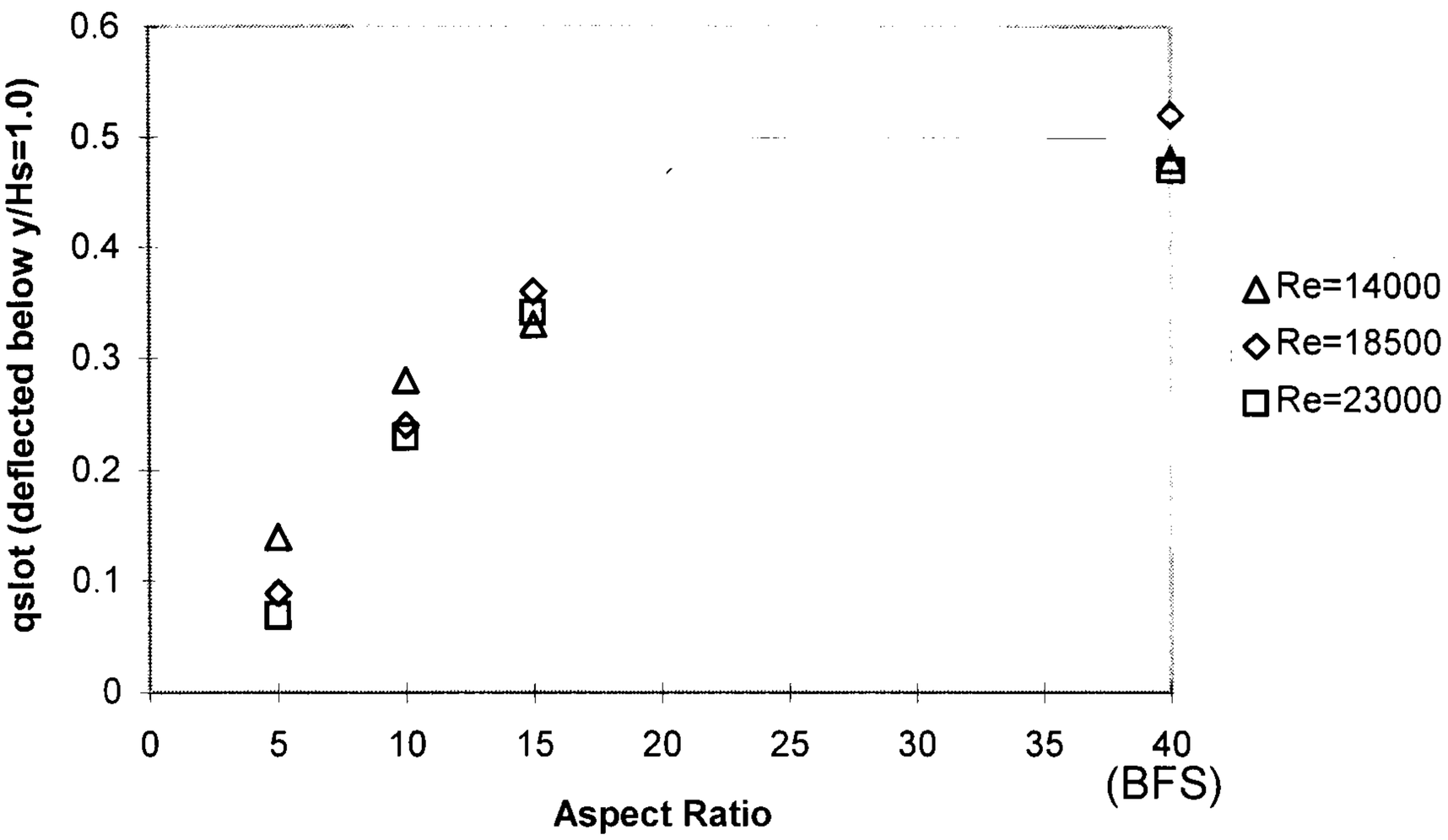

Figure 5.19(a) - Streamline=0 Location in Recirculation Zone: BFS-1

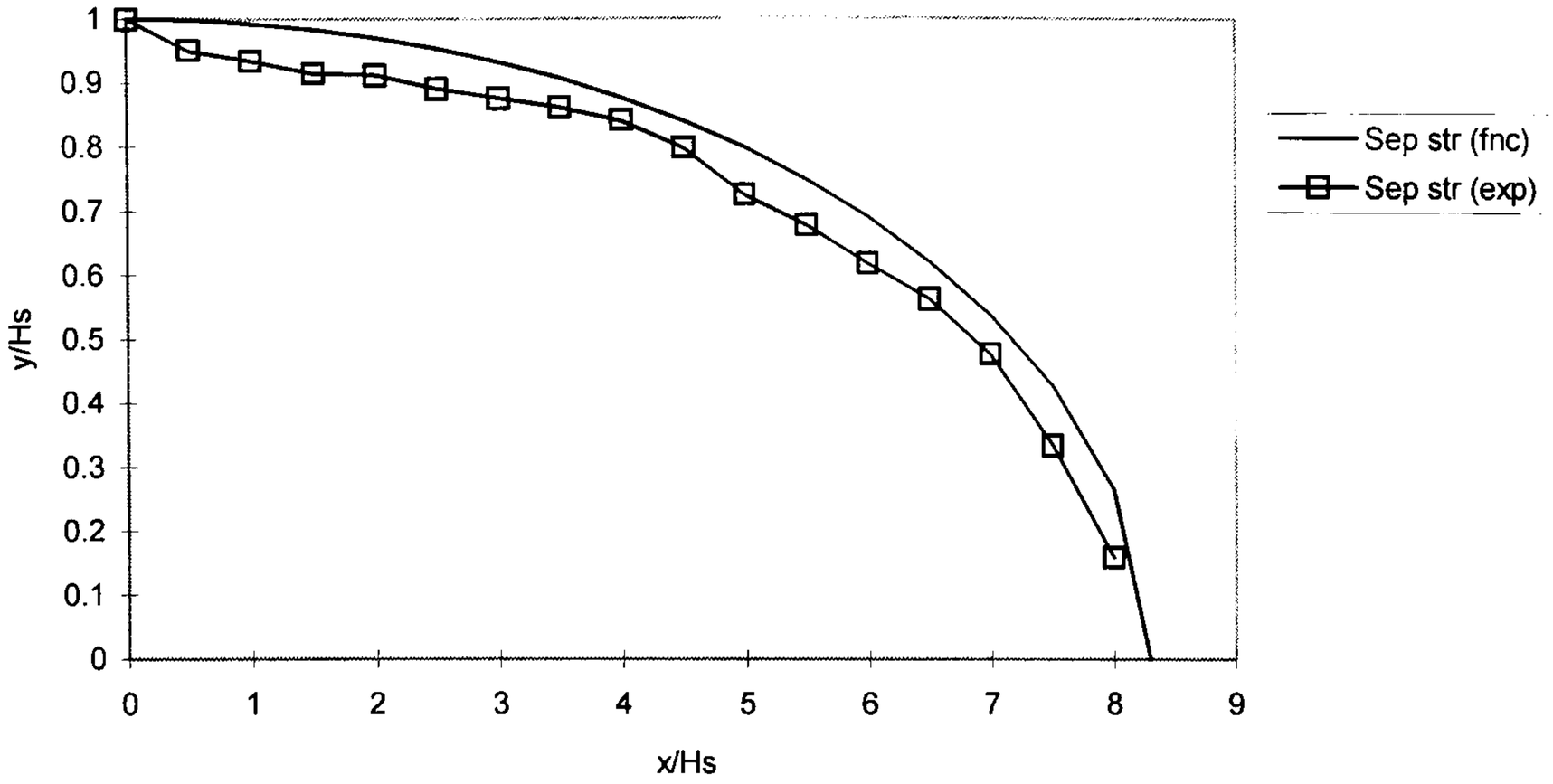

Figure 5.19(b) - Streamline=0 Location in Recirculation Zone: BFS-2

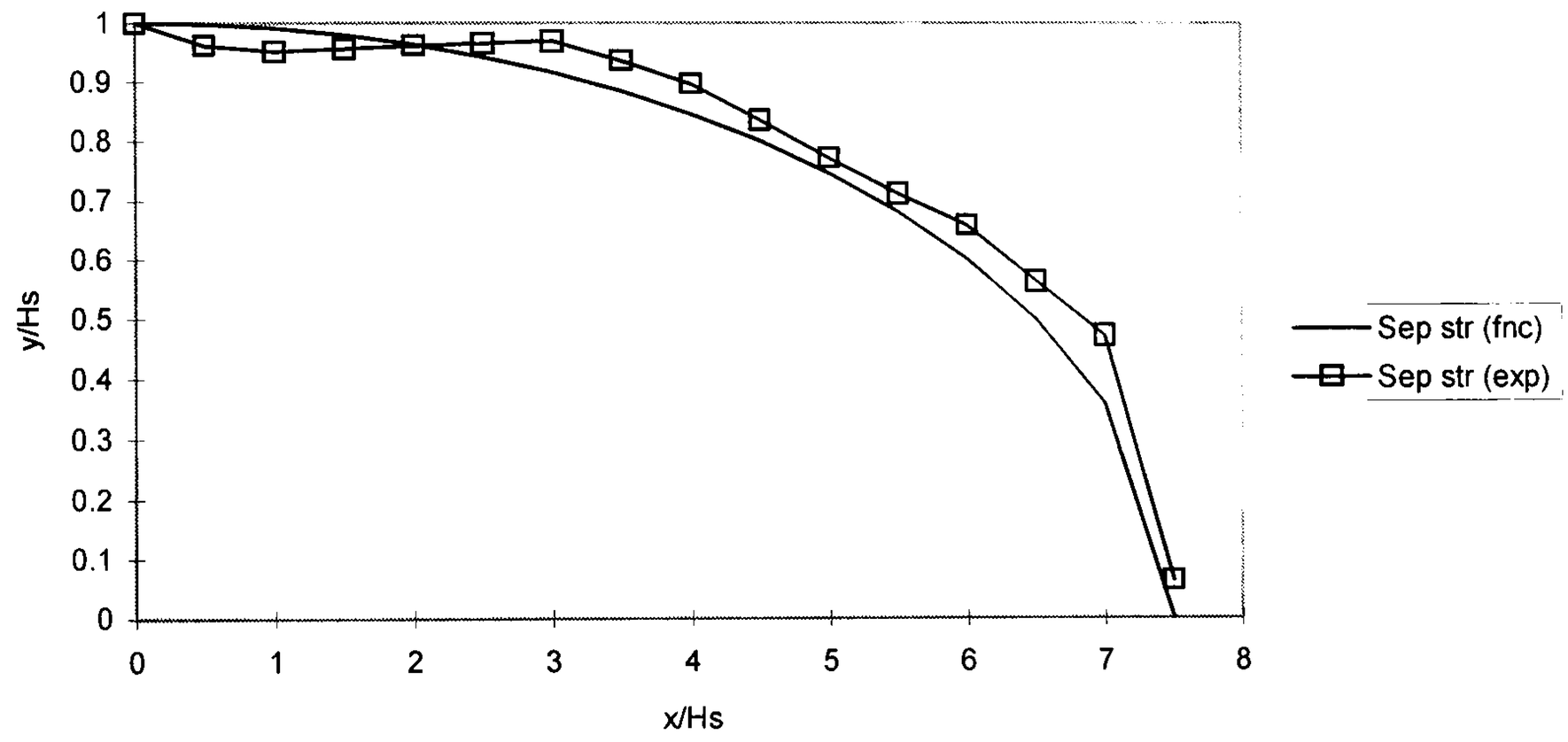

Figure 5.19(c) - Streamline=0 Location in Recirculation Zone: BFS-3

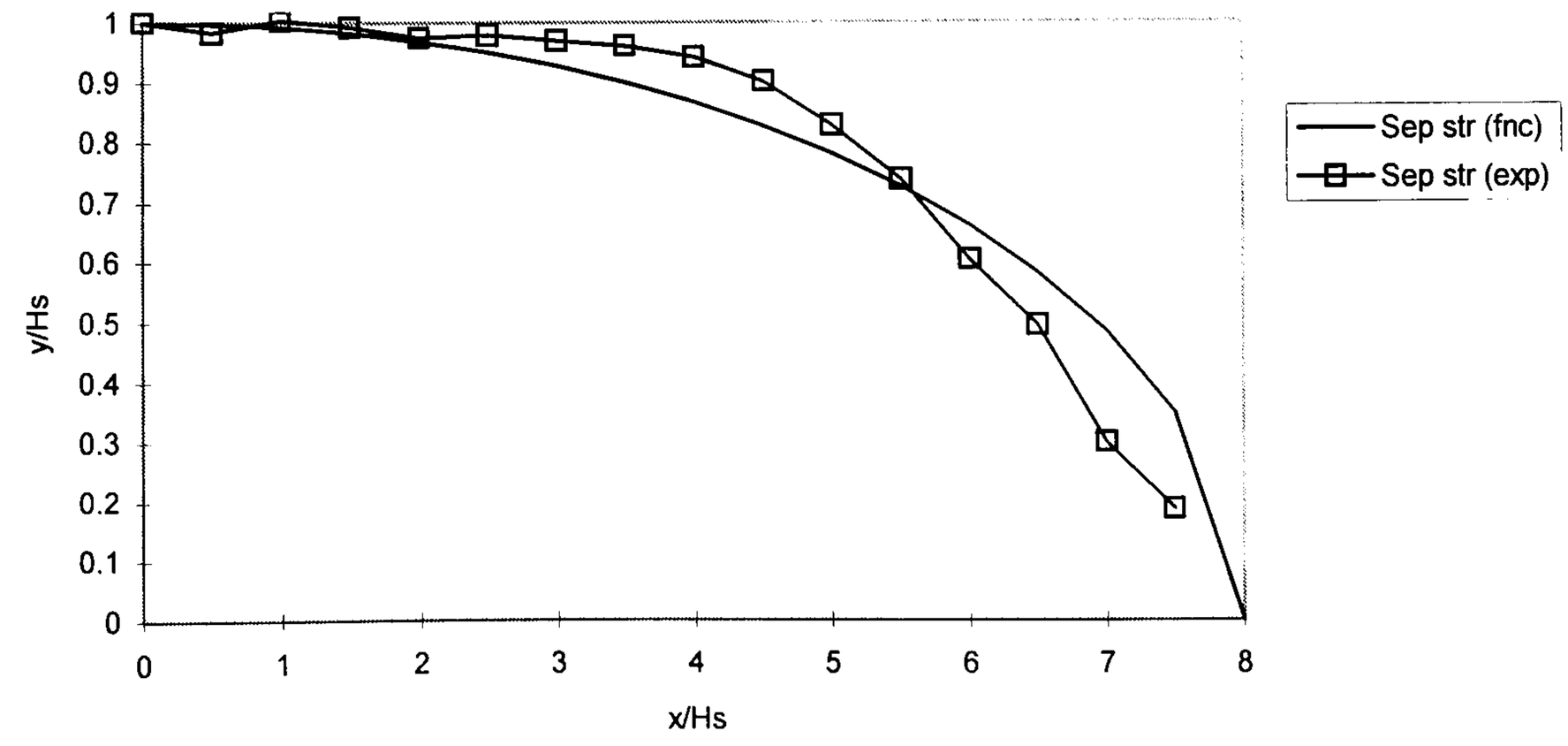

Figure 5.20(a) - Streamline=0 Location in Recirculation Zone: 15-1

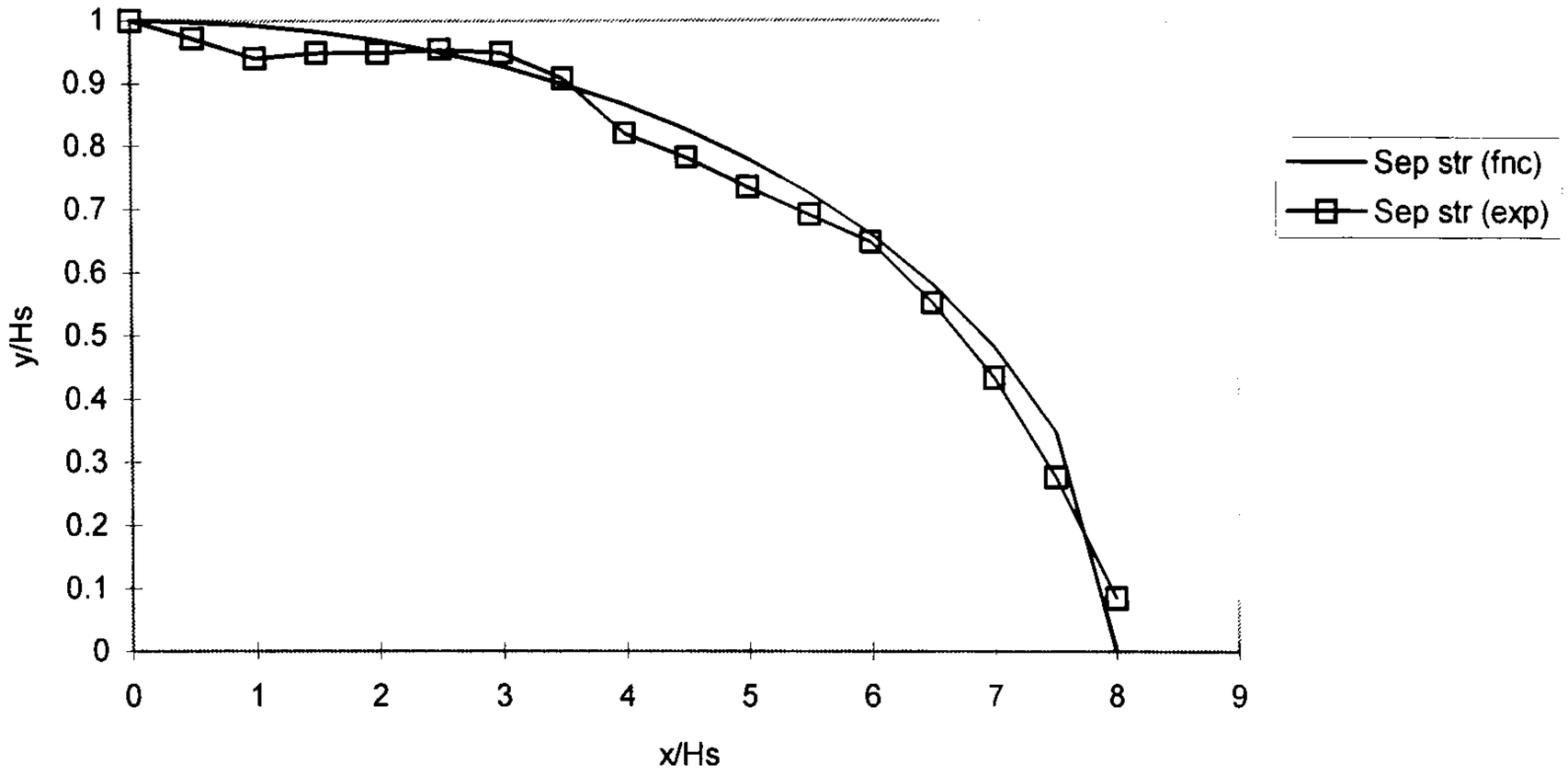

Figure 5.20(b) - Streamline=0 Location in Recirculation Zone: 15-2

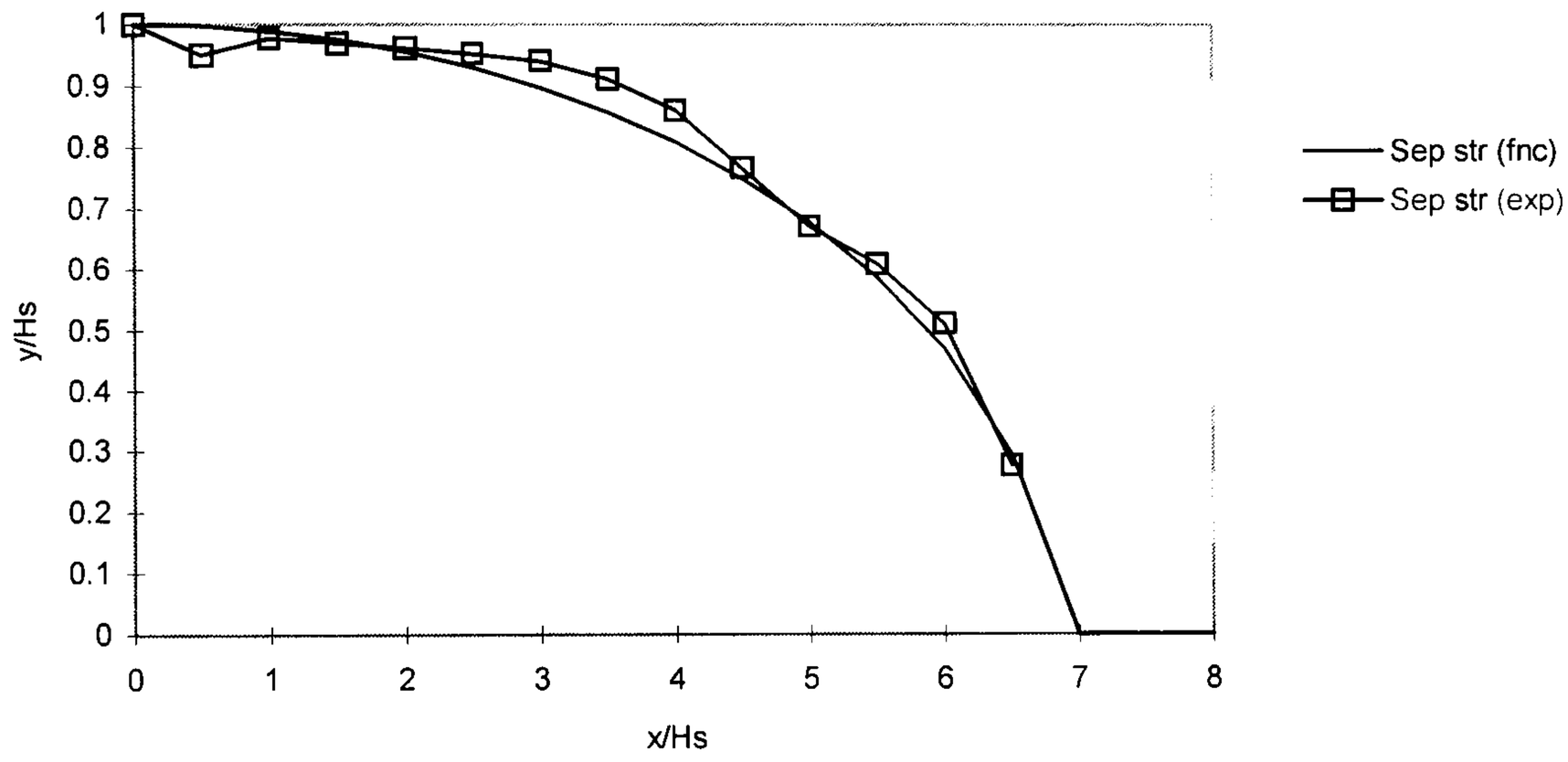

Figure 5.20(c) - Streamline=0 Location in Recirculation Zone: 15-3

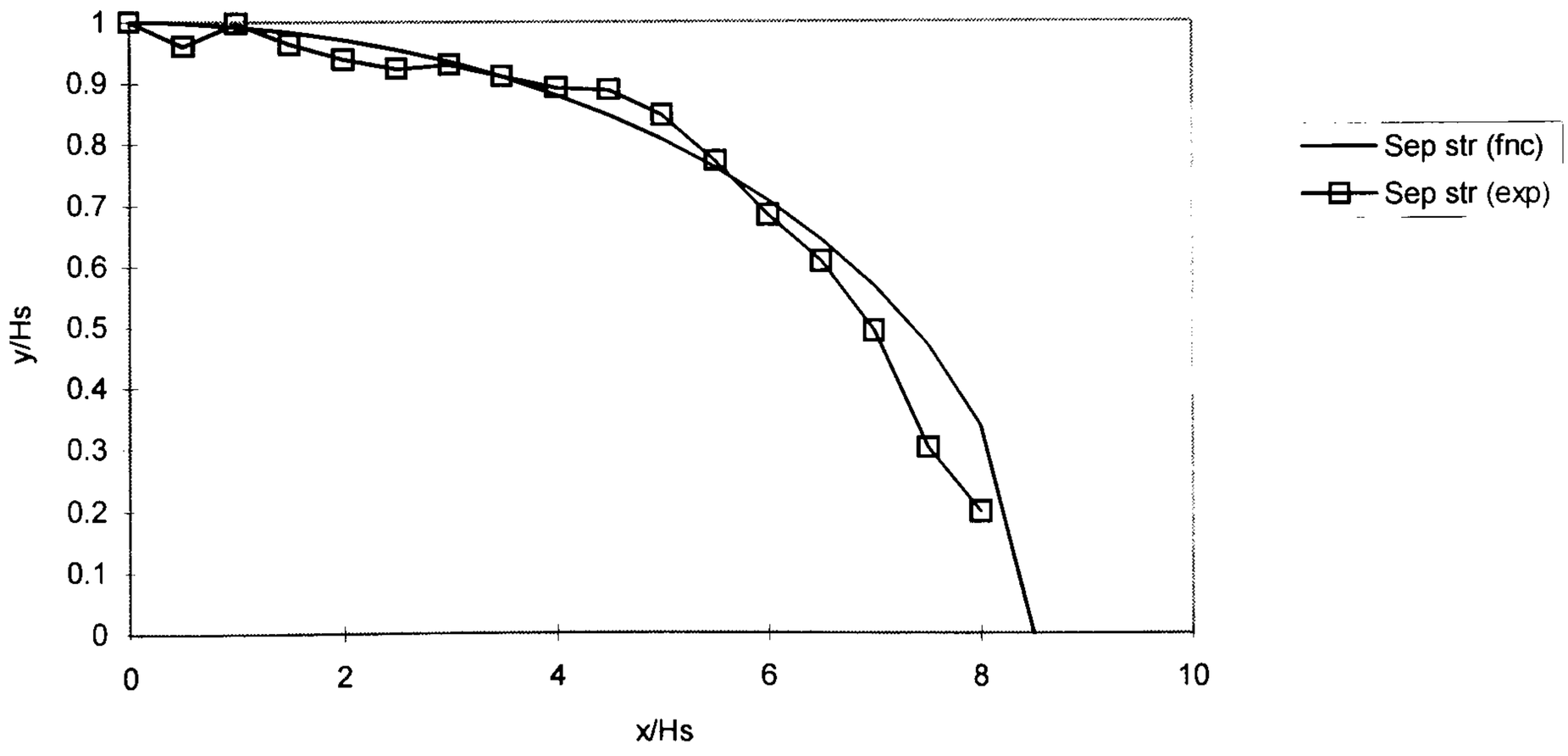

Figure 5.21(a) - Streamline=0 Location in Recirculation Zone: 10-1

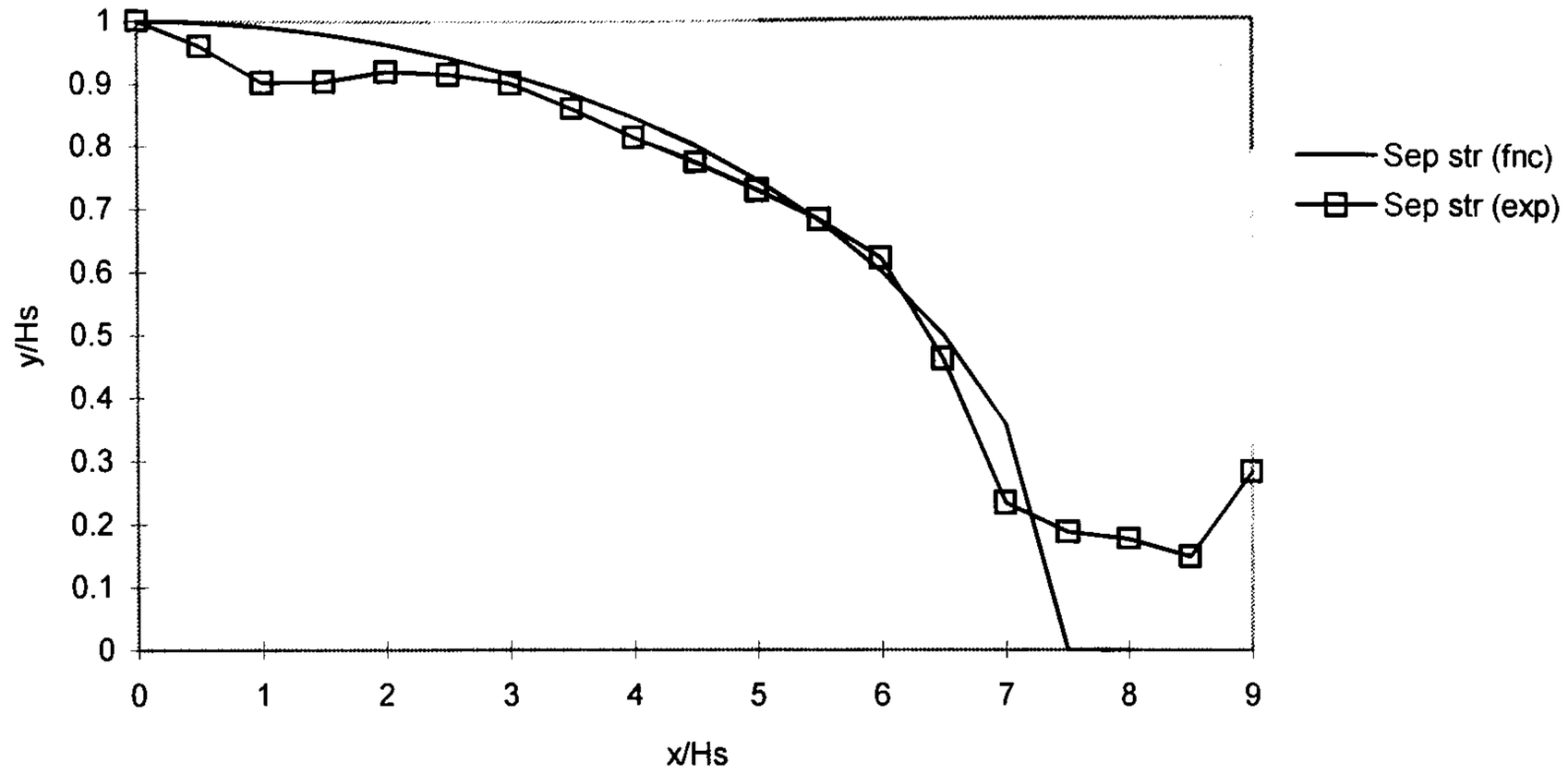

Figure 5.21(b) - Streamline=0 Location in Recirculation Zone: 10-2

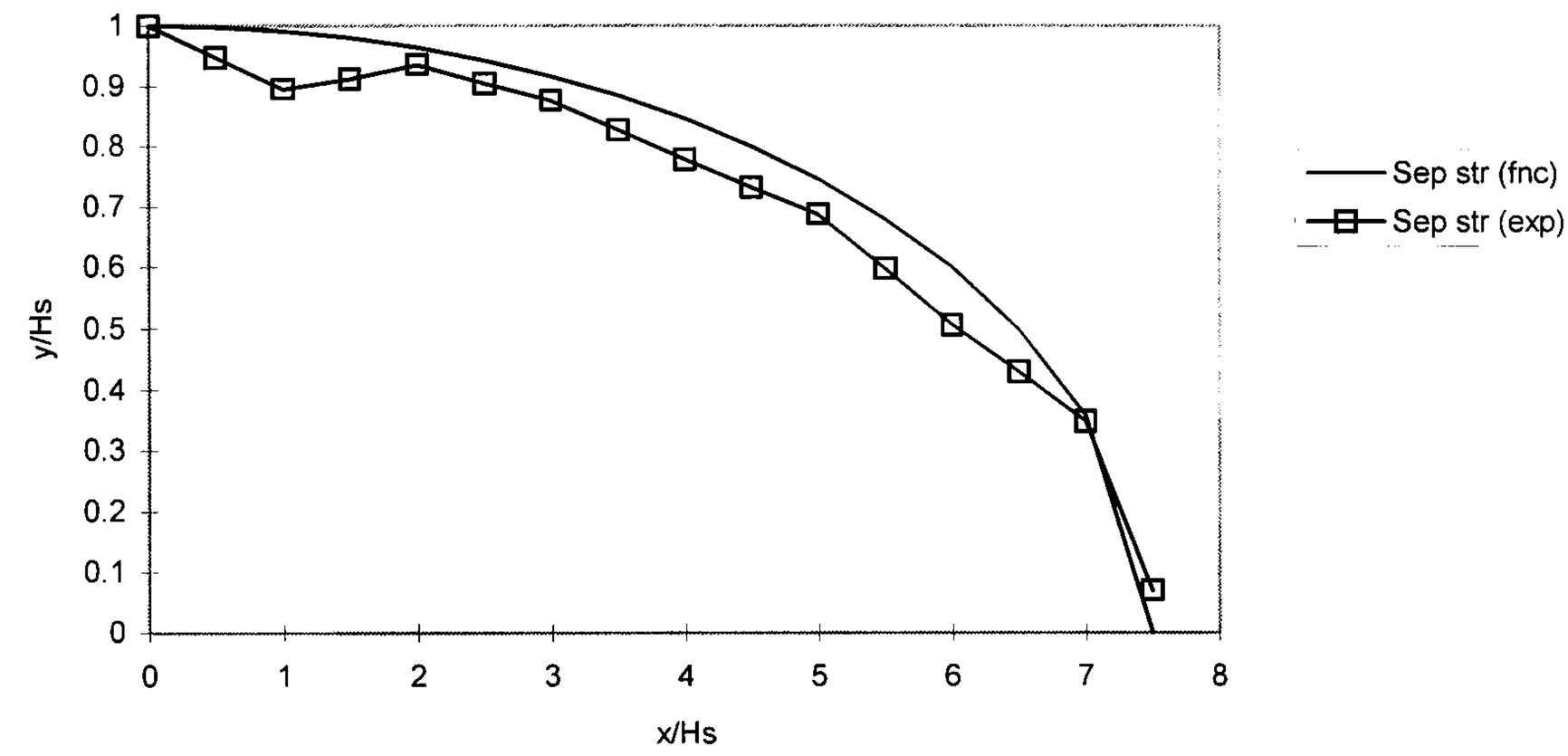

Figure 5.21(c) - Streamline=0 Location in Recirculation Zone: 10-3

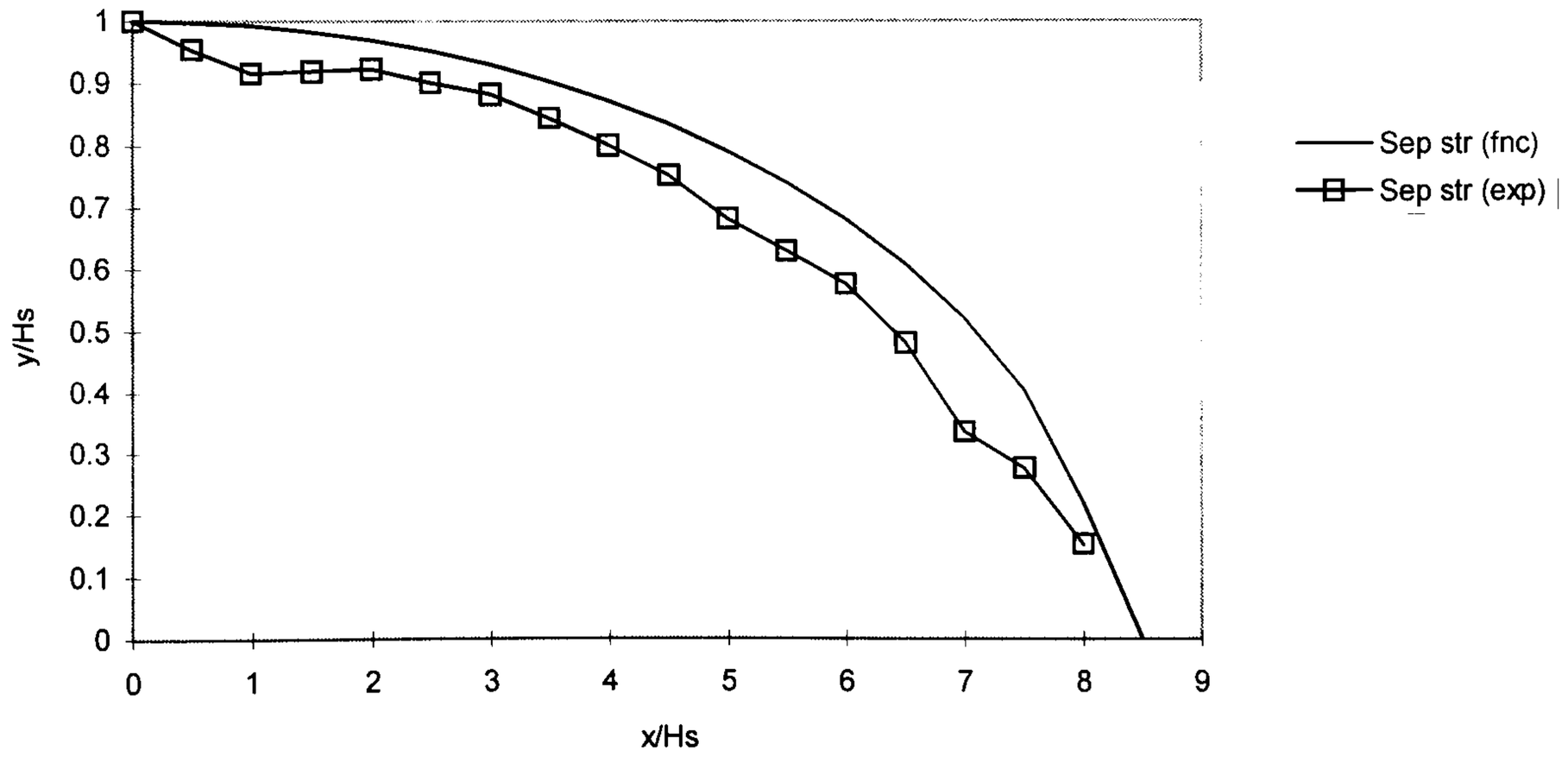

Figure 5.22 - Schematic Representation of Terms used in Shear Layer Analysis

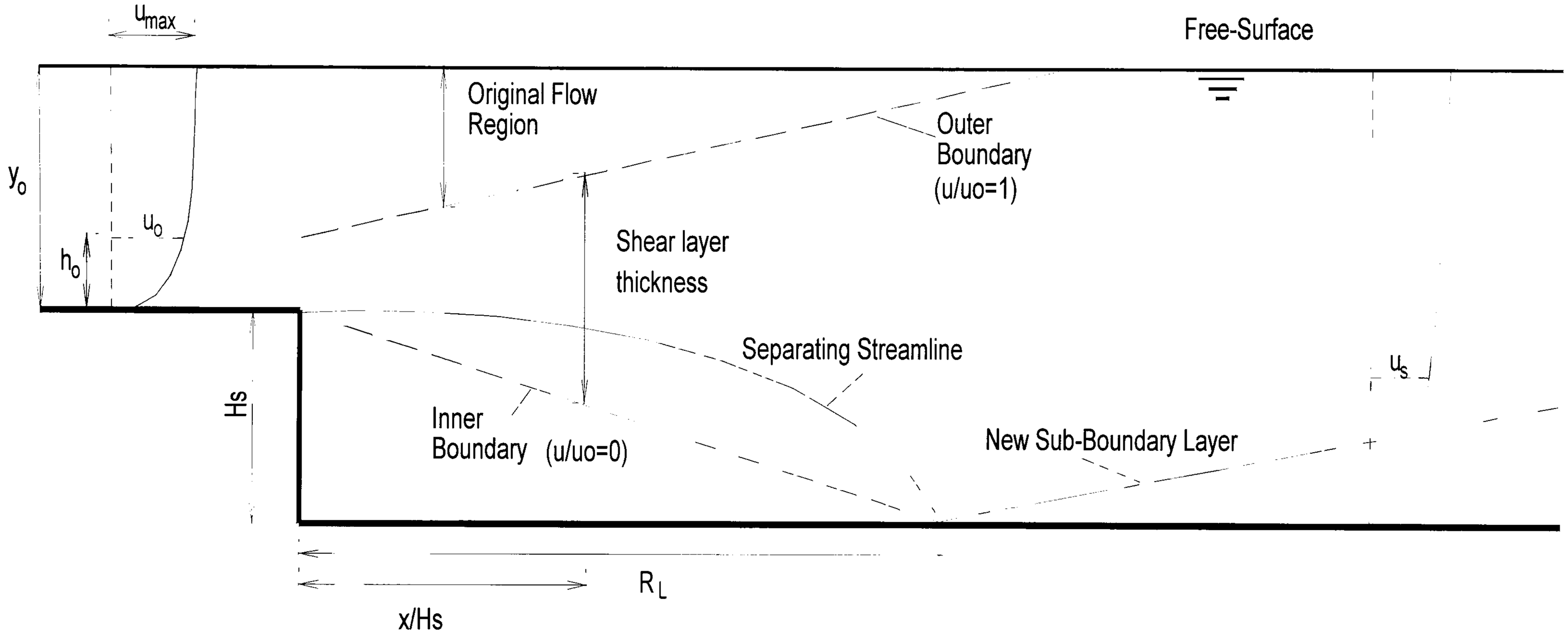

Figure 5.23 - Co-Ordinate System Used in Interpolation Technique

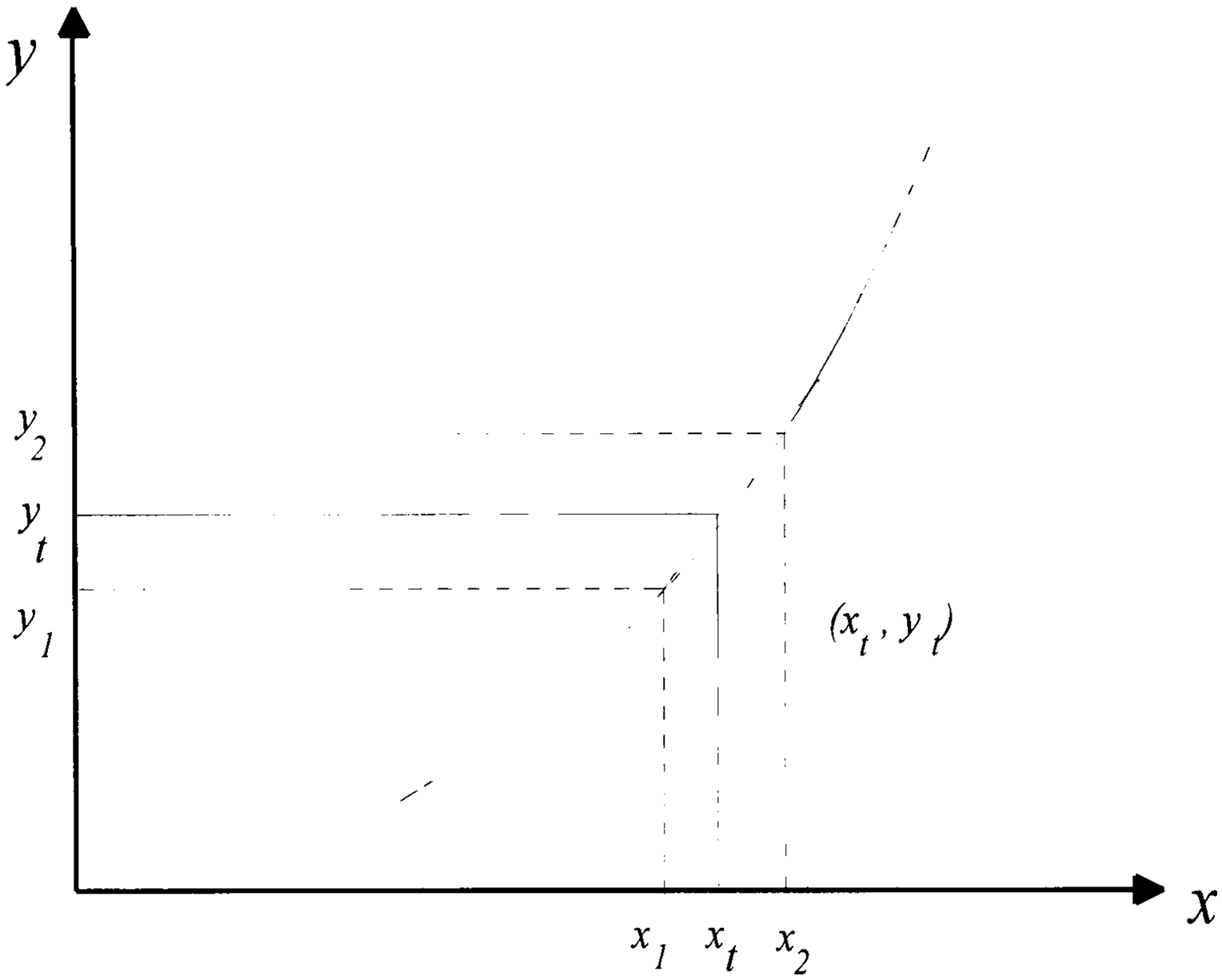

Figure 5.24(a) - Shear Layer Boundaries: BFS Cases

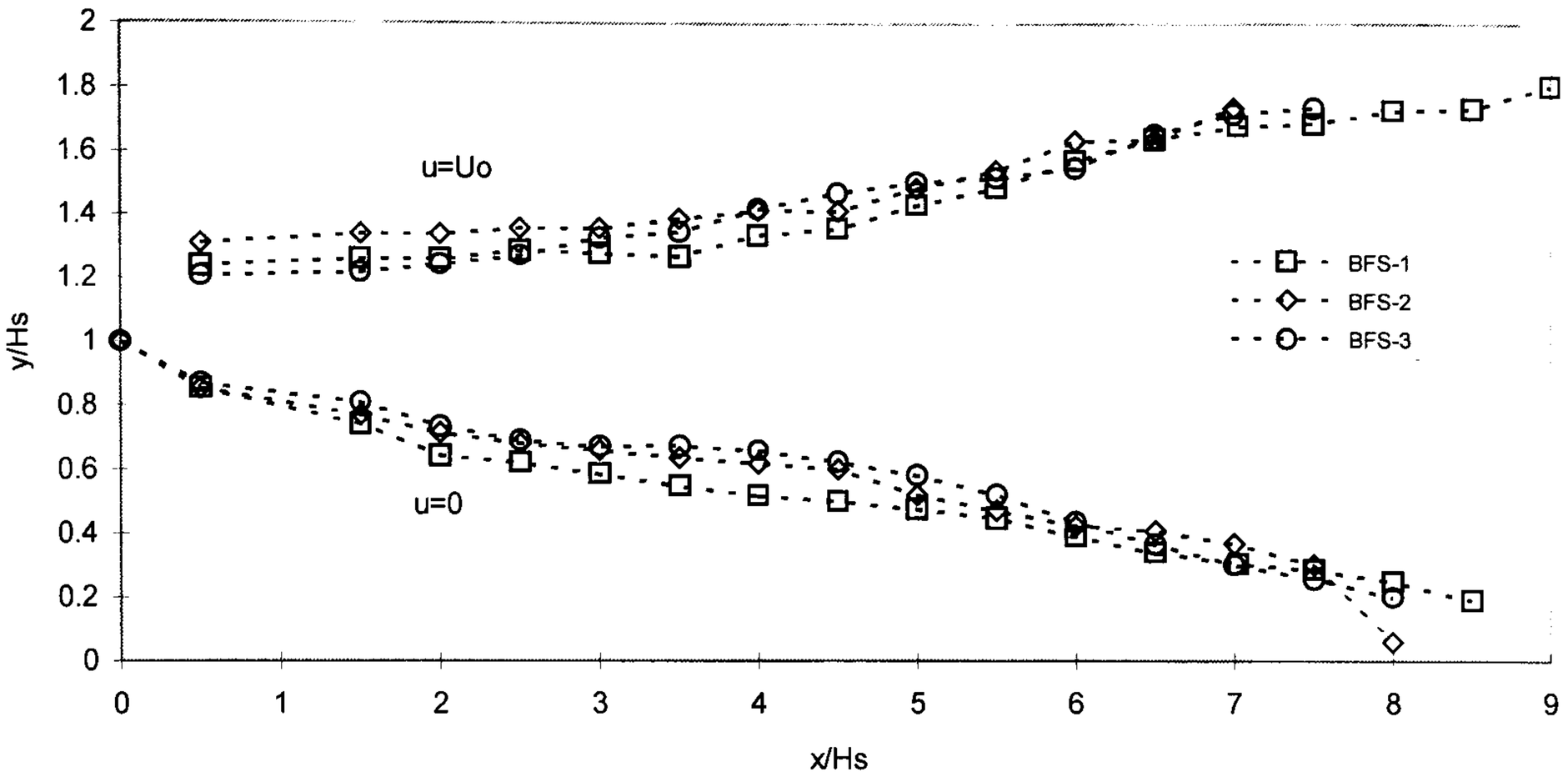

Figure 5.24(b) - Shear Layer Boundaries: As=15 Cases

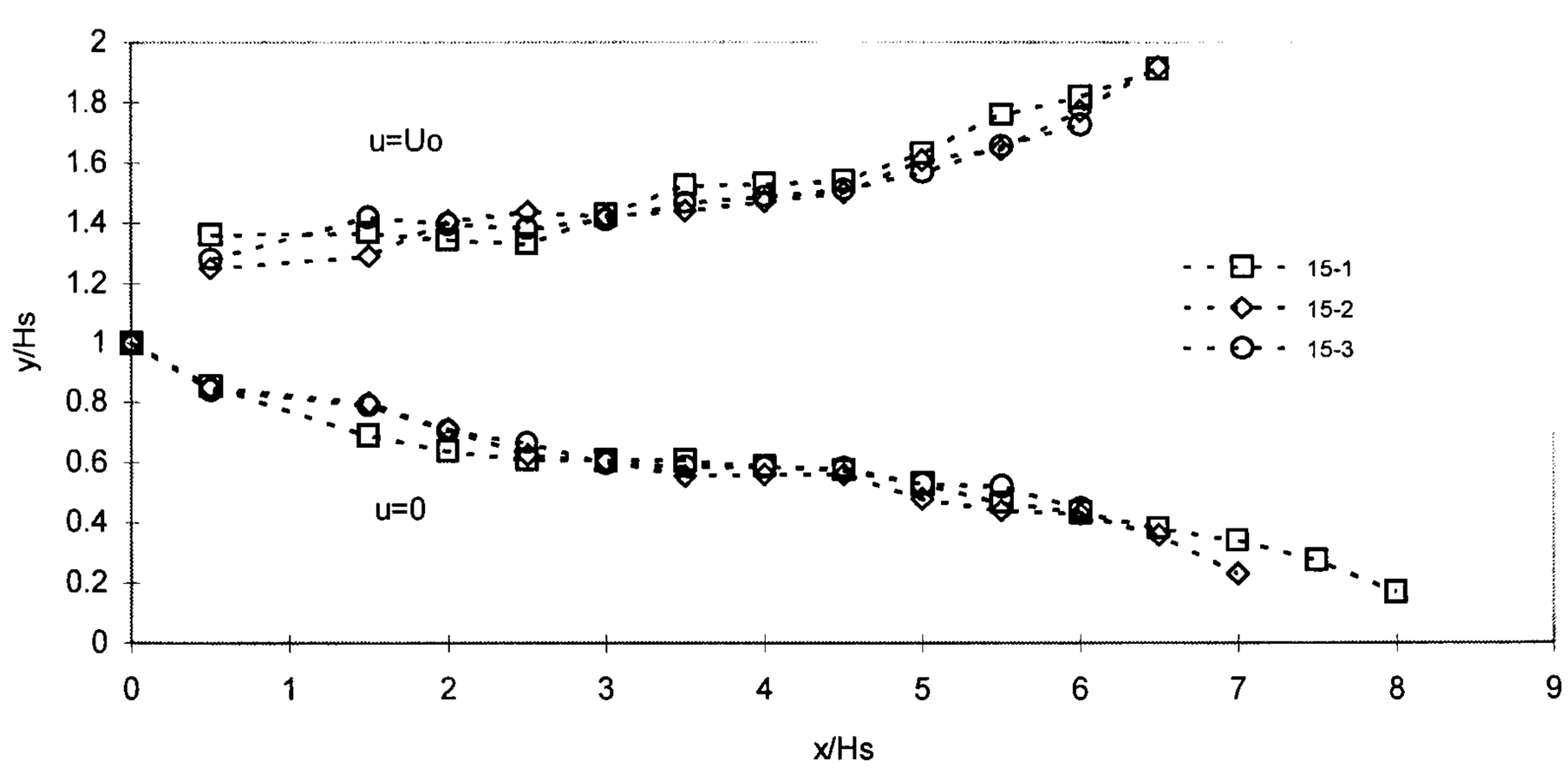

Figure 5.24(c) - Shear Layer Boundaries: As=10 Cases

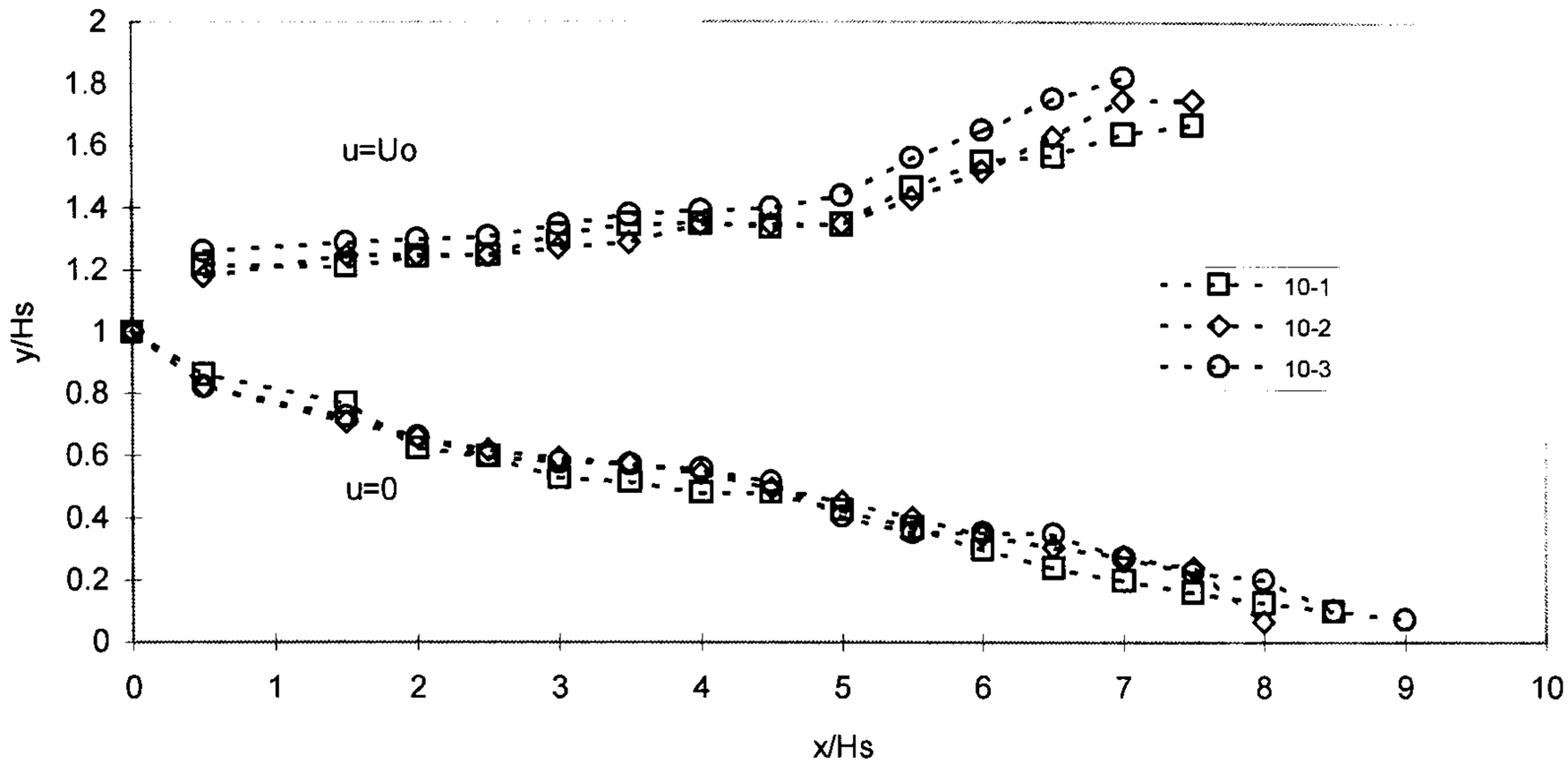

Figure 5.24(d) - Shear Layer Boundaries: As=5 Cases

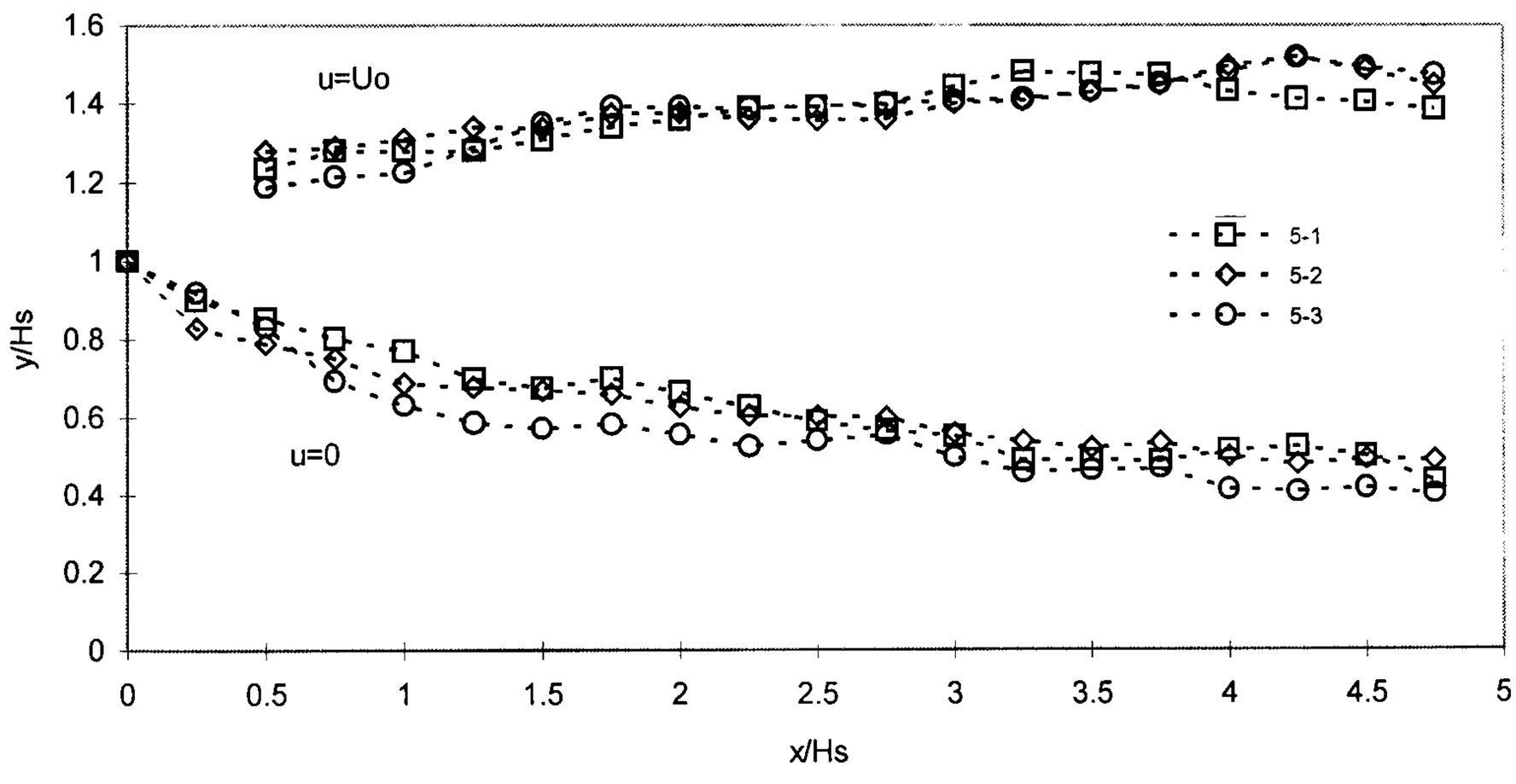

Figure 5.25 - Universal Profile for the Outer Boundary of a Shear Layer

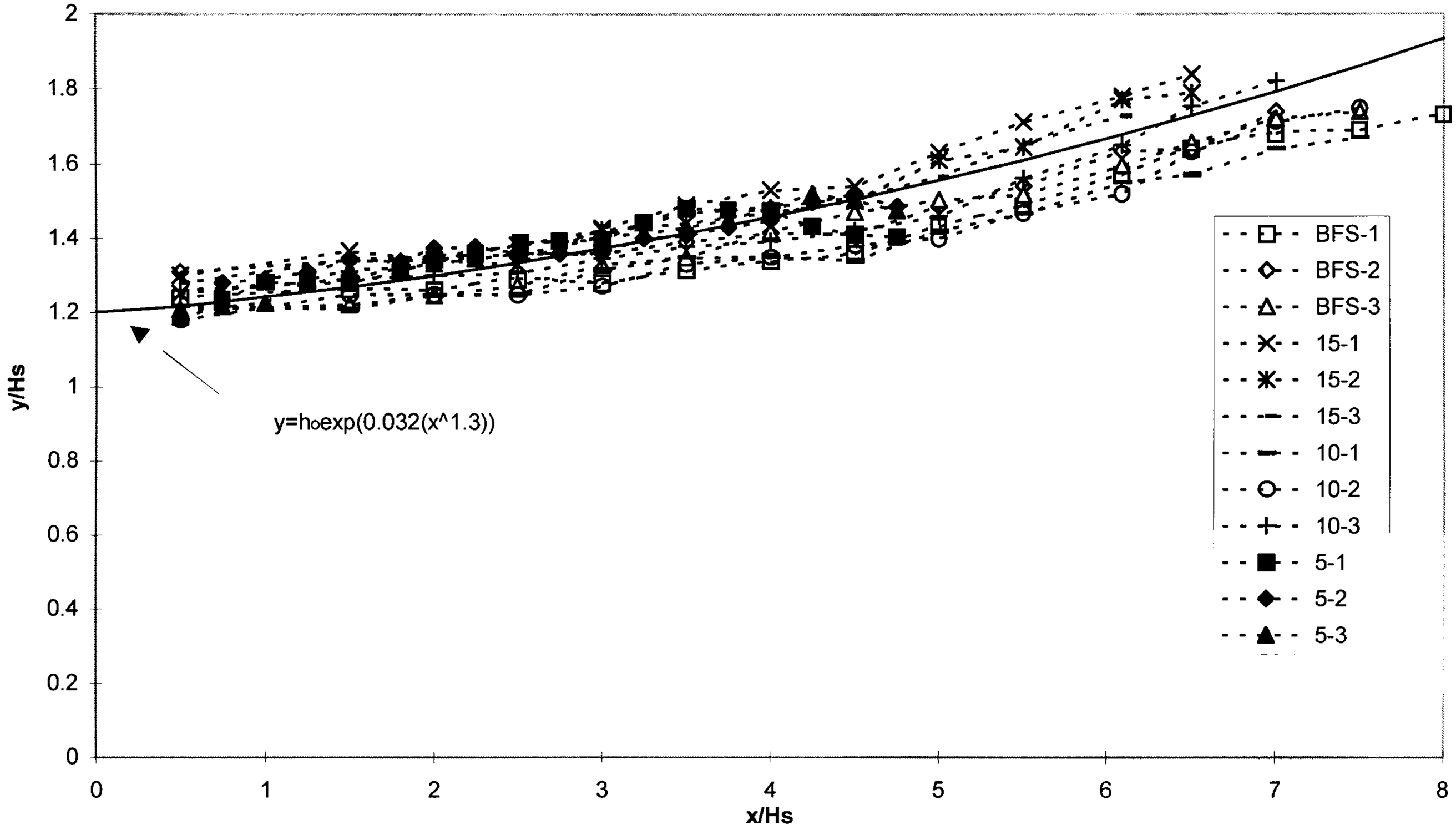

Figure 5.26(a) - Inner Shear Layer Boundary (u/u_0) in Recirculation Zone: BFS-1

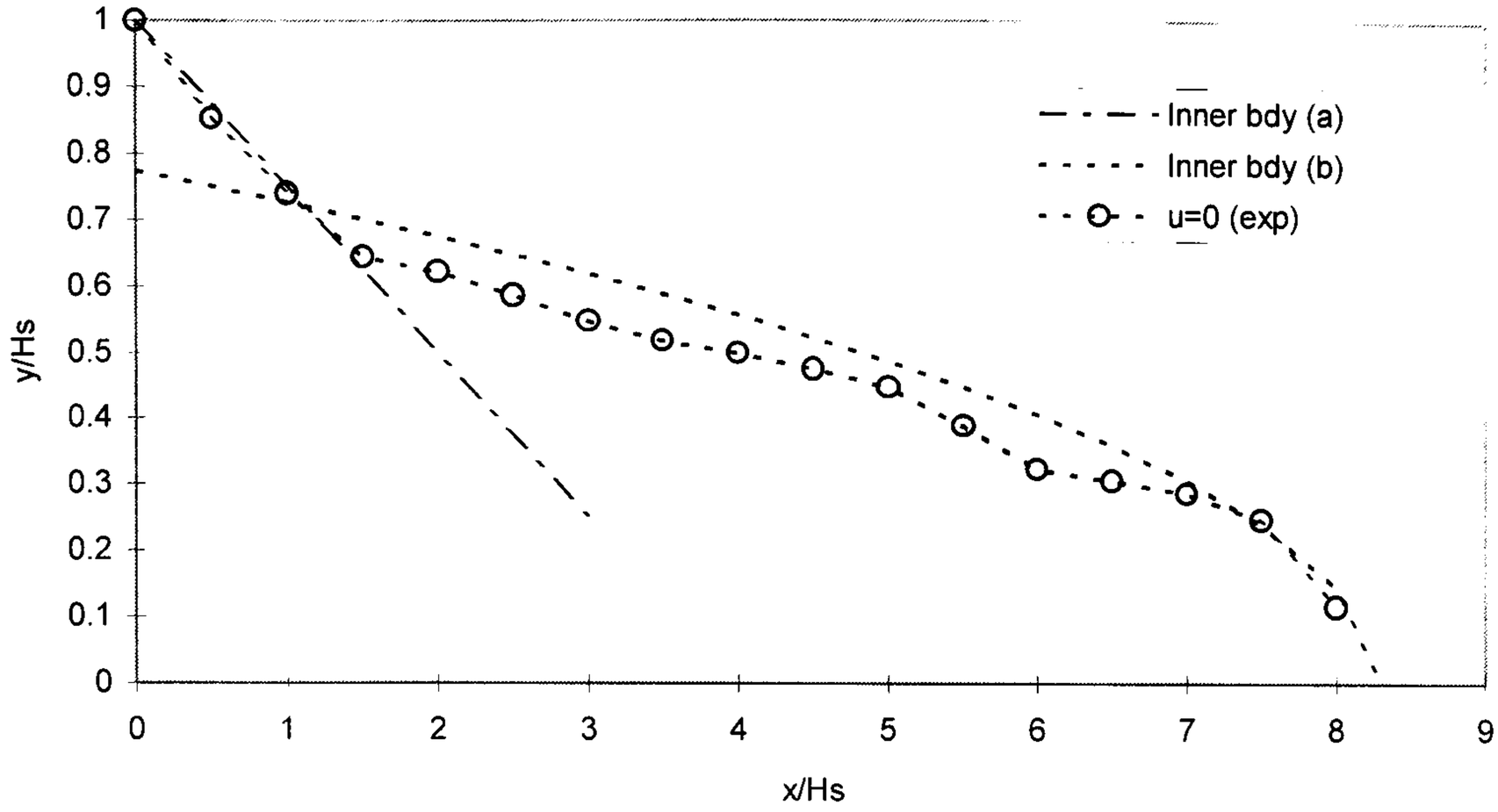

Figure 5.26(b) - Inner Shear Layer Boundary (u/u_0) in Recirculation Zone: BFS-2

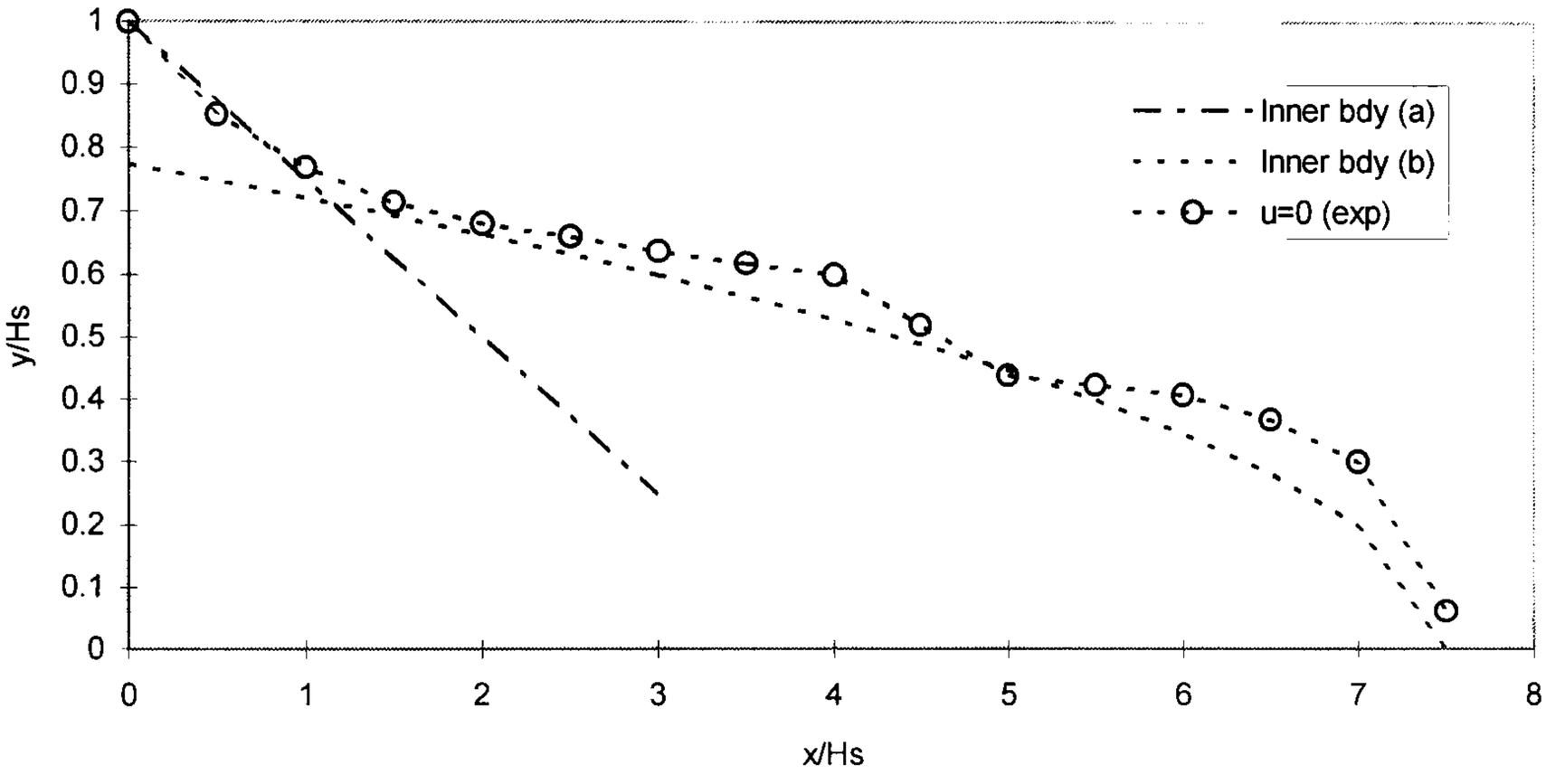

Figure 5.26(c) - Inner Shear Layer Boundary (u/u_0) in Recirculation Zone: BFS-3

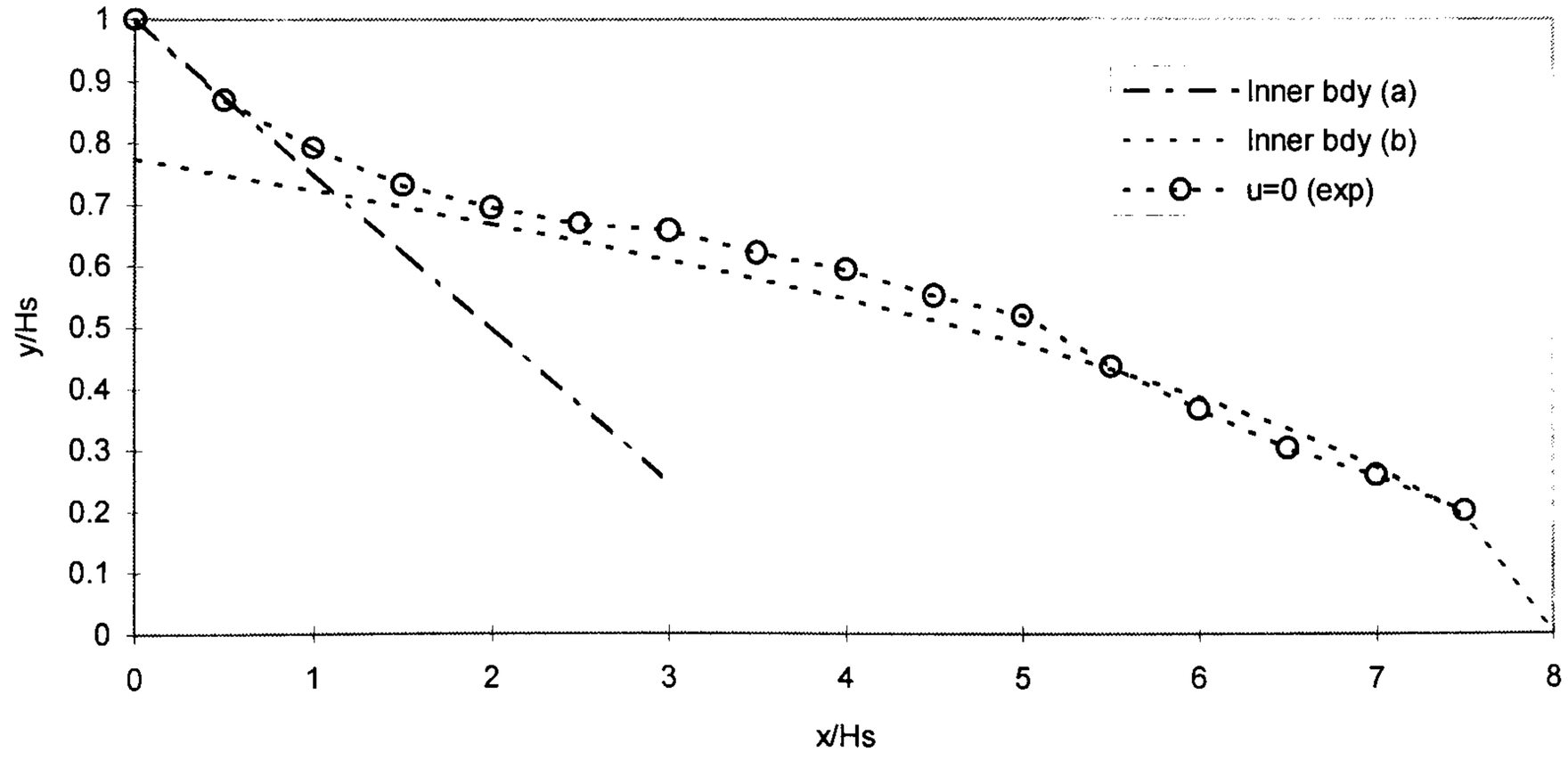

Figure 5.27(a) - Inner Shear Layer Boundary (u/u_o) in Recirculation Zone: 15-1

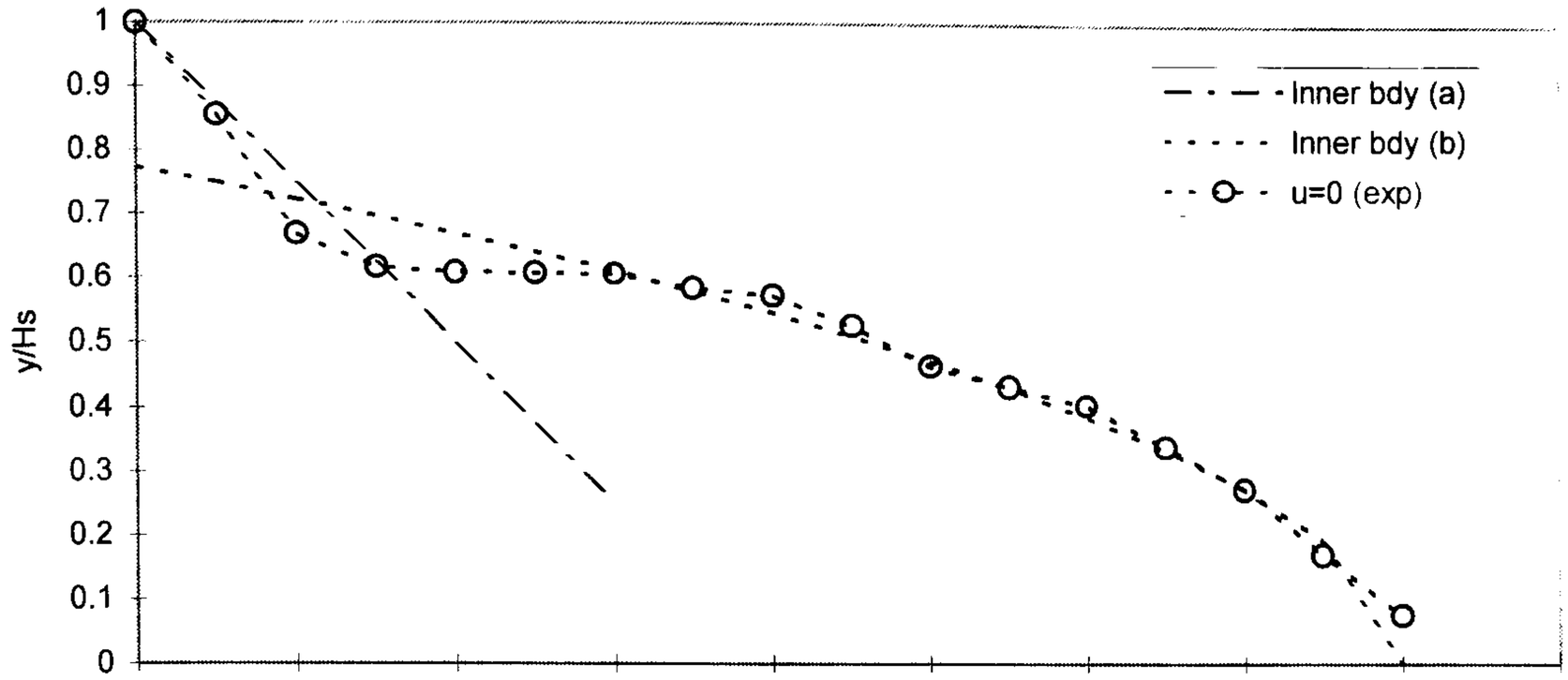

Figure 5.27(b) - Inner Shear Layer Boundary (u/u_o) in Recirculation Zone: 15-2

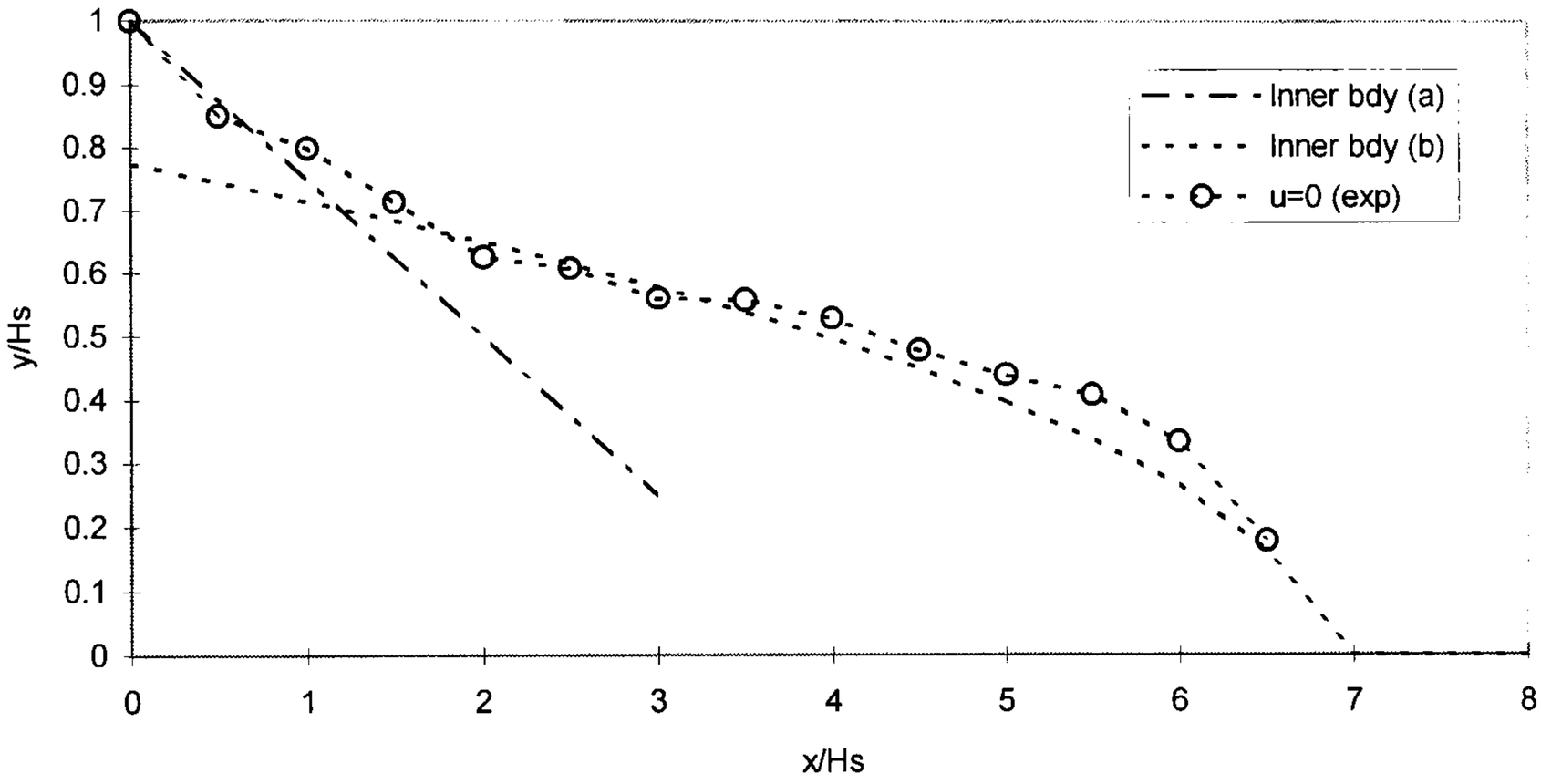

Figure 5.27(c) - Inner Shear Layer Boundary (u/u_o) in Recirculation Zone: 15-3

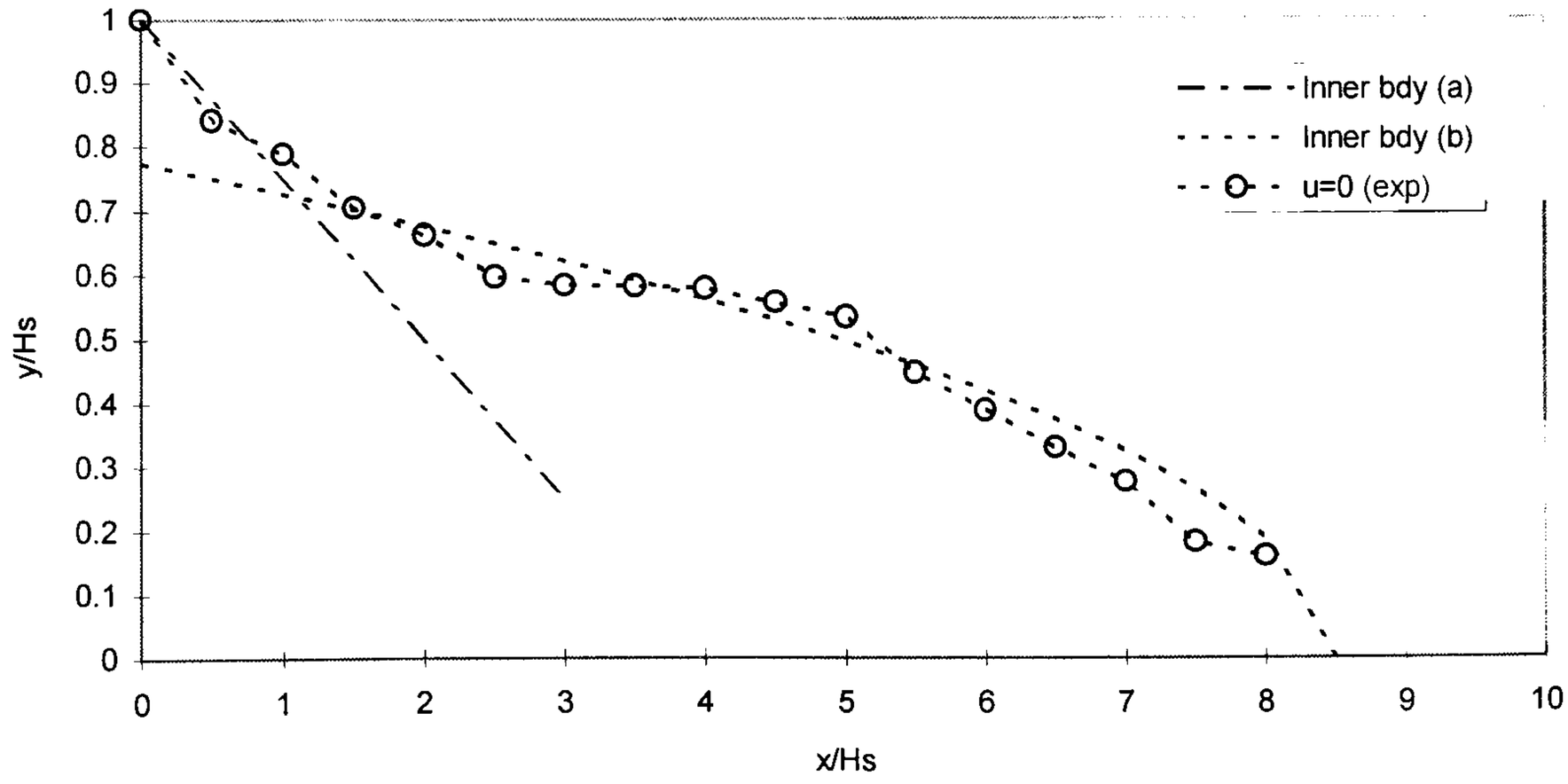

Figure 5.28(a) - Inner Shear Layer Boundary (u/u_0) in Recirculation Zone: 10-1

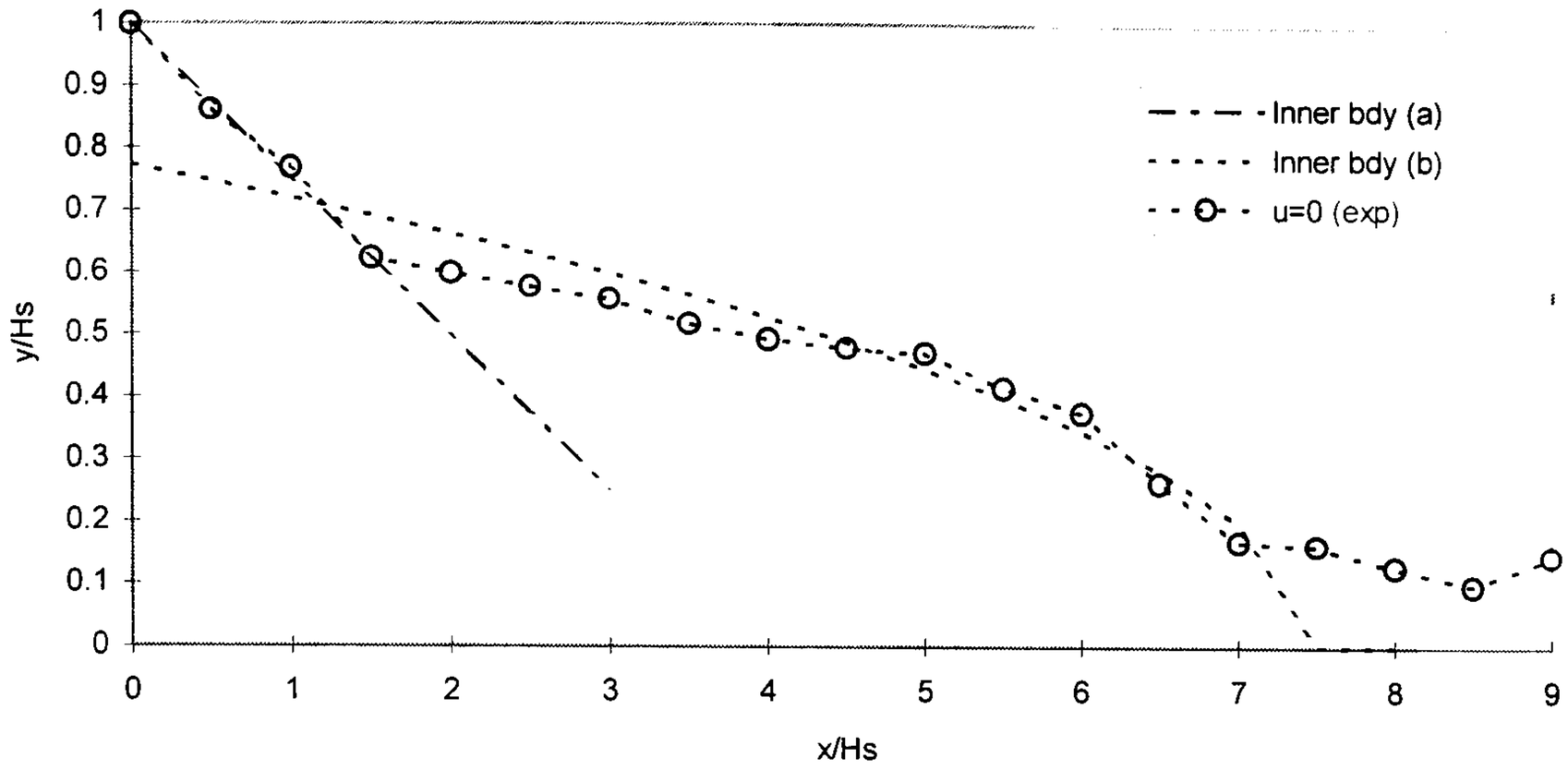

Figure 5.28(b) - Inner Shear Layer Boundary (u/u_0) in Recirculation Zone: 10-2

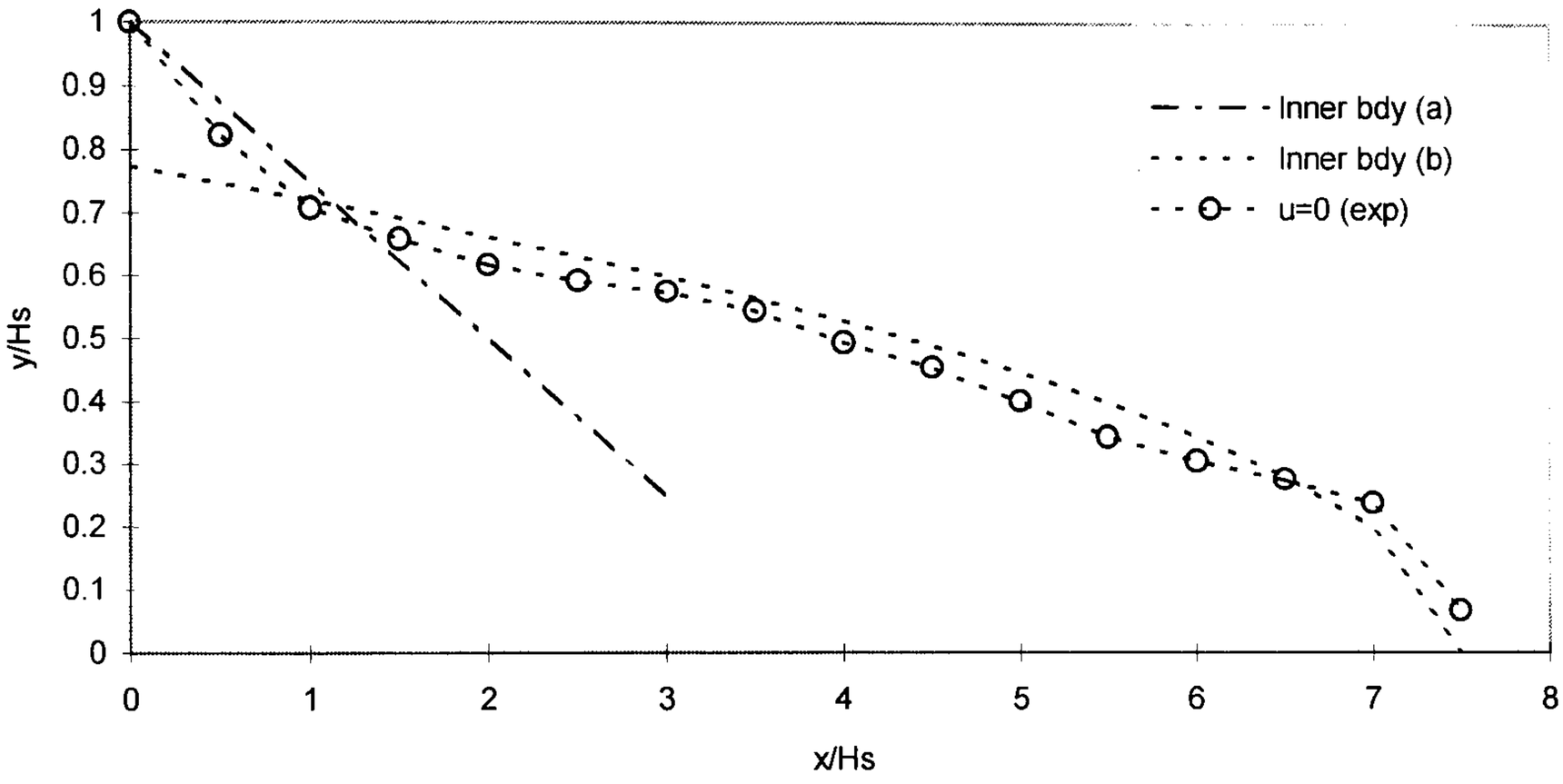

Figure 5.28(c) - Inner Shear Layer Boundary (u/u_0) in Recirculation Zone: 10-3

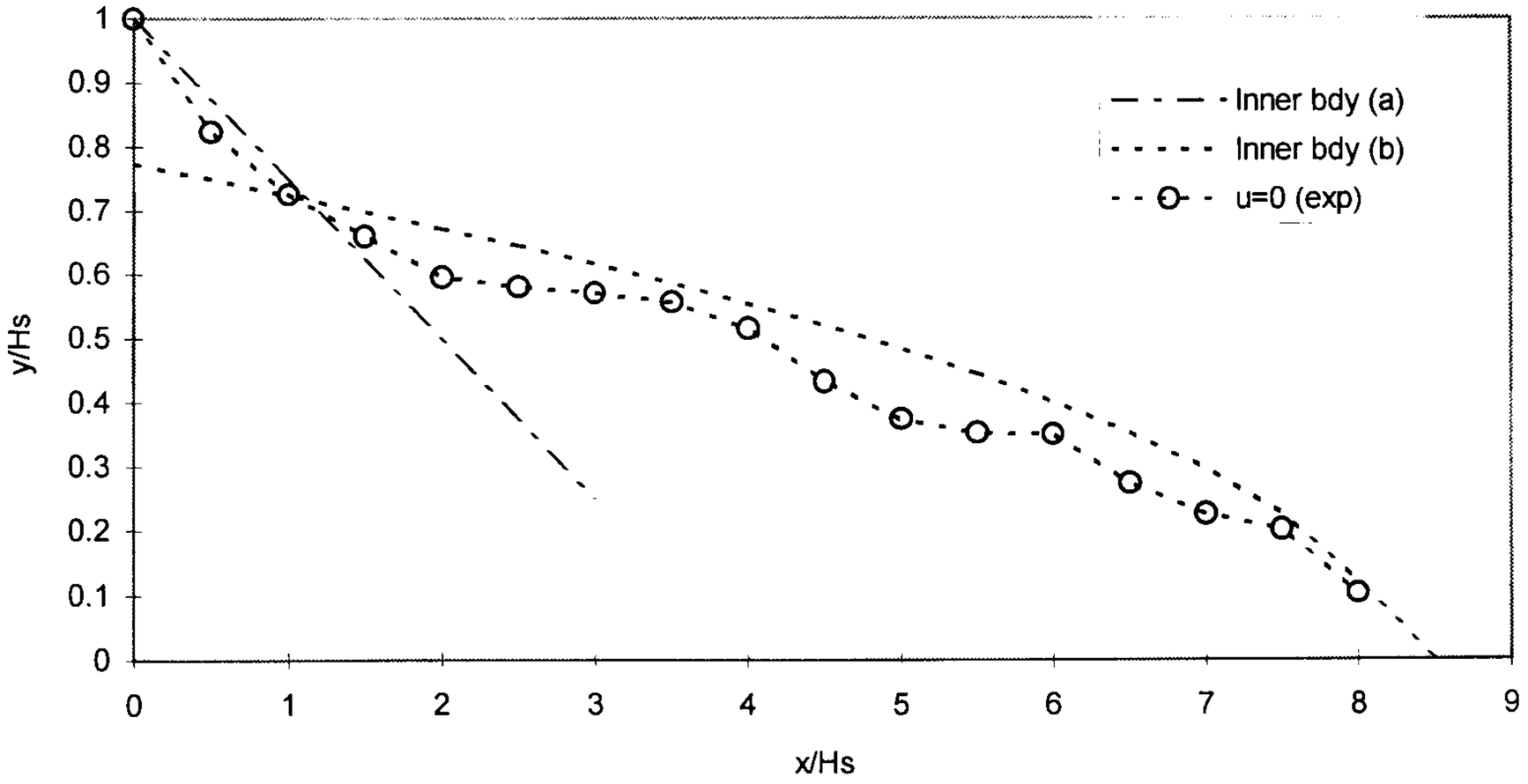

Figure 5.29 - Shear Layer Thickness: Based on Distance Between Shear Layer Boundaries

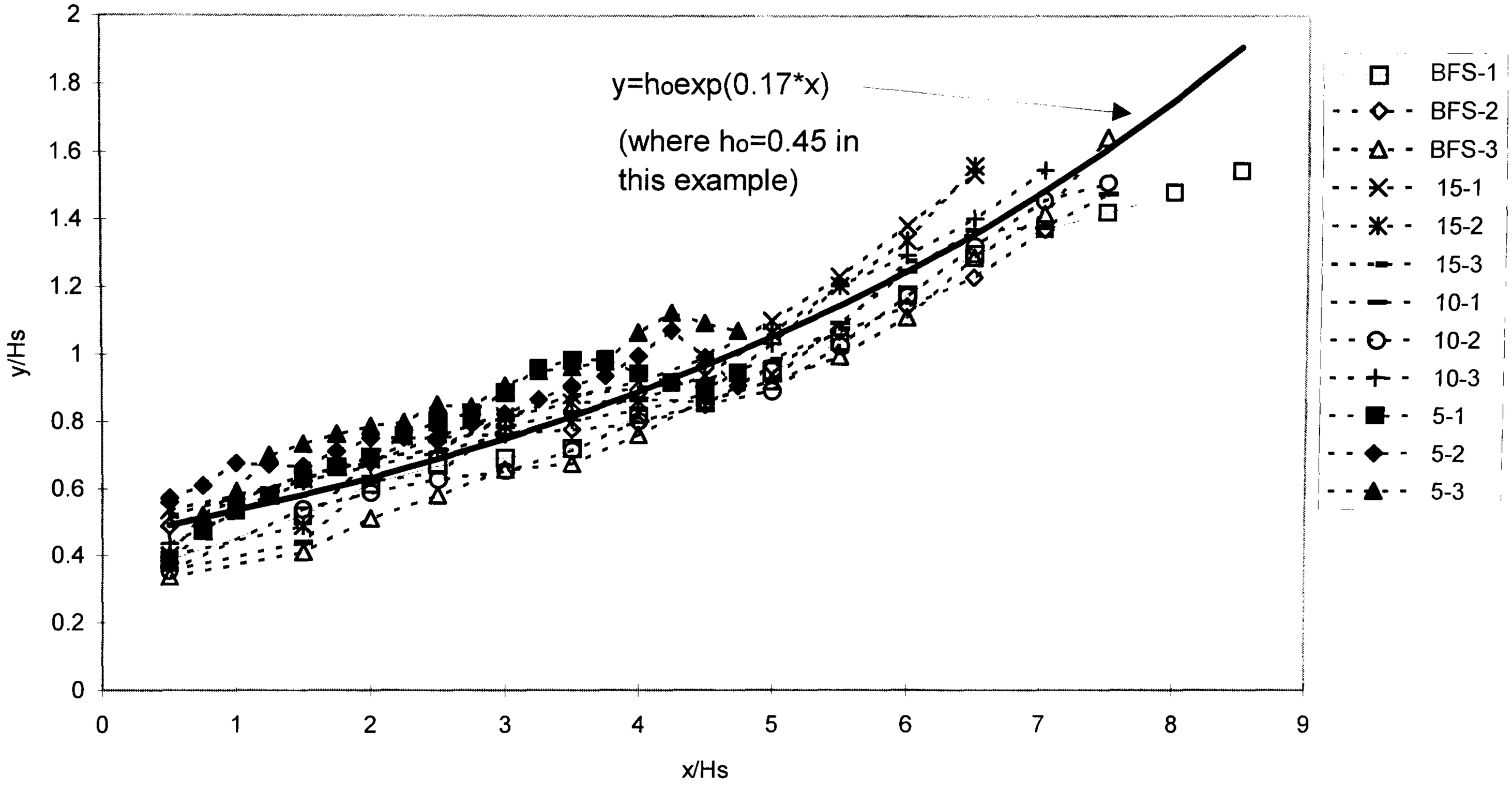

Figure 5.30 - Shear Layer Thickness Based on Constant Velocity Gradient

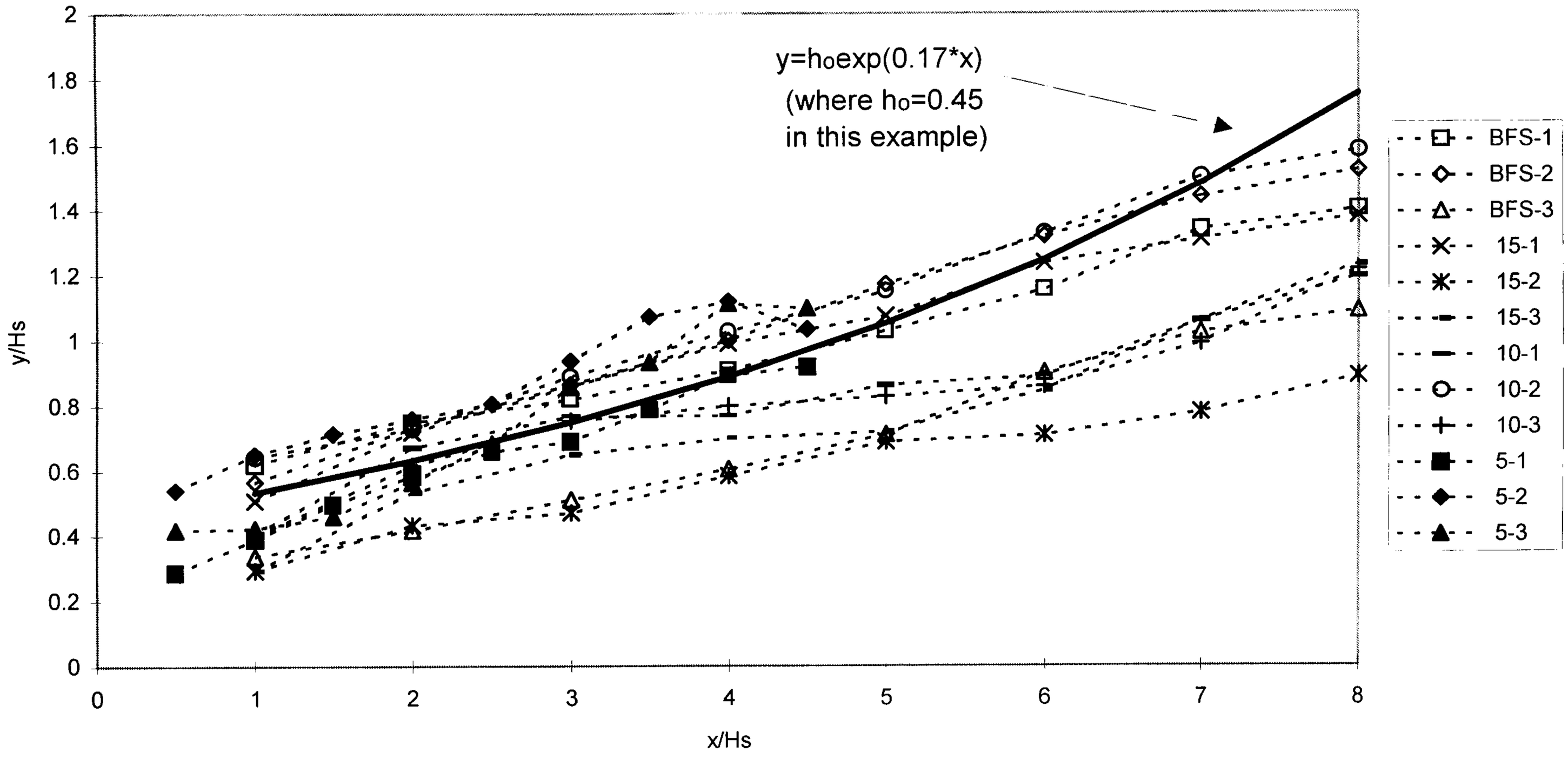

Figure 5.31(a) - Universal Velocity Profile (Nakagawa and Nezu, 1987) Downstream of a BFS: BFS-1, $x/H_s<R_L$

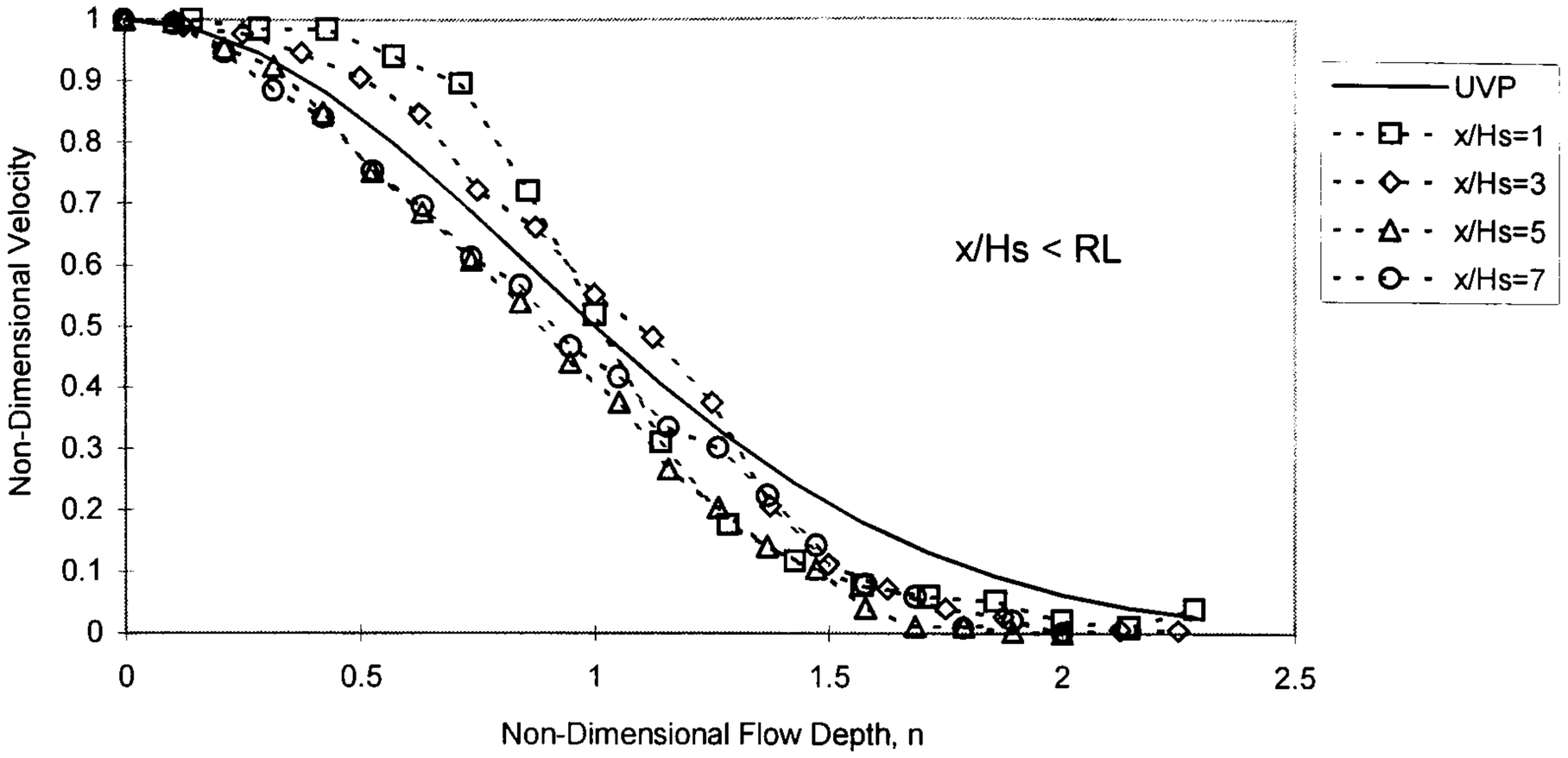

Figure 5.31(b) - Universal Velocity Profile (Nakagawa and Nezu, 1987) Downstream of a BFS: BFS-1, $x/H_s>R_L$

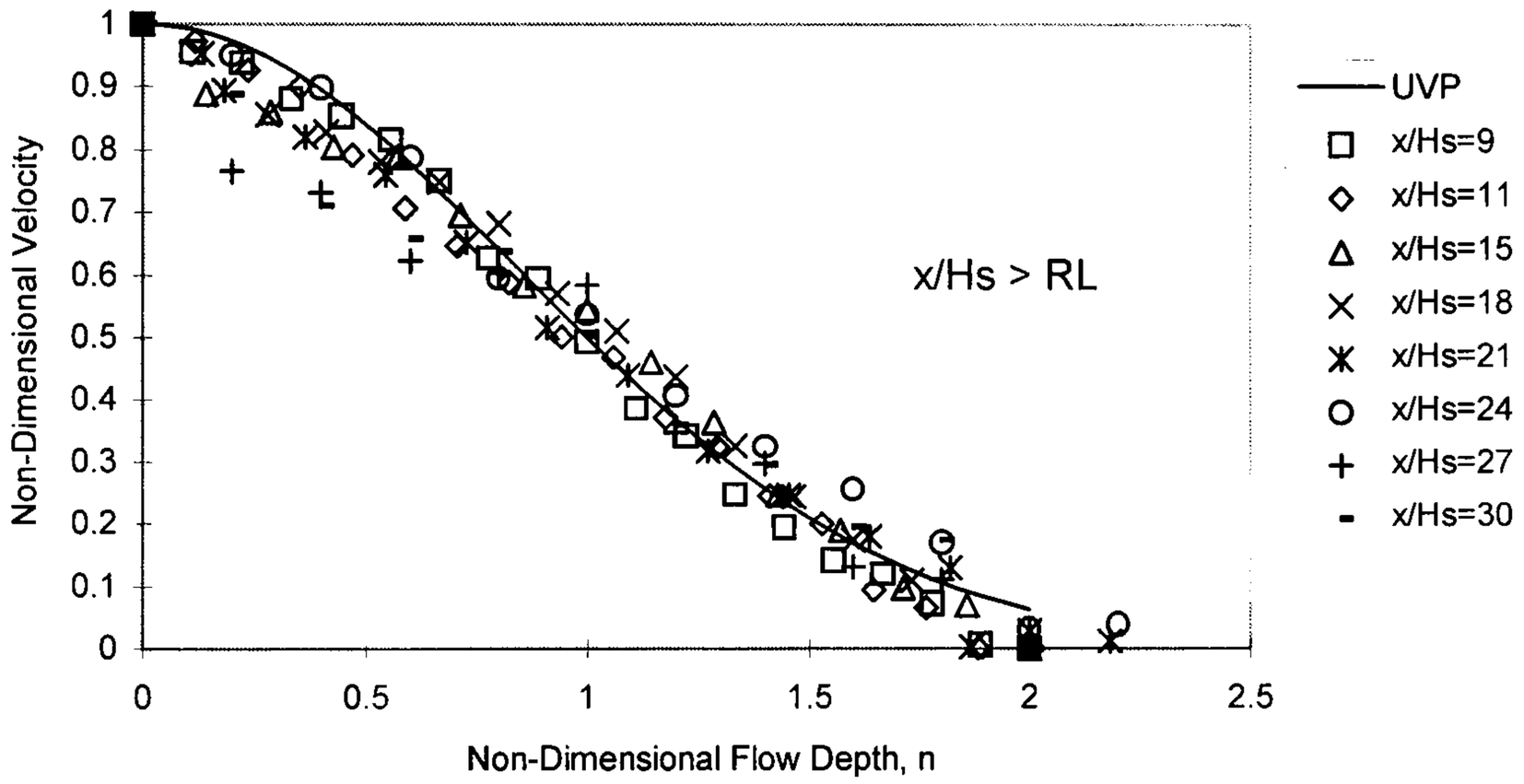

Figure 5.32(a) - Universal Velocity Profile (Nakagawa and Nezu, 1987) Downstream of a BFS: BFS-2, $x/H_s<R_L$

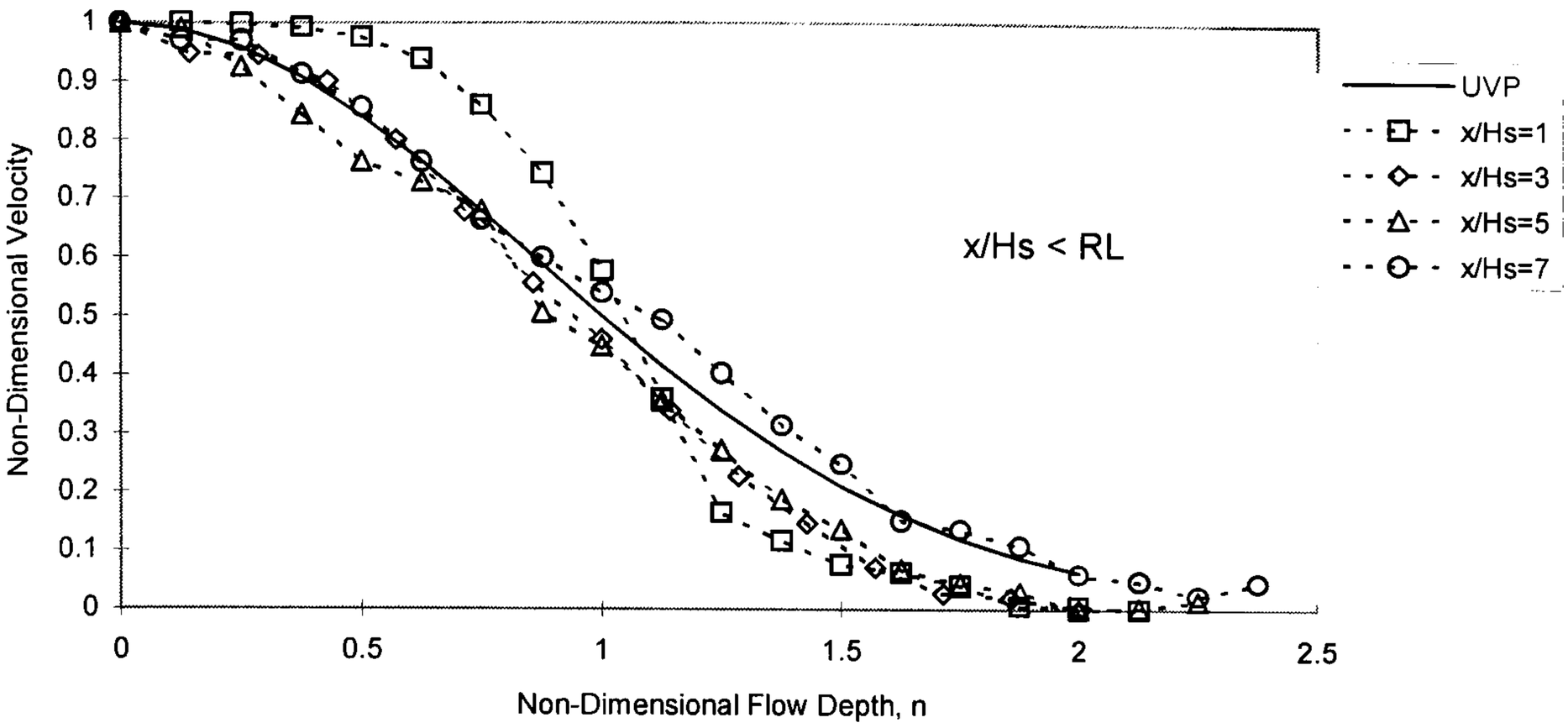

Figure 5.32(b) - Universal Velocity Profile (Nakagawa and Nezu, 1987) Downstream of a BFS: BFS-2, $x/H_s>R_L$

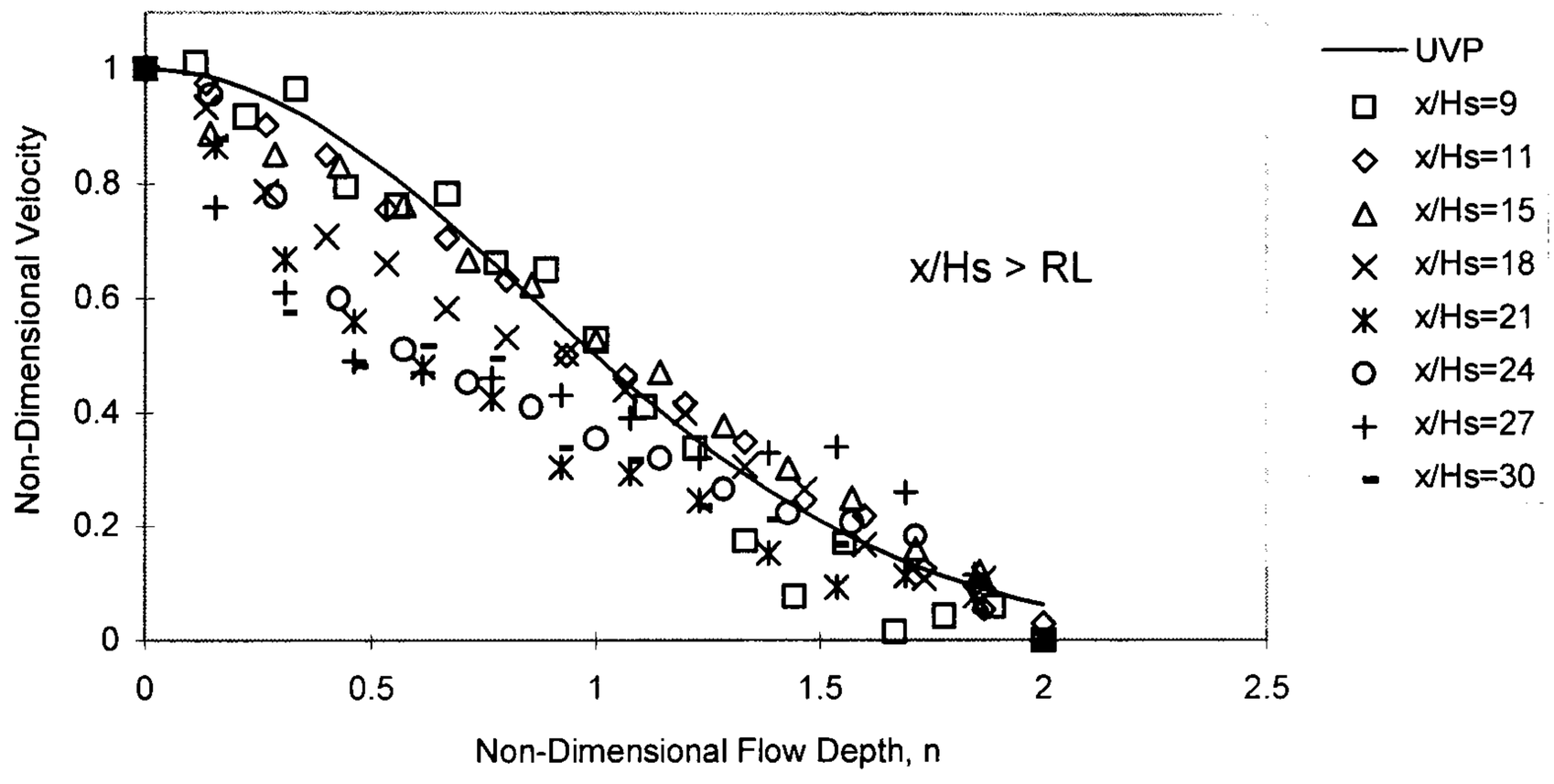

Figure 5.33(a) - Universal Velocity Profile (Nakagawa and Nezu, 1987) Downstream of a BFS: BFS-3, $x/H_s<R_L$

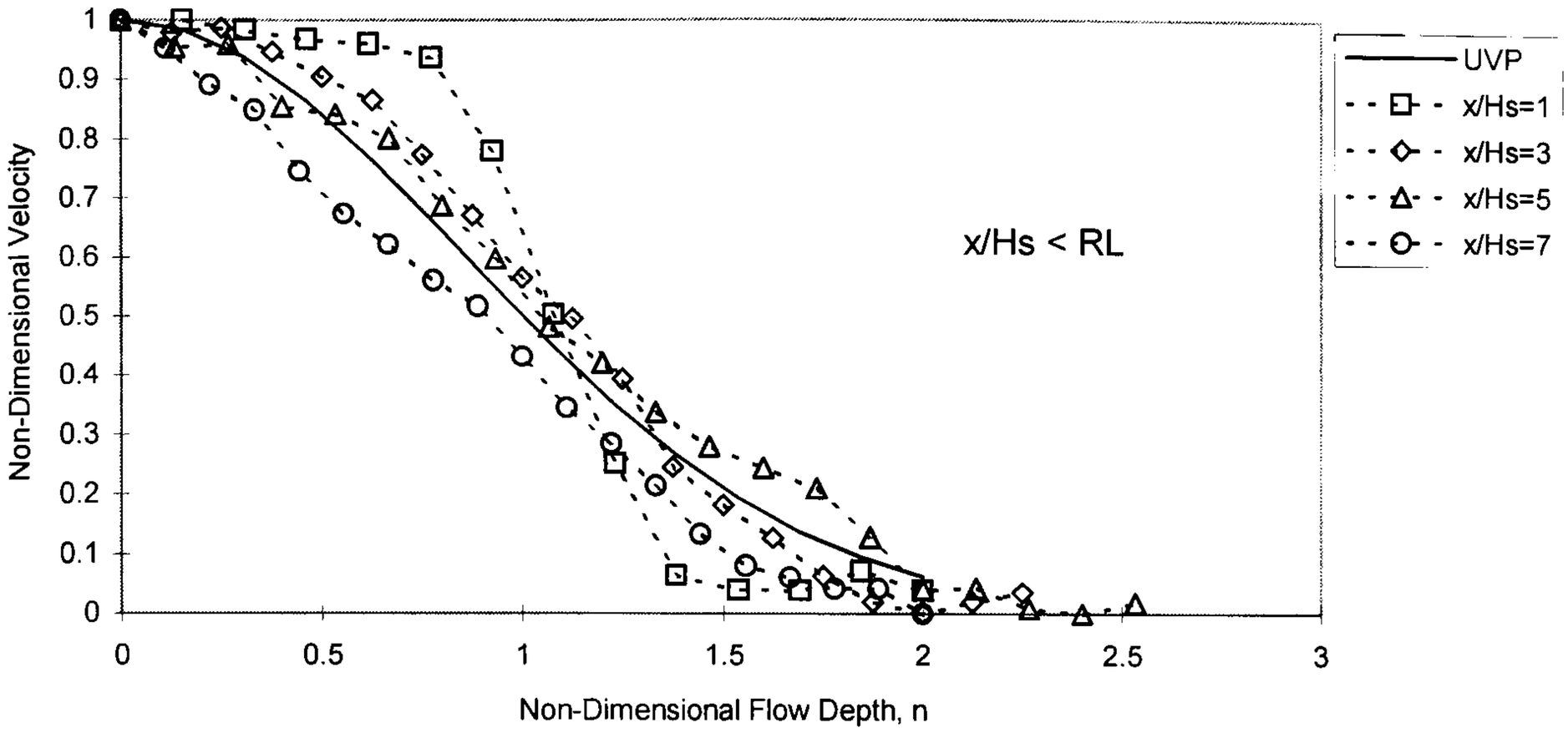

Figure 5.33(b) - Universal Velocity Profile (Nakagawa and Nezu, 1987) Downstream of a BFS: BFS-3, $x/H_s>R_L$

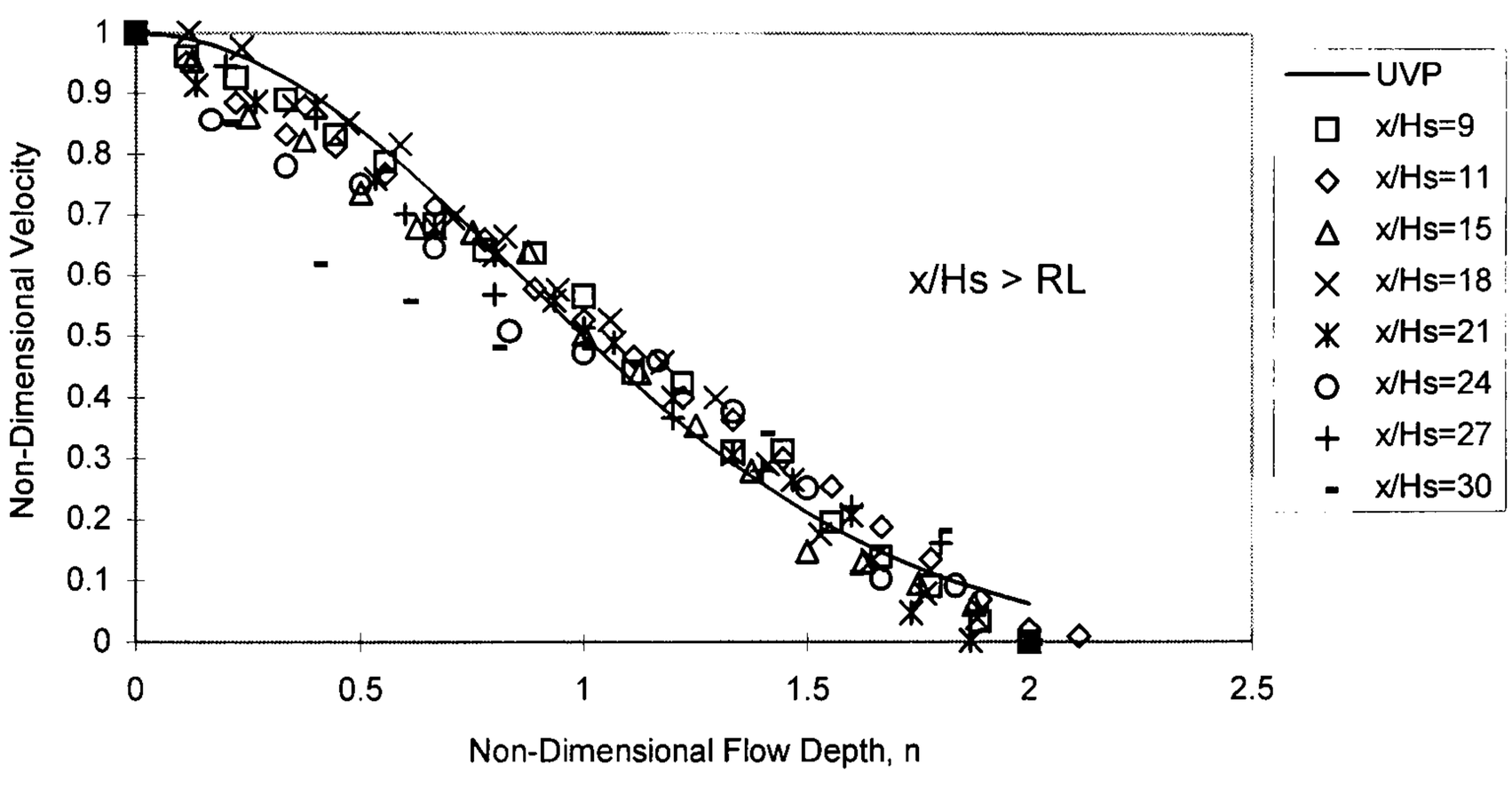

Figure 5.34(a) - Universal Velocity Profile Downstream of a BFS (Jasem, 1990): BFS-1

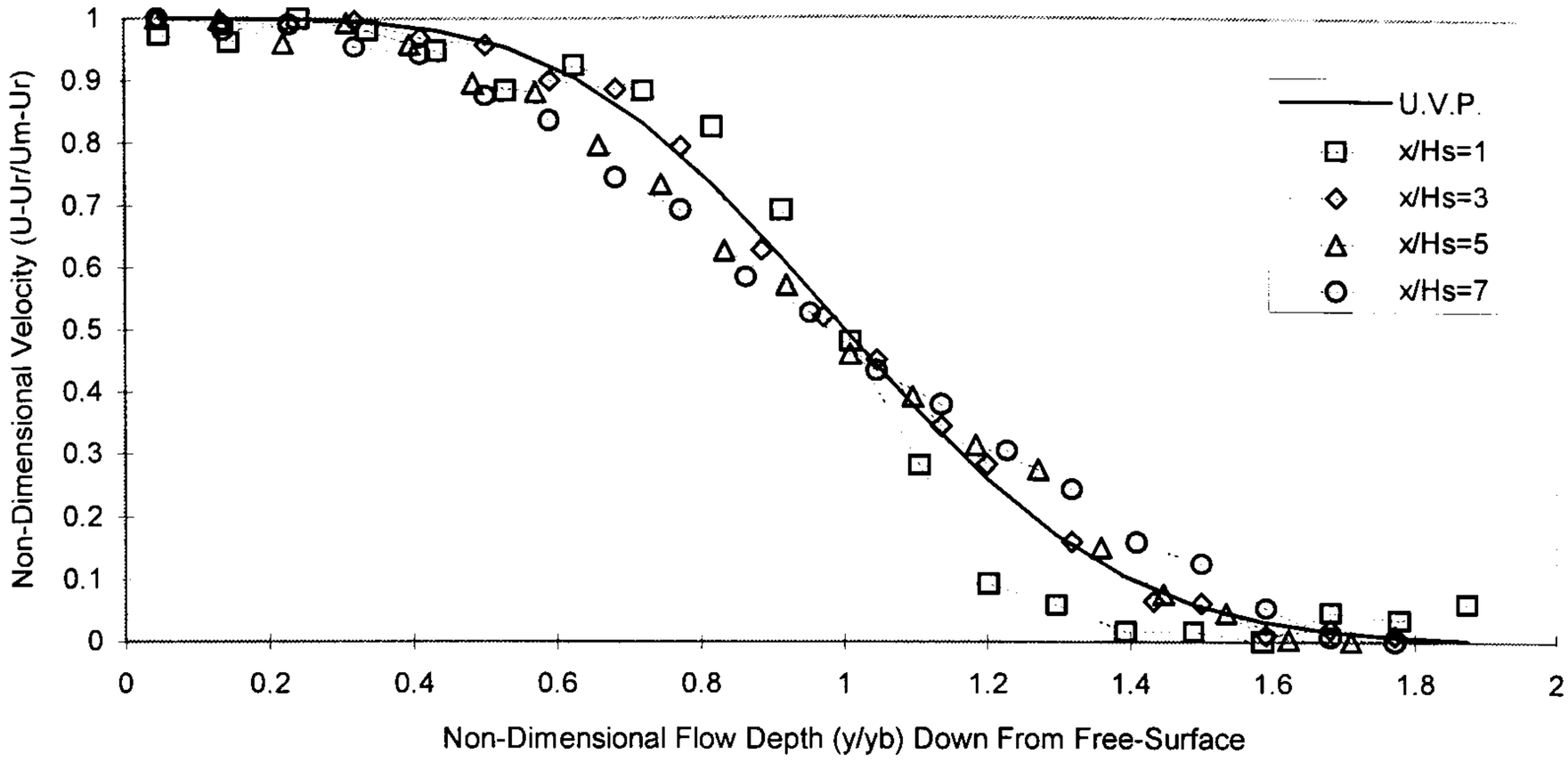

Figure 5.34(b) - Universal Velocity Profile Downstream of a BFS (Jasem, 1990): BFS-2

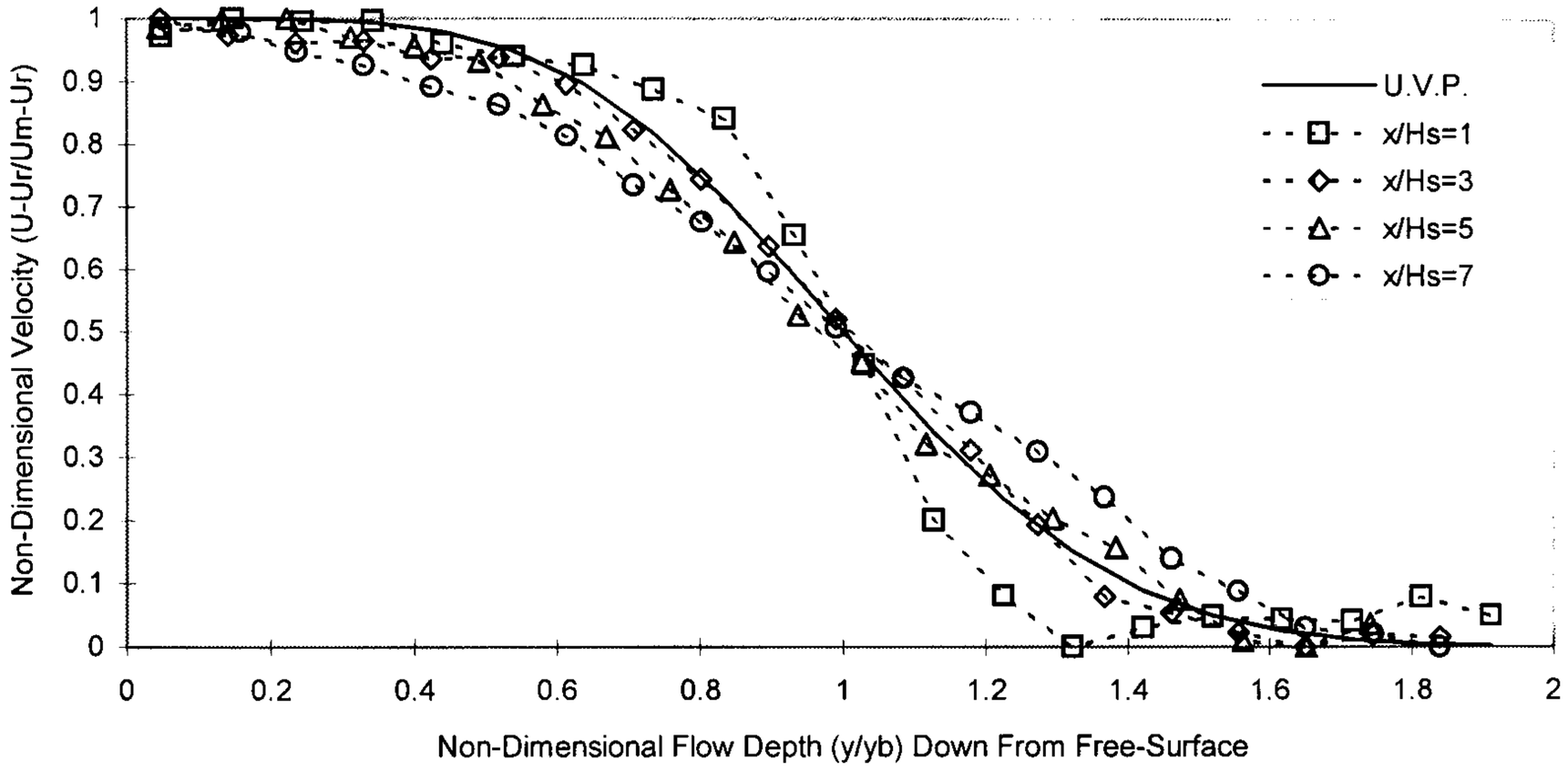

Figure 5.34(c) - Universal Velocity Profile Downstream of a BFS (Jasem, 1990): BFS-3

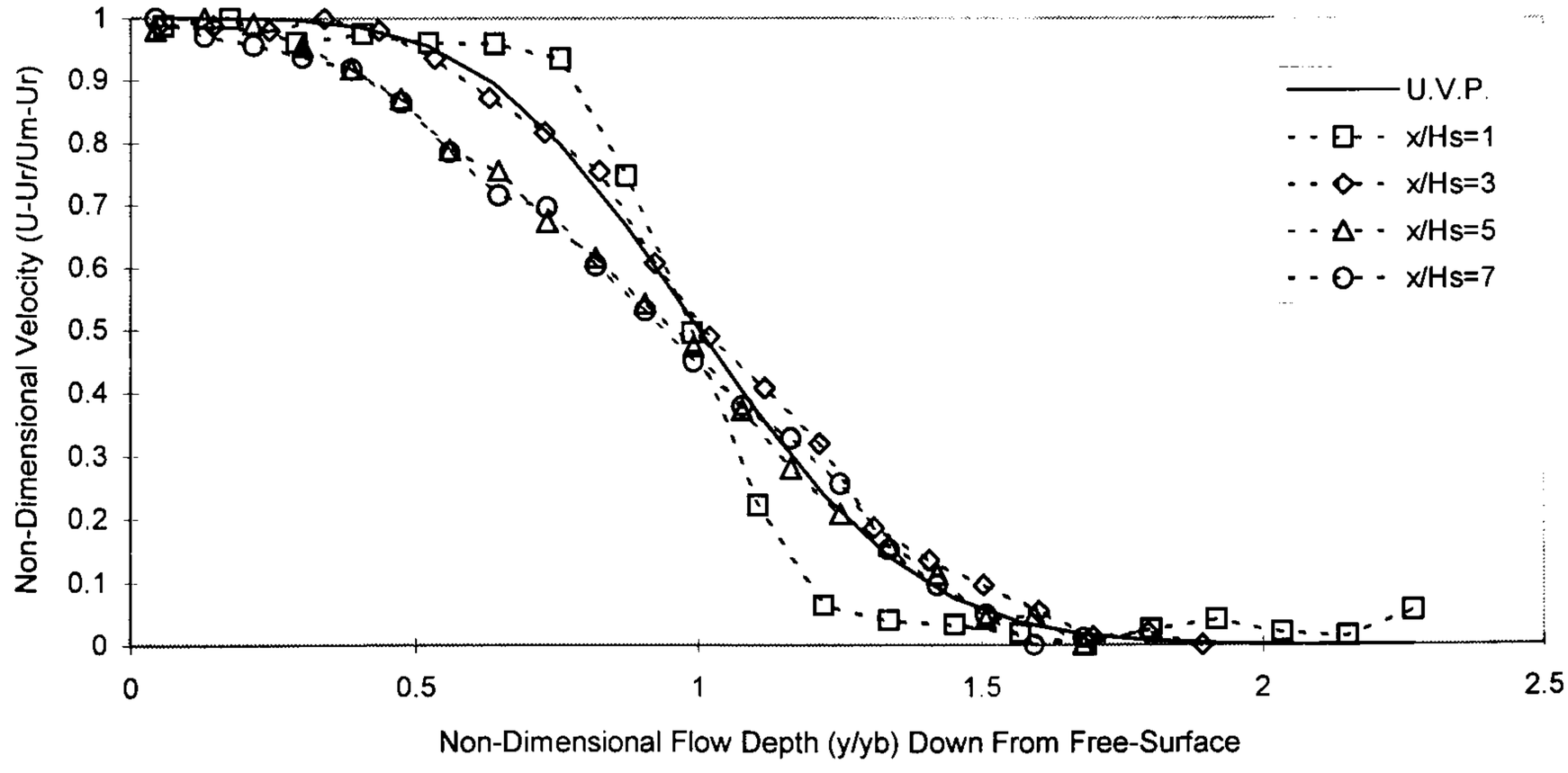

Figure 5.34(d) - Universal Velocity Profile Downstream of a BFS (Jasem, 1990): Initial Investigation (Re=10000)

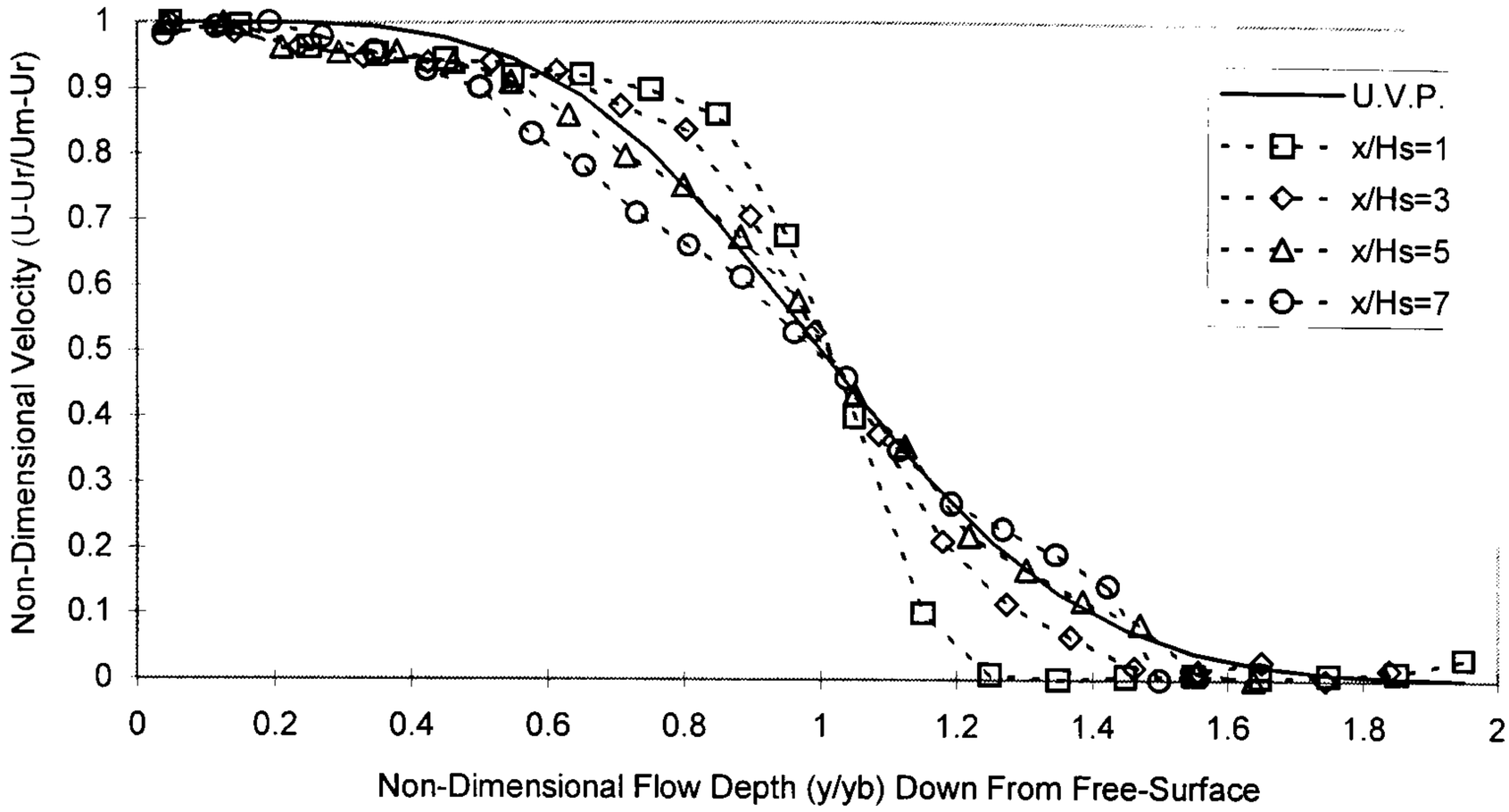

Figure 5.35(a) - Universal Velocity Profile Downstream of a BFS (Jasem, 1990): 15-1

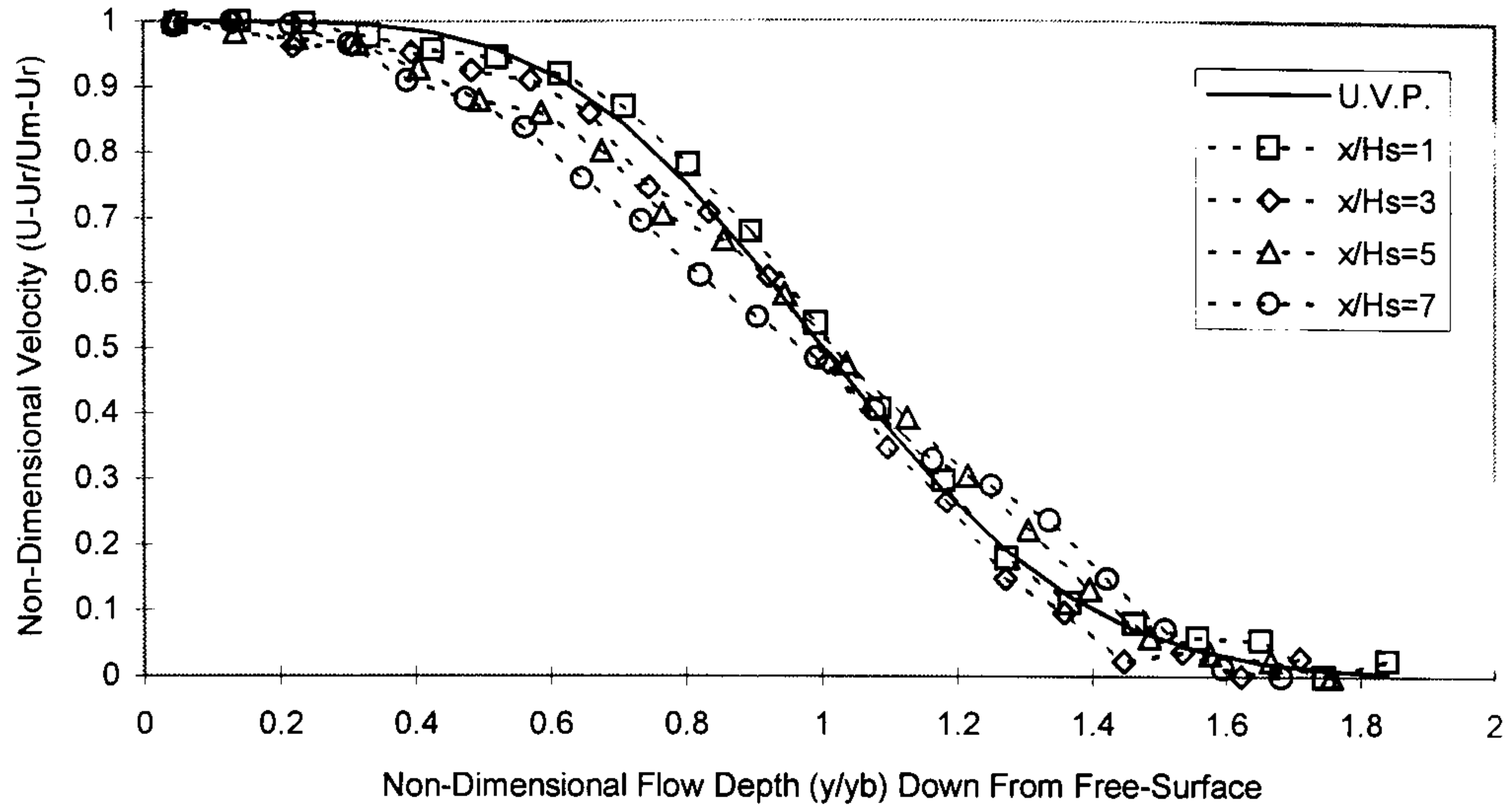

Figure 5.35(b) - Universal Velocity Profile Downstream of a BFS (Jasem, 1990): 15-2

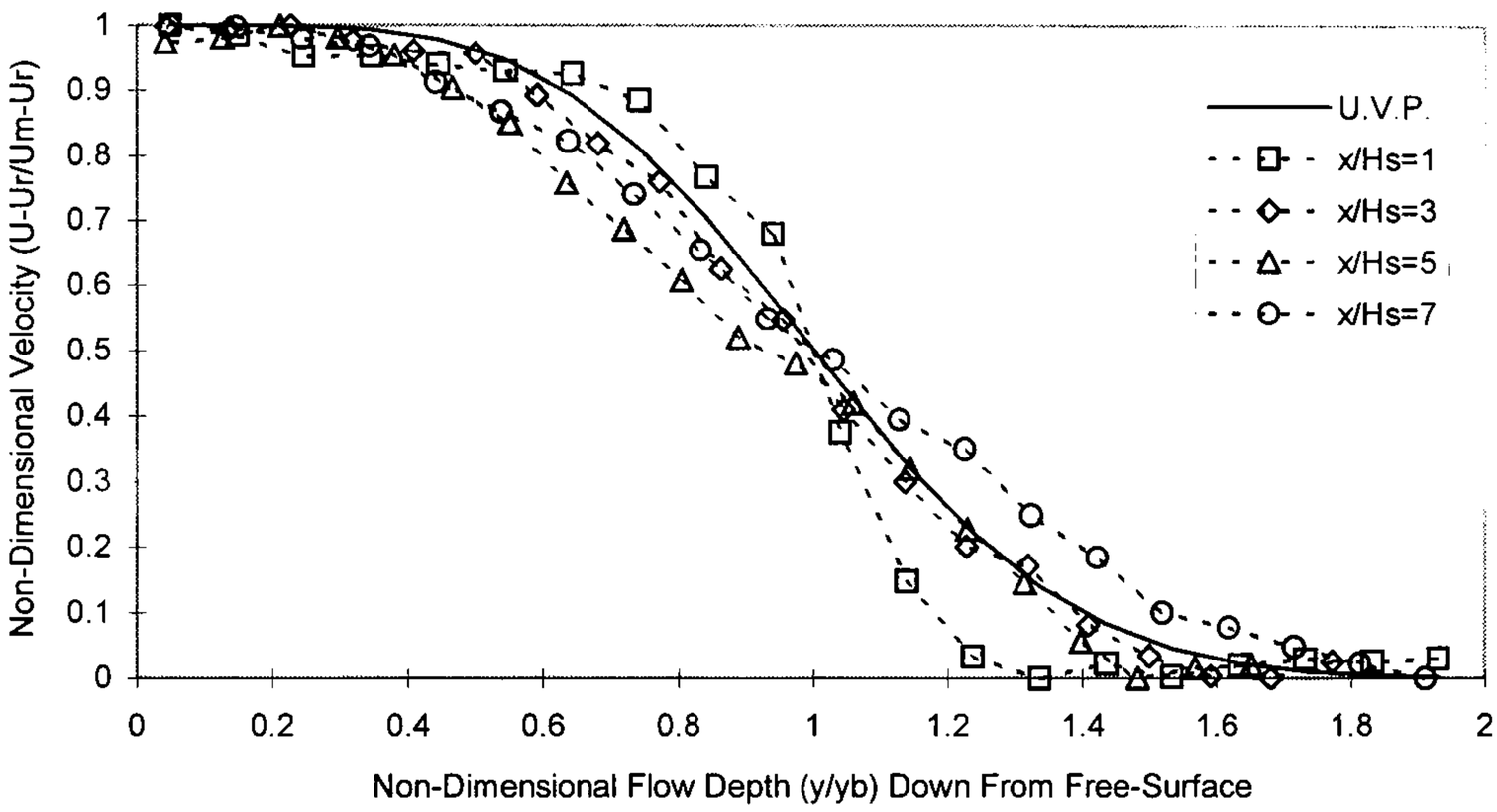

Figure 5.35(c) - Universal Velocity Profile Downstream of a BFS (Jasem, 1990): 15-3

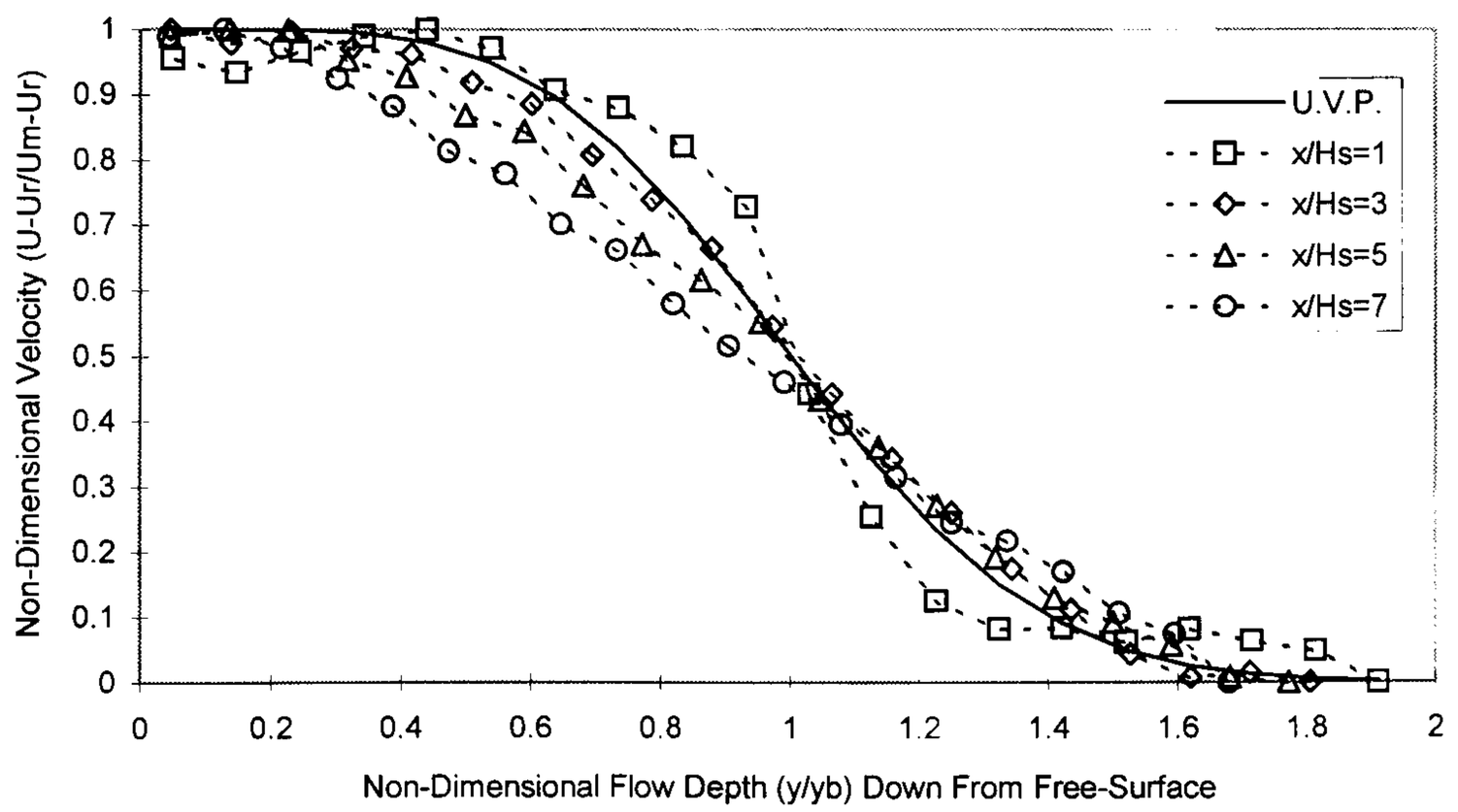

Figure 5.36(a) - Universal Velocity Profile Downstream of a BFS (Jasem, 1990): 10-1

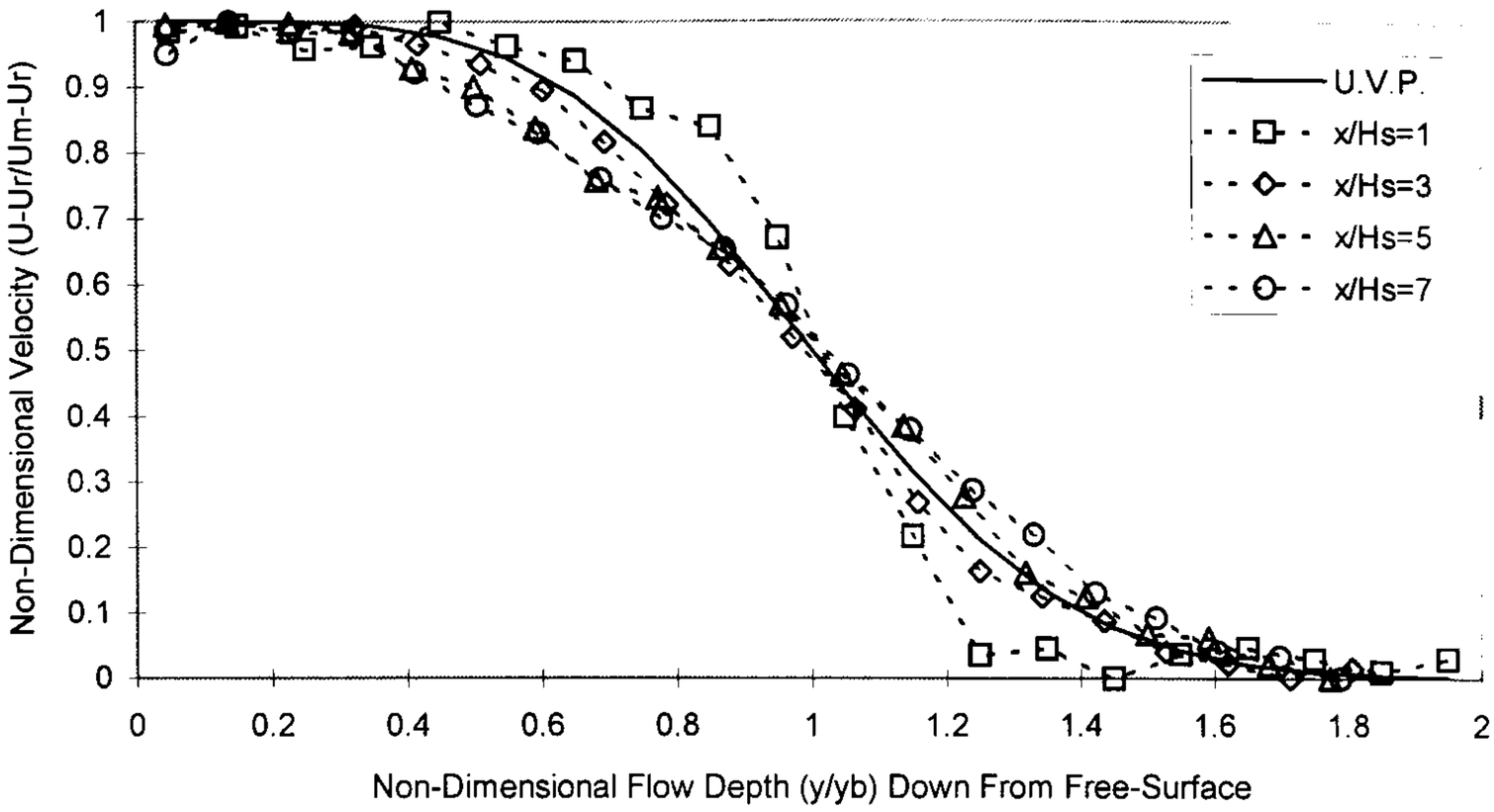

Figure 5.36(b) - Universal Velocity Profile Downstream of a BFS (Jasem, 1990): 10-2

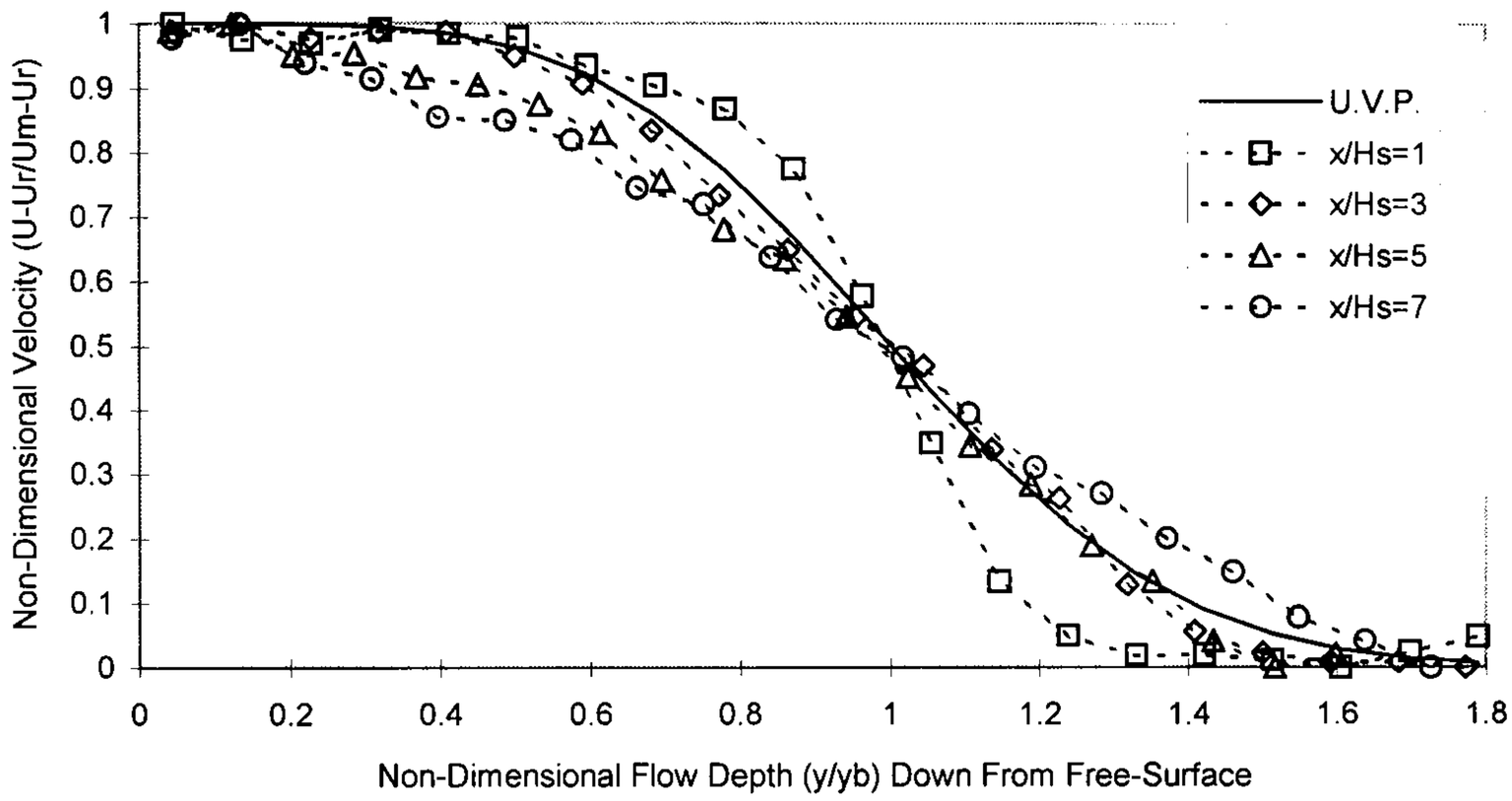

Figure 5.36(c) - Universal Velocity Profile Downstream of a BFS (Jasem, 1990): 10-3

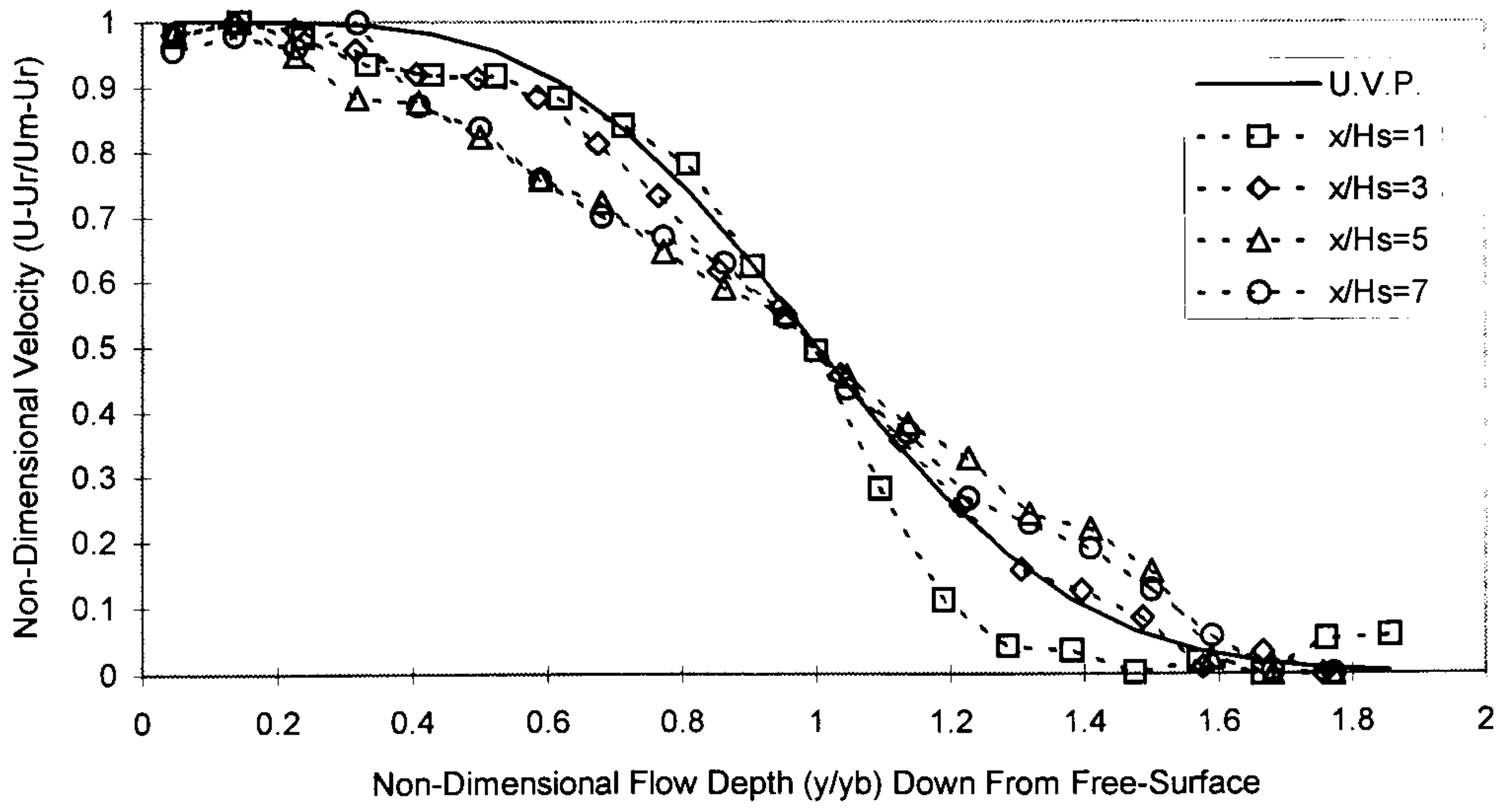

Figure 5.37(a) - Universal Velocity Profile Downstream of a BFS (Jasem, 1990): 5-1

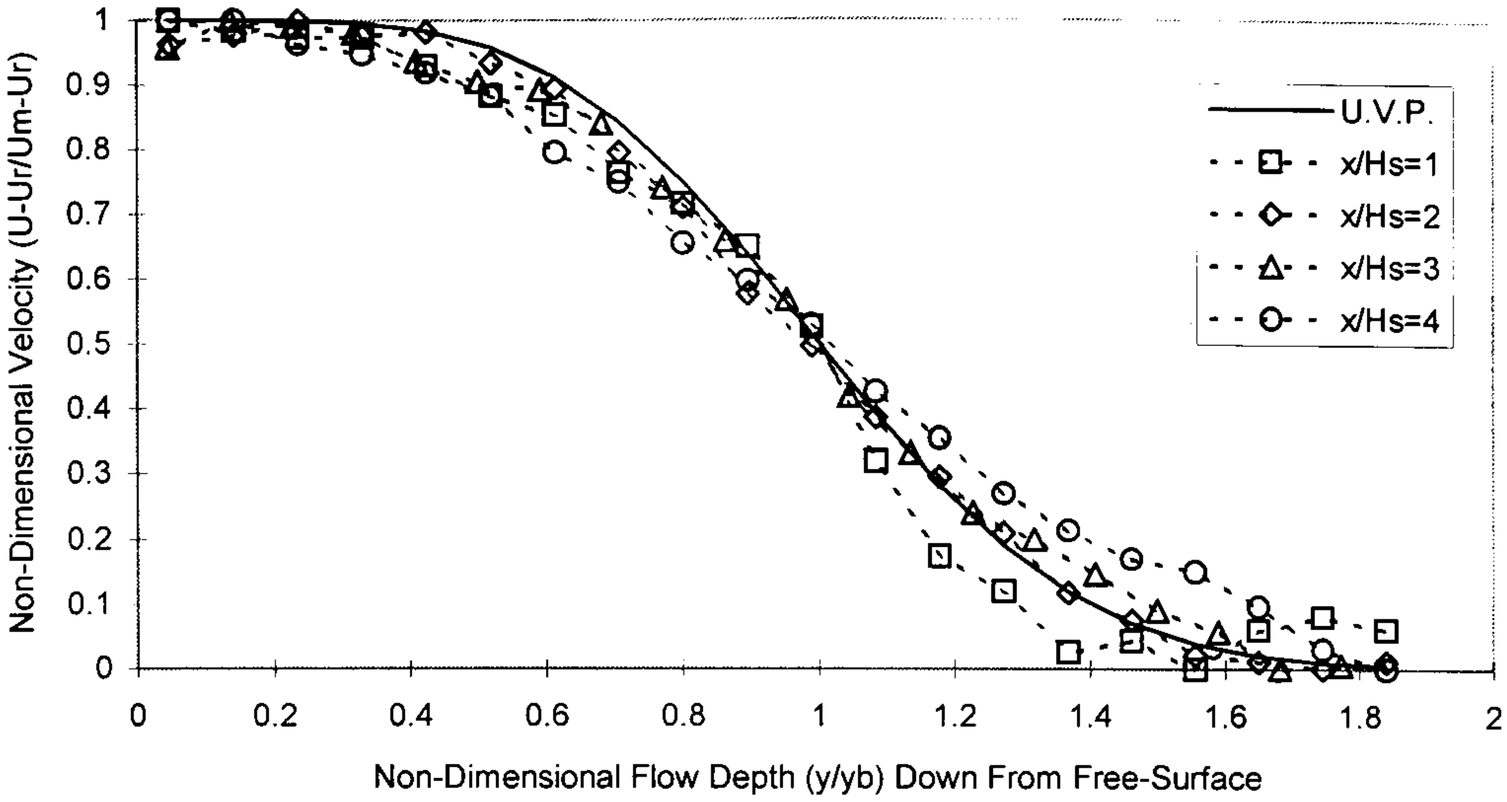

Figure 5.37(b) - Universal Velocity Profile Downstream of a BFS (Jasem, 1990): 5-2

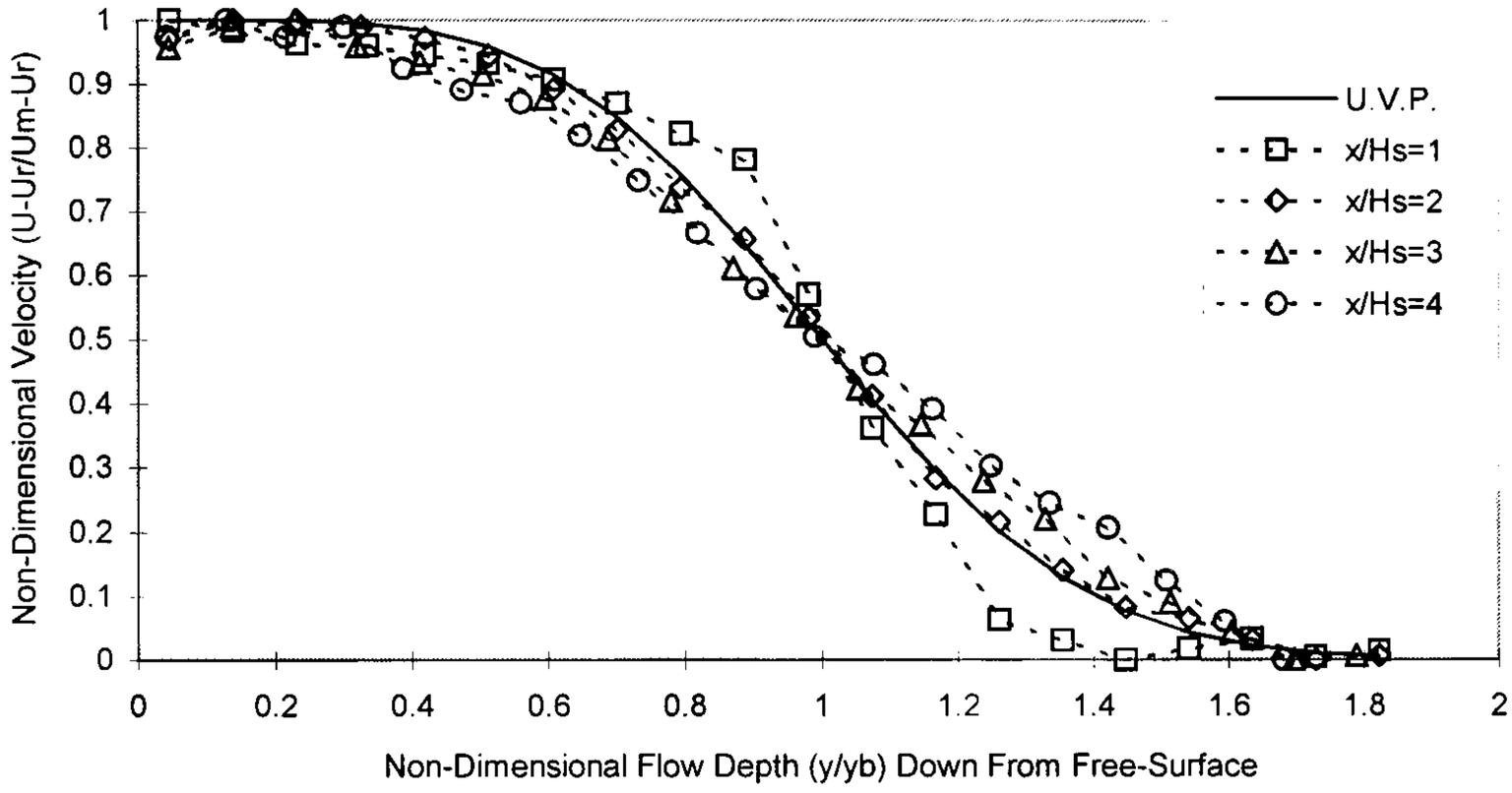

Figure 5.37(c) - Universal Velocity Profile Downstream of a BFS (Jasem, 1990): 5-3

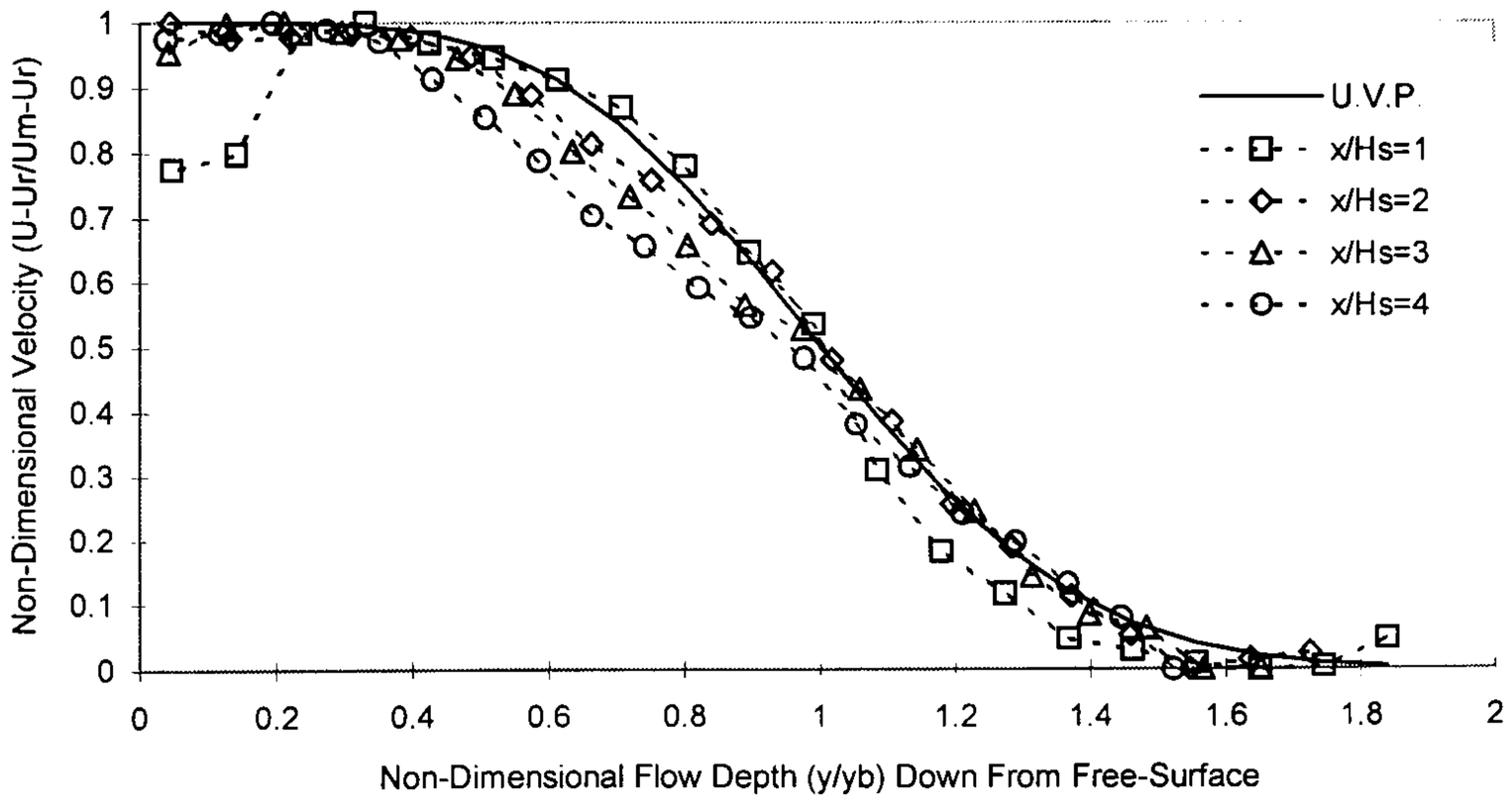

Figure 5.38(a) - Updated Universal Velocity Profile for x/Hs=1

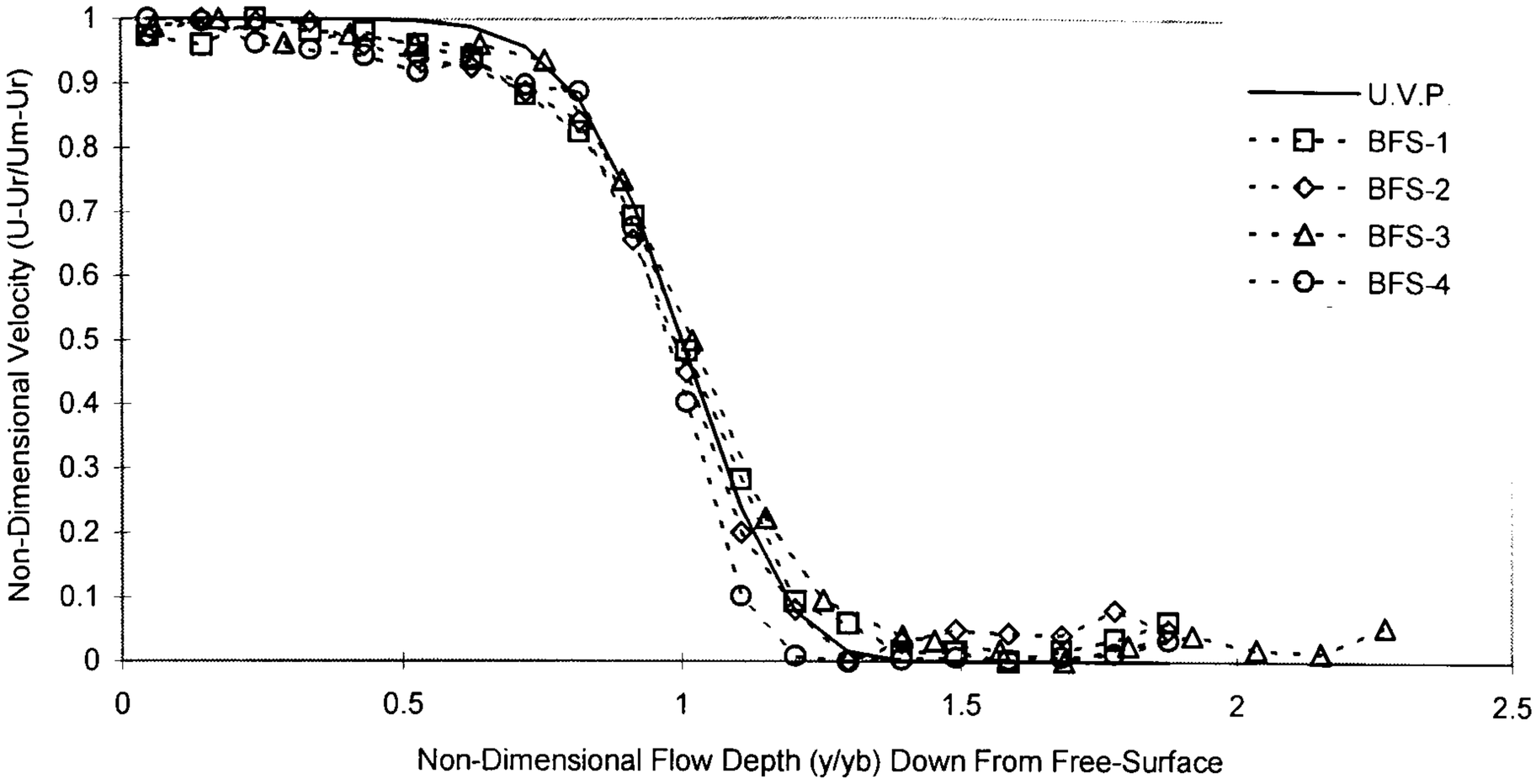

Figure 5.38(b) - Updated Universal Velocity Profile for x/Hs=3

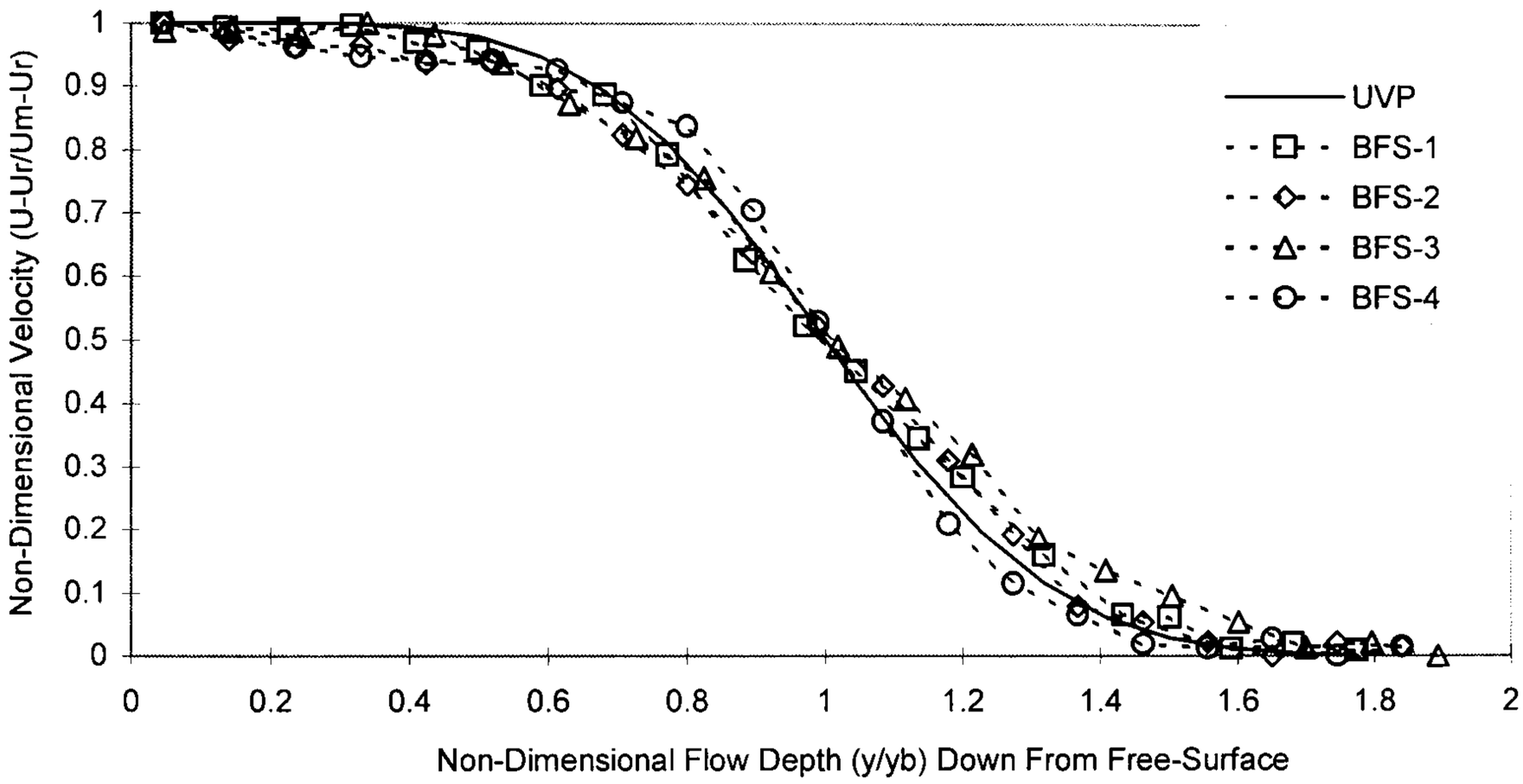

Figure 5.38(c) - Updated Universal Velocity Profile for x/Hs=5

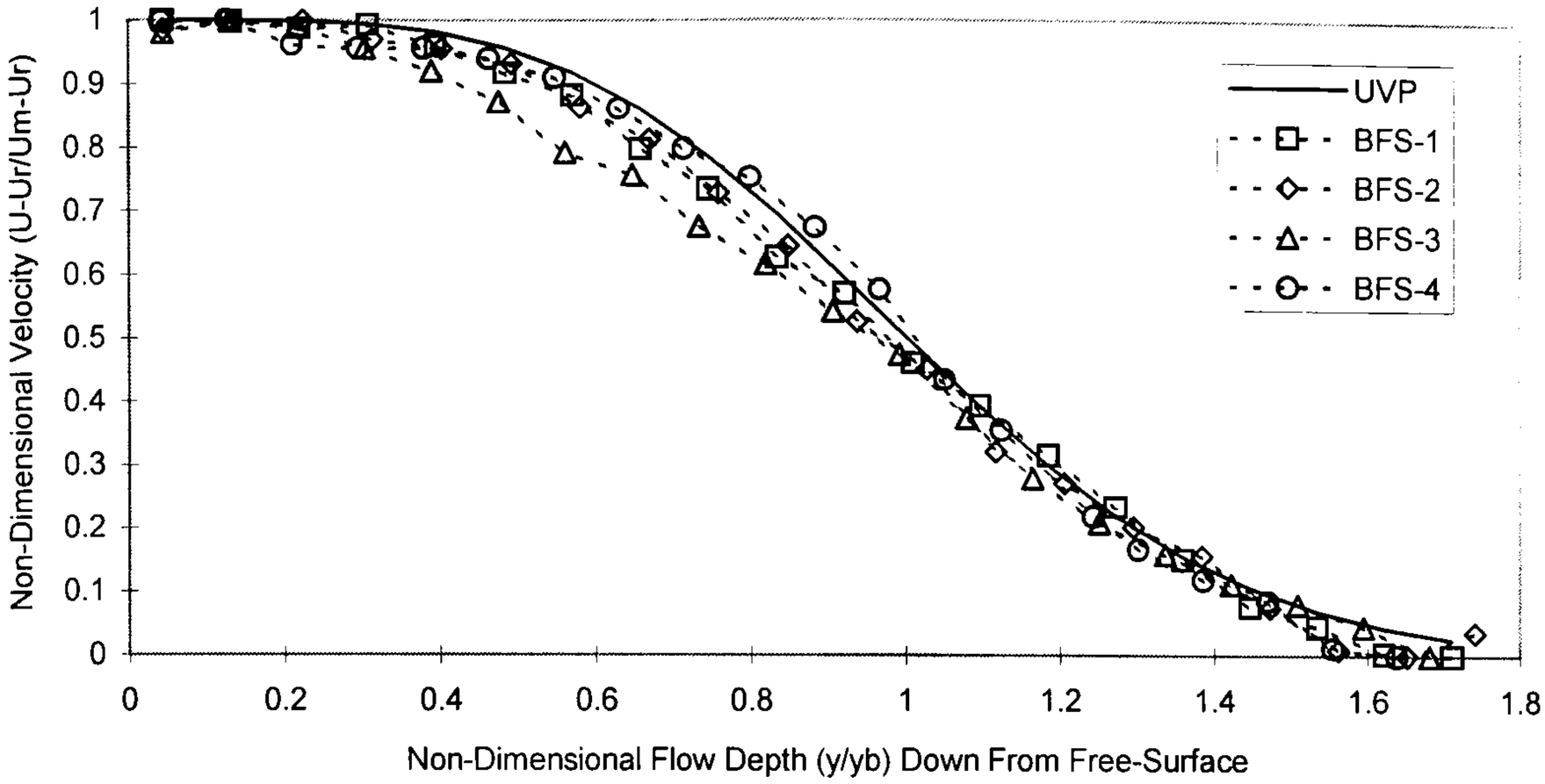

Figure 5.38(d) - Updated Universal Velocity Profile for x/Hs=7

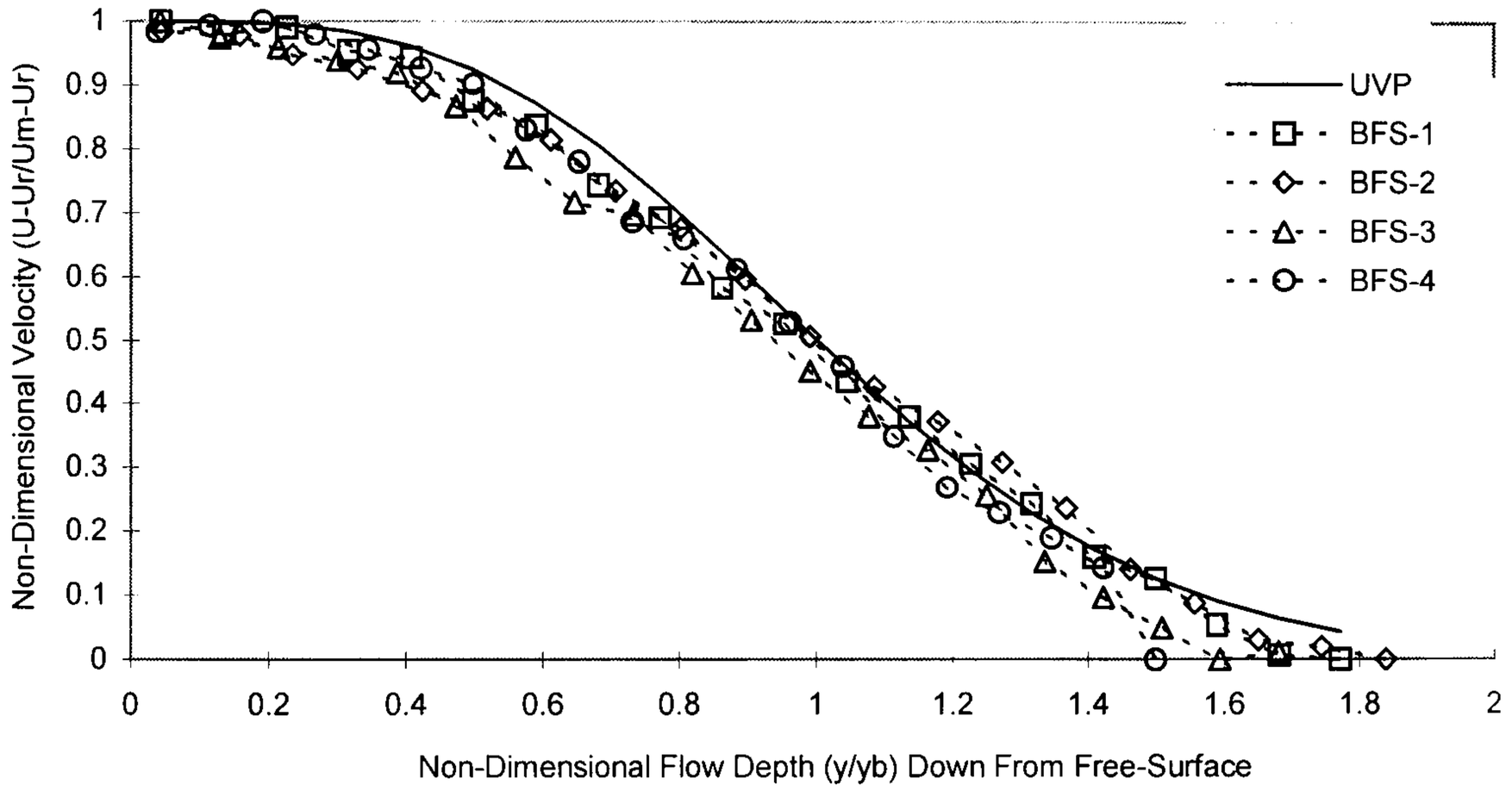

Figure 5.39(a) - Log-Law Velocity Profiles Downstream of Flow Reattachment: BFS-1

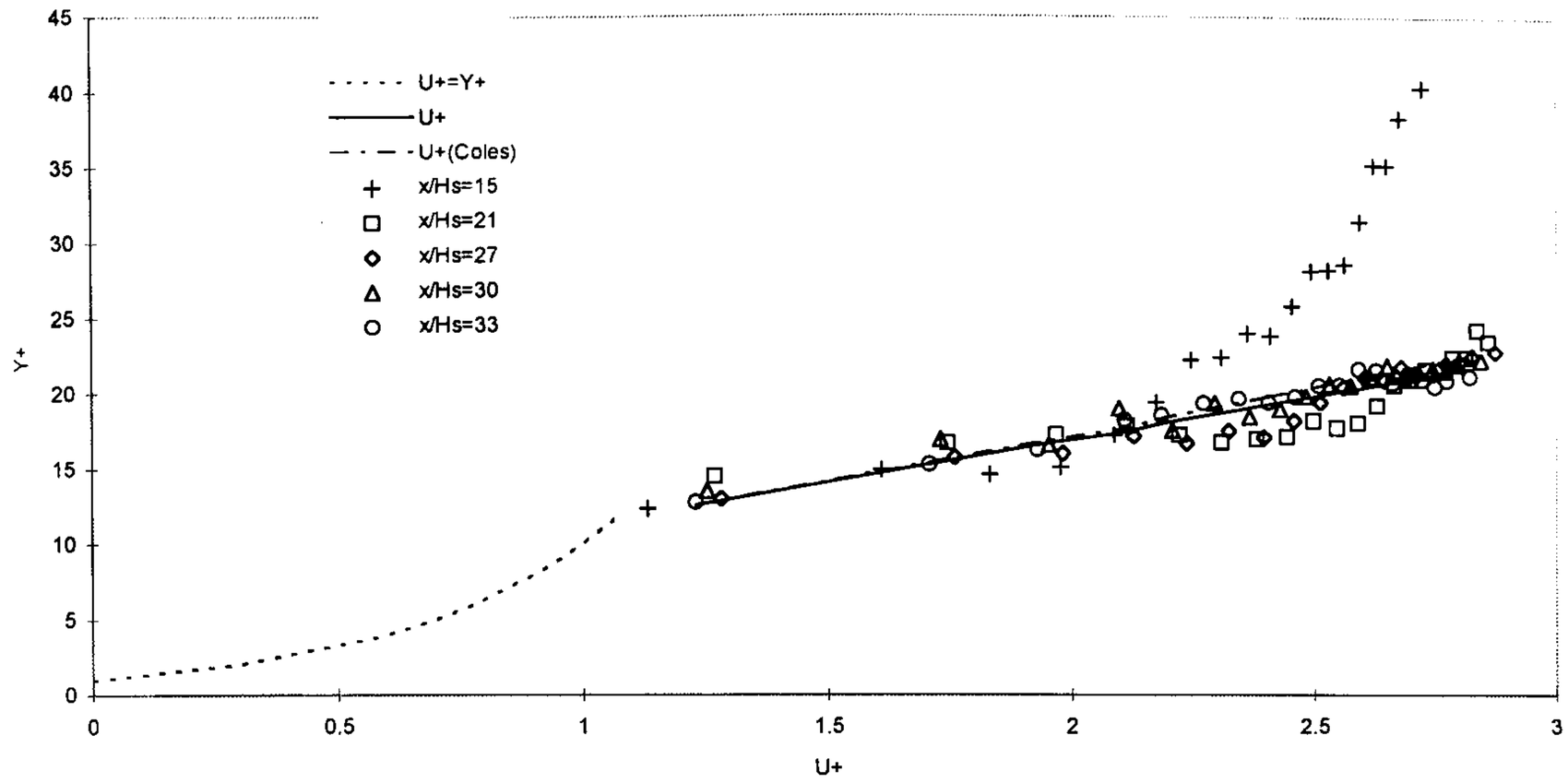

Figure 5.39(b) - Log-Law Velocity Profiles Downstream of Flow Reattachment: BFS-2

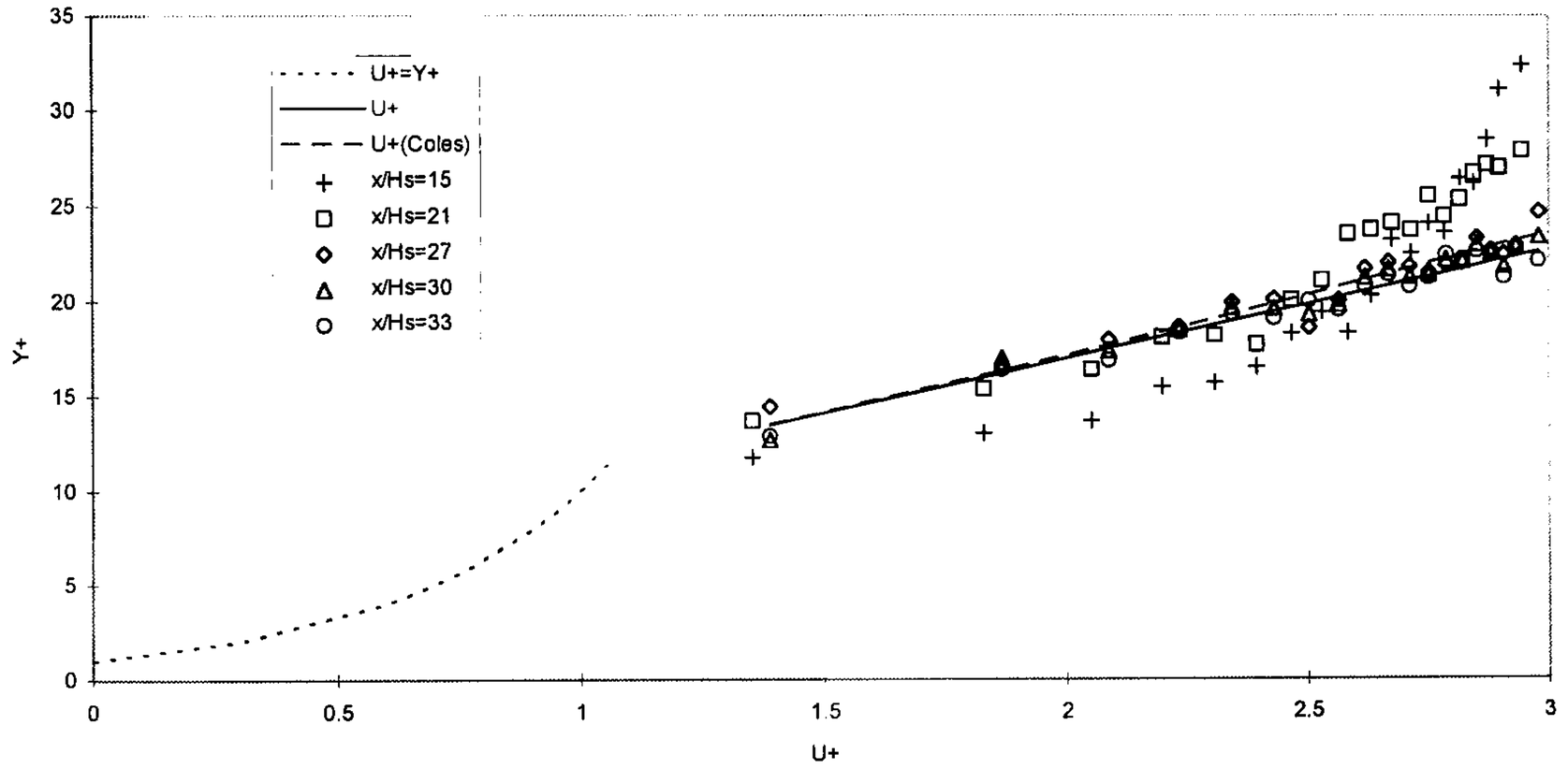

Figure 5.39(c) - Log-Law Velocity Profiles Downstream of Flow Reattachment: BFS-3

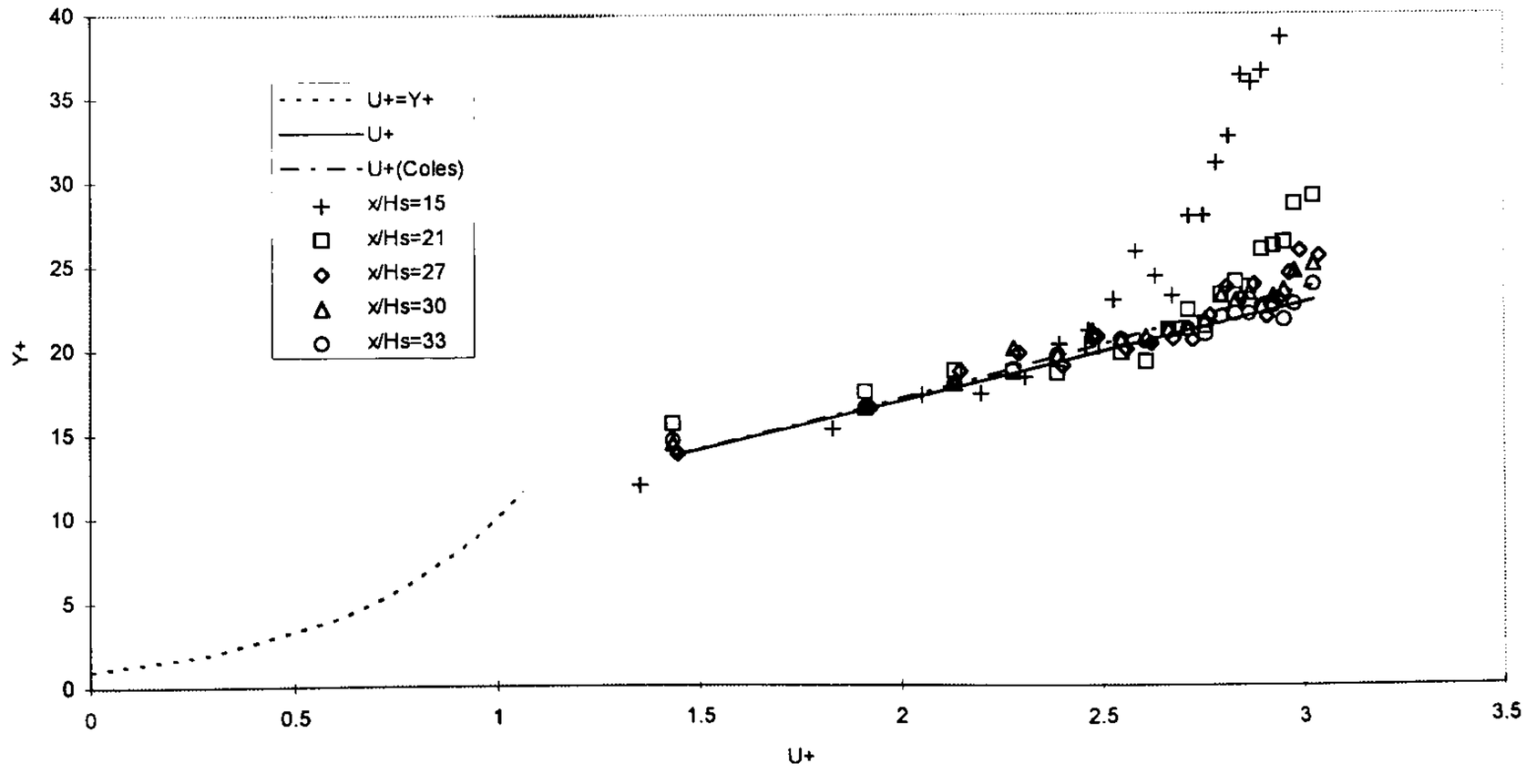

Figure 5.40(a) – Non-Dimensionalised Turbulent Kinetic Energy (Total): BFS-1

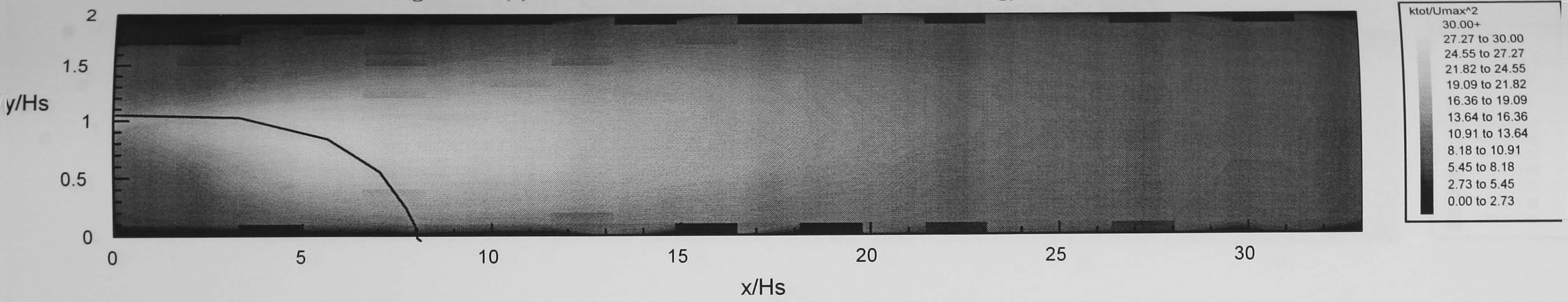

Figure 5.40(b) - Non-Dimensionalised Turbulent Kinetic Energy (Total): BFS-2

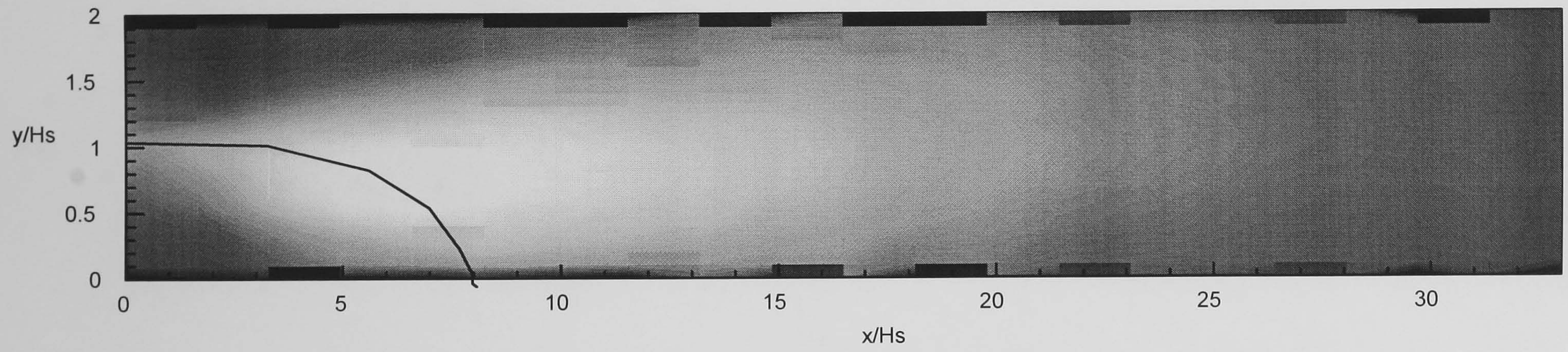

Figure 5.40(c) - Non-Dimensionalised Turbulent Kinetic Energy (Total): BFS-3

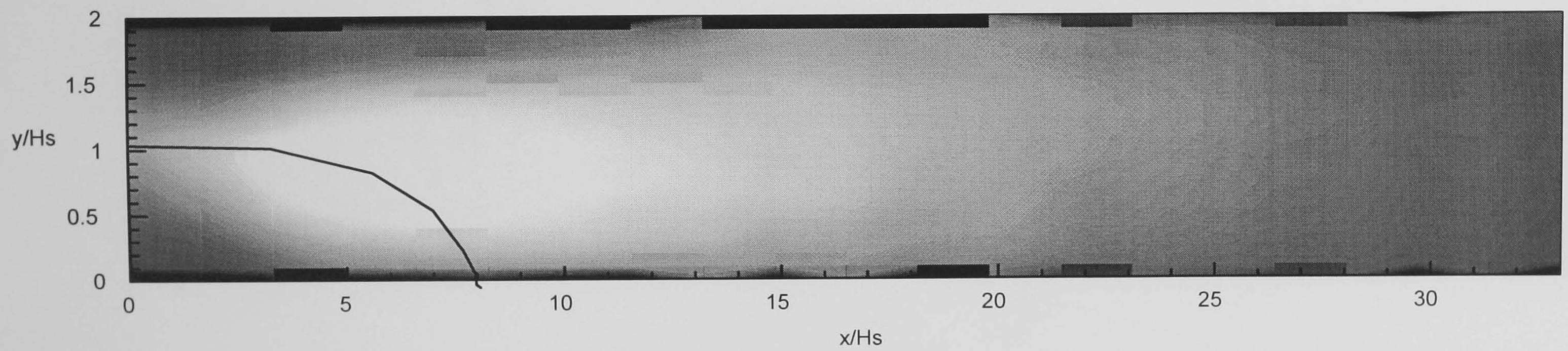

Figure 5.41(a) - Non-Dimensionalised Turbulent Kinetic Energy (u'): BFS-1

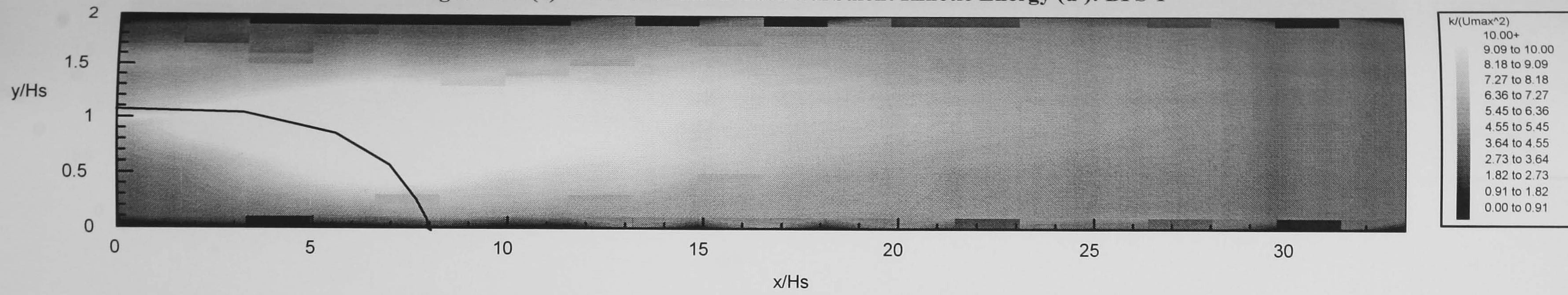

Figure 5.41(b) - Non-Dimensionalised Turbulent Kinetic Energy (v'): BFS-1

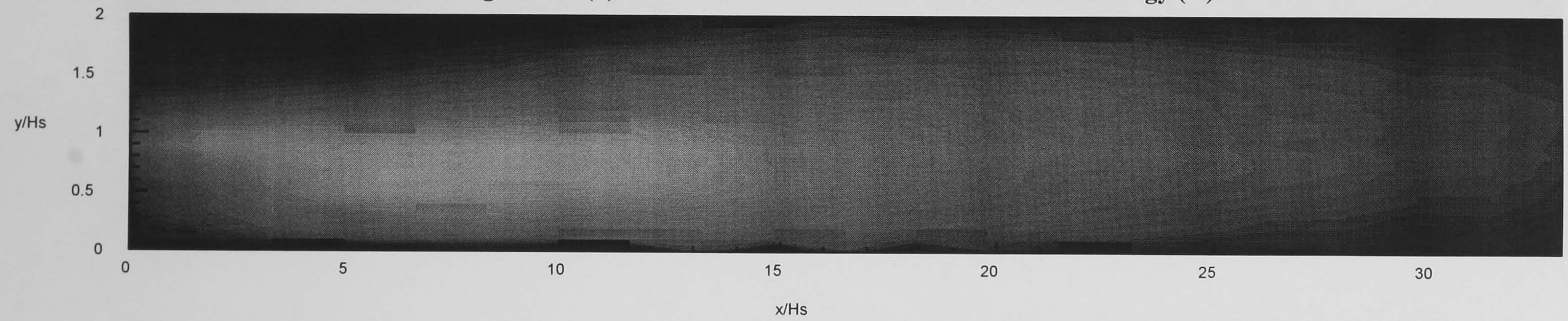

Figure 5.41(c) - Non-Dimensionalised Turbulent Kinetic Energy (w'): BFS-1

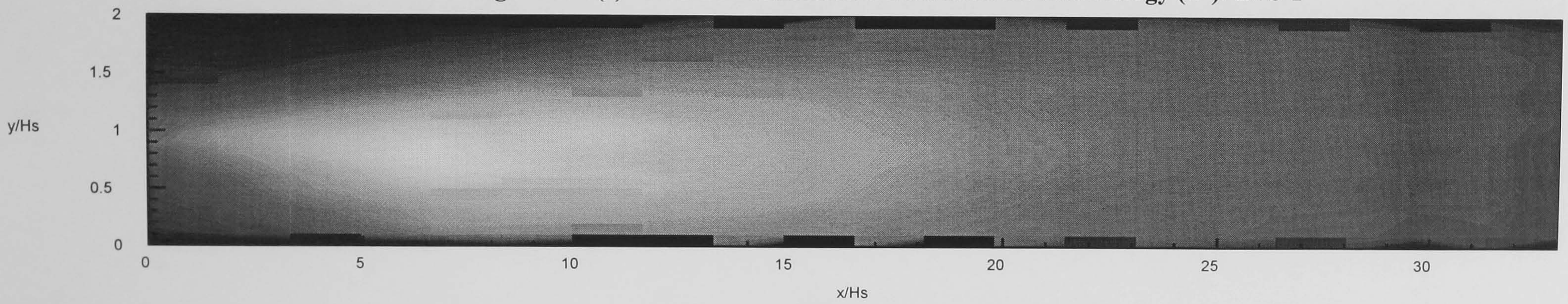

Figure 5.42(a) - Non-Dimensionalised Turbulent Kinetic Energy (u'): BFS-2

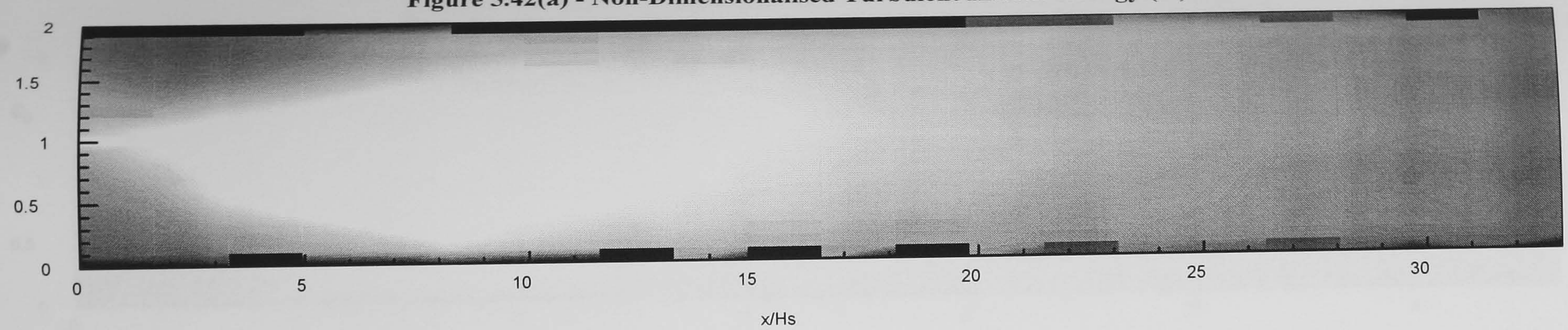

Figure 5.42(b) - Non-Dimensionalised Turbulent Kinetic Energy (v'): BFS-2

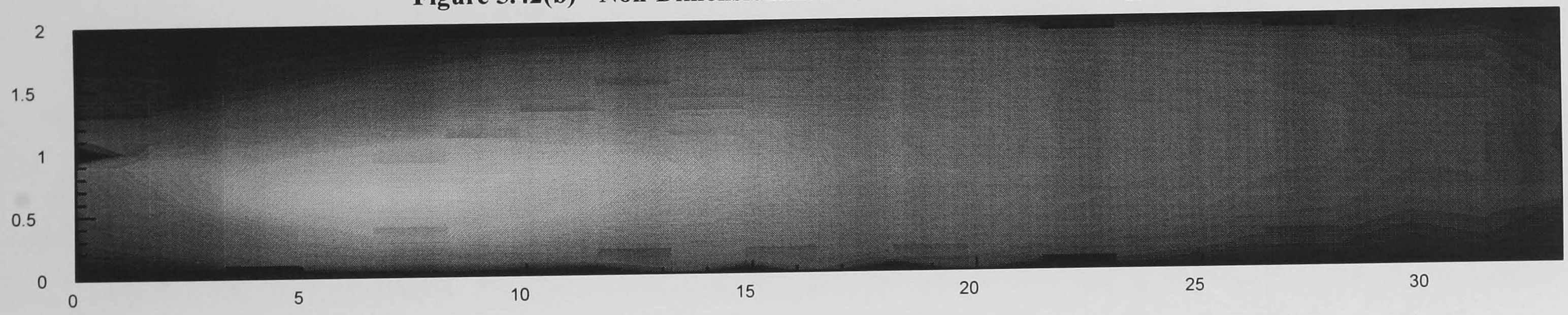

Figure 5.42(c) - Non-Dimensionalised Turbulent Kinetic Energy (w'): BFS-2

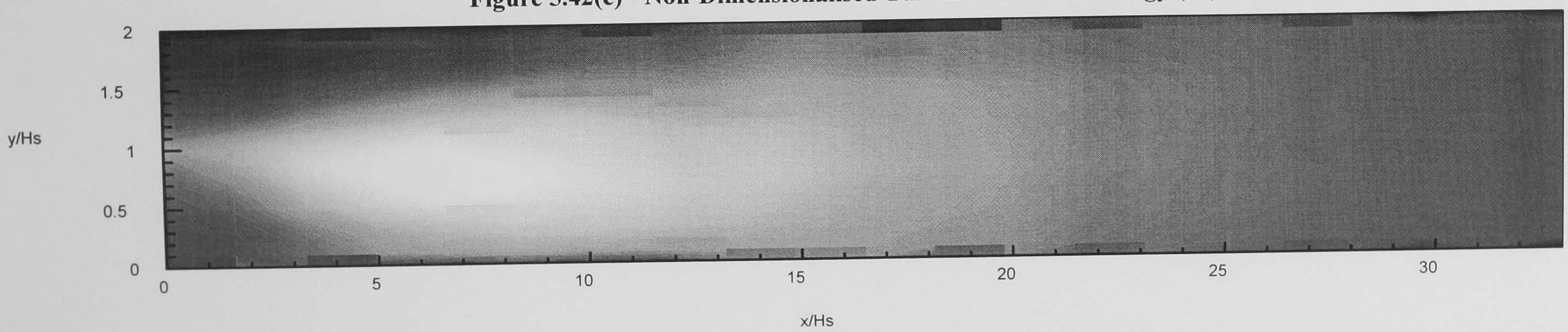

Figure 5.43(a) - Non-Dimensionalised Turbulent Kinetic Energy (u'): BFS-3

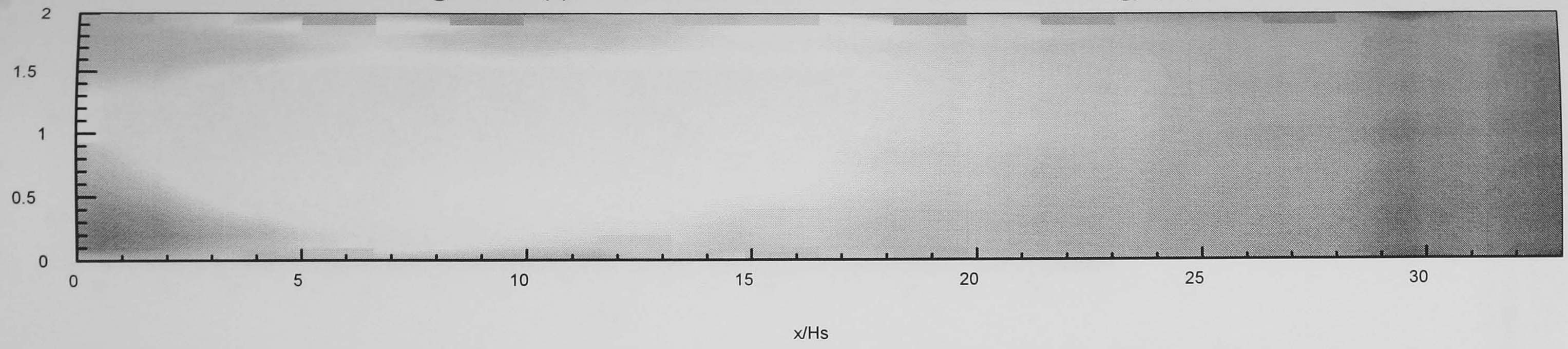

Figure 5.43(b) - Non-Dimensionalised Turbulent Kinetic Energy (v'): BFS-3

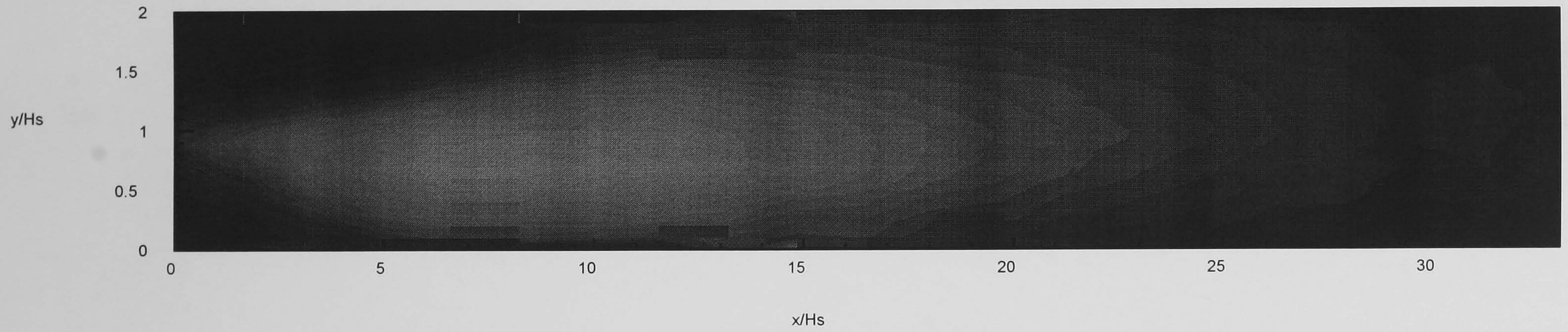

Figure 5.43(c) - Non-Dimensionalised Turbulent Kinetic Energy (w'): BFS-3

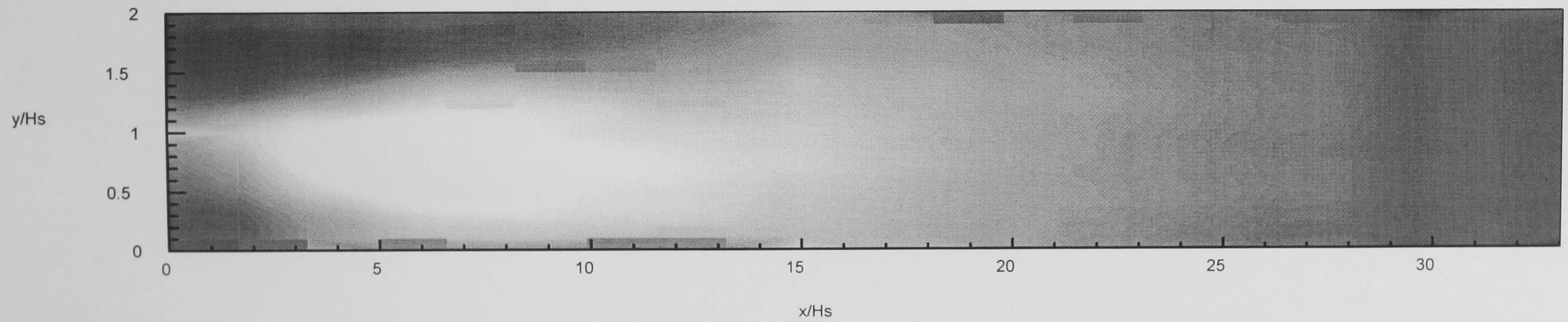

Figure 5.44(a) - Non-Dimensionalised Turbulent Kinetic Energy (Total) - As=15-1

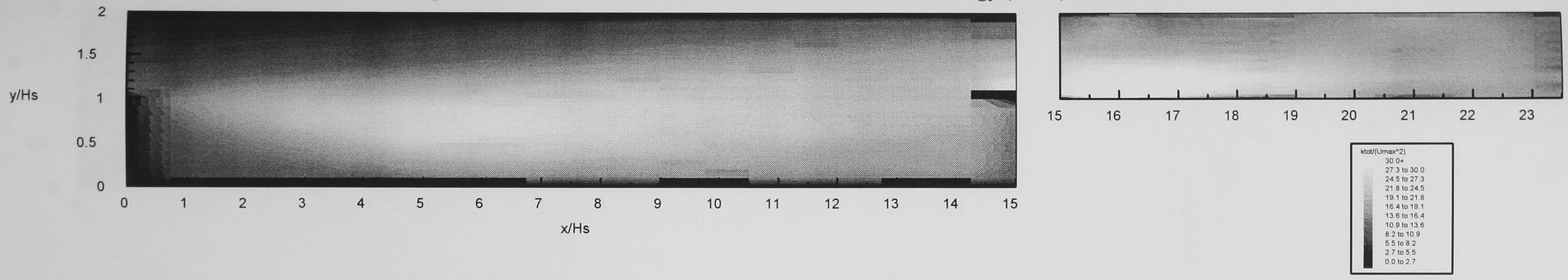

Figure 5.44(b) - Non-Dimensionalised Turbulent Kinetic Energy (Total) - As=15-2

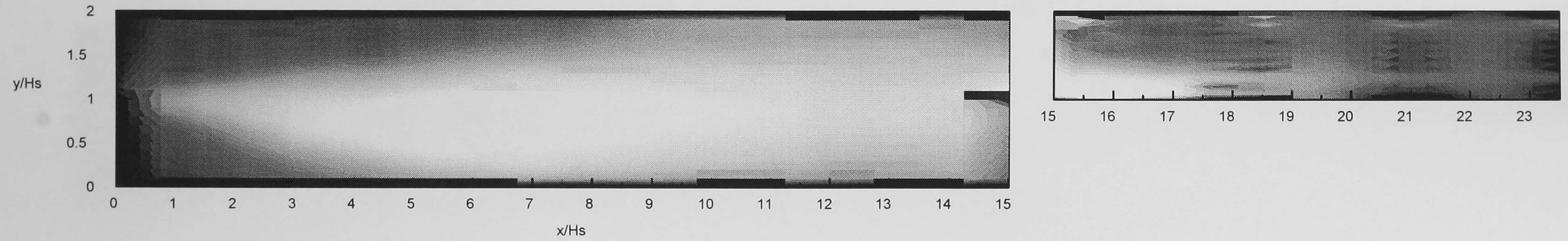

Figure 5.44(c) - Non-Dimensionalised Turbulent Kinetic Energy (Total) - As=15-3

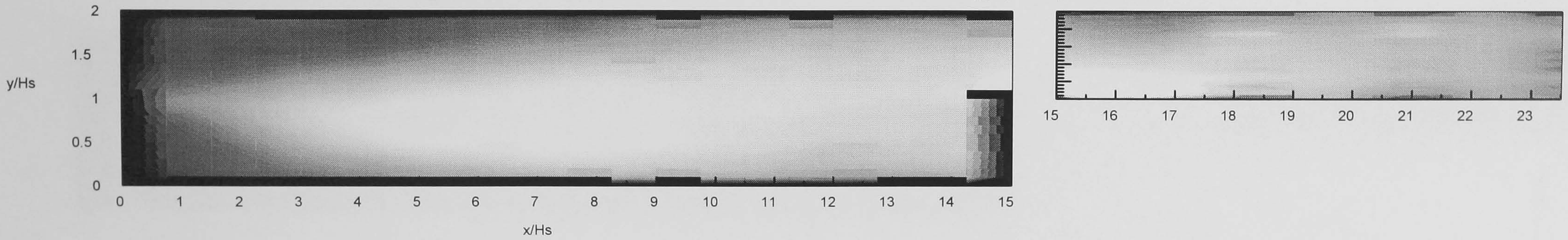

Figure 5.45(a) – Non-Dimensionalised Turbulent Kinetic Energy (u'): As=15-1

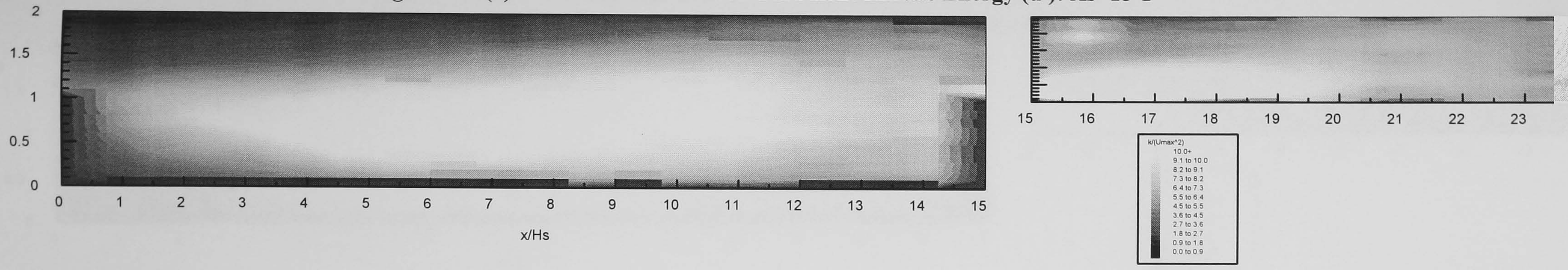

Figure 5.45(b) - Non-Dimensionalised Turbulent Kinetic Energy (v'): As=15-1

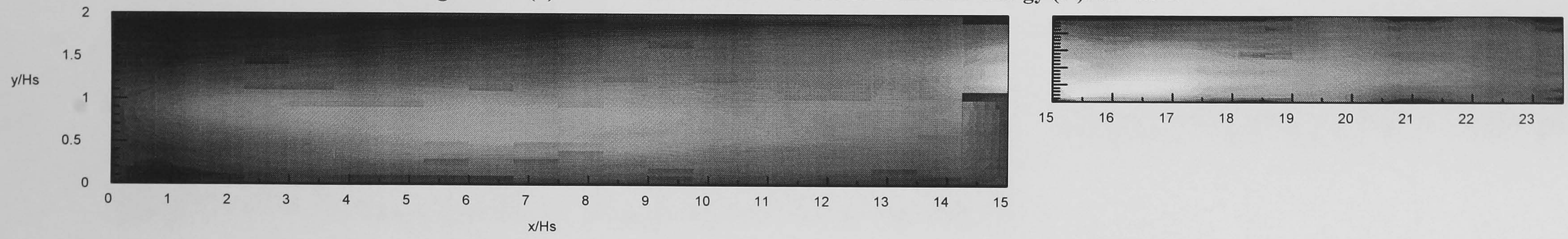

Figure 5.45(c) - Non-Dimensionalised Turbulent Kinetic Energy (w'): As=15-1

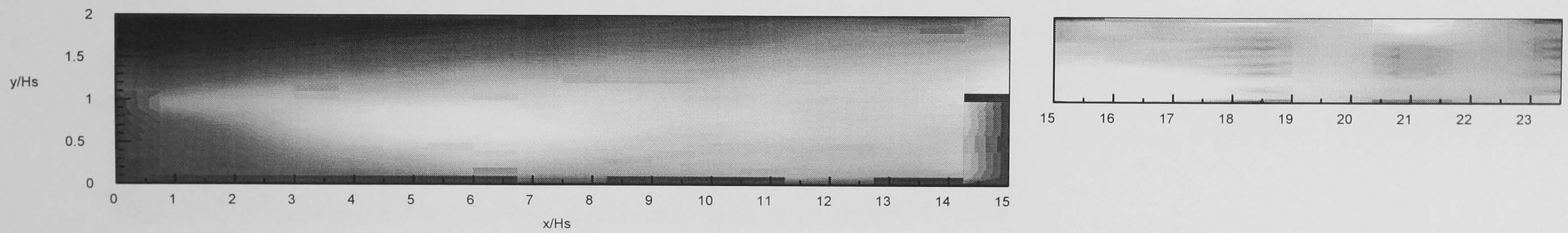

Figure 5.46(a) - Non-Dimensionalised Turbulent Kinetic Energy (u'): As=15-2

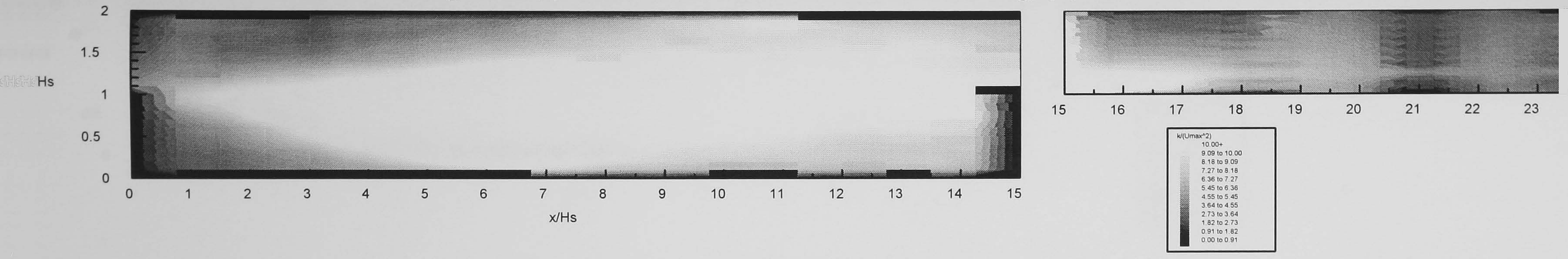

Figure 5.46(b) - Non-Dimensionalised Turbulent Kinetic Energy (v'): As=15-2

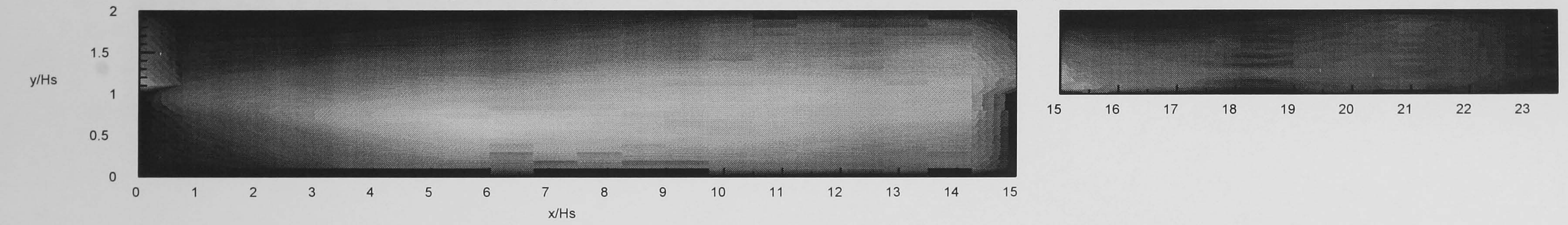

Figure 5.46(c) - Non-Dimensionalised Turbulent Kinetic Energy (w'): As=15-2

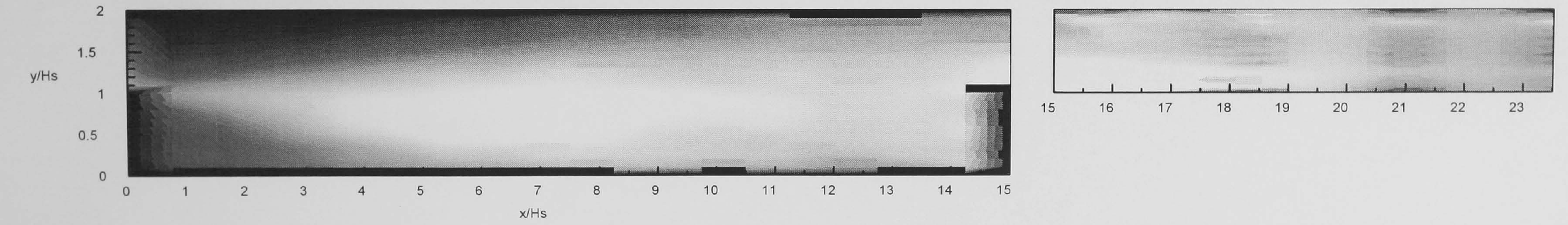

Figure 5.47(a) - Non-Dimensionalised Turbulent Kinetic Energy (u'): As=15-3

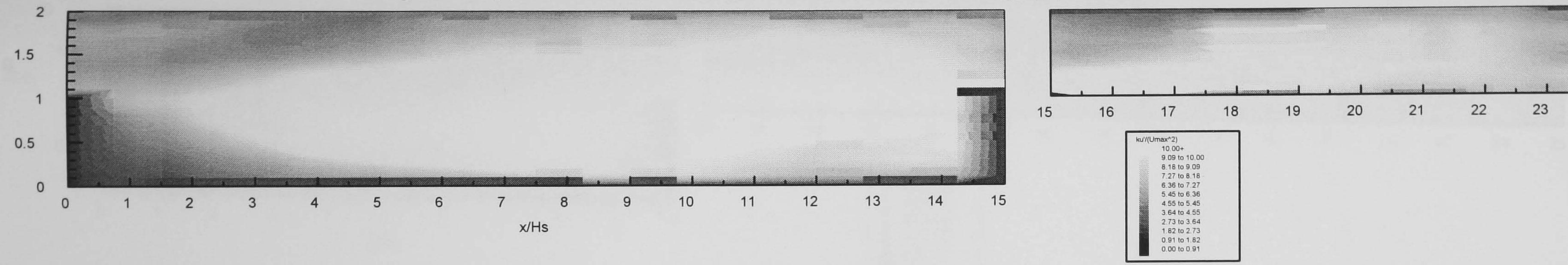

Figure 5.47(b) - Non-Dimensionalised Turbulent Kinetic Energy (v'): As=15-3

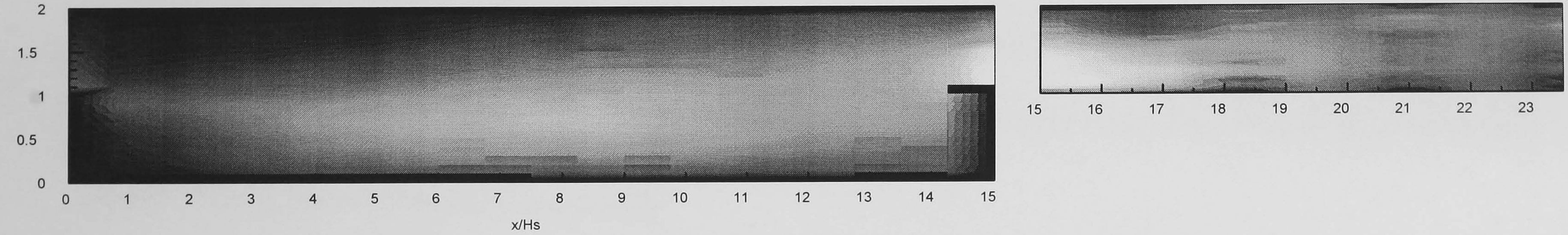

Figure 5.47(c) - Non-Dimensionalised Turbulent Kinetic Energy (w'): As=15-3

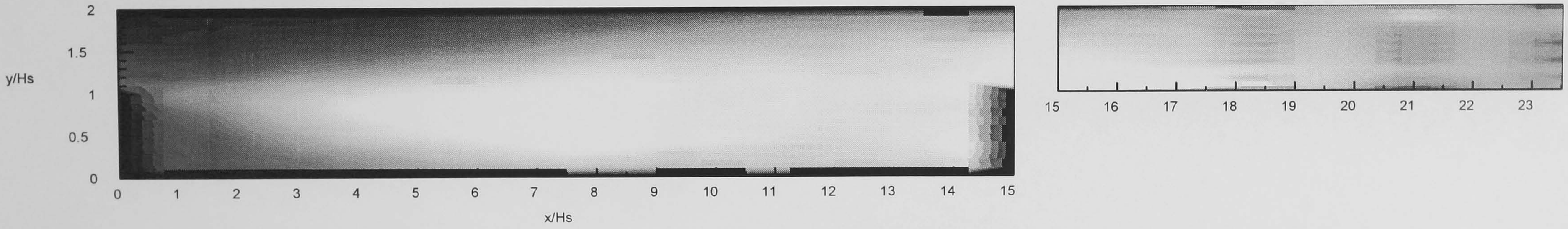

Figure 5.48(a) - Non-Dimensionalised Turbulent Kinetic Energy (Total) - As=10-1

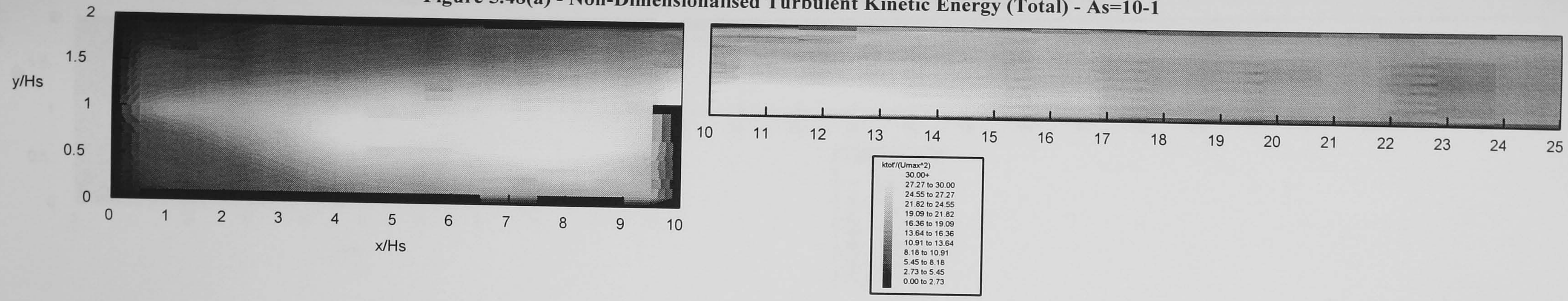

Figure 5.48(b) - Non-Dimensionalised Turbulent Kinetic Energy (Total) - As=10-2

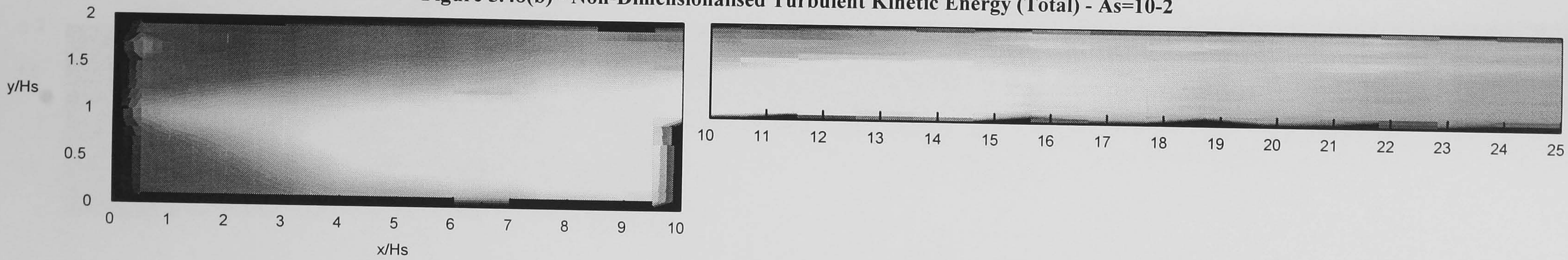

Figure 5.48(c) - Non-Dimensionalised Turbulent Kinetic Energy (Total) - As=10-3

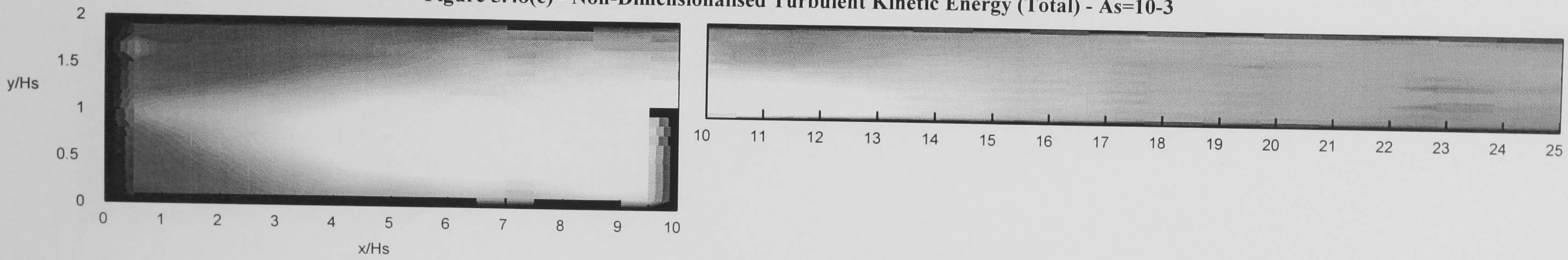

Figure 5.49(a) - Non-Dimensionalised Turbulent Kinetic Energy (u'): As=10-1

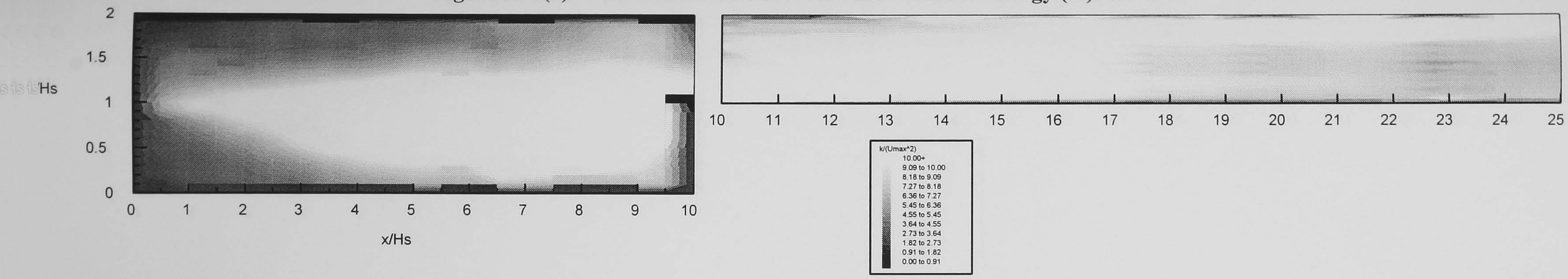

Figure 5.49(b) - Non-Dimensionalised Turbulent Kinetic Energy (v'): As=10-1

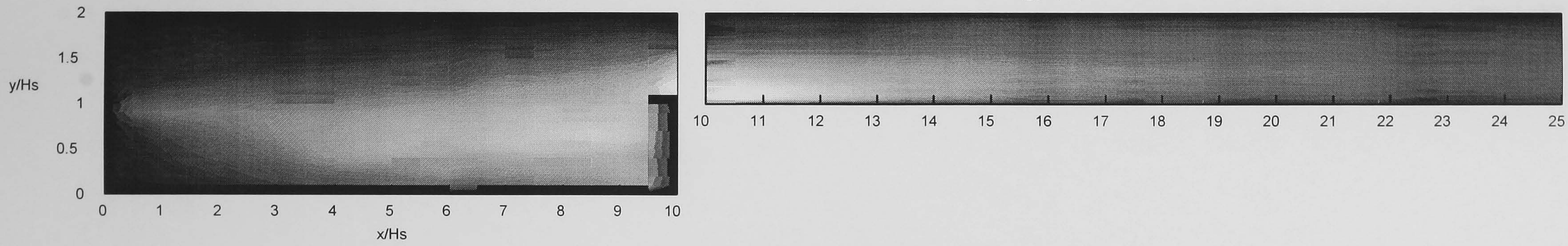

Figure 5.49(c) - Non-Dimensionalised Turbulent Kinetic Energy (w'): As=10-1

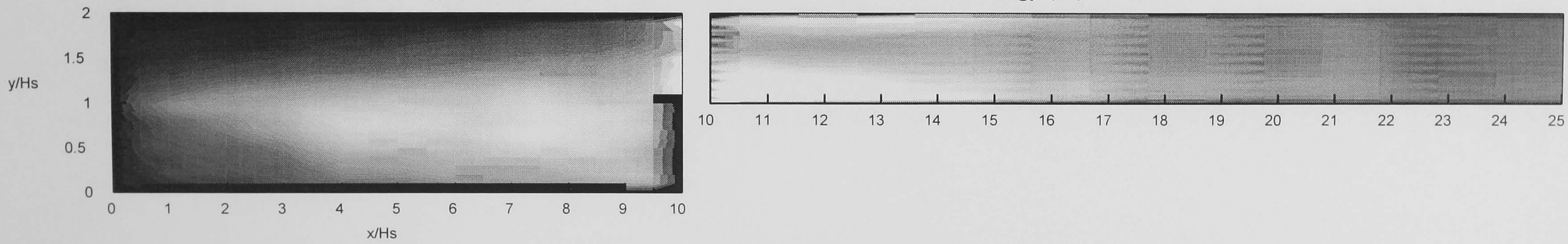

Figure 5.50(a) - Non-Dimensionalised Turbulent Kinetic Energy (u'): As=10-2

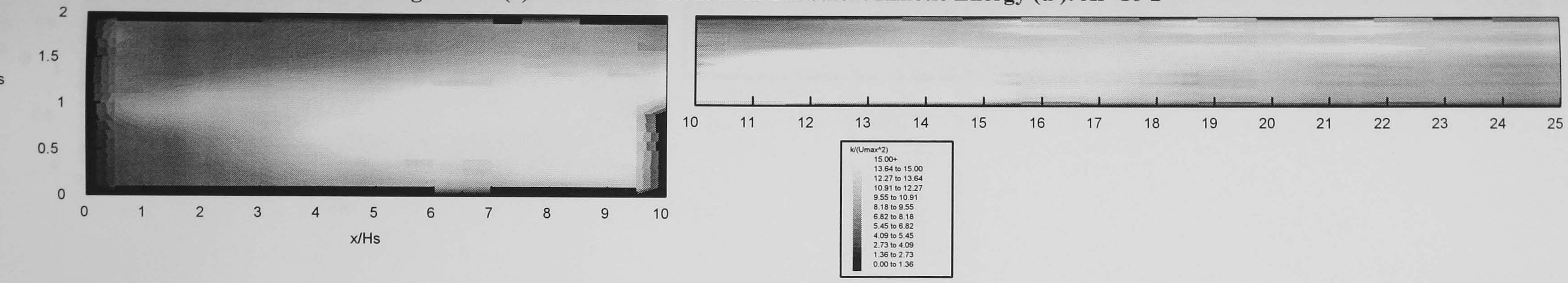

Figure 5.50(b) - Non-Dimensionalised Turbulent Kinetic Energy (v'): As=10-2

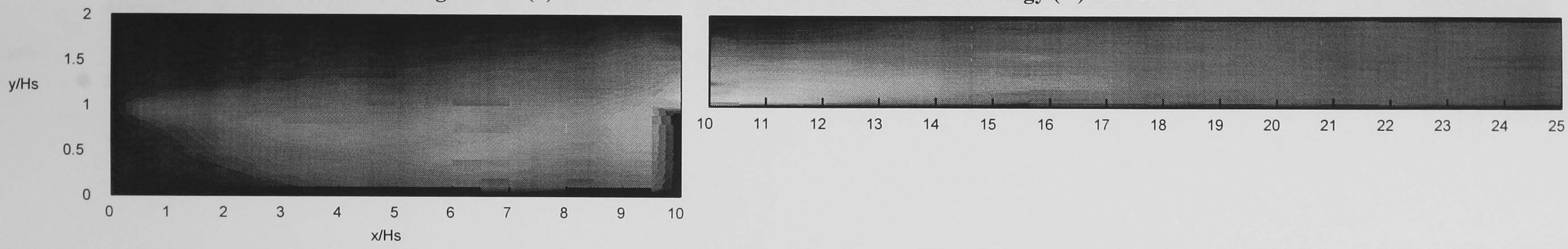

Figure 5.50(c) - Non-Dimensionalised Turbulent Kinetic Energy (w'): As=10-2

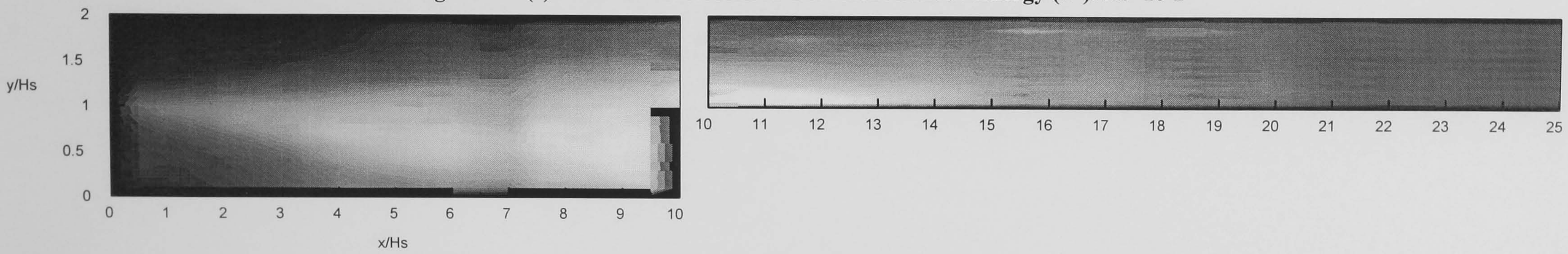

Figure 5.51(a) - Non-Dimensionalised Turbulent Kinetic Energy (u'): As=10-3

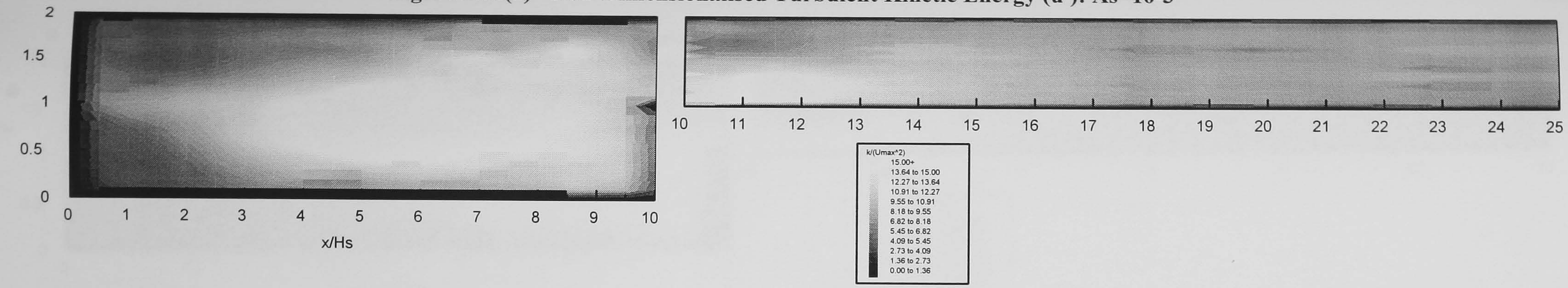

Figure 5.51(b) - Non-Dimensionalised Turbulent Kinetic Energy (v'): As=10-3

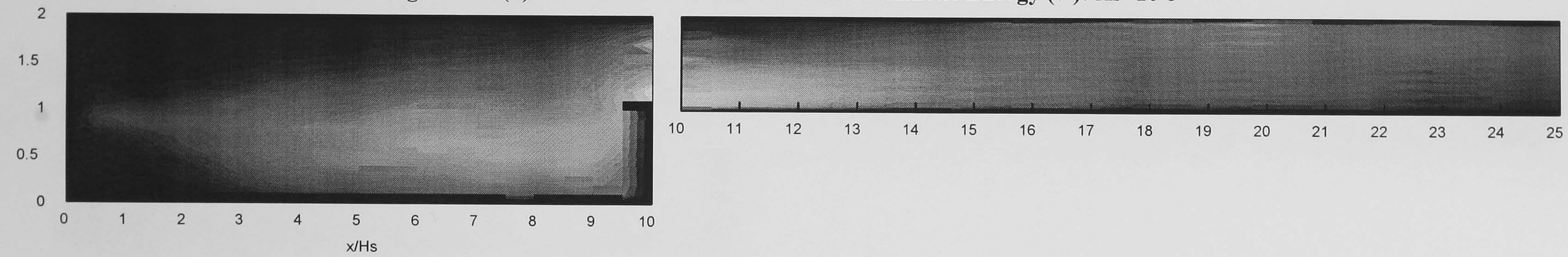

Figure 5.51(c) - Non-Dimensionalised Turbulent Kinetic Energy (w'): As=10-3

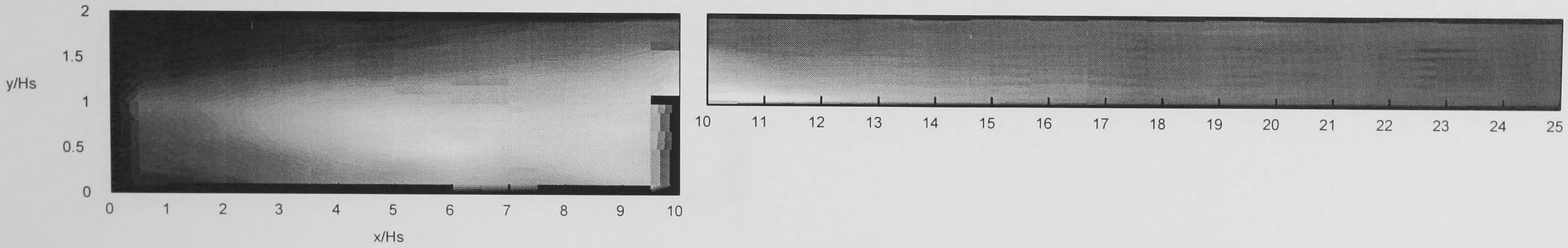

Figure 5.52(a) - Non-Dimensionalised Turbulent Kinetic Energy (Total) - As=5-1

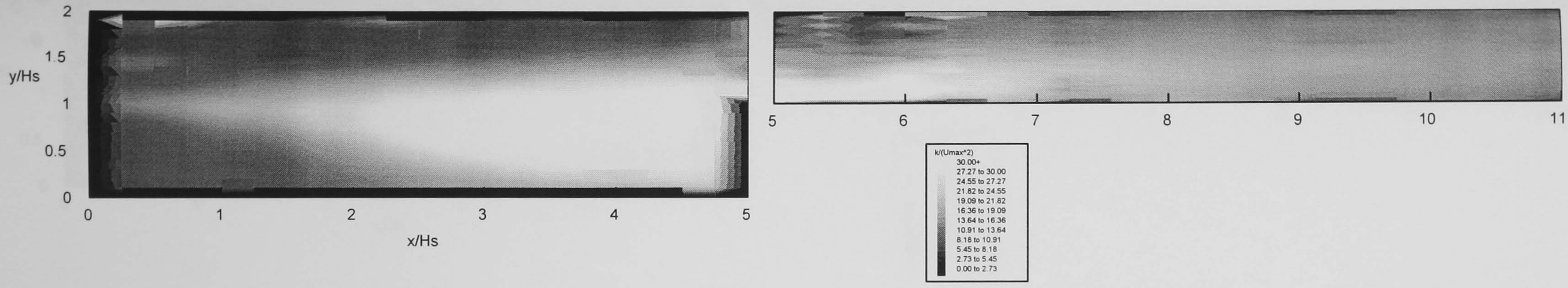

Figure 5.52(b) - Non-Dimensionalised Turbulent Kinetic Energy (Total) - As=5-2

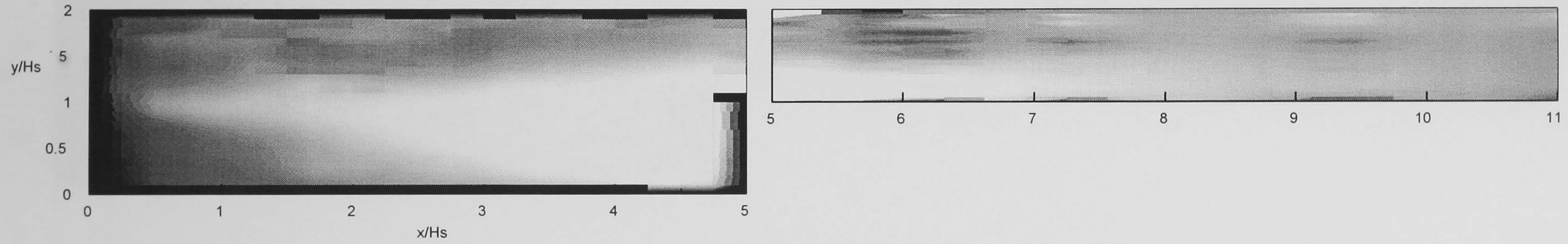

Figure 5.52(c) - Non-Dimensionalised Turbulent Kinetic Energy (Total) - As=5-3

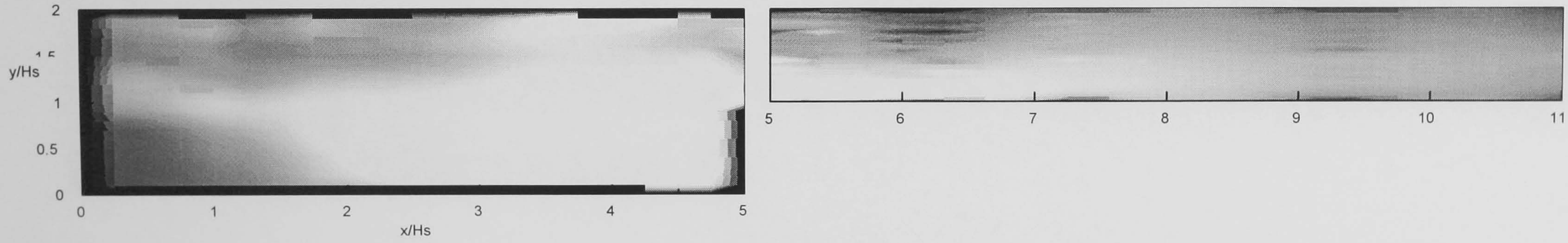

Figure 5.53(a) - Non-Dimensionalised Turbulent Kinetic Energy (u'): As=5-1

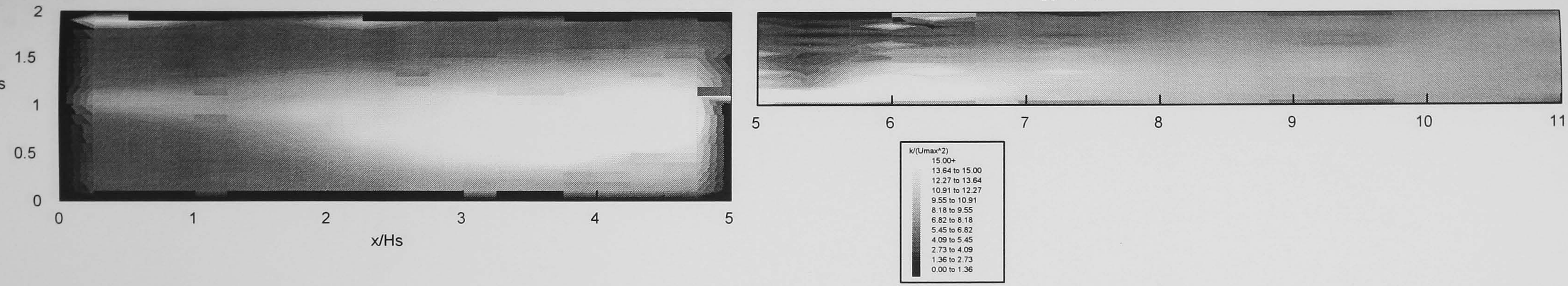

Figure 5.53(b) - Non-Dimensionalised Turbulent Kinetic Energy (v'): As=5-1

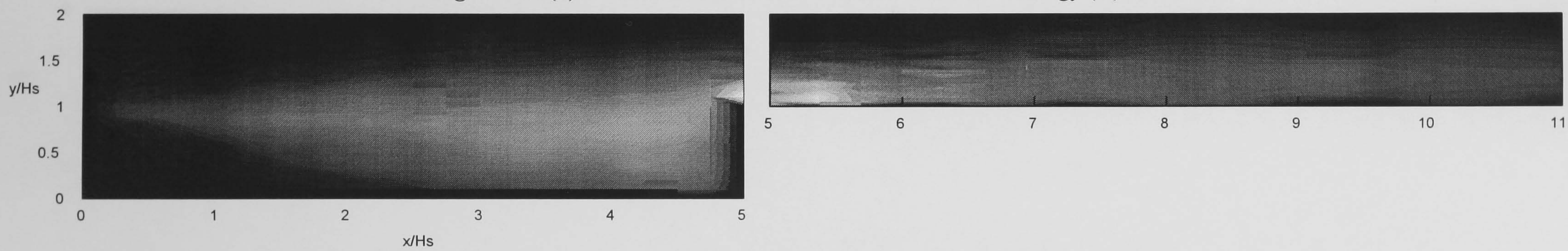

Figure 5.53(c) - Non-Dimensionalised Turbulent Kinetic Energy (w'): As=5-1

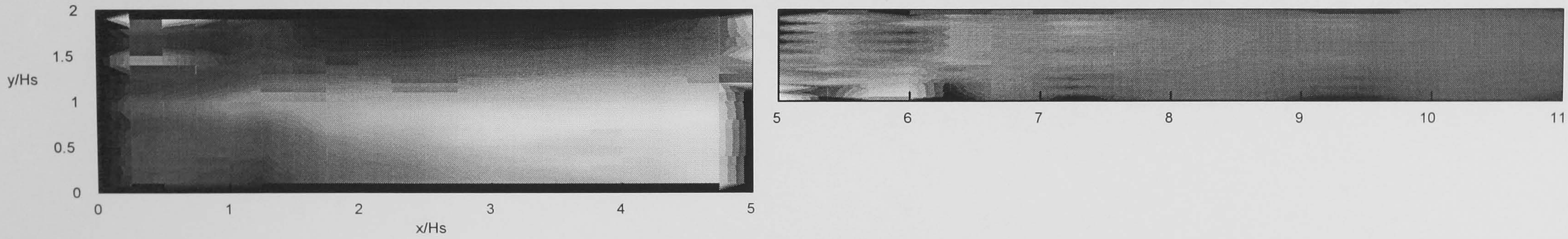

Figure 5.54(a) - Non-Dimensionalised Turbulent Kinetic Energy (u'): As=5-2

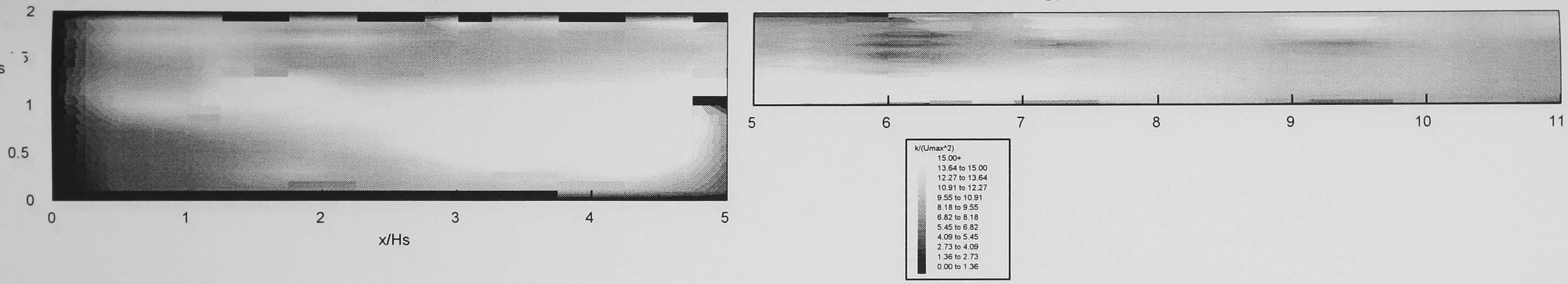

Figure 5.54(b) - Non-Dimensionalised Turbulent Kinetic Energy (v'): As=5-2

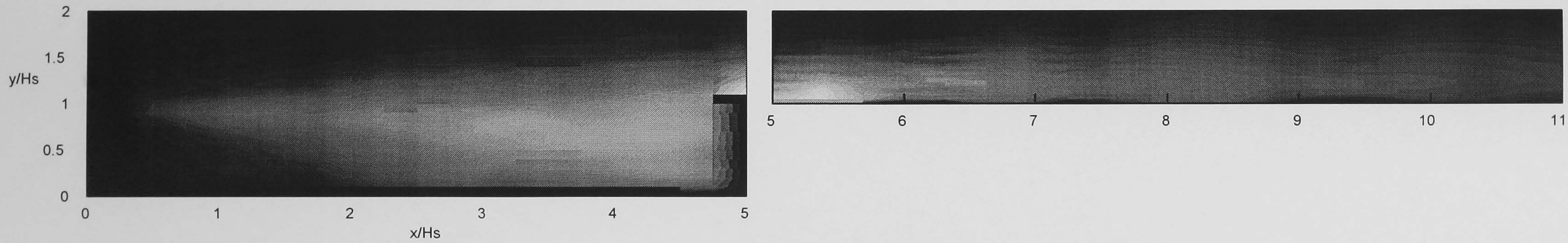

Figure 5.54(c) - Non-Dimensionalised Turbulent Kinetic Energy (w'): As=5-2

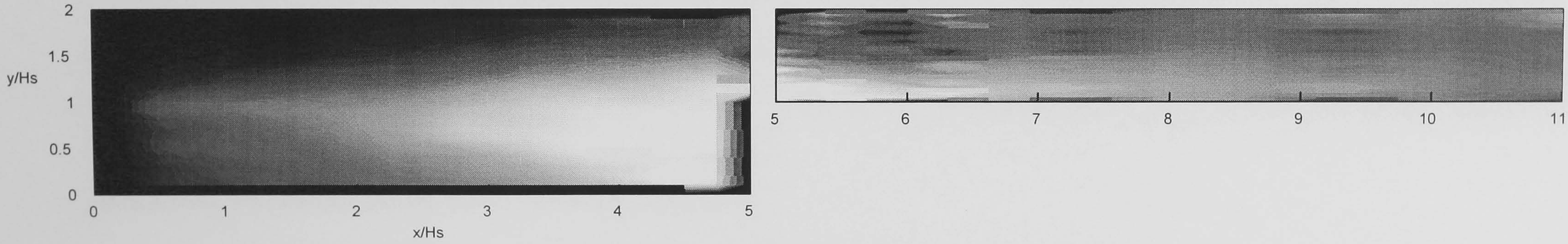

Figure 5.55(a) - Non-Dimensionalised Turbulent Kinetic Energy (u'): As=5-3

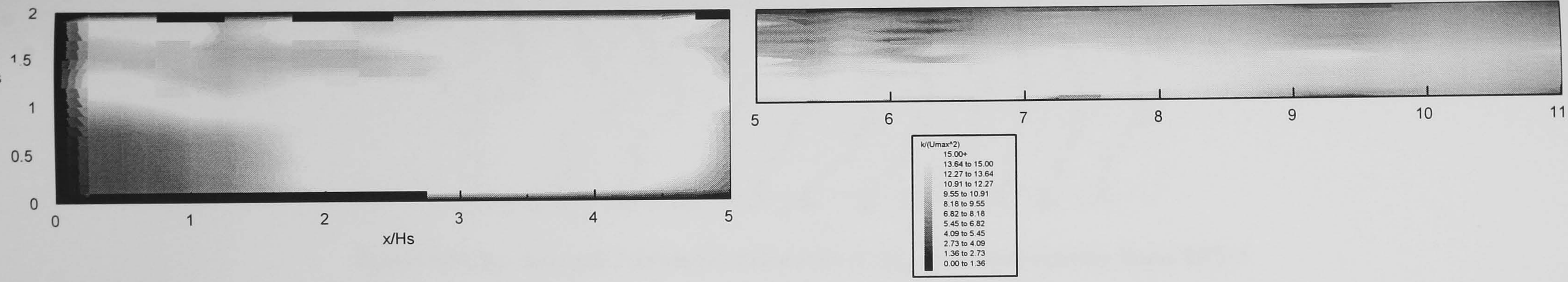

Figure 5.55(b) - Non-Dimensionalised Turbulent Kinetic Energy (v'): As=5-3

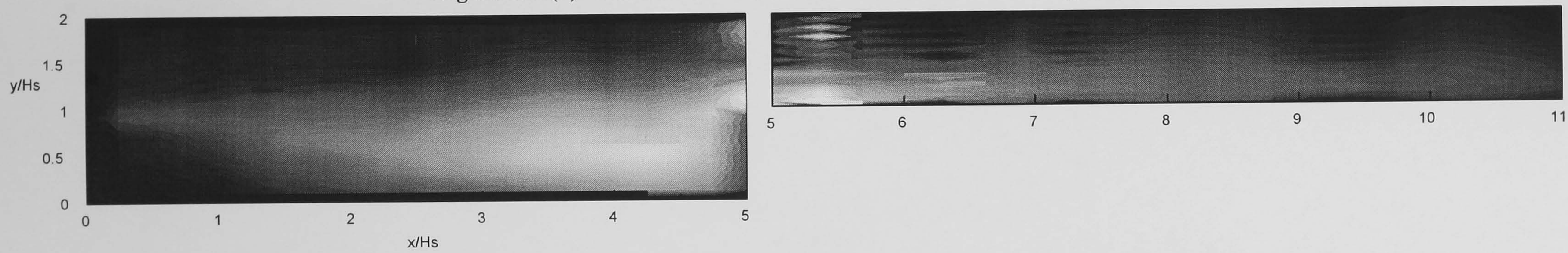

Figure 5.55(c) - Non-Dimensionalised Turbulent Kinetic Energy (w'): As=5-3

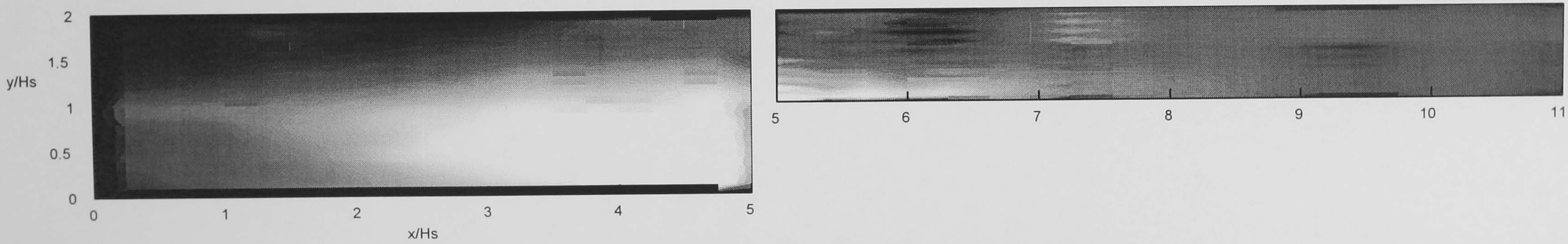

Figure 5.56(a) - Selected Turbulence Intensities (u'/U_{max}) in Recirculation Zone: BFS-1

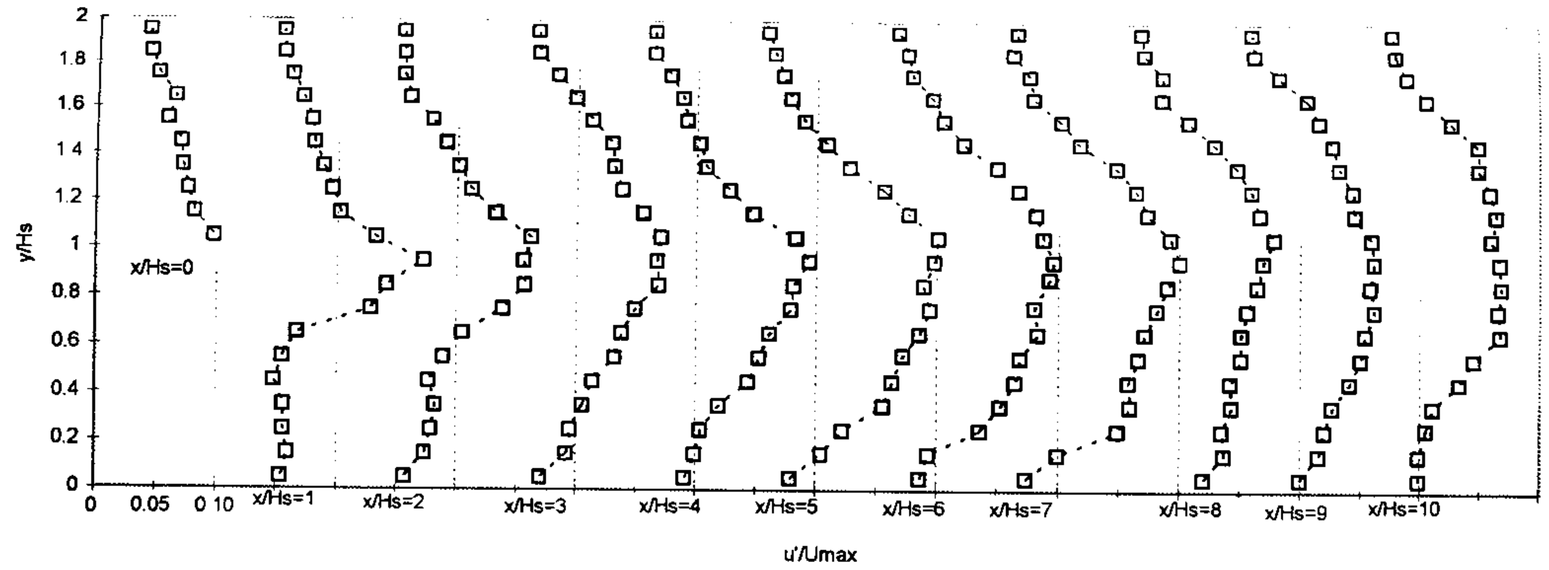

Figure 5.56(b) - Selected Turbulence Intensities (v'/U_{max}) in Recirculation Zone: BFS-1

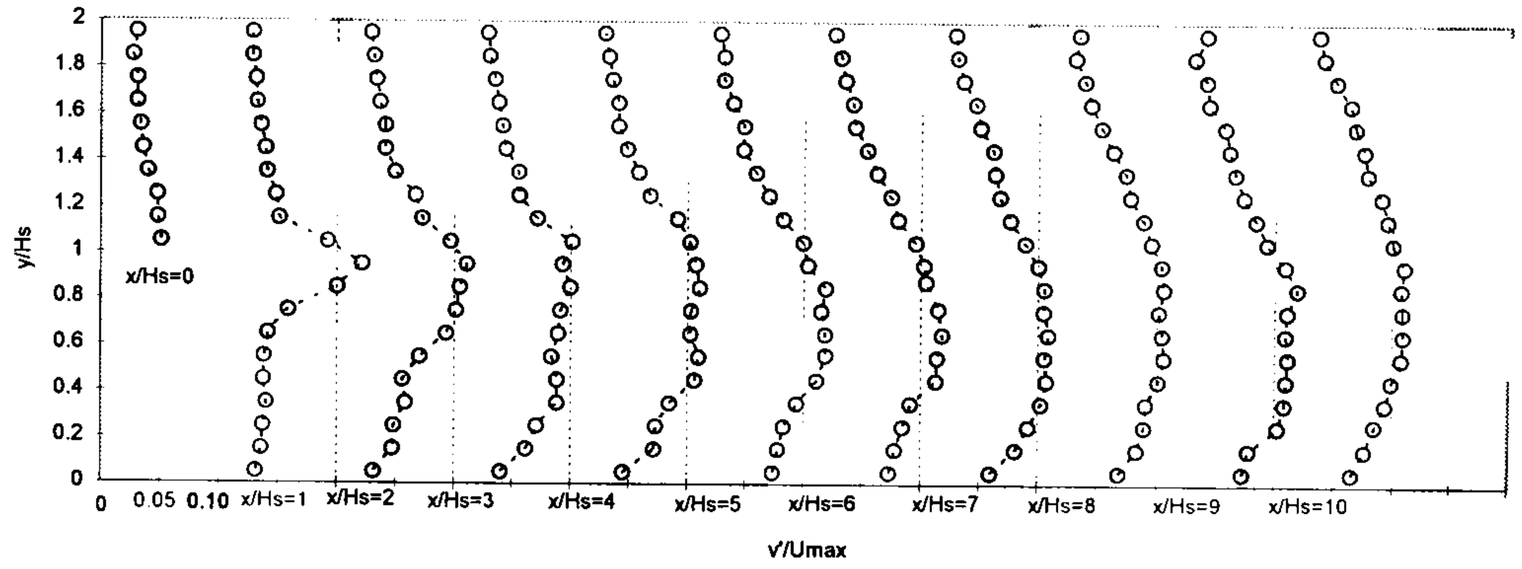

Figure 5.56(c) - Selected Turbulence Intensities (w'/U_{max}) in Recirculation Zone: BFS-1

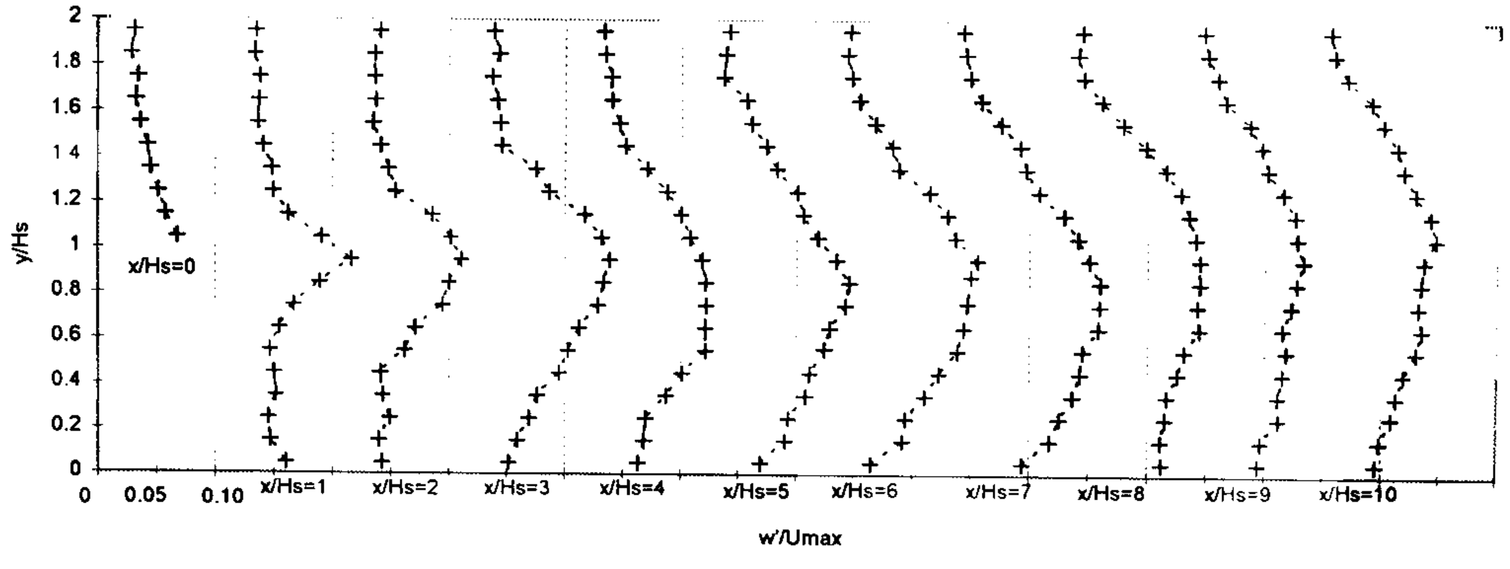

Figure 5.57(a) - Selected Turbulence Intensities (u'/U_{max}) in Recirculation Zone: BFS-2

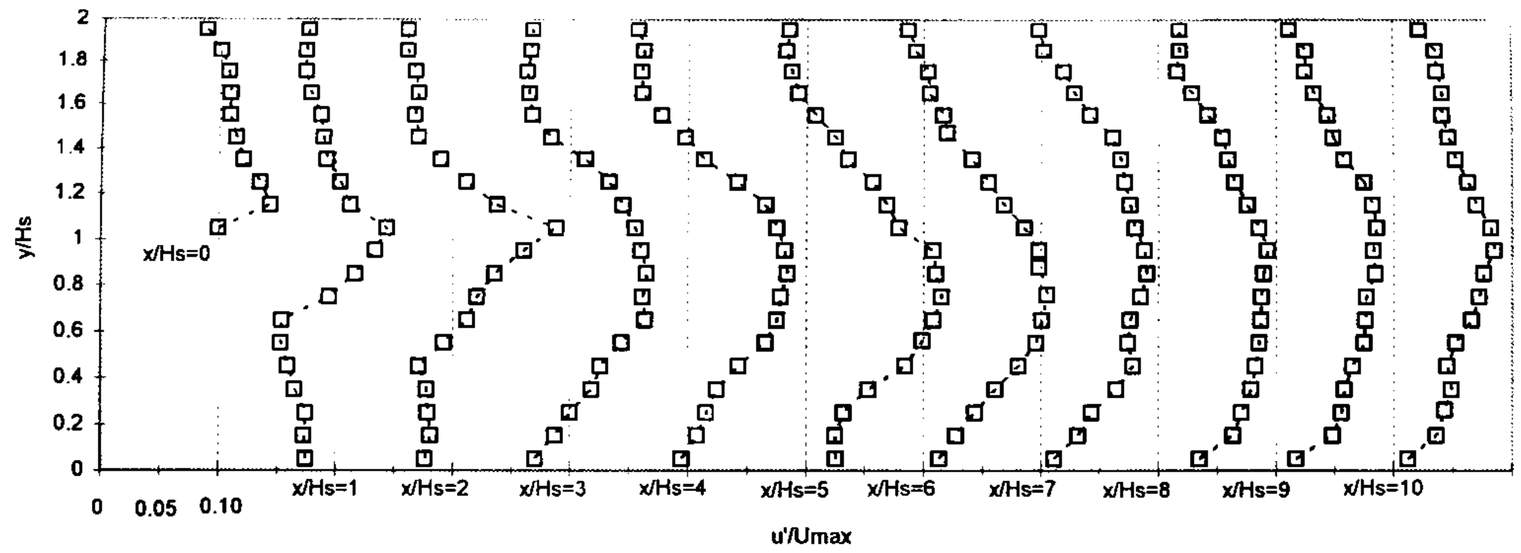

Figure 5.57(b) - Selected Turbulence Intensities (v'/U_{max}) in Recirculation Zone: BFS-2

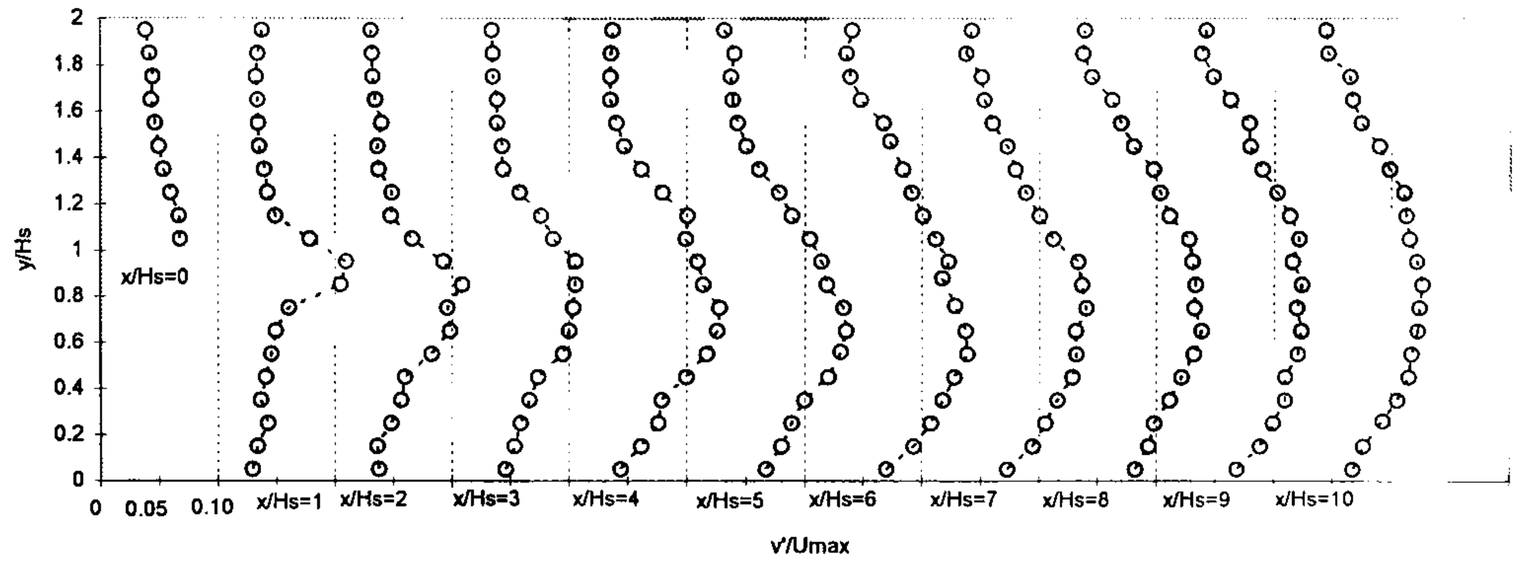

Figure 5.57(c) - Selected Turbulence Intensities (w'/U_{max}) in Recirculation Zone: BFS-2

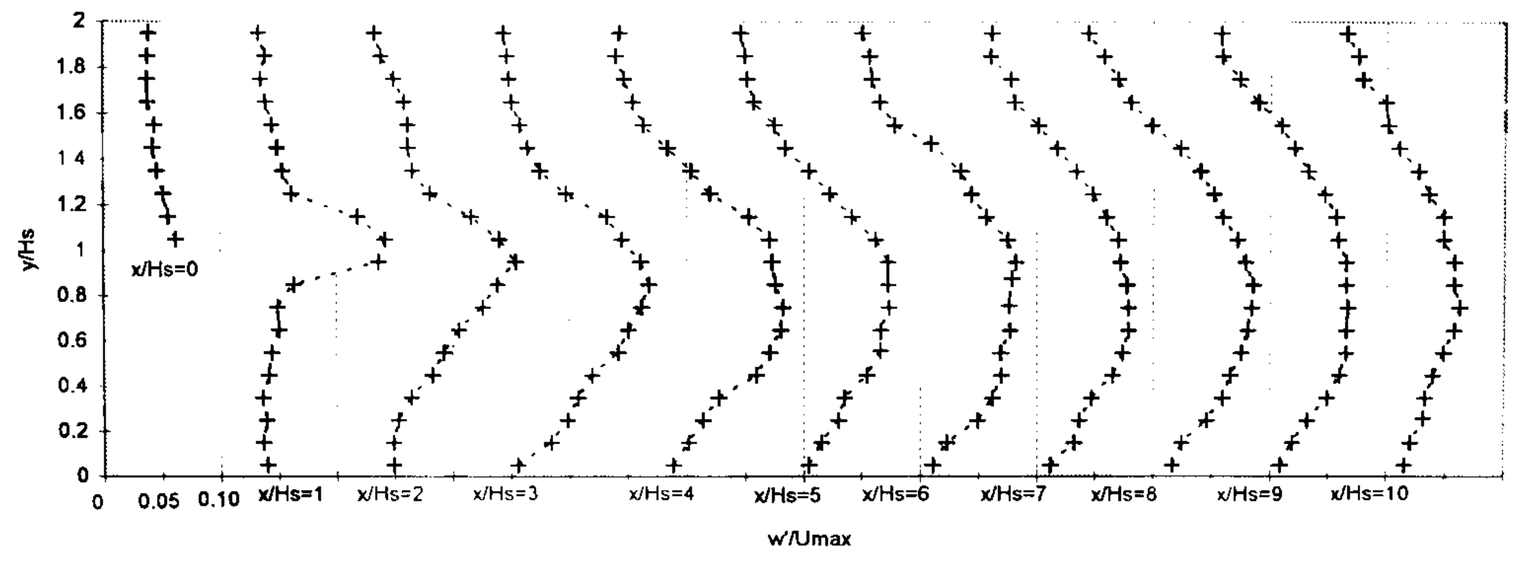

Figure 5.58(a) - Selected Turbulence Intensities (u'/U_{max}) in Recirculation Zone: BFS-3

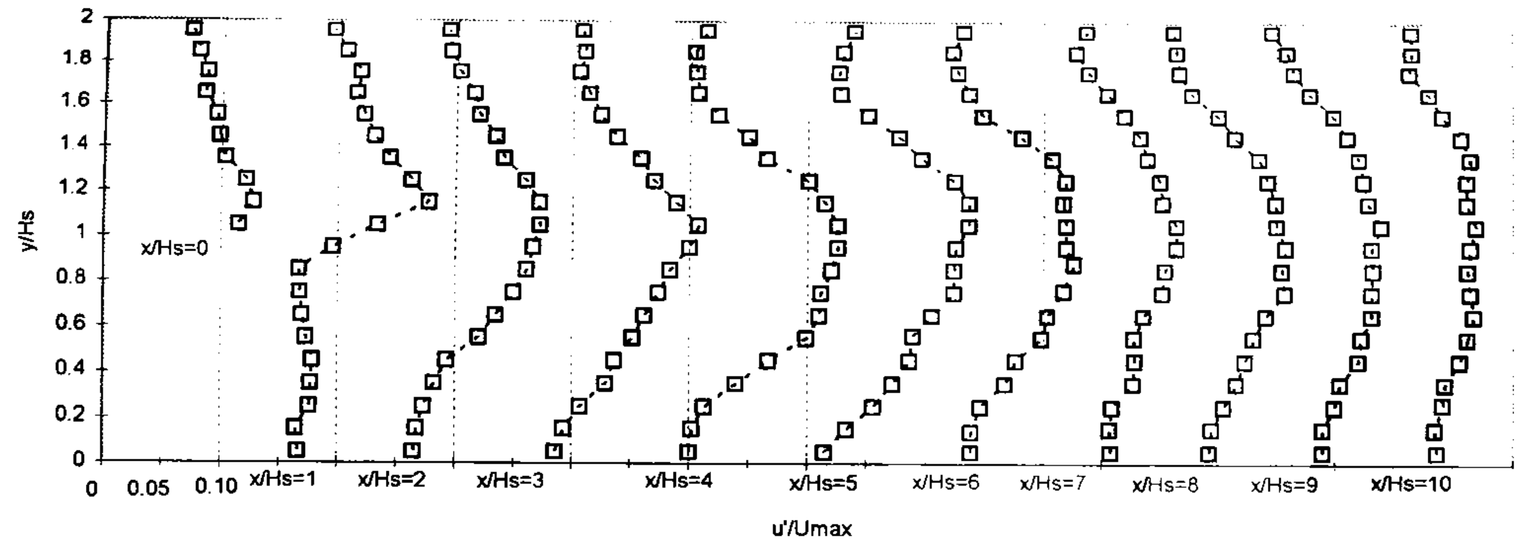

Figure 5.58(b) - Selected Turbulence Intensities (v'/U_{max}) in Recirculation Zone: BFS-3

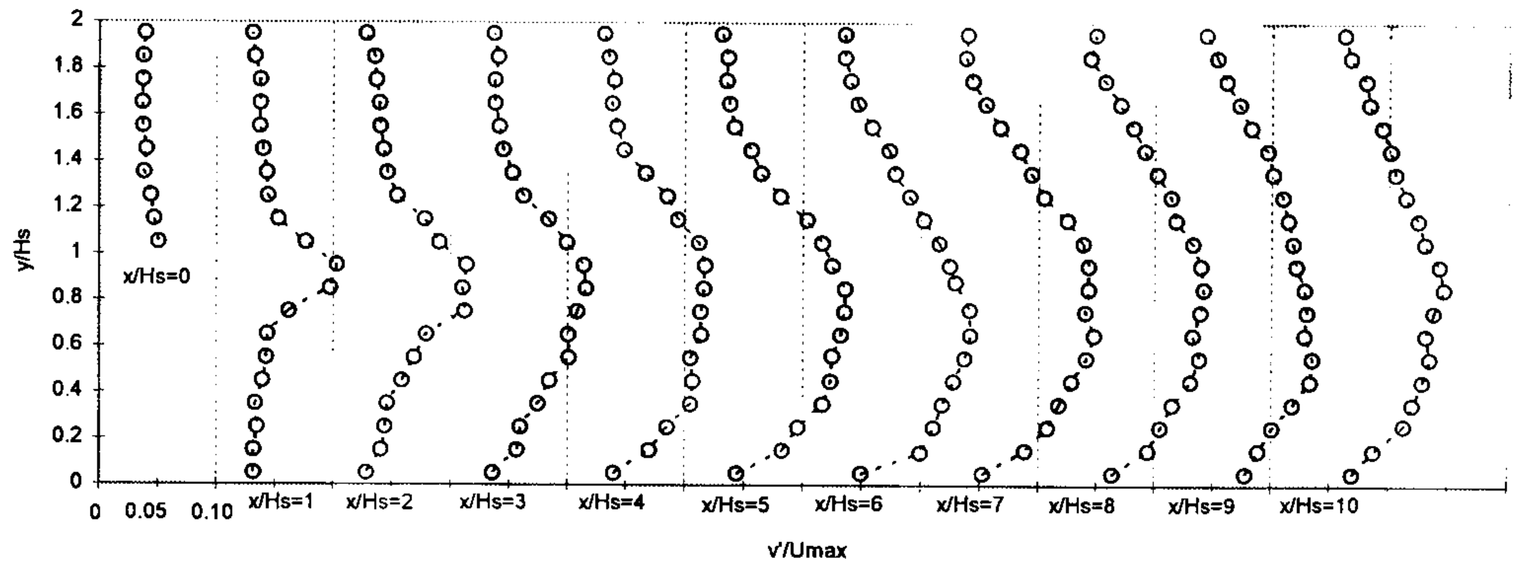

Figure 5.58(c) - Selected Turbulence Intensities (w'/U_{max}) in Recirculation Zone: BFS-3

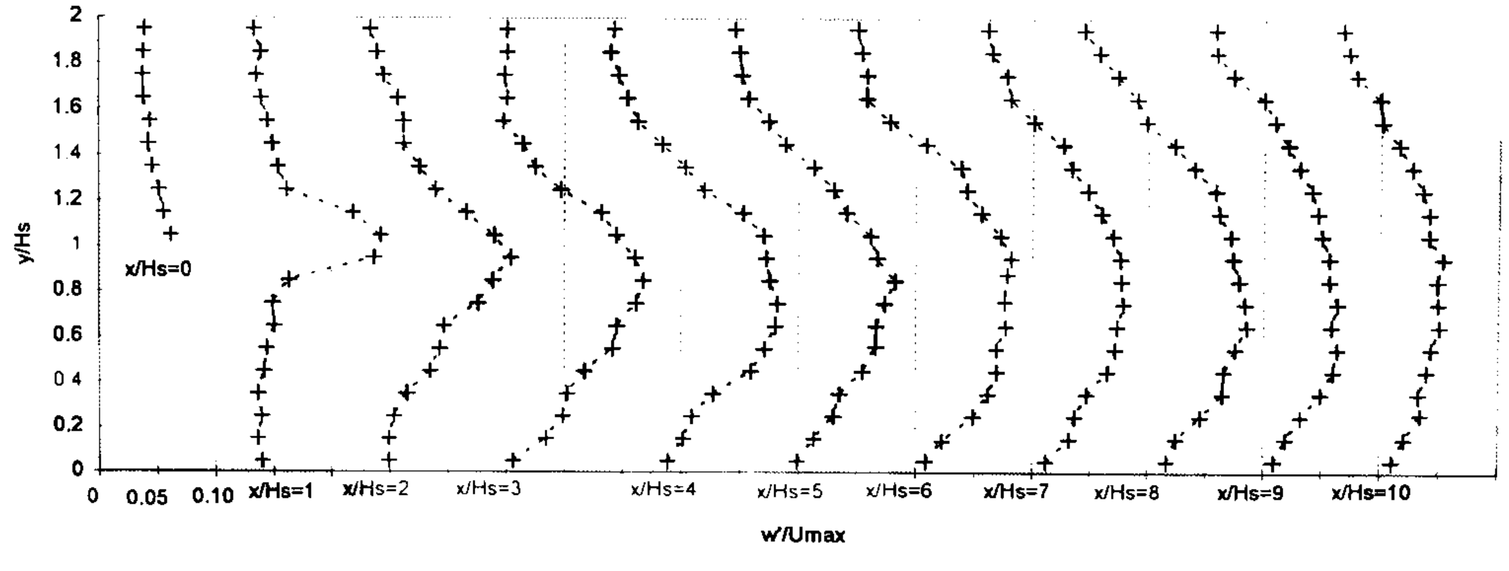

Figure 5.59(a) - Selected Turbulence Intensities (u'/U_{max}) in Recirculation Zone: 15-1

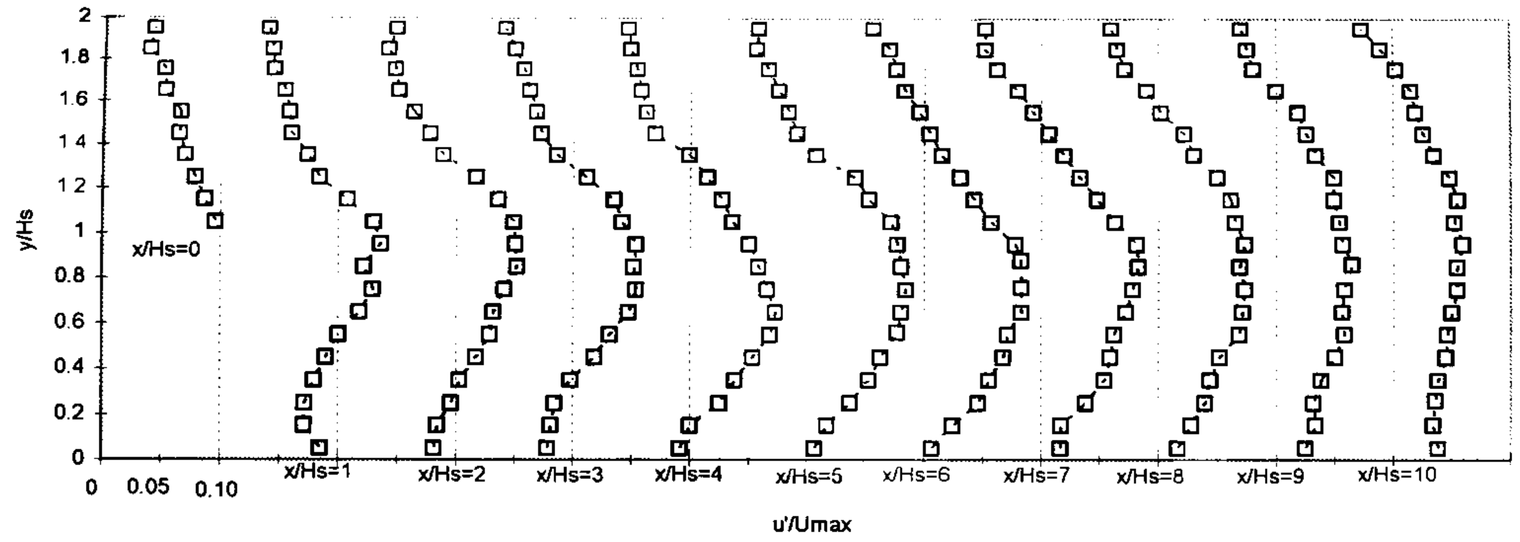

Figure 5.59(b) - Selected Turbulence Intensities (v'/U_{max}) in Recirculation Zone: 15-1

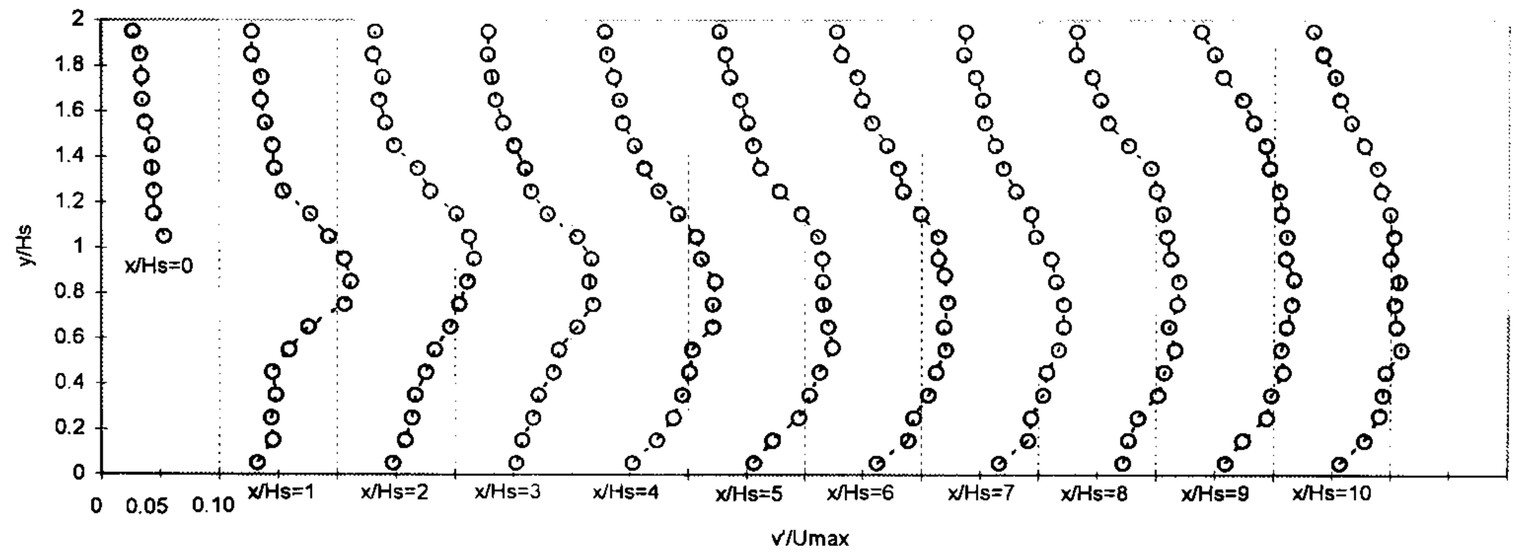

Figure 5.59(c) - Selected Turbulence Intensities (w'/U_{max}) in Recirculation Zone: 15-1

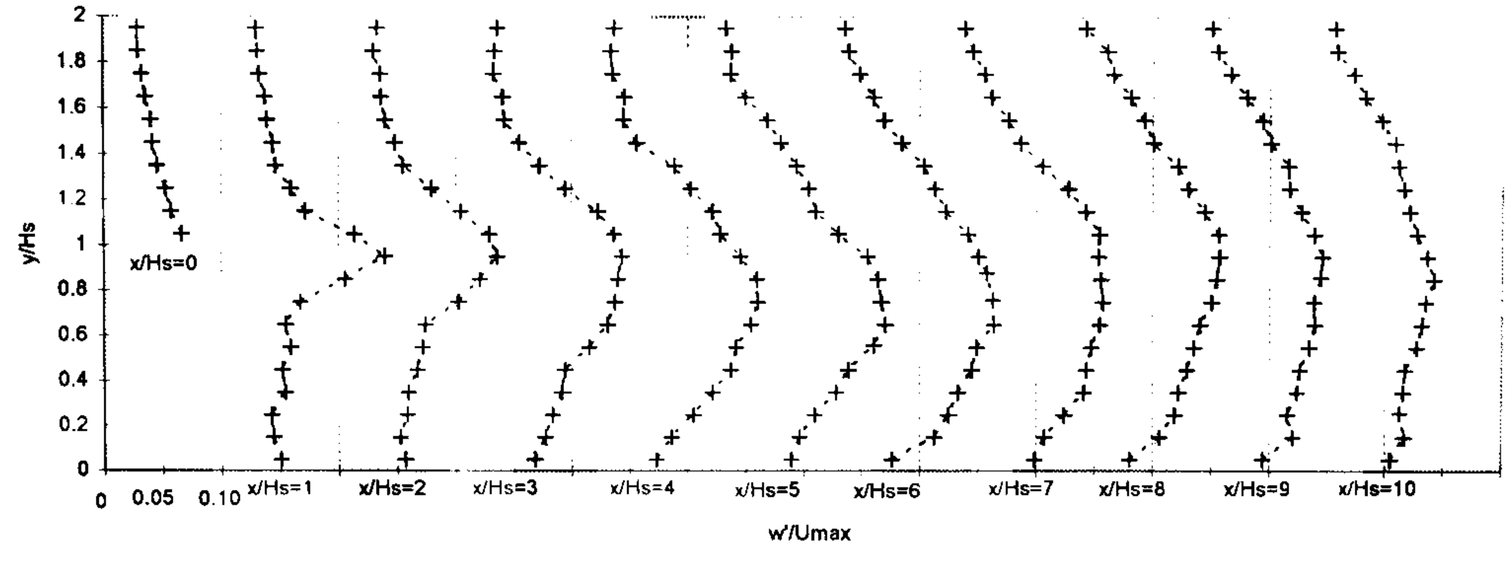

Figure 5.60(a) - Selected Turbulence Intensities (u'/U_{max}) in Recirculation Zone: 15-2

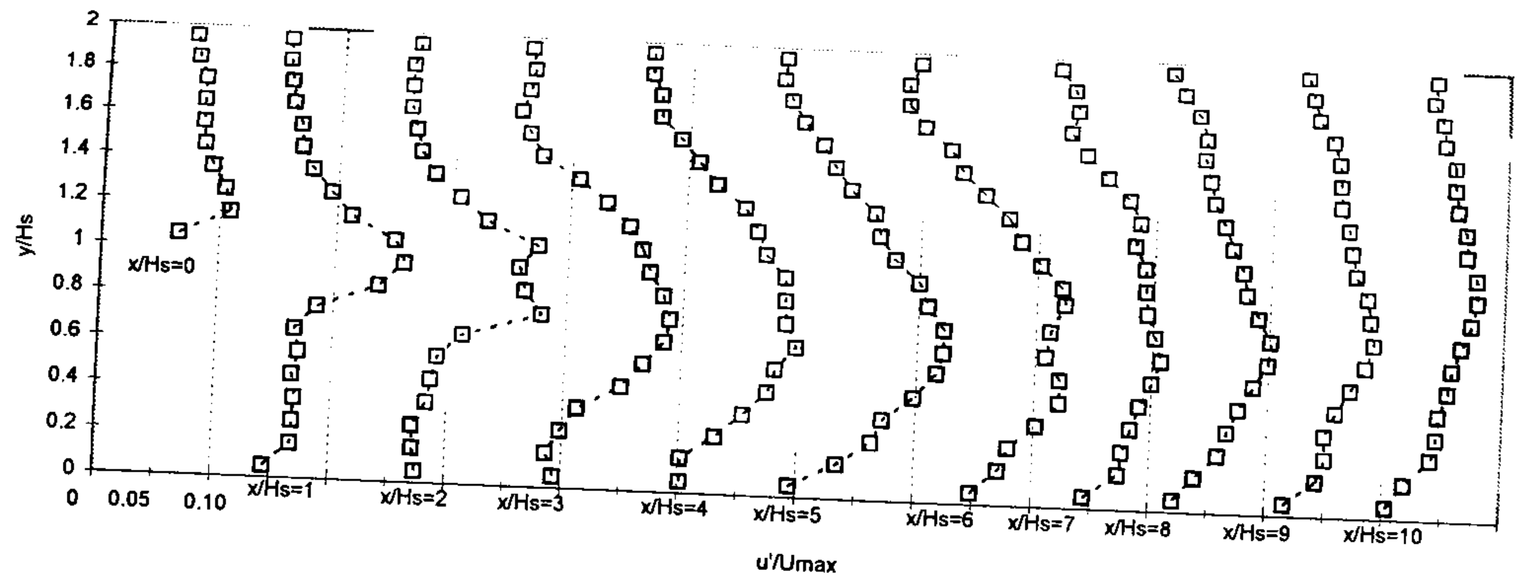

Figure 5.60(b) - Selected Turbulence Intensities (v'/U_{max}) in Recirculation Zone: 15-2

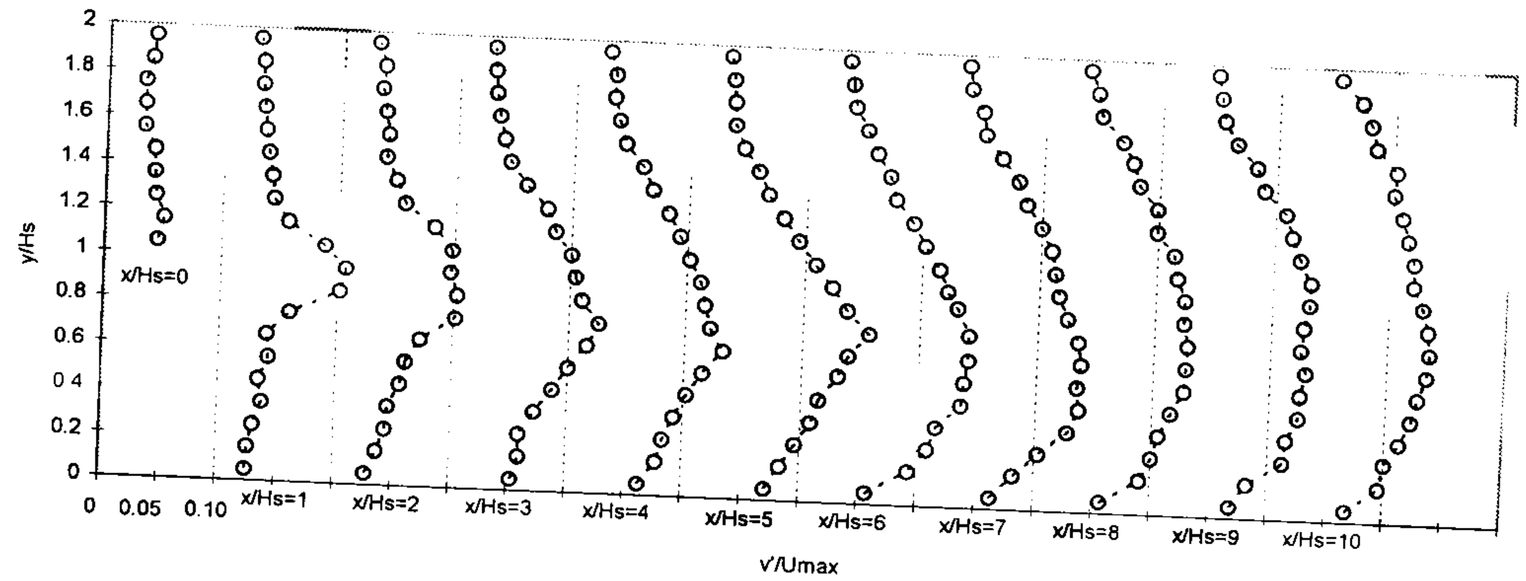

Figure 5.60(c) - Selected Turbulence Intensities (w'/U_{max}) in Recirculation Zone: 15-2

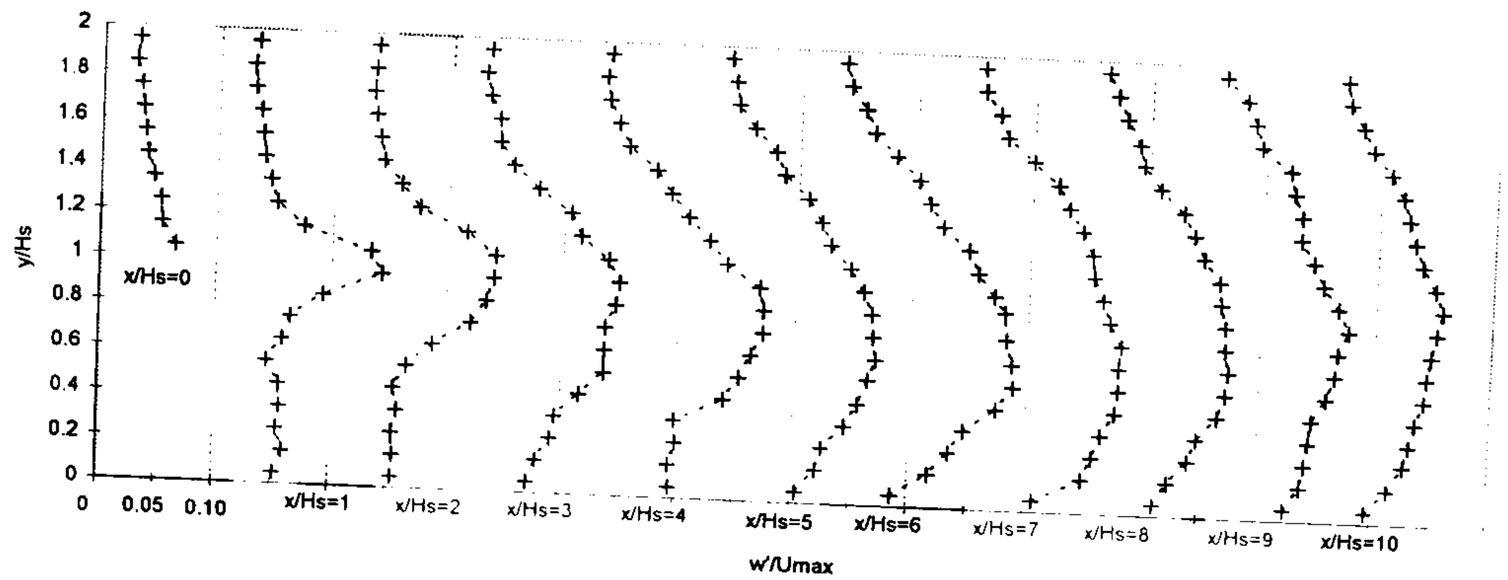

Figure 5.61(a) - Selected Turbulence Intensities (u'/U_{max}) in Recirculation Zone: 15-3

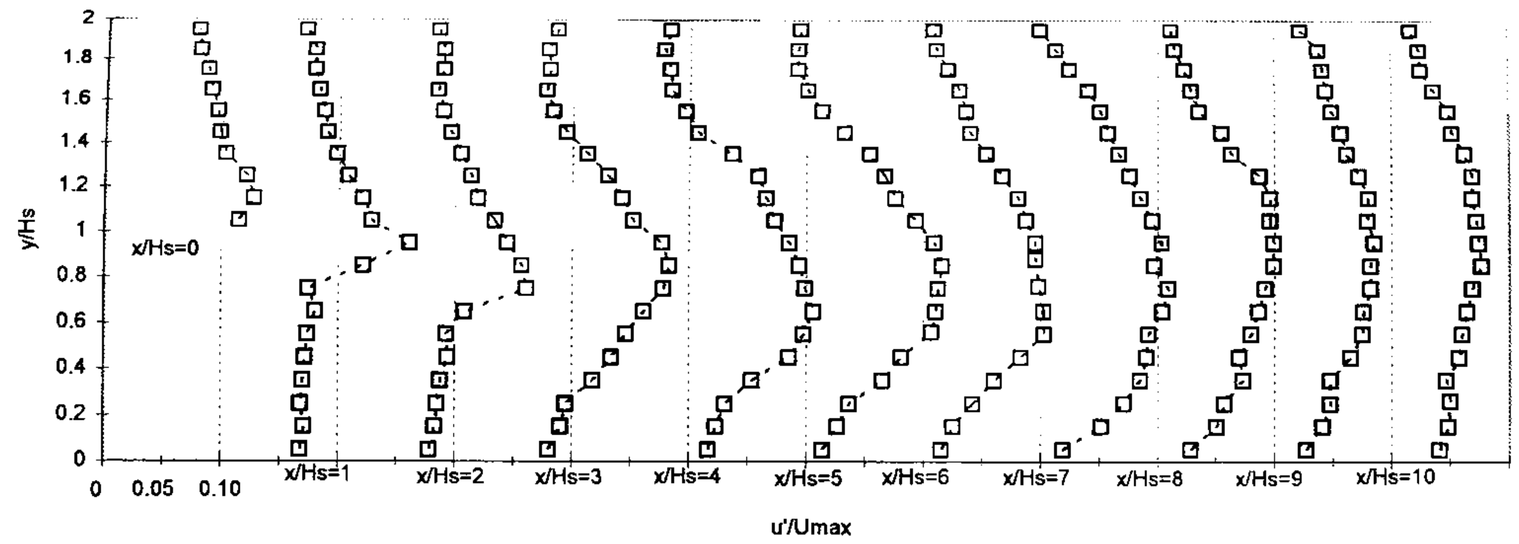

Figure 5.61(b) - Selected Turbulence Intensities (v'/U_{max}) in Recirculation Zone: 15-3

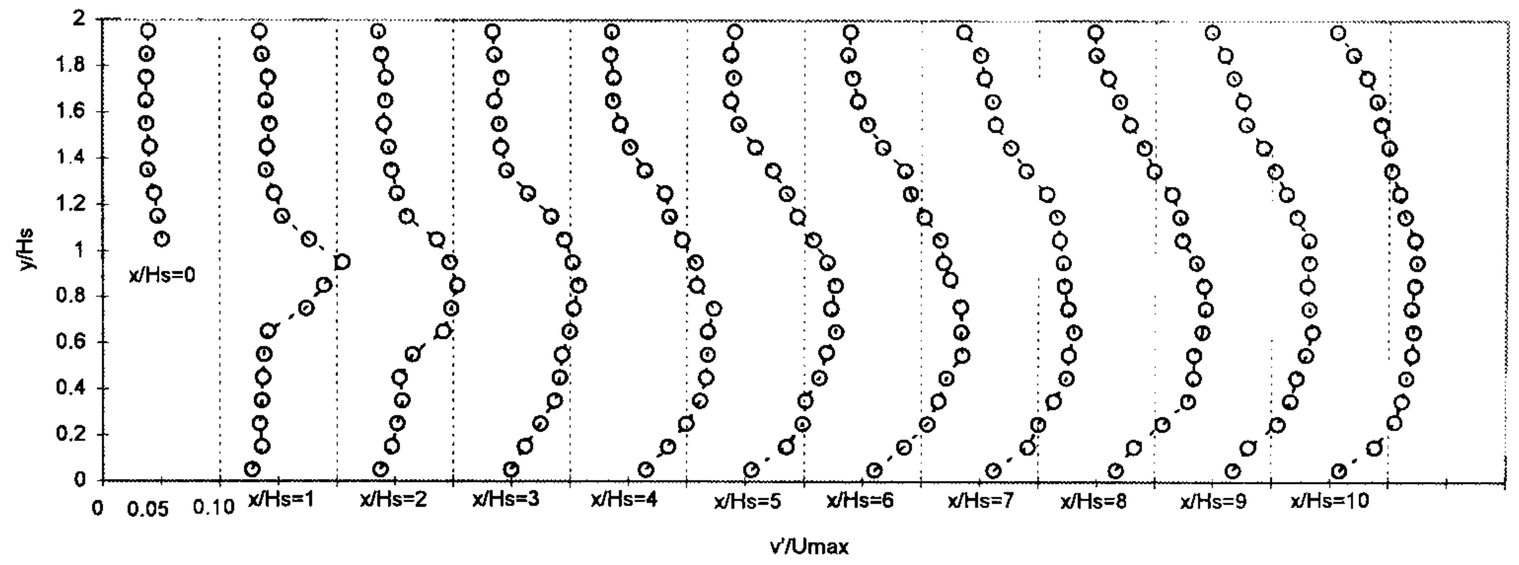

Figure 5.61(c) - Selected Turbulence Intensities (w'/U_{max}) in Recirculation Zone: 15-3

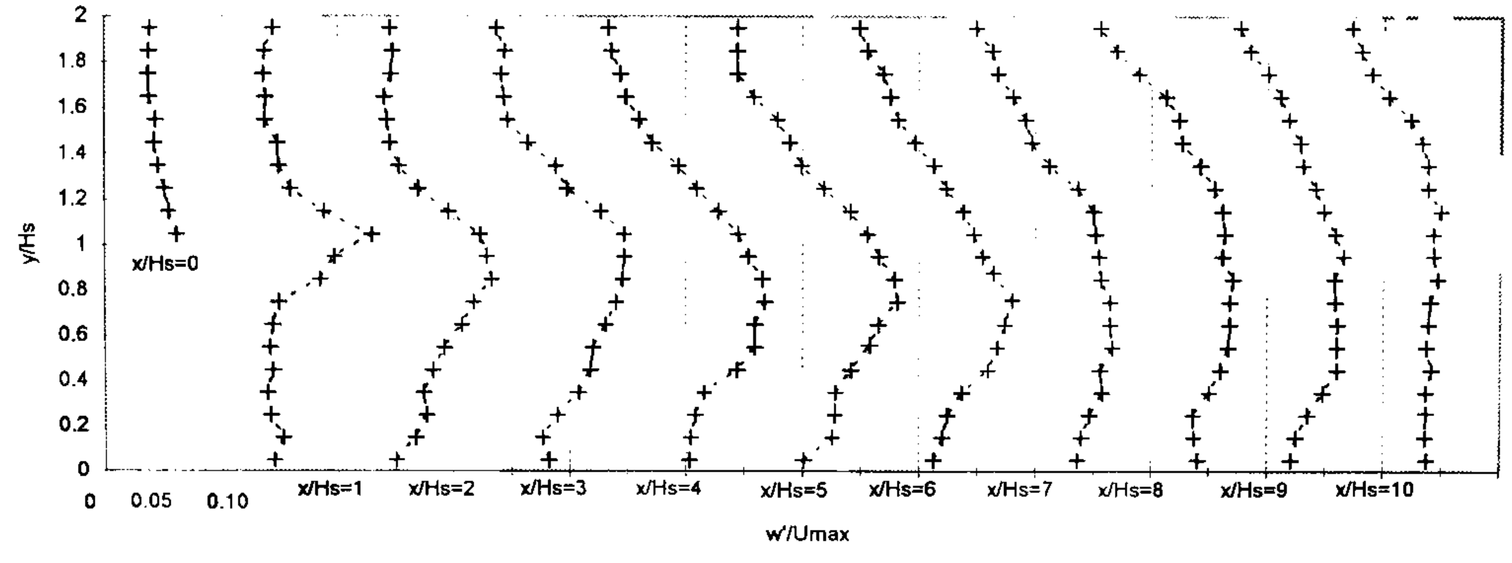

Figure 5.62(a) - Selected Turbulence Intensities (u'/U_{max}) in Recirculation Zone: 10-1

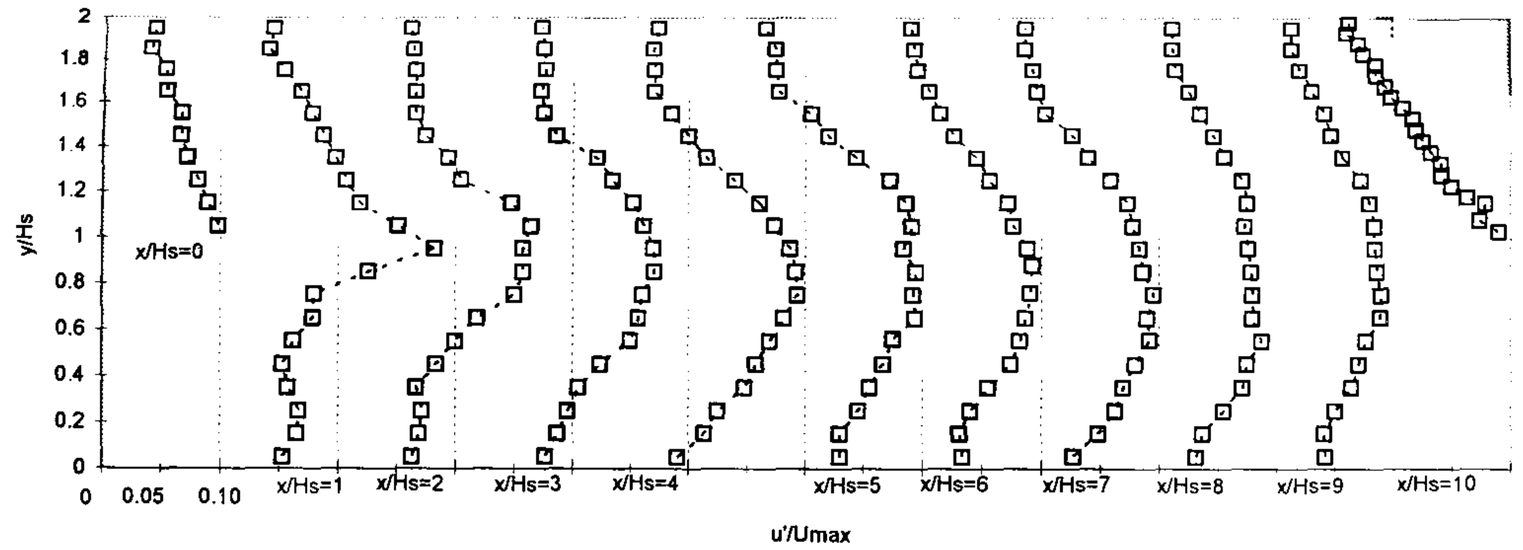

Figure 5.62(b) - Selected Turbulence Intensities (v'/U_{max}) in Recirculation Zone: 10-1

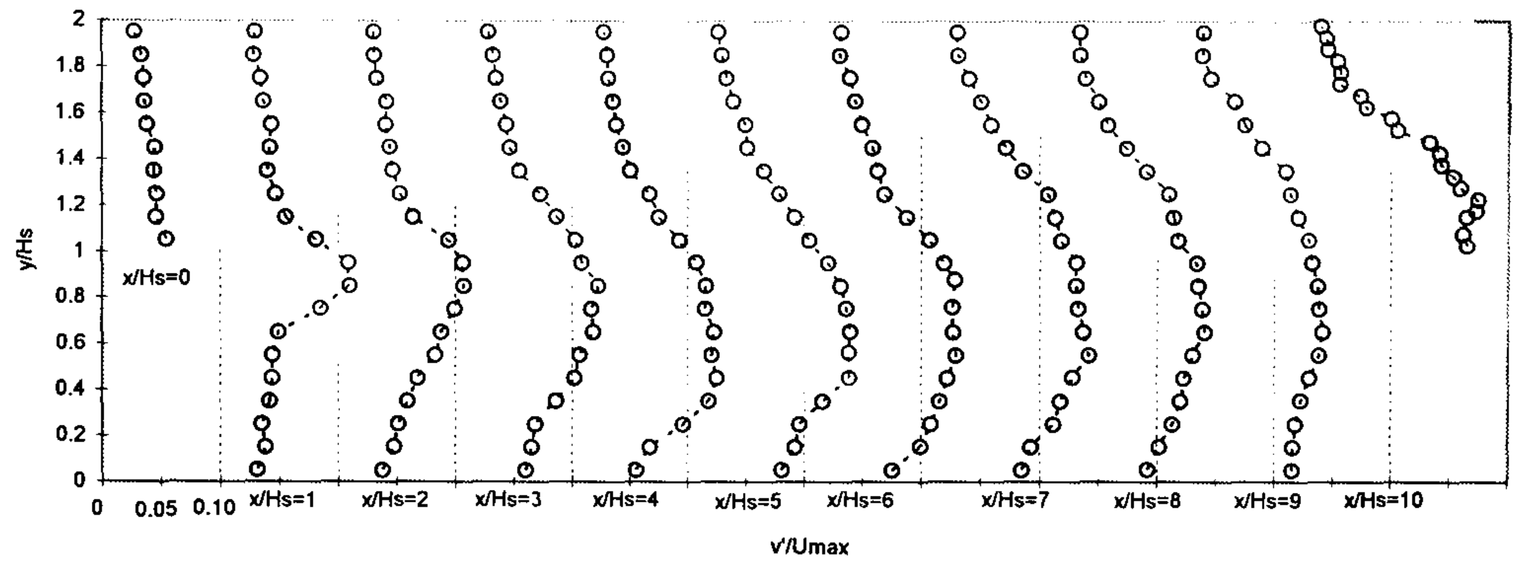

Figure 5.62(c) - Selected Turbulence Intensities (w'/U_{max}) in Recirculation Zone: 10-1

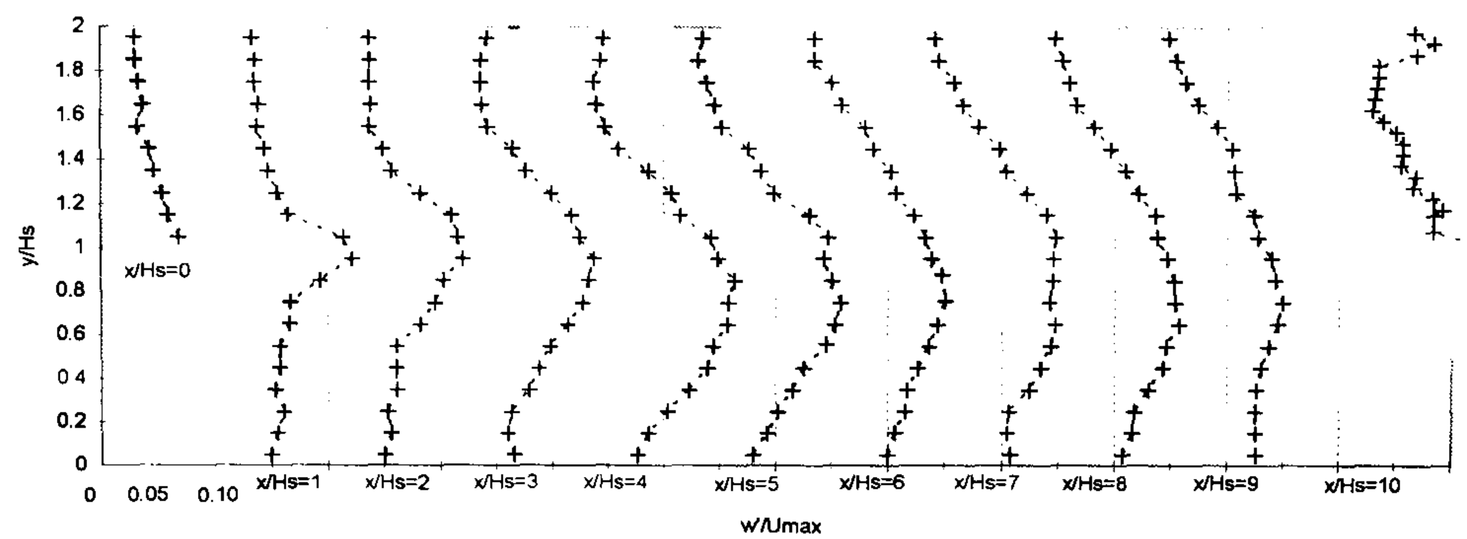

Figure 5.63(a) - Selected Turbulence Intensities (u'/U_{max}) in Recirculation Zone: 10-2

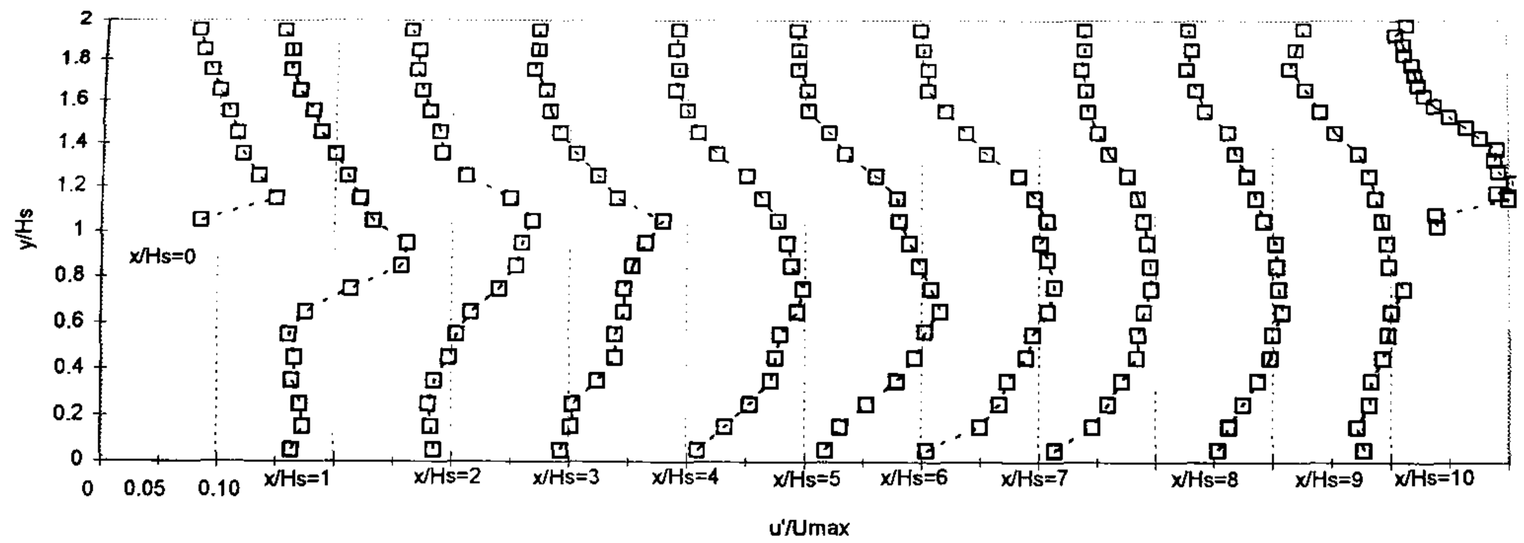

Figure 5.63(b) - Selected Turbulence Intensities (v'/U_{max}) in Recirculation Zone: 10-2

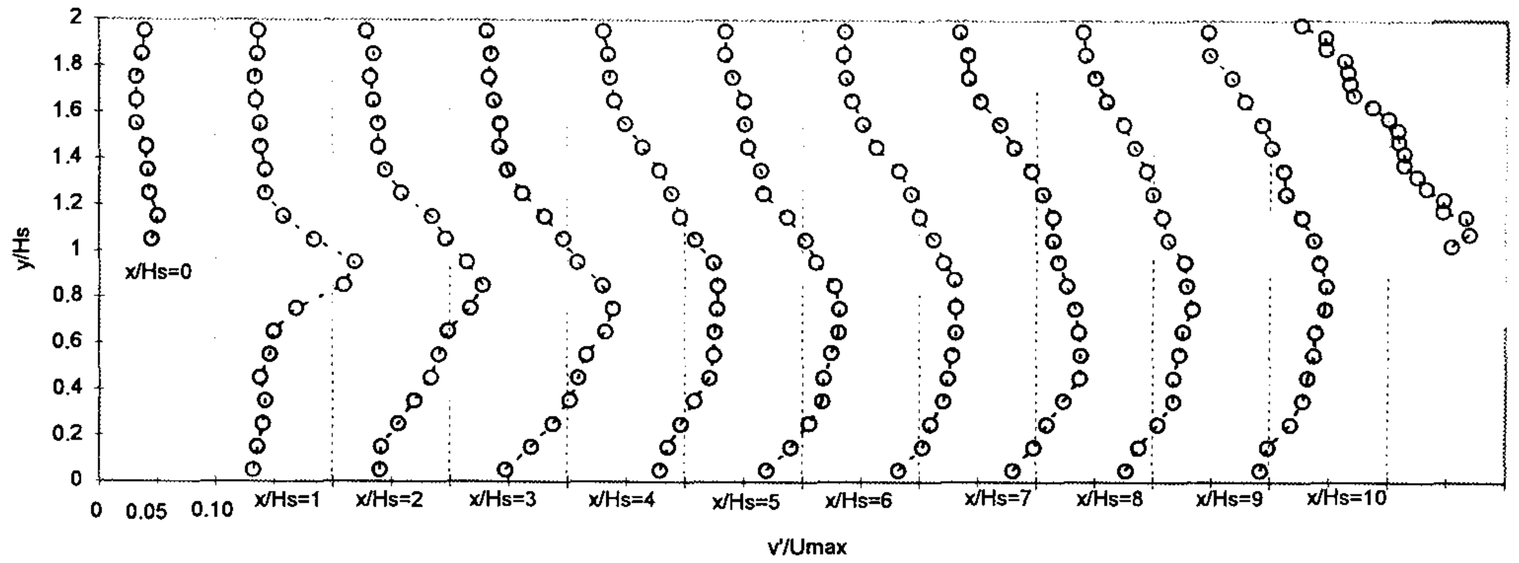

Figure 5.63(c) - Selected Turbulence Intensities (w'/U_{max}) in Recirculation Zone: 10-2

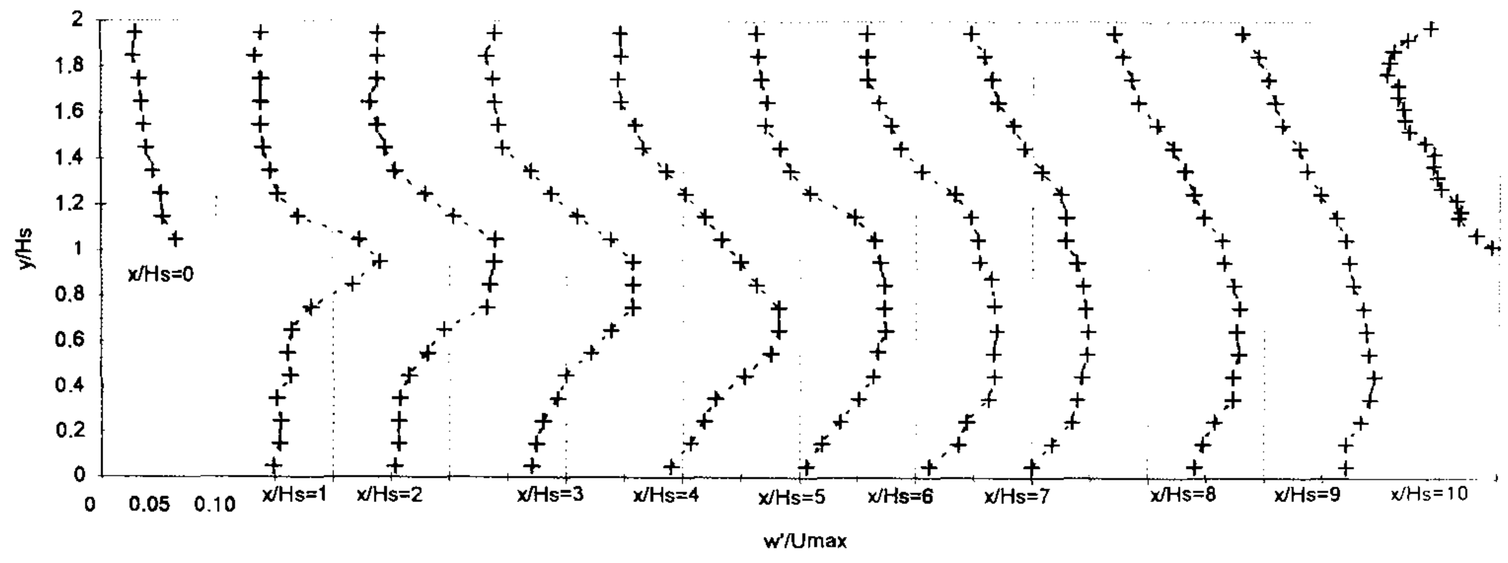

Figure 5.64(a) - Selected Turbulence Intensities (u'/U_{max}) in Recirculation Zone: 10-3

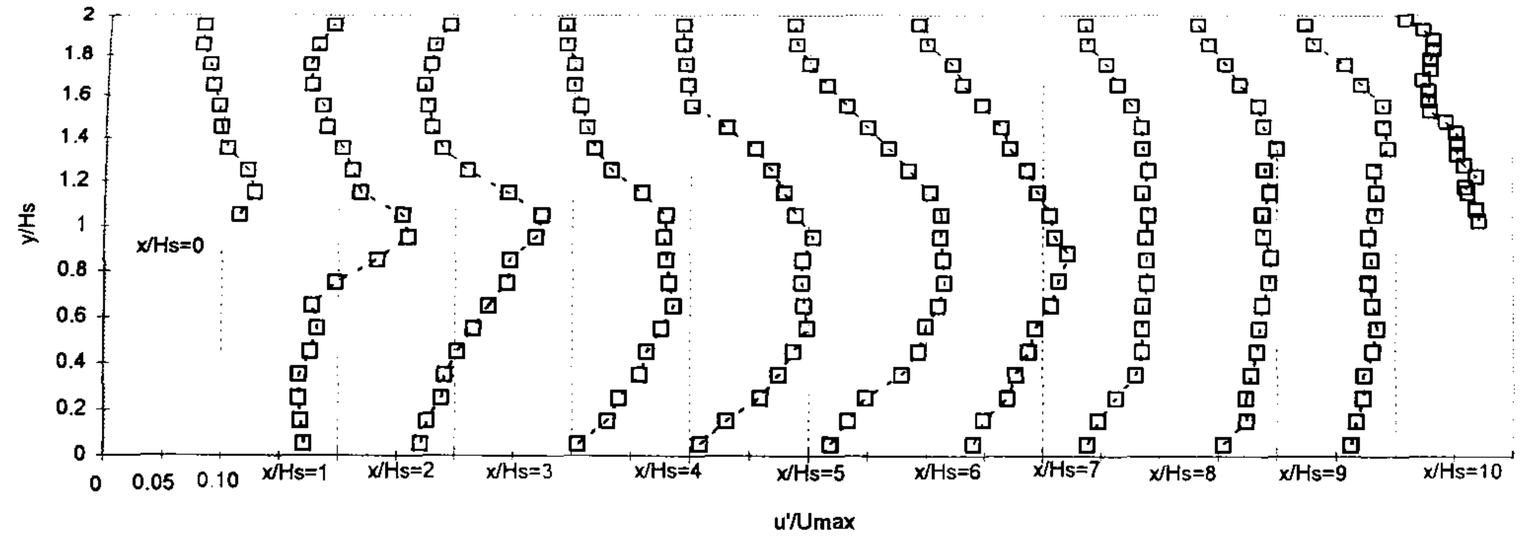

Figure 5.64(b) - Selected Turbulence Intensities (v'/U_{max}) in Recirculation Zone: 10-3

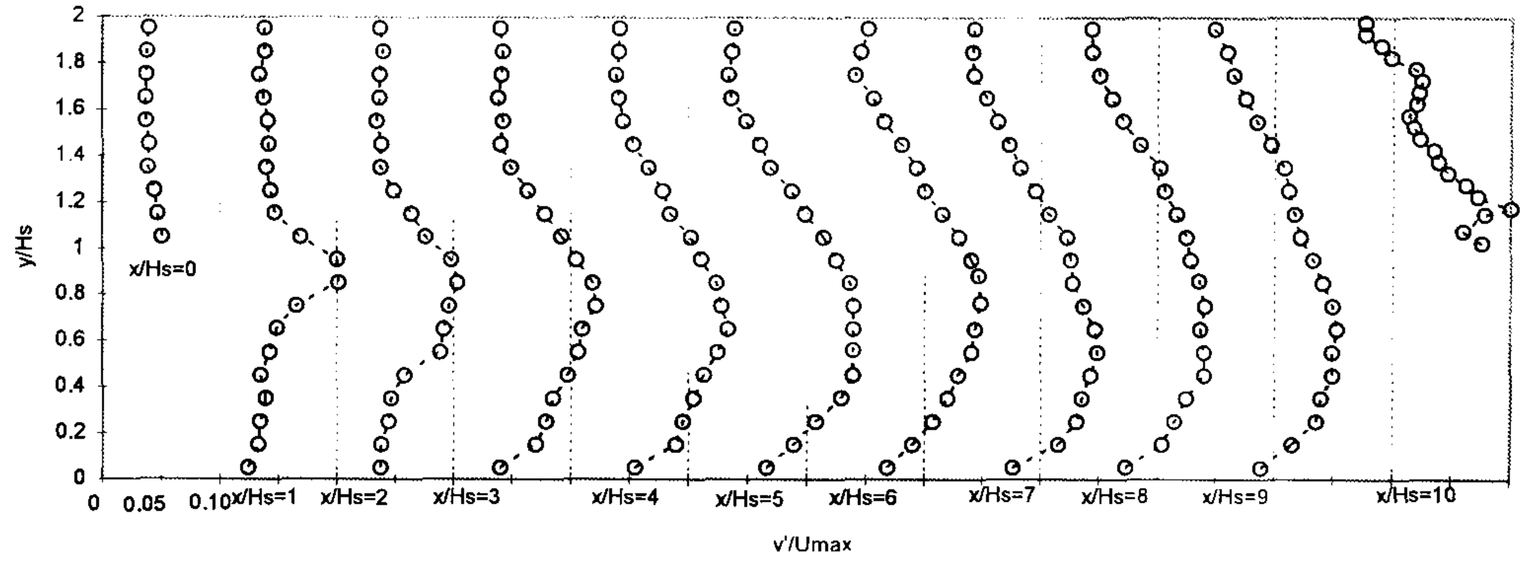

Figure 5.64(c) - Selected Turbulence Intensities (w'/U_{max}) in Recirculation Zone: 10-3

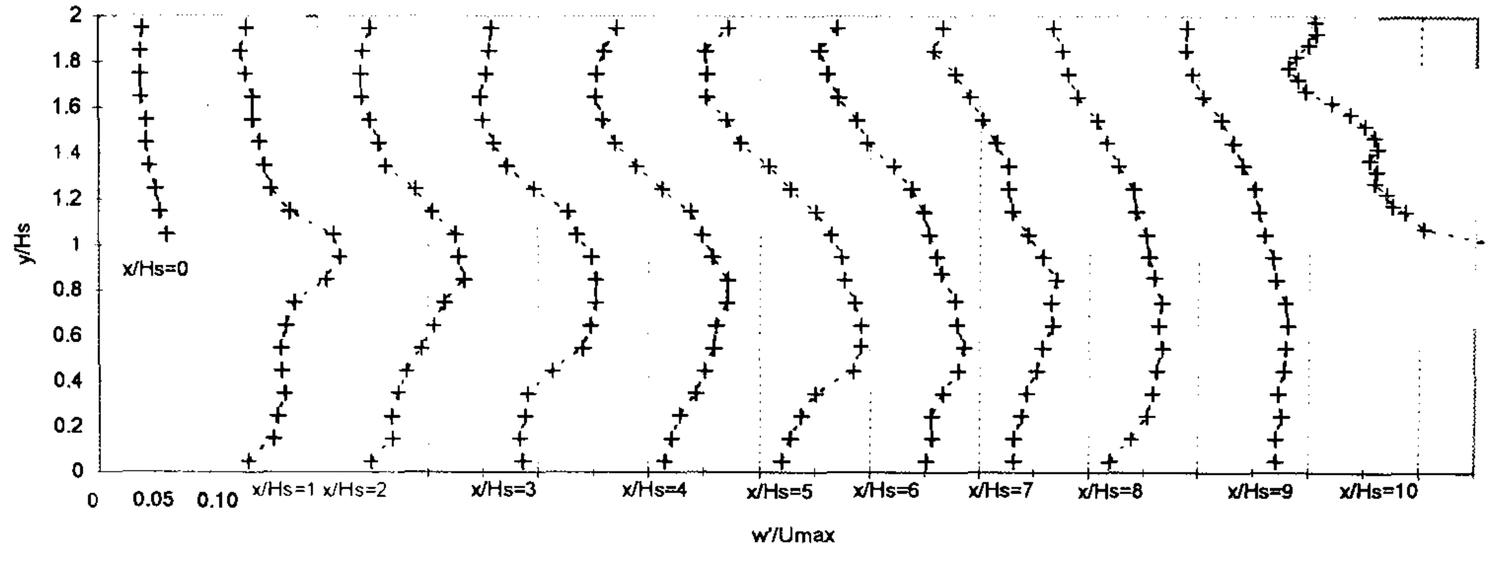

Figure 5.65(a) - Selected Turbulence Intensities (u'/U_{max}) in Recirculation Zone: 5-1

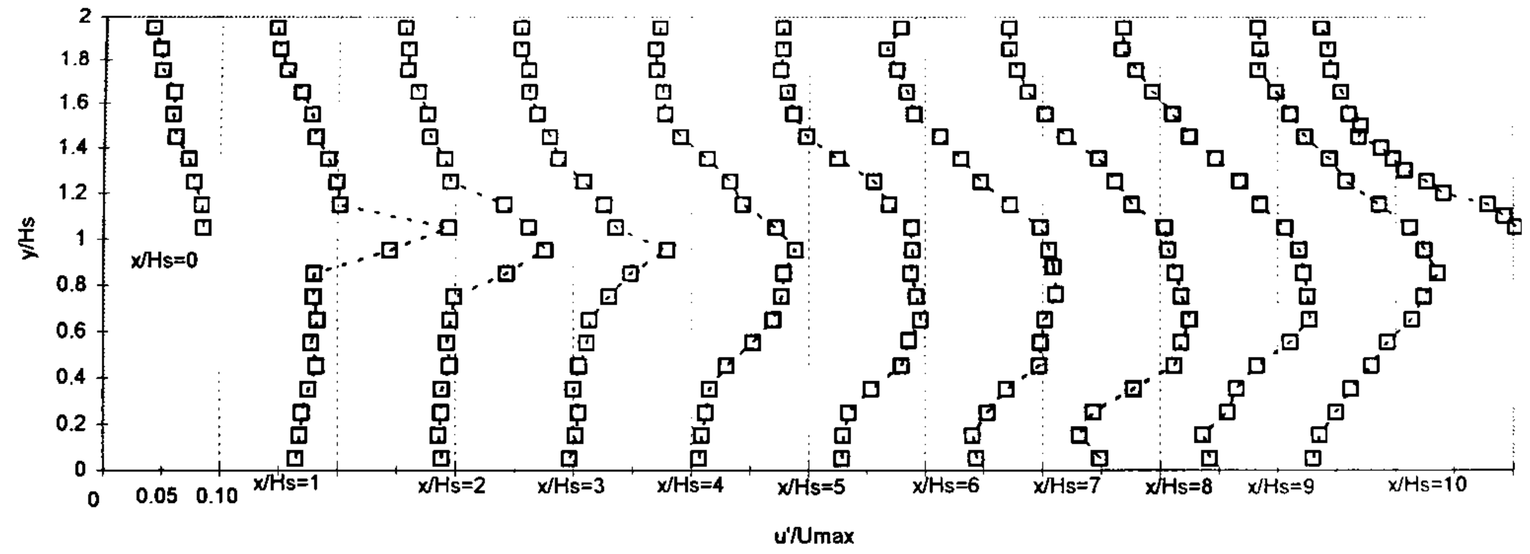

Figure 5.65(b) - Selected Turbulence Intensities (v'/U_{max}) in Recirculation Zone: 5-1

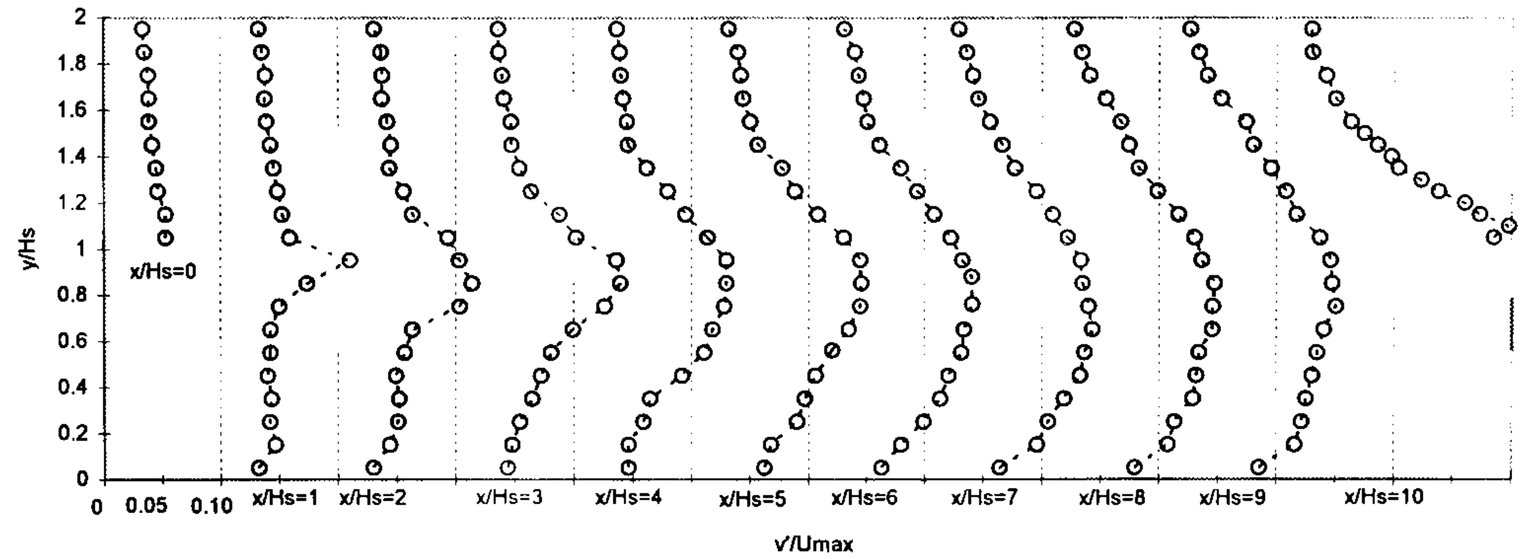

Figure 5.65(c) - Selected Turbulence Intensities (w'/U_{max}) in Recirculation Zone: 5-1

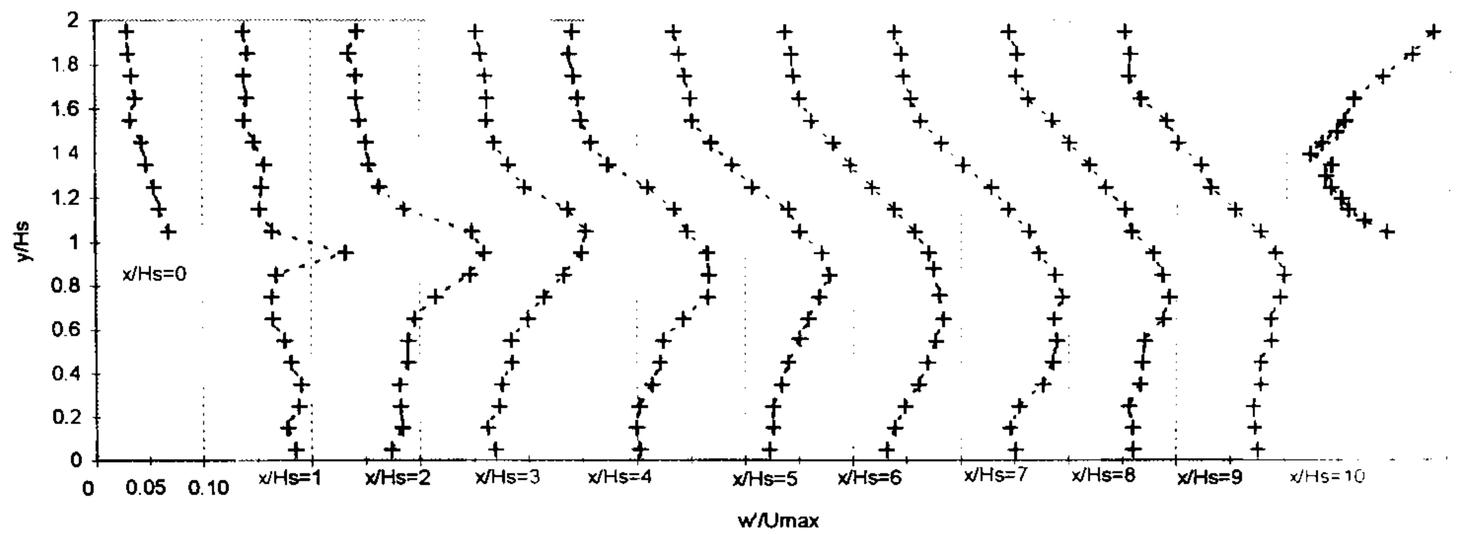

Figure 5.66(a) - Selected Turbulence Intensities (u'/U_{max}) in Recirculation Zone: 5-2

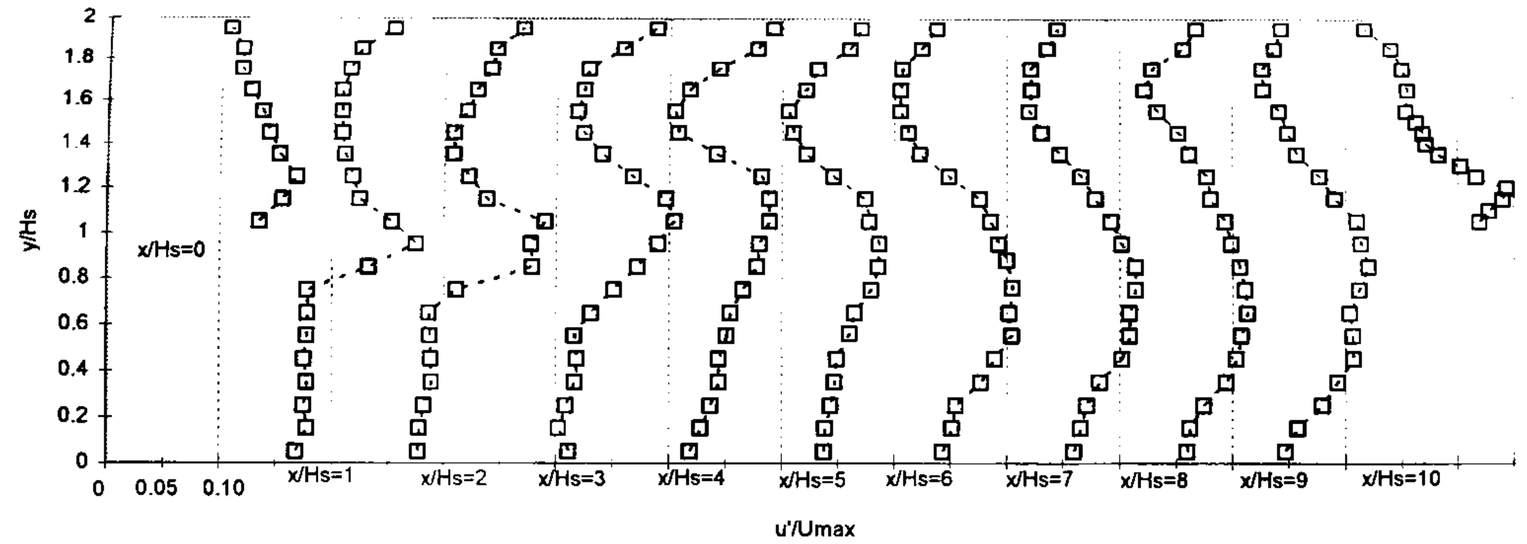

Figure 5.66(b) - Selected Turbulence Intensities (v'/U_{max}) in Recirculation Zone: 5-2

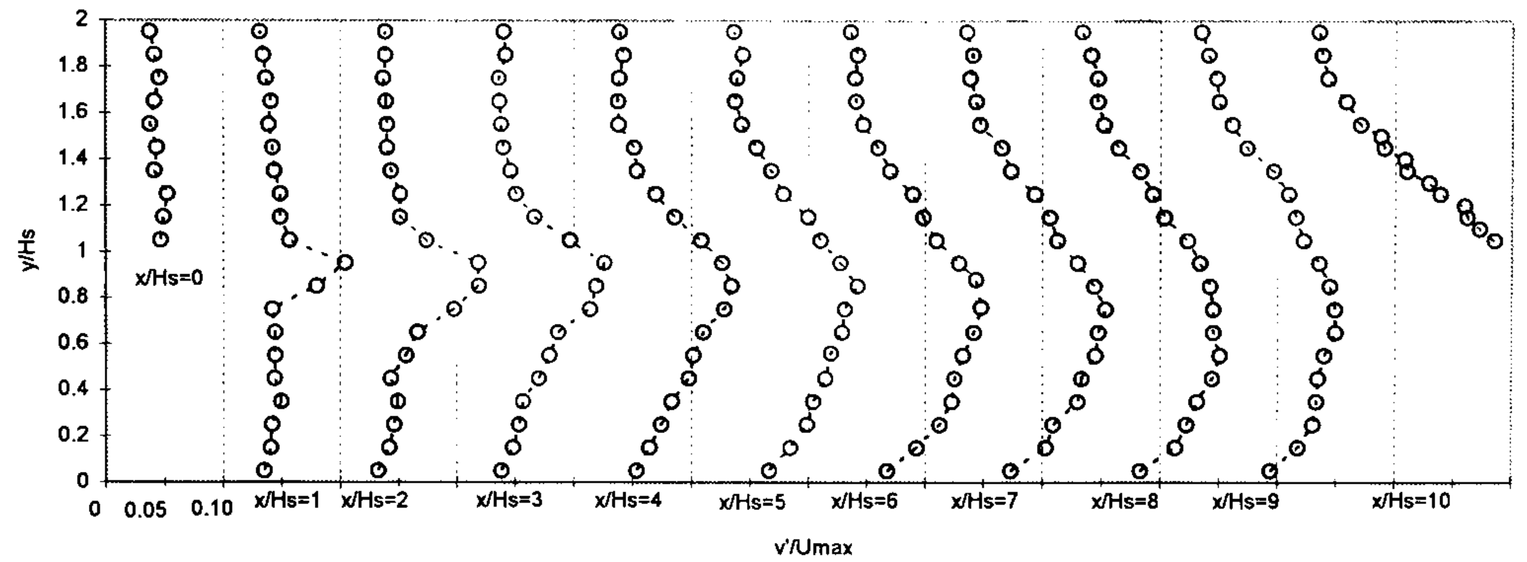

Figure 5.66(c) - Selected Turbulence Intensities (w'/U_{max}) in Recirculation Zone: 5-2

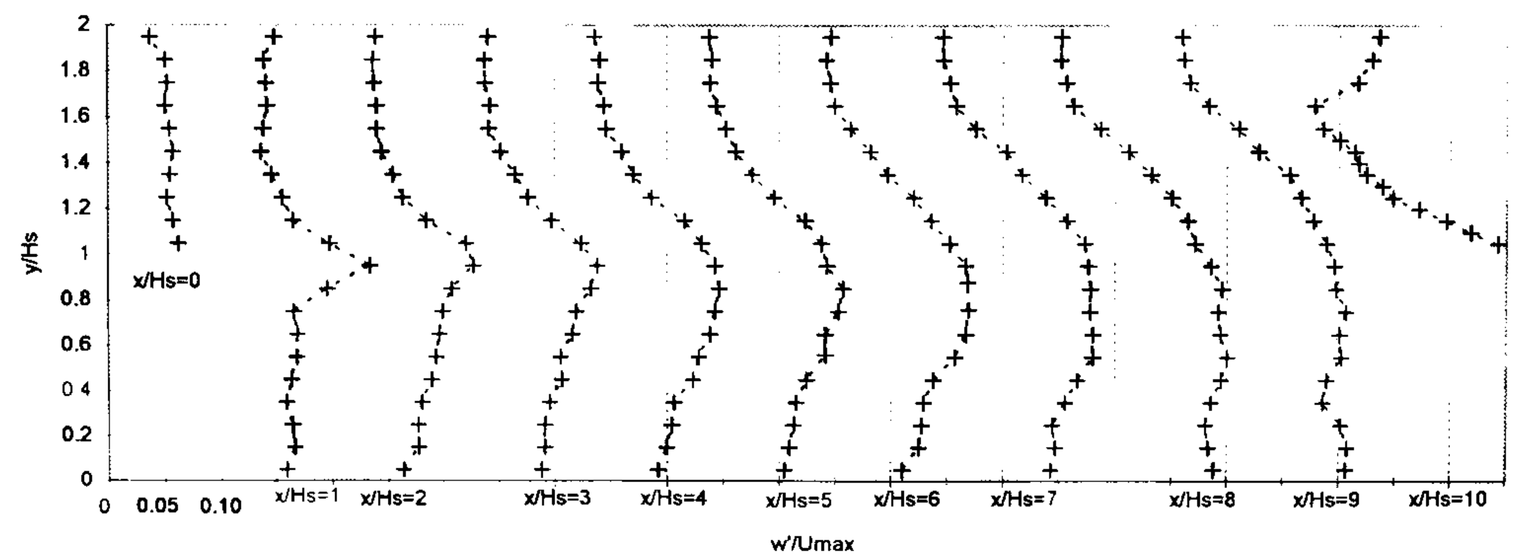

Figure 5.67(a) - Selected Turbulence Intensities (u'/U_{max}) in Recirculation Zone: 5-3

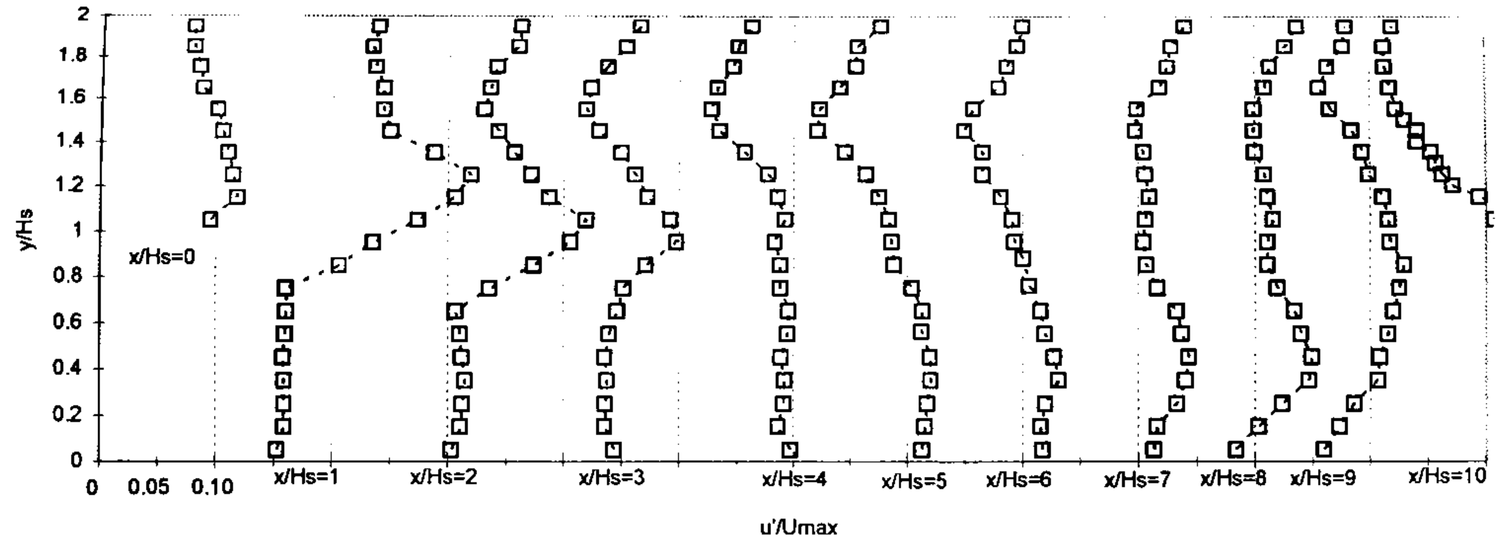

Figure 5.67(b) - Selected Turbulence Intensities (v'/U_{max}) in Recirculation Zone: 5-3

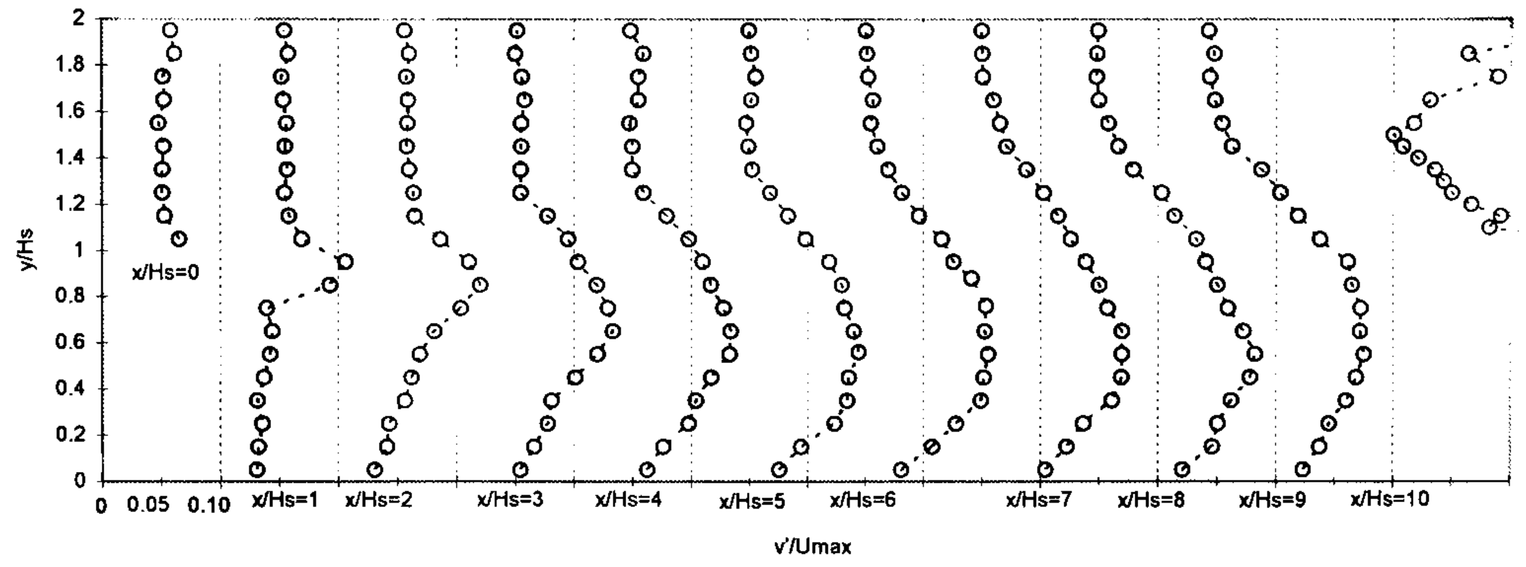

Figure 5.67(c) - Selected Turbulence Intensities (w'/U_{max}) in Recirculation Zone: 5-3

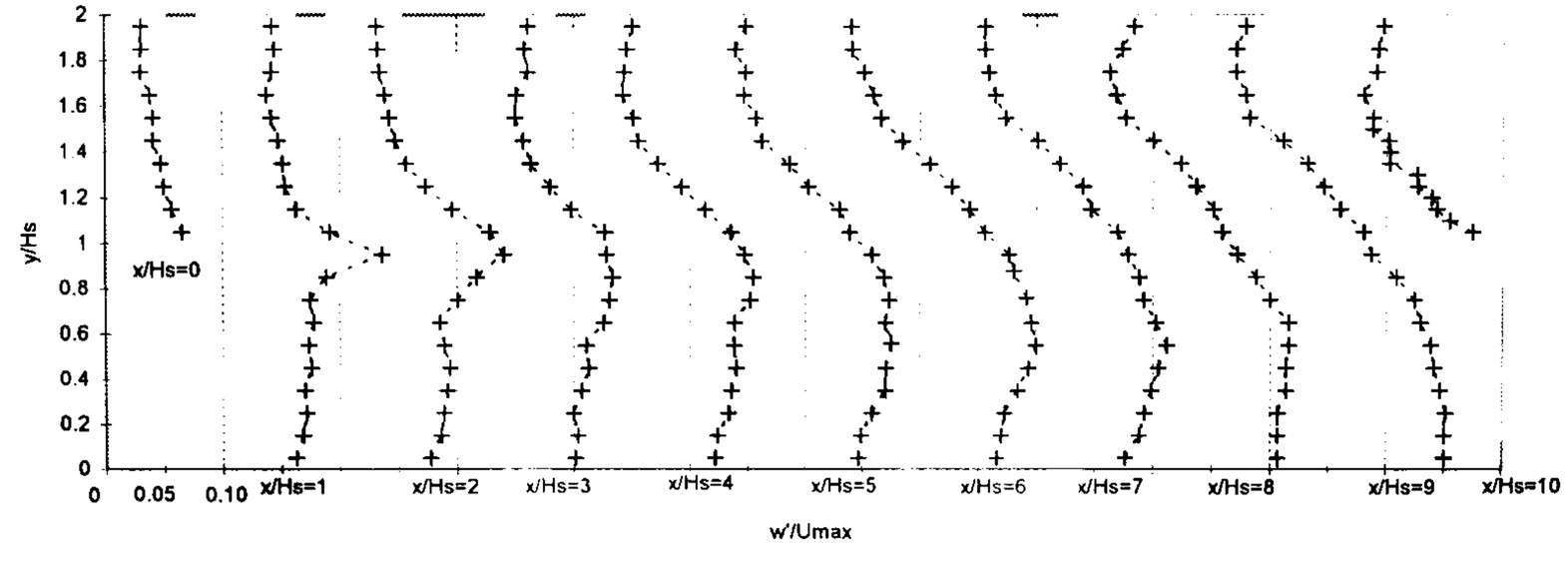

Figure 5.68(a) - Selected Turbulence Intensity Profiles ($u'/u*$) Downstream of Reattachment: BFS-1

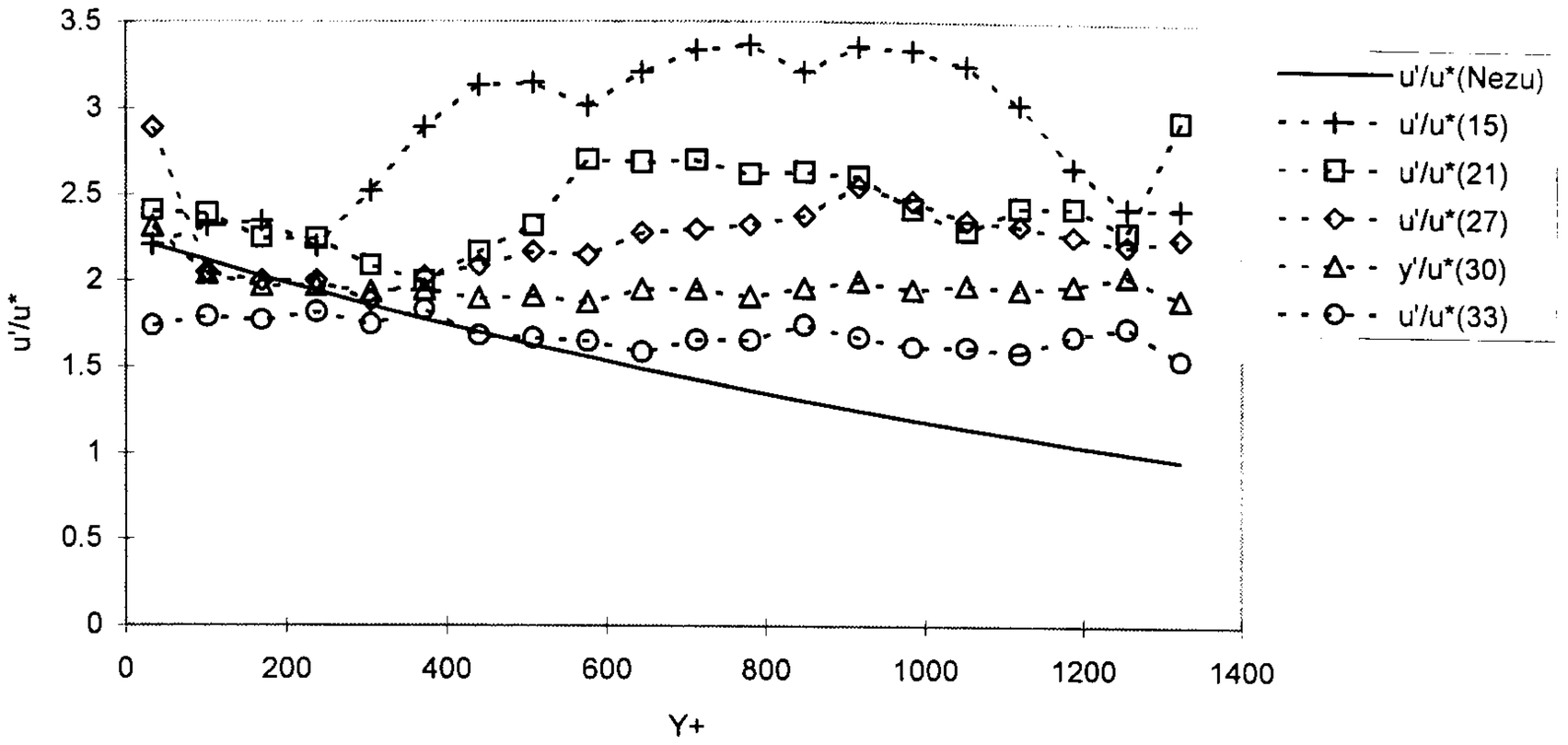

Figure 5.68(b) - Selected Turbulence Intensity Profiles ($u'/u*$) Downstream of Reattachment: BFS-2

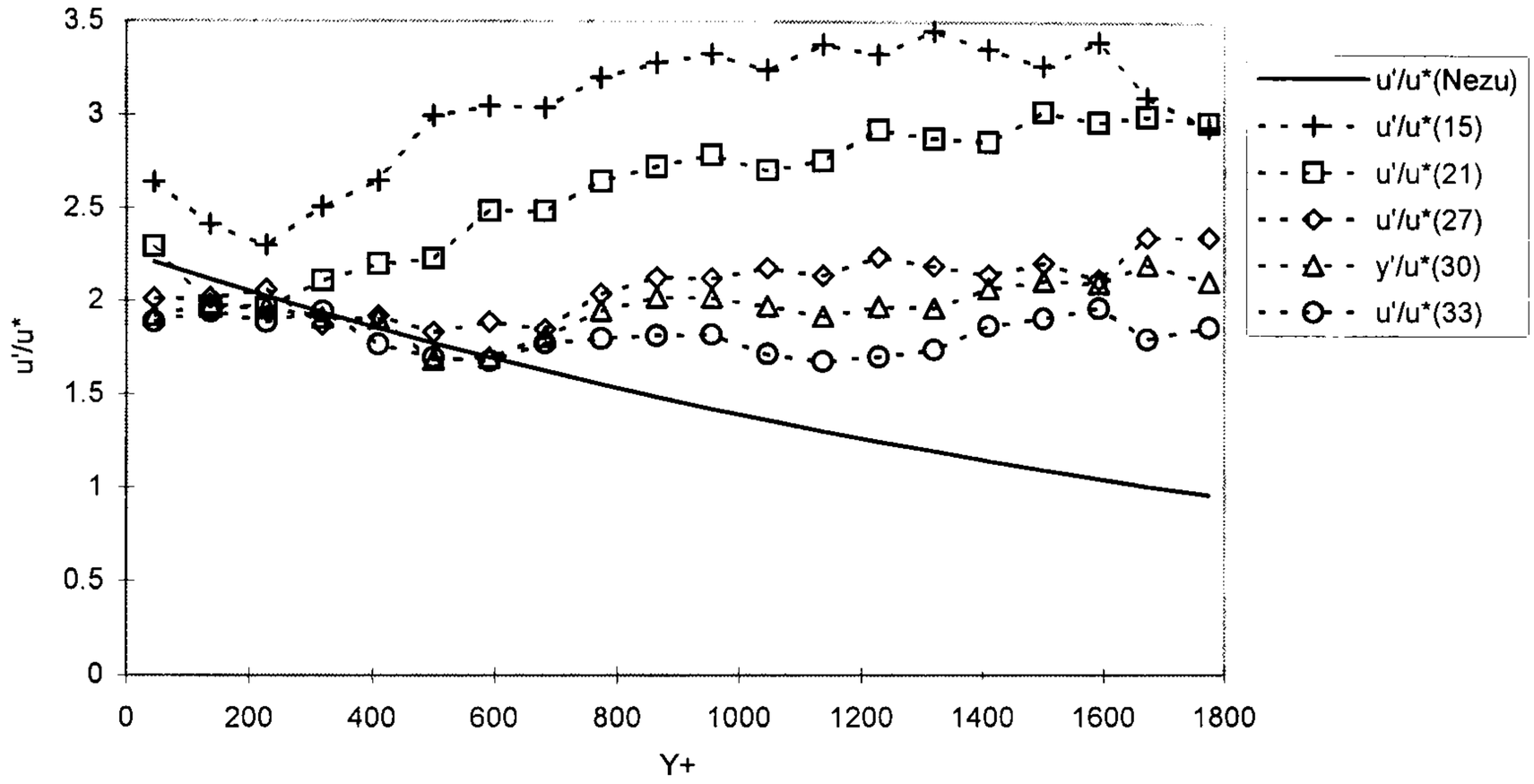

Figure 5.68(c) - Selected Turbulence Intensity Profiles ($u'/u*$) Downstream of Reattachment: BFS-3

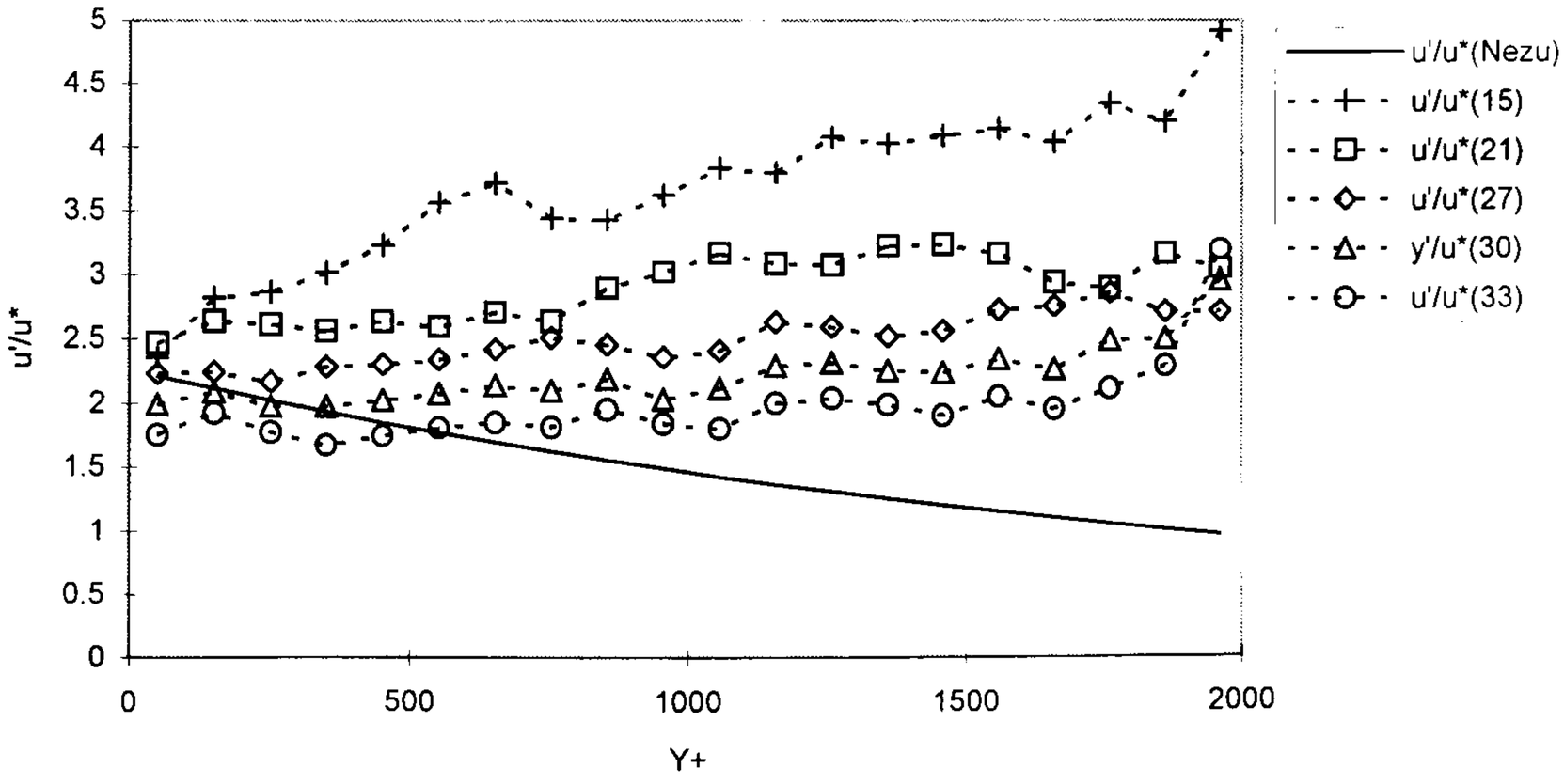

Figure 5.69(a) - Selected Turbulence Intensity Profiles ($v'/u*$) Downstream of Reattachment: BFS-1

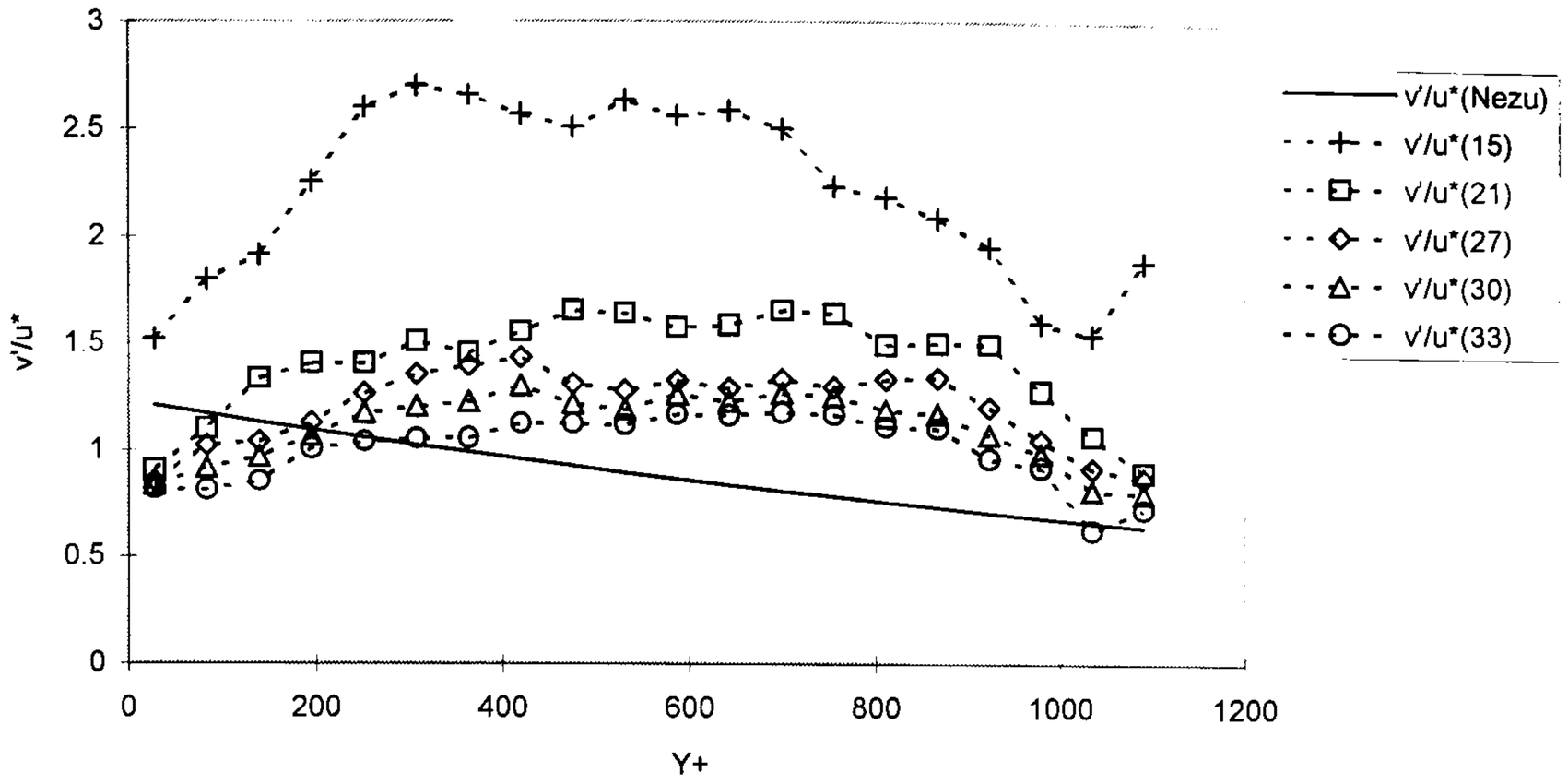

Figure 5.69(b) - Selected Turbulence Intensity Profiles ($v'/u*$) Downstream of Reattachment: BFS-2

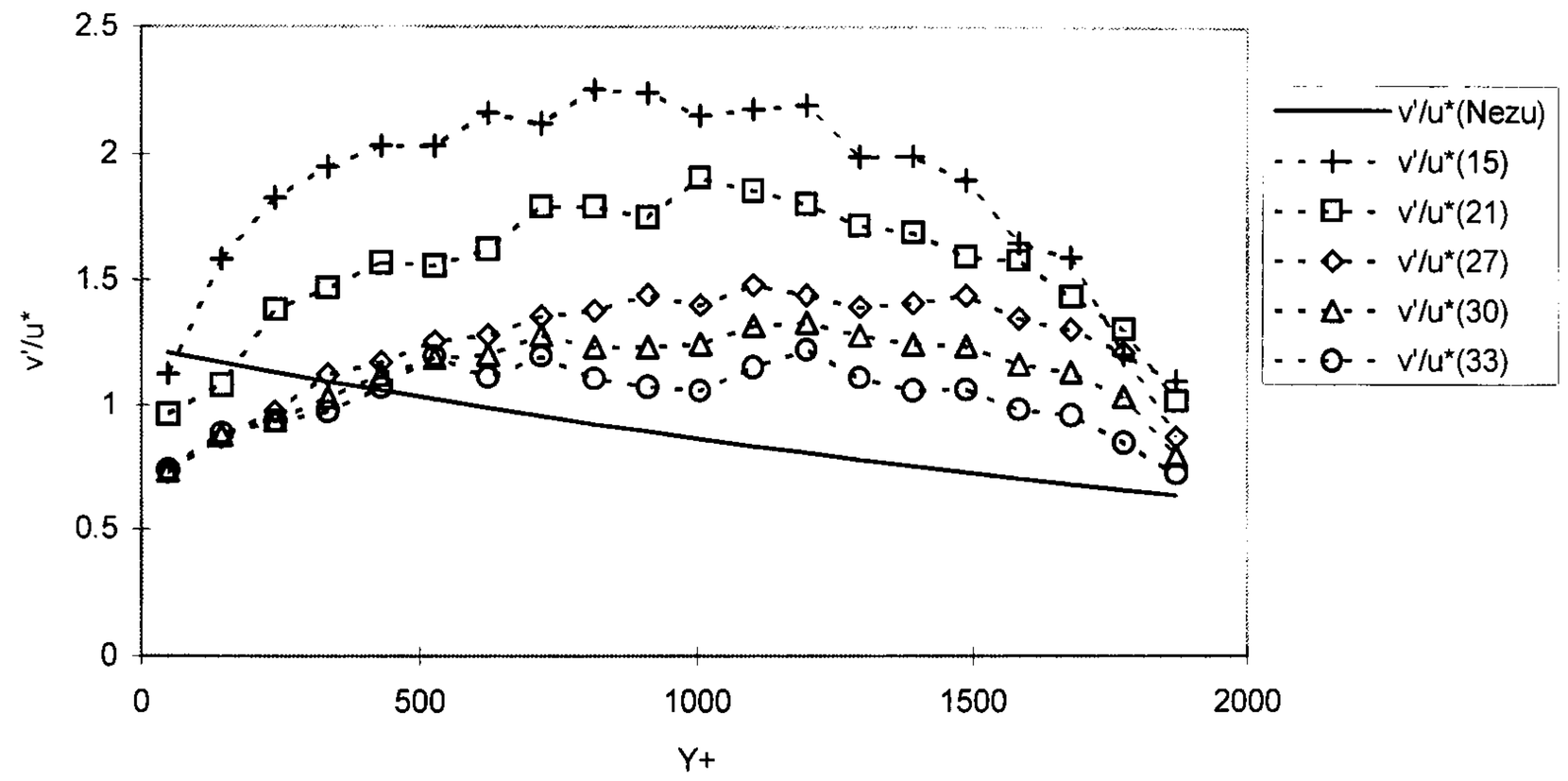

Figure 5.69(c) - Selected Turbulence Intensity Profiles ($v'/u*$) Downstream of Reattachment: BFS-3

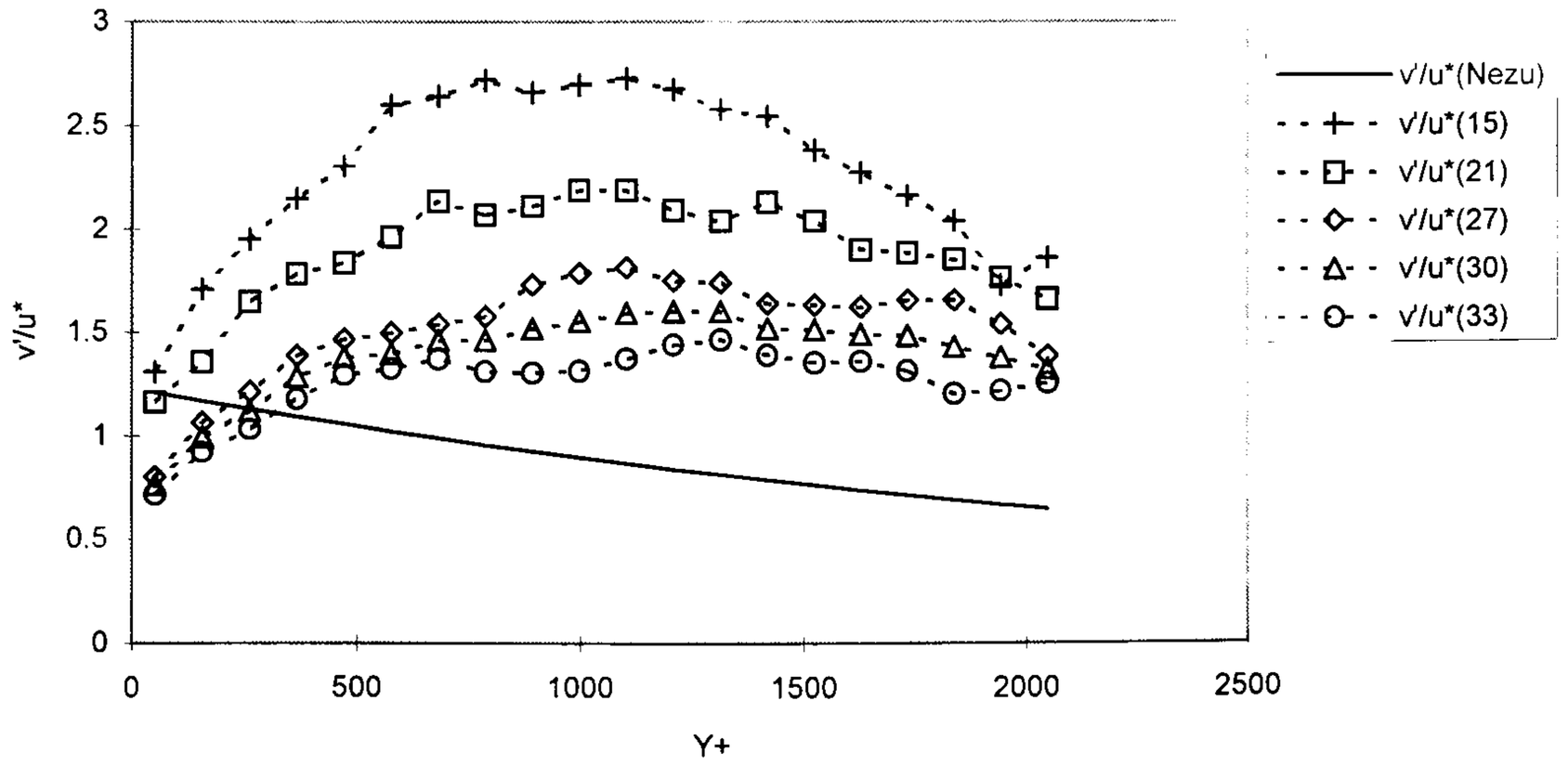

Figure 5.70(a) - Selected Turbulence Intensity Profiles ($w'/u*$) Downstream of Reattachment: BFS-1

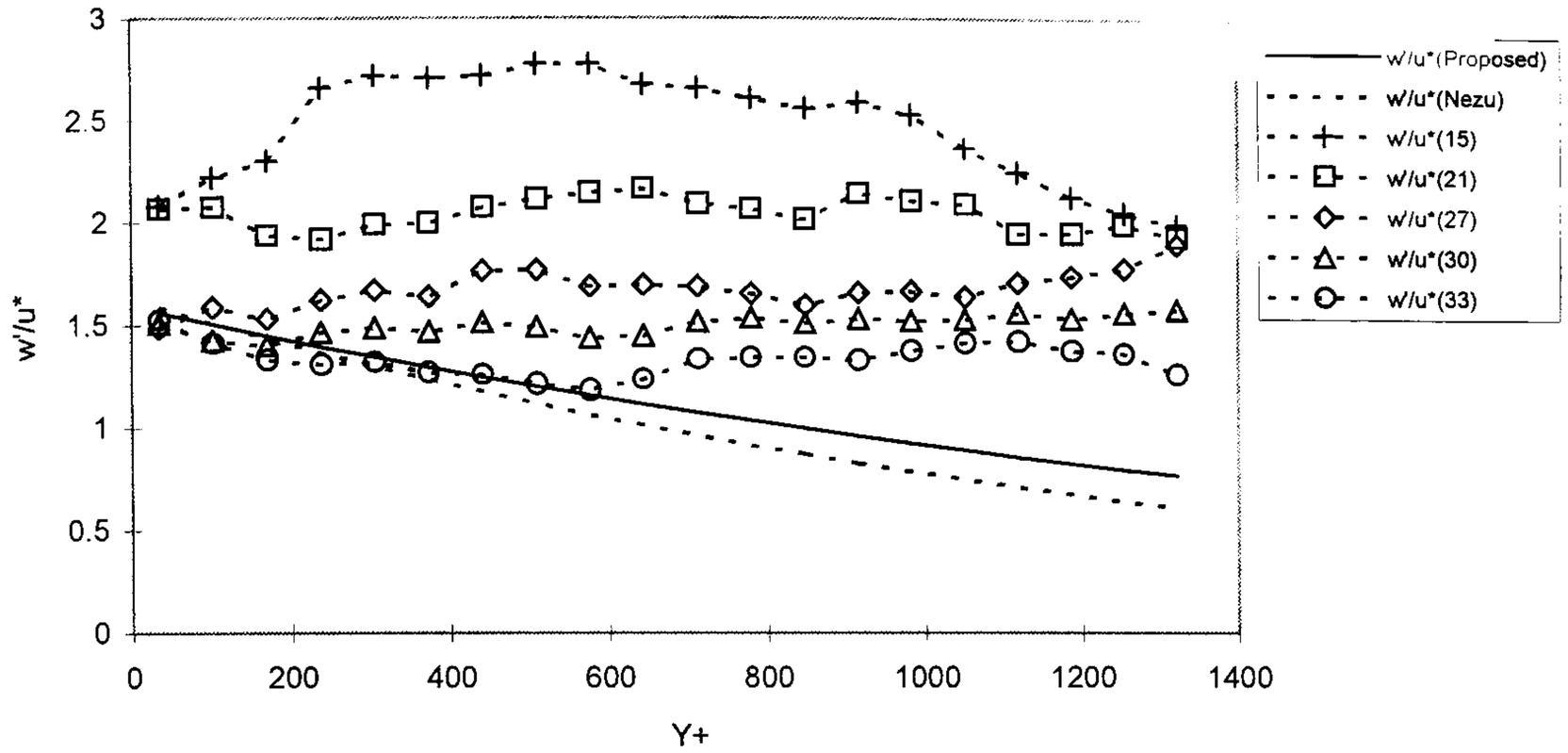

Figure 5.70(b) - Selected Turbulence Intensity Profiles ($w'/u*$) Downstream of Reattachment: BFS-2

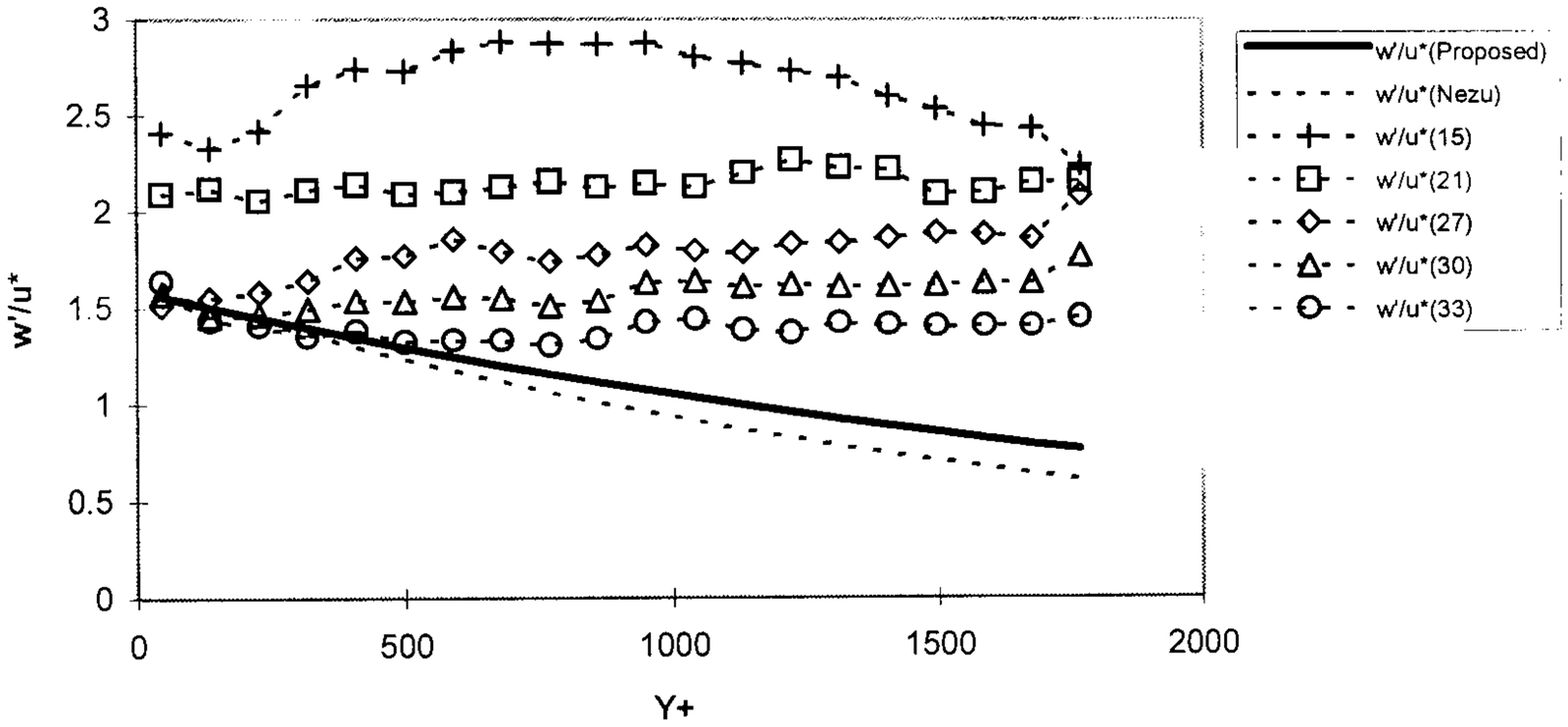

Figure 5.70(c) - Selected Turbulence Intensity Profiles ($w'/u*$) Downstream of Reattachment: BFS-3

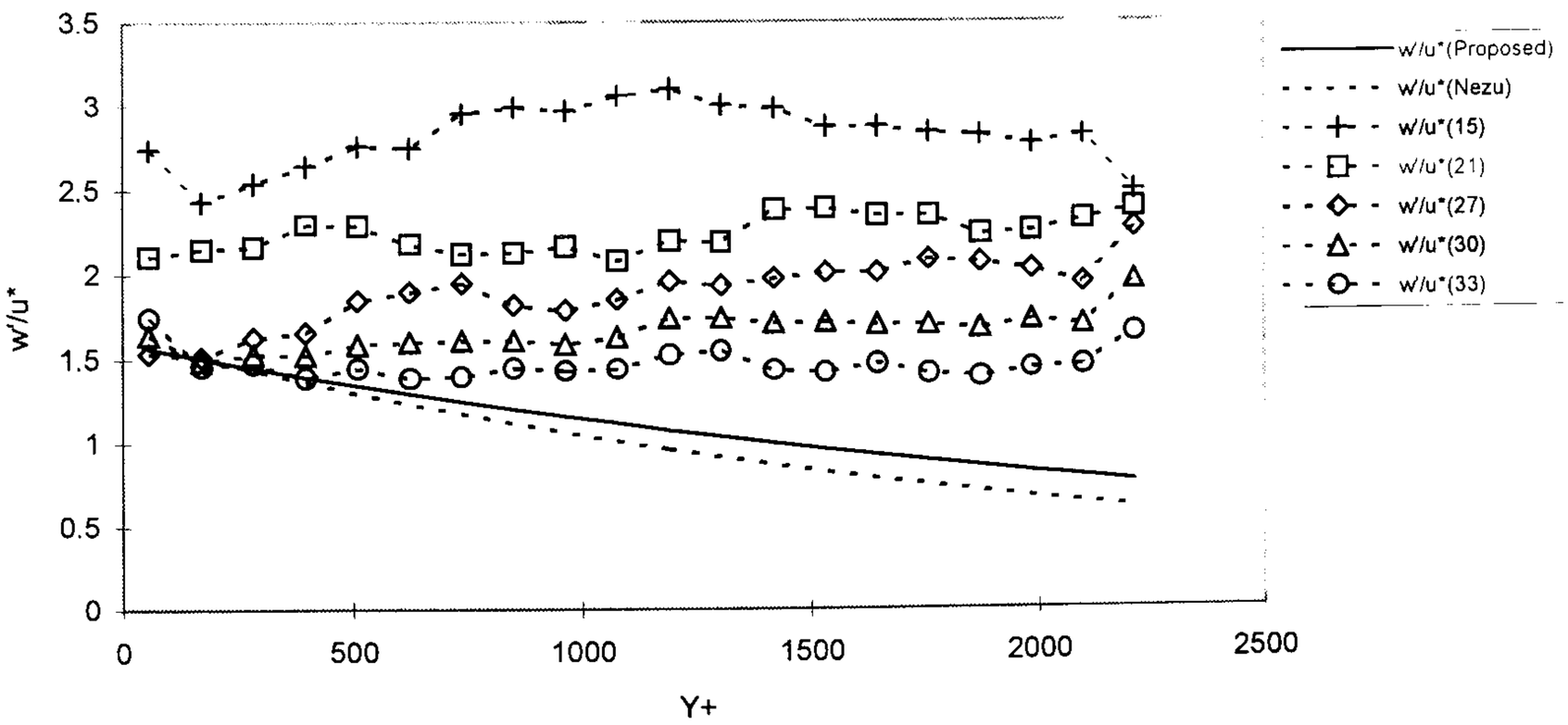

CHAPTER 6

CONCLUSIONS

6.1 INTRODUCTION

6.2 CONCLUSIONS FROM THIS INVESTIGATION

6.2.1 Testing Equipment: Laser Probe Support-Traverse, Main Flume Design and LDV Validation

6.2.2 Rectangular Open-Channel Flow

6.2.3 Reattachment Length

6.2.4 Open-Channel Slot Flow

6.3 RECOMMENDATIONS FOR FUTURE RESEARCH

CHAPTER 6

CONCLUSIONS

6.1 INTRODUCTION

The aim of this research was to investigate the influence of a FFS at varying distances downstream of a BFS in open-channel slot flow. In order to achieve this, three key objectives were established, these were:

(1) To undertake a preliminary study using the LDV system in a laboratory teaching flume.
(2) To construct a purpose built experimental flume.
(3) To undertake a comprehensive study of open-channel slot flow using the purpose built flume.

An initial investigation was undertaken in an existing laboratory flume. The main limitation of this flume was its inability to provide lateral velocity measurements, thereby limiting the investigation to 2-components, namely U and V. Despite this, a series of slot flow fields of varying slot aspect ratio were investigated. The results clearly illustrated the mean flow characteristics, such as the recirculation zones and flow reattachment locations. The turbulent flow characteristics, such as the growth, shape and intensity of the turbulent shear layers located downstream of the BFS and the FFS were also examined. Although much of the initial study was aimed at confirming the general flow characteristics of open-channel slot flow, it also provided a detailed insight into the use of the LDV system.

A purpose built flume was required for this study in order to provide the correct physical and hydraulic conditions, and to allow 3-component data acquisition using a 1-component LDV system. The constructed flume consisted of a transparent perspex channel with a built in slot section. This slot section could be changed (or omitted completely) with the addition of perspex blocks. Initial LDV measurements in this flume concentrated on rectangular open-channel flows, primarily to confirm existing empirical formulae and flow characteristics of this flow type. A more detailed discussion on this investigation is given later in this chapter.

An investigation of the length of flow reattachment was undertaken for a BFS and a series of slots with varying slot aspect ratios. This allowed the influence of the flow depth and Reynolds number to be evaluated with respect to the reattachment length. The conclusions

drawn from this were used to determine the slot geometries and hydraulic conditions used for the detailed measurements of the slot flow field. Using a constant flow depth, the slot flow field was measured in detail for three different Reynolds numbers for slot aspect ratios of 5, 10, 15 and a BFS only case. Point velocities were taken along the centreline of the flume for all three components of velocity. The mean longitudinal velocities for these point measurements were used to examine relationships describing the flow in the recirculation zone, and beyond reattachment to examine the relaxation of the flow back to a thin shear layer state. The growth of the free shear layer from the point of flow separation to the point of flow reattachment was examined using the mean velocities. The fluctuating velocities were converted to turbulence intensities to illustrate the production of turbulent energy within the shear layer and its subsequent dissipation.

6.2 CONCLUSIONS FROM THIS INVESTIGATION

This section contains a summary of the main conclusions drawn from this project. Further details on each of the areas covered below are given at the end of each chapter.

6.2.1 Testing Equipment: Laser Probe Support-Traverse, Main Flume Design and LDV Validation

In order to conduct this project, there was a requirement to design and construct testing equipment and confirm the validation process of LDV measurements. The following remarks and conclusions were drawn from this phase of the project.

(a) A support-traverse was constructed from mild steel with moveable plates allowing accurate movement of the laser probe to ±0.1mm in all three directions. This also facilitated a change in orientation of the laser probe, a feature required to measure all three components of velocity from different locations around the flume. Although automated versions could be purchased from the LDV supplier, the system developed proved to be a cost efficient and highly versatile alternative.

(b) It was a requirement of the main flume construction that the channel base and sidewalls were made from a transparent material allowing laser light penetration, and in addition, to be of sufficient length and scale to support 2-dimensional open-channel flow. A limited budget for this construction meant that a self built flume was the only option. The design and construction took approximately 18 months.

(c) The completed flume had a length of 5.7m, a width of 0.6m, a depth of 0.3m, with an in-built slot 2.0m in length and 0.1m in depth which was located 2.6m downstream of the channel inlet. Although the main flume was designed with an in-built step of height 0.1m, this was later reduced to 0.05m. This reduction of the slot height increased the width to depth ratio, thereby increasing the central 2-dimensional flow region of the channel.

(d) A detailed examination of the flume geometry was undertaken to minimise errors from this source. This involved a survey of the bed contours, the sidewall spacing and the step height. It was concluded from these investigations that the construction of the flume met the design specifications to an acceptable degree of accuracy.

(e) It was anticipated that a changeable centre section of the flume (which contains the slot) would allow greater use of the flume for future investigations. Despite this feature being incorporated in the constructed flume, the connection of the centre section to both the upstream and downstream channel sections break the continuity of the channel bed and sidewalls. In hindsight, this problem would be reduced on limiting the centre section to the slot only.

(f) From the initial 2-dimensional slot flow investigation, it became apparent that the method of LDV data acquisition required validation with respect to the statistical properties of the measured data, and should be configured with respect to certain properties of the flow itself. Based on the maximum response frequency of the flow, f_{max}, (Nezu and Nakagawa, 1993b), where:

$$f_{\max} = k_{\max}.u/(2\pi) \geq 100.u/(2\pi L_x) \approx (50/\pi).(u/y) \qquad \textbf{Equation 4.2}$$

Then the minimum sampling frequency for data acquisition was obtained by satisfying $f_{min}>2f_{max}$. Using this minimum sampling frequency, velocity time series taken at various locations in the flow were analysed to determine a minimum number of samples (or time duration). This ensured that the statistical properties of the measurements were reliable, and that time taken for both data acquisition and processing was kept to a minimum. The minimum number of samples was based upon achieving a standard deviation less than 2% of a long-term average of u and u'_{RMS}. It was observed that u'_{RMS} took longer to achieve this condition than u, and therefore this became the deciding condition for the minimum number of samples.

6.2.2 Rectangular Open-Channel Flow

A series of investigations were undertaken to determine the hydraulic conditions which would provide fully developed turbulent flow in a rectangular open-channel (i.e. without the presence of a slot). The 'law of the wall' and turbulence intensity models were examined to obtain the maximum flow depth which provided a central region of flow unaffected by sidewall contamination. The following conclusions were drawn form this phase of the investigation.

(a) The most accurate method of determining the friction velocity, $u*$, was the use of the log-law relationship. The more direct method using the channel slope was found to agree within 5% of the log-law method.

(b) The log-law was used successfully to describe the inner-region of flow, $y/h \leq 0.2$, and the velocity defect law for the outer-region, $y/h > 0.2$.

(c) The universal functions proposed by Nezu (1977) and Nezu and Rodi (1986) were used to describe the turbulence intensity distribution. The experimental profiles agreed with the modified turbulence intensity function $u'/u*$ for the outer-region and with the damping function extension for the inner-region of flow. The modified turbulence intensity function for the vertical fluctuations, $v'/u*$, was also found to agree with the experimental profiles. Whilst the lateral turbulence intensity function, $w'/u*$, proposed by Nezu (1977) was also found to agree with the experimental profiles, a modified set of constants for this function have not been documented in the literature. The present investigation proposes a modified set of values for D_w and C_w providing a more accurate correlation. This takes the form:

$$\frac{w'}{u_*} = D_w . \exp(-C_w \frac{y}{h})$$

where, D_w=1.59, and C_w=0.75.

(d) From the literature, the minimum span/depth ratio, B/h, which provides a central region of 2-dimensional flow has been found to range from B/h=5-10. Using various flow depths and Reynolds numbers, it was observed that a central 2-dimensional region of flow existed for the condition where B/h>5-7.

6.2.3 Reattachment Length

The current literature has limited information on the influence of the upstream flow conditions on the flow which develops downstream of a BFS. The reattachment length of the flow has often been used to examine these, as it is highly sensitive to changes in these conditions and it can provide much information on the flow in general. A detailed investigation of the influence of the upstream conditions on the reattachment length was therefore undertaken, both to confirm and expand on the existing knowledge. As this present study aimed to investigate the effects of a FFS at various locations downstream of a BFS, then the influence of the FFS on the reattachment length was also investigated. The following conclusions have been drawn from this phase of the investigation.

(a) It was observed that irrespective of the flow depth, the reattachment length initially increased with Reynolds number, reaching a maximum value and subsequently decreasing to a stable value as the Reynolds number continued to increase. Over a Reynolds number range of 3000<Re<60000, reattachment lengths between $5<R_L<9$ were observed.

(b) Given the above nature of the R_L vs Re profiles, it was observed that the reattachment length produced by a given Re increased with a reduction in flow depth. This was found to stabilise at depths of $y_o/H_s \leq 1.0$.

(c) It was observed that as the FFS moves closer to the point of flow reattachment, the greater is its influence on the reattachment length. For large aspect ratios (i.e. greater than 20), the reattachment lengths are similar to those observed for a BFS, with values of $R_{L\max}$ reaching a distance of $9H_s$. This indicates that the FFS does not affect the reattachment length at distances greater than this. As the FFS moves closer to the BFS, to a distance of $x/H_S=10$, the value of $R_{L\max}$ did not exceed $8H_s$. This reduction of the reattachment length results from a decrease in the velocity gradient *du/dx* forced by the presence of the FFS. The reduced velocity is coupled with a decrease in flow momentum along the separation streamline, and therefore the reattachment point is forced upstream.

(d) The spanwise distribution of reattachment length was investigated for different flow depths and Reynolds numbers. It was observed that a central region of the channel produced similar reattachment lengths, with a reduction in length observed closer to the sidewalls. This reduction is attributed to the 3-dimensional flow effects created

by the sidewall increasing the turbulence intensities, and hence increasing the rate of shear layer development.

6.2.4 Open-Channel Slot Flow

Based on conclusions drawn from the reattachment length investigation, the slot geometries and hydraulic conditions for the slot flow investigation were determined. The mean and turbulent components of velocity were each used to illustrate several characteristics of slot flow. The following conclusions were made from this part of the study.

(a) For slot bed reattached flows, the mass-flow deflected upstream at reattachment was found to be 1/10th of the total mass-flow. This value is less than the 1/6th observed by Etheridge and Kemp (1978), however, this difference is attributed to the definition of the outer boundary of the shear layer, which, in the current investigation was based upon the depth where u/u_o=1.0, whereas a Reynolds stress based function was adopted by Etheridge and Kemp (1978).

(b) The outer boundary of the shear layer was found to be similar for all the cases where the slot aspect ratio ≥10. The boundary can be expressed by a single universal equation which does not rely on any parameter other than the longitudinal distance, x/H_s, and the initial depth of the mean velocity, h_O, at x/H_s=0:

$$\frac{y}{H_s} = \frac{h_o}{y_o} e^{0.032\left(\frac{x}{H_s}\right)^{1.3}}$$

Equation 5.4

This equation is valid in the region $0<x/H_s<R_L$, however, at this stage there is no evidence that it holds for depths where $y_o>H_s$.

(c) The inner boundary of the shear layer was found experimentally to be described by the following expression:

$$\frac{y}{H_s} = H_s\sqrt{0.6\left(1-\frac{x}{H_s R_L}\right)}$$

Equation 5.5

This was accurate for the region $1.5<x/H_s<R_L$, however, in order to include the initial stage of the profile, an additional expression has been introduced. The region bounded by $0\leq x/H_S\leq 1.5$ was found to take the linear form:

$$y/H_s=1-(0.25x/H_s) \qquad \textbf{Equation 5.6}$$

(d) The shear layer thickness, δ_S, can be defined as the difference in height between the inner and outer boundaries of the shear layer. However, another definition of the shear layer is based upon the assumption that the local maximum of mean velocity gradient, du/dy, within the shear layer is constant and applies to the region between these boundaries i.e. $u=0$ and $u=u_O$. Both of these methods were investigated, where the method using the shear boundaries produced a consistent exponential growth of the shear layer with longitudinal distance. The shear layer thickness using the velocity gradient, du/dy, resulted in lower thicknesses, and there was a large scatter between the different cases investigated. The problem associated with this method is that the velocity gradient has a Gaussian distribution and is not constant across the shear layer. Therefore, the maximum velocity gradient is not representative of the whole shear layer, and as a result, the shear layer thickness is less.

(e) The streamwise velocity distribution downstream of a BFS was shown to have a Gaussian form. There were good similarities between the results and current Gaussian models. However, the distribution of the experimental results were influenced by their longitudinal location, which the existing Gaussian distributions did not cater for. The following modified Gaussian equation is therefore proposed which accounts for the longitudinal location:

$$\widetilde{U} \equiv (1+\mathrm{t})\mathrm{e}^{-\mathrm{t}} \qquad \textbf{Equation 5.11}$$

where,

$$\mathrm{t} = 1.67(y/y_b)^c \qquad \textbf{Equation 5.15}$$

and,

$$c = \frac{5}{\sqrt{x/H_s}} \qquad \textbf{Equation 5.16}$$

(f) Vertical profiles downstream of reattachment were plotted against the log-law distribution for the BFS flow. It was observed that the profiles were described by the log-law after a distance of $x/H_S=27$ downstream of the BFS. The turbulence intensities were also plotted against their respective universal functions, however, these did not compare favourably within the downstream limit of observation. From

the developing profiles, it was expected that u' and w' would compare after a distance of $x/H_S \approx 40$ downstream of the BFS, however, v' was expected to be greater than this.

(g) The turbulence intensities throughout the entire flow field were found to have the relationship $u' > w' > v'$. The ratios of these intensities, with respect to u', however, did alter between different locations in the flow field.

(h) The maximum turbulence intensities observed in the slot shear layer were approximately 2-3 times the initial upstream values. This increased to approximately 3-4 times for the smaller shear zone generated at the top of the FFS.

(i) In general, the influence of a FFS on the flow characteristics downstream of a BFS are limited to a distance of $x/H_S \approx 15$-20 from the BFS. Beyond this, the FFS and BFS can be treated independently.

6.3 RECOMMENDATIONS FOR FUTURE RESEARCH

(a) A method of acquiring accurate 3-component data measurements was achieved using a 1-component LDV system. This may be largely attributed to the ability of the main flume to: provide accurate flow conditions; facilitate various channel geometries; and support laser penetration through both sidewalls and channel bed. These features of the flume make it suitable for use in future investigations. The design and construction of the flume took approximately 18 months in this project, however, data acquisition should commence much earlier in future investigations after only minor modifications and maintenance to the flume.

(b) This project aimed at improving the knowledge of the flow characteristics which develop in open-channel slot flow. The results presented provide much information taken from the mean velocity characteristics, such as the reattachment length, shear layer development, velocity profiles in the recirculation zone, and the relaxation of the flow back to the thin shear layer state. However, the information gained from the instantaneous velocities are restricted to the distribution of the turbulence intensities. An important flow property used to investigate the turbulent nature of flow is the Reynolds shear stress. This property is difficult to measure using a 1-component LDV system, and is normally acquired from 2 and 3-component systems. Although a method does exist for 1-component LDV systems, this requires an additional set of two velocities per measurement point, namely $\overline{u'v'}$ at $\pm 45^{o}$ to the x-direction in the

x-y plane (and similarly for the other two planes $u'w'$ and $v'w'$). To achieve this with a 1-component system would be time consuming, and therefore any such attempt would be restricted to a limited data set. The Reynolds stress distribution is an important property of turbulent flow, and should therefore be considered as an extension to the current investigation.

(c) The current investigation has highlighted that the addition of a FFS within 2-3 step heights downstream of reattachment results in a reduction in the reattachment length. For an A_S=10 and 12.5, it was difficult in some cases to obtain a reattachment point, suggesting that the flow is neither reattached flow (on the slot bed) or skimming type flow over a slot. It would appear that the flow was unstable, flipping between these two conditions. This may be an inherent property of the flow for a FFS close to the point of flow reattachment, however, due to the lack of observations of this phenomena in the current investigation, no conclusive findings can be drawn at this stage.

(d) A feature of BFS and slot flows not presented in this thesis is the fluctuation of the flow caused by the hydrodynamic instability of the free-shear layer and by the interaction of the flow with the flow boundaries. This oscillation of the flow creates vortices (over a wide range of frequencies) which amplify as they convect downstream, prior to dissipating. The production of these vortices can be periodic, and are largely influenced by a basic feedback mechanism (i.e. pressure variations in the recirculation region). This fluctuation of the flow may lead to a variation in the hydrodynamic loading on structures, and therefore, the reduction of this undesirable feature may be required in many engineering problems. Although information on this property of BFS and slot flows exist in the literature (Rubin and McDonald, 1995; Chun and Sung, 1996), much of this information is limited to BFS flow, however, slot flow has received some attention (Ethambabaoglu, 1978). Despite this, more information is required on this particular feature, specifically in relation to the slot geometries presented in this thesis.

(e) The slots used in this study were limited to a BFS and FFS with vertical faces, however, a similar investigation could be undertaken for positive and negative facing slopes (see below), and combinations thereof. This may yield geometries with different flow properties such as hydrodynamic loading, reverse flows, and the generation and dissipation of turbulent energy. This could be beneficial in reducing the hydrodynamic loading on structures, and provide optimum conditions for sediment traps and reducing (or increasing) the rate of bed erosion.

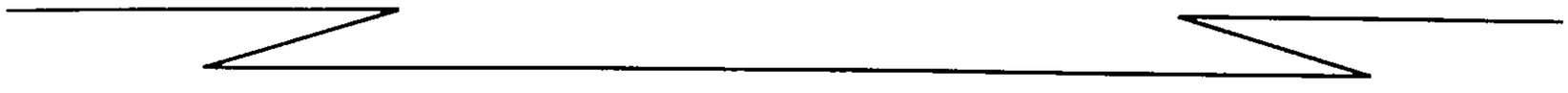

(a) Slot with Negative Facing Slopes

(b) Slot with Positive Facing Slopes

(f) This project was also limited to channel geometries with fixed beds, however, the slot geometries used in this investigation can also occur in mobile beds, both naturally (e.g. floodplain flow) and artificially (e.g. drenched trenches). The flow characteristics which are influenced by the location of the FFS, such as the magnitude of the reverse flow and areas of low velocity, will subsequently influence rates of erosion and deposition in a slot with a mobile granular bed. Although the literature provides information on the sediment processes in dunes and over backward-facing steps with mobile beds, there is limited information on slot flows. It is therefore recommended that a similar investigation is conducted on mobile granular beds, with emphasis on the influence of the location of the FFS. This could also include slots with positive and negative facing slopes (see above), thereby establishing desired geometries for maximum or minimum slope erosion and sediment deposition.

APPENDICES

Appendix A

SNELL'S LAW

APPENDIX A

SNELL'S LAW

When light strikes an interface between two transparent media, different optical phenomena may occur. When the interface is smooth, i.e. when its irregularities are small compared to the light wavelength, the wave is partly reflected and partly transmitted into the second medium where it undergoes refraction. Reflection obeys the law that the incoming, or incident, wave approaching a reflective surface at angle θ_i to the normal will produce a reflected wave at the same angle θ_r. Therefore, the total angle between incident and reflected wave will be $\theta_i + \theta_r$, or $2\theta_i$. With the phenomena of refraction, the incident wave meets the new medium at an angle θ_i to the normal, but alters its direction by an angle θ_b in this new medium. This beam is known as the refracted ray. For the purpose of this investigation, the incident medium is air (denoted by, a), and the refractive medium is water (denoted by, w). According to Snell (1591-1626), this refracted angle θ_w is determined by the law:

$$n_a \sin \theta_a = n_w \sin \theta_w \qquad \text{Equation A-1a}$$

Therefore, $$\sin \theta_w = (n_a/n_w) \sin \theta_a \qquad \text{Equation A-1b}$$

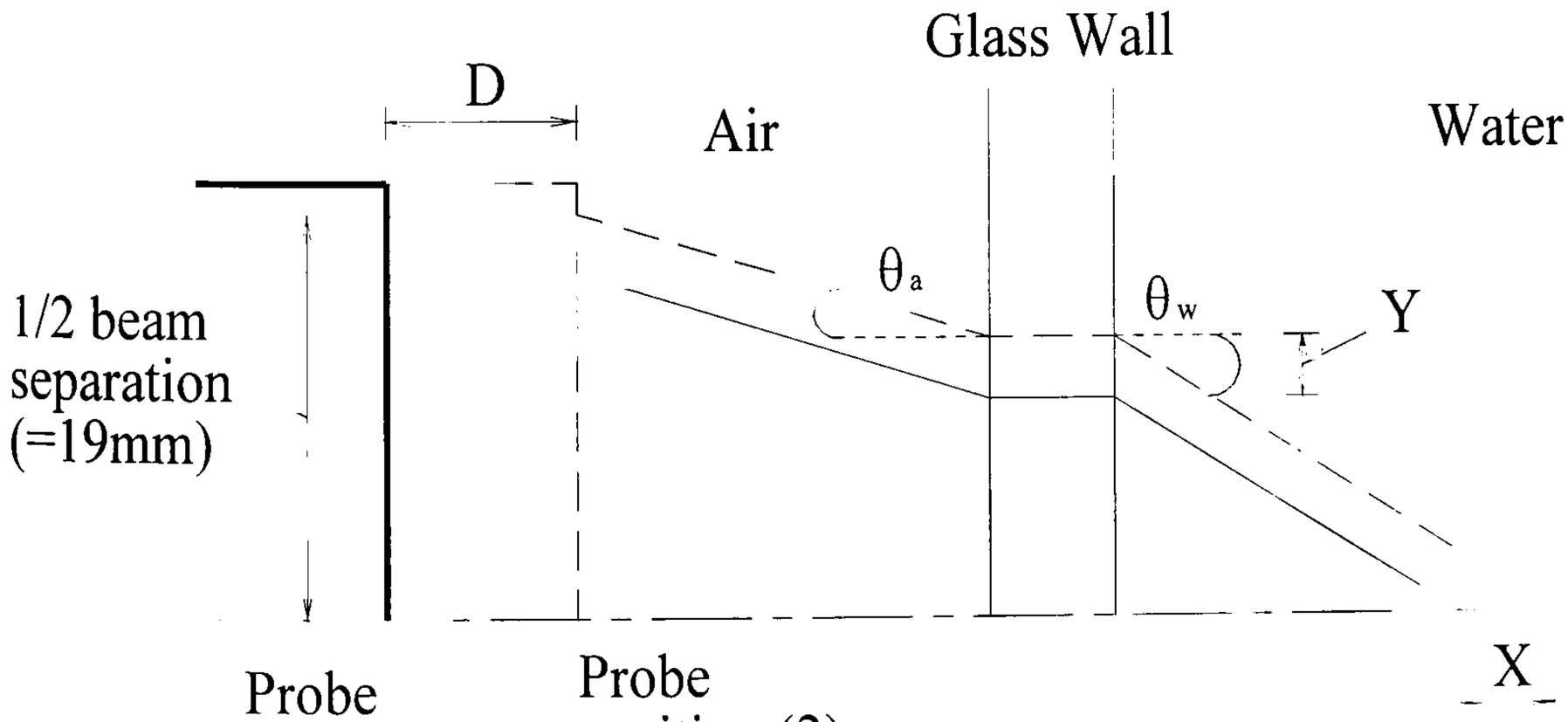

If we consider the above diagram as representing one of the two laser beams emitted from the laser probe, then using Snell's Law we can calculate the position of the laser intersection with respect to movement of the laser probe.

Let,

$$\tan \theta_a = Y/D$$

$$\tan \theta_w = Y/X$$

Then,

$$D.\tan \theta_a = Y = X.\tan \theta_w$$

$$\Rightarrow \quad D.(\sin \theta_a / \cos \theta_a) = X.(\sin \theta_w / \cos \theta_w)$$

$$\Rightarrow \quad D/X = (\sin \theta_w \cos \theta_a) / (\sin \theta_a \cos \theta_w)$$

From Snell's Law, equation A-1b, then

$$\sin \theta_a = (n_w / n_a)\sin \theta_w$$

$$\Rightarrow \quad D/X = (\sin \theta_w \cos \theta_a) / ((n_w / n_a)\sin \theta_w \cos \theta_w)$$

$$\Rightarrow \quad (D/X)(n_w / n_a) = \cos \theta_a / \cos \theta_w$$

$$\Rightarrow \quad ((D/X)(n_w / n_a))^2 = (\cos \theta_a / \cos \theta_w)^2 = \cos \theta_a^2 / (1- \sin \theta_w)^2$$

$$\Rightarrow \quad ((D/X)(n_w / n_a))^2 = \cos \theta_a^2 / (1- (n_a^2 \sin \theta_a^2 / n_w^2))$$

$$\Rightarrow \quad D^2/X^2 = \cos \theta_a^2 / ((n_w^2 / n_a^2) - \sin \theta_a^2)$$

$$\Rightarrow \quad D/X = \cos \theta_a / \sqrt{((n_w^2 / n_a^2) - \sin \theta_a^2)} \qquad \text{Equation A-2}$$

θ_a is obtained from the half-beam separation and focal length, whereby:

$\theta_{a1} = 6.772^o$, from $\tan^{-1} \theta_a$= (half beam separation)/(focal length in air) = 19/160

$\theta_{a2} = 2.719^{o}$, from $\tan^{-1} \theta_a$= (half beam separation)/(focal length in air) = 19/399.8

and, $n_w = 1.33$

$n_a = 1.00$

Therefore, solving the right hand side of equation A-2 we obtain:

For $lens_1$ (f.l. = 160mm), $D = 0.7496 \, . \, X$

For $lens_2$ (f.l. = 399.8mm), $D = 0.7516 \, . \, X$

It was assumed that for both of the lens' the relationship between probe movement, D, and intersection, X, can be described by the expression,

$$D = 0.75 \, X \qquad \text{Equation A-3}$$

Appendix B

FREE-SURFACE AND CHANNEL BED LIMITATION ON LASER PENETRATION

APPENDIX B

FREE-SURFACE AND CHANNEL BED LIMITATION ON LASER PENETRATION

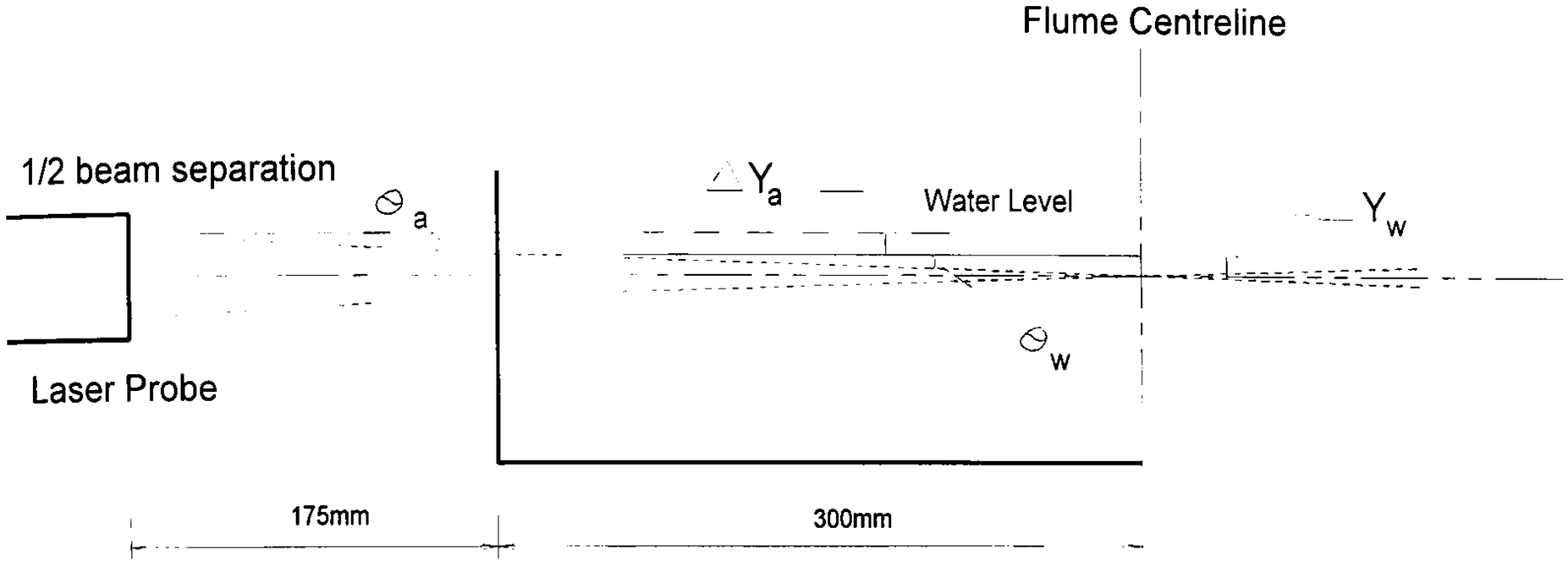

Let maximum penetration in flume = distance to centreline = 300mm

Using the 400mm lens for this penetration, the distance of the probe to the flume sidewall:

= focal length - (penetration x refraction correction)

= 400 - (300 x 0.75)

= 175mm

From calculations, $\theta_a = 2.719^o$

$\theta_w = 2.045^o$

Therefore, just prior to the upper laser-beam intercepting the free-surface (when the probe is 175mm from the sidewall), the control volume will occur at a distance ΔY_w below the free-surface:

$$\Delta Y_w = \tan \theta_w \, . \, X = \tan 2.045 \times 300 = 10.7\text{mm}$$

Similarly, $\Delta Y_a = \tan \theta_a \, . \, X = \tan 2.719 \times 175 = 8.3\text{mm}$

where, $\Delta Y_a + \Delta Y_w = 8.3 + 10.7 = 19\text{mm} = 1/2$ beam separation

Therefore, when acquiring the *v*-component of velocity in a vertical profile at the centreline of the flume, the first and last 10.7mm of the profile cannot be measured due to physical limitations. This reduces the range of measurements for the *v*-component by 21.4mm at the channel centreline.

Appendix C

EXAMPLE FILES FROM FLOWARE Ver3.2

APPENDIX C

EXAMPLE FILES FROM FLOWARE Ver3.2

This appendix contains examples of the files and graphs used from the LDV software package Floware Ver 3.2. This includes:

(1) MOMENT FILE: This file summarises the statistical information gained from a series of velocity files (see next). This normally corresponds to a velocity profile (or traverse) through the flow depth.

(2) VELOCITY FILE: This file contains the instantaneous velocities of a single point measurement.

(3) TIME SERIES: This graphically illustrates (chronologically) the instantaneous velocities obtained from the velocity file.

(4) HISTOGRAM: This indicates the number of counts that each velocity occurs in the velocity file. It can be seen that this graph displays a Gaussian distribution, as expected from this flow type.

1. MOMENT FILE

Parameter file : FLWCAL5.PAR
Data file : FLWCAL5.MOM
File date : 5/15/99
File time : 19:23:13
Number of Traverse Points : 15
Dimension : 1-D
Encoder : Yes

PT.	X (mm)	Y (mm)	Z (mm)	U Mean (m/s)	U RMS (m/s)	U Skew	U Flat %	U Turb
0	1.000000	0.000000	0.000000	0.297470	0.009820	-0.432166	3.782668	3.301269
1	2.000000	0.000000	0.000000	0.296013	0.010305	-0.247965	2.864876	3.481141
2	3.000000	0.000000	0.000000	0.296879	0.011005	-0.284330	3.149098	3.706755
3	4.000000	0.000000	0.000000	0.298725	0.012835	-0.291687	3.714743	4.296592
4	5.000000	0.000000	0.000000	0.296370	0.013816	-0.535892	3.834450	4.661707
5	6.000000	0.000000	0.000000	0.294490	0.013744	-0.594210	3.736161	4.667025
6	7.000000	0.000000	0.000000	0.285277	0.016936	-0.786789	3.611692	5.936623
7	8.000000	0.000000	0.000000	0.279228	0.021144	-0.562269	3.124800	7.572272
8	9.000000	0.000000	0.000000	0.279656	0.017956	-0.474939	2.942693	6.420618
9	10.000000	0.000000	0.000000	0.281034	0.019906	-0.556734	3.207986	7.083261
10	11.000000	0.000000	0.000000	0.256497	0.022382	-0.144385	2.555100	8.726007
11	12.000000	0.000000	0.000000	0.258162	0.024598	-0.271050	2.453387	9.528049
12	13.000000	0.000000	0.000000	0.222826	0.029032	0.033595	2.778995	13.028893
13	14.000000	0.000000	0.000000	0.182740	0.032058	-0.337145	3.265754	17.543102
14	14.000000	0.000000	0.000000	0.182740	0.032058	-0.337145	3.265754	17.543102

2. VELOCITY FILE

NB: Original file contains 4000 data samples - reduced to 80 samples for brevity

Parameter file : <FLWCAL5.PAR>
Data file : <FLWCAL5V.00C>
File date : <1/25/96>
File time : <18:2:57>
Log > :<>
Dimension : <1-D>
Encoder : <yes>
A/D board 1 : <No>
A/D board 2 : <No>

Attempted Samples : <4000>
Validated Samples : <4000>
Data rate : <0.075772> kHz
Elapsed time : <52.789928> sec
Traverse x-pos : <13.000000> mm
Traverse y-pos : <0.000000> mm
Traverse z-pos : <0.000000> mm

PT.	STAT	A.T.(sec)	T.T.(msec)	UVEL(m/s)	ENCODER
0	63	0.004554	0.204400	0.209692	0.004554
1	63	0.007774	0.255500	0.204515	0.007774
2	63	0.022526	0.357700	0.214130	0.022526
3	63	0.048654	0.204400	0.234101	0.048654
4	63	0.055646	0.255500	0.243716	0.055646
5	63	0.056077	0.153300	0.238539	0.056077
6	63	0.078457	0.408800	0.209692	0.078457
7	63	0.088376	0.204400	0.190461	0.088376
8	63	0.093278	0.204400	0.190461	0.093278
9	63	0.115769	0.204400	0.190461	0.115769
10	63	0.131845	0.255500	0.190461	0.131845
11	63	0.137027	0.255500	0.180846	0.137027
12	63	0.139320	0.306600	0.180846	0.139320
13	63	0.155107	0.204400	0.190461	0.155107
14	63	0.179964	0.306600	0.194899	0.179964
15	63	0.195979	0.204400	0.214130	0.195979
16	63	0.244222	0.459900	0.180846	0.244222
17	63	0.252528	0.562100	0.171230	0.252528
18	63	0.254860	0.255500	0.176408	0.254860
19	63	0.266730	0.459900	0.180846	0.266730
20	63	0.301342	0.255500	0.190461	0.301342
21	63	0.307289	0.306600	0.190461	0.307289
22	63	0.329027	0.306600	0.224485	0.329027
23	63	0.335037	0.255500	0.214130	0.335037
24	63	0.347105	0.408800	0.219308	0.347105
25	63	0.369435	0.306600	0.214130	0.369435
26	63	0.375108	0.306600	0.228923	0.375108
27	63	0.375420	0.204400	0.228923	0.375420
28	63	0.389729	0.306600	0.224485	0.389729
29	63	0.427199	0.306600	0.204515	0.427199

30	63	0.445336	0.562100	0.200077	0.445336
31	63	0.448486	0.306600	0.194899	0.448486
32	63	0.450315	0.255500	0.204515	0.450315
33	63	0.489351	0.153300	0.204515	0.489351
34	63	0.492652	0.408800	0.190461	0.492652
35	63	0.529807	0.306600	0.171230	0.529807
36	63	0.539030	0.408800	0.171230	0.539030
37	63	0.581302	0.357700	0.204515	0.581302
38	63	0.588132	0.255500	0.204515	0.588132
39	63	0.591977	0.255500	0.209692	0.591977
40	63	0.604006	0.204400	0.219308	0.604006

----------Points 41-3960 deleted for illustrative purposes----------

3961	63	52.473686	0.204400	0.262948	52.473682
3962	63	52.482868	0.255500	0.258510	52.482868
3963	63	52.491756	0.204400	0.262948	52.491756
3964	63	52.495323	0.153300	0.248154	52.495323
3965	63	52.501698	0.102200	0.253332	52.501698
3966	63	52.508720	0.204400	0.248154	52.508720
3967	63	52.511997	0.306600	0.258510	52.512001
3968	63	52.512566	0.153300	0.258510	52.512569
3969	63	52.518978	0.102200	0.262948	52.518978
3970	63	52.520016	0.204400	0.253332	52.520016
3971	63	52.523216	0.153300	0.262948	52.523216
3972	63	52.524651	0.255500	0.253332	52.524651
3973	63	52.530212	0.255500	0.248154	52.530216
3974	63	52.550995	0.306600	0.238539	52.550991
3975	63	52.553928	0.204400	0.243716	52.553928
3976	63	52.564079	0.306600	0.243716	52.564079
3977	63	52.570667	0.357700	0.238539	52.570663
3978	63	52.571213	0.306600	0.243716	52.571213
3979	63	52.573635	0.153300	0.234101	52.573635
3980	63	52.576099	0.255500	0.238539	52.576096
3981	63	52.579163	0.255500	0.238539	52.579163
3982	63	52.584141	0.255500	0.243716	52.584141
3983	63	52.596626	0.255500	0.238539	52.596626
3984	63	52.607868	0.306600	0.253332	52.607868
3985	63	52.611248	0.153300	0.268125	52.611248
3986	63	52.613083	0.153300	0.262948	52.613079
3987	63	52.627209	0.153300	0.272563	52.627209
3988	63	52.643642	0.204400	0.282918	52.643639
3989	63	52.643940	0.204400	0.277741	52.643940
3990	63	52.649582	0.204400	0.277741	52.649586
3991	63	52.656841	0.306600	0.272563	52.656841
3992	63	52.657631	0.153300	0.268125	52.657631
3993	63	52.702991	0.153300	0.234101	52.702991
3994	63	52.728065	0.204400	0.224485	52.728065
3995	63	52.749863	0.255500	0.243716	52.749863
3996	63	52.760952	0.153300	0.243716	52.760952
3997	63	52.768803	0.153300	0.248154	52.768799
3998	63	52.787861	0.153300	0.282918	52.787861
3999	63	52.789928	0.204400	0.282918	52.789928

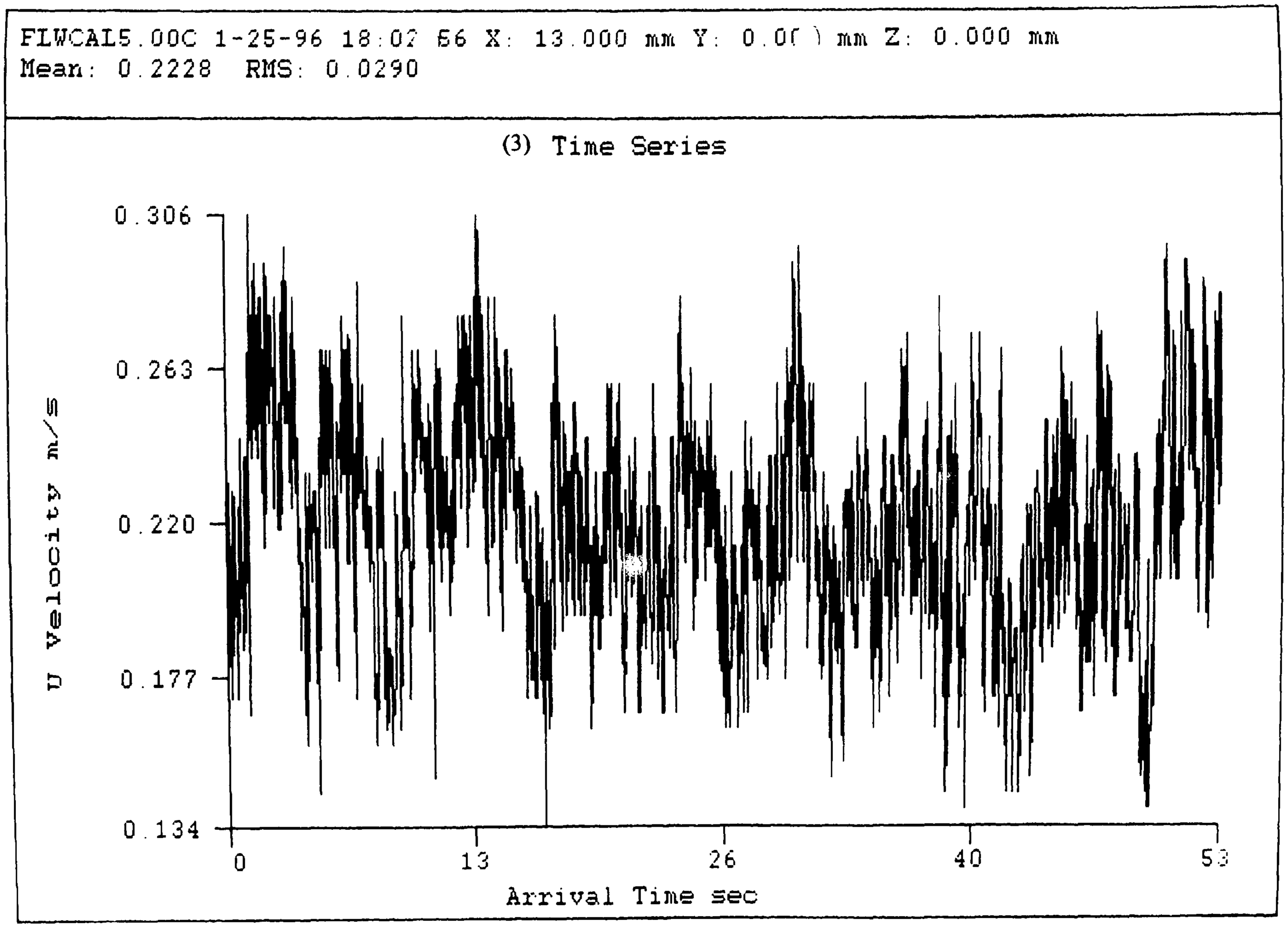
FLWCAL5.00C 1-25-96 18:07 56 X: 13.000 mm Y: 0.000 mm Z: 0.000 mm
Mean: 0.2228 RMS: 0.0290
(3) Time Series
0.306
0.263
0.220
0.177
0.134
U Velocity m/s
0
13
26
40
53
Arrival Time sec

FLWCAL5.00C 1-25-96 10.02.56 X. 13.000 mm Y. 0.000 mm Z. 0.000 mm
Mean. 0.2220 RMS. 0.0290 Skew. 0.0336 Flat. 2.7790

(4) Histogram

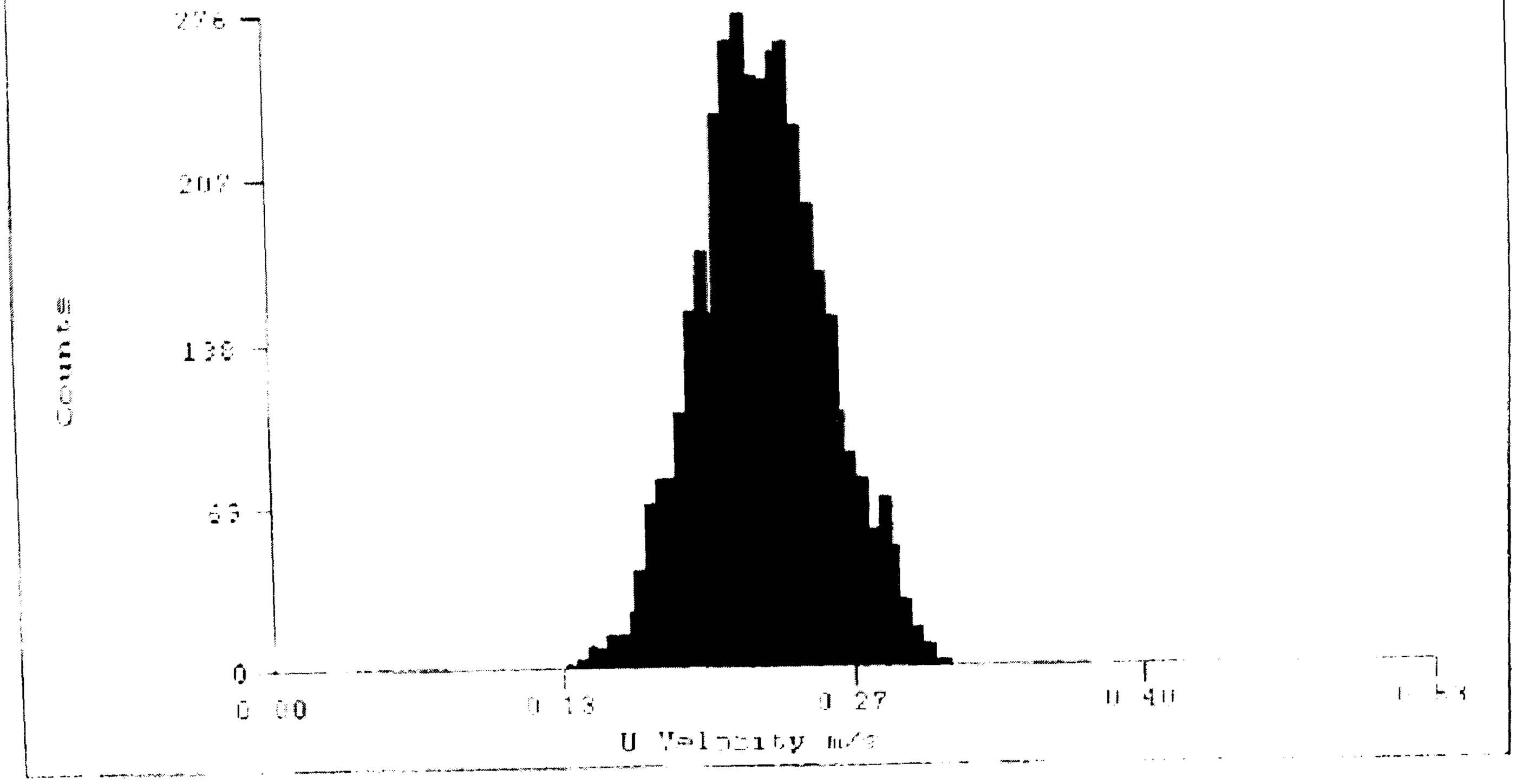

Appendix D

LASER PROBE SUPPORT-TRAVERSE

APPENDIX D

LASER PROBE SUPPORT-TRAVERSE

The support-traverse consisted of several moveable plates, each of which could be moved independently allowing the laser probe (or volume) to be accurately positioned within the flow field. The laser probe housing could be adjusted through 90^{o}, allowing the laser probe to be aligned vertically for lateral measurements. An additional supporting cup (not illustrated here, see figure 3.2) was installed for this alignment.

The support-traverse was supported on a series of supporting frames (see figure 3.3), depending on the location of the support-traverse around the flume. Many measurements could be obtained without relocation of the support-traverse, and all areas of the flow field could be measured with this system.

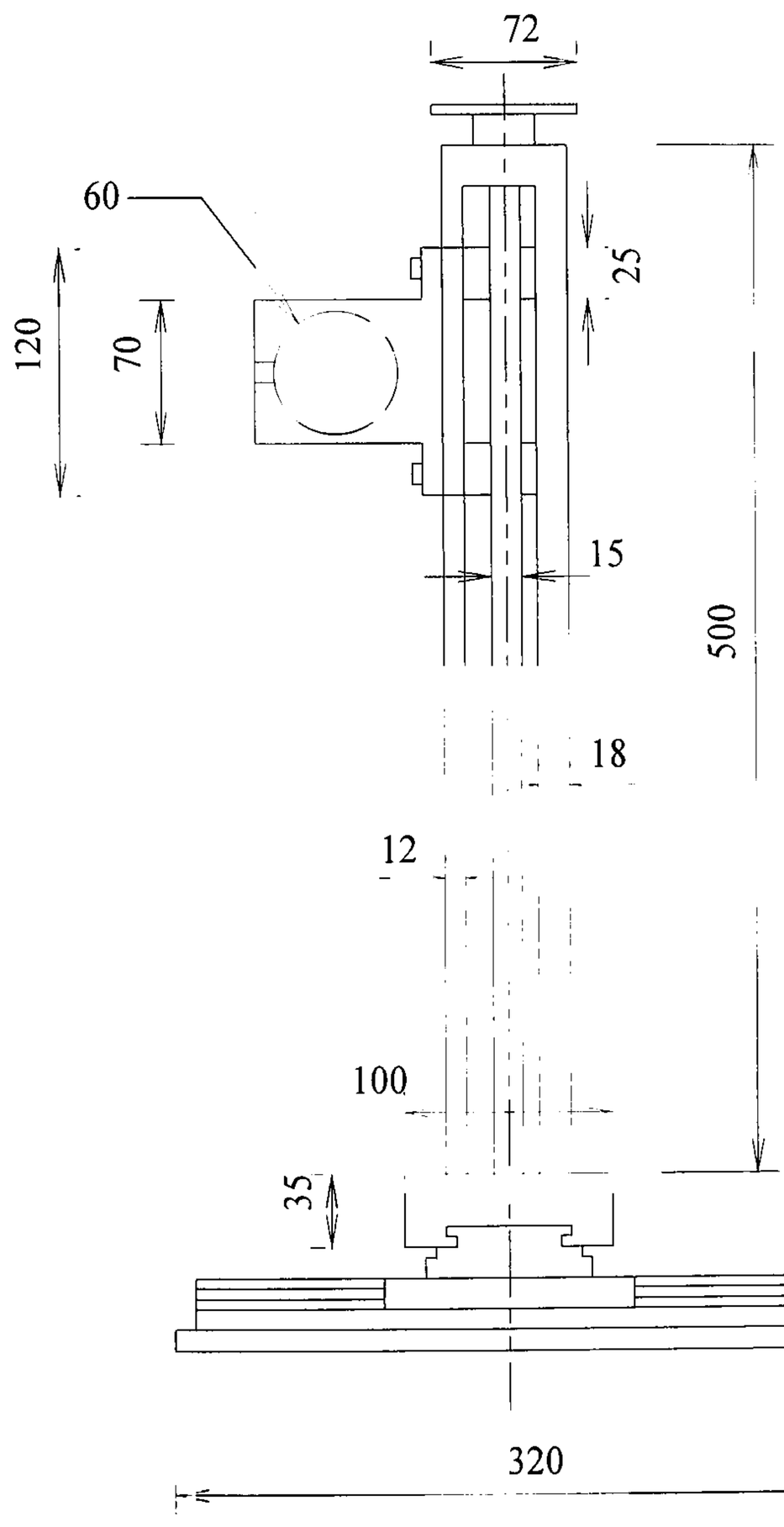

ELEVATION

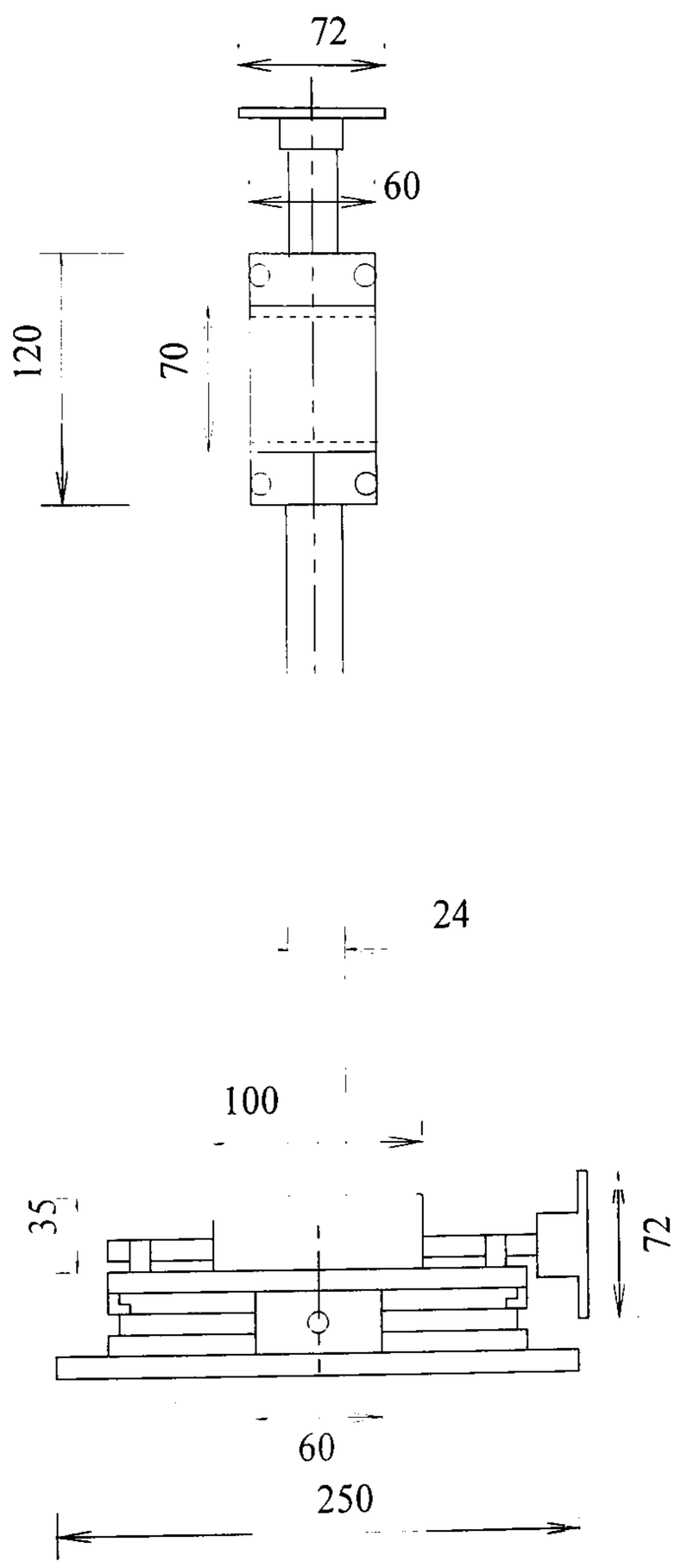

END ELEVATION

(All Dimensions in mm)

Appendix E

MAIN FLUME DESIGN DETAILS

APPENDIX E

MAIN FLUME DESIGN DETAILS

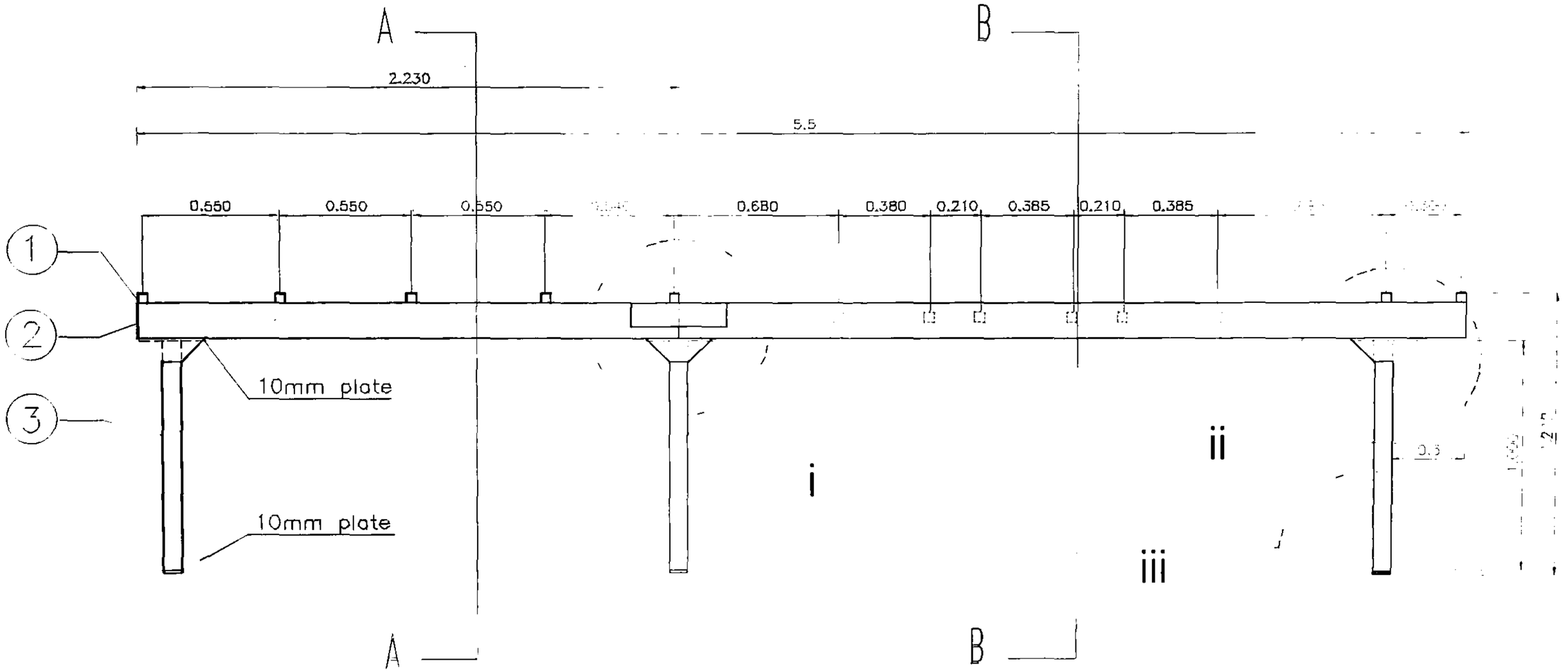

ELEVATION

PROJECT: Flume Sub-Frame
DRAWING TITLE: Elevation
Drawing 1 of 6
DRAWN BY: Darren P. Keogh
DIMENSIONS: metres
SCALE:
DATE: 8/6/94
NOTES: Sections - 1. - 40x40x3 SHS 2. - 152x76 RSC 3. - 75x75x3.2 SHS See drawing nos. 4, 5 and 6 for details i, ii and iii

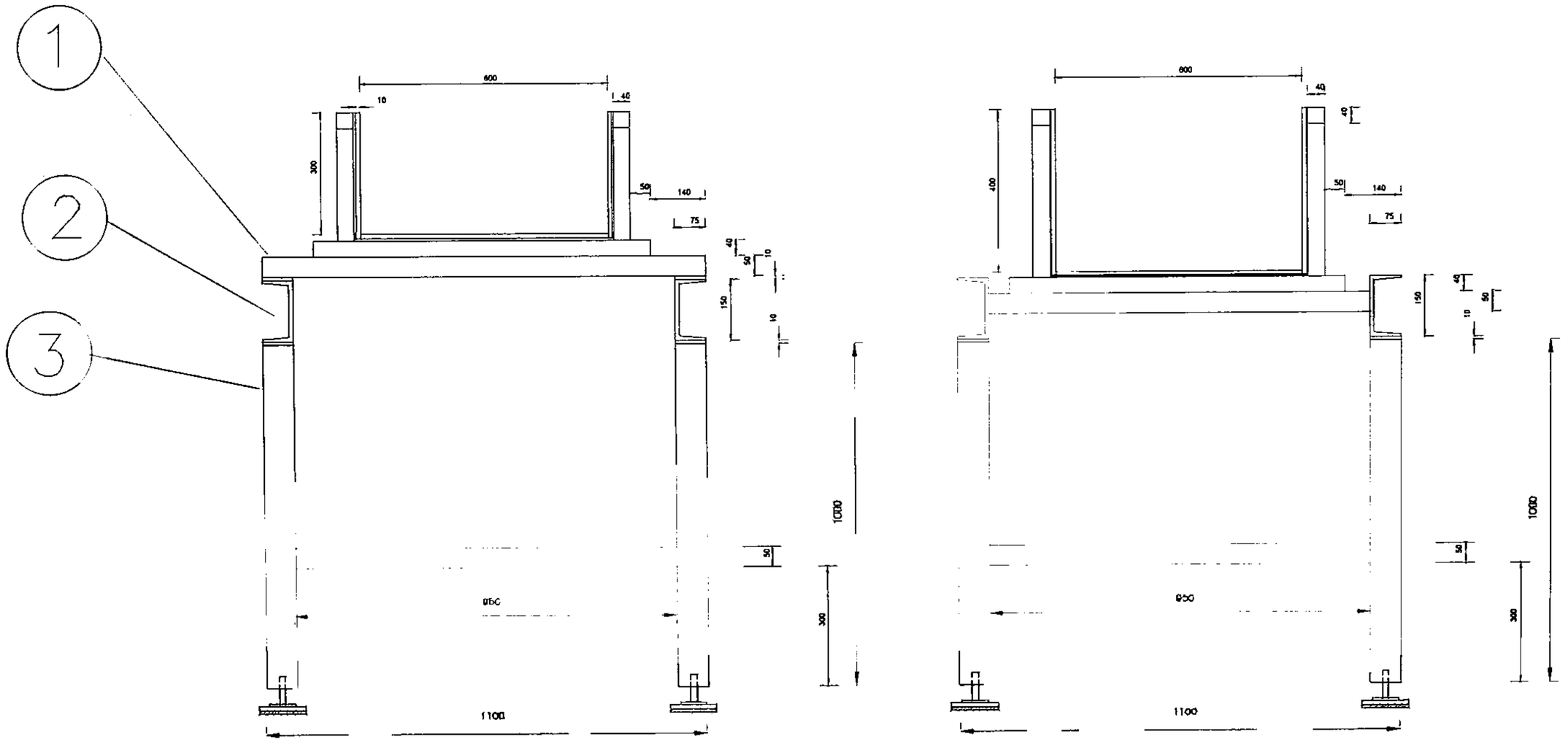

END ELEVATION
SECTION A–A

END ELEVATION
SECTION B–B

PROJECT:
Flume Sub-Frame

DRAWING TITLE:
End Elevations A,B

Drawing 2 of 6

DRAWN BY:
Darren P. Keogh

DIMENSIONS: metres

SCALE:

DATE: 8/6/94

NOTES:

Sections -
1. - 40x40x3 SHS
2. - 152x76 RSC
3. - 75x75x3.2 SHS

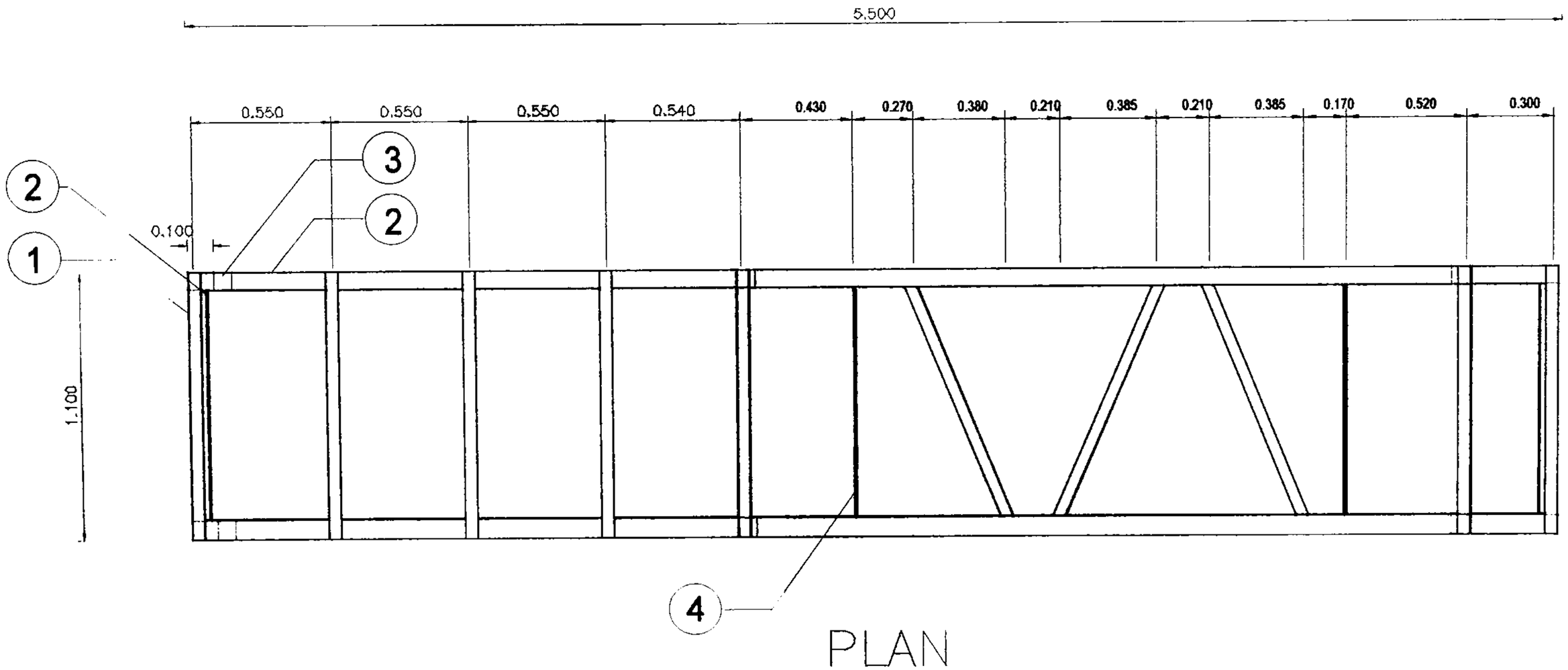

PLAN

PROJECT:
Flume Sub-Frame

DRAWING TITLE:
Plan

Drawing 3 of 6

DRAWN BY:
Darren P. Keogh

DIMENSIONS: metres

SCALE:

DATE: 8/6/94

NOTES:

Sections -
1. - 40x40x3 SHS
2. - 152x76 RSC
3. - 75x75x3.2 SHS
4. - 10x10 Steel Bar

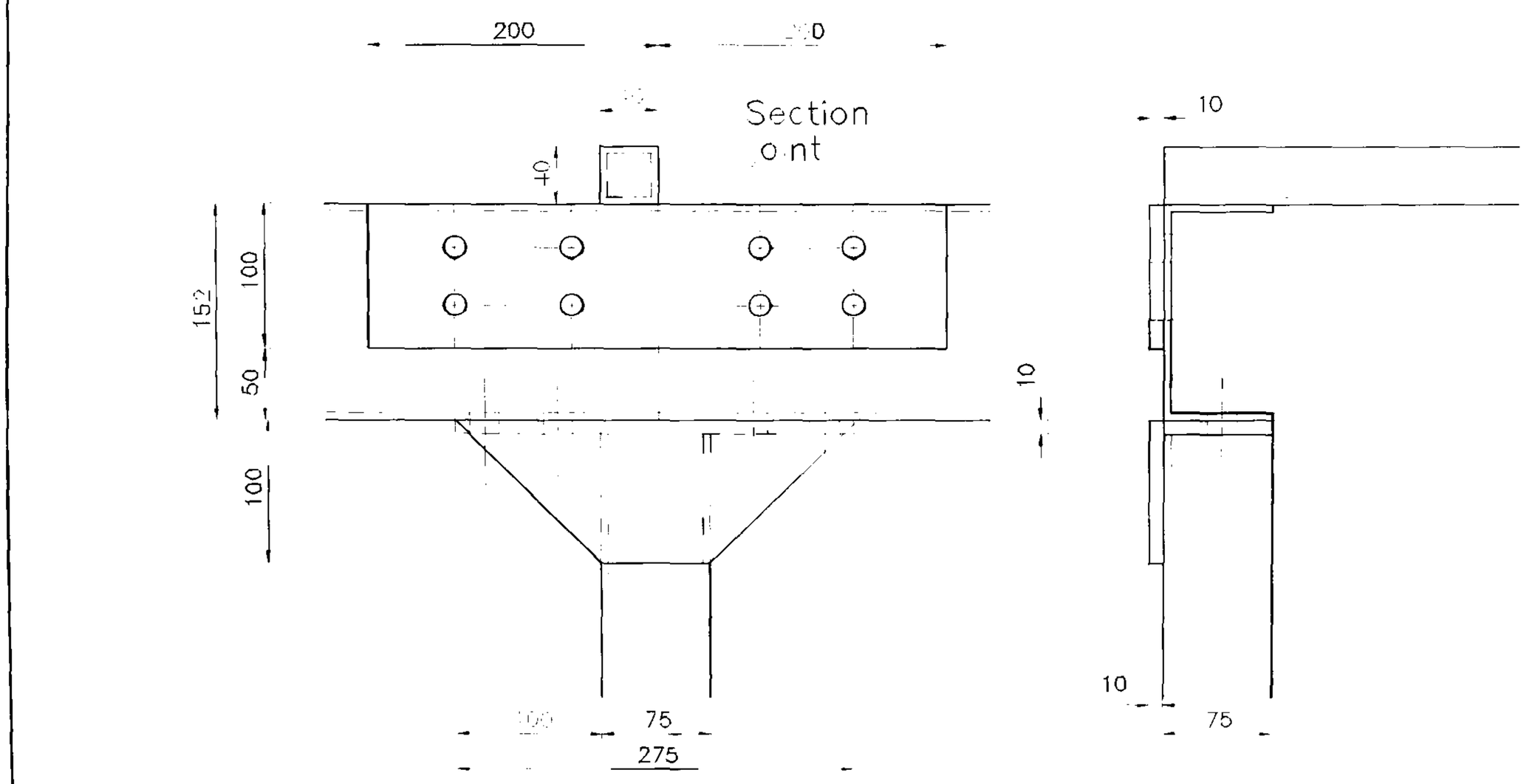

ELEVATION

END ELEVATION

PROJECT: Flume Sub-Frame
DRAWING TITLE: DETAIL (i) - Centre Gusset
DRAWING 4 OF 6
DRAWN BY: Darren P. Keogh
DIMENSIONS: mm
SCALE:
DATE: 8/6/94
NOTES: All bolt holes 12mm diameter Location of bolt holes at approximately that in drawing.

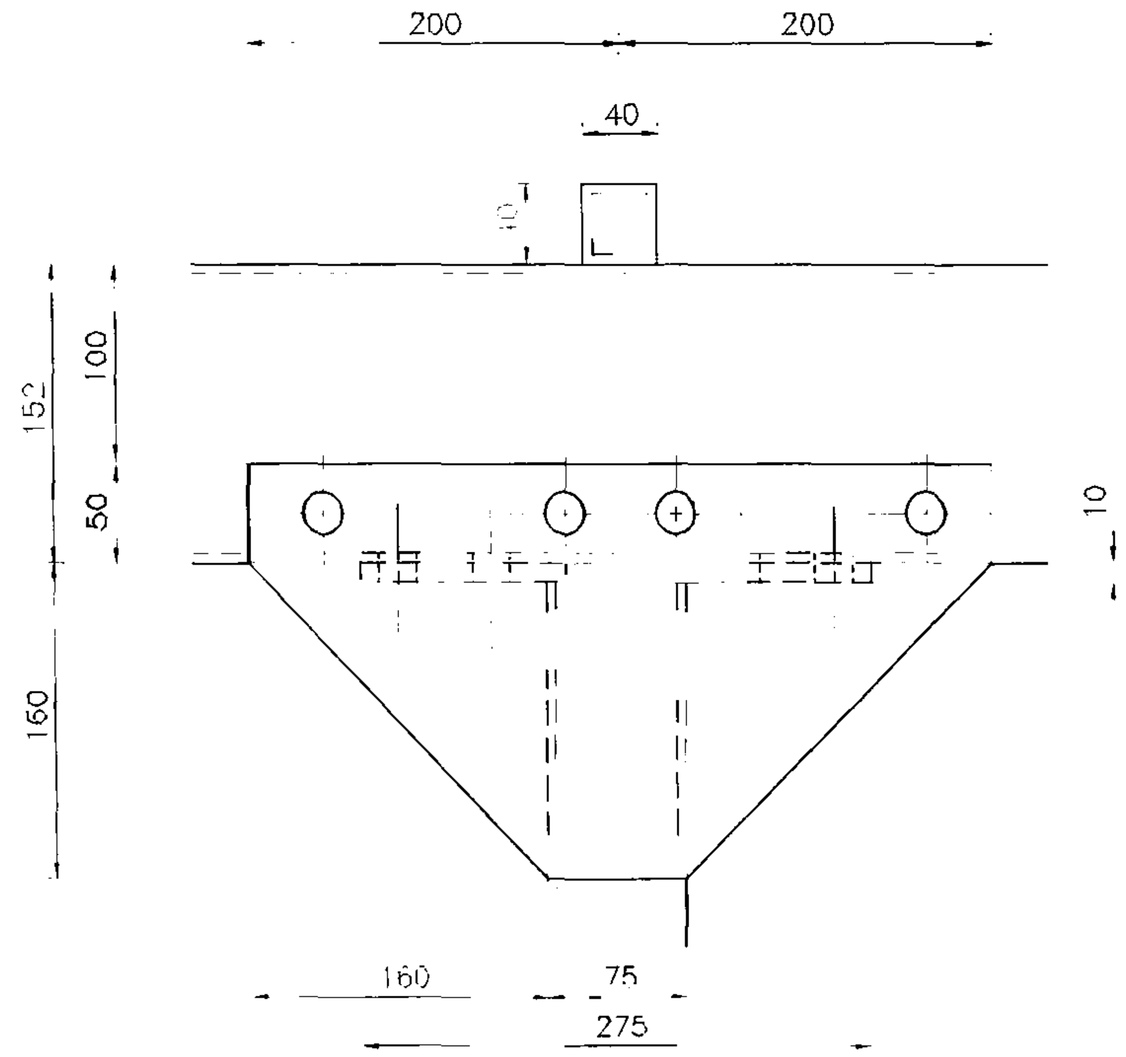

ELEVATION

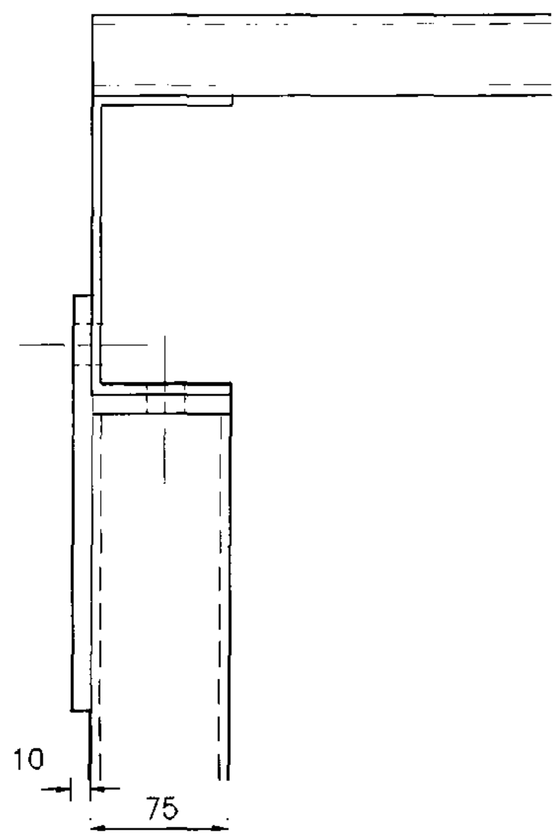

END ELEVATION

PROJECT: Flume Sub-Frame
DRAWING TITLE: DETAIL (i)
DRAWING 4 OF 6
DRAWN BY: Darren P. Keogh
DIMENSIONS: mm
SCALE:
DATE: 8/6/94
NOTES: All bolt holes 20mm diameter. Locations of bolt holes to be similar to drawing.

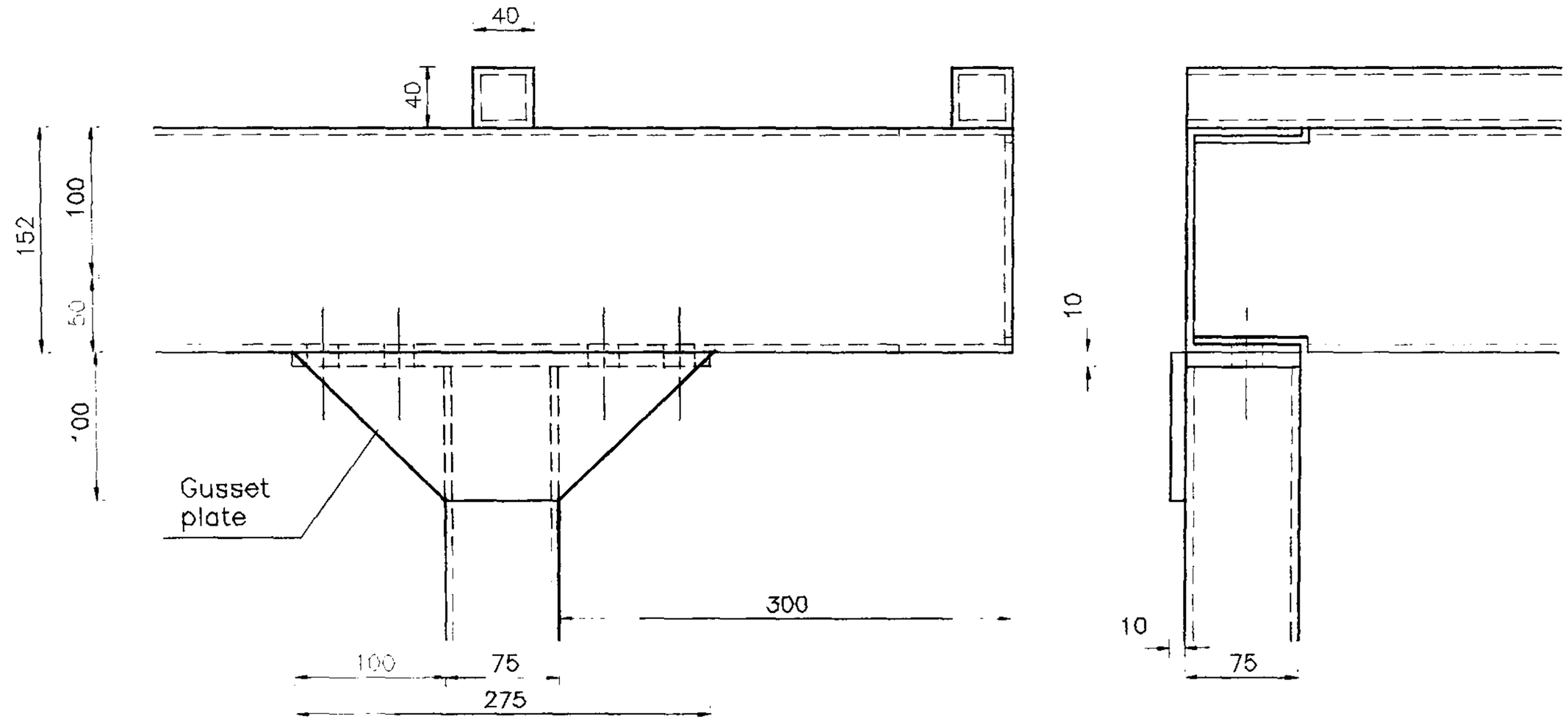

ELEVATION

END ELEVATION

PROJECT:	Flume Sub-Frame
DRAWING TITLE:	DETAIL (ii) - End Gusset
	DRAWING 5 of 6
DRAWN BY:	Darren P. Keogh
DIMENSIONS:	mm
SCALE:	
DATE:	8/6/94

NOTES:

All bolt holes 12 mm diameter.

Locations of bolt holes to be similar to drawing.

152x76 RSC cross-member is to be cut and welded to fit longitudinal members.

Gusset plate used to connect longitudinal members to legs. Welded to legs and bolted to long. member.

4 gussets (type ii) used in frame
2 gussets (type i) used in frame

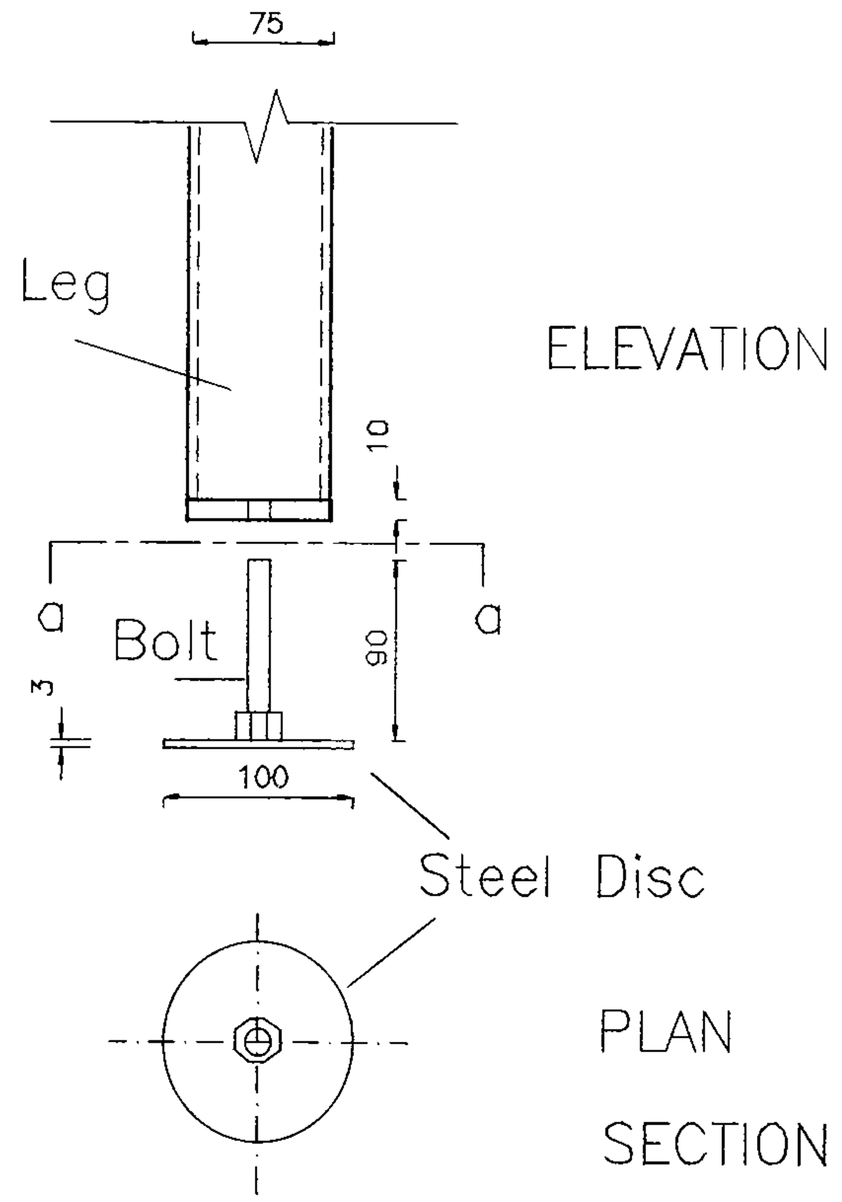

PROJECT:	Flume Sub-Frame
DRAWING TITLE:	DETAIL (iii) - Foot Connection
DRAWING 6 OF 6	
DRAWN BY:	Darren P. Keogh
DIMENSIONS:	mm
SCALE:	
DATE:	8/6/94

NOTES:

10mm thick steel plate welded to base of leg

Bolt, nut and disc welded together.

Appendix F

FLOWMETER MANUFACTURERS CERTIFICATE OF CALIBRATION

CERTIFICATE OF CALIBRATION.

FISCHER & PORTER

Customer Details

Primary Serial No. : 9503L1006A1
Secondary Serial No. :N/A
Customer : NAPIER UNIVERSITY EDINBURGH
Model No. PRI : L10DX3311AAA17C1A2BA1112*OACAA11B1
Model No. SEC : N/A
Customer Tag No(s) : N/A

Technical Data

Size : 150 mm
Liner : UKWFBS RUBBER
Electrode Material : 316 STAINLESS/STEEL
Flange : ANSI 150 M/S
METER FACTOR : 1000 l\min\m\sec
Supply Volts : 240V AC
Current : .05 A
Excitation Frequency : 6.25 Hz
K-Factor : 2.614286
Volts (K2 - 3a) : 183 mV
Reference Volts (I6 - 3a) : 70 mV
System Zero : -.18 Hz
Analogue Output : 4-20 mA
Scaled Pulse / Datalink : N/A

Calibration Data

Reference Meter Serial No. PRI : REF-11
Reference Meter Serial No. SEC : SE 51
Test Flow Rate (MAX) : 9000 (Litres / min)
Rig Ident : Rig 2 : Traceability : N.A.M.A.S. lab 0031.
Test fluid : Water.
Meter under test stated accuracy :

Customer Setting Details.

Flowrate 0 - 50 LT/SEC, Pulse Setting N/A
Calibrated by : J.MORRIS
Date : 03: April :1995 TIME : 09:20:52

Test no.	Temp deg C	Time Secs	Flowrate(%)	Volume (Litres) Ref.	Test	Diff.	Rate Error(%)
1	20.2	100	95.680	14352.00	14370.00	18.00	0.1254
2	20.3	100	77.519	11627.90	11658.90	31.00	0.2666
3	20.4	100	52.806	7920.88	7948.58	27.70	0.3497
4	20.5	100	26.471	3970.62	3977.84	7.22	0.1818

Calibrator's Signature :.....

Q.C. Dept.:.....

FP/QAR/14.03. Issue No 1 Jan 1992.

Certificate No. FM 20896
STAT 606

REGISTERED NUMBER: 457 068 (ENGLAND)
FISCHER & PORTER LTD · WORKINGTON · CUMBRIA · ENGLAND CA14 5DS
Telephone: 01946 830 611 · Fax: 01946 832 661

REFERENCES

ABBOT, D. E. and KLINE, S. J. (1962).
Experimental investigation of subsonic turbulent flow over single and double backward facing steps,
Journal of Basic Engineering, ASCE, 84, pp 317-325.

ACKERS, P. (1992).
Hydraulic design of two-stage channels.
Journal of Water , Maritime and Energy, Proc. ICE, 96, Dec., pp247-257.

ADDISON, P.S., CURRIE, J.I., LOW, D.J. and McCANN, J.M. (1999a - *in press*).
An integrated approach to modelling traffic pollution in the urban environment.
Traffic Engineering Control.

ADDISON, P.S., McCANN, J.M., LOW, D.J. and CURRIE, J.I. (1999b).
An integrated approach to Street Canyon Pollution Modelling.
Urban Air Quality: Measurement, Modelling and Management,
2nd International Conference, Madrid.

ALFRINK, B.J. (1982).
Value of refined turbulence modelling for the flow over a trench.
Proceedings Symposium on Refined Modelling of Flows.

ALFRINK, B.J. and VAN RIJN, L.C. (1983).
Two-equation turbulence model for flow in trenches.
Journal of Professional Issues in Engineering, Vol.109, No. 3, July, ASCE, pp941-958.

ALLERBORN, N., NANDAKUMAR, K., RASZILLIER, H. and DURST, F. (1997).
Further contributions on the two-dimensional flow in a sudden expansion.
Journal of Fluid Mechanics, Vol.330, pp169-188.

AMANO, R.S. and GOEL, P. (1985).
Computations of turbulent flow beyond backward-facing steps using Reynolds-stress closure.
Journal of American Institute of Aeronautics and Astronautics, Vol.23, No.9, pp 1356-1361.

ARMALY, B. F., DURST, F., PEREIRA, J. C. F. and SCHONUNG, B. (1983).
Experimental and theoretical investigation of a backward-facing step flow.
Journal of Fluid Mechanics, Vol. 127, pp 473-496.

ARNELL, N.W. (1992).
Impacts of climatic change on river flow regimes in the UK.
Journal of the Institute of Water and Environmental Management, Vol.6, August.

BABARUTSI, S., GANOULIS, J. and CHU, V.H. (1989).
Experimental investigation of shallow recirculating flows.
Journal of Hydraulic Engineering, ASCE, Vol.115, No.7, July, pp 906-924.

BAKER, G.R., BARKER, S.J., BOFAH, K.K. and SAFFMAN, P.G. (1974).
Laser anemometer measurements of trailing vortices in water.
Journal of Fluid Mechanics, Vol. 65, Part 2, pp 325-336.

BARTON, I.E. (1995).
A numerical study of flow over a confined backward-facing step.
International Journal for Numerical Methods in Fluids, Vol. 21, pp653-665.

BASARA, B. and YOUNIS, B. A. (1995)
Prediction of turbulent flows in dredged trenches.
Journal of Hydraulic Research, IAHR, Vol. 33, No. 6, pp 813-824.

BATCHELOR, G.K. (1950).
Note on free turbulent flows, with special reference to the two dimensional wake.
Journal of Aeronautical Science, Vol. 17, p441-463.

BAYAZIT, M. (1976).
Free surface flow in a channel of large relative roughness.
Journal of Hydraulic Research, IAHR, Vol. 14, No. 2, pp 115-126.

BAZIN, H. E. (1865).
Recherches Hydrauliques, Memoires presentes par divers savants.
Science Mathematiques et physiques, Series 2, Vol. 19, Paris, 1865.

BERBEE, J. G. and ELLZEY, J. L. (1989).
The effect of aspect ratio on the flow over a rearward-facing step.
Experiments in Fluids, Vol. 7, pp447-452.

BERGELES, G. and ATHANASSIADIS, N. (1983).
The flow past a surface-mounted obstacle.
Journal of Fluids Engineering, ASME, Vol. 105, pp 461-463.

BETTS, P. L. (1972).
Self induced oscillations in an open water-channel with slotted walls.
Journal of Fluid Mechanics, Vol. 55, part 3, pp 401-417.

BHATTACHARJEE, S., SCHEELKE, B. and TROUTT, T.R. (1986).
Modification of vortex interactions in a reattaching separated flow.
AIAA Journal, Vol. 24, No. 4, pp623-629.

BLINCO, P.H. and PARTHENIADES, E. (1971).
Turbulence characteristics in free surface flows over smooth and rough boundaries.
Journal of Hydraulic Research, IAHR, Vol. 9, No. 1, pp 43-71.

BOYLE, D. R. and GOLAY, M. W. (1983)
Measurements of a recirculating, two-dimensional, turbulent flow and comparison to turbulence model predictions. I: Steady state case.
Journal of Fluids Engineering, ASME, Vol. 105, pp 439-446.

BOYLE, D. R. and GOLAY, M. W. (1983)
Measurements of a recirculating, two-dimensional, turbulent flow and comparison to turbulence model predictions. II: Transient case.
Journal of Fluids Engineering, ASME, Vol. 105, pp 447-460.

BRADSHAW, P. and GALEA, P.V. (1967).
Step-indiced separation of a turbulent boundary layer in incompressible flow.
Journal of Fluid Mechanics, Vol. 27, Part I, pp 111-130.

BRADSHAW, P. and WONG, F. Y. F. (1972).
The reattachment and relaxation of a turbulent shear layer.
Journal of Fluid Mechanics, Vol. 52, pp 113-135.

CA, V.T., ASAEDA, T., ITO, M. and ARMFIELD, S. (1995).
Characteristics of wind field in a street canyon.
Journal of Wind Engineering and Industrial Aerodynamics, Vol. 57, pp63-80.

CELIK, I. and RODI, W. (1984).
Simulation of free-surface effects in turbulent channel flows.
PCH PhysicoChemical Hydrodynamcs, Vol. 5, No. 3/4, pp217-227.

CHAPMAN, D.R., KUEHN, D. M. and LARSON, H. K. (1957).
Investigation of separated flows in supersonic and subsonic streams with emphasis on the effect of transition.
NACA TA-3869.

CHOW, V.T. (1959).
Open Channel Hydraulics.
McGraw-Hill, Inc..

CHUNG, K.B. and SUNG, H.J. (1996).
Control of turbulent separated flow over a backward-facing step.
Experiments in Fluids, Vol.21, pp417-426.

CLARK, J.A. (1968).
A study of incompressible turbulent boundary layer in channel flow.
Journal of Basic Engineering, Proc. ASCE, pp455-468.

CLAUSER, F.H. (1956).
Advances in Applied Mechanics, Vol.4, New York, N.Y., p1.

COLEMAN, N.L. (1981).
Velocity profiles with suspended sediment.
Journal of Hydraulic Research, IAHR, Vol.19, pp211-229.

COLEMAN, N.L. and ALONSO, C.V. (1983).
Two-dimensional channel flows over rough surfaces.
Journal of Hydraulic Engineering, ASCE, Vol. 109, pp175-188.

COLES, D (1956).
The law of the wake in turbulent boundary layer.

Journal of Fluid Mechanics, Vol.1, pp191-226.

COLES, D (1968).
The Young Persons Guide to the Data.
Proceedings AFOSR-IFP Stanford Conference on Computation of Turbulent Boundary Layers, Vol.2, pp1-45.

DE BREDERODE, V. and BRADSHAW, P. (1972).
Three-dimensional flow in nominally two-dimensional separation bubbles, I. Flow behind a rearward-facing step.
Imperial College of Science and Technology, Aero Report 72-19.

DEPAUL, F.T. and SHEIH, C.M. (1986).
Measurement of wind velocities in a street canyon.
Atmospheric Environment, Vol.20, No.3, pp455-459.

DELLEUR, J.W. (1957).
The boundary layer development in open channels, paper 1138.
Proceedings, ASCE, Journal Engineering Mechanics Division, vol. 83, no.EM1, pp1-24, January, 1957.

DEMUREN, A. O. AND WILSON, R. V. (1994).
Estimating uncertainty in computations of two-dimensional separated flows.
Journal of Fluids Engineering, ASME, June, Vol. 116, pp 216-220.

DIMACZEK, G., KESSLER, R., MARTINUZZI, R. and TROPEA, C. (1989).
The flow over two-dimensional surface mounted obstacles at high Reynolds numbers', in Pollard, A. and Wakarani, N. (1996), Genesis and morphology of erosional shapes associated with turbulent flow over a forward facing step.
Coherent Flow Structures in Open-Channels, John Wiley and Sons, pp249-265.

DRIVER, D.M. and SEEGMILLER, H.L. (1985).
Features of a reattaching turbulent shear layer in divergent channel flow.
Journal of AIAA, Vol.23, No.2, pp163-171.

DURST, F., MELLING, A. and WHITELAW, J.H. (1974).
Low Reynolds number flow over a plane symmetric sudden expansion.
Journal of Fluid Mechanics, Vol.64, Pt 1, pp 111-128.

DURST, F. and RUCK, B. (1987).
Effective particle size range in laser-Doppler anemometry.
Experiments in Fluids, Vol. 5, pp 304-314.

EATON, J. K. and JOHNSTON, J. P. (1981).
A review of research on subsonic turbulent flow reattachment.
AIAA Journal, Vol. 19, No. 9, pp1093-1100.

EATON, J. K. and JOHNSTON, J. P. (1982).
Low frequency unsteadiness of a reattaching turbulent shear layer.
Turbulent Shear Flow III, pp162-170.

ENGEL, P. (1981).

Length of Flow Separation over dunes.
Journal of the Hydraulics Division, ASCE, Vol.104, No.HY10, pp1133-1143.

ERVINE, D.A., WILLETS, B.B., SELLIN, R.H.J. and LORENA, M. (1993).
Factors affecting conveyance in meandering compound flows.
Journal of Hydraulic Engineering, ASCE, Vol.119, No.12, pp1383-1399.

ERVINE, D.A. and JASEM, H.K. (1995).
Observations on flows in skewed compound channels.
Proceedings of the Institute of Civil Engineers - Water, Maritime and Energy,
Vol. 112, No.3, pp249-259.

ERVINE, D.A. and MACLEOD, A.B. (1999).
Modelling a river channel with distant floodbanks.
Proceedings of the Institute of Civil Engineers - Water, Maritime and Energy,
Vol. 136, No.1, pp21-33.

ETHEMBABAOGLU, S. (1978).
Some characteristics of unstable flow past slots.
Journal of the Hydraulics Division, ASCE, Vol. 104, No. HY5,pp 649-666.

ETHERIDGE, D.W. and KEMP, P.H. (1978).
Measurements of turbulent flow downstream of a rearward-facing step.
Journal of Fluid Mechanics, Vol.86, Part 3, pp545-566.

FARES, Y.R. and HERBERTSON, J.G. (1993).
Behaviour of flow in a channel bend with a side overflow (flood relief) channel.
Journal of Hydraulic Research, IAHR, Vol. 31, No. 3.

FARES, Y.R. and HERBERTSON, J.G. (1993).
Behaviour of flow in a channel bend with a side overflow (flood relief) channel.
Journal of Hydraulic Research, Vol. 31, No. 3.

FINAISH, F., FREYMOUTH, P. AND BANK, W. (1986).
Starting flows over spoilers, double steps and cavities.
Journal of Fluid Mechanics, Vol. 168, pp383-392.

FRANCIS R. and HAMA, (1954).
Boundary layer characteristics for smooth and rough surfaces.
Transactions, Society of Navel Architects and Marine Engineers, vol. 62, pp333-351.

FREITAS, C. J., STREET, R. L., FINDIKAKIS, A. N. and KOSEFF, J. R. (1985).
Numerical simulation of three-dimensional flow in a cavity.
International Journal for Numerical Methods in Fluids, Vol. 5, pp561-575.

FRENCH, R.H. (1994).
Open Channel Hydraulics.
McGraw-Hill Inc. Singapore.

FUJITA, I., KOMURA, S. and KANDA, T. (1993).
Measurements of turbulent flow in a trench using an image processing technique.

Refined Flow Modelling and Turbulence Measurements.
Proceedings of the 5th International Symposium, Paris, France, pp309-316.

GRANT, I., OWENS, E., YAN, Y.-Y. and SHEN, X. (1992).
Particle image velocimetry measurements of the separated flow behind a rearward facing step.
Experiments in Fluids, Vol. 12, pp 238-244.

GREENHILL, R.K. and SELLIN, R.H.J. (1993).
Development of a simple method to predict discharges in compound meandering channels.
Journal of Water , Maritime and Energy, Proc. ICE, 101, March, pp37-44.

HERBERT, J.M., JOHNSON, G.T. and ARNFIELD, A.J. (1997).
Coupling of a scalar dispersion and an urban canyon energy budget model.
Mathematics and Computers in Simulation, Vol. 43, pp277-283.

HOYDYSH, W.G. and DABBERDT, W.F. (1988).
Kinematics and dispersion characteristics of flows in asymmetric street canyons.
Atmospheric Environment, Vol.22, No.12, pp2677-2689.

HUFFMAN, D.G. and BRADSHAW, P. (1972).
A note on Von Karmens constant in low Reynolds number turbulent flows.
Journal of Fluid Mechanics, Vol. 53, Part 1, pp55-60.

HUNTER, J., WATSON, I.D. and JOHNSON, G.T. (1990)
Modelling air flow regimes in urban canyons.
Energy and Buildings, Vol. 15-16, pp315-324.

ISOMOTO, K. and HONAMI, S. (1989).
The effect of inlet turbulence intensity on the reattachment process over a backward-facing step.
Journal of Fluid Engineering, ASME, Vol. 111, pp87-92.

JASEM, H.K. (1990).
Flow in Two Stage Channels with the Main Channel Skewed to the Flood Plain Direction.
PhD Thesis submitted to the University of Glasgow.

JOHNS, B., SOULSBY, R. L. AND XING, J. (1993).
A comparison of numerical model experiments of free surface flow over topography with flume field observations.
Journal of Hydraulic Research, Vol.31, No. 2.

KELLER, R.J. and RODI, W. (1988).
Prediction of flow characteristics in main channel/flood plain flows.
Journal of Hydraulic Research, IAHR, Vol.26, No.4, pp425-441.

KEOGH, D.P. & ADDISON, P.S. (1996a)
Coherent flow structures in open-channel slot flow.

Coherent flow structures in open channels, Edited by Ashworth, Bennett, Best and McLelland, 1996, John Wiley and Sons, pp267-280.

KEOGH, D.P. & ADDISON, P.S. (1996b)
Turbulent Mechanisms in Open-Channel Slot Flow.
6th International Symposium on Flow Modelling and Turbulence Measurements, Florida (1996), pp75-81.

KESTIN, J., SOKOLOV,K. and WAKEHAM, W. A. (1978)
Viscosity of liquid water in the range -8^{o}C to 150^{o}C.
Journal of Physical Chemistry, Vol. 7, No. 3, pp941-948

KRISHNAPPAN, B.G. and LAU, Y.L. (1986).
Turbulence modelling of flood plain flows.
Journal of Hydraulic Engineering, ASCE, Vol.112, No.4, April, pp251-266.

KUELEGAN, G.H. (1938).
Laws of turbulent flow in open channels.
Journal of National Bureau of Standard, Washington, D.C. Research Paper 1151, Vol. 21, pp707-741.

LEAN, G.H. and WEARE, T.J. (1979).
Modeling two-dimensional circulating flow.
Proc. of ASCE, Journal of the Hydraulics Division, Vol.105, No.HY1, pp17-26.

LEE, H.Y. and HWANG, S.T. (1994).
Migration of a backward-facing step.
Journal of Hydraulic Engineering, ASCE, Vol.120, No.6, pp693-705.

LAUFER, J. (1954).
National Advisory Committee for Aeronautics.
Technical Report, No.1174.

LI, R.-M., SCHALL, J. D. and SIMONS, D. B. (1980)
Turbulence prediction in open channel flow.
Journal of the Hydraulics Division, ASCE, Vol. 106, No. HY4, pp 575-587.

LIEPMANN, H.W. and LAUFER, J. (1947).
Investigation of free turbulent mixing.
NACA, Technical Note, 1257.

LIGRANI, P.M. and MOFFAT, R.J. (1986).
Structure of transitionally rough and fully rough turbulent boundary layers.
Journal of Fluid Mechanics, Vol. 162, pp 69-98.

MANNING, R. (1890).
On the flow in water in open channels and pipes.
Trans. Institute of Civil Engineers, Ireland, Vol. 20, pp161-207.

MANSON, J.R. (1994).
The development predictive procedure for localised three dimensional river flows.
PhD Thesis, Dept. of Civil Engineering, University of Glasgow.

McQUIVEY, R.S. and RICHARDSON, E.V. (1969).
Some turbulence measurements in open channel flow.
Journal of the Hydraulics Division, Proc. A.S.C.E., Vol. 95, No. HY1, January.

MENDOZA, C. and SHEN, H.W. (1990).
Investigation of turbulent flow over dunes.
Journal of Hydraulic Engineering, ASCE, Vol.116, No.4, pp459-477.

MORROUGH, O'BRIEN, P and JOHNSON J. W. (1934).
Velocity-head correction for hydraulic flow.
Enginnering News-Record, Vol. 113, No.7, pp214-216.

MOTOHASHI, T. and BLACKWELDER, R. F. (1983).
Decreasing the side wall contamination in wind tunnels.
Journal of Fluids Engineering, ASME, Vol. 105, pp 435-438.

MUNSON, B. R., YOUNG, D. F. and OKIISHI, T. H. (1990)
Fundamentals of Fluid Mechanics.
John Wiley & Sons, Inc, Canada.

NAKAGAWA, H., NEZU, I. and UEDA, H. (1975).
Turbulence of open channel flow over smooth and rough beds.
Proc. JSCE, No. 241, pp155-168.

NAKAGAWA, H., TSUJIMOTO, T. and SHIMIZU, Y. (1988).
Velocity profile of flow over rough permeable bed.
6th Congress of Asian and Pacific Regional Division of IAHR, Kyoto, Japan, pp 449-456.

NAKAGAWA, H. and NEZU, I. (1987).
Experimental investigation on turbulent structure of backward facing step flow in an open-channel.
Journal of Hydraulic Research, IAHR, Vol.25, No1, pp67-88.

NAKAMURA, Y. and OKE, T.R. (1988).
Wind, temperature and stability conditions in an east-west orientated urban canyon.
Atmospheric Environment, Vol.22, No.12, pp2691-2700.

NELSON, J.M., SHREVE, R.L., MCLEAN, S.R. and DRAKE, T.G. (1995).
Role of near-bed turbulence structure in bed load transport and bed form mechanics.
Water Resources Research, Vol.31, No.8, pp2071-2086.

NEZU, I. (1977a).
Turbulence intensities in open channel flows.
Proceedings of the Japanese Society of Civil Engineers, No. 261, pp67-76.

NEZU, I. (1977b).
Turbulent structure in open channel flows.

Thesis presented to Kyoto University, Japan, in partial fulfilment of the degree of doctor of philosophy.

NEZU, I. and RODI, W. (1986).
Open channel flow measurement with a laser doppler anemometer.
Journal of Hydraulic Engineering, Proceedings ASCE, Vol. 112, No. 5, pp335-355.

NEZU, I. and NAKAGAWA, H. (1993a)
Three-dimensional structures of coherent vortices generated behind dunes in turbulent free-surface flows.
Proceedings of the Japanese Society of Civil Engineers, pp603-612.

NEZU, I. and NAKAGAWA, H. (1993b).
Turbulence in open channel flows.
IAHR/AIRH Monograph.
Balkema/Rotterdam.

O'BRIEN, M.P. and HICKOX, G.H. (1937).
"Applied Fluid Mechanics".
McGraw-Hill Book Company Inc., New York, 1st Ed., p.272.

ÖTÜGEN, M.V. (1991).
Expansion ratio effects on the separated shear layer and reattachment downstream of a backward facing step.
Experiments in Fluids, No. 10, pp 273-280.

ÖTÜGEN, M.V., PAPADOPOULOS, G., VRADIS, G. and MUCKENTHALER, G. (1992).
Spanwise characteristics of the separated flow in a suddenly expanding duct.
Experiments in Fluids 11, pp213-216.

ÖTÜGEN, M.V., and MUCKENTHALER, G. (1992).
A study of separated shear layer in moderate Reynolds number plane sudden expansion flows.
Journal of the AIAA, Vol. 30, pp 1808-1814.

PENDER, G. (1992).
Maintaining numercial stability of flood plain calculations by time increment splitting.
Journal of Water , Maritime and Energy, Proc. ICE, 26, March, pp35-42.

PENDER, G., KEOGH, D.P., ADDISON, P.S. and MANSON, J.R. (1995)
Verification of a three-dimensional river flow model with experimental data.
Hydra 2000, IAHR, Vol.1, London, pp290-295.

PERRY, A.E. and ABELL, C.J. (1975).
Scaling Laws for pipe flow turbulence.
Journal of Fluid Mechanics, Vol. 67, pp 257-271.

POLLARD, A. and WAKARANI, N. (1996).

Genesis and morphology of erosional shapes associated with turbulent flow over a forward facing step.
Coherent Flow Structures in Open-Channels, John Wiley and Sons, pp249-265.

PRANDTL, L. (1925)
Über die ausgebildete turbulenz.
2nd International Congress of Applied Mechanics, Zurich, ZAMM, 5, p26.

PRANDTL, L. (1932)
Recent results of turbulent research.
Translation by National Advisory Committee for Aeronautics, TM, No. 720.

PRANDTL, L. (1952)
Essentials of Fluid Dynamics.
Blackie, London.

QURAAISHI, A.A. and AL_BRAHIM, A.M. (1992).
Hydraulic jump in sloping channel with positive or negative step.
Journal of Hydraulic Research, IAHR, Vol.30, No.6, pp769-782.

RAICHLEN, F. (1967).
Some turbulence measurements in water,
Journal of the Engineering Mechanics Division, ASCE, Vol. 93, No. EM2, pp 73-97.

RAJARATNAM, N. (1976)
Turbulent Jets, Elsevier Sc. Publ., Co., Amsterdam, p304.

RAJARATNAM, N. and AHMADI, R. (1981).
Hydraulics of channels with flood plains.
Journal of Hydraulic Research, IAHR, Vol. 19, No. 1., pp43-60.

REYNOLDS, O. (1883).
An experimental investigation of the circumstances which determine whether the motion of water shall be direct or sinuous and of the law of resistence in parallel channels.
Phil. Transactions of the Royal Society, Vol.174, pp935-982.

RICHARDSON, E.V. and McQUIVEY, R.S. (1968).
Measurement of turbulence in water.
Journal of Hydraulic Division, Proceedings ASCE, Vol. 94, No. HY2, pp411-429.

ROUSE, H. and INCE, S. (1957).
History of Hydraulics.
Iowa Institute of Hydraulic Research.

RUBEN, D.K. and McDONALD, R.R. (1995).
Nonperiodic eddy pulsations.
Journal of Water Resources Research, Vol. 31, No. 6, pp1595-1605.

SARMA, K.V.N., LAKSHMINARAYANA, P. and LAKSHMANA RAO, N.S. (1983).
Velocity Distribution in Smooth Rectangular Open Channels.
Journal of Hydraulic Engineering, ASCE, Vol.109, No.2, February, pp270-289.

SCHLICHTING, H. (1955).
"Boundary Layer Theory", translated from the German by J.Kestin.
McGraw-Hill Book Company, Inc., New York, Pergamom Press Ltd., London, and Verlag G. Braun, Karlsuhe, 1955.

SELLIN, R.H.J., GILES, A. and VAN BEESTEN, D.P. (1990).
Post-implementation appraisal of a two-stage channel in the River Roding, Essex.
Journal of the Institute of Water and Environmental Management, Vol.4, April.

SELLIN, R.H.J., ERVINE, D.A. and WILLETS, B.B. (1993).
Behaviour of Meandering 2-stage channels.
Proceedings of the Institute of Civil Engineers - Water, Maritime and Energy, Vol. 101, No.2, pp99-111.

SHIH, C. AND HO, C.-M. (1994).
Three-dimensional recirculation flow in a backward facing step.
Journal of Fluids Engineering, ASME, Vol. 116, June, pp 228-232.

SMITH, B.T. and ETTEMA, R. (1997).
Ice-cover influence on flow structure over dunes.
Journal of Hydraulic Research, IAHR, Vol.35, No.5, pp707-719.

SOHN, J. L. (1988).
Evaluation of FIDAP on some classical laminar and turbulent benchmarks.
International Journal for Numerical Methods in Fluids, Vol. 8, pp 1469-1490.

SPALDING, D. B. (1961).
A single formula for the "Law of the Wall".
Journal of Applied Mechanics, September, pp 455-457.

STEFFLER, P.M., RAJARATNAM, N. and PETERSON, A.W. (1985).
LDA measurements in open channel.
Journal of Hydraulic Engineering, Proceedings ASCE, Vol. 111, pp119-130.

THOMAS, N. H. and HANCOCK, P.E. (1977).
Grid turbulence near a moving wall.
Journal of Fluid Mechanics, 82, pp481-490

TOEBES, G.H. and SOOKY, A.A. (1967).
Hydraulics of meandering rivers with flood plains.
J. of the Waterways and Harbours Div., Proc. ASCE, Vol.93, No.WW2, May, pp213-236.

TOWNSEND, A.A. (1956).
The structure of turbulent shear flow.
Cambridge University Press, New York, N.Y.

TRACY, H.J. and LESTER, C.M. (1961).
Resistence coefficients and velocity distribution - smooth rectangular channel.
Water Supply Paper 1592-A, U.S. Geological Survey.

TRITTON, D.J. (1988).

"Physical Fluid Dynamics".
Oxford University Press Inc., 2nd Ed, UK.

VANONI, V.A. (1941).
Velocity distribution in open channels.
Proceedings ICE, Vol.11, No.6, June, pp356-357.

WANG, J., DONG, Z., CHEN, C. and XIA, Z. (1993).
The effects of bed roughness on the distribution of turbulent intensities in open-channel flow.
Journal of Hydraulic Research, IAHR, Vol. 31, No. 1, pp89-97.

WILLETTS, B.B. and HARDWICK, R.I. (1993).
Stage dependancy for overbank flow in meandering channels.
Journal of Water , Maritime and Energy, Proc. ICE, 101, March, pp45-54.

XINYU, L., ZENGNAN, D. and CHANGZHI, C. (1995).
Turbulent flows in smooth-wall open channels with different slope.
Journal of Hydraulic Research, IAHR, Vol. 33, No. 3, pp 333-347.

YEN, C. and OVERTON, D.E. (1973).
Shape effects on the resistence in floof-plain channels.
Journal of the Hydraulics Division, Proc. ASCE, Vol.99, No.HY1, January, pp219-238.

YOSHIAKA and IWASA (1957).
Boundary layer growth of open channel flows on a smooth bed and it's contribution to practical application to channel design, Memoirs of the Faculty of Engineering, Kyoto University, Japan, Vol. XIX, No.III, pp229-254, July.